Handbook of Computational Chemistry Research

Charles T. Collett

Christopher D. Robson

Editors

NOVA

HANDBOOK OF COMPUTATIONAL CHEMISTRY RESEARCH

HANDBOOK OF COMPUTATIONAL CHEMISTRY RESEARCH

CHARLES T. COLLETT
AND
CHRISTOPHER D. ROBSON
EDITORS

For permission to use material from this book please contact us:
Telephone 631-231-7269; Fax 631-231-8175
Web Site: http://www.novapublishers.com

NOTICE TO THE READER

The Publisher has taken reasonable care in the preparation of this book, but makes no expressed or implied warranty of any kind and assumes no responsibility for any errors or omissions. No liability is assumed for incidental or consequential damages in connection with or arising out of information contained in this book. The Publisher shall not be liable for any special, consequential, or exemplary damages resulting, in whole or in part, from the readers' use of, or reliance upon, this material. Any parts of this book based on government reports are so indicated and copyright is claimed for those parts to the extent applicable to compilations of such works.

Independent verification should be sought for any data, advice or recommendations contained in this book. In addition, no responsibility is assumed by the publisher for any injury and/or damage to persons or property arising from any methods, products, instructions, ideas or otherwise contained in this publication.

This publication is designed to provide accurate and authoritative information with regard to the subject matter covered herein. It is sold with the clear understanding that the Publisher is not engaged in rendering legal or any other professional services. If legal or any other expert assistance is required, the services of a competent person should be sought. FROM A DECLARATION OF PARTICIPANTS JOINTLY ADOPTED BY A COMMITTEE OF THE AMERICAN BAR ASSOCIATION AND A COMMITTEE OF PUBLISHERS.

CONTENTS

PREFACE

This book presents ways in which computers can be used to solve chemical problems. One approach develops synoptic algebraic scaling laws to use in place of the case-by-case numerical integrations prescribed by traditional quantum chemistry. The ONIUM hybrid method combines a quantum mechanical method with the molecular mechanical method. One study includes placing functional constraints and testing the performance of the resulting constrained functionals for several chemical properties. A review of the known approximations for the temperature integral is included.

Some of the other areas of research discussed include protein coarse-grain models, a specific application of spherical harmonics, use of the FERMO concept to better explain reactions that are HOMO driven, wavelet based approaches and high resolution methods with successful application to a fixed-bed adsorption column model. There is a discussion of stability and thermodynamics, as well as kinetic properties of heterophosphetes and phosphole oxides. A model is proposed that applies methods and concepts in mathematical morphology paradigms to solve the problem of offset curves as well as a description of the solvent effects through the in silico procedures by the use of continuum and discrete models. A simulation method attempts to relate the microscopic details of a system to macroscopic properties of experimental interest. Techniques to retain the use of simple potential functions are also discussed, but with the possibility of allowing them to readjust their properties to fit the potential energy curves of the more complex functions. The Chapman-Cruzen mechanism is also studied using the ideas of the theory of dynamical systems.

Chapter 1 reprises and extends the development of a new approach to fundamental problems in chemistry, now known as 'Algebraic Chemistry'. It collects and summarizes all results so far produced. Problems addressed here include **1)** the nominal pattern of single-electron state filling across all of the elements, **2)** the exceptions to that pattern that occur for about 20% of elements; **3)** the numerical patterns in the experimental data about ionization potentials of all elements and all orders, and **4)** plausible reasons for the existence of chemical periodicity and **5)** some insights on the possible nature of chemical bonds. The approach develops synoptic algebraic scaling laws to use in place of the case-by-case numerical integrations prescribed by traditional Quantum Chemistry. The development of Algebraic Chemistry requires an initial re-examination of *two* pillars of twentieth century physics: not just Quantum Mechanics (QM), but also Special Relativity Theory (SRT). The reader is asked to entertain an 'Expanded SRT', in which an additional 'speed' concept appears, and several additional mathematical relationships among speed concepts appear. This Expanded SRT

allows an 'Expanded QM', in which the main actors are not the modern, and very abstract, probability-amplitude waves, but the old-fashioned, and very concrete, point particles. Although the hundred years elapsed since SRT and QM were first introduced may make this sort of re-work seem troublesome, the practical utility of the results produced makes the effort clearly worthwhile.

The ONIOM hybrid method, which combines a quantum mechanical (QM) method with the molecular mechanical (MM) method, is one of the powerful methods that allow to calculate large molecular systems with the high accuracy afforded for smaller molecular systems. The notable feature of this method is that it can include the environmental effects into the high level QM calculation through a simple extrapolation procedure. This is a significant difference from the conventional QM/MM methods. The definition of the layer is simple, and also the layer is easily extended to the multiple-layers. Contrary to this, the traditional QM/MM method that adopts the sophisticated link between the QM and MM regions makes the handling difficult. The ONIOM method is thus more flexible and versatile than the conventional QM/MM method, and is therefore increasingly adopted as an efficient approach beneficial to many areas of chemistry.

Recently, the ONIOM-molecular dynamics (MD) method has been developed to analyze the more complicated large molecular system where the thermal fluctuations of the environment play an important role. For example, when the target is a biomolecule, such as an enzyme, the property of the entire system is strongly affected by its dynamical behavior. In such case, the ONIOM method is not satisfactory. The coupling of the ONIOM method with the molecular dynamics (MD) method is necessary to account for the thermal fluctuations of the environment. Newly developed ONIOM-MD method has made it possible to characterize the function of enzyme etc. in a realistic simulation of the thermal motion, retaining the concept embodied in the ONIOM method. In Chapter 2, the basic concept of the ONIOM and ONIOM-MD methods we developed and their applications to typical cases are introduced.

Several recent studies (*J. Phys. Chem. A* 2004, *108*, 5479; *J. Comput. Chem.* 2007, *28*, 2431) have shown impressive results when replacing the non-empirical PBE density functional by the empirical OPBE or OLYP functionals, i.e. replacing the PBE exchange functional by Handy and Cohen's OPTX functional. To investigate the origin of the improvements, we have placed constraints from the non-empirical PBE exchange functional on the empirical OPTX exchange functional, and tested the performance of the resulting constrained functionals for several characteristic chemical properties.in Chapter 3, the performance of the new functionals is tested for a number of standard benchmark tests, such as the atomization energies of the G2 set, accuracy of geometries for small molecules, atomic exchange energies, and proton affinities of anionic and neutral molecules. Furthermore, the new functionals are tested against a benchmark set of nucleophilic substitution S_N2 reactions, for which we have recently compared DFT with high-level coupled cluster CCSD(T) data (*J. Comput. Chem.* 2007, *28*, 1551). Our study makes clear that the performance depends critically on the number of constraints, and on the reference data to which the constrained functionals are optimized. For each of these properties studied, there is at least one functional that performs very well. Although a new promising functional ($ML_{ff}OLYP$) emerged from the set of constrained functionals that approaches coupled-cluster accuracy for geometries and performs very well for the energy profile of S_N2 reactions, there is no one of the newly constructed functionals that performs equally well for all properties.

The temperature integral, which frequently occurs in the kinetic analysis of solid-state reactions, does not have an exact analytical solution. Instead of performing the numerical integration, most of the researchers prefer to circumvent the problem by using approximate expressions.

The main aim of Chapter 4 is to carry out a review of the known approximations for the temperature integral, to establish a ranking of those temperature integral approximations and to present some applications of the temperature integral approximations.

The design of protein coarse-grain (CG) models and their corresponding interaction potentials is an active field of research, especially for solving problems such as protein folding, docking… Among the essential parameters involved in CG potentials, electrostatic interactions are of crucial importance since they govern local and global properties, *e.g*., their stability, their flexibility…

Following our development of an original approach to hierarchically decompose a protein structure into fragments from its electron density (ED) distribution, the method is applied in Chapter 5 to molecular electrostatic potential (MEP) functions, calculated from point charges as implemented in well-known force fields (FF). To follow the pattern of local maxima (and minima) in an ED or a MEP distribution, as a function of the degree of smoothing, we adopted the following strategy. First, each atom of a molecule is considered as a starting point (a peak, or a pit for negative potentials in a MEP analysis). As the smoothing degree increases, each point moves along a path to reach a location where the ED or MEP gradient value vanishes. Convergences of trajectories lead to a reduction of the number of points, which can be associated with molecular fragments.

Practically, to determine the protein backbone representations, we analyzed CG models obtained for an extended strand of polyglycine. The influence of the different amino acid side chains was then studied for different rotamers by substituting the central glycine residue. Regarding the determination of charges, we adopted two procedures. First, the net charge of a fragment was calculated as the summation over the charges of its constituting atoms. Second, a fitting algorithm was used to assign charges to the obtained local maxima/minima.

Applications to a literature case, a 12-residue β-hairpin peptide, are also presented. It is observed that classical CG models are more similar to ED-based models, while MEP-based descriptions lead to different CG motifs that better fit the MEP distributions.

A simulation method attempts to relate the microscopic details of a system (atomic masses, interactions between them, molecular geometry, etc.) to macroscopic properties of experimental interest (equation of state, structural parameters, etc.). The first step in performing a molecular simulation requires knowledge of the potential energy of interaction between the particles of the system, and one of the simplest methods used to obtain this treats the intermolecular energy as the sum of pairwise additive potentials (as in the force-field method). The model presented in Chapter 6 does not consider the molecules as formed by rigid spherical particles (atoms or assemblies of atoms) but as continuum distributions of matter (without electrical charge), and this has two effects: it can be applied to many kinds of systems and extends the information on the system, relating a microscopic property (such as the interaction energy) with macroscopic properties (such as the structural parameters of the molecules). To simulate the interaction energy between β–cyclodextrin (β–CD) and molecules with different structure (cyclic, spherical and linear geometry), a model was constructed from a simple pairwise-additive Lennard-Jones potential combined with a continuum description of the cyclodextrin cavity and the guest molecule. This model

reproduces the main energetic and structural features of the physisorption, in particular that guest molecule positions inside the cavity are more stable than outside the CD, as amply confirmed by molecular mechanics calculations. Therefore this model cannot explain the existence of non-inclusion complexes, and this is not a consequence of model assumptions such as rigidity of molecules or ignoring the effects of solvent. Neither does this model allow the effect of temperature to be included in the process. The aim of the present chapter is to analyse the effect of molecular structure on the mobility of the guest inside and around the β–CD, and the influence of temperature on inclusion complex formation. It was carried out by molecular dynamics, because this simulation method is based on the resolution of classical equations of motion to determine the trajectories of the particles. From these trajectories we also determine the preferential binding site of the guest molecule and the probability of forming β–CD inclusion complex.

Petroleum fractions are essentially complex mixtures of cyclic and non-cyclic hydrocarbons. Given the complex nature of these systems and even the difficulty of identifying the components present in such mixtures, developing a viscosity correlation accounting for all the composition details becomes a challenging task. Numerous estimation methods have been developed to represent the effect of the temperature on the viscosity of different crude oil fractions at atmospheric pressure. Most of these methods are empirical in nature since no fundamental theory exists for the transport properties of liquids. In Chapter 7 the authors carry out both a brief review of the empirical correlations commonly used and an evaluation of their degree of accuracy. Unfortunately, the absence of information about the accuracy of the physical magnitudes used as input parameters in the correlations and the experimental data of kinematic viscosity used in the different fittings prevents a conclusive assessment of the percentage of average absolute deviation reported in the literature. Finally, the authors apply the error theory to a set of equations recently derived (and published), which has been proved to fit successfully the data of the chart of the ASTM standard D 2502-92 (reapproved 2004). This standard provides a means of calculating the mean molecular weight of petroleum oils from kinematic viscosity measurements and it is partially based on the Walter equation, that is, one of the correlations previously discussed. The use of a PC program designed in order to carry out this new analysis permits a preliminary evaluation of the errors of this ASTM standard.

Notwithstanding their simplicity, semi-empirical interatomic potential energy functions are indispensable in computational chemistry as a result of their ease of execution. With over eight decades of interatomic potential functions since the days of Lennard-Jones, numerous potential energy functions have been proposed. The potential functions developed over the decades have increased in complexities through additions of many parameters for the sake of improving the modeling accuracy. However, many established computational chemistry software still incorporate simple potential functions due to the multi-body and dynamical nature in computational chemistry. The use of highly complex potential functions would give a limited improvement in accuracy at the expense of the computational time and cost. An economical and technically feasible solution would be to retain the use of simple potential functions, but with the possibility of allowing them to readjust their properties to fit the potential energy curves of the more complex functions. Chapter 8 discusses the techniques developed recently for attaining such purpose.

In Chapter 9, we carried out Hartree-Fock (HF) and density functional theory calculations on the conjugated bases of phenols, alcohols, organic acids, and amines compounds and

analyzed their acid-base behavior using molecular orbital (MO) energies and their dependence on solvent effects. Despite the well-known correlation between highest-occupied MO (HOMO) energies and pKa, we observed that HOMO energies are inadequate to describe the acid-base behavior of these compounds. Therefore, we established a criterion to identify the best frontier MO for describing pKa values and also to understand why the HOMO approach fails. The MO that fits our criterion provided very good correlations with pKa values, much better than those obtained by HOMO energies. Since they are the frontier molecular orbitals that drive the acid-base reactions in each compound, they were called frontier effective-for-reaction MOs, or FERMOs. By use of the FERMO concept, the reactions that are HOMO driven, and those that are not, can be better explained, independent from the calculation method used, since both HF and Kohn-Sham methodologies lead to the same FERMO.

Many industrial processes and systems can be modelled mathematically by a set of Partial Differential Equations (PDEs). Finding a solution to such a PDF model is essential for system design, simulation, and process control purpose. However, major difficulties appear when solving PDEs with singularity. Traditional numerical methods, such as finite difference, finite element, and polynomial based orthogonal collocation, not only have limitations to fully capture the process dynamics but also demand enormous computation power due to the large number of elements or mesh points for accommodation of sharp variations. To tackle this challenging problem, wavelet based approaches and high resolution methods have been recently developed with successful applications to a fixed-bed adsorption column model.

Our investigation has shown that recent advances in wavelet based approaches and high resolution methods have the potential to be adopted for solving more complicated dynamic system models. Chapter 10 will highlight the successful applications of these new methods in solving complex models of simulated-moving-bed (SMB) chromatographic processes. A SMB process is a distributed parameter system and can be mathematically described by a set of partial/ordinary differential equations and algebraic equations. These equations are highly coupled; experience wave propagations with steep front, and require significant numerical effort to solve. To demonstrate the numerical computing power of the wavelet based approaches and high resolution methods, a single column chromatographic process modelled by a Transport-Dispersive-Equilibrium linear model is investigated first. Numerical solutions from the upwind-1 finite difference, wavelet-collocation, and high resolution methods are evaluated by quantitative comparisons with the analytical solution for a range of Peclet numbers. After that, the advantages of the wavelet based approaches and high resolution methods are further demonstrated through applications to a dynamic SMB model for an enantiomers separation process.

This research has revealed that for a PDE system with a low Peclet number, all existing numerical methods work well, but the upwind finite difference method consumes the most time for the same degree of accuracy of the numerical solution. The high resolution method provides an accurate numerical solution for a PDE system with a medium Peclet number. The wavelet collocation method is capable of catching up steep changes in the solution, and thus can be used for solving PDE models with high singularity. For the complex SMB system models under consideration, both the wavelet based approaches and high resolution methods are good candidates in terms of computation demand and prediction accuracy on the steep front. The high resolution methods have shown better stability in achieving steady state in the specific case studied in this Chapter.

Molecular structures are often influenced by aromatic stabilization and antiaromatic destabilization effects. In spite of nearly a century's effort – from *Kekulé* 1871 to *Breslow* and *Dewar* 1965 – to synthesize cyclobutadiene, these attempts have proved to be unsuccessful [1–6]. Only theoretical chemistry was able to explain this failure by introducing the concept of antiaromaticity as a new phenomenon. The synthesis of these antiaromatic compounds has long been considered as desirable target of preparative chemistry in order to examine experimentally their species chemical properties, but only a few compounds could be prepared and studied. One of the examples may be the family of phosphole oxides exhibiting a slightly antiaromatic character [7–10]. At the same time, heterophosphetes, are of more considerable antiaromatic character and they manifest only as high energy intermediate or transition state (TS) [11–20]. In Chapter 11, stability and thermodynamic, as well as kinetic properties of heterophosphetes and phosphole oxides are discussed.

As discussed in Chapter 12, the description of the solvent effects through the *in silico* procedures can be realized by using continuum and discrete models. Based on the classic works of Born, Onsager and Kirkwood, the continuum models became an important tool in the study of the solvent effects in several chemical process. In its formalism, the insertion of the solute into a arbitrary cavity modelled by overlap spheres and the description of the solvent as a dielectric unleashed a popular growth of the continuum models. All this methodologic advance provided the development of many other current implementations, such as PCM and COSMO, which have been used successfully in the study of many molecular systems. However, the description of solvent as a dielectric yields some limitations, i.e. the underestimates of specific interactions between solvent and solute, in particular hydrogen bonds.

Offsets are one of the most important problems in Computational Geometry. They can be used in many fields, such as geometric modelling, CAD/CAM and robot navigation. Although some efficient algorithms have been developed to solve this problem, their lack of generality makes them efficient in only a limited number of cases.

The aim of Chapter 13 is to propose a model that applies methods and concepts used in mathematical morphology paradigms to solve the problem of general offset curves.

Presented in the work there is a method for offsetting any kind of curve at any distance, constant or not. As a consequence, we will obtain a geometrical abstraction which will provide solutions to typically complex problems.

The resulting method avoids any constraint in curve shape or distance to the offset and obtains valid and optimal trajectories, with a low temporal cost of $O(n \cdot m)$, which is corroborated by the experiments. It also avoids some precision errors that are present in the most popular commercial CAD/CAM libraries.

The use of morphology as the base of the formulation avoids self intersections and discontinuities and allows the system to obtain general offsets to free-form shapes without constraints. Most numerical and geometrical problems are also avoided. Obtaining a practical algorithm from the theoretical formulation is straightforward, as it will be shown with the application of the method to an algorithm to obtain tool paths for contour-parallel pocketing. The resulting procedure is simple and efficient.

The work has been divided into next parts:

Introduction provides the reader with background information on existing offset methods and their associated problems in offset computation. The new concept of general offset is also introduced.

Second section develops the morphological system resulting from applying the conventional morphological model to *which the feature of primitives ordering has been added. The new model, called DTM model,* owns features for order establishment of morphologic primitives. The use of morphology as the base of the formulation allows the system to obtain general offsets to free-form shapes without constraints. A computational model which enables the morphological operations defined in the DTM to be carried out is also developed. Its existence makes the new model (DTM) operative and permits its efficiency to be checked through testing.

Morphologic primitives are translated into *offset computation* and are applied to real machining tests in order to probe the correct behaviour of the model. The proposed model has been successfully implemented in a commercial CAD/CAM system specialised in shoe last making. Finally, some illustrative examples are shown.

Conclusion and discussion part summarizes this investigation and offers recommendations for future work.

Dobson and Doig (D and D) reported an important but somehow complicated non-linear model for alignment-free prediction of 3D-structures of enzymes opening the search of simpler Computational Chemistry models. In Chapter 14 we have used Markov Chain Models (MCM) to calculate electrostatic potential, hydrophobic interactions (HINT), and van der Waals (vdw) interactions in 1371 protein structures (essentially the D and D data set). Next, we developed a simple linear model that discriminates 73.5% of enzyme/no-enzyme proteins using only one electrostatic potential while the D and D reaches 80% of accuracy with a non-linear model based on more than 30 parameters. We both analyzed ROC and constructed Complex Networks for the first time in order to study the variations of the three fields in enzymes. Finally, we illustrated the use of the model predicting drug-target enzymes and antibiotic enzymes (enzybiotics). In closing, this MCM allowed fast calculation and comparison of different potentials deriving accurate protein 3D structure-function relationships and protein-protein Complex networks obtained in a way notably simpler than in the previous way.

In recent years, density functional theory (DFT) has emerged as one of the most successful and powerful approaches in electronic structure calculation of atoms, molecules and solids, as evidenced from burgeoning research activities in this direction. Chapter 15 concerns with the recent development of a new DFT methodology for accurate, reliable prediction of many-electron systems. Background, need for such a scheme, major difficulties encountered, as well as their potential remedies are discussed at some length. Within the realm of non relativistic Hohenberg-Kohn-Sham (HKS) DFT and making use of the familiar LCAO-MO principle, relevant KS eigenvalue problem is solved numerically. Unlike the commonly used atom-centered grid (ACG), here we employ a 3D cartesian coordinate grid (CCG) to build atom-centered localized basis set, electron density, as well as all the two-body potentials directly on grid. The Hartree potential is computed through a Fourier convolution technique via a decomposition in terms of short- and long-range interactions. Feasibility and viability of our proposed scheme is demonstrated for a series of chemical systems; first with homogeneous, local-density-approximated XC functionals followed by nonlocal, gradient- and Laplacian-dependent functionals. A detailed, systematic analysis on obtained results relevant to quantum chemistry, are made, *for the first time*, using CCG, which clearly illustrates the significance of this alternative method in the present context. Quantities such as component energies, total energies, ionization energies, potential energy curve, atomization

energies, etc., are addressed for pseudopotential calculations, along with a thorough comparison with literature data, wherever possible. Finally, some words on the future and prospect of this method are mentioned. In summary, we have presented a new CCG-based *variational* DFT method for accurate, dependable calculation of atoms and molecules.

Infinite series are probably one of major tools that was elaborated in the early days of modern mathematics for the purpose of answering practical and theoretical questions. In chemistry and physics, infinite series in terms of spherical harmonics, also known as multipole expansions, are routinely used to solve a variety of problems particularly those with spherical symmetry, *eg.* an electron moving in the field created by a fixed nucleus. Chapter 16 addresses a specific application of spherical harmonics, namely the so-called two-range addition theorems. Such mathematical constructs essentially allow one to expand a function $f(r+a)$ in terms of $Y_l^m(\theta_r, \phi_r)$ hence leading to a separation of the angular and radial parts of the variable r. In fact such a problem is very common in quantum chemistry where it is used to express a given charge distribution as a sum of multipolar contributions and multicenter integrals over Exponential Type Functions (ETFs) are just one of many such problems. As a consequence and in order to illustrate the mechanics behind the two-range addition theorems, we will use the case of multicenter integrals over ETFs as working example. In addition to numerical algorithms, symbolic computation which is perfectly geared to obtain analytical expressions, we will purposely address in some detail the convergence of the multipole expansion, in the context of multicenter integrals, since this aspect is often overlooked by researchers.

Following the work of Guo, Thompson, and Sewell (Y.Guo, D.L.Thompson, and T.D. Sewell, J.Chem.Phys. **104**, 576 (1996)) on the zero point energy correction of classical trajectories, Chapter 17 emphasizes that the zero-point energy of a molecule is a quantum phenomenon with no classical counterpart, rooted soundly in the positionmomentum uncertainty principle. As a consequence certain quantum "ingredients," such as those introduced using Heller's thawed Gaussian wavepacket dynamics (E.J. Heller, J.Chem.Phys. **62**, 1544 (1975)), are probably necessary to avoid the computational difficulties in applying zero-point energy corrections to classical molecular dynamics trajectories which have been described in the literature to date.

In Chapter 18, the dynamics of stratospheric ozone is studied using the ideas introduced by Chapman including the role of nitrogen oxides as proposed by Crutzen. We refer to these ideas as the Chapman–Crutzen mechanism that gives a system of five ordinary differential equations. This set of differential equations is studied using the ideas of the theory of dynamical systems. In particular, mass conservation is used to reduce the set to three differential equations by using certain constants of motion, we obtain the critical points of this reduced set of equations, analyze the eigenvalues of the Jacobian matrix evaluated at the critical points in order to determine whether or not they are hyperbolic, and compare them with the corresponding critical points of the Chapman mechanism. Several numerical methods, like Adams' method and the backward differentiation formula, are used to solve the initial value problem for the reduced set of ordinary differential equations seeking to obtain a more global picture of the orbits than that provided by the local analysis consisting in analyzing the nature of the critical points.

Chapter 1

RECENT PROGRESS IN 'ALGEBRAIC CHEMISTRY'

Cynthia Kolb Whitney[*]

Galilean Electrodynamics, Proceedings of the Natural Philosophy Alliance
141 Rhinecliff Street, Arlington, MA 01476-7331, U.S.A.

Abstract

This work reprises and extends the development of a new approach to fundamental problems in chemistry, now known as 'Algebraic Chemistry'. It collects and summarizes all results so far produced. Problems addressed here include **1)** the nominal pattern of single-electron state filling across all of the elements, **2)** the exceptions to that pattern that occur for about 20% of elements; **3)** the numerical patterns in the experimental data about ionization potentials of all elements and all orders, and **4)** plausible reasons for the existence of chemical periodicity and **5)** some insights on the possible nature of chemical bonds. The approach develops synoptic algebraic scaling laws to use in place of the case-by-case numerical integrations prescribed by traditional Quantum Chemistry. The development of Algebraic Chemistry requires an initial re-examination of *two* pillars of twentieth century physics: not just Quantum Mechanics (QM), but also Special Relativity Theory (SRT). The reader is asked to entertain an 'Expanded SRT', in which an additional 'speed' concept appears, and several additional mathematical relationships among speed concepts appear. This Expanded SRT allows an 'Expanded QM', in which the main actors are not the modern, and very abstract, probability-amplitude waves, but the old-fashioned, and very concrete, point particles. Although the hundred years elapsed since SRT and QM were first introduced may make this sort of re-work seem troublesome, the practical utility of the results produced makes the effort clearly worthwhile.

Keywords: single-electron state filling, ionization potentials, chemical periodicity, chemical bonds, expanded special relativity theory, expanded quantum mechanics.

---

[*] E-mail address: Galilean_Electrodynamics@comcast.net

1. Introduction

Chemistry possesses a gift of inestimable value for physics, if physicists will be so wise as to embrace the gift. Chemistry possesses a wealth of empirical data that often seems mysterious because it has yet to be fully interpreted in physical terms. A physicist could be occupied for a lifetime with the existing chemical data, and never have to wait on far-off, fickle funding for a particle accelerator, a deep mine shaft experiment, or a deep space satellite mission. The chemical data will drive a physicist just as hard toward new physics (or perhaps back to old physics) as would any of the other investigative techniques.

This paper reviews and extends my own journey along this path [1-3]. Section 2 shows how far into the past I have now been driven: all the way back to Maxwell's Electromagnetic Theory (EMT), for an exploration of the implications of his equations that were not forcefully articulated in his own time, or even later, although they would have been the key to more effective development of twentieth century physics, and now for twenty first century chemistry.

The subsequent trail goes from Maxwell's EMT through major parts of twentieth-century physics: Einstein's Special Relativity Theory (SRT), then to Quantum Mechanics (QM) for Hydrogen atoms, Positronium, spinning electron rings, and to spinning positive charge rings. Much of that work has been published, or is in press, elsewhere, and so is here summarized and collected as Appendices.

Sections 3 through 7 review applications of the newly developed ideas to problems in chemistry. The first such problem concerns the nominal pattern of single-electron state filling across all of the elements. What was generally known about the order in which single-electron states fill was described in terms of QM. As one progresses through the elements, more and more electrons are involved in a multi-electron state that is envisioned as a product of single-electron states like the states that QM attributes to the prototypical Hydrogen atom. These single-electron states are characterized by quantum numbers: the radial quantum number n, the orbital angular momentum quantum number l, and the electron spin quantum number s. There existed some order to the way in which available quantum numbers enter into the mix, and it was characterized by almost-reliable empirical rules. With occasional exceptions, single-electron state filling follows Madelung's and Hund's rules for the nominal filling order: advance with the linear combination $n+l$, and within a given value of $n+l$, advance with n, and within a given n,l combination, fill all of one s state, then the other.

Within the context of modern QM, there is no good reason why the sum of the two physically different quantum numbers like n and l should mean something. The only justification for any such thing comes from the huge database of spectroscopy, which was being accumulated even before QM existed, and which suggests, when viewed from a modern perspective, that sums of integers, like $n+l$, correlate with single electron state energies proportional to $-1/(n+l)^2$. But the $n+l$ parameter itself is pretty limited: it does not even give a clue about the second part of the $n+l$ state-filling directive: "within a given value of $n+l$, advance with n."

Furthermore, about 20% of known elements break those rules in some way. Ref. [1] suggests refining the $n+l$ parameter in a way that at least calls attention to places where the violations occur. The refined parameter is

$$R = \frac{1}{2}\left[4n + 2(l + s)\right] \qquad (1)$$

Like the original $n + l$, R is a linear combination of disparate quantum numbers, and has no rationale in QM. But it is useful. It has regressions and repeats that mark the places in the Periodic Table (PT) where violations of the expected filling order occur. See figure 1.1.

	n,l,s designations in periods 1 to 7	numerical values of parameter R
1	$1s(-) \rightarrow 1s(+)$	$1 \rightarrow 2$
	↵	↵
2	$2s(-) \rightarrow 2s(+) \rightarrow 2p(-) \rightarrow 2p(+)$	$3 \rightarrow 4 \rightarrow 4 \rightarrow 5$
	↵	↵
3	$3s(-) \rightarrow 3s(+) \rightarrow 3p(-) \rightarrow 3p(+)$	$5 \rightarrow 6 \rightarrow 6 \rightarrow 7$
	↵	↵
4	$4s(-) \rightarrow 4s(+) \rightarrow 3d(-) \rightarrow 3d(+) \rightarrow 4p(-) \rightarrow 4p(+)$	$7 \rightarrow 8 \rightarrow 7 \rightarrow 8 \rightarrow 8 \rightarrow 9$
	↵	↵
5	$5s(-) \rightarrow 5s(+) \rightarrow 4d(-) \rightarrow 4d(+) \rightarrow 5p(-) \rightarrow 5p(+)$	$9 \rightarrow 10 \rightarrow 9 \rightarrow 10 \rightarrow 10 \rightarrow 11$
	↵	↵
6	$6s(-) \rightarrow 6s(+) \rightarrow 4f(-) \rightarrow 4f(+) \rightarrow 5d(-) \rightarrow 5d(+) \rightarrow 6p(-) \rightarrow 6p(+)$	$11 \rightarrow 12 \rightarrow 10 \rightarrow 11 \rightarrow 11 \rightarrow 12 \rightarrow 12 \rightarrow 13$
	↵	↵
7	$7s(-) \rightarrow 7s(+) \rightarrow 5f(-) \rightarrow 5f(+) \rightarrow 6d(-) \rightarrow 6d(+) \rightarrow 7p(-) \rightarrow 7p(+)$	$13 \rightarrow 14 \rightarrow 12 \rightarrow 13 \rightarrow 13 \rightarrow 14 \rightarrow 14 \rightarrow 15$

Figure 1.1. The evolution of the parameter R through all the periods of elements.

Suppose single-electron state energies are characterized simply by $E \propto -1/R^2$. Repeats in R mean repeats in E. That can create opportunities for replacements, which are seen as violations of the expected single-electron state filling order. But the filling order was still not fully explained by this notion. So there remained good reason to try out a different approach on this filling-order problem. The idea of spinning charge rings, arrived at through the development recounted in the Appendices, provides such an approach [2]. It is applied in Section 3. Section 4 goes on to identify more detailed physical reasons for the exceptions to that pattern that occur for about 20% of elements.

Since the time of Mendeleev, the PT has been the fundamental organizing tool of Chemistry. The big question is: Why does chemical periodicity exist? Section 5 discusses plausible reasons for the existence of chemical periodicity, based on the ideas about electron clusters of spinning electron rings developed in Sections 3 and 4.

Section 6 recounts from [3] the numerical patterns in the experimental data about ionization potentials of all elements and all orders. Section 7 expands from [3] with some new insights on the possible nature of chemical bonds, based on the information about ionization potentials. Section 8 concludes this paper and points to future investigations.

2. Maxwell Revisited

It is generally believed that QM is a departure from EMT necessitated by failures of EMT at the atomic level, such as failure to account for the existence of the ground state of the Hydrogen atom, which was thought to be vulnerable to destruction by the radiative energy loss mandated in EMT. The present author believes the QM departure actually had a different cause; namely, the failure of EMT practitioners to analyze fully the situation that develops in Maxwell propagation of a radiation wave packet with finite total energy (a photon) from one atomic system (a source) to another (a receiver). (Please take note that I say 'atomic system' here, and not 'atom'. That is because, for reasons that will emerge later in this article, I do not believe that a single isolated atom can by itself either emit a photon, or absorb a photon. Please bear with me on this.).

One may ask: What is so interesting about the propagation of a finite energy wave packet? Surely it can be well understood from Huygens' analysis of an expanding spherical wave front: each point on the spherical wave front launches little spherical wavelets, and the wavelets tend to cancel in the backward direction and reinforce in the forward direction, resulting in ever increasing radius R of the overall spherical wave front, with amplitude diminishing as $1/R^2$, and with profile limited in R, and invariant in R^2-normalized shape.

All of that is indeed true for a scalar wave. But Maxwell waves are not scalar waves; they are vector waves. There is an electric vector $\mathbf{E}$ and a magnetic vector $\mathbf{B}$, transverse to each other, and both transverse to the radiation propagation direction. This circumstance mandates several departures from the Huygens situation. First, it is not even possible to make a uniform spherical wave front for this situation. The simplest possible idealization that one can make is a plane wave. This means thinking 'rectangular' or 'cylindrical' rather than 'spherical'. We have one definite propagation direction and two transverse field directions.

Second, finite total energy is a constraint, a kind of generalized 'boundary condition'. Any discussion of any differential equation is incomplete without detailed consideration of boundary conditions, or other similar constraints, that serve to select a particular solution from the many possible solutions.

For finite energy, the Maxwell fields have to be limited to a finite volume. That means they have to be limited in all three spatial directions. After several centuries, we know extremely well what limitation in the two transverse directions leads to: the phenomenon of 'diffraction' creates interference fringes or rings, and overall spreading in the transverse directions. [4,5] But throughout all of that time, we should also have been asking: What about limitation in the *longitudinal* direction? Will waveform shape be preserved, like in the Huygens scalar wave situation? Or will some spreading phenomenon like diffraction come into play?

Many people would expect the waveform shape to be preserved, on the basis that free space has no dispersion (light speed variation with wave number), and the whole propagation process is linear (no fields squared, cross multiplied, exponentiated, *etc*., involved in Maxwell's equations; products occur only in the formulations of field energy density and Poynting vector). But the 'linearity' of Maxwell propagation only means that adding two inputs results in adding two outputs; it does *not* mean the system responds to a delta-function input with a delta function output. In the parlance of modern engineering science, the system

can reshape the profile of the input, amplify some parts of it, kill some parts, delay some, put some through a 'feedback loop', *etc*.

The Maxwell equations need to be considered with allowance for such complexity. Consider that the Maxwell wave is a *vector* wave, and that there are two vectors involved, $\mathbf{E}$ and $\mathbf{B}$, and that these vectors are coupled through the Maxwell differential equations. This makes a classic feedback loop. Induction happens: spatial variation in $\mathbf{E}$ (captured in modern notation as $\nabla \times \mathbf{E}$) drives temporal changes in $\mathbf{B}$ (captured in modern notation as $\partial \mathbf{B} / \partial t$), and *vice versa*.

Here is how induction plays out over time. If $\mathbf{E}$ starts out spatially bounded in the propagation direction, the boundaries are the loci of extra spatial change in $\mathbf{E}$, and hence extra temporal change in $\mathbf{B}$ orthogonal to $\mathbf{E}$. In short, a pulse in $\mathbf{E}$ induces two peaks in $\mathbf{B}$ beyond each of its two edges. The newly induced $\mathbf{B}$ peaks then induce two more $\mathbf{E}$ peaks orthogonal to $\mathbf{B}$ further beyond. The 'then' means 'a little later'; the system has 'delay'. More and more peaks appear, sequentially over time, symmetrically over space. Thus the originally very confined waveform spreads out longitudinally.

Naturally, as the overall waveform spreads, its central amplitude must decrease to conserve total energy. In detail, each new pair of $\mathbf{E}$ or $\mathbf{B}$ peaks not only induces another pair of $\mathbf{B}$ or $\mathbf{E}$ peaks further out in the waveform, but also induces diminution of $\mathbf{B}$ or $\mathbf{E}$ peaks further in, thereby maintaining the integral over all space of the energy density $\frac{1}{2}(E^2 + B^2)$.

How fast does the waveform spreading proceed? There is only one speed in the free-space Maxwell equations, the so-called 'light speed' c. It is the only speed available to describe this spreading by induction. There are two limiting cases of interest, and in both, the spread speed must be c.

In the first case, the process is seeded with just one pulse, either of $\mathbf{E}$ or of $\mathbf{B}$. This seed pulse is spatially bounded, but oscillatory in time. It sets the stage for an electromagnetic wave expanding from the pulse location. At the extremities, new crests come into existence by induction. So both $\mathbf{E}$ and $\mathbf{B}$ exist in this wave, with their crests interleaved so that they form a kind of 'standing wave'. But here nothing confines the standing waveform, so it spreads, with greater or lesser amplitude, in all directions, except exactly coincident with the seed field direction. In any other direction, the two ends of the waveform recede at speeds $\pm c$.

The other limiting case of interest is seeded with *two* pulses, one $\mathbf{E}$ and the other $\mathbf{B}$ orthogonal to $\mathbf{E}$, with equal energy in each pulse. This situation sets the stage for a 'traveling wave'. The presence of the $\mathbf{B}$ and $\mathbf{E}$ pulses together creates a Poynting vector proportional to $\mathbf{E} \times \mathbf{B}$, and the combined waveform travels at speed c in the direction of $\mathbf{E} \times \mathbf{B}$. Like the standing wave, the traveling wave also spreads at $\pm c$ from its middle, but unlike the standing wave, the middle itself is moving at $+c$ away from its source, as indeed are all of its induced wave crests. With greater or lesser amplidude, the waveform spread is in all directions. But the direction of greatest interest here is the longitudinal one. Transverse spread is related to diffraction, an important subject, but already much studied. The corresponding longitudinal spread has not yet had equal attention.

Longitudinal spread means that one end of the wave form always remains with the source, and the other end always extends forward to a distance twice as far away as the waveform center. It is as if the 'tail' end of the waveform did not travel at all, while the 'nose'

end traveled at speed $2c$. Note that this does *not* mean that any identifiable wave front travels at a speed different from c. Those wave fronts at the 'tail' and 'nose' ends of the waveform have *not* gotten there by *travel* from somewhere else; they have *arisen* there by induction.

Note that, to arrive at this picture for the longitudinal spread of a traveling waveform, we have reversed a common way of thinking about things. It has always been customary to think of a standing wave as the combination of two traveling waves. The conceptual reversal is to think of a traveling wave as the combination of two standing waves, with each one being forced to move along on account of the presence of the other one.

The story about longitudinal waveform spread implies a corresponding story about wave momentum (*i.e.* wave number k). Suppose at a given time t the waveform is describable by some function $f(x, ct)$. That means it has a Fourier amplitude function $F(k, ct)$ such that

$$f(x, ct) = \int_{-\infty}^{+\infty} F(k, ct) e^{ikx} dk \qquad (2.1)$$

This Fourier amplitude function can be found from

$$F(k, ct) = \frac{1}{2\pi} \int_{-\infty}^{+\infty} e^{-ikx} f(x, ct) dx \qquad (2.2)$$

For example, we could have $f(x, ct)$ be a traveling complex oscillation with nominal wave number k_0, but cut off below $x = 0$ and above $x = 2ct$, and normalized by the length $2ct$.

$$f(x, ct) = \frac{1}{2ct} \exp\left[ik_0(x - ct)\right] \text{ for } 0 < x < 2ct \text{, } 1/2$$

at $x = 0$, $x = 2ct$, 0 elsewhere $\qquad (2.3)$

The cut-offs make this $f(x, ct)$ function a combination of two so-called 'Heaviside step functions'. The normalization by $2ct$ means that in the limit $ct \to 0$ $f(x, ct)$ is a so-called 'Dirac delta function'. The Fourier amplitude function corresponding to this $f(x, ct)$ function is

$$
\begin{aligned}
F(k, ct) &= \frac{1}{2\pi} \int_{x=0}^{2ct} e^{-ikx} \frac{1}{2ct} \exp\left[ik_0(x - ct)\right] dx \\
&= \frac{1}{2\pi} \left\{ \frac{\exp\left[-i(k - k_0)x\right]}{-i(k - k_0)2ct} \right\} \Big|_{x=0}^{2ct} e^{-ik_0ct} = \frac{1}{2\pi} \left\{ \frac{\exp\left[-i(k - k_0)2ct\right] - 1}{-i(k - k_0)2ct} \right\} e^{-ik_0ct} \\
&= \frac{1}{2\pi} \left\{ \frac{\exp\left[-i(k - k_0)ct\right] - \exp\left[+i(k - k_0)ct\right]}{-i(k - k_0)2ct} \right\} \exp\left[-i(k - k_0)ct\right] e^{-k_0ct} \\
&= \frac{1}{2\pi} \frac{\sin\left[(k - k_0)ct\right]}{(k - k_0)ct} e^{-ikct}
\end{aligned}
\qquad (2.4)
$$

The limit of any `sin(variable)/ variable′` as `variable′ → 0` is unity. So for $ct → 0$, the scalar amplitude $\frac{1}{2\pi}\sin\left[(k-k_0)ct\right]\big/(k-k_0)ct$ of this $F(k,ct)$ approaches the constant value $1/2\pi$ for all k. All wave numbers are present in equal amount; with total localization in x (position) space, but no localization at all in k (wave-number, *i.e.*, momentum) space. For $ct → 0$, the pulse is so short that it does not contain even one nominal wavelength, so it possesses all wave numbers in equal amount. For large ct, the situation reverses: there is a large spread in x space, but very little spread in k space.

A reciprocal relationship between the spreads in Fourier function pairs exists generally, including for Maxwell fields **E** or **B** fields. Such behavior in a Maxwell wave anticipates the kind of behavior discovered later for probability waves in QM. This is a clue that the Maxwell theory was not really so deficient as was thought at the advent of QM: it anticipates Heisenberg's Uncertainty Principle.

The actual shape of the functions $f(x,ct)$ and $F(k,ct)$ representing the energy in the actual **E** and **B** fields in a spreading waveform can be inferred on logical grounds. Observe that the induction process takes energy out of any local peak, say in **E**, and casts it equally into the two neighboring peaks in the other field, *i.e.* **B**. In terms of energy, the induction process over time is much like the row-by-row construction of Pascal's famous triangle (figure 2.1):

```
                    1
                1       1
            1       2       1
        1       3       3       1
    1       4       6       4       1
  1     5      10      10      5      1
1     6     15      20      15     6      1
                  etc.
```
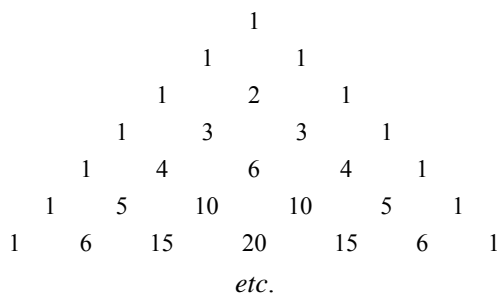
Figure 2.1. Pascal's triangle.

Labeling the rows in Pascal's triangle with index $n = 0,1,2,...$, the elements in row n are the 'binomial coefficients' for $(1+1)^n = 2^n$, *i.e.* $n!/m!(n-m)!$. The only difference is that the conservation of energy over time needs to be represented by normalization of the numbers over rows (figure 2.2):

```
                      1
              1/2           1/2
          1/4         2/4         1/4
       1/8        3/8         3/8        1/8
    1/16       4/16        6/16       4/16       1/16
  1/32      5/32      10/32      10/32       5/32      1/32
1/64     6/64     15/64      20/64      15/64     6/64     1/64
                      etc.
```
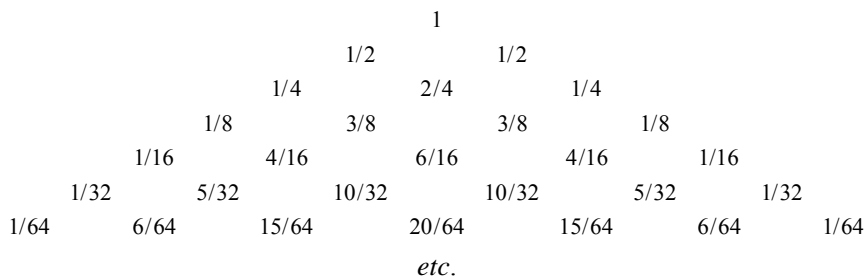
Figure 2.2. Pascal's triangle normalized.

Thus the shape of the function $f(x,ct)$ that represents the energy profile of the $\mathbf{E}$, or the $\mathbf{B}$, field is a series of peaks with areas matching the binomial probability distribution. The function $f(x,ct)$ representing the energy profile of both fields together is the sum of two such series, one for some number n and the other for $n+1$, interleaved with the first one. For large n, the resulting sum function $f(x,ct)$ is indistinguishable from a smooth Gaussian distribution. This means that its Fourier amplitude function $F(k,ct)$ is also indistinguishable from a smooth Gaussian. Function pairs $f(x,ct)$ and $F(k,ct)$ that are Gaussian minimize the product of spreads x and k. That means the Maxwell fields in this limit are conforming to Heisenberg's Uncertainty Principle with the '$\geq$' approaching the '$=$'.

The existence of such product relationships has been long known in the context of transverse spreading; *i.e.* 'diffraction'. For example, in an optical system, large aperture means small focal spot. The 'diffraction integral' that relates aperture to focal spot is basically a Fourier transform. More generally, the similarity between all diffraction integrals and Fourier transforms accounts for the existence of the whole technologically important discipline called 'Fourier optics' [4].

The corresponding situation concerning longitudinal spreading has not been similarly developed. The present paper contains the beginning of the missing development. It too leads to technologically important results – those in Chemistry being especially noted here.

The first step of development is to recognize that Maxwell's equations generally support time-reversed solutions. That means we can have not only solutions that expand from a source, but also solutions that contract to a receiver. Their combination can explain how energy transfer from a source to a receiver can occur. Imagine that the 'nose' of the expanding waveform encounters some atomic system that can serve as receiver for the energy contained in the wave. The presence of this new system creates a new, and hard, boundary condition: the spreading waveform can spread no further. But a time-reversed solution that contracts to the receiver can match exactly the now stymied waveform that has expanded from the source. This time-reversed solution can therefore proceed, and complete the energy transfer.

Speaking in more detail, the time reversal means $\partial \mathbf{E} / \partial t$ and $\partial \mathbf{B} / \partial t$ reverse sign, and this reverses the whole induction process that drove the expansion, and makes it drive the contraction instead. The 'nose' and 'tail' of the waveform shrivel, and the 'heart' of the waveform re-fills, thus contracting the waveform over all to the point where the receiver can swallow it.

Thus we can understand the natural history of energy transfer by radiation from one atomic system to another as follows: Light is emitted from a source in a pulse very localized in space, and totally spread out in momentum (wave number). The wave packet then spreads in space and becomes defined in wave number. Then the receiver is then encountered, and the whole process reverses. At the end of the scenario, the pulse in space with spread in momentum is restored, and the now fully delivered energy is absorbed all at once into the receiver.

The behavior described here apparently *is* what is needed to satisfy the Maxwell differential equations and the desired radiation condition, $\mathbf{E} \cdot \mathbf{B} = 0$, and the desired energy condition, finite and constant spatial integral of $\frac{1}{2}(E^2 + B^2)$. I believe it is the behavior that

Nature actually exhibits. But can we witness this 'exhibition'? Not necessarily. Consider that the proposed waveform evolution is a behavior of 'light in flight'. 'Observing' light means 'capturing' light, whereupon it is no longer 'light in flight'. We can at best witness consequences of this waveform evolution, not the evolution itself.

So what consequences can there be? Absolutely none, if the source and receiver are at rest with respect to each other. But physics is generally a science of things that move. The possibility of witnessing some consequence emerges when there is relative motion between the source and receiver. We find that much of 20th century physics needs review in consideration of the finite-energy solutions to Maxwell's equations, and that there is considerable spillover into chemistry. The remainder of this paper looks at just a few things. The ones that are specifically about chemistry are in the following Sections 3-7. The ones that are not fundamentally about chemistry, but precursors to it, are in the Appendices. What the chemist needs to know from those Appendices is summarized as follows:

- Some post-Maxwell EMT results need to be revisited in light of the finite-energy analysis. In particular, the directionality of Coulomb force and radiation from a rapidly moving source must reconcile to 'half-retarded'. This is important for modeling atoms.
- Einstein's SRT depends on his Second Postulate, and it changes when the Postulate is replaced with the finite energy analysis. In particular, superluminal Galilean speeds become a natural part of the theory. This is important for modeling electron populations in atoms.
- The Hydrogen atom ground state can be found by asserting balance between energy loss due to radiation and energy gain due to torquing within the system. It does *not* require the QM departure from EMT. This is important for modeling all other atoms.
- The Hydrogen atom has a spectrum of sub states that are not accounted for in traditional QM. The Hydrogen sub-state analysis is important as a prototype for many other analyses that ultimately get to the chemistry problems.
- The Hydrogen sub-state math applies to many other attractive two-body systems. In particular, Positronium exemplifies all equal-mass systems, the situation opposite to the Hydrogen atom, where the positive charge is overwhelmingly more massive than the negative charge.
- The equal-mass analysis also applies to binary pairs of charges of the same sign, and then to larger same-charge clusters in the form of spinning charge rings. In all such same-charge spinning charge rings, the individual charges move at super-luminal speeds.
- Same-charge super-luminal spinning charge rings figure in atomic 'excited states' and hence atomic spectroscopy. Charge clusters are important, and probably ubiquitous in atoms. They figure in all of the discussions of chemistry problems below.

3. Single Electron State Filling Across the Elements – Nominal Order

Same-charge super-luminal spinning charge rings provide another tool that can help explain the observed facts of single-electron state filling. This Section addresses the nominal pattern of single-electron state filling. It is a summary of the relevant Section in [2]. Where that paper addressed every element, this summary focuses on the elements where something in process finishes or something new starts: the noble gasses, and the metals two charges beyond the noble gasses.

To describe the spinning charge rings, we first of all need some words. For charge number $N = 2$, call the 'ring' a 'binar' for 'binary'; for $N = 3$, 'tert'; for $N = 4$, 'quart'; for $N = 5$, 'quint'; for $N = 6$, 'hex'; for $N = 7$, 'sept', and so on, if ever needed.

Except for the case of two electrons, we only occasionally see cases of even numbers of electrons; such cases would usually form two rings instead of one big ring. So for describing atomic charge clusters, the rings most often needed are 'binars', 'terts', 'quints', 'septs', and of course 'singletons'.

Let us now develop visual images for the spinning electron rings in atoms. In general, the axes of all the electron rings should be parallel to the axis of the orbit that the whole electron cluster executes around the nucleus. If we imagine this atomic orbit axis to be horizontal on the page, and we imagine the various electron rings to be viewed edge-on, then those rings look like vertical lines. So we can use vertical lines as a visual notation for electron rings. The Appendix on Spinning Charge Rings shows that rings with successively more charges must spin faster, and so at smaller radii. That means the vertical lines are shorter when the number of charges is greater. Representing singleton electrons as points then completes the visual vocabulary:

$$
\begin{array}{cccccc}
| & | & | & | & | & | \\
\text{binar } 2, & \text{tert } 3, & \text{quart } 4, & \text{quint } 5, & \text{hex } 6, & \text{sept } 7, \ldots \text{ singleton} \bullet \\
| & | & | & | & | & | \\
\end{array}
$$

All of the spinning charge rings essentially amount to permanent electrical 'currents' within the low-temperature/high-temperature/no-temperature-exists 'superconductor' that otherwise-empty space provides. They constitute tiny charged super magnets.

We are accustomed to thinking of magnetic interactions as producing small perturbations on effects that are dominated by Coulombic interactions. That is so because we are accustomed to thinking only of very sub-luminal particle speeds, both for charges creating magnetic fields and for charges responding to magnetic fields. The situation is different when charged particles move at super luminal speeds. Then magnetic interactions dominate.

The tiny charged super magnets like to stack, just like macroscopic magnets do. Since magnetic effects dominate in their world, they go ahead and do stack. That is how they form big electron clusters.

Observe that between the two binars there exists a region where the magnetic field lines must form a 'bottle'; *i.e.* the sort of thing familiar in the macro world of magnetic confinement for controlled fusion technology. So a pair of rings of any size can contain other

things: *i.e.*. a pair of smaller rings, or such a pair of rings plus whatever they in turn contain. So we can have structures like

$$| \;_|\; | \quad | \;_{||}\; | \quad | \;_{|||}\; | \quad | \;_{||||}\; | \quad | \;_{|||||}\; | \quad | \;_{||||||}\; |$$
$$2\;3\;2 \;\text{ or }\; 2\;3\;3\;2 \;\text{ or }\; 2\;3\;5\;3\;2 \;\text{ or }\; 2\;3\;5\;5\;3\;2, \text{ or } 2\;3\;5\;7\;5\;3\;2, \text{ or } 2\;3\;5\;7\;7\;5\;3\;2,$$
$$| \;^|\; | \quad | \;^{||}\; | \quad | \;^{|||}\; | \quad | \;^{||||}\; | \quad | \;^{|||||}\; | \quad | \;^{||||||}\; |$$

etc.

That is, the iconic image is *not* a *sphere* of electron *shells* nested *around* the nucleus, with larger electron counts *outside* of smaller ones, it is a *cylinder* of stacked electron *rings*, located at a nominal orbit radius *away from* the nucleus, with larger electron counts *inside* of smaller ones.

Observe that the space between the two terts constitutes a magnetic confinement region with a *double* wall: not just a magnetic 'bottle', but rather a magnetic 'thermos jug'. Similarly, the space between two quints constitutes a magnetic bottle with a *triple* wall, which is not just a 'magnetic bottle', or even a 'magnetic thermos jug'; it is really a 'magnetic Dewar flask'. But note too that singletons can move along any charge population axis, and such motion is parallel to the magnetic field along the axis, so no magnetic restraint is exercised. Singletons can always escape magnetic confinement.

Describing the elements in terms of electron rings generally requires some 'punctuation'. This punctuation makes the association between specific charge rings in an atom and the conventional QM single-electron state designations. This information appears below and/or above the ring: below for lower energy, above for higher energy. For example, one may see

$$
\begin{array}{cccccccc}
1s+ & 2s- & 2s+ & & 2p+ & & 4d+ & \\
| & | & | & | & | & | & | & \\
2 & 2 & 2 & 3 & 3 & 5 & 5 & , etc. \\
| & | & | & | & | & | & | & \\
1s- & 1s- & 1s+ & 2p- & & 4d- & &
\end{array}
$$
(or ... or ... or ... or ... or ... or ...)

The first of these ring examples show two single-electron states differing only in spin. They make something like a 'Cooper pair', something familiar from solid-state physics. The second and third examples involve two different radial quantum numbers. That means the ring does not have its multiple electrons in a particular single-electron state; instead, it has its multiple electrons in linear combinations of single-electron states. For different electrons, the coefficients might differ in phase, but not amplitude, so that in the end all the state linear combinations in a ring have the same mixed-state average energy. The fourth and fifth examples have all three electrons alike. The two rings together make a sort of 'super Cooper pair', made out of electron rings instead of individual electrons. The same is true of the last two examples.

Describing the elements in terms of this 'vocabulary' and 'punctuation' also requires some 'grammar rules'. Here are some rules:

1. Being the largest of all electron rings, binars make the exterior framework for the stack.
2. The stack is always straight, centered with respect to the nucleus, and as symmetric as its total electron count permits.
3. The equi-potential surfaces around a nucleus are spherical, so the stack center falls at lowest energy, and the stack ends fall at highest energy.
4. The electron ring being filled is always just inside the magnetic bottle created by an end binar.
5. Rings of the same size but more out-lying positions have higher energies.
6. At a given position, a larger ring probes further into the concave nuclear potential well, and so has lower energy.
7. As soon as a pair of binars is present, terts can be confined; as soon as two pairs of terts are present, quints can be confined; as soon as two pairs of quints are present, septs can be confined.

In [2], the nominal electron configurations of all the elements are described with the given vocabulary, punctuation, and grammar rules, along with whatever explanations of their behavior seem to emerge from the visualization model. The competing factors that determine state energy can make the nominal stacking order look more complicated than it really is. It can be appreciated pretty well by looking ahead to the end, to element $_{118}?$. Note that the question mark just means that this element has not been discovered yet, or even imagined, so it does not have a name.

For the present summary, the first noble gas and the first element after it are:

$$
\begin{array}{ccccc}
1s+ & & 2s- & 2s+ \\
| & & | & | \\
{}_2\mathrm{He}:\ 2 & \text{and} & {}_4\mathrm{Be}:\ 2 & 2 \\
| & & | & | \\
1s- & & 1s- & 1s+
\end{array}
$$
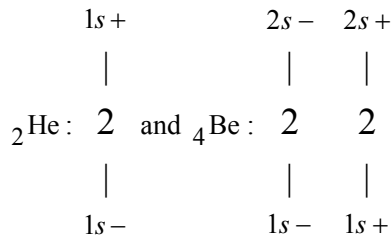
Note that the completion of two binars with $_4\mathrm{Be}$ permits the filling of terts to begin. This filling is completed with the next noble gas:

$$
\begin{array}{ccccc}
2s- & & 2p+ & 2s+ \\
| & | & | & | \\
{}_{10}\mathrm{Ne}:\ 2 & 3 & 3 & 2 \\
| & | & | & | \\
1s-\ 2p- & & & 1s+
\end{array}
$$
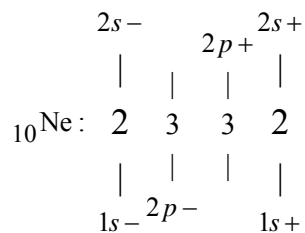
Two electrons further on we switch to three binars, with single terts confined:

```
              3s −        1s +    3s +
                               2p +
               |      |    |   |   |
   12Mg :  2   3    2   3   2
               |    |    |   |   |
              2s − 2p − 1s −      2s +
```
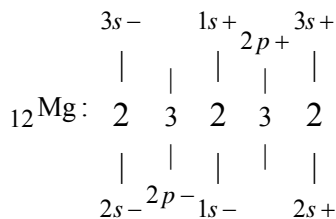
It is now possible to fill more terts. This filling is completed with the next noble gas:

```
           2s −            1s +       3s +
                                2p +3p +
            |    |    |    |    |    |    |
   18Ar :  2   3   3   2   3   3   2
            |    |    |    |    |    |    |
           3s − 3p −2p − 1s −           2s +
```
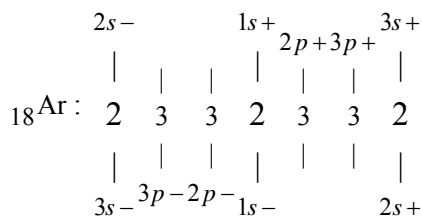
Two electrons further on, we switch to four binars, with only single terts at the outside.

```
      4s −      2s −          2s +   4s +
                         2p +     3p +
       |    |    |    |    |    |    |   |
   20Ca :  2   3   2   3   3   2   3   2
       |    |    |    |    |    |    |   |
      3s − 3p − 1s − 2p −      1s +   3s +
```
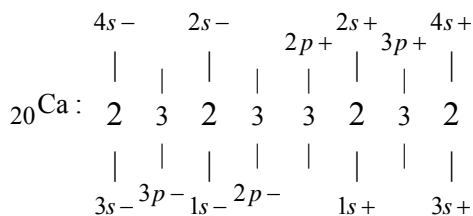
Enough terts are now present for quints to start filling. When two quints are full, then more terts can be filled. This filling is completed with the next noble gas:

```
      4s −                  2s −      2s +          4s +
                                  2p +   3p +3d +4p +
       |    |    |    |    |    |    |    |    |    |   |
   36Kr :  2   3   5   3   2   3   3   2   3   5   3   2
       |    |    |    |    |    |    |    |    |    |   |
      3s − 4p −3d −3p − 1s − 2p −      1s +          3s +
```
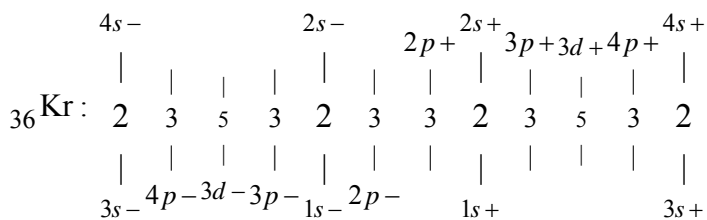
Two electrons further on, we switch to five binars, with six terts and two quints confined:

```
      5s −          3s −          1s +       3s +          5s +
                                        2p +3p +   4p +3d +
       |    |    |    |    |    |    |    |    |    |    |   |
   38Sr :  2   5   3   2   3   3   2   3   3   2   3   5   2
       |    |    |    |    |    |    |    |    |    |    |   |
      4s − 3d −4p − 2s − 3p −2p − 1s −      2s +          4s +
```
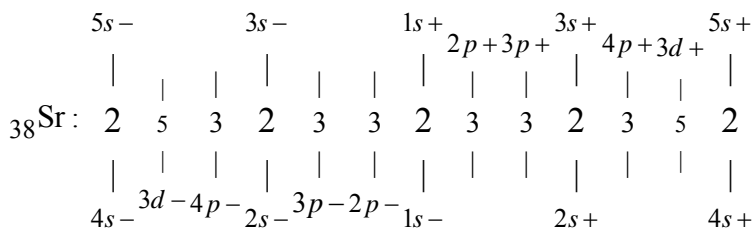
Observe how the switch rearranges the terts for symmetry. Now two more quints can fill, and then two more terts can fill. This all completes with the next noble gas.

$$
\begin{array}{c}
5s- \qquad\qquad 3s- \qquad\quad 1s+ \;_{2p+\,3p+}\;^{3s+}\;_{4p+\,3d+\,4d+\,5p+}\;\;5s+ \\
\mid \quad\mid\;\mid\;\mid\;\mid\;\mid\;\;\mid\;\mid\;\mid\;\;\mid\;\mid\;\mid\;\mid\;\mid\;\mid\;\mid\;\mid \\
_{54}\mathrm{Xe}:\; 2\;\;3\;\;_5\;\;_5\;\;3\;\;2\;\;3\;\;3\;\;2\;\;3\;\;3\;\;2\;\;3\;\;_5\;\;_5\;\;3\;\;2 \\
\mid\;\;\mid\;\;\mid\;\;\mid\;\;\mid\;\;\mid\;\;\mid\;\;\mid\;\;\mid\;\;\mid\;\;\mid\;\;\mid\;\;\mid\;\;\mid\;\;\mid\;\;\mid\;\;\mid \\
4s-\;^{5p-\,4d-\,3d-\,4p-}\,_{2s-}\;^{3p-\,2p-}\,_{1s-}\qquad\quad 2s+\qquad\qquad\quad 4s+
\end{array}
$$
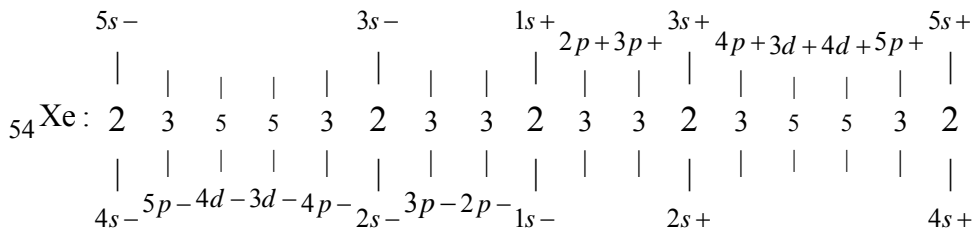
Two electrons further on, we switch to six binars with terts and quints confined.

$_{56}\mathrm{Ba}:$

$$
\begin{array}{c}
6s- \qquad 4s- \qquad\qquad 2s- \;\;^{2s+}_{2p+}\;_{3p+\,3d+\,4p+}\;\;^{4s+}\;_{5p+\,4d+}\;\;6s+ \\
\mid\quad\mid\;\mid\;\mid\;\mid\;\mid\;\mid\;\mid\;\mid\;\mid\;\mid\;\mid\;\mid\;\mid\;\mid\;\mid\;\mid \\
2\;\;_5\;\;3\;\;2\;\;3\;\;_5\;\;3\;\;2\;\;3\;\;3\;\;2\;\;3\;\;_5\;\;3\;\;2\;\;3\;\;_5\;\;2 \\
\mid\;\;\mid\;\;\mid\;\;\mid\;\;\mid\;\;\mid\;\;\mid\;\;\mid\;\;\mid\;\;\mid\;\;\mid\;\;\mid\;\;\mid\;\;\mid\;\;\mid\;\;\mid\;\;\mid \\
5s-\;^{4d-\,5p-}\,_{3s-}\;^{4p-\,3d-\,3p-}\,_{1s-}\,^{2p-}\qquad 1s+\qquad\qquad 3s+\qquad 5s+
\end{array}
$$
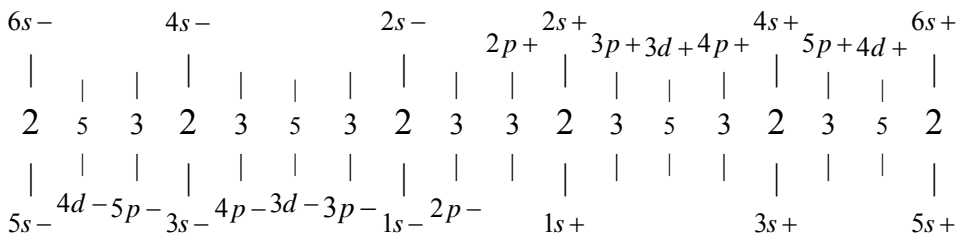
Observe how the switch moves terts and quints. It is now possible to fill two septs, two more quints, and two more terts. All this is completed with the next noble gas.

$$
\begin{array}{c}
6s- \qquad\qquad\qquad 4s- \qquad\qquad\qquad 2s- \\
\mid\quad\mid\;\;\mid\;\;\mid\;\;\mid\;\;\mid\;\;\mid\;\;\mid\;\;\mid\;\;\mid\;\;\mid\;\;\mid \\
_{86}\mathrm{Rn}:\; 2\;\;3\;\;_7\;\;5\;\;3\;\;2\;\;3\;\;_5\;\;_5\;\;3\;\;2\;\;3\;\;\text{-} \\
\mid\;\;\mid\;\;\mid\;\;\mid\;\;\mid\;\;\mid\;\;\mid\;\;\mid\;\;\mid\;\;\mid\;\;\mid\;\;\mid \\
5s-\;^{6p-\,4f-\,4d-\,5p-}\,_{3s-}\;^{4p-\,4d-\,3d-\,3p-}\,_{1s-}\,^{2p-}
\end{array}
$$

$$
\begin{array}{c}
_{2p+}\;^{2s+}\;_{3p+\,3d+\,4d+\,4p+}\;\;^{4s+}\;_{5p+\,5d+\,4f+\,6p+}\;\;^{6s+} \\
\mid\;\;\mid\;\;\mid\;\;\mid\;\;\mid\;\;\mid\;\;\mid\;\;\mid\;\;\mid\;\;\mid\;\;\mid\;\;\mid \\
\text{-}\;\;3\;\;2\;\;3\;\;_5\;\;_5\;\;3\;\;2\;\;3\;\;_5\;\;_7\;\;3\;\;2 \\
\mid\;\;\mid\;\;\mid\;\;\mid\;\;\mid\;\;\mid\;\;\mid\;\;\mid\;\;\mid\;\;\mid\;\;\mid\;\;\mid \\
1s+\qquad\qquad 3s+\qquad\qquad 5s+
\end{array}
$$
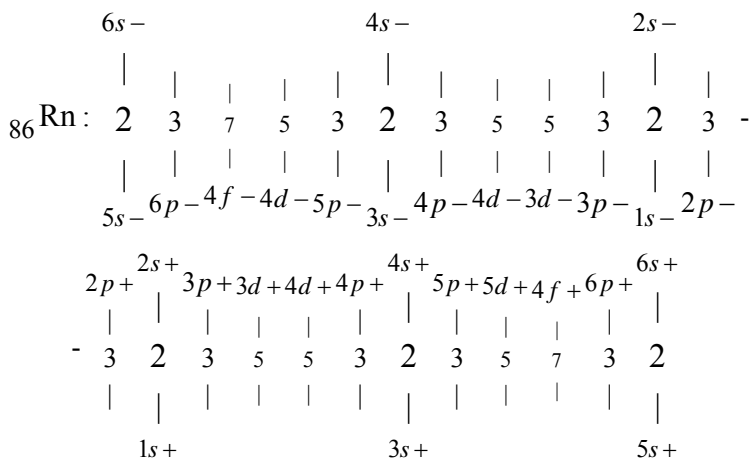
Two electrons further on, we switch to seven binars, with four tert pairs, two terts, two quint pairs, two quints, two septs:

$$_{88}\text{Ra}:$$

Diagram for Ra (element 88):

```
 7s −              5s −                    3s −        1s +
  |     |   |   |    |   |   |   |   |    |   |   |    |
2   7   5   3   2    3   5   5   3   2    3   3   2  -
  |   |   |   |    |   |   |   |   |    |   |   |    |
6s − 4f −5d −6p − 4s − 5p −4d −3d −4p − 2s − 3p −2p − 1s −
```

```
        3s +                    5s +              7s +
2p +3p +   4p +3d +4d +5p +   6p +5d +4f +         |
  |   |   |   |   |   |   |    |   |   |   |       |
- 3   3   2   3   5   5   3    2   3   5   7       2
  |   |   |   |   |   |   |    |   |   |   |       |
        2s +                    4s +              6s +
```

Observe how the switch moves quints and terts. At this point, septs can fill, then quints, then terts. That brings us to an element not yet discovered, and therefore not named:

$$_{118}?:$$

```
  7s −                         5s −                    3s −        1s +
   |    |   |   |   |   |   |    |   |   |   |   |    |   |   |    |
 2   3   5   7   7   5   3    2   3   5   5   3    2   3   3   2  -
   |   |   |   |   |   |   |    |   |   |   |   |    |   |   |    |
 6s − 7p −6d −5f −4f −5d −6p − 4s − 5p −4d −3d −4p − 2s − 3p −2p − 1s −
```

```
                                                              -
```

```
        3s +                    5s +
2p +3p +   4p +3d +4d +5p +   6p +5d +4f +5f +6d +7p +      7s +
  |   |   |   |   |   |   |    |   |   |   |   |   |   |      |
- 3   3   2   3   5   5   3    2   3   5   7   7   5   3      2
  |   |   |   |   |   |   |    |   |   |   |   |   |   |      |
        2s +                    4s +                        6s +
```

Element $_{118}?$ completes the present discussion of nominal electron configurations. Observe how the idea of magnetic confinement explains the otherwise mysterious nominal order in which QM single-electron states fill. When characterized partly in terms of the traditional angular momentum quantum number l, that order sometimes looks backwards. But Nature is not paying attention to this purely mathematical construct; it is building a physical situation based on magnetic confinement.

4. Single Electron State Filling Across the Elements – Exceptions

For about 20% of elements, the nominal single-electron state filling order is wrong, based on a 'singleton' displacement, or on chemical properties, or on known single-electron quantum state occupations. This Section identifies reasons for the 19 presently known

exceptions to the pattern. Based on the present visualization model, a few more exceptions are predicted for elements not yet discovered. Ref. [2] presents them all, along with whatever insight about them can be gathered from the visualization model. Here we summarize the possible exceptions with examples of distinct kinds.

The first exception is $_{24}$Cr . It should nominally be

$$
\begin{array}{ccccccccc}
4s- & & 2s- & & & 2s+ & & 4s+ & \\
 & & & & 2p+ & & 3p+ & & \\
| & | & | & | & | & | & | & | & | \\
2 & 4 & 3 & 2 & 3 & 3 & 2 & 3 & 2 \;\cdot \\
| & | & | & | & | & | & | & | & | \\
3s- & 3d-3p- & 1s- & 2p- & & 1s+ & & 3s+ &
\end{array}
$$
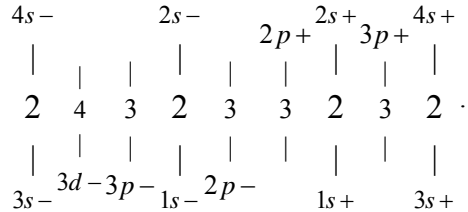
But $_{24}$Cr seems actually to be

$$
\begin{array}{cccccccc}
4s- & & 2s- & & & 2s+ & & \\
 & & & & 2p+ & & 3p+ & \\
| & | & | & | & | & | & | & \\
2 & 5 & 3 & 2 & 3 & 3 & 2 & 3 \quad \mathsf{g} \;\cdot \\
| & | & | & | & | & | & | & | \; 3s+ \\
3s- & 3d-3p- & 1s- & 2p- & & 1s+ & &
\end{array}
$$
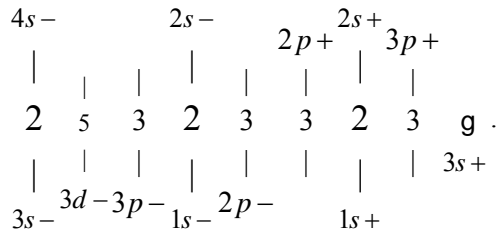
The higher-energy right-most binar ($3s+/4s+$) has been broken and cannibalized: its $4s+$ electron has been taken to complete the lower-energy $3d-$ quint. The net energy change is negative because the binar was at higher enegy than the quint is. The single $3s+$ electron left resting unstably outside the magnetic confinement region makes $_{24}$Cr obviously conductive.

The next exception is $_{29}$Cu . It is similar to $_{24}$Cr except that now it is the second quint that is being filled, and cannibalizes the same right-most binar.

The next exception is $_{41}$Nb. The situation is similar to $_{24}$Cr , with cannibalization of the rightmost binary ($4s+/5s+$) binar to improve the lower-energy $4d-$ ring from tert to quart (still not a quint though), leaving the singleton $4s+$ electron outside the confinement region, with the result that $_{41}$Nb is obviously conductive.

The next exception is $_{42}$Mo . It too is similar to $_{24}$Cr , with a cannibalization of the higher-energy $4s+/5s+$ binar, this time to complete the lower-energy $4d-$ quint, leaving the single $4s+$ electron outside, and so leaving $_{42}$Mo obviously conductive.

The next exception is $_{44}$Ru . Again the $4s+/5s+$ binary is cannibalized, this time to improve the lower-energy $4d+$ from a singleton to a binar. The single $4s+$ electron left outside makes $_{44}$Ru obviously conductive.

The next exception is $_{45}$Rh. Again the higher-energy $4s+/5s+$ binar is cannibalized, this time to improve the lower-energy $4d+$ ring from binar to tert. The single $4s+$ electron thus left outside makes $_{45}$Rh obviously conductive.

The next exception is $_{46}$Pd. This one is unique among cannibalizations. It should nominally be

$$
\begin{array}{c}
5s- \qquad\qquad 3s- \qquad\qquad 1s+ \quad\; 3s+ \qquad\qquad 5s+ \\
\qquad\qquad\qquad\qquad\qquad\qquad\quad 2p+3p+\quad 4p+3d+4d+ \\
|\quad\;\;|\;\;|\;\;|\quad|\quad|\;\;|\;\;|\quad|\;\;|\;\;|\;\;|\quad|\;\;|\;\;|\quad| \\
2\quad 5\;\;5\;\;3\quad 2\;\;3\;\;3\quad 2\;\;3\;\;3\;\;2\quad 3\;\;5\;\;3\;\;2\;\cdot \\
|\quad|\;\;|\;\;|\quad\;|\quad|\;\;|\;\;|\quad|\;\;|\;\;|\;\;|\quad|\;\;|\;\;|\quad| \\
4s-\;\;4d-3d-4p-\;_{2s-}\;3p-2p-\;_{1s-}\qquad 2s+\qquad\qquad 4s+
\end{array}
$$

But $_{46}$Pd seems actually to be

$$
\begin{array}{c}
3s- \qquad\qquad 1s+ \qquad 3s+ \\
\qquad\qquad\qquad\quad 2p+3p+\quad 4p+3d+4d+ \\
|\;\;|\;\;|\quad|\;\;|\;\;|\quad|\;\;|\;\;|\quad|\;\;|\;\;|\;\;| \\
g\quad 5\;\;5\;\;3\quad 2\;\;3\;\;3\quad 2\;\;3\;\;3\;\;2\quad 3\;\;5\;\;5\quad g \\
4s-\;\;|\;\;|\;\;|\quad|\;\;|\;\;|\quad|\;\;|\;\;|\quad|\;\;|\;\;|\;\;4s+ \\
4d-3d-4p-\;_{2s-}\;3p-2p-\;_{1s-}\qquad 2s+
\end{array}
$$

where *both* the $4s-/5s-$ and $4s+/5s+$ binars have been cannibalized to complete the $4d+$ quint, which leaves *two* singleton exterior electrons, and makes $_{46}$Pd very conductive.

The next exception is $_{47}$Ag. This time, only the $4s+/5s+$ binar is cannibalized, and that suffices to complete the $4d+$ quint. That leaves a singleton $4s+$ electron outside to make $_{47}$Ag obviously conductive.

The next exception is $_{57}$La. This one introduces a different kind of exception; not cannibalization of an existing electron ring, but rather anticipation or one to come later. $_{57}$La should nominally be

$$
\begin{array}{c}
6s- \qquad\qquad 4s- \qquad\qquad 2s- \qquad 2s+ \qquad\qquad 4s+ \qquad\qquad 6s+ \\
\qquad\qquad\qquad\qquad\qquad\qquad\qquad 2p+\quad 3p+3d+4p+\quad 5p+4d+ \\
|\qquad\quad|\;\;|\;\;|\;\;|\;\;|\;\;|\quad|\;\;|\;\;|\quad|\;\;|\;\;|\quad|\;\;|\;\;|\;\;| \\
2\quad g\;\;5\;\;3\quad 2\;\;3\;\;5\;\;3\quad 2\;\;3\;\;3\;\;2\quad 3\;\;5\;\;3\;\;2\;\;3\;\;5\;\;2\;\cdot \\
|\;\;4f-\;|\;\;|\;\;|\quad|\;\;|\;\;|\;\;|\quad|\;\;|\;\;|\quad|\;\;|\;\;|\quad|\;\;|\;\;|\quad| \\
5s-\qquad 4d-5p-\;_{3s-}\;4p-3d-3p-\;_{1s-}\;2p-\qquad 1s+\qquad\qquad 3s+\qquad\qquad 5s+
\end{array}
$$

But $_{57}$La seems actually to be

$6s-$ $4s-$ $2s-$ $2s+$ $4s+$ $6s+$

                 $2p+$ $3p+3d+4p+$ $5p+4d+$

```
 6s−        4s−              2s−      2s+                 4s+          6s+
                                    2p+    3p+3d+4p+    5p+4d+
  |    |   |   |   |   |   |    |     |    |   |   |    |   |   |    |
g 2   5  3  2  3  5  3   2    3    3   2  3  5  3  2  3  5  2
5d−  |   |   |   |   |   |   |    |    |   |   |   |    |   |   |    |
   5s−  4d−5p− 3s− 4p−3d−3p− 1s− 2p−      1s+          3s+          5s+
```

where a single exterior $5d-$ electron has replaced the single interior $4f-$ electron, and made $_{57}$La conductive.

The next exception is $_{58}$Ce. It is like $_{57}$La in that a $5d-$ electron replaces one of two $4f-$ electrons, creating a mixed $4f-/5d-$ binar.

The next exception is $_{64}$Gd. A single exterior $5d-$ electron replaces the single $4f+$ interior electron, making $_{64}$Gd conductive.

The next exception is $_{78}$Pt. This is the typical cannibalization scenario again: the $5s+/6s+$ binar is cannibalized to improve the $5d+$ ring from tert to quart, leaving a singleton $5s+$ electron outside to make $_{78}$Pt obviously conductive.

The next exception is $_{79}$Au. The $5s+/6s+$ binar is cannibalized to complete the $5d+$ quint, leaving a singleton $5s+$ outside, which makes $_{79}$Au obviously conductive.

The next exception is $_{89}$Ac. A single exterior $6d-$ electron replaces the single interior $5f-$ electron, making $_{89}$Ac obviously conductive. This is the $_{57}$La 'anticipation' scenario again.

The next exception is $_{90}$Th. It is unique among 'anticipation' scenarios: there are *two* anticipations: a *pair* of $6d-$ electrons replaces a *pair* of $5f-$ electrons. That is, $_{90}$Th should nominally be

```
  7s−                    5s−              3s−        1s+
   |  |                  |                |   |    |    |
   2  2   7   7   5   3  2  3  5   5  3  2  3   3  2  -
   |  |  |   |   |   |   |   |   |   |   |   |   |   |  |
  6s−5f− 4f−4f−5d−6p− 4s−5p−4d−3d−4p− 2s−3p−2p− 1s−

       3s+              5s+              7s+
   2p+3p+  4p+3d+4d+5p+   6p+5d+4f+     |
   |   |   |   |   |   |   |   |    |   |   |
 - 3  3  2  3  5  5  3  2  3  5  7  2  .
   |   |  |   |   |   |   |   |   |   |   |
       2s+              4s+              6s+
```

But $_{90}$Th seems actually to be

$$7s- \quad\quad\quad 5s- \quad\quad\quad 3s- \quad\quad 1s+$$

```
7s−                    5s−                    3s−          1s+
 |   |      |   |   |   |   |   |   |   |   |   |   |   |
 2   2   7   5   3   2   3   5   5   3   2   3   3   2  -
 |   |      |   |   |   |   |   |   |   |   |   |   |   |
6s−6d− 4f−5d−6p− 4s−5p−4d−3d−4p− 2s− 3p−2p−1s−

             3s+                 5s+              7s+
    2p+3p+       4p+3d+4d+5p+       6p+5d+4f+      |
     |   |   |   |   |   |   |   |   |   |   |      |
  -  3   3   2   3   5   5   3   2   3   5   7   2  .
     |   |   |   |   |   |   |   |   |   |   |      |
             2s+                 4s+              6s+
```

The next exception is $_{91}$Pa . Again we have an 'anticipation' scenario: a single exterior $6d-$ electron replaces one of three interior $5f-$ electrons, making $_{91}$Pa obviously conductive.

The next exception is $_{92}$U . An exterior $6d-$ electron replaces one four interior $4f-$ electrons, making $_{92}$U obviously conductive.

The next exception is $_{93}$Np . We have another 'anticipation' scenario: an exterior $6d-$ electron replaces one of the five interior $5f-$ electrons, making $_{93}$Np obviously conductive. This scenario is unusual in that a perfectly good quint is spoiled. That is, $_{93}$Np should nominally be

```
7s−                    5s−                    3s−          1s+
 |      |   |   |   |   |   |   |   |   |   |   |   |   |
 2   5   7   5   3   2   3   5   5   3   2   3   3   2  -
 |   |   |   |   |   |   |   |   |   |   |   |   |   |   |
6s− 5f−4f−5d−6p− 4s−5p−4d−3d−4p− 2s− 3p−2p−1s−

             3s+                 5s+              7s+
    2p+3p+       4p+3d+4d+5p+       6p+5d+4f+      |
     |   |   |   |   |   |   |   |   |   |   |      |
  -  3   3   2   3   5   5   3   2   3   5   7   2  .
     |   |   |   |   |   |   |   |   |   |   |      |
             2s+                 4s+              6s+
```

But $_{93}$Np seems actually to be

$7s-$ $5s-$ $3s-$ $1s+$

```
7s−                     5s−                  3s−         1s+
 |    |   |   |   |    |   |   |   |   |    |   |   |   |
 g  2  4  7  5  3  2  3  5  5  3  2  3  3  2  -
6d−  |  |  |  |  |  |  |  |  |  |  |  |  |  |
 6s− 5f −4f −5d −6p − 4s− 5p −4d −3d −4p − 2s− 3p −2p −1s−

        3s+              5s+              7s+
 2p+3p+     4p+3d+4d+5p+     6p+5d+4f+     |
   |   |   |   |   |   |   |   |   |   |   |
 - 3  3  2  3  5  5  3  2  3  5  7  2  .
   |   |   |   |   |   |   |   |   |   |   |
       2s+              4s+              6s+
```

The next exception is $_{96}$Cm. It is a typical 'anticipation' scenario: an exterior $6d+$ replaces the single $5f+$ electron, making $_{96}$Cm obviously conductive

Though not known yet, the next exception is likely to be $_{110}$Uun. It should nominally be

```
7s−                     5s−                  3s−         1s+
 |    |   |   |   |    |   |   |   |   |    |   |   |   |
 2  5  7  7  5  3  2  3  5  5  3  2  3  3  2  -
 |  |  |  |  |  |  |  |  |  |  |  |  |  |
 6s− 6d −5f −4f −5d −6p − 4s− 5p −4d −3d −4p − 2s− 3p −2p −1s−

        3s+              5s+              7s+
 2p+3p+     4p+3d+4d+5p+     6p+5d+4f+5f+6d+  |
   |   |   |   |   |   |   |   |   |   |   |   |
 - 3  3  2  3  5  5  3  2  3  5  7  7  3  2  .
   |   |   |   |   |   |   |   |   |   |   |
       2s+              4s+              6s+
```

But $_{110}$Uun will probably follow $_{78}$Pt, with cannibalization of the $6s+/7s+$ binar to improve the $6d+$ ring from tert to quart:

```
7s −                        5s −                    3s −            1s +
 |       |    |    |    |    |    |    |    |    |    |    |    |    |
 2   5   7   7   5   3   2   3   5   5   3   2   3   3   2  -
 |    |    |    |    |    |    |    |    |    |    |    |    |    |
6s − 6d −5f −4f −5d −6p − 4s −5p −4d −3d −4p − 2s −3p −2p −1s −

        3s +           5s +
   2p +3p + | 4p +3d +4d +5p + | 6p +5d +4f +5f +6d +
    |    |    |    |    |    |    |    |    |    |    |    |
 -  3    3    2    3    5    5    3    2    3    5    7    7    4    g   .
    |    |    |    |    |    |    |    |    |    |    |    | 6s +
        2s +                4s +
```

Or $_{110}$Uun may even follow $_{46}$Pd, with complete cannibalization of the $6s+/7s+$ binar to complete the $6d+$ quint:

```
7s −                        5s −                    3s −            1s +
 |       |    |    |    |    |    |    |    |    |    |    |    |    |
 2   5   7   7   5   3   2   3   5   5   3   2   3   3   2  -
 |    |    |    |    |    |    |    |    |    |    |    |    |    |
6s − 6d −5f −4f −5d −6p − 4s −5p −4d −3d −4p − 2s −3p −2p −1s −

        3s +           5s +
   2p +3p + | 4p +3d +4d +5p + | 6p +5d +4f +5f +6d +
    |    |    |    |    |    |    |    |    |    |    |    |
 -  3    3    2    3    5    5    3    2    3    5    7    7    5   .
    |    |    |    |    |    |    |    |    |    |    |    |
        2s +                4s +
```

The next exception will probably be $_{111}$Uuu. It will probably follow $_{79}$Au, $_{47}$Ag, and $_{29}$Cu in cannibalizing the rightmost binary, $6s+/7s+$, to complete the $6d+$ quint, and hence becoming obviously conductive.

Element $_{111}$Uuu completes the present discussion of exceptional electron configurations. We see that generally exceptions occur because any charge ring that is not yet completed can still be the wrong size for its confinement location. For example, singleton electrons are too small to be confined at all, and binars are too big even for other binars to confine very well.

5. Numerical Patterns in Ionization Potentials

It is desirable now to strive for more quantitative assessment of single-electron state energies. Experimental evidence related to such energies is available in measured ionization potentials (represented here as scalar variables, IP's). IP's represent the strength with which electrons are bound to atoms. Data are generally available for several ionization orders (as integer variables, IO's) of most elements. It is a rich database to explore. This Section reveals numerical patterns in the experimental data about ionization potentials of all elements and all orders.

Even the IP's of atoms are not yet generally understood as well as they need to be. I have been studying the problem for some years, and figure 5.1 expresses my current best understanding of it. The figure depicts the behavior of IP's for all elements (nuclear charge $Z = 1$ to $Z = 120$ shown). Element Z actually allows Z ionization potentials, but for larger Z, many IP's are not so easy to measure. Readily available data go only to seventh order, so that is how many orders are shown here.
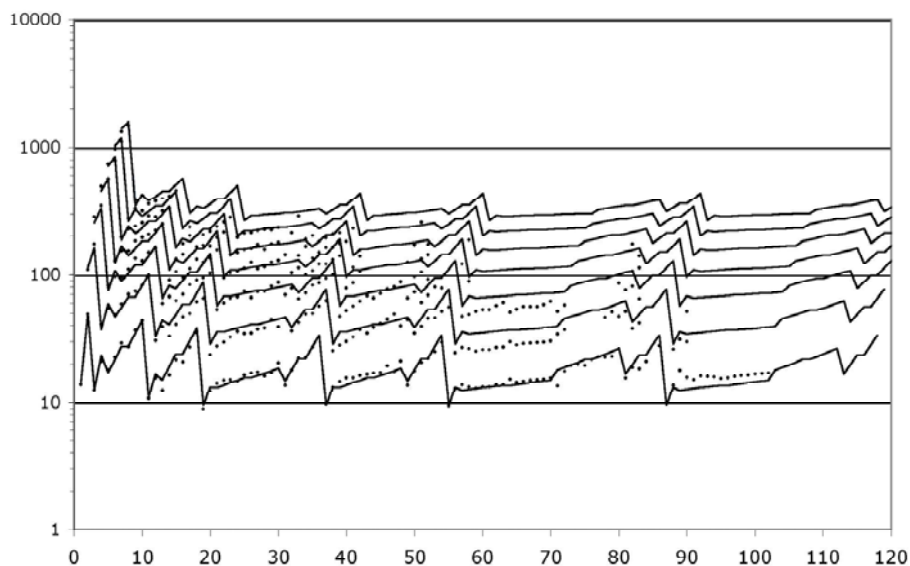
Figure 5.1. Ionization potentials, scaled appropriately and modeled algebraically.

The points on figure 5.1 are measured IP electron volts, scaled for comparison with each other as indicated by a new theory summarized in subsequent Sections of this paper. The scale factor is M / Z where M is nuclear mass number. This scale factor is in no way indicated by traditional QM. Its origin lies in the variant approach to QM explained in Appendix A3 on QM. That variant approach in turn arises in turn from the expanded development of SRT explained in the Appendix A2 on SRT, and the field directionality resolution in Appendix A1.

The lines on figure 5.1 represent my algebraic model for IP's, rendered in its current best state of development. The model is capable of producing plausible estimates for all M / Z-scaled IP's for all IO's, even beyond those measured, and all Z's, even beyond those known to exist.

The model-development approach is called 'data mining'. Figure 5.1 has less than 400 out of approximately 5000 desired data points. But that is enough data points to support the development of the algebraic model.

The work involved is a good example of continuing positive feedback between theory and experiment. Theory shows what to look for; experiment shows what to try to understand.

The first development step was fundamentally observational: for $IO = 1$, with M/Z scaling, there are consistent rises on periods, and consistent mid-period similarity to Hydrogen ($Z = 1$). For $IO > 1$, there is consistent scaling with IO. There are several ways that the scaling can be described, and the simplest way found so far is previewed as follows:

1. First-order IP's contain ALL the information necessary to predict ALL higher-order IP's via scaling.
2. Every ionization potential IP of any order IO can be expressed as a function of at most two first-order IP's.
3. For a given ionization order $IO > 1$, the ionization potentials for all elements start at element $Z = IO$, and follow a pattern similar to the IP's for $IO = 1$, except for a shift to the right and a moderation of excursions.

Details follow.

For a given value of IO, the first element that has an IP value for that IO is the element with nuclear charge $Z = IO$. This IP represents completely stripping all the electrons from the atom, thus leaving an ion fully charged to $+IO$. The IP is given by

$$IP_{IO,IO} = C \times IP_{1,1} \times IO^2 , \tag{5.1}$$

where $IP_{1,1}$ is the one and only ionization potential for atomic Hydrogen, and C is a constant factor. Incarnations of this work prior to [3] expressed my early opinion that this factor, like so many others to be revealed shortly, involved a 7, and some 2's, and therefore had to be $7/4$. I saw that the data were slightly off from $7/4$, and attributed that discrepancy to experimental error. I was wrong. I am now sure that the factor is not $7/4$; it is 2, exactly, without any discernable experimental error in the data. *Mea culpa*. The '2' shows the ongoing interplay between theory and experiment at work: looking at real data for long enough can finally open one's eyes!

The second element having an IP of order IO is the element having nuclear charge $Z = IO + 1$. This IP is given by

$$IP_{IO,IO+1} = IP_{IO,IO} + \frac{1}{2} \times IP_{1,2} \times IO . \tag{5.2}$$

Then inserting Eq. (5.1) with the value $C = 2$,

$$IP_{IO,IO+1} = 2 \times IP_{1,1} \times IO^2 + \frac{1}{2} \times IP_{1,2} \times IO . \tag{5.3}$$

Eq. (5.3) for $IP_{IO,IO+1}$ makes clear that for $Z = IO + 1$ there exists not only a contribution that scales with the quadratic IO^2, but also a contribution that scales with the linear IO. The presence of the quadratic term again suggests a physical process involving all of the IO electrons being removed. The presence of the linear term suggests a SECOND physical process, involving just the one remaining electron, perhaps a 'resettling' into a system of net charge $+IO$.

Eq. (5.3) for $IP_{IO,IO+1}$ presages the form of the IP of order IO for the third element that has one. This element has nuclear charge $Z = IO + 2$. This IP refers, not to Hydrogen, but rather to Lithium, the start of the second period in the PT/PA. It is given by

$$IP_{IO,IO+2} = \frac{1}{2} \times IP_{1,3} \times IO^2 + \frac{1}{2} \times IP_{1,3} \times IO . \qquad (5.4)$$

This IP has the same form as Eq. (5.3) for $IP_{IO,IO+1}$, but with the coefficient $1/2$ replacing the coefficient $C = 2$, and $IP_{1,3}$ replacing $IP_{1,1}$. Now we have two electrons remaining, instead of just one, as in $IP_{IO,IO+1}$. The linear 'resettling' term is essentially the same in form, as if only the net positive charge of the ion actually matters, not the individual numbers of protons or electrons.

The fourth element having an IP of order IO is the one having nuclear charge $Z = IO + 3$. The formula for that IP refers to Beryllium as well as Lithium:

$$IP_{IO,IO+3} = \frac{1}{2} \times IP_{1,3} \times IO^2 + (IP_{1,4} - \frac{1}{2} \times IP_{1,3}) \times IO . \qquad (5.5)$$

And in fact, Eq. (5.5) is just a special case of a general formula that applies for $Z = IO + 3$ through $Z = IO + 9$, or $N_{next} = N_{start} = 3$ through $N_{next} = 9$ in:

$$IP_{IO,IO+N_{next}} = \frac{1}{2} IP_{1,3} IO^2 + (IP_{1,N_{next}+1} - \frac{1}{2} IP_{1,3}) IO . \qquad (5.6)$$

The 11'th element that has an IP of order IO is that with nuclear charge $Z = IO + 10$. For that atom, and for all atoms in the period $N_{next} = N_{start} = 11$ through $N_{next} = 17$, we have

$$IP_{IO,IO+N_{next}} = \frac{1}{2} IP_{1,11} IO^2 + (IP_{1,N_{next}+1} - \frac{1}{2} IP_{1,11}) IO . \qquad (5.7)$$

Every subsequent period is like that. We always have:

$$IP_{IO,IO+N_{next}} = \frac{1}{2} IP_{1,N_{start}} IO^2 + (IP_{1,N_{next}+1} - \frac{1}{2} IP_{1,N_{start}}) IO , \qquad (5.8)$$

where $N_{\text{start}} = 3, 11, 19, 37, 55, 87, ...$

Figure 5.1 shows that the weakest area of the model for higher order IP's in terms of first-order IP's is its fit to second-order and third-order IP's for elements in the sixth and seventh periods. Because the model works so well elsewhere, it is natural to scrutinize those points especially closely for clues to the mismatches there. It may be important that the reported second- and third-order IP's there are very close to 2 and 3 times the corresponding first-order IP's. It is possible that the physical process that produced the data was actually different from what was intended: coincident production of multiple atoms each singly-ionized instead of production of a single atom multiply-ionized.

The algebraic model gives an exceedingly prominent role to terms in squared ionization order, IO^2. This raises a question to face head on. When one speaks of ionization at order IO, should one imagine removal of one more electron from a previously prepared ion of charge $+IO - 1$? Or should one imagine removal of IO electrons all at once? Some may favor the former vision because it fits with theory we have been taught. But having seen all the data, with its prominent IO^2 scaling, I now believe the latter vision absolutely.

Overall, the model for for higher order IP's in terms of first-order IP's seems to convey a simple message: Evidently, the typical IP of order IO involves THREE physical processes:

1. Removal of IO electrons from an atomic system, which is thereby left with net positive charge of $+IO$. The energy required for this process must scale with IO^2. So it has to be the term $\frac{1}{2} IP_{1, N_{\text{start}}} IO^2$ in Eq. (5.8).

2. But before that must come removal of IO electrons from the atom's electron population, which will then be left with $Z - IO$ electrons. The energy required for this process must depend on the specific Z, which enters Eq. (5.8) only through the variable N_{next}. So it has to be the term $IP_{1, N_{\text{next}}+1} IO$ in Eq. (5.8).

3. There must also be reconstruction/reinstallation of the smaller population of $Z - IO$ electrons. As the reverse of destruction/removal, the energy 'required' for this process is negative. So it has to be the term $-\frac{1}{2} \times IP_{1, N_{\text{start}}} IO$ in Eq. (5.8).

The first two IP's of any order $IO > 1$ are not quite typical. The general case is Eq. (5.8), but for total ionization, $IP_{Z,Z} = IP_{IO,IO} = \underline{2} \times IP_{1,1} \times IO^2$ [Eq. (5.1) with C correctly set at 2], and for removing $IO - 1$ electrons, thus leaving just one electron, $IP_{Z-1,Z} = IP_{IO,IO+1} = \underline{2} \times IP_{1,1} \times IO^2 + \frac{1}{2} \times IP_{1,2} \times IO$ [Eq. (5.3)]. Why are the underlined factors $\underline{2}$ instead of $1/2$? Observe that Hydrogen is exceptional: it has no electron-electron interactions. So only process 1 exists; there is no Process 2 or Process 3. So Hydrogen's $IP_{1,1}$ is deficient in information as a period-start reference for other more normal elements. Observe that the general sum of the absolute coefficients in Eq. (5.8) is $1/2 + 1 + |-1/2| = 2$.

This suggests that Hydrogen's information needs to be scaled up by 2 rather than down by $1/2$ in the IO^2 terms for the first two IP's of order IO.

These comments complete the demonstration that first-order IP's contain ALL the information necessary to predict ALL the higher-order IP's via scaling laws.

We come now to the problem of the input first-order IP's themselves. As shown on figure 5.1, first-order IP's exhibit consistent rises on periods, and consistent mid-period similarity to Hydrogen. The rise factors are all $7/2$. After the first three periods, the period maxima are all similar to each other, and the period minima are all similar to each other, and the period mid regions are all similar to Hydrogen. Figure 5.2 details these facts.

Observe that the neighboring IP's are connected to each other by scale factors, such as $7/2$, $1/4$, $7/8$, *etc*. These scale factors correspond to alternate and redundant paths through the data. The path actually used in the excel program that created figure 5.1 is indicated by the scale factors that are displayed in bold font.

	$_1$H	$IP_{1,1} = 13.72$	→ **7/2** →	$49.24 = IP_{1,2}$	$_2$He	
7/8	↓	[	← **1/4** ←	[	↓	7/8
	$_3$Li	$IP_{1,3} = 12.48$	→ **7/2** →	$43.56 = IP_{1,10}$	$_{10}$Ne	
7/8	↓	[	← **1/4** ←	[	↓	7/8
	$_{11}$Na	$IP_{1,11} = 10.75$	→ **7/2** →	$35.01 = IP_{1,18}$	$_{18}$Ar	
7/8	↓	[	← **1/4** ←	[	↓	7/8
	$_{19}$K	$IP_{1,19} = 8.94$	→ **7/2** →	$32.62 = IP_{1,36}$	$_{36}$Kr	
1	↓		← 2/7 ←		↓	1
	$_{37}$Rb	$IP_{1,37} = 9.66$	→ **7/2** →	$29.51 = IP_{1,54}$	$_{54}$Xe	
1	↓		← 2/7 ←		↓	1
	$_{55}$Cs	$IP_{1,55} = 9.42$	→ **7/2** →	$27.77 = IP_{1,86}$	$_{86}$Rn	
1	↓		← 2/7 ←		↓	1
	$_{87}$Fr	$IP_{1,87} = ?.??$	→ **7/2** →	$??.?? = IP_{1,118}$	$_{118}$??	

Figure 5.2. First-order IP's: map of main highways through the periods.

The consistency of the rises of $7/2$ can be appreciated, if not fully understood, as a manifestation of periodicity: all periods in the PT/PA are fundamentally similar. The numerical value $7/2$ can be understood in relation to the already noted connections between IP's of order 1 and those of higher order $IO > 1$. The expression

$$IP_{1,2} = \frac{7}{2} IP_{1,1} \qquad (5.9a)$$

can be written

$$IP_{1,2} = 2 \times IP_{1,1} \times 2 \times 1 + (0 - \frac{1}{2} IP_{1,1}) \times 1 \qquad (5.9b)$$

or

$$IP_{IO,1+IO} = 2 \times IP_{1,1} \times (IO+1) \times IO + (0 - \frac{1}{2} IP_{1,1}) \times IO \tag{5.9c}$$

with $IO = 1$, which for general IO resembles Eq. (5.8) except for the following differences:

1. The factor of 2 instead of the factor $1/2$, which any reference to Hydrogen requires;

2. The factor $(IO+1) \times IO$ in place of the IO^2 factor, which is appropriate because Helium has nuclear charge $Z = 2 = IO + 1$;

3. The zero in place of $IP_{1,N}$, which is appropriate because there exists no input $IP_{1,2}$ to use.

All of this suggests that the connections between first IP's of different elements resemble the connections between IP's of different orders. This suggests in turn that all IP's of all orders can ultimately be related back to Hydrogen. However, there exist many more details to specify. Within the periods beyond the first one, the rise is nowhere steady; there is a lot of detailed structure in the IP plots. On the log scale of figure 5.1, there appear to be straight-line runs interrupted by discontinuities. The straight-line runs are associated with the nominal blocks of the traditional angular momentum quantum number l. Every straight-line run is characterized by:

1. A total rise over the run, and
2. An intercept with the 'main-highway' straight line through the period.

The rise appears to be a function of the parameter $N = 1,2,2,3,3,4,4$ that belongs to the period, and the angular momentum quantum number l that varies within the period from 0 to $N-1$. The rise for $l = 0$ is just the full period rise for $N = 1$, and for $N > 1$ it appears to decline with each period. The sequence plotted in figure 5.1 is $1,1/2,1/3,1/4$, with $1/4$ repeated thereafter.

The rise for $l > 0$ offers a lot more data to support a choice of model. The following function was developed for use in figure 5.2 for all $l > 0$:

$$\text{incremental rise} = \text{total rise} \times \text{fraction}, \tag{5.10a}$$

where

$$\text{fraction} = \left[(2l+1) / N^2 \right] \left[(N-l)/l \right]. \tag{5.10b}$$

The first factor in square brackets is just the ratio of the multiplicity of l states, $2(2l+1)$, to the period length, $2N^2$. The second factor, $(N-l)/l$, captures the real variability in slopes. Figure 5.3 gives the overall fraction for all N,l pairs of interest.

N	period	l	fraction	l	fraction	l	fraction	l	fraction
1	1	0	1						
2	2	0	$1/2$	1	$3/4$				
2	3	0	$1/3$	1	$3/4$				
3	4	0	$1/4$	2	$5/18$	1	$2/3$		
3	5	0	$1/4$	2	$5/18$	1	$2/3$		
4	6	0	$1/4$	3	$7/48$	2	$5/16$	1	$9/16$
4	7	0	$1/4$	3	$7/48$	2	$5/16$	1	$9/16$

Figure 5.3. First-order IP's: map of local roads through the periods.

The intercepts for $l=0$ and $l=1$ are fixed by the period boundaries: the first $l=0$ point is tied to the period start, and the last $l=1$ point is tied to the period end. The intercepts for $l=2$ and $l=3$ are set at the midpoints of those runs. Because $2(2l+1)$ is an even number, midpoints fall between elements. The data often shows some type of discontinuity at run midpoints (where the spin quantum number s changes sign). For the model, the IP's just above and below these mid points are set equal, making a tiny flat spot on the plotted curves on figure 5.1.

Figure 5.1 shows that the weakest area of the model fit to first-order IP's is in the seventh period, in the Actinide series. The model is systematically low in comparison to the first order IP data there. The present study on single-electron state filling order may help explain why this happens.

It is often assumed that when ionization occurs, what gets removed from the mix of single-electron states is a state that has the largest n radial quantum number involved, and so seems to be on the 'outside' of the atomic system. This is certainly true for elements that begin periods: $_1$H, $_3$Li, $_{11}$Na, $_{19}$K, $_{37}$Rb, $_{55}$Cs, $_{87}$Fr. It has to be true for $_2$He and $_4$Be too. It is probably true for $_{12}$Mg, $_{20}$Ca, $_{38}$Sr, $_{56}$Ba, and $_{88}$Ra. But it may not be true in general.

Nor is it necessarily true that the single-electron state that gets deleted is the last one added. For example, in the d runs of Periods 4 and 5, there are many d for s replacements in building the atoms, so there might also be such replacements in ionizing them. For example, $_{30}$Zn might give up a d state rather than the s state added last, because the two s states now present are like a Cooper pair, which is very resistant to parting, as $_2$He shows us, whereas the 10 d states present are only like a Cooper pair when all taken together, so that removing just one d state should be less difficult – apparently by a factor of about $2/5$.

Just before $_{30}$Zn, $_{29}$Cu tells the opposite sort of story: $_{29}$Cu has one of those anomalous d-for-s replacements, and as a result, it has just one s state present, which it readily gives up for ionization.

In short, complications in the single-electron state filling story lead to complications in the story about IP's. In the Period 7 Actinide series, there are many d-for-f replacements present. Suppose 'splitting' due to magnetic effects sends a d state down and an f state up in energy, resulting in the replacement, and then ionization results in deletion of the d state. The algebraic model does not know about this complication, so it somewhat underestimates this anomalous data point.

More generally, the obvious regularities present in the mass of IP data seem to be trying to tell us something. It remains our duty to figure out more of what the message really is. Some further ideas are discussed in the last of the Appendices, which is devoted to spectroscopy.

6. Comments on Chemical Periodicity

This paper has so far discussed two manifestations of 'periodicity'. Sect. 3 discussed the nominal pattern for single-electron state filling in terms of superluminal spinning charged rings and magnetic confinement thereof. The resulting model shows a structural manifestation of periodicity. It gives some clues for understanding the exceptions that do occur, as discussed in Sect. 4. Section 5 then identified the nominal pattern for ionization potentials of all elements and all ionization orders, and noted that slight departures correlate with exceptions in single-electron state filling. The basic pattern in the ionization-potential data is a physical manifestation of periodicity.

We turn now to the heart of Chemistry: *chemical* periodicity. The development of the Mendeleev's Periodic table (PT), based on chemical periodicity, marks the beginning of a real science. The PT has been the fundamental organizing tool for all of Chemistry. Eric Scerri documents the extensive history of PT development, and our present understanding of its significance, in [6].

The existence of chemical periodicity has long been considered a mystery. People have imagined electron shells nested around the nucleus of an atom, and supposed that the number of electrons in the outermost shell determines the chemical properties. This idea is useful for smaller atoms, but becomes cumbersome and unhelpful for larger ones. Just consider that periods 6 and 7 have 32 members each, suggesting outer shells of 32 electrons each. Are there as many as 32 distinguishable chemical behaviors?

My own opinion is that chemical periodicity correlates better with the structural periodicity and the physical periodicity discussed in earlier Sections of this paper. That is, the sizes and positions of spinning charged rings correlate with chemical properties, just as do the patterns in ionization potentials.

Since the structural periodicity is all about filling spinning charged rings, the chemical behavior may well have more to do with what is *absent* than with what is *present*. For example, any element a few electrons short of a 'quint' will strongly seek those few electrons. Indeed, Section 4 showed many instances of self-cannibalization of 'binars' in those cases. Conversely, any element with only one or a few of the electrons needed to fill the currently

filling ring will strongly seek to lose those electrons. The quantitative meaning of 'strongly' has to do with ionization potentials, as described in the next Section.

In preparation for that, we need a purpose-built version of the iconic visual display concerning chemical periodicity: the Periodic table. The goal of organizing the elements according to chemical properties, like valence, has previously produced the wheels, spirals, helixes, three-dimensional pretzels, conics, trees, and more, collected and richly displayed by Spronsen [7]. The goal of organizing the elements according to shell structure or electron configuration has produced some more linear types of displays, which are generally favored by Mazurs [8]. These have elements arranged in columns for chemical similarity.

I like the idea of using an architectural metaphor in general, but not the column metaphor in particular. As the PT has grown to accommodate more and more newly discovered elements, the columns have come to include some very short ones to the center left, where the Lanthanide and Actinide series must go. Being unable to support any metaphorical 'roof' of all-encompassing understanding, those columns are generally stored away in the 'basement' (footnotes), to be remembered and retrieved as needed by the user. This is awkward.

My preferred remedy for the situation is to change the architectural metaphor: instead of thinking 'columns', think 'arch'. Figure 6.1 shows the 'Periodic Arch' (PA). Some information appears in red, for reasons to be explained next.

Any architectural metaphor naturally attracts one's attention to the idea of a 'foundation'. The foundation of the PA is the red information along the bottom of the arch: the N parameter, the arch layer lengths L, and the noble gasses and their atomic numbers Z_{noble}:

$$L = 2N^2 \text{ for } N = 1, 2, 2, 3, 3, 4, 4, ...,$$
$$Z_{noble} = \sum_N L(N) = 2, 10, 18, 36, 54, 86, 118, ... \quad (6.1)$$

Although actual element discovery is presently only up to $Z = 112$, one can anticipate that the pattern identified will be followed by any heavier elements that may be found in the future. Should we ever reach and progress beyond $Z = 118$, we will be into the regime of $N = 5$ and $2N^2 = 2(5)^2 = 50$, and so on, according to the pattern.

While the pattern, $2N^2$ for $N = 1, 2, 2, 3, 3, 4, 4, ...$, was also detectable in the rows of the traditional PT, it was rather hidden there because of the confusing footnotes for insertions. Mingos [9] noted the numbers, and described them by an algebraic formula (numerically equivalent though formally different), but did not pursue a deeper meaning. Siekierski & Burgess [10] discussed in some detail the believed reasons why each atom turns out the way it does, but not why the overall pattern is what it is.

The arch metaphor further draws one's attention to the idea of 'keystone'. The keystones in the PA are the red elements up the middle of figure 6.1: starting with Hydrogen, and above it Carbon, Silicon, Cobalt, Rhodium, Ytterbium, and Nobelium. These keystone elements play an important role in chemical bonding, discussed next.

101Md 102No 103Lr
100Fm 104Rf
99Es 69Tm 70Yb 71Lu 72Hf 105Db
98Cf 68Er 73Ta 106Sg
67Ho 74W
97Bk 66Dy 75Re 107Bh
96Cm 65Tb 45Rh 76Os 108Hs
95Am 64Gd 44Ru 46Pd 77Ir 109Mt
94Pu 63Eu 43Tc 27Co 47Ag 78Pt 110Uun
93Np 62Sm 42Mo 26Fe 28Ni 48Cd 79Au 111Uuu
92U 61Pm 25Mn 29Cu 80Hg 112Uub
60Nd 41Nb 24Cr 30Zn 49In
91Pa 59Pr 40Zr 23V 14Si 31Ga 50Sn 81Tl 113??
90Th 58Ce 39Y 22Ti 13Al 6C 15P 32Ge 51Sb 82Pb 114??
89Ac 57La 21Sc 12Mg 5B 7N 16S 33As 52Te 83Bi 115??
88Ra 56Ba 38Sr 20Ca 4Be 1H 8O 34Se 84Po 116??
87Fr 55Cs 37Rb 19K 11Na 3Li $N=1$ 9F 17Cl 35Br 53I 85At 117??
2He 10Ne 18Ar 36Kr 54Xe 86Rn 118??

$N=4$ | $N=4$ | $N=3$ | $N=3$ | $N=2$ | $N=2$

$L=32$ | $L=32$ | $L=18$ | $L=18$ | $L=8$ | $L=8$ | $L=2$ | $L=2N^2$ | $Z=\Sigma L\text{'s}=2,10,18,36,54,86,118$

Figure 6.1. The Periodic Arch (PA).

7. Comments on Chemical Bonds

The foundation algebra and the keystone elements of the PA turn out to be useful for developing comments on the nature of chemical bonds. We know that some molecules tend to be stable, whereas some tend to be highly reactive. For example, some simple dimers, like H_2 or $NaCl$, *etc*., may escape into air, or dissolve and dissociate in water, but they will not react explosively without a spark or catalyst of some kind. But some monomers, like atomic Hydrogen and metallic sodium, are more risky. The present understanding for these simple cases is often phrased in terms of 'complete' and 'incomplete' electron 'shells', which are said to surround atoms. But what should be said about larger molecules, with many atoms in them? Evidently, molecules that are relatively stable must have strong chemical bonds throughout, and molecules that are strongly reactive must have some weak chemical bonds somewhere. In order to extend the somewhat limited 'shell' understanding to larger molecules, consider the following more general candidate statement:

> **Proposition 1:** Molecules that are relatively stable have total electron counts such that every atom present can be assigned an electron count equal to that of a noble gas, or else zero.

The proposition is saying that chemical bonding has less to do with pair-wise connection between individual atoms, and more to do with molecule-wide collective status of all atoms.

The means for improving collective status is redistribution of electron resources. The idea is that electrons are like cash money: they are totally fungible – even more so than cash money, since they have no serial numbers or other individually distinguishing characteristics. Atoms are like citizens of a society: they aspire to some recognized status that has something to do with sense of wealth: either 'noble gas' (possessing a comfortable number of electrons), or else 'priestly class' (needing no worldly electrons at all). Strong bonding is about attending to every atom present. If that goal can be achieved, then the molecule can have a population of well-satisfied atoms, constituting a relatively stable society.

The reader can readily verify that Proposition 1 is satisfied by the simple dimers like H_2, NaCl, *etc*., as well as water H_2O, CO_2, and many other simple trimers. Table 7.1 gives a half dozen of the increasingly complex other examples that prompted the articulation of Proposition 1. There exist many more examples; there are, for example, many hydrocarbon fuels, and so far all of them examined do have electron counts that can be redistributed in the way that Proposition 1 describes. Maybe the stability thus implied is why the hydrocarbon fuels are commercially viable.

Table 7.1. Electron redistributions in relatively stable molecules to give to all of the atoms an electron count equal to that of a noble gas, or else zero

Name	Chemical formula	Electron contributions	Electron redistributions
Ammonia	NH_3	N : 7, H 's: 1 each total 10	N : 10, H 's: all 0 total 10
Sodium hydroxide	NaOH	Na : 11, O : 8, H : 1 total 20	Na : 10, O : 10, H : 0 total 20
Potassium carbonate	K_2CO_3	K 's: 19 each, total 38 O 's: 8 each, total 24 C : 6; total 68	K 's: 18 each; total 36 O 's: 10 each, total 30 C : 2; total 68
Bornyl acetate	$CH_3CO_2C_{10}H_{17}$	C 's: 6 each, total 72 H 's: 1 each, total 20 O 's: 8 each, total 16 total 108	C 's: 6@2, 6@10; total 72 H 's: 8@2, 8@0, total 16 O 's: 10 each, total 20 total 108
Lead acetate	$(CH_3CO_2)_2Pb \cdot 3H_2O$	C 's: 6 each, total 24 H 's: 1 each, total 12 O 's: 8 each, total 56 Pb : 82; total 174	C 's: 2 each: total 8 H 's: 5@2, 7@0, total 10 O 's: 10 each, total 70 Pb : 86; total 174
Calcium stearate	$(C_{17}H_{35}CO_2)_2Ca$	C 's: 6 each; total 216 H 's: 1 each, total 70 O 's: 8 each, total 32 Ca : 20; total 338	C 's: 18@10, 18@2, tot. 216 H 's: 38@0, 32@2, total 64 O 's: 10 each, total 40 Ca : 18; total 338

Observe in table 7.1 that the noble-gas number (or zero) assigned to each atom is generally for the noble gas (or zero) as close as possible to that element. Observe that the 'keystone' elements are all special, being equidistant from *two* noble gasses, or in the case of Hydrogen, equidistant from a noble gas and a priestly-class 0. An equidistant condition allows two choices of electron reassignment. The equidistant condition of Hydrogen perhaps explains something mysterious observed in deep space. Evidently, any Hydrogen atom would

want either to form a Hydrogen molecule (2 electrons total), or if that were not possible, then to dissociate and form plasma (proton with no electron). Plasma is indeed frequently observed in deep space. The amazing possibilities for Carbon-Carbon bonds are well known (chains, rings, sheets, tubes, balls…life…), and seem likely to trace to its special equidistant condition. Silicon is known to be very similar to Carbon, and the other keystone elements may also turn out to be more similar than is presently recognized.

Sometimes, the condition specified in Proposition 1 cannot be achieved. For example, it cannot be achieved for any molecule that has an electron count that is an odd number. Also, it cannot be achieved for some atmospheric gasses, such as O_2, O_3, or NO. These molecules are often rather highly reactive. These situations prompt one to consider a second candidate statement that is the converse to Proposition 1:

> **Proposition 2:** Molecules that are highly reactive have total electron counts such that *not* every atom present can be assigned an electron count equal to that of a noble gas, or else zero.

The kinds of molecules that prompt the statement of Proposition 2 invite some further discussion of the 'society' of atoms. We have so far identified the 'priestly class': $_1H$, with no electrons needed, and the 'noble gasses': $_2He$, $_{10}Ne$, $_{18}Ar$, $_{36}Kr$, $_{54}Xe$, $_{86}Rn$, $_{118}?$, with period-finishing electron counts. There is also a somewhat less prestigious 'gentry class' with sub-period-finishing electron counts: $_4Be$, $_{12}Mg$, $_{20}Ca$, $_{38}Sr$, $_{56}Ba$, $_{88}Ra$; $_{30}Zn$, $_{48}Cd$, $_{80}Hg$, $_{112}?$; $_{70}Yb$, and $_{102}No$,. Then we have a hard-working 'middle class' with electron counts that finish the first half of a sub-period: $_7N$, $_{15}P$, $_{33}As$, $_{51}Sb$, $_{33}Bi$; $_{115}?$; $_{43}Tc$, $_{75}Re$, $_{107}Bh$; $_{63}Eu$, and $_{95}Am$,. Nitrogen is a typical middle-class element; for example, it imposes some moderation on Oxygen. Oxygen is from the remaining 'feckless mass': subject to rearrangements and exceptions of the sort documented in Section 4, plus other alarming behaviors. For example, Oxygen burns things. Finally, drawn from almost the whole of this diverse society, we have a peace keeping police force of 'keystone elements': $_1H$, $_6C$, $_{14}Si$, $_{27}Co$, $_{45}Rh$, $_{70}Yb$, $_{102}No$; these 'keystone cops' include priests, gentry, and feckless individuals, all working together for molecular stability.

Both Propositions stated about molecules are fundamentally qualitative in nature. The data about ionization potentials can now be enlisted to provide quantitative backup for the Propositions. For example, consider for example the reaction $CH_4 + 2O_2 \rightarrow CO_2 + 2H_2O$. The methane CH_4 is a stable molecule with 6 electrons from the Carbon atom and 1 from each Hydrogen atom, for a total of 10 electrons, admitting the reassignments 10 to Carbon, none to any Hydrogen. The Carbon becomes like the noble gas $_{10}Ne$, with M/Z-scaled first $IP_{1,10}$ of 43.64eV. The four H's enter the 'priestly class', and have no associated IP. The two oxygen molecules are both unstable, with 16 electrons total. They cannot make any fully noble-gas reassignment. The best they can achieve is 10 electrons to one Oxygen atom, 6 electrons to the other. That makes one oxygen atom like $_{10}Ne$ at scaled IP of 43.64eV,

and the other like $_6C$, at 21.57 eV. The total for each oxygen molecule is 65.21 eV. On the other side of the reaction, CO_2 is a stable molecule with 22 electrons, admitting the reassignment of two electrons to the Carbon atom, ten to each Oxygen atom. That makes the Carbon atom like $_2He$, at 49.875 eV, and each Oxygen atom like $_{10}Ne$, at 43.64 eV. The two water molecules are stable, with a total of 10 electrons each, all reassigned to the Oxygen atom, which thereby becomes like $_{10}Ne$ at 43.64 eV. The sum on the left side of the reaction is $43.64 + 2 \times 65.21 = 174.06$ eV. The sum on the right side of the reaction is $49.875 + 4 \times 43.64 = 224.435$ eV. The larger sum on the right is a quantitative reason for the fact that the reaction goes to the right. The amount of the excess correlates with the energy produced, although there remains Z/M scaling to be re-introduced in some appropriate way to specify that energy numerically.

8. Conclusion

If science is to have the firmest foundation possible, no stone potentially useful for that foundation can be left unturned. An important stone was left unturned during the time that the world possessed Maxwell's electromagnetic theory, but did not fully possess the mathematical tools necessary to explore all of its implications; tools such as linear system theory (Fourier transforms) and generalized functions (Heaviside step, Dirac delta). The problem concerns the propagation of a finite-energy packet of light, like a photon.

The theory and proper use of generalized functions occasioned many years of debate, mainly because any representation for them, whether by a parameter that goes to infinite value, or by Fourier integrals, or sums, that go to infinite limits, lacks the normal and usual mathematical property of 'uniform convergence'. (The term 'uniform convergence' would mean that one could set an arbitrarily small error limit, and guarantee that some finite parameter value, or integral limit, or sum limit, would meet the error limit everywhere. No such luck here. The unavoidable penalty is that familiar math operators, like integration, differentiation, and limit, cannot be trusted to commute.)

No risky operator commutations are involved in the analysis given here, so one has to wonder: Why was this analysis not done a century ago, and well remembered today? The work of Oliver Heaviside was vital for the wide adoption of Maxwell theory, because he developed the modern vector notation for it. He is also credited with the idea of the 'step function', which involved in the present analysis? So why didn't he do this analysis, or if he did, why isn't it remembered today? Perhaps his mind was 'compartmentalized': the 'Maxwell-equation' physics mind not communicating with the 'step-function' engineering mind. Or perhaps, like many useful things, it was forgotten.

Too late to restrain the excesses of SRT or QM, generalized functions finally became familiar enough for routine use, most often in modern engineering science, sometimes in physics, although not always correctly, engineers would argue. In particular, in electromagnetic theory, the generalized functions have been used to 'modernize' the derivation of an early application of Maxwell theory, the Liénard-Wiechert potentials and fields. Although the end results comport with the original derivations, the reader will find many risky operator exchanges involved in getting to those results.

The fact is: the original Liénard-Wiechert results, and many related results involving high relative speeds produced by Einstein's SRT, embed an assumption that contradicts Maxwell theory. That assumption concerns the 'speed of light'. The assumption has been overly simple: just 'c'. The Maxwell analysis given here suggests something more complicated. That makes the foundation for an otherwise questionably postulate-based tower of theoretical development that is summarized in the Appendices. The first Appendix shows how the Liénard-Wiechert results change. The next articulates and illustrates the natural history of a photon through emission, expansion, encounter with a candidate receiver, contraction, and absorption by this receiver. Two Step Light then provides a foundation for an expanded version of SRT, a 'covering theory' for Einstein's SRT. Since expanded SRT contains Einstein's SRT, researchers who are happy with SRT need not sacrifice anything. But researchers who need something more can perhaps find what they need in the expanded SRT.

Most notably, through the expanded SRT, Two Step Light leads to an expanded version of QM. We need not postulate the value of Planck's constant, or the nature of its involvement in the mathematics of 'probability' waves, *etc*. Planck's constant can be an output *from*, rather than an input *to*, the expanded QM. It comes from the model for a Hydrogen atom with its single proton and its single electron in balance through two competing effects: the well-known loss or energy through radiation, and the newly exposed gain of energy from internal torquing within the system.

The approach for expanded QM resembles the early Thomas-Fermi approach, and the more recent density-functional approaches, in the sense that it seeks a universal solution, particularized to individual elements by scaling laws. But the approach for expanded QM differs from those other approaches, in that it does not use a spatial density function, or involve any spatial integration to estimate any values of any variables. All it uses is algebra. Results include 'sub-states' for Hydrogen and other atoms, plus 'spinning electron rings' to form 'charge clusters'. This charge cluster idea brings within reach some new approaches for fundamental problems in Chemistry. The basic idea is that all atoms resemble Hydrogen, except with a more positive and heavier nucleus instead of a proton, and an electron cluster instead of a single electron.

Thus the expanded QM leads to 'Algebraic Chemistry'. Some results from the main part of the paper are summarized and commented as follows:

- We have a way of thinking about single-electron state filling across the elements. It is all about building an orbiting charge cluster from super-luminal spinning rings of electrons in successively larger electron counts and smaller geometric extent, each magnetically confined between geometrically larger, lower electron-count rings. The process might well be described as 'fractal'.
- We also have a way of thinking about the exceptions to nominal single-electron state filling order that occur for about 20% of elements. They have to do with incomplete electron rings being the wrong size: single electrons too small, and able to escape along the axis of the confining rings, or low-electron count rings being too geometrically large to fit where they belong.
- The charge-cluster model for electron populations offers some explanation for the otherwise totally mysterious Hund's rule: fill all of one spin state first, then the other. The mystery is that when paired, opposite spin electrons seem to make a stable configuration (a Cooper pair), so why doesn't Nature fill atomic spin states in

alternating order? The explanation offered by the present model is that an electron ring that is more filled, which makes it geometrically smaller, so that it can be well confined magnetically, is more stable than two less-filled, geometrically-larger rings, which are hence not so well confined magnetically.

- We have an algebraic model for ionization potentials, *IP*'s. This model is synoptic: it extends to all possible elements and all possible ionization orders. It shows that there exists repeated sameness of ionization potentials from period to period, and it has to do with the sameness of the electrostatic attraction between a positive nucleus and a negative electron cluster. There also exist clear differences between ionization potentials from atom to atom within a period, and it has to do with the difference between the electron clusters that the atoms have.

- The *IP* model could be important and useful in a practical way. For example, there exist some really 'bad actors' among the known elements - think of Plutonium, Polonium, Thallium, or Uranium. There are also some very short-lived elements beyond Uranium. Supposing that there exists some good reason to know more about these dangerous and difficult elements, it is a good thing to have a single, safe and reliable model, instead of many dangerous and difficult experiments, to estimate all their ionization potentials.

- We have a way of thinking about chemical periodicity. It has to do with recurrent situations that occur in the filling of spinning electron rings in the atomic electron cluster. In short, the chemical character of an element has more to do with what is present in, or what is absent from, the spinning electron ring that is currently being filled than with any characterization in terms of a nucleus surrounded with 'electron shells' (which the present author doesn't believe in).

- We also have a purpose-built new display format for the Periodic Table (PT); namely, the Periodic Arch (PA) The historically numerous revisits to the PT do express the strong tradition in science for looking at the same, known, information again and again, but arranged in a variety of different ways. This sort of exercise is important for scientists to do, and *keep* doing, regularly. Experience has shown over and over that looking at any information from a different angle can reveal aspects of that information not consciously noted before, and so can trigger new and interesting insights and new questions to ask. The PA invites one to pay attention to 'keystone' elements, which facilitate chemical bonding by being equally able to give or take electrons.

- We have a way of thinking about chemical bonding that is holistic: not about individual atom-to-atom connections, more about molecule-wide conditions. It appears that all bonding between atoms in a molecule, however complex that molecule may be, does involve reassignment of electrons, described by the offered Propositions 1 and 2.

- Any reassignment of electrons gives the individual atoms a net charge. It would then appear that, while electron populations in atoms are held together magnetically, atoms overall are held together in molecules by electrostatic forces.

- Bond strengths must have some correlation with ionization potentials of the elements corresponding to the reassigned electron counts. We have gotten far enough with that idea to see what direction a reaction goes. We still need to detail further how to calculate exact reaction energies.

- There is a great deal of other work yet to be done too. The presentation of the algebraic model in [3] prompted the Guest Editor Prof. Dr. Mihai V. Putz to call my attention to his related works [11-13]. Ref. [11] reveals, like the present work does, energy increments that are linear and quadratic in electron numbers. Reaction energies of 'hard acid' (H^+) and 'soft acid' (HO^+) with 'hard base' (OH^-) and 'soft bases' (many kinds exist) are studied in [12]. They, and other reaction energies, must be related to the *IP* data here codified in terms of the PT/PA. Trends across the PT/PA are addressed for electro-negativity and hardness in [13]. I believe there exists much related data here to be further mined!

Just for one more example, there exists a whole body of work in mathematics, especially topology and structural analysis, by my colleague Don Briddell [14], and it all looks potentially useful for thinking about complicated orbits traversed by electron clusters in molecules.

Appendices

The following Appendices provide the path through theoretical physics that leads from the Maxwell analysis to the practical chemistry applications featured in the main part of this paper. We begin at a point in time late in the 19th century and work forward.

A1. Retarded Potentials and Fields

Maxwell's equations contain the free-space electric permittivity ε_0 and magnetic permeability μ_0, which together imply a light speed c. Einstein stated this fact in a formalized way as his famous Second Postulate, but it was known and used well before that. One early use was in the now-standard expressions for electromagnetic potentials and fields created by rapidly moving sources. These were developed in the works of Liénard (1898; [15]) and Wiechert (1901; [16]).

Expressed in Gaussian units [17], the Liènard-Wiechert scalar and vector potentials are:

$$\Phi(\mathbf{x},t) = e\left[1/\kappa R\right]_{\text{retarded}} \text{ and } \mathbf{A}(\mathbf{x},t) = e\left[\boldsymbol{\beta}/\kappa R\right]_{\text{retarded}}, \qquad (A1.1a)$$

where $\kappa = 1 - \mathbf{n}\cdot\boldsymbol{\beta}$, with $\boldsymbol{\beta}$ being source velocity normalized by c, and $\mathbf{n} = \mathbf{R}/R$ (a unit vector), and $\mathbf{R} = \mathbf{r}_{\text{observer}}(t) - \mathbf{r}_{\text{source}}(t - R/c)$ (an implicit definition for the terminology 'retarded'). The Liènard-Wiechert fields expressed in Gaussian units are then

$$\mathbf{E}(\mathbf{x},t) = e\left[(\mathbf{n}-\boldsymbol{\beta})(1-\beta^2)\Big/\kappa^3 R^2 + \mathbf{n}\times\left((\mathbf{n}-\boldsymbol{\beta})\times d\boldsymbol{\beta}/dt\right)\Big/c\kappa^3 R\right]_{\text{retarded}}$$

$$\text{and } \mathbf{B}(\mathbf{x},t) = \mathbf{n}_{\text{retarded}} \times \mathbf{E}(\mathbf{x},t). \qquad (A1.1b)$$

The $1/R$ fields are radiation fields, and they make a Poynting vector **P** that lies along $\mathbf{n}_{\text{retarded}}$:

$$\mathbf{P} = \mathbf{E}_{\text{radiative}} \times \mathbf{B}_{\text{radiative}} = \mathbf{E}_{\text{radiative}} \times (\mathbf{n}_{\text{retarded}} \times \mathbf{E}_{\text{radiative}}) = E_{\text{radiative}}^2 \mathbf{n}_{\text{retarded}} . \quad \text{(A1.1c)}$$

But the $1/R^2$ fields are Coulomb-Ampère fields, and the Coulomb field does *not* lie along $\mathbf{n}_{\text{retarded}}$ as one might naively expect; instead, it lies along $(\mathbf{n} - \boldsymbol{\beta})_{\text{retarded}}$.

Consider the following scenario, designed specifically for an instructive exercise in *reductio ad absurdum*. A source executes a motion comprising two components: **1)** inertial motion at constant $\boldsymbol{\beta}$, plus **2)** oscillatory motion at small amplitude and high frequency, so that there exists a small velocity $\Delta\boldsymbol{\beta}_{\text{retarded}}$ and a not-so-small acceleration $d\Delta\boldsymbol{\beta} / dt \big|_{\text{retarded}}$. Observe that the radiation and the Coulomb attraction/repulsion come from different directions. The radiation comes along $\mathbf{n}_{\text{retarded}}$ from the retarded source position, but the Coulomb attraction/repulsion lies along $(\mathbf{n} - \boldsymbol{\beta})_{\text{retarded}}$, which is basically $(\mathbf{n}_{\text{retarded}})_{\text{projected}}$, and lies nearly along $\mathbf{n}_{\text{present}}$. This behavior seems peculiar. Particularly from the perspective of modern Quantum Electrodynamics (QED), all electromagnetic effects are mediated by photons – real ones for radiation and virtual ones for Coulomb-Ampere forces. How can these so-similar photons come from different directions?

This is a paradox. It is a clue that the usage of c in so simplistic a way may presume too much. It is thus a clue that Einstein's Second Postulate may have presumed too much too. Witness that SRT has produced an extensive literature about paradoxes, especially featuring twins, clocks, trains, meter sticks, or barns, or spinning disks, *etc*. The Liénard- Wiechert problem is not generally counted among them, but there it is.

The Maxwell-based analysis of the finite-energy pulse developed in the present paper resolves the directionality paradox inherent in the Lènard-Wiechert potentials and fields. It introduces various $2c$'s into the mathematics. Because of all the $2c$'s, the radiation direction $\mathbf{n}_{\text{retarded}}$ changes to $\mathbf{n}_{\text{half retarded}}$, and the Coulomb attraction/repulsion direction $(\mathbf{n}_{\text{retarded}})_{\text{projected}}$ changes to $(\mathbf{n}_{\text{retarded}})_{\text{half projected}}$. These two directions are now physically the same; namely the source-to-receiver direction at the mid point of the scenario, *i.e.* $\mathbf{n}_{\text{mid point}}$. The potentials and fields become:

$$\Phi(\mathbf{x},t) = e\Big[1/R \Big]_{\text{mid point}} \text{ and } \mathbf{A}(\mathbf{x},t) = e\Big[\mathbf{V}/cR \Big]_{\text{mid point}} \quad \text{(A1.2a)}$$

and

$$\mathbf{E}(\mathbf{x},t) = e\bigg[\mathbf{n}/R^2 + \big(\mathbf{n}/cR \big) \times \big(\mathbf{n} \times d(\mathbf{V}/c)/dt \big) \bigg]_{\text{mid point}} \text{ and }$$

$$\mathbf{B}(\mathbf{x},t) = \mathbf{n}_{\text{mid point}} \times \mathbf{E}(\mathbf{x},t) \quad \text{(A1.2b)}$$

so

$$\mathbf{P} = \mathbf{E}_{\text{radiative}} \times \mathbf{B}_{\text{radiative}}$$
$$= \mathbf{E}_{\text{radiative}} \times (\mathbf{n}_{\text{mid point}} \times \mathbf{E}_{\text{radiative}}) = E_{\text{radiative}}^2 \mathbf{n}_{\text{mid point}} \qquad (A1.2c)$$

Observe that the Coulomb attraction or repulsion is now aligned with the direction of the radiation propagation.

A2. Expanded SRT: Reintroduction of Galilean Speed

People often think of Einstein's SRT as another face of Maxwell's EMT, since so much of either theory can be derived from the other. But this assessment is not quite accurate, since the finite-energy propagation analysis presented in this paper really is part of EMT, although a late arrival, and it conflicts with Einstein's famous Second Postulate, upon which he based SRT. [18,19]

Maxwell's equations contain the free-space electric permittivity ε_0 and magnetic permeability μ_0, which together imply a light speed c that is entirely determined by space, without reference to matter. This fact influenced Einstein in formulating his famous Second Postulate, asserting that this light speed is the same constant c for all inertial observers, independent of any particular circumstance, such as motion of the source. This assertion is the foundation for SRT.

But given the finite energy analysis developed in the present paper, the assertion needs to be refined to embody the characteristics of a finite-energy wave packet: emission and expansion from one atomic system, followed by contraction to and absorption by another atomic system. The main refinement needed concerns the 'reference' for the light speed c. The finite energy analysis requires that it be not so reference-free as Einstein made it. In the expansion phase of the scenario, c has to be speed relative to the source that has emitted the energy, and in the contraction phase of the scenario, c has to be relative to the receiver that will absorb the energy.

A bit of history: because of all the paradoxes generated by SRT, there have always been researchers questioning Einstein's Second Postulate, and evaluating alternatives to it. Ritz (1908; [20]) was an early, and famous, but ultimately unsuccessful, example. The Ritz postulate had the light moving at velocity $\mathbf{c} + \mathbf{V}$, where $\mathbf{V}$ was the velocity vector of the source at the moment of emission, and $\mathbf{c}$ is the velocity vector of the light if it had come from a stationary source at that moment. This postulate was put to rest because of conflict with data from binary star systems.

More successful with the binary star problem, and with many other interesting problems as well, is the work of P. Moon, D. Spencer, E. Moon, and many of Spencer's students. (1950's to present; [21-23]) Their key idea has been a propagation process with continuing control by the source, even after the initial 'emission' event, so that the light continues to move away from the source at speed c relative to the source, however arbitrarily the source itself may move. Most notably, this sort of Postulate permits the recovery of Newtonian Universal Time.

Observe that continuing control by the source implies that 'light', whatever it is, has a longitudinal extent (Of course! Light possesses wavelength, does it not?), and the longitudinal extent is expanding in time. That expansion naturally raises the question: exactly what *feature* of the expanding light packet is it that moves at speed c relative to the source? The tacit assumption in the work of Moon-Spencer-Moon *et al*. is that the c-speed part is the leading tip of the light packet.

My own work in SRT [24, 25] has followed Moon-Spencer-Moon *et al*. in maintaining control by the source after emission. But the speed c relative to the source characterizes, not the leading tip of the light packet, but rather the mid point of the light packet. The leading tip moves relative to the source, not at c, but rather at $2c$. And then when this leading tip encounters a viable receiver, control switches to the receiver, and the whole process proceeds in reverse, with the mid point of the light packet moving at c relative to the receiver, and the tail reeling in at speed $2c$,

My process description was originally cast as a Postulate, in the spirit of all the earlier work investigating alternative Postulates. However, the present paper offers something less arbitrary than a Postulate; namely, an analysis of the implications of Maxwell's equations for a finite-energy light pulse. Since Maxwell is linked through Faraday to deep empirical roots, I believe reference to his work is a foundation for further developments that is less arguable than any postulate can be.
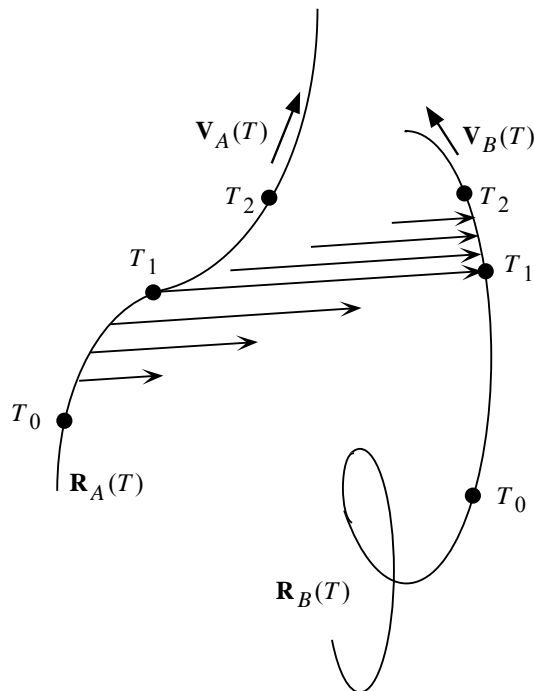
Figure A2.1. Illustration of Two-Step Light propagation.

In any event, the process described here has been called 'Two-Step Light'. It is illustrated in figure A2.1. The subscripted T's are Universal Times: T_0 at the beginning of the scenario, T_1 at the mid point, and T_2 at the end. Particle A is the source, and particle B is

the receiver (one of possibly many candidate receivers, selected by the accidental collision with the expanding light arrow at T_1).

The mid points of the light arrows may be said to behave like the Moon-Spencer-Moon *et al*. favored postulate in the expansion phase of the scenario, and then like the Einstein postulate in the contraction phase of the scenario.

Analysis of this process produces some interesting results. Consider the problem of processing data consisting of successive light signals from a moving source in order to estimate the speed V of that source. If the light propagates according to the Two-Step process, but the data gets processed under the assumption of the one-step Einstein postulate, then there will be a systematic error to the estimate. In fact, the estimate turns out to be:

$$v = V / (1 + V^2 / 4c^2).$$
(A2.1)

The estimate v is always less than V, and in fact is limited to c, which value occurs at $V = 2c$. Thus v has the property that is characteristic of any observable speed in Einstein's SRT. The obvious implication is that v is an Einsteinian speed, whereas V is a Galilean speed.

One is obviously invited to look also at a related construct

$$V^\uparrow = V / (1 - V^2 / 4c^2).$$
(A2.2)

The superscript $\uparrow$ is used to call attention to the fact that $V^\uparrow$ has a singularity, which is located at $V = 2c$, or $v = c$. That is, $V^\uparrow$ has the property of the so-called 'proper' or 'covariant' speed. Interestingly, past the singularity, $V^\uparrow$ changes sign. This behavior mimics the behavior that SRT practitioners attribute to 'tachyons', or 'super-luminal particles': they are said to 'travel backwards in time'. The sign change is a mathematical description, while the 'travel backwards in time' is a mystical description.

The relationships expressed by (A2.1) and (A2.2) can be inverted, to express V in terms of v or $V^\uparrow$. The definition $v = V / (1 + V^2 / 4c^2)$ rearranges to a quadratic equation $(v / 4c^2)V^2 - V + v = 0$, which has solutions

$$V = \frac{1}{v / 2c^2}\left(+1 \pm \sqrt{1 - v^2 / c^2}\right).$$
(A2.3a)

Multiplying numerator and denominator by $\left(+1 \mp \sqrt{1 - v^2 / c^2}\right)$ converts these to the form

$$V = v \left/ \frac{1}{2}\left(1 \mp \sqrt{1 - v^2 / c^2}\right)\right.,$$
(A2.3b)

which makes clear that for small v, V has one value much, much larger than v, and another value essentially equal to v.

Similarly, the definition $V^\uparrow = V / (1 - V^2 / 4c^2)$ rearranges to a quadratic equation $(-V^\uparrow / 4c^2)V^2 - V + V^\uparrow = 0$, which has solutions

$$V = \frac{1}{-V^\uparrow / 2c^2}\left(+1 \pm \sqrt{1 - V^{\uparrow 2} / c^2}\right). \qquad \text{(A2.4a)}$$

Multiplying numerator and denominator by $\left(+1 \mp \sqrt{1 + V^{\uparrow 2} / c^2}\right)$ converts these to the form

$$V = V^\uparrow \Big/ \frac{1}{2}\left(1 \mp \sqrt{1 + V^{\uparrow 2} / c^2}\right), \qquad \text{(A2.4b)}$$

which makes clear that for small $V^\uparrow$, V has one value much larger in magnitude than $V^\uparrow$ (which is negative there), and another value essentially equal to $V^\uparrow$.

To see that v and $V^\uparrow$ are not only qualitatively *like* Einsteinian speed and covariant speed, but in fact quantitatively *equal* to them, one can do a bit more algebra. Substitute (A2.3b) into (A2.2) and simplify to find

$$V^\uparrow = mv \Big/ \sqrt{1 - v^2 / c^2}, \qquad \text{(A2.5a)}$$

which is the definition of covariant speed familiar from SRT, made slightly more precise by inclusion of the minus sign for situations beyond the singularity.

Similarly, substitute (A2.4b) into (A2.1) and simplify to find

$$v = mV^\uparrow \Big/ \sqrt{1 + V^{\uparrow 2} / c^2}, \qquad \text{(A2.5b)}$$

which is again a relationship familiar from SRT, made slightly more precise by inclusion of the minus sign for situations beyond the singularity.

The information contained in Eqs. (A2.1) to (A2.5a,b) is displayed graphically in figure A2.2. Both plot axes denote multiples of nominal light speed c. Galilean particle speed V is the independent variable. To save space beyond the singularity, where $V^\uparrow$ goes negative, it is the absolute value of $V^\uparrow$ that is plotted.

Speed can be seen as a proxy for many other interesting things in SRT, like momentum, relativistic mass, *etc*. Observe that with only two speed concepts, SRT only can offer only two speed relationships, whereas with three speed concepts, Two Step Light offers six speed relationships. This constitutes three times the information content. This is what makes Two

Step Light a 'covering theory' for SRT. Two Step Light offers additional opportunities for explaining all the interesting things in SRT.
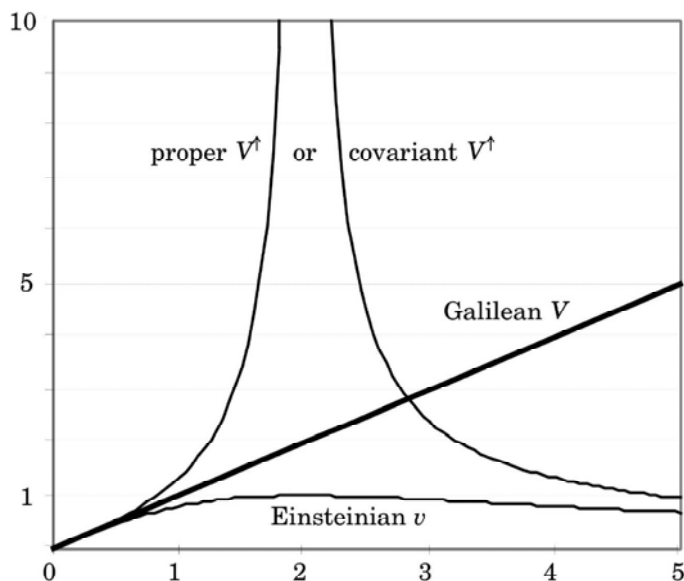
Figure A2.2. Numerical relationships among three speed concepts.

Uses of the word 'interesting' can include use as a euphemism for 'paradoxical'. The fact that Galilean speed V is missing from the language of SRT means that Einsteinian speed v gets conflated with Galilean speed V in SRT. Any conflation of different physical concepts causes confusion and misinterpretation of both theoretical and experimental results. That is why the literature of SRT contains so much discussion of 'paradoxes'. But there are no paradoxes in physical reality, and there are none in Two Step Light theory.

A3. Redeveloping QM: Ground State of Hydrogen Atom

The basis for an redeveloping QM lies in the expanded SRT. The present Appendix reviews the redevelopment [26] of QM.

Consider the Hydrogen atom. The electron orbits at r_e and the proton orbits at much, much smaller r_p. Figure A3.1 illustrates in an exaggerated manner how each experiences Coulomb attraction to the 'half-retarded' position of the other (as if the Coulomb force vector propagated at speed $2c$).

This situation implies that the forces within the Hydrogen atom are not central, and not even balanced. This situation has two major implications:

1. The unbalanced forces mean that the system as a whole experiences a net force. That means the system center of mass (C of M) can move.
2. The non-central individual forces, and the resulting torque, mean the system energy can change.
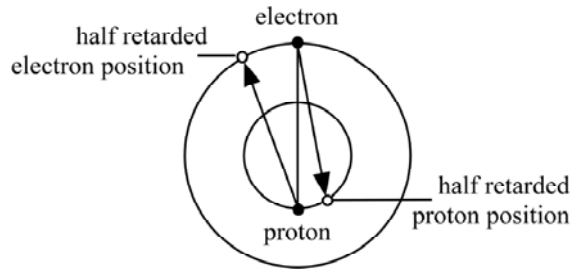
Figure A3.1. Coulomb force directions within the Hydrogen atom.

These sorts of bizarre effects never occur in Newtonian mechanics. But electromagnetism is not Newtonian mechanics. In electromagnetic problems, the concepts of momentum and energy 'conservation' have to include the momentum and energy of fields, as well as those of matter. Momentum and energy can both be exchanged between matter and fields. 'Conservation' applies only to the system overall, not to matter alone (nor to fields alone either).

Looking in more detail, the unbalanced forces in the Hydrogen atom must cause the C of M of the whole atom to traverse its own circular orbit, on top of the orbits of the electron and proton individually. This is an additional source of accelerations, and hence of radiation. It evidently makes even worse the original problem of putative energy loss by radiation that prompted the development of QM. But on the other hand, the torque on the system implies a rate of energy gain to the system. This is a candidate mechanism to compensate the rate of energy loss due to radiation. That is why the concept of 'balance' emerges: there can be a balance between radiation loss of energy and torquing gain of energy.

The details are worked out quantitatively as follows. First, ask what the circulation can do to the radiation. A relevant kinematic truth about systems traversing circular paths was uncovered by L.H. Thomas back in 1927, in connection with explaining the then-anomalous magnetic moment of the electron: just half its expected value [27]. He showed that a coordinate frame attached to a particle driven around a circle naturally rotates at half the imposed circular revolution rate. Figure A3.2 illustrates.

Applied to the old scenario of the electron orbiting stationary proton, the gradually rotating x, y coordinate frame of the electron meant that the electron would see the proton moving only half as fast as an external observer would see it. That fact explained the electron's anomalous magnetic moment, and so was received with great interest in its day. But the fact of Thomas rotation has since slipped to the status of mere curiosity, because Dirac theory has replaced it as the favored explanation for the magnetic moment problem.

Now, however, there is a new problem in which to consider Thomas rotation: the case of the C of M of a whole Hydrogen atom being driven in a circle by unbalanced forces. In this scenario, the gradually rotating local x, y coordinate frame of the C of M means that the atom system doing its internal orbiting at frequency Ω_e relative to the C of M will be judged by an external observer to be orbiting twice as fast, at frequency $\Omega' = 2\Omega_e$ relative to inertial space.
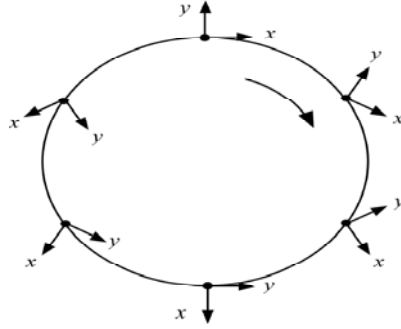
Figure A3.2. Thomas rotation. When the particle traverses the full circle, its internal frame of reference rotates 180°.

This perhaps surprising result can be established in at least three ways:

1. By analogy to the original problem of the electron magnetic moment;
2. By construction of Ω' in the lab frame from Ω_e in the C of M frame as the power series $\Omega' = \Omega_e \times (1 + 1/2 + 1/4 + 1/8 + ...) \rightarrow \Omega_e \times 2$;
3. By observation that in inertial space Ω' must satisfy the algebraic relation $\Omega' = \Omega_e + \Omega'/2$, which implies $\Omega' = 2\Omega_e$.

The relation $\Omega' = 2\Omega_e$ means the far field radiation power, if it really ever manifested itself in the far field, would be even stronger than classically predicted. The classical Larmor formula for radiation power from a charge e (e in electrostatic units) is $P_e = 2e^2 a^2 / 3c^3$, where a is total acceleration. For the classical electron-proton system, most of the radiation comes from the electron orbiting with $a_e = r_e \Omega_e^2$, Ω_e. But with $\Omega' = 2\Omega_e$, the effective total acceleration is $a' = a_e \times 2^2$. With electron-proton total separation $r_e + r_p$, the Coulomb force is approximately $F_e = e^2 / (r_e + r_p)^2$, $a_e = F_e / m_e$, and the total radiation power is approximately

$$P_R = \underline{2}^4 (2e^2 / 3c^3) a_e^2 = \underline{2}^5 (e^6 / m_e^2) / 3c^3 (r_e + r_p)^4 . \tag{A3.1a}$$

However, that outflow of energy due to radiation is never manifested in the far field because it is compensated by an inflow of energy due to the torque on the system. This is what overcomes the main problem about Hydrogen that was a main driver in the development of QM; namely, that the Hydrogen atom ought to run down due to radiative energy loss.

Generally, the inflow power $P_T = T\Omega_e$, where T is the total torque $T = |\mathbf{r}_e \times \mathbf{F}_e + \mathbf{r}_p \times \mathbf{F}_p|$, and $\mathbf{r}_e \times \mathbf{F}_e \equiv \mathbf{r}_p \times \mathbf{F}_p$, so $T = \underline{2}|\mathbf{r}_e \times \mathbf{F}_e|$. With two-step light, the angle

between $\mathbf{r}_e$ and $\mathbf{F}_e$ is $r_p\Omega_e/2c = (m_e/m_p)(r_e\Omega_e/2c)$. So the torque $T = (m_e/m_p)(r_e\Omega_e/c)[e^2/(r_e+r_p)]$ and the power

$$P_T = (m_e/m_p)(r_e\Omega_e^2/c)[e^2\big/(r_e+r_p)] = (e^4/m_p)\big/c(r_e+r_p)^3 \ . \qquad \text{(A3.1b)}$$

Now posit a balance between the energy gain rate due to the torque and the energy loss rate due to the radiation. The balance requires $P_T = P_R$, or

$$(e^4/m_p)\big/c(r_e+r_p)^3 = (2^5 e^6/m_e^2)\big/3c^3(r_e+r_p)^4 \ . \qquad \text{(A3.1c)}$$

This equation can be solved for $r_e + r_p$:

$$r_e + r_p = 32m_p e^2\big/3m_e^2 c^2 = 5.5\times10^{-9} \text{ cm.} \qquad \text{(A3.2a)}$$

Compare this value to the accepted value 5.28×10^{-9} cm. The match is fairly close, running just about 4% high. That means the concept of torque versus radiation does a fairly decent job of modeling the ground state of Hydrogen.

The result concerning the Hydrogen atom invites a comment on Planck's constant h, which is generally presumed to be a fundamental constant of Nature. In conventional QM, $r_e + r_p$ is expressed in terms of h:

$$r_e + r_p = h^2\big/4\pi^2\mu e^2 \ . \qquad \text{(A3.2b)}$$

Here μ is the so-called 'reduced mass', defined by $\mu^{-1} = m_e^{-1} + m_p^{-1}$. Using $\mu \approx m_e$ in (A3.2b) and equating (A3.2b) to (A3.2a) gives

$$h \approx \frac{\pi e^2}{c}\sqrt{128m_p/3m_e} \ . \qquad \text{(A3.3)}$$

This expression comes to a value of 6.77×10^{-34} Joule-sec, about 2% high compared to the accepted value of 6.626176×10^{-34} Joule-sec. Is this result meaningful? To test it, a more detailed analysis accounting more accurately for 'sin' and 'cos' functions of the small angle $r_p\Omega_e/2c$, here represented by the small angle itself, and by unity. That exercise made the estimate of h more accurate too, and suggests that the model is indeed meaningful, and that Planck's constant need not be regarded as an independent constant of Nature.

The analysis so far is for the ground state of Hydrogen. To contribute to a covering theory for QM, that analysis has to be extended in several ways. The first of these extensions is most important to chemistry: we need to cover trans-Hydrogenic atoms. For this, we need to replace the proton in Hydrogen with other nuclei. This replacement immediately gives the reason for the M/Z scaling used in this paper for relating ionization potentials of different elements to each other. With replacement, the subscript p for proton changes to Z. Eqs. (A3.1a) and (A3.1b) are both scaled by Z^2, and (A3.1b) is additionally scaled by $1/M$. As a result, (A3.2a) changes to $r_e + r_Z = M(r_e + r_p)$. The electron energy in the Hydrogen case is $E_H = e^2/(r_e + r_p)$; for the element Z case, the e^2 changes to Ze^2, so overall, the single-electron energy changes to

$$E_Z = \not{Z}Ze^2 / M(r_e + r_Z) = (Z/M)E_H . \tag{A3.4}$$

If it weren't for neutrons, the scale factor Z/M would be unity. But because of neutrons, Z/M varies from 1 for Hydrogen, immediately to 0.5 for Helium, and eventually to 0.4 for the heaviest elements we presently know about. So in order to put the IP data for different elements onto a common basis, we must remove the Z/M factor from raw data by scaling with its inverse M/Z.

A4. Expanding QM: Sub States of Hydrogen Atoms

In earlier works, I called the redevelopment of QM 'Variant QM', because I was not then certain it could actually do more than the standard QM. Now I am certain that it can, so it has become 'Expanded QM'. This Appendix details the first example of that expansion.

The basic concept of the ground state analysis from Appendix 3 (A3) is a balance between two effects: the familiar energy loss by radiation, and the newly identified energy gain by torquing. The torquing is a consequence of electromagnetic signal propagation in two steps as described in A3.

The ground-state analysis in A3 has two 'small-angle' approximations in it. In the expression for energy loss rate by radiation, there are vector projections, and hence angle cosines, which are approximated by unity. In the expression for energy gain rate due to torquing, there are vector cross products, and hence angle sines, which are approximated by the angle values in radians. The sub-ground states of Hydrogen are found by replacing these 'small-angle' approximations with actual trigonometric functions.

Figure A4.1 illustrates the Hydrogen atom with the electron and proton both orbiting, all dimensions exaggerated for visibility. The small angles are indicated by appropriately labeled small arrows. The angle α is measured at the system origin, between present and half-retarded positions of the electron or equivalently of the proton. The angle β is measured at the electron, and is smaller than α. The angles $\alpha - \beta$ and β are the angles from which the two particles, electron and proton, each receive the half-retarded attractive signal from their partner.
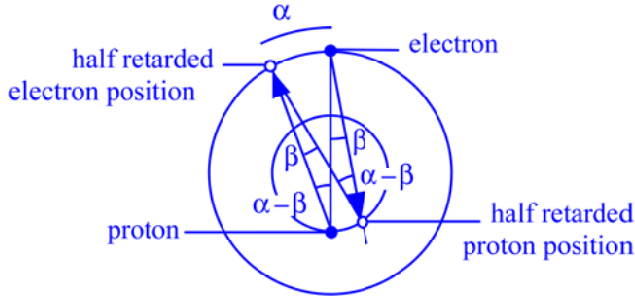
Figure A4.1. Identification of small-angle approximations in Hydrogen analysis.

The larger arrows on figure A4.1 point in the directions of these charge attractions. The proton attraction to the electron has a radial component proportional to $\cos(\alpha - \beta)$ and a tangential component proportional to $\sin(\alpha - \beta)$. The electron attraction to the proton has a radial component proportional to $\cos(\beta)$ and a tangential component proportional to $\sin(\beta)$. The small-angle approximations assumed for the Hydrogen analysis in A3 were:

$$\cos(\alpha - \beta) \approx \cos(\beta) \approx 1 \ , \ \sin(\alpha - \beta) \approx \alpha \ , \ \sin(\beta) \approx \beta \qquad (A4.1)$$

The small angle approximations allowed straightforward solution of the equation of balance between energy loss rate due to radiation and energy gain rate solution due to torquing. This was done algebraically by equating the energy gain rate due to torquing,

$$P_T = (e^4 / m_p) \Big/ c(r_e + r_p)^3 \qquad (A4.2)$$

to the energy loss rate due to radiation,

$$P_R = (2^5 e^6 / m_e^2) \Big/ 3c^3 (r_e + r_p)^4 \qquad (A4.3)$$

The relaxation of the small-angle approximations mandates the following complications:
1) The condition defining the angle α is:

$$\alpha = (V_e / 2c) \times [(r_e + r_p) / r_e] \qquad (A4.4)$$

Because $r_p << r_e$, Eq. (A4.4) simplifies to $\alpha \approx V_e / 2c$.

2) The condition defining the angle β is

$$\tan(\beta) = r_p \sin(\alpha) \Big/ \Big[r_e + r_p \cos(\alpha) \Big] \qquad (A4.5)$$

Whatever angle α is, β will be near zero. But like α, angle β does depend upon V_e.

3) The condition defining V_e is

$$m_e V_e^2 / r_e = e^2 / (r_e + r_p)^2 \qquad \text{(A4.6)}$$

Because $r_p \ll r_e$, the approximation $V_e \approx e / \sqrt{m_e(r_e + r_p)}$ is acceptable.

4) Because the solution sought is a balance between torquing and radiation reaction, there is no net acceleration of the charges in the angular direction. So the rate of energy loss due to radiation P_R depends only upon the radial components of forces. These components are proportional to $\cos(\alpha - \beta)$ and $\cos(\beta)$. Because they are generally less than unity, the rate of energy loss due to radiation is lessened. The scaling down is expressed by:

$$P_R \rightarrow \left\{ \frac{1}{2} \left[\cos(\alpha - \beta) + \cos(\beta) \right] \right\}^2 P_R \qquad \text{(A4.7)}$$

5) The torque on the system has contributions arising from forces on both the electron and the proton. Those contributions involve cross products between the forces and the radial position vectors, and hence involve the $\sin(\alpha - \beta)$ and $\sin(\beta)$. The scaling down of the rate of energy gain due to torquing is expressed by

$$P_T \rightarrow \left\{ \frac{1}{2} \left[\sin(\alpha - \beta)/(\alpha - \beta) + \sin(\beta)/\beta' \right] \right\} P_T \qquad \text{(A4.8)}$$

where β' is the factor within P_T that $\sin(\beta)$ replaces. For small α, $\beta' = \beta$ [from (A4.5)], but for the full range of arbitrary α, $\beta' = \alpha / 1838$.

The changes developed above make the Hydrogen balance problem significantly more complicated. Algebraic solution is no longer a practical approach. So graphical solution becomes a more attractive approach. A simple EXCEL program is sufficient for a perfectly reasonable graphical solution approach. To set the stage for graphical solution of the more complicated problem with the small-angle approximations removed, figure A4.2 illustrates the graphical solution approach as applied to the original problem, with the small-angle approximations still embedded in it.

In figure A4.2, the independent variable is the system radius, $r_e + r_p$. It is plotted on a log scale, starting at $r_e + r_p = 10^{-11}$ cm and going through 6 decades to $r_e + r_p = 10^{-5}$ cm. There are 301 data points for each dependent variable plotted. 'Series 1' refers to the steeper line, representing energy loss rate due to radiation. 'Series 2' refers to the shallower line, referring to energy gain rate due to torquing. The two lines on figure A4.2 are straight because the energy gain and loss rates are power laws plotted on log scales. The graphical solution comes approximately in the middle of the plots, approximately at point 138,

approximately at $r_e + r_p = 5.5 \times 10^{-9}$ cm, *i.e.* approximately the same as the algebraic solution

$r_e + r_p = 5.5 \times 10^{-9}$ cm, and fairly close to the accepted value $r_e + r_p = 5.28 \times 10^{-9}$ cm.

Figure A4.2 reveals something that was not obvious in the purely algebraic approach used in [1]: the ground-state solution for Hydrogen is *not stable*. Any small perturbation right, to higher energy, is encouraged by energy gain due to torquing, and any perturbation further left, to lower energy, is encouraged by energy loss due to radiation. The revealed instability does comport with observed facts: here on Earth, Hydrogen atoms tend to come together to form molecules, and deep in space they tend to come apart to form a plasma. Nowhere do they appear abundantly as individual atoms.
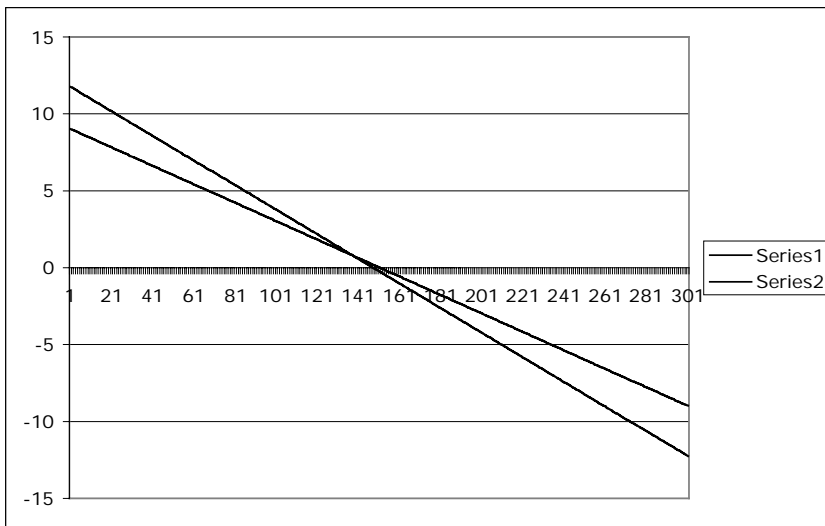
Figure A4.2. Graphical solution for the Hydrogen ground state.

When the small-angle approximations are removed, the straight lines on figure A4.2 become the curved lines on figure A4.3. Again there are 301 data points, but now starting at system radius $r_e + r_p = 10^{-15}$ cm and proceeding to $r_e + r_p = 10^{-5}$ cm.

The familiar first solution is located where the lines cross on the right side of figure A4.3, between points 203 and 204, between $r_e + r_p = 5.41 \times 10^{-9}$ cm and $r_e + r_p = 5.84 \times 10^{-9}$ cm.

The lower value comes a bit closer to the accepted value $r_e + r_p = 5.28 \times 10^{-9}$ cm than did the

$r_e + r_p = 5.5 \times 10^{-9}$ cm previously obtained with small-angle approximations. As one might hope, including more trigonometric detail produces more numerical accuracy.

On the left side of figure A4.3, some dramatic features emerge. They are all associated with $\alpha \geq \pi$. Note that in the vicinity of $\alpha = \pi$, the electron speed is in the vicinity of $V_e = 2\pi c$. This kind of speed is dramatically superluminal. Note that it does occur *deep*

inside an atom – hardly the kind of 'free-space' situation for which the Einstein particle-speed limit c was legislated.
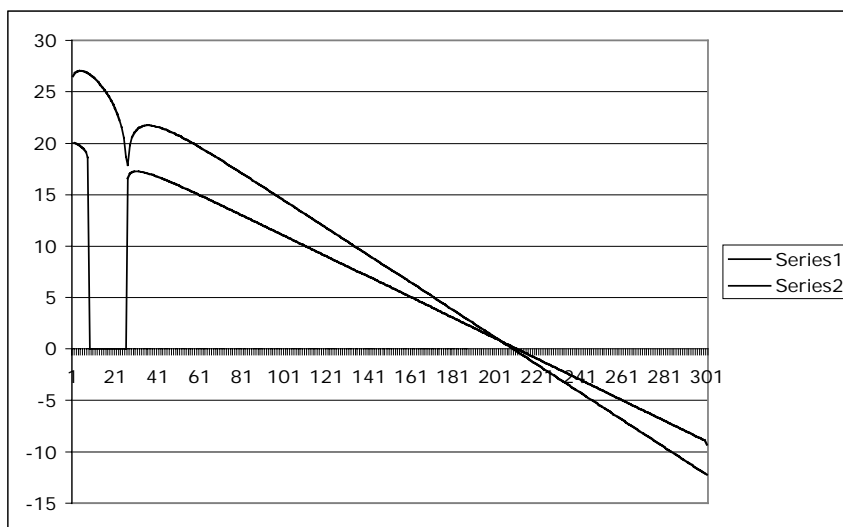
Figure A4.3. Extended graphical solution to the Hydrogen balance problem.

The first dramatic feature is a dip in the curve representing the rate of energy loss due to radiation. This dip occurs where the cosine sum in Eq. (A4.7) touches zero. That happens as angle α passes through π. The dip on figure A4.3 actually goes to zero, but since the plot is on a log scale, the calculations have been set up to avoid having a data point occur exactly where the zero occurs.

The second dramatic feature is a gap in the curve that represents the rate of energy gain due to torquing. This gap occurs for the interval $\pi < \alpha < 2\pi$. In this interval, the $\sin(\alpha - \beta)$ and the $\sin(\beta)$ in Eq. (A4.8) for P_T are negative. That means the sign of P_T is negative, and P_T cannot be plotted on a log scale. In this interval, the torquing effect on the system does not *oppose* the radiation effect; it *augments* it. So system balance is not possible in this interval.

But the third and most dramatic feature is that an additional solution emerges. It is located just to the right of the radiation dip and torquing gap, between data points 26 and 27. This second solution is clearly where the Hydrogen system would be driven to, should it be perturbed from its first solution in the direction downward in radius, and hence downward in energy. Throughout the radius regime from the first solution to the second solution, energy loss due to radiation dominates energy gain due to torquing, and ever more energy is lost.

Looking further to the left on figure A4.3, it is clear that a family of viable superluminal solutions is developing. Figure A4.4 begins at even smaller system radius, and shows even more solutions. Superluminal solutions correlate with $\alpha = \pi + 4\pi n$, $n = 0,1,2,3,...$, These solutions occur just to the right of the dips. Solution-prohibiting regions of negative torque occur to the left of the dips. The dips themselves actually go to zero, but since the plots are on a log scale, there are no data points placed exactly at the zeros. The depths of dips look ragged, but that is just a computational artifact without physical meaning.

The graphical analysis here gives an initial insight into the otherwise puzzling issue of stability *vs.* instability of the Hydrogen ground-state solution to the problem of Hydrogen torque *vs.* radiation balance. That solution is off the right side of figure A4.4, and it is obviously unstable. The graphical analysis has then arrived at an infinite family of additional solutions for Hydrogen torque *vs.* radiation balance. These solutions are on the left side of figure A4.4, all below the ground state of Hydrogen in total energy, so they are 'sub-ground' states. They all have superluminal orbit speeds: with $\alpha \approx V_e / 2c$, we have $V_e = 2\pi c, 10\pi c, 18\pi c, \dots$.
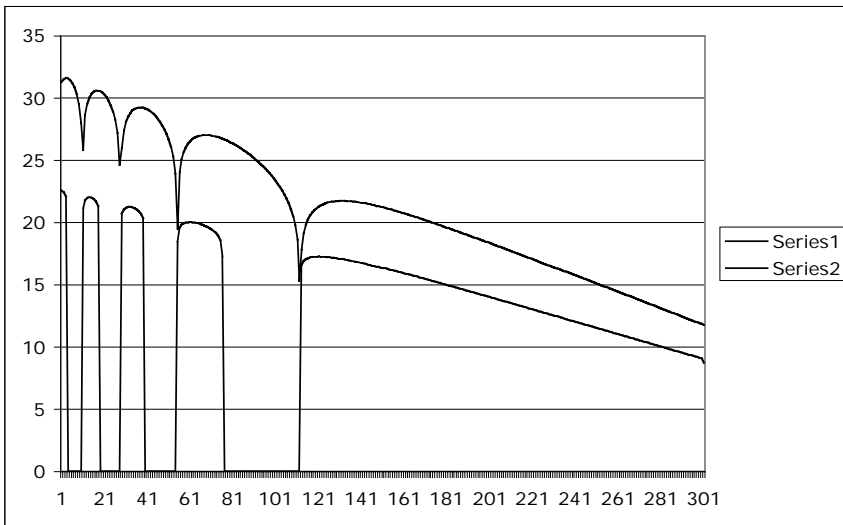
Figure A4.4. Multiple solutions to the Hydrogen balance problem.

The superluminal velocity results imply very high kinetic energies. Rewriting the results as $V_e = 2\pi c(1 + 4n)$, $n = 0, 1, 2, 3 \dots$, we see that kinetic energies, if proportional to V_e^2, must advance with n^2. This behavior is like having a radial quantum number that is fractional. A fractional radial quantum number is a phenomenon simply not within the current paradigm of QM.

Though not the main topic of the present paper, these results are of further interest for the future because there exists an extensive experimental literature on the spectroscopy of Hydrogen, and some of it seems inexplicable in terms of traditional QM. In particular, the work of Dr. Randall L. Mills and associates shows some extreme UV lines that are suggestive of Hydrogen atom states with fractional radial quantum numbers. Dr. Mills tells that story quite comprehensively in [28].

The refined Hydrogen analysis provides a stepping-stone to the analysis of systems in which the participant charges are not of very dissimilar mass, as in Hydrogen, but rather of equal mass, such as in the electron cloud in a trans-Hydrogenic atom.

A5. An Example with Equal Masses: Positronium

The mass symmetry of Positronium makes for angle symmetry, illustrated by figure A5.1.
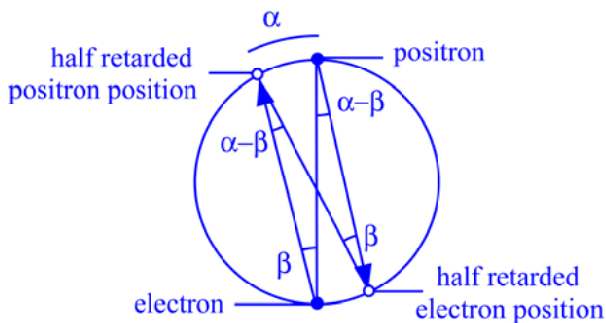
Figure A5.1. Positronium.

From figure A5.1,

$$\alpha - \beta \equiv \beta \equiv \alpha / 2 . \tag{A5.1}$$

The small-angle approximation for energy gain rate due to torquing becomes

$$P_T = (e^4 / m_e)\big/ c(2r_e)^3 . \tag{A5.2}$$

The small-angle approximation for energy loss rate due to radiation becomes

$$P_R = (2^5 e^6 / m_e^2)\big/ 3c^3 (2r_e)^4 . \tag{A5.3}$$

The analysis then follows:

1) The condition defining the angle α becomes

$$\alpha = (V_e / 2c) \times (2r_e) / r_e \to V_e / c \tag{A5.4}$$

2) The formal condition for defining angle β becomes

$$\tan(\beta) = \frac{\sin(\alpha)}{1+\cos(\alpha)} = \frac{2\sin(\alpha/2)\cos(\alpha/2)}{1+\cos^2(\alpha/2)-\sin^2(\alpha/2)} = \frac{\sin(\alpha/2)\cos(\alpha/2)}{\cos^2(\alpha/2)} = \tan(\alpha/2) \tag{A5.5}$$

This relationship is indeed satisfied by $\beta = \alpha / 2$.

3) The condition defining V_e becomes

$$m_e V_e^2 / r_e = e^2 / (2r_e)^2 \qquad\qquad (A5.6)$$

The solution is then $V_e \approx e \big/ \sqrt{m_e (2r_e) \times (1/2)}$.

4) The factors for removing the small-angle approximations from P_T and P_R simplify. The expression for energy loss rate due to radiation changes from

$$P_R \to \left\{ \frac{1}{2} \big[\cos(\alpha - \beta) + \cos(\beta) \big] \right\}^2 P_R \ \text{ to } \ P_R \to \big[\cos(\alpha/2) \big]^2 P_R \qquad (A5.7)$$

5) The expression for the energy gain rate due to torquing changes from

$$P_T \to \left\{ \frac{1}{2} \big[\sin(\alpha - \beta)/(\alpha - \beta) + \sin(\beta)/\beta' \big] \right\} P_T \ \text{ to } \ P_T \to \big[\sin(\alpha/2)/(\alpha/2) \big] P_T \quad (A5.8)$$
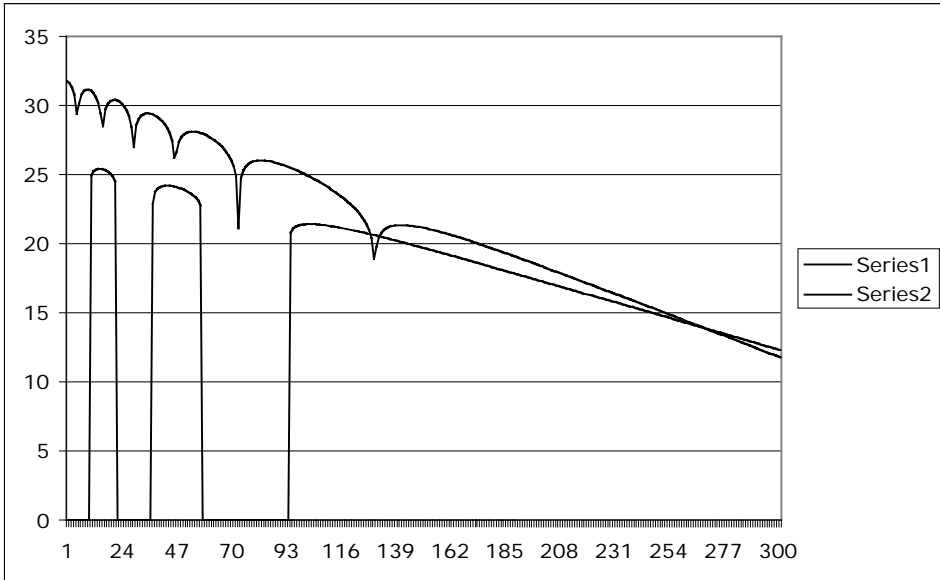
Figure A5.2. Positronium solutions.

Being formally analogous to Hydrogen, Positronium also has a 'ground-state', low-speed solution, plus a family of high-speed sub-ground solutions. Figure A5.2 illustrates the solutions. The range of system radii starts at 10^{-16} cm, and goes to 10^{-11} cm via 301 points. The ground-state solution occurs between points 269 and 270, at system radius of about 3×10^{-12} cm (quite a bit smaller than the 5.28×10^{-9} cm for the Hydrogen atom), with orbit

speed of about $0.22\,c$. The other solutions are superluminal, occurring in the vicinity of $V = \pi c, 5\pi c, 9\pi c, 13\pi c,...$

The 'ground-state' solution for Positronium occurs at about point 270, where system radius is about 3.04×10^{-12} cm and $V = 0.22c$. This state is qualitatively like the ground-state solution for Hydrogen: it is unstable. Any perturbation to the right, to higher energy, is amplified by energy gain due to torquing, and any perturbation to the left, to lower energy, is amplified by energy loss due to radiation. As we know from experience, Positronium is indeed quite unstable; it tends to annihilate itself quite quickly.

The sub-ground solutions for Positronium are startlingly different from the corresponding sub-ground solutions for Hydrogen: they occur where the energy gain rate due to torquing is near maximum, not near where it is passing through zero. This is a consequence of the perfect mass equality of the two particles in Positronium, opposite to the extreme mass inequality of the particles in Hydrogen. While both Positronium and Hydrogen have dips in the energy loss rate due to radiation at angle $\alpha = \pi, 3\pi, 5\pi, 7\pi,....$, Hydrogen has its energy gain rate due to torquing pass through zero there, whereas Positronium has it passing through maximum there. The reason for this difference is visible within the mathematics describing energy gain rate due to torquing:

1. Hydrogen always has angle $\beta \approx 0$, so for $\alpha = \pi, 3\pi, 5\pi, 7\pi,....$, both the $\sin\beta$ and the $\sin(\alpha - \beta)$ involved in the expression for energy gain rate due to torquing pass through zero.
2. Positronium always has angle $\beta = \alpha / 2$, so $\sin\beta = \sin(\alpha - \beta) = \sin(\alpha / 2)$. The $\sin(\alpha / 2)$ passes through unity at $\alpha = \pi, 3\pi, 5\pi, 7\pi,....$

As a result of this difference between Hydrogen and Positronium, all of the Positronium superluminal solutions are actually doublets: a solution to the right with higher system radius, lower orbit speed, and a solution to the left with lower system radius and higher orbit speed. Within each doublet, the solution to the right is extremely stable: the plot shows that any perturbation further right, to higher energy, is driven back by energy loss due to radiation, and any small perturbation left, to lower energy, is driven back by energy gain due to torquing. The solution to the left is then just the reverse, extremely *un*stable: any small perturbation right, to higher energy, is encouraged by energy gain due to torquing, and any perturbation further left, to lower energy, is encouraged by energy loss due to radiation. Something even worse is *not* obvious in the plot, although it *is* obvious in the mathematics. For this solution to the left, the factor $\cos(\alpha / 2)$ that enters the radial force components is actually slightly negative. So no such circular orbit can exist at all, unless a retaining radial force arises from some external circumstance.

The conclusion to remember for future reference is that the Positronium solutions occur at orbit speeds just slightly below $V = (\pi c, 5\pi c, 9\pi c, 13\pi c)$.

A6. Charges of the Same Sign

Technical journals occasionally feature reports and commentary about the apparently incomprehensible phenomenon of electrons clustering together. Some of these articles have been in the Galilean Electrodynamics journal I now edit [29-31]. The phenomenon is widely known; related literature cited in the third of those references is quite extensive, and some of it appears in the most widely circulated physics journals.

The non-central forces illustrated in figure A5.1 for Positronium can also provide a mechanism that can explain charge clusters. As is emphasized by Appendix 2 (A2), there is no limitation on Galilean speed V ; it can exceed c . Figure A6.1 illustrates a case where two like charges are orbiting each other at speed $V = \pi c$. Because of the 'mid-point' feature of Eqs. (A1.2b), the Coulomb 'repulsion' between the two charges is half-retarded, and because of the super luminal orbit speed, the 'repulsion' actually works as attraction.
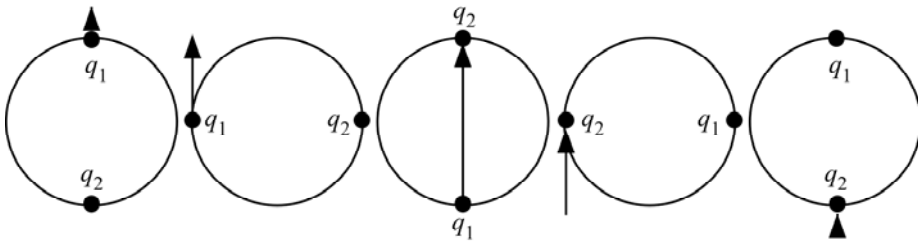
Figure A6.1. Attraction between two like charges orbiting at superluminal speed $V = \pi c$.

Figure A6.1 just constitutes a 'proof of existence': there do exist circumstances in which like charges attract. More detailed analysis of the binary same-charge system begins with figure A6.2, which is similar to the figure A5.2 for Positronium. The angle α is the sum of the half retardation angles, both of which are $\beta = \alpha / 2$.
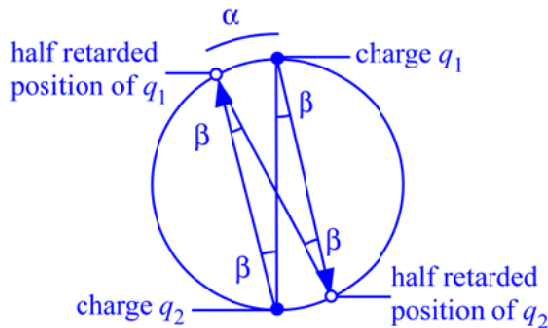
Figure A6.2. Binary charge cluster.

Let us identify exactly what changes are needed to adapt the existing Positronium analysis to the binary charge cluster. The change from an opposite-charge to a same-charge system requires that:

1. The two charges nominally repel each other, instead of attracting each other as in the Positronium case.
2. The radiation created by the system changes form to quadrupole, rather than dipole, as it was in the Positronium case.
3. The torque on the system everywhere reverses sign from what it was in the Positronium case.

The Positronium analysis identified intervals $\pi < \alpha < 3\pi$, $5\pi < \alpha < 7\pi$, $9\pi < \alpha < 11\pi$, *etc.*, within which the attraction between electron and positron works as if it were repulsion. The complementing intervals $3\pi < \alpha < 5\pi$, $7\pi < \alpha < 9\pi$, $11\pi < \alpha < 13\pi$, *etc.*, must play a similar role for the same-charge pair: within these intervals, the repulsion between same charges must work as if it were attraction. Note that figure A6.1 basically illustrated the first point of the first such interval: $\alpha = \pi$.

The radiation from the same-charge system is quadrupole, instead of dipole as it was for the opposite-charge Positronium system. The kind of radiation does not matter very much qualitatively, inasmuch as solutions are associated with dips to zero radiation that are in turn keyed to speeds at multiples of πc, regardless of what kind of radiation it is.

The sign of torquing is more significant. The Positronium solutions displayed the existence of regimes of negative torque within which both radiation and torquing cause energy *loss* from the system considered. No solution for system balance between radiation and torquing can exist in these regimes. The excluded intervals for Positronium were $2\pi < \alpha < 4\pi$, $6\pi < \alpha < 8\pi$, $10\pi < \alpha < 12\pi$,... The complementing intervals $4\pi < \alpha < 6\pi$, $8\pi < \alpha < 10\pi$, $12\pi < \alpha < 14\pi$,… are excluded for the same-charge system.

The details of the analysis follow. The angles again satisfy:

$$\alpha - \beta \equiv \beta \equiv \alpha / 2 \tag{A6.1}$$

The initial formula for energy gain due to torquing changes slightly; *i.e.*, from

$$P_{\mathrm{T}} = (e^4 / m_{\mathrm{e}}) \Big/ c(2r_{\mathrm{e}})^3 \ \text{ to } \ P_{\mathrm{T}} = (q^4 / m_q) \Big/ c(2r_q)^3 \tag{A6.2}$$

The 'same-charge' condition causes several changes in the initial formula for energy loss due to radiation. For Positronium we had (slightly rearranged for easy in conversion)

$$P_{\mathrm{R}} = 2^5 (e^6 / m_{\mathrm{e}}^2) \Big/ 3c^3 (2r_{\mathrm{e}})^4 = 2^4 (2e^6 / m_{\mathrm{e}}^2) \Big/ 3c^3 (2r_{\mathrm{e}})^4 \tag{A6.3}$$

For one thing, we have q's instead of e's, as in P_{T} above. In addition, we have quadrupole radiation instead of dipole radiation. To quantify this, we start with Eq. (9.52) from Jackson [4], $P = ck^6 Q_0^2 / 240$, and insert, $Q_0 = 2qd^2$ with $d = 2r_q$, and $k = \Omega / c$ with $\Omega^2 = q^2 / mr_q d^2$, plus a factor of 2^6 for the Thomas rotation [28] that this system experiences due to unbalanced forces. We end up with

$$P_{\mathrm{R}} = 2^6 \left(64 q^8 / m_q^3 \right) \Big/ \left[240 c^5 (2 r_q)^5 \right] = 2^6 \left(4 q^8 / m_q^3 \right) \Big/ \left[15 c^5 (2 r_q)^5 \right] \qquad \text{(A6.4)}$$

The condition defining the angle α becomes

$$\alpha = (V_q / 2c) \times (2 r_q / r_q) \rightarrow V_q / c \qquad \text{(A6.5)}$$

The condition defining the angle β remains

$$\beta \equiv \alpha / 2 \qquad \text{(A6.6)}$$

The condition defining V_q becomes

$$m_q V_q^2 / r_q = e^2 / (2 r_q)^2 \qquad \text{(A6.7)}$$

which implies $V_q = q \Big/ \sqrt{m_q (2 r_q) \times (1/2)}$. The scaling of P_{R} , is

$$P_{\mathrm{R}} \rightarrow \left[\cos(\alpha / 2) \right]^2 P_{\mathrm{R}} \qquad \text{(A6.8)}$$

The scaling of P_{T} is

$$P_{\mathrm{T}} \rightarrow \left[\sin(\alpha / 2) / (\alpha / 2) \right] P_{\mathrm{T}} \qquad \text{(A6.9)}$$

The analog of figure A5.2 from Appendix 5 is then figure A6.3. Again, the plot starts at system radius 10^{-16} cm, a progresses to 10^{-11} cm in 301 data points. Observe that the radiation curve is generally steeper than it was for Positronium. That is because the radiation is quadrupole rather than dipole. Observe too that there is no 'ground-state' solution for like charges, but there are superluminal sub-ground solution doublets, just as for Positronium, except that they occur at orbit speeds just slightly below $V = 3\pi c, \acute{7}\pi c, \acute{A} 1\pi c, \acute{A} 5\pi c...$ instead of $V = \pi c, \acute{5}\pi c, \acute{9}\pi c, \acute{A} 3\pi c, ...$. Within a doublet, the solutions to the right are stable, and the solution to the left is unstable.

For present purposes, the stable solution near $V = 3\pi c$ is probably of greatest interest. The system radius in this vicinity is about 1.58×10^{-15} cm. This is much smaller than the believed Hydrogen atom radius $r_e + r_p = 5.28 \times 10^{-9}$ cm, confirming the premise of this model, that atomic charge clusters are small compared to atoms. It is smaller even than the so-called 'classical radius of the electron', $r_c = e^2 / m_e c^2 = 2.82 \times 10^{-13}$ cm. Note that this

'classical radius' involves the rest energy $m_e c^2$, which is a concept from standard SRT, which in turn assumes the 'speed limit' c. Its meaning in the expanded SRT, with its unlimited superluminal speeds, is not clear.
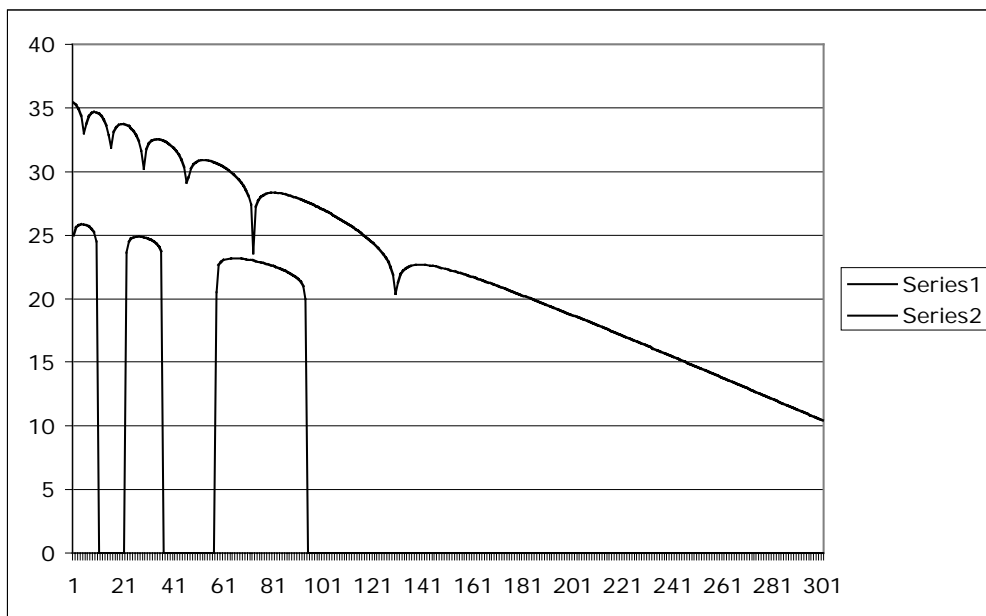
Figure A6.3. Same-charge solutions.

A7. Systems of Many Charges

The analysis for two charges is a stepping-stone to analyses involving three, and more, electrons. For three electrons, the analog of figure A6.1 is figure A7.1.

The condition expressed by figure A7.1 is that the light vector expansion at $2c$ across a chord of the circle synchronizes with the particle transit halfway around the circumference of the circle. Therefore, the particle transit has to be at $V_q = \pi c \times (\text{diameter} / \text{chord length}) = \pi c / \sin(\pi / 3)$. The $\sin(\pi / 3)$ for the ternary case, in place of $\sin(\pi / 2) = 1$ for the binary case, recurs throughout the full analysis of ternary charge cluster.
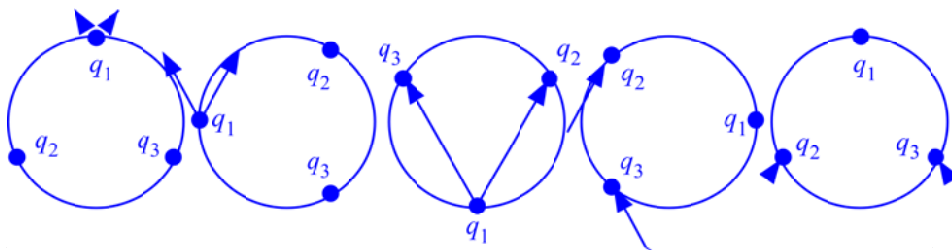
Figure A7.1. Attraction between three like charges orbiting at speed $V = \pi c / \sin(\pi / 3)$.

The ternary analog for figure A6.2 is figure A7.2. The angle β is smaller than in the binary case, and that affects both the torque energy gain and the radiation energy loss.
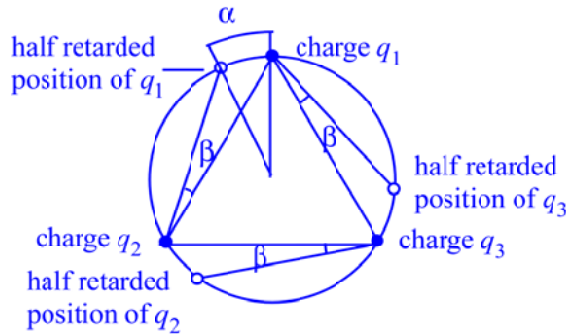
Figure A7.2. Angles involved in analysis of ternary charge cluster.

Another type of change required concerns the radiation. It is not the dipole formula, and it is not the quadrupole formula. It is perhaps a 'hexapole' formula. In any case, it can be worked out from the dipole formula, just as the quadrupole formula can be worked out in that way. The quadrupole formula is the difference of two dipoles. To put it another way, it is the sum of two dipoles at phases of 0° and 180°. Correspondingly, the radiation from this ternary system is the sum of *three* dipoles, at phases 0°, 120°, and 270°. This exercise about the radiation formula is interesting and challenging, but as we already know, does not affect the solutions very much. Solutions will be doublets surrounding orbit speeds

$$V_q = \frac{1}{\sin(\pi/3)}\left(3\pi c, 7\pi c, 11\pi c, 13\pi c...\right) \qquad (A7.1)$$

Of these, the solution at orbit speed just below $V_q = 3\pi c / \sin(\pi/3)$ is probably of greatest interest.

The system radius for the ternary case can be expressed by scaling from the system radius for the binary case. Two factors affect it. One is the increase of velocity for which radius is sought, by the factor of $1/\sin(\pi/3)$. This decreases the solution radius by a factor of $\sin^2(\pi/3) = 3/4$. The other factor is the change in the force attracting a subject charge, which now has two contributing charges instead of one, both at closer distance, but at off-radial direction. This changes the attractive force by a factor of $2\sin(\pi/3)/\sin^2(\pi/3) = 2/\sin(\pi/3) = 2.3094$, and hence changes the solution radius by the inverse of that factor. Altogether then, the solution radius decreases by $0.75/2.3094 = 0.3248$.

In the general case of N charges in a ring, the solution velocities are

$$V_q = \frac{1}{\sin(\pi/N)}\left(3\pi c, 7\pi c, 11\pi c, 15\pi c...\right) \qquad (A7.2)$$

Of these, the solution just below $V_q = 3\pi c / \sin(\pi / N)$ is probably of greatest interest.

The system radius for the general case involves two factors. One is the 'velocity' factor $\sin^2(\pi / N)$, and the other is the 'attraction' factor, which in general can be written as

$$\sum_{k=1}^{N-1} \left[1 / \sin(k\pi / N) \right] \qquad (A7.3)$$

Altogether then, the solution radius scales down by

$$\sin^2(\pi / N) \Big/ \sum_{k=1}^{N-1} \left[1 / \sin(k\pi / N) \right] \qquad (A7.4)$$

The resulting sizes for charge rings decrease as N increases: Using 1 for $N = 2$ (call it a 'binar' for 'binary'), we have 0.3248 for $N = 3$ ('tert'), 0.1306 for $N = 4$ ('quart'), 0.06275 for $N = 5$ ('quint'), 0.0342 for $N = 6$ ('hex'), 0.0204 for $N = 7$ ('sept'). All these spinning charge rings essentially amount to permanent electrical 'currents' within the low-temperature/high-temperature/no-temperature-exists 'superconductor' that otherwise-empty space provides. The superluminal charge rings provide a tool for understanding electron clusters in atoms.

A8. Excited States of Hydrogen

The conventional idea for the so-called 'excited states' of the Hydrogen atom involves an electron teetering in an upper 'shell' around the nucleus, ready to fall back to a lower 'shell' closer to the nucleus. But the present simple two-body analysis of Hydrogen does not allow anything so complicated. The simple torque *vs.* radiation balance has only one low-speed solution, corresponding to the ground state. The absence of lower-speed, higher-energy solutions means that in this analysis the term 'excited state' cannot describe a condition of a single Hydrogen atom.

A viable alternative idea for an 'exicted state' of Hydorgen involves, not just a single Hydrogen atom, but rather a system of multiple Hydrogen atoms that can emit or absorb energy as a system. In short, it is not really states of an individual atom that account for the quantization observed; it is instead the integer number of atoms in an atomic system.

A 'system of multiple atoms' as the conceptual model for an 'excited atomic state' is similar to the 'Superatom Model' for the structures or nanopartcles that atoms form in the gas phase, and possibly in solution as well [32]. Support for an atomic excitation model based on multiple atoms comes from the known fact that light emission is always a little bit laser-like, in that photons are emitted, not as singletons, but rather in bursts. [33] This behavior suggests that atoms become excited, not as singletons, but as groups.

The concept for creating such an extension to the analysis is to replace the single electron and the single proton in Hydrogen with multiple electrons and multiple protons, the charges of each sign bound together in 'charge clusters'.

So suppose that 'excitation' of Hydrogen up to state n actually involves $n = n_H$ Hydrogen atoms all working together in a coherent way. In particular, suppose that the n_H electrons make a negative cluster, and the n_H protons make a positive cluster, and the two clusters together make a scaled-up Hydrogen super-atom.

The replacement of single charges with charge clusters must affect both the radiation energy loss rate and the torquing energy gain rate, and the balance between them. Every factor of e and every factor of m_e or m_p scales by n_H. Starting from (12a) for the radiation, one finds that the energy loss rate scales by $(n_H)^4$. Starting from (12b) for the torquing, one finds that the energy gain rate scales by $(n_H)^3$. The solution radius for system balance therefore scales as $r_e + r_p \rightarrow r_{n_H} = n_H(r_e + r_p)$. [Note: if this multi-atom model captures the real behavior behind atomic excitation, and if one attempts to model that behavior in terms of a single atom with discrete radial states identified with a principal quantum number n, then the radial scaling has to be $r_1 \rightarrow r_n = n^2 r_1$, as is seen in standard QM.]

The overall system orbital energy then scales as $E_1 \rightarrow E_{n_H} = (n_H)^2 E_1 / n_H = n_H E_1$. This energy result is exactly the same as the orbital energy of n_H *separate* atoms *not* clustered together in a super atom. The implication is that when the system disintegrates, the energy that exits as photons does *not*, as is generally believed, correspond to a change in orbit around the nucleus. It is instead the positive energy required to form the charge clusters. This is a completely novel view of excitation.

The charge-cluster model for excitation suggests that there ought to be some similarity between Hydrogen in its first excited state ($n_H = 2$) and a Hydrogen dimer molecule. Both have two electrons; both are favored, just like a Helium atom is favored. The preference for a two-atom excited state would explain why the spectrum of Hydrogen so strongly features transitions that terminate, not with the ground state, but rather with the first excited state.

A9. Ties to Spectroscopy

Being a tool of extreme sensitivity, spectroscopy is the tool of choice for both chemists and physicists studying the structure of atoms and molecules. But while the tool is incisive, the interpretations of its results and its prospects for new investigations leave room for further discussion in light of the theoretical developments summarized above, as well as the data reported in the main part of the paper.

First of all, spectroscopy can help us interpret some mathematical details about the atomic excitation model on offer here. The spectroscopic data about Hydrogen indicates that the energy required to bring the last Hydrogen atom from complete separation to complete integration into an existing super atom of $n_H - 1$ atoms, thus forming a super atom of n_H atoms, is $|E_1|[(n_H - 1)^{-2} - (n_H)^{-2}]$. The inverse squares can be understood as follows. The

radial scaling $r_{n_H} = n_H(r_e + r_p)$ suggests that all linear dimensions scale linearly with n_H. If so, the volume of the clusters scales as $(n_H)^3$. The number density of charges in clusters therefore scales as $n_H / n_H^3 = (n_H)^{-2}$. The positive energy locked in the pair of clusters therefore depends on the number density in the clusters. This is something like having energy proportional to pressure, as is seen in classical thermodynamics.

Furthermore, spectroscopy offers a way of testing the atomic structure model on offer here. Spectroscopic data for Hydrogen samples that include sensible amounts of deuterium and/or tritium would be extremely helpful in this regard. Recall the Z/M scale factor that occurs in the model; it implies a significant isotope effect. Being extremely sensitive, spectroscopy may be able to detect and quantify any such isotope effect.

Spectroscopic data about trans-Hydrogenic atoms invites analysis in terms of charge clusters in general, positive well as negative, and offers an opportunity to apply what has been revealed about ionization potentials (IP's). All spectral series for neutral atoms terminate with a spectral line whose energy corresponds to a first-order IP. Historically, spectral series have been characterized in terms of the famous Rydberg constant R. The value of R for a hypothetical nucleus of infinite mass is called R_∞, and the value of R for a real atom is said to scale from R_∞ according to the rule $R_Z = R_\infty \times Z^2 /(1 + m_e / m_{nucleus})$. The spectral limit for the real atom is then proportional to R_Z times $1/n^2$, where n reflects the largest radial quantum number the atom's electron population offers.

Where IP's are expressed in units of electron volts (eV's), R_∞ is expressed in inverse wavelengths (cm^{-1} or Å^{-1}). Other than that dimensional detail, the presumption is that the spectral limit would be the same as $IP_{1,Z}$. But the algebraic model for IP's involves no quantum number n, no nuclear charge Z, and its nuclear mass dependence is much stronger - $1/M$, where M is the nuclear mass number.

Consider an element toward the end of the Periodic Table. Its top radial quantum number n will be 5, its Z will be of order 100. So its R_Z will be of order $R_1 \times (10,000/25) = R_1 \times 400$. By contrast, its measured and M/Z-scaled first order $IP_{1,Z}$ will be of order $IP_{1,1}$, and the raw data without the M/Z scaling will be of order $IP_{1,1} \times 0.4$. That is three orders of magnitude smaller than the application of textbook scaling to the Rydberg constant predicts. It would seem that there is no empirical evidence *whatever* for that kind of scaling deep into the Periodic Table. It seems likely that the standard scaling for R was just an early guess, offered before spectroscopy was so well developed, or so many IP's had been measured. It now lies fossilized in the pedagogical literature, and needs to be dug out.

The only Z^2 involved in the IP data occurs for *total* ionization (not any kind of single-electron 'state' elevation). With the M/Z-scaled total IP for Hydrogen given by $IP_{1,1}$, all others are given by $2 \times Z^2 IP_{1,1}$. What does that universal factor of 2 mean? I believe it

reveals a form of 'equi-partition of energy': for any atom that *has* an electron cluster, that electron cluster involves an amount of internal energy equal in magnitude to the atomic orbit energy in the atom.

If this is true, then the spectral data tells us something about the relationship between electrons and photons. The traditional QM model has a one-for-one correspondence between a photon emitted and a single electron state change in a single atom. The present model has an electron cluster made up of electrons from several atoms coming apart, and possibly several new, smaller electron cluster, made up of electrons from fewer atoms, being formed.

Consider Hydrogen again. Consider a decay that starts with a cluster of N and ends with a cluster of $M < N$. With cluster energies N^2 and M^2, one expects photon energies $\propto N^2 - M^2$. The relationship is 'proportional', not 'equal', because the number $N^2 - M^2$ is generally large compared to unity. The spectral lines traditionally attributed to normal H atomic state transitions never exhibit photon energy greater than one unit of orbit energy. (Higher-energy transitions do occur, but without the attribution 'normal'. I believe they involve the un-recognized 'sub states' of H .)

A proportionality factor $1/N^2 M^2$ will guarantee photon energies limited to one unit of orbit energy. It makes the photon energies $= (N^2 - M^2)/N^2 M^2 = 1/M^2 - 1/N^2$. Spectroscopic data do indeed confirm this functional form for normal spectral lines.

The present model offers a different interpretation for one important spectral datum. Observe that when the final state is the ground state $M = 1$, the numerator in the present model involves is no $-M^2$ energy consumption for formation of a new cluster because there *is* no new cluster. The photon energy for a drop to the ground state is then $1/M^2 = 1$, regardless of N. In conventional terms, photon energy $= 1$ looks like a drop from dissociated plasma to ground state, *i.e.* $N \to \infty$. The present model suggests the more mundane interpretation that the photon energy for a drop to the ground state is $1/M^2 = 1$, regardless of the starting state N.

The present model also offers an explanation for why one never sees just one spectral line; one always sees a spectrum, plus some sort of noise. Observe that all transitions are at least binary: $N \to M \& (N - M)$, That means the cluster energies are $N^2 \to M^2 \& (N - M)^2$. The energy left for formation of photons is never more than $E = N^2 - M^2 - (N - M)^2$, except for the special case $M = 1$, where $E \to N^2 - (N-1)^2$. In the general binary case, the photon energies are

$$\frac{(N^2 - M^2)}{N^2 M^2} = \frac{1}{M^2} - \frac{1}{N^2} \text{ and } \frac{N^2 - (N-M)^2}{N^2 (N-M)^2} = \frac{1}{(N-M)^2} - \frac{1}{N^2} \qquad \text{(A8.1)}$$

If they did not have to be binary, the two kinds of transitions would consume energies $N^2 - M^2$ and $N^2 - (N - M)^2$, which would require a total energy of

$2N^2 - M^2 - (N - M)^2$. But there isn't that much energy available; there is only $N^2 - M^2 - (N - M)^2$. The scaled-down energies available for each kind of transition are

$$(N^2 - M^2) \frac{N^2 - M^2 - (N - M)^2}{2N^2 - M^2 - (N - M)^2} \text{ \& } [N^2 - (N - M)^2] \frac{N^2 - M^2 - (N - M)^2}{2N^2 - M^2 - (N - M)^2} \quad \text{(A8.2)}$$

Dividing these energies by the requisite photon energies produces photon counts

$$N^2 M^2 \frac{N^2 - M^2 - (N - M)^2}{2N^2 - M^2 - (N - M)^2} \text{ \& } N^2 (N - M)^2 \frac{N^2 - M^2 - (N - M)^2}{2N^2 - M^2 - (N - M)^2} \quad \text{(A8.3)}$$

Note that in general, the total photon count from a transition $N \to M \, \& \, (N - M)$ is not equal to the number N of electrons in the scenario. There is no one-for-one correspondence between electrons and photons here, as there is in standard quantum theory.

Note too that photon counts from (A8.3) are in general real numbers. Actual photon counts have to be integers. The leftover fractions have to appear in some other way, such as thermal background and Doppler line broadening. This type of scenario can account for the fact that some spectral lines, especially toward the infra red, look 'diffuse', while others, especially toward the ultra violet, look 'sharp'.

Spectroscopy is a huge subject in its own right, deserving of much more discussion in light of the present research. But here we must stop at this point. Because of its deep involvement of ionization potentials, spectroscopy marks a transition from Physics to Chemistry, and so now returns the reader to the main part of this paper.

References

[1]   Whitney, C. K. Single-Electron State Filling Order Across the Elements, forthcoming *in International Journal of Chemical Modeling* (2008) 1, (1).

[2]   Whitney, C. K. *Visualizing Electron Populations in Atoms*, submitted to *International Journal of Chemical Modeling*.

[3]   Whitney, C. K. *Closing in on Chemical Bonds by Opening up Relativity Theory*. *International Journal of Molecular Sciences*, Special Issue on The Chemical Bond and Bonding (2008) No. 9, pp. 272-298.

[4]   Goodman, J. W. *Introduction to Fourier Optics*; McGraw-Hill: New York, 1968.

[5]   Born, M.; Wolff, E. *Principles of Optics*, Fifth Edition; Pergamon: Oxford, 1975.

[6]   Scerri, E. R. *The Periodic Table – Its Story and Its Significance*; Oxford University Press: Oxford, England, 2007).

[7]   Spronsen, J. W. *The Periodic System of Chemical Elements*; Elsevier: Amsterdam, Netherlands, 1969.

[8]   Mazurs, E. G. *Graphic Representations of the Periodic System During One Hundred Years*; University of Alabama Press, AL, USA, 1974.

[9]   Mingos, D. M. P. *Essential Trends in Inorganic Chemistry*, page 10; Oxford University Press: Oxford, England, 1998.

[10] Siekierski S.; Burgess J. *Concise Chemistry of the Elements*; Horwood Publishing Series in Chemical Science; Horwood Publishing Ltd.: Chichester, England, 2002.

[11] Putz, M. V. *Systematic Formulation for Electronegativity and Hardness and Their Atomic Scales within Densitiy Functional Softness Theory*, *International Journal of Quantum Chemistry* (2006), 106, 361-386; URL: http://www3.interscience.wiley.com/ cgi-bin/abstract/112093056/START.

[12] Putz, M.V.; Russo N.; Sicilia, E. *On the Application of the HSAB Principle through the use of Improved Computational Schemes for Chemical Hardness Evaluation*, *Journal of Computational Chemistry* (2004), 25, 994-1003; URL: http://www3.interscience. wiley.com/ cgi-bin/abstract/107637137/START.

[13] Putz, M.V. *Semiclassical Electronegativity and Chemical Hardness*. *Journal of Theoretical and Computational Chemistry* (2007) 6, 33-47; URL: http://www.worldscinet.com/jtcc/06/0601/S0219633607002861.html.

[14] Briddell, D. *Field Structure Theory* (2007), http://www.fieldstructure.org

[15] Liénard, A. *Champ Electrique et Magnétique produit par une Charge Electrique Concentrée en un Point et Animée d'un Movement Quelconque*. *L'Eclairage Electrique*, XVI (1898) (27) 5-14, (28) 53-59, (29) 106-112.

[16] Wiechert, E. *Elektrodynamische Elementargesetze*. *Archives Néerlandesises des Sciences Exactes et Naturelles série II, Tome IV* (1901).

[17] Jackson, J.D. *Classical Electrodynamics*, First Edition, Chapter 14 (John Wiley & Sons, New York, NY, USA, 1962).

[18] Einstein, A. *On the Electrodynamics of Moving Bodies* (1905), as translated in *The Collected Papers of Albert Einstein*, Volume 2, pages 140-171 (Princeton University Press, Princeton NJ, USA, 1989).

[19] Einstein, A. "On the Relativity Principle and the Conclusions Drawn from it" (1907), as translated in *The Collected Papers of Albert Einstein*, Volume 2, pages 252-311 (Princeton University Press, Princeton NJ, USA, 1989).

[20] Ritz, W. "Recherches critiques sur l'electrodynamique generale", *Ann, Chim. et Phys.* (1908) 13, 145-256.

[21] Moon, P.; Spencer, D. E. *On the establishment of a universal time*. *Phil. Sci.* (1956) 23, 216-229.

[22] Moon, P.; Spencer D. E.; Moon E.E, *The Michelson-Gale experiment and its effect on the postulates on the velocity of light*. *Physics Essays* (1990) 3, 421-428.

[23] Spencer, D. E. *The development of the new Gaussian equation for the force between moving charges*. *Infinite Energy Magazine* (2005) (No. 63) 39-46.

[24] Whitney, C. K. *Editor's Essays*. *Galilean Electrodynamics* (2005) 16, Special Issues 3, Winter, 41-60.

[25] Whitney, C. K. *Essays on Special Relativity Theory*. *Hadronic Journal* (2006) 29, 47-110.

[26] Whitney, C.K. *Algebraic Chemistry*. *Hadronic Journal* (2006) 29, 1-46.

[27] Thomas, L. H. *The Kinematics of an Electron with an Axis*, *The London, Edinburgh, and Dublin Phil. Mag. and J. of Sci.* (1927) seventh series, 1-22.

[28] Mills, R.L. *The Nature of the Chemical Bond Revisited and an Alternative Maxwellian Approach, Physics Essays* (2004) 17 (3) 342-389.

[29] Beckmann, P. *Electron Clusters*. *Galilean Electrodynamics* (1990) 1, 55-58; *erratum* on p. 82.

[30] Aspden, H. *Electron Clusters* (1990) (Correspondence) Galilean Electrodynamics 1, 81-82.

[31] Piestrup, M. A.; Puthoff H. E.; Ebert, P. J. *Correlated Emissions of Electrons*. *Galilean Electrodynamics* (1998) 9, 43-49.

[32] Walter, M.; *et al*. *A Unified view of ligand-protected gold clusters as superatom complexes*. *Proceedings of the National Academy of Sciences* (8 July, 2008) 105 (27) 9157-9162; noted in 'Editor's Choice' column, *Science* (18 July, 2008) 321, 319.

[33] Wesley, J. P. *Classical Quantum Theory*; Benjamin Wesley: Weiherdammstrasse 24, 78176 Blumberg Germany, 1996; Chapter 7.

Chapter 2

ONIOM AND ONIOM-MOLECULAR DYNAMICS METHODS: PRINCIPLES AND APPLICATIONS

Toshiaki Matsubara[*]

Center for Quantum Life Sciences and Graduate School of Science, Hiroshima
University, 1-3-1, Kagamiyama, Higashi-Hiroshima 739-8530, Japan

Abstract

The ONIOM hybrid method, which combines a quantum mechanical (QM) method with the molecular mechanical (MM) method, is one of the powerful methods that allow to calculate large molecular systems with the high accuracy afforded for smaller molecular systems. The notable feature of this method is that it can include the environmental effects into the high level QM calculation through a simple extrapolation procedure. This is a significant difference from the conventional QM/MM methods. The definition of the layer is simple, and also the layer is easily extended to the multiple-layers. Contrary to this, the traditional QM/MM method that adopts the sophisticated link between the QM and MM regions makes the handling difficult. The ONIOM method is thus more flexible and versatile than the conventional QM/MM method, and is therefore increasingly adopted as an efficient approach beneficial to many areas of chemistry.

Recently, the ONIOM-molecular dynamics (MD) method has been developed to analyze the more complicated large molecular system where the thermal fluctuations of the environment play an important role. For example, when the target is a biomolecule, such as an enzyme, the property of the entire system is strongly affected by its dynamical behavior. In such case, the ONIOM method is not satisfactory. The coupling of the ONIOM method with the molecular dynamics (MD) method is necessary to account for the thermal fluctuations of the environment. Newly developed ONIOM-MD method has made it possible to characterize the function of enzyme etc. in a realistic simulation of the thermal motion, retaining the concept embodied in the ONIOM method. In this chapter, the basic concept of the ONIOM and ONIOM-MD methods we developed and their applications to typical cases are introduced.

---

[*] E-mail address: matsu05@hiroshima-u.ac.jp

1. Introduction

We have usually adopted the molecular mechanics (MM) method with molecular force fields such as MM3, Charmm, Amber, and UFF, when we treat large organic molecules, solution, and biological systems [l]. However, if molecular system includes a strong interaction where large charge transfer or electron reorganization is involved, it is not accurate enough. The molecular mechanics method cannot predict transition state structures and energies of chemical reactions. High-level ab initio molecular orbital (MO) methods are necessary to obtain reliable structures with strong chemical interactions and energetics of chemical reactions. However, high-level MO calculations have a problem of the computational time, because computational time increases as a large power of the size of molecules. Therefore, the application of the high-level MO method has been limited in the size of the molecule. Even calculations at a relatively low level of the MO method also face the same problem especially for geometry optimizations. To resolve this problem of the computational time, large and complicated substituents of real molecules, which are chemically less important, have been very often replaced by a smaller atom or group [2]. The model molecule obtained in this way, where its size is reduced enough, allows us to calculate with the ab initio MO method. This approximation can evaluate the major electronic effect. However, the steric or electrostatic effect of the replaced part cannot be taken into account. One of possible solutions to this dilemma is to integrate the MO and the MM methods, where the active and important part of the molecule and the remainder, such as bulky substituents or other chemical environments, are treated by the MO and MM methods, respectively. This method thus makes it possible to calculate the real molecule saving the computational time and without losing the accuracy. A combination of the MO and MM methods, which is the so-called QM/MM method, has been proposed by some groups [3-6]. However, there is a significant difference in the definition of the MO and MM layers between the conventional QM/MM and our ONIOM methods, as mentioned later.

In the initial stage, we optimized the entire molecule by the 'MO-then-MM' approach. The geometry of a model molecule without bulky groups is first optimized by the MO method, and then some hydrogen atoms of the model molecule are replaced by the original substituents, whose geometries are re-optimized using the MM method, leaving the geometry of the MO part frozen. This approach was used for organometallic reactions with bulky substituents and ligands [7-9]. To fully optimize the geometry of the entire molecule, the Integrated Molecular Orbital + Molecular Mechanics (IMOMM) method was developed [10]. We tested this IMOMM method on the conformation and energetics of n-butane [11] and applied to a few examples, for example, the transition states for the S_N2 reaction, $Cl^- + RCl \rightarrow ClR + Cl^-$, where R is methyl in the model system and propyl, isobutyl, and neopentyl in the real systems, and potential energy profiles for the oxidative addition reaction of H_2 to $Pt(PR_3)_2$, where in the model system R is H and in the real system methyl, tert-butyl, and phenyl [12]. The test calculations showed that the IMOMM method can reproduce the geometries and energetics by a full ab initio MO method. It should be noted that the geometry optimization for the reaction system, $H_2 + Pt[P(t-Bu)_3]_2$, at the IMOMM(MP2:MM3) level requires only 1/253 of the computational time required for a MP2 full geometry optimization.

The MP2 full geometry optimizations for the systems with R = t-Bu or Ph is practically impossible.

Some cases need a more accuracy in geometries and energies. For such cases, the integrated Molecular Orbital + Molecular Orbital (IMOMO) method combining different levels of molecular orbital approximations was designed [13,14]. The active or more important part of a molecule is treated at a higher level of approximation, which is similar to the IMOMM method, and the remainder at a lower level of approximation. We further extended this concept of the IMOMM and IMOMO approaches and developed the ONIOM (our own n-layered integrated molecular orbital and molecular mechanics) method [15]. A molecular system is partitioned into an onion-like multilayer. For example, a three-layered system is handled by a high level of ab initio method taking account of the electron correlation on the most important core part of the system, an intermediate level of MO theory to describe the electronic effects of functional groups or ligands in the vicinity of the active region, and a MM level of theory to describe the steric and electrostatic effects of the outer layer of the system. In practice, we can use any combination of molecular orbital approximations, i.e., ab initio, density functional to semi-empirical method, and molecular mechanics method in the ONIOM method.

Huge molecular systems in nano and biological science, where the 'true features' of the environmental effects remain unresolved, would be excellent targets of the ONIOM method. However, for example, in many cases of biomolecules, the dynamical behaviors would be strongly related to their properties. In such cases, the ONIOM method, in which the thermal motion of the molecular system is not taken into account, is not appropriate in itself. We therefore recently developed the ONIOM-molecular dynamics method by coupling the ONIOM method with the molecular dynamics (MD) method [16]. In the ONIOM-MD method, a direct MD simulation is performed calculating the ONIOM energy and its gradients on the fly. We first applied the ONIOM-MD method to cytidine and cytosine deaminase and showed that the thermal motion of the amino acid residues environment perturbs and destabilizes in energy the substrate trapped in the active site of the enzyme to promote the reaction [16,17]. To examine the environmental effects on the reaction in more detail, we recently applied the ONIOM-MD method to a simple reaction of the organometallic compound, cis-$(H)_2$Pt$(PR_3)_2 \rightarrow H_2$ + Pt$(PR_3)_2$, where the environment at the active site is quite similar to that of enzymes, and newly found the 'dynamical' environmental effects [18].

2. ONIOM Method

In this section, the principle and description of the ONIOM method is first mentioned in section 2.1. Then, the first application of the ONIOM method to the organometallic reaction, H_2 + Pt$(PR_3)_2 \rightarrow$ cis-$(H)_2$Pt$(PR_3)_2$, is introduced in the subsequent section 2.2.

2.1. Principle and Description of the ONIOM Method

The idea of the combination of the MO and MM methods is not first one for the ONIOM method. We can found it in the previous literatures for the QM/MM method [3-6]. There exists a significant difference between our ONIOM and traditional QM/MM methods in the

definition of the linkage between the QM and MM parts. The total energy E(X-Y) of the entire system X-Y (X is the inner part and Y is the outer part) is expressed as follows by the QM/MM and ONIOM methods.

$$E^{QM/MM}(X-Y) = E_{high}(X) + E_{low}(Y) + E_{int\,erlayer}(X,Y)$$

(1)

$$E^{ONIOM}(X-Y) = E_{high}(X) + E_{low}(X+Y) - E_{low}(X)$$

(2)

Eq. (1) for the QM/MM method includes the third term to describe the interaction energy between the inner and outer parts. We know that it is not easy to calculate this third term. A sophisticated definition of the interaction energy is necessary. On the other hand, eq. (2) for the ONIOM method is quite simple. We do not need to calculate a term corresponding to the third term of eq. (1). Both energy of the outer part and interaction energy between inner and outer parts are included in the easily calculated second and third terms. This is readily understood when we assume, for example, a water dimmer presented in figure 1. Here, one and the other H_2O molecules belong to the inner and outer parts, respectively. If a covalent bond exists between the inner and outer parts, we have to define a link atom to construct a model molecule of the inner part, as mentioned later. The total energy E(X-Y) of the entire system is thus expressed by a connection scheme for the QM/MM method and an extrapolation scheme for the ONIOM method. A notable feature of the ONIOM method is that it can include the environmental effects into the high level QM calculation through a simple extrapolation procedure. The definition of the layer is simple, and then the layer is easily extended to the multiple-layers. On the other hand, the traditional QM/MM method that adopts the sophisticated link between the QM and MM parts makes the handling difficult. The ONIOM method is more flexible and versatile than the conventional QM/MM method, and is therefore increasingly adopted as an efficient approach beneficial to many areas of chemistry.
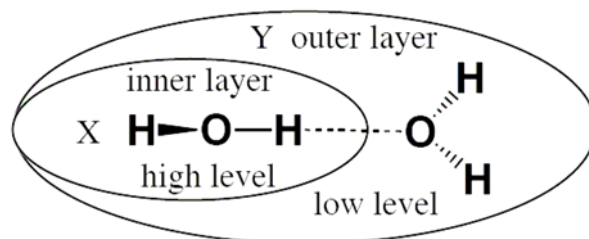
Figure 1. Two-layered ONIOM partition of a water dimmer.

The partitioning of the entire system in the case of the three-layered ONIOM methodology is presented in figure 2. The entire system is divided into three layers, i.e., the center of the system and intermediate and outer layers. The core part of the center of the system is the most important and active part, which includes a change in the elecronic configuration. The intermediate layer includes functional groups that have an electronic effect on the active part. The steric and electrostatic effects are taken into account by the outer layer. This partitioning is arbitrary but is an important issue that determines the calculation

accuracy. The core part is calculated at the highest level, and the calculation level is lowered in turn toward the outer layer, taking account of the electronic, electrostatic, and steric effects appropriately. Thus, we can save the computational time without losing the calculation accuracy.
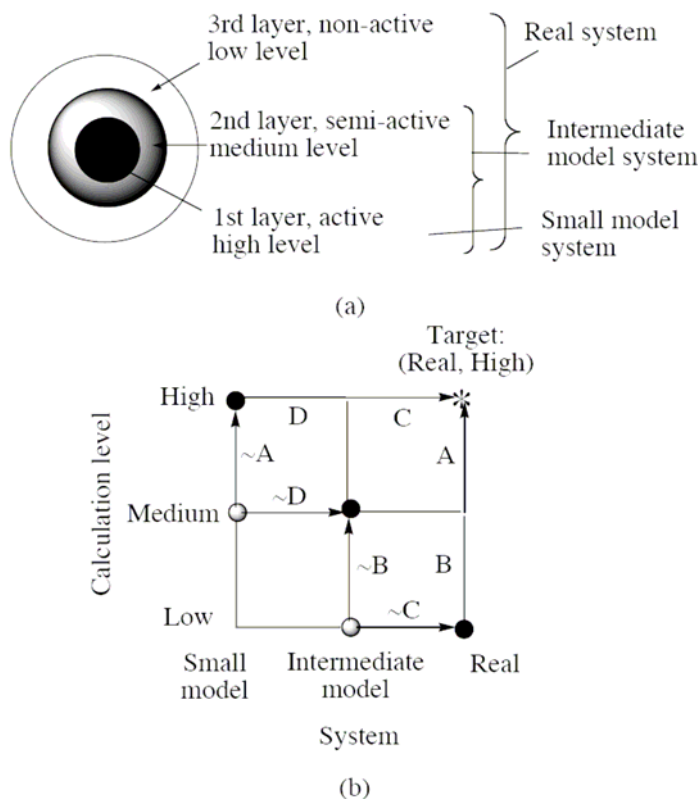
Figure 2. Concept of the ONIOM method.

The total energy of the entire system is defined as a sum of the energy of three layers as follows.

$$E(ONIOM3) = E(Small,High) + \Delta E(Int \leftarrow Small,Med)$$
$$+ \Delta E(Real \leftarrow Int,Low) \qquad (3)$$

Here,

$$\Delta E(Int \leftarrow Small,Med) = E(Int,Med) - E(Small,Med) \qquad (4)$$

$$\Delta E(Real \leftarrow Int,Low) = E(Real,Low) - E(Int,Low) \qquad (5)$$

The number of the layer is shown by the suffix n and described as ONIOMn. ONIOM3 means that the entire system is divided into three layers. The calculation level adopted to each layer is written as ONIOM3(High:Med:Low). In an actual calculation, we have to construct the

intermediate and small models, as mentioned later. To get an ONIOM energy of the entire system according to eqs. (3)-(5), we carry out five calculations for the real, intermediate, and small models at the different levels. Here, for example, the energy of the small model at a high level is written as E(Small,High). The energies expressed by eqs. (4) and (5), ~D and ~C, correspond to D and C, respectively, as shown in figure 2, which teach us that the ONIOM method obtain the total energy of the entire system at a high level E(Real,High) by an extrapolation procedure.

The partitioning of a molecular system using a link atom in the case of 3,3-dimethyl-1-butene is presented in figure 3. The vinyl group with the double bond is included in the inner part and the remainder t-Bu group in the outer part. In the model system of the inner part, the set 3 atom is replaced by the set 2 link atom. In this case, the t-Bu is replaced by the H link atom, and the model system ethylene is formed. If the bond between the set 1 and set 3 atoms is not a covalent bond but a hydrogen bond, the link atom is not necessary. Since the set 2 link atom is on the bond between the set 1 and set 3 atoms, the position of the set 2 link atom is shown by eq. (6).

$$\mathbf{r}_2 = \mathbf{r}_1 + g\,(\mathbf{r}_3 - \mathbf{r}_1) \tag{6}$$

$$\theta_2 = \theta_3,\ \phi_2 = \phi_3 \tag{7}$$

Here, g is a scale factor and constant. When the distance of the C-C bond $|\mathbf{r}_3 - \mathbf{r}_1|$ changes in the optimization of the structure, the distance of C-H bond $|\mathbf{r}_2 - \mathbf{r}_1|$ also changes, the link atom H following the set 3 C atom. The bond angle and dihedral angle of the link atoms are the same as those of the corresponding set 3 atoms.

The definition of the integrated ONIOM gradients is straightforward. Let us assume a two-layered ONIOM. The ONIOM energy is expressed as follows.

$$E(ONIOM2) = E(Small,High) + \Delta E(Real \leftarrow Small,Low) \tag{8}$$

$$\Delta E(Real \leftarrow Small,Low) = E(Real,Low) - E(Small,Low) \tag{9}$$

Then, the two-layered ONIOM energy gradients are obtained as

$$gradE(ONIOM2) = gradE(Real,Low) + gradE(Small,High)*\mathbf{J}(\mathbf{R}_2;\mathbf{R}_1,\mathbf{R}_3)$$
$$- gradE(Small,Low)*\mathbf{J}(\mathbf{R}_2;\mathbf{R}_1,\mathbf{R}_3) \tag{10}$$

Here, $\mathbf{R}$ is the coordinate of the atom. The forces on the set 2 link atoms ($\mathbf{R}_2$) are projected onto the set 1 ($\mathbf{R}_1$) and set 3 ($\mathbf{R}_3$) atoms by the Jacobian matrix $\mathbf{J}$. The second derivatives of the ONIOM energy with respect to the nuclear coordinates are also obtained in the same manner [19]. The ONIOM gradients and second derivatives are used for the geometry optimization, normal mode analysis, and so on, of the real system.
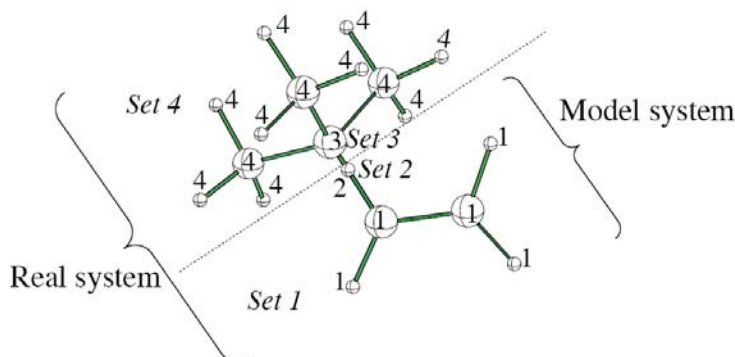
Figure 3. Two-layered ONIOM partitioning of 3,3-dimethyl-1-butene.

2.2. Application to the Organometallic Reaction, H_2 + $Pt(PR_3)_2 \rightarrow$ cis-$(H)_2Pt(PR_3)_2$ (R= Me, Ph, and t-Bu)

It is well-known that the substituents of the ligands play an important role in the organometallic reactions. The reaction is very often controlled by their steric and electronic effects and then a selectivity of the reaction appears. Therefore, organometallic reactions are excellent targets of the ONIOM method. We made a first test and application of the ONIOM method to the simplest prototype organometallic reaction, the oxidative addition of the H_2 molecule to the bisphosphine platinum complex $Pt(PR_3)_2$, shown in Scheme 1, for R = Me, Ph, and t-Bu.
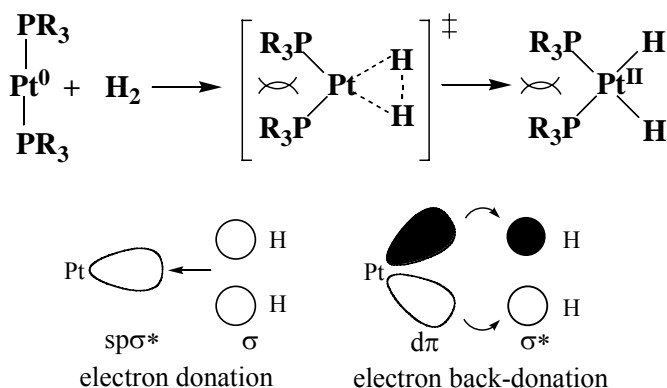
Scheme 1.

The reactivity of the platinum(0) complex with H_2 has been experimentally investigated [20]. The cis-bishydrido complex with a chelating phosphine ligand cis-$(H)_2Pt[(t-Bu)_2P(CH_2)_3P(t-Bu)_2]$ is produced from the reaction of $Pt[(t-Bu)_2P(CH_2)_3P(t-Bu)_2]$ with H_2 in toluene [21]. The two-coordinate phosphine complexes $Pt(PR_3)_2$ (R=c-C_6H_{11} and i-Pr) also react with H_2 at room temperature under atmospheric pressure to give finally the energetically stable trans-$(H)_2Pt(PR_3)_2$ product through the isomerization of the cis-$(H)_2Pt(PR_3)_2$ product [20(a)]. However, in the case of $P(t-Bu)_3$ and $PPh(t-Bu)_2$, the reaction practically does not

take place under the same reaction conditions. The reactivity of $Pt(PR_3)_2$ toward H_2 increases in the following order: $P(t-Bu)_3 < PPh(t-Bu)_2 < P(c-C_6H_{11})_3 < P(i-Pr)_3$.

This reaction has been studied extensively with ab initio MO method for the model system with R = H [22]. The process of cis addition is well-understood in the electronic aspects [22(a),(b)]. The reaction proceeds by the two kinds of orbital interactions, electron donation from the H_2 σ orbital to a Pt spσ* vacant orbital and electron back-donation from an occupied Pt dπ orbital to the H_2 σ* orbital, as shown in Scheme 1. The latter interaction is important to complete the reaction. An occupied dπ orbital of the Pt is destabilized in energy by the electronically donative phosphine ligand bent toward the cis position in the transition state, which allows an easier interaction of the Pt dπ with the H_2 σ*.

However, the reactivity of $Pt(PR_3)_2$ depending on the substituents R of the real system has not been investigated due to the problem of the computational time. We carried out the ONIOM calculations for geometries and energies of the reactants, transition states, and products of the reaction for the substituted systems with R=Me, Ph, and t-Bu at the ONIOM2(MP2:MM3) level taking account of the electron correlation for the core part. In the ONIOM method, we used $H_2 + Pt(PH_3)_2$ as a model system for the real system, for example, of $H_2 + Pt(P(t-Bu)_3)_2$, as shown in Scheme 2. The set 2 link atoms, the H atoms on PH_3, in the model system are replaced by the tert-C atoms on $P(t-Bu)_3$, set 3 atoms, in the real system.
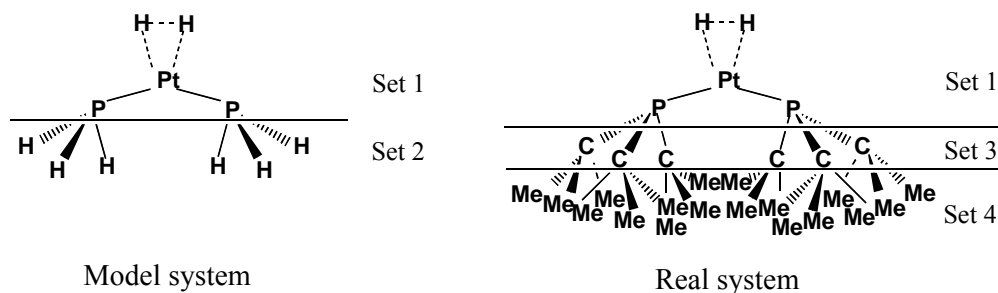
Scheme 2.

The transition state has been theoretically determined to be rather early for R=H [22(a)-(d)]. The H-H distance is stretched by only 4 %, and the Pt-H distance is much longer than that of the cis-product. The energy barrier is calculated to be only several kilocalories per mole due to the large exothermicity. The ONIOM calculations for the cases of R=Me and Ph also gave similar results in both geometry and energetics. Contrary to this, the ONIOM calculations showed significant differences in the case of R=t-Bu. The effects of the substituents t-Bu are remarkably reflected in the ∠P-Pt-P angle in the geometry. The ∠P-Pt-P angle of 151° for R=t-Bu is larger by 6-9° than those for the other R=Me and Ph in the transition state. Although the ∠P-Pt-P angle decreases to 107° in the cis-product for R=Me and Ph, it does not become smaller than 127° for R=t-Bu. These tendencies for R=t-Bu are due to the strong steric repulsion between the bulky t-Bu substituents caused by the bend of the P-Pt-P axis during the reaction. It is also interesting that the congested environment of t-Bu forces the H_2 to rotate out from the P-Pt-P plane by 32° in the transition state. The energetics also dramatically changes by the steric effect of t-Bu. The reaction is largely endothermic and then the energy barrier becomes very large in the case of R=t-Bu as shown

by **f**igure 4. This is because an occupied $d\pi$ orbital of the Pt is not sufficiently destabilized in energy for the electron back-donation to the H_2 σ^* orbital due to the large $\angle$P-Pt-P angle in the transition state and the product. Thus, it is successfully revealed by the ONIOM method that the steric effect of the substituents of the ligands is an important factor controlling the H_2 oxidative addition. This is a first case that the role of the substituent of the ligand of the organometallic compound is computationally clarified.
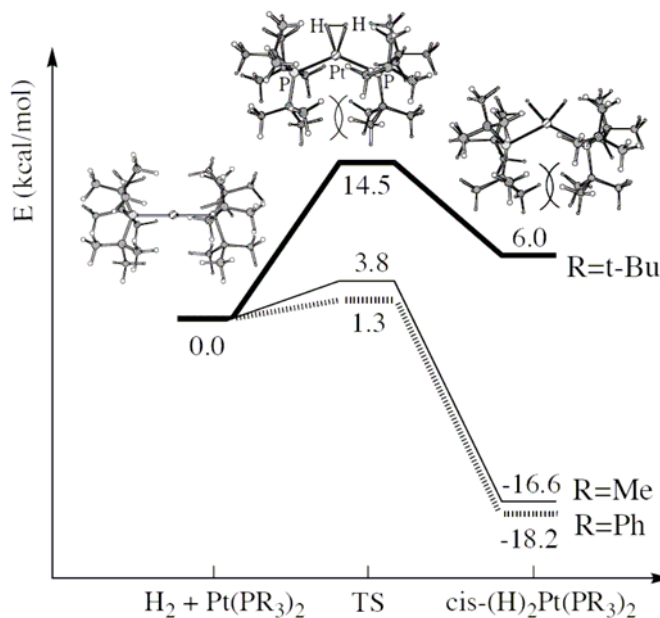
Figure 4. Potential energy surfaces of the reaction, $H_2 + Pt(PR_3)_2 \rightarrow$ cis-$(H)_2Pt(PR_3)_2$ (R=Me, Ph, and t-Bu), calculated by the ONIOM2(MP2:MM3) method.

3. ONIOM-Molecular Dynamics (MD) Method

In this section, after the explanation of the ONIOM-molecular dynamics (MD) method in section 3.1, the first applications of the ONIOM-MD method to cytidine deaninase and the organometallic reaction, cis-$(H)_2Pt(PR_3)_2 \rightarrow H_2 + Pt(PR_3)_2$, are introduced in section 3.2 and 3.3, respectively.

3.1. Principle and Description of the ONIOM-Molecular Dynamics (MD) Method

The ONIOM method is now routinely used all over the world to examine the large molecular systems, since it is implemented in GAUSSIAN03 program package. The ONIOM method is a very powerful method allowing us to calculate large molecular systems [10-15,19,23,24] without losing the accuracy afforded for smaller molecular systems. Due to the simple definition of the QM and MM layers [19], which easily includes the environmental

effects into the high level QM calculation, the ONIOM method is increasingly adopted as an efficient approach beneficial to many areas of chemistry, as mentioned earlier.

The biological system is one of excellent targets for the ONIOM method. For enzymes that include a reaction region at the active site, the QM method that can treat the electron configuration of the molecule is indispensable. In this case, we have been forced to reduce a real molecule to a model molecule, which is restricted to only active region, disregarding the environment so far, due to the limitation of the computational time. The ONIOM method resolved this problem by including the environment in the MM part, as the MM level of theory is good enough to describe the amino acid residues environment of enzymes.

However, the ONIOM method is not satisfactory in itself, when the target is a biomolecule, such as an enzyme, in which the property of the entire system is strongly affected by its dynamical behavior. For example, we have to take account of the thermal fluctuations of the environment to examine the environmental effects of the biomolecular system appropriately. We therefore recently developed the ONIOM-molecular dynamics method by coupling the ONIOM method with the molecular dynamics (MD) method [16(a)].
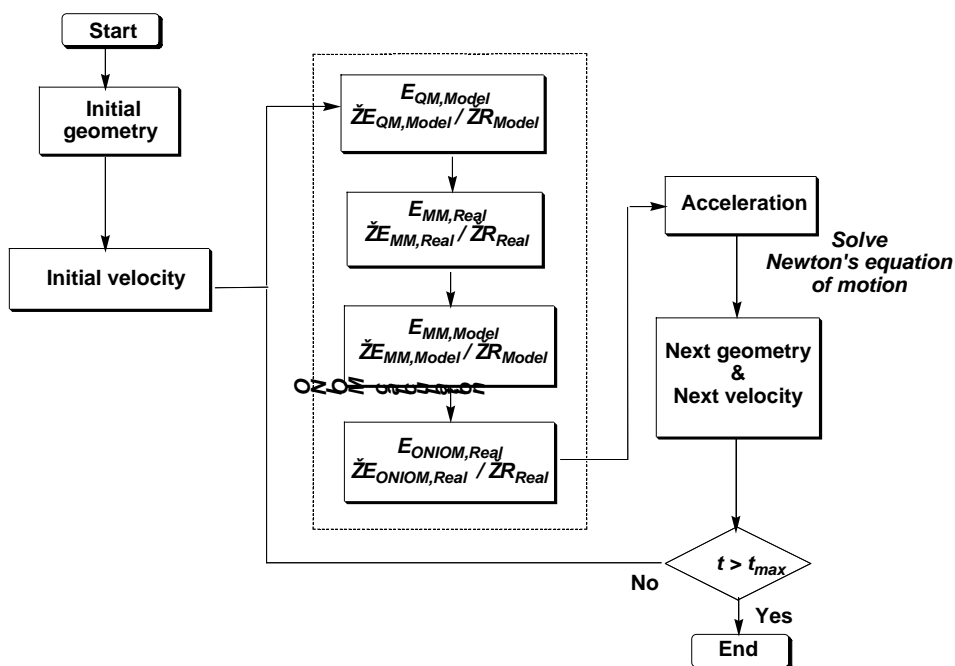
Figure 5. Flowchart of the ONIOM-molecular dynamics (MD) calculation.

The flowchart of the ONIOM-MD calculation is presented in figure 5. The time evolution of the atomic nuclei is performed according to the conventional MD procedure. Here, the Newton's equation of motion is solved by calculating the ONIOM gradients on the fly:

$$F(GradE_{ONIOM,Real}) = ma \qquad (11)$$

The ONIOM-MD method made it possible to characterize the function of enzymes in a realistic simulation of the thermal motion retaining the concept embodied in the ONIOM

method. In the next section, we introduce a first application of the ONIOM-MD method to cytidine deaminase.

3.2. Application to Cytidine Deaminase

Cytidine deaminase has attracted much attention from pharmaceutical point of view, because it plays an important role on the activation of the anticancer drug in the human body. Recently, the oral therapy by capesitabine has been popularized for the metastatic breast and colorectal cancer. The administered prodrug capesitabine undergoes some conversion processes by enzymes step by step inside the human body, and is finally converted to 5-fuluorouracil (5-FU) that attacks tumor tissues when it reaches the cancer cell, as presented in figure 6. Cytidine deaminase catalyzes the deamination of the intermediate 5'-deoxy-5-fluorocytidine (5'-DFCR) and produces 5'-deoxy-5-fluorouridine (5'-DFUR) that is the precursor of 5-FU [25,26]. This is an essential step of the entire process.
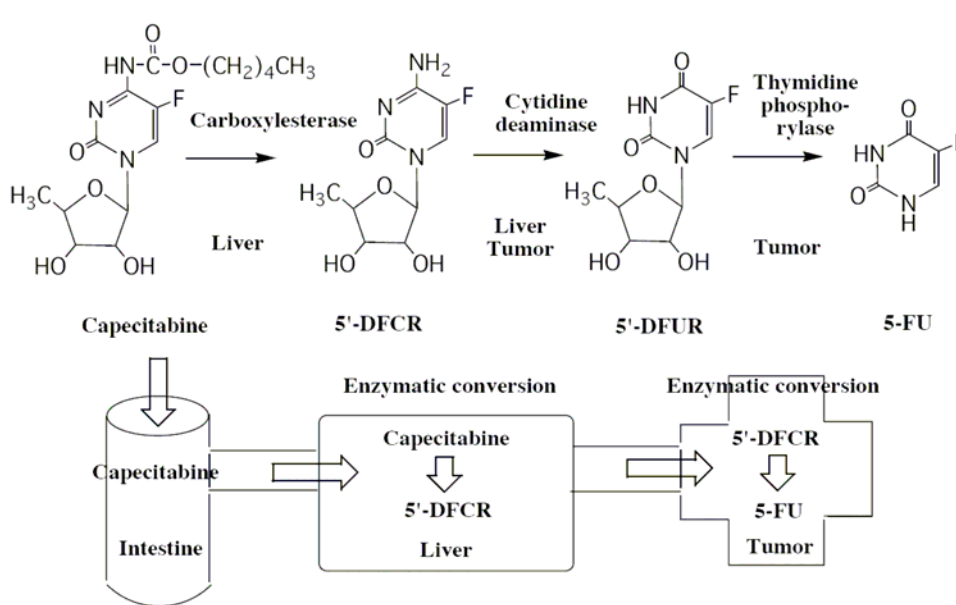
Figure 6. Activation process of anticancer drug capecitabine inside the human body.

The reaction mechanism in the active site proposed on the basis of the experimental results is presented in figure 7. Uridine and ammonia is produced from cytidine and water, where it is considered that the reaction undergoes an intermediate **B** usually referred to as the tetrahedral intermediate [26]. The participation of Glu104 in the deamination reaction has been speculated from the observed crystal structures that combine with the substrates [27,28]. The incoming H_2O molecule is first trapped at the empty site of the Zn atom in **E**. One of the H of the coordinated H_2O is abstracted by the glutamic acid and is transferred to the cytidine, which induces the nucleophilic attack of the hydroxyl anion on the Zn atom to the cytidine (**E→A**). As a result, the tetrahedral intermediate **B** is formed. This is the first process of the catalytic cycle. In the second process of the catalytic cycle, the -OH hydrogen in **B** is carried

toward the -NH$_2$ group by the glutamic acid to form NH$_3$ and the product uridine (**B→C→D**). This mediation of the glutamic acid is thought to lower the energy barrier of the deamination reaction. We have also recently shown that the glutamic acid significantly contributes to lower the energy barrier of the deamination reaction by means of the density functional theory (DFT) method using a small model of the active site [29], where the environmental effects of the amino acid residues in the pocket of the active site are ignored. The previous experimental studies have indicated that the second process of the catalytic cycle after the formation of the tetrahedral intermediate **B** is a rate-determining step [26,30].
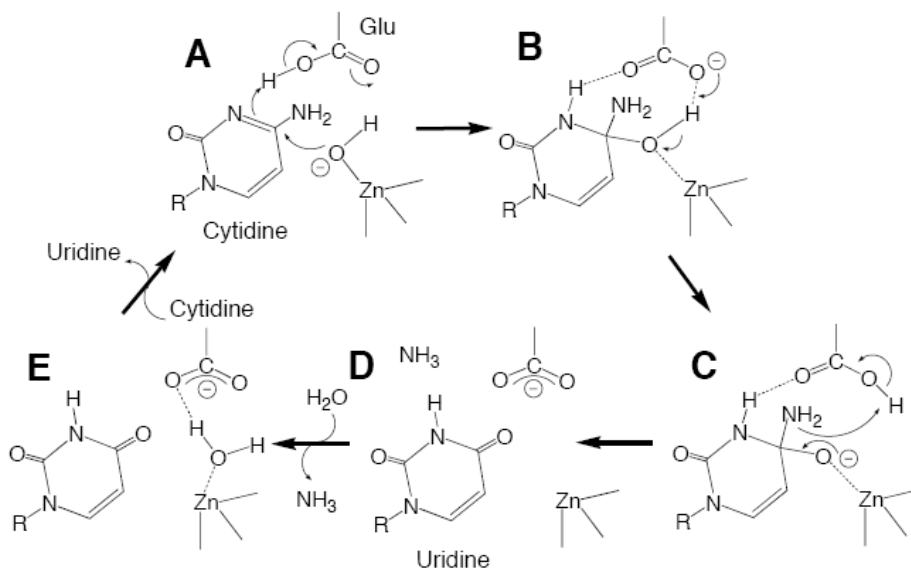
Figure 7. Experimentally proposed catalytic cycle of the hydrolytic deamination of cytidine in the active site of cytidine deaminase.

The crystal structure of cytidine deaminase was used as a realistic model of the enzyme for the ONIOM-molecular dynamics (MD) simulations. Water molecules are placed around the enzyme to mimic the water solvent. The entire system is divided into two layers of the core and outer parts. The active region was cut out from the active site of the real enzyme to form a model system, CH$_3$COO$^-$ + H$_2$O + (cytosine)Zn(SH)$_2$(H$_2$O), capping the dangling bonds with the H atoms. We included in the model system the –COO$^-$ group of Glu104 that mediates the deamination reaction and the three-coordinate Zn complex that binds with the substrate besides the substrate and the H$_2$O molecule. The ribose ring of cytidine is replaced by the H atom and cytosine is used instead of cytidine in the model system. To mimic the lone electron-pair of the N of the histidine that coordinates to the Zn atom in the real system, a H$_2$O molecule was used in the model system. The core part were treated by the HF level of theory and the outer part, i.e., the other part of the enzyme and the water solvent, by the MM level of theory with the AMBER99 and TIP3P force field parameters. The simulations were run under a constant temperature.

The second process of the deamination, which is considered to includes a rate-determinig step, starts from the tetrahedral intermediate **12**. The active site with the substrate of **12** of the realistic model optimized by the ONIOM-MD method at 0 K is displayed in figure 8. The

tetrahedral intermediate experimentally proposed is successfully reproduced. The Zn atom binds with the O5 atom with the distance of 1.985 Å, and the –COO⁻ of Glu104 interacts with the H25 and H13 atoms with the distances of 1.506 Å and 1.703 Å, respectively. It should be noted that the main chain of the CO oxygen of Tyr126 interacts with the H23 with the distance of 2.829 Å and affects the behavior of the -NH₂ group (see below). Three H-bonds between the substrate and the amino acid residues, Ala103, Asn89, and Glu91, found in the crystal structure are reproduced. The carbonyl group of the 6-membered ring forms the H-bond with Ala103. One of the –OH groups attached to the ribose ring forms the H-bonds with Asn89 and Glu91. Here, Glu91 more strongly interacts with the substrate than Ala103 and Asn89. These H-bonds prevent the substrate from relaxing, when the substrate is sterically perturbed by other amino acid residues [16(a),17]. Thus, these H-bonds play an important role to destabilize the substrate in energy.

Figure 8. Structure and its illustration of the active site of the tetrahedral intermediate 12 of the realistic model of cytidine deaminase in the water solvent optimized by the ONIOM-MD method. The optimized geometric parameters (Å) are also presented together.

The H-bonds between the substrate and the amino acid residues, Ala103, Asn89, and Glu91, are maintained in the ONIOM-MD simulation at 298.15 K, although the O---H distances are lengthened by 0.070-0.164 Å compared to those of the optimized structure, as presented in table 1. The tendencies in the distance and angle of three H-bonds found in the optimized structure are not changed in the ONIOM-MD simulation. The occurrence of these three H-bonds decreases in the order, Glu91 > Ala103 > Asn89, which reflects the strength of the H-bond. Ala103 as well as Glu91 strongly interacts with the substrate whereas Asn89 weakly interacts. Asn89 comes close to and goes away from the substrate repeatedly due to its thermal fluctuation.

Table 1. Occurrence of the H-bonds between the substrate and the neighboring amino acid residues and the average and standard deviation of the geometric parameters of their H-bonds in the ONIOM-MD simulation of the tetrahedral intermediate 12 of the realistic model of cytidine deaminase in the water solvent at 298.15 K [a]

Amino acid residue	Occurrence (%)	d (O---H) (Å)		∠(O---H-X) (degree)	
		Average	Standard deviation	Average	Standard deviation
Ala103	76.3	1.925(1.842)	0.113	159.6(140.7)	8.9
Asn89	46.9	2.057(1.893)	0.207	163.9(162.2)	8.9
Glu91	100.0	1.535(1.465)	0.088	170.1(173.0)	5.2

[a] The values in parentheses are the optimized geometric parameters. The occurrence was calculated on the basis of the geometries during the MD simulation with the requirements of the O---H distance less than 2.0 Å and the ∠O---H-X angle more than 120°. The standard deviation σ was calculated by the following equation; $\sigma = \sqrt{\dfrac{1}{n}\sum_{i=1}^{n}\left(X_i - \overline{X}\right)^2}$. See Figure 8 for the H-bonds.

The thermal motion of Tyr126 and Phe71, which are outside of the pocket of the active site and contact with the water solvent, is remarkably large, as shown by the mean square displacement calculated by the following equation (figure 9)

$$D_{MSD} = \frac{1}{3N}\sum_{i}^{N}\left|R_i(t) - R_i(0)\right|^2$$

(12)

Here, N is the number of the atoms included in each unit of the amino acid residues and substrate. The large thermal motion of Tyr126 and Phe71, which sandwich the substrate with His102, affects the substrate fixed by the H-bonds with other amino acid residues through the steric contact. In fact, the standard deviation of the QM energy of the substrate in the ONIOM-MD simulation is about two times larger for the realistic model (7.4 kcal/mol) than for the small model without the amino acid residues environment (4.2 kcal/mol). The energy fluctuations of the substrate are enlarged by the perturbation from the surrounding amino acid residues. These effects of the thermal motion of the neighboring amino acid residues are the 'dynamical environmental effects', which is a new concept we found. The dynamical environmental effects verify the general consensus that the substrate trapped in the pocket of the active site is destabilized in energy. When a part of energy fluctuations of the substrate larger than the energy barrier concentrates on a normal mode of the reaction coordinate, the reaction of the substrate proceeds. Therefore, the reactivity is enhanced when the energy fluctuations of the substrate are increased by the dynamical environmental effects. The high reactivity of enzymes thus originates from the dynamical environmental effects of the neighboring amino acid residues.
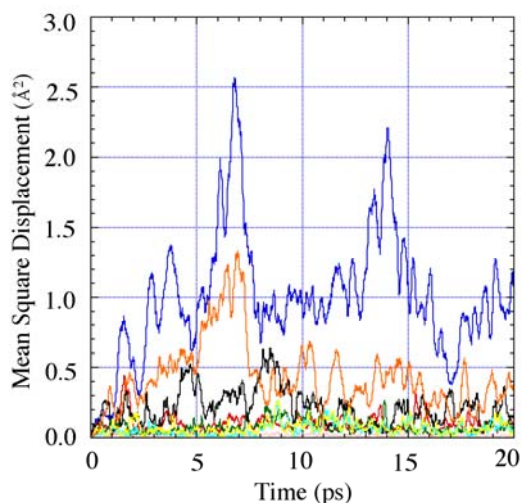
Figure 9. Change in the mean square displacement of the local units, the substrate and the neighboring amino acid residues, in the ONIOM-MD simulation of the tetrahedral intermediate 12 of the realistic model of cytidine deaminase in the water solvent at 298.15 K. The color of the lines represents the local units as follows; green: Asn89; blue: Phe71; red: ribose ring of the substrate; black: Glu91; pink: His102; pale blue: Ala103; yellow: Glu104; orange: Tyr126.

The intermediate **12** was converted to the intermediate **13** at 13.5 ps as presented in figure 10. The $-NH_2$ group rotates clockwise taking the energetically favorable channel with the increase in the kinetic energy of both H23 and H24. When the lone electron-pair of the $-NH_2$ is directed toward the $-COO^-$ of Glu104, the H25 migrates from the O5 to the O18 as a proton. Although the magnitude of the oscillation of the O18---H25 distance is large, the H25 never migrates to the O18 unless the lone electron-pair of the $-NH_2$ is directed toward the $-COO^-$ of Glu104 by the rotation of the $-NH_2$. The migration of the H25 takes place at the same time as the rotation of the $-NH_2$. On the other hand, the $-NH_2$ group freely rotates around the C6-N22 axis in the case of the small model without the amino acid residues environment. Consequently, the H25 migrates between the O18 and O5 atoms again and again. The rotation of the $-NH_2$ group is locked by the attractive interaction of the $-NH_2$ hydrogen with the CO oxygen of the main chain of Tyr126 in the realistic model (see figure 8). On the other hand, one of the H of the hydroxyphenyl group of Tyr126 keeps staying in the vicinity of the $-NH_2$ with the distance of less than 2.5 Å, and facilitates the rotation of the $-NH_2$ through the steric contact due to the thermal motion. Thus, the neighboring amino acid residues support the H migration step.
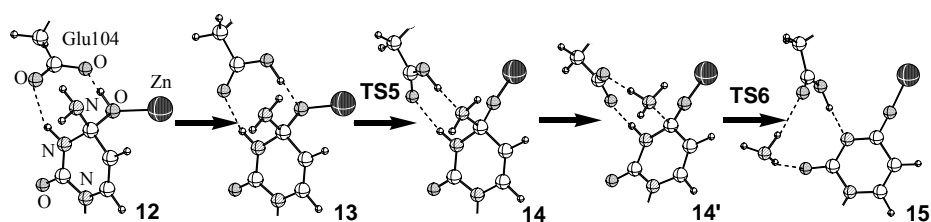
Scheme 3.
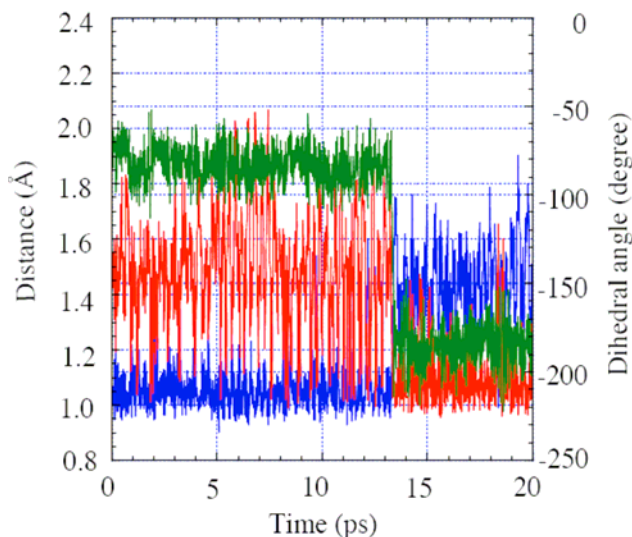
Figure 10. Change in the distances of the H-bond O5-H25---O18 and the dihedral angle ∠H24-N22-C6-O5 in the ONIOM-MD simulation of the tetrahedral intermediate 12 of the realistic model of cytidine deaminase in the water solvent at 298.15 K. The color of the lines represents the geometric parameters as follows; blue: d(O5-H25); red: d(H25---O18); green: ∠H24-N22-C6-O5.

The O16---H13-N7 H-bond between the –COO⁻ of Glu104 and the substrate is maintained in the realistic model, but not in the small model. The formation and dissociation of the O16---H13-N7 and O16---H23-N22 H-bonds are repeated alternately in the small model due to the large thermal motion of the O16 atom. In the realistic model, the position of the O16 and the O18 is kept so as to always form the O16---H13-N7 and O18---H25-O5 H-bonds. As a matter of course, the motion of the –COO⁻ of Glu104 is restricted, because the space inside the pocket of the active site is limited. However, the space provided for Glu104 is well designed to permits the O18 to merely shuttle between the O5 and the N22 as a carrier of the proton. This is responsible for the fact that Glu104 efficiently functions as a mediator of the proton transfer.

According to the potential energy surface of the deamination reaction calculated for the small model by the quantum mechanical method, at least, the energy of 10.2 kcal/mol is required to pass through the transition state **TS6** that is at the highest point [29]. In the MD simulation, the magnitude of the oscillation of the potential energy of the QM part of the realistic model is 14.8 kcal/mol. This suggests that the deamination reaction is in principle completed when more than 70 % of 14.8 kcal/mol concentrates on the normal mode corresponding to the reaction coordinate. However, in order to complete the deamination reaction within a limited time of the MD simulation, we increased the probability of the occurrence of the deamination reaction raising the temperature of the system.

When the temperature of the entire system is raised up to 600 K, the intermediate **14** was formed for a while after 9.6 ps. We found that besides **14** another intermediate **14'** exists between **14** and the transition state **TS6**. In the intermediate **14'**, the C6-N22 bond is hardly lengthened, although the H25 is almost transferred to the N22. We further increased intentionally the kinetic energy of the local unit including the reaction part, i.e., N7, C8, C9, N10, C11, O12, N22, H23, and H24, after 9.6 ps, at which the intermediate **14** is formed,

because the formed intermediate **14** goes back to the intermediate **13** without going to **15**. This selection of the atoms is reasonable, because the thermal energy would be localized on a vibrational mode corresponding to the reaction coordinate when the reaction proceeds (The H25 and H13 atoms are already sufficiently 'thermally activated' at 600 K). By this procedure, the formed NH_3 molecule on the C6 is released 3 ps later and the deamination reaction is successfully completed (figure 11). This result suggests that the release of the NH_3 molecule from the C6 (**14**→**15**) is the rate-determining step. During 3 ps from 9.6 to 12.6 ps before releasing the NH_3, the intermediate **14** was included 22.3 %, and the intermediate **14'** was also included 8.7 %. Although the intermediate **14** once retuned to the intermediate **13** after increasing the kinetic energy of the local unit, **14** was formed again at 11.3 ps. The H25 showed a reciprocating motion between the O18 and the N22 during 1.4 ps (from 11.3 to 12.7 ps) just before the release of the NH_3 molecule, which suggests that the NH_3 molecule is released when the motions of both H25 and N22 match to each other.
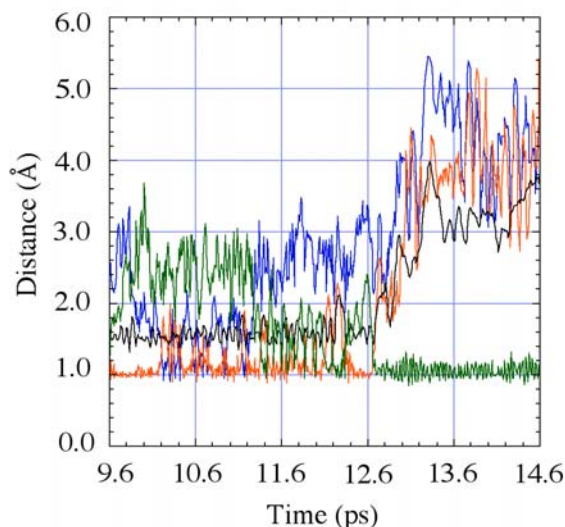
Figure 11. Change in the selected distances of the active site in the ONIOM-MD simulation of the tetrahedral intermediate 12 of the realistic model of cytidine deaminase in the water solvent at 600 K. The kinetic energy of the local unit consisting of the N7, C8, C9, N10, C11, O12, N22, H23, and H24 atoms was intentionally increased by two times after 9.6 ps. The color of the lines represents the distances as follows; green: d(N22-H25); blue: d(O5-H25); red: d(O18-H25); black: d(C6-N22).

3.3. Application to the Organometallic Reaction, cis-(H)$_2$Pt(PR$_3$)$_2$ → H$_2$ + Pt(PR$_3$)$_2$ (R=Me, Ph, and t-Bu)

As mentioned in section 2, the ONIOM calculations have demonstrated that the steric effect of the environment significantly changes the potential energy surface of the organometallic reaction, $H_2 + Pt(PR_2)_2 \rightarrow$ cis-(H)$_2$Pt(PR$_3$)$_2$. The steric effect might be one of reasons to determine the reactivity. However, the thermal motion of the environment should be taken into account to describe more realistic feature of the reaction, as our ONIOM-MD simulations have evidenced that the thermal motion is a crucial factor of the environmental

effects for enzymes. The 'dynamical environmental effects' on the active site is readily expected for the reverse reaction, cis-$(H)_2Pt(PR_3)_2 \rightarrow H_2 + Pt(PR_3)_2$. The inner (active) part of cis-$(H)_2Pt(PH_3)_2$ would be affected by the thermal motion of the outer part of the substituent R, because the inner part is surrounded by the outer part, as presented in Scheme 4. This situation of the inner part is similar to that of the substrate trapped in the pocket of the enzyme.
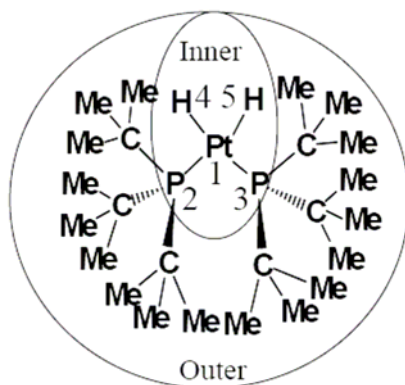
Scheme 4.

As mentioned aerlier, according to the ONIOM method, the sterically congested t-Bu substituent makes the cis-product unstable in energy, and then the oxidative addition of H_2 becomes difficult. On the other hand, the less congested Me and Ph substituents readily lead to the cis-product. Therefore, the reverse reaction, the H_2 reductive elimination, cis-$(H)_2Pt(PR_3)_2 \rightarrow H_2 + Pt(PR_3)_2$, would be the most facile in the case of the congested substituent t-Bu. We gave by ONIOM-MD method a further insight into the dynamical aspects of the environmental effects and more realistic feature of the H_2 reductive elimination, and revealed a dynamical factor of the environmental effects controlling the reactivity and a new feature of the reaction process.

We adopted the two-layered ONIOM methodology for the system, cis-$(H)_2Pt(PR_3)_2 \rightarrow H_2 + Pt(PR_3)_2$ (R=Me, Ph, and t-Bu). The inner part is cis-$(H)_2Pt(PH_3)_2 \rightarrow H_2 + Pt(PH_3)_2$, where all the P-C bonds are cut and the formed dangling bonds are capped with the H atoms. The outer part is substituent R. This ONIOM partition is the same as that used in section 2 for the H_2 oxidative addition. The inner and outer parts are also similarly treated by the quantum mechanical (QM) method at the Hartree-Fock (HF) level of theory and by the molecular mechanics (MM) method with the MM3 force field parameters, respectively. The MP2 level, which makes the MD simulation difficult due to the high computational cost, is not adopted, because the tendency in the potential energy surface for R=Me, Ph, and t-Bu is similar even at the HF level.

As far as we tried, the H_2 elimination from cis-$(H)_2Pt(PR_3)_2$ occurred only when R is t-Bu in the ONIOM-MD simulations during 100 ps. Figure 12 shows that the H_2 eliminates at 87.2 ps. Figure 12(c) focuses on the changes in the geometric parameters in the short time domain from 86.5 to 87.5 ps where the H_2 eliminates. The H_2 bond is at first formed at 87.16 ps. At this moment, the H4-H5 already shortens to 0.781 Å. On the other hand, the distances of the Pt-H4 and Pt1-H5 are 1.883 Å and 1.811 Å, respectively, which are not significantly

stretched. The angle ∠P2-Pt1-P3 of 138.2° is also still within its fluctuations (see figure 12(a)). It is interesting that one of the terminal H of t-Bu comes close to the Pt just before the H_2 elimination.
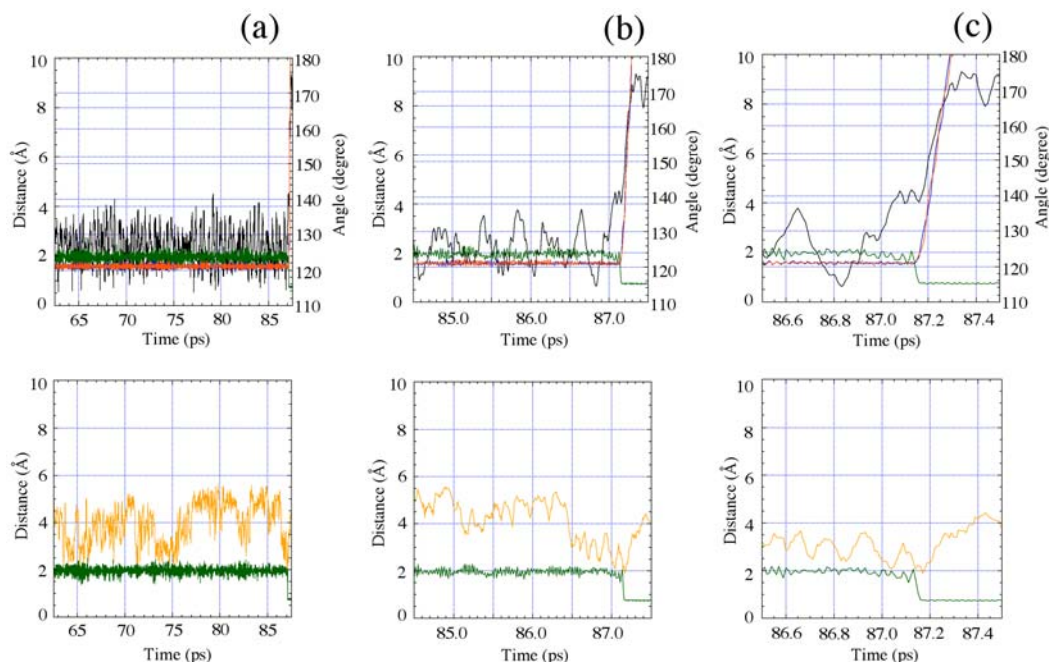
Figure 12. Change in the geometric parameters in the reaction, cis-(H)$_2$Pt[P(t-Bu$_3$)$_2$] → H_2 + Pt[P(t-Bu$_3$)$_2$], in the ONIOM-MD simulation at 900 K. The color of the lines represents the geometric parameters as follows; red: d(Pt1-H4); blue: d(Pt1-H5); green: d(H4-H5); orange: d(Pt1-H62(t-Bu)); black: ∠P2-Pt1-P3. a, b, and c have a different time scale.

As shown in figure 12(a), the magnitude of the fluctuations of the H4-H5 distance and that of the Pt1-H4 and Pt1-H5 distances repeat the increase and the decrease with a same cycle. The magnitude of the fluctuations of the H4-H5 distance obviously increases, when the H(t-Bu) atom comes close to the Pt. It is rational to think that two hydrido ligands are energetically enhanced through the steric contact of a H(t-Bu) with the Pt. This approach of the H(t-Bu) atom would also cause a C-H σ electron donation to the Pt and prevent the H_2 σ electron donation to the Pt, if the electronic effect is taken into account. The magnitude of the fluctuations of the ∠P2-Pt1-P3 angle also changes with a cycle. When the H4-H5 distance shortens, the ∠P2-Pt1-P3 angle has to enlarge in order to eliminate H_2. However, before the H_2 elimination takes place at 87.2 ps, both cycles of the changes in the magnitudes of the H4-H5 distance and the ∠P2-Pt1-P3 angle do not match as shown in figure 12(b). Both cycles match to each other in the time domain from 87.0 to 87.2 ps just before the H_2 elimination takes place. A H(t-Bu) atom also attacks the Pt for a while after 86.5 ps, until the H_2 eliminates. In the time domain from 87.0 to 87.2 ps where all the factors to eliminate the H_2 are prepared, two hydrido ligands, H4 and H5, start the reaction as shown by the change in the H4-H5 distance. After the H_2 is detached from the Pt at 87.2 ps, the ∠P2-Pt1-P3 angle increases (figure 12(c)) along the downhill energy surface of the outer part (figure 14(a)).

As shown by the snapshots of the H_2 elimination process (figure 13), when the H_2 molecule is formed on the Pt at 87.16 ps, the H_2 axis suddenly rotates to become perpendicular to the P2-Pt1-P3 plane. One of charge transfer interactions, the electron back-donation from an occupied Pt $d\pi$ orbital to the H_2 σ^* orbital, is broken by this rotation of the H_2. The formed H_2 still interacts with the Pt due to the other charge transfer interaction, the electron donation from the H_2 σ orbital to an unoccupied Pt $sp\sigma*$ orbital. This electron donative interaction is broken by the attack of a H(t-Bu) atom at 87.17 ps. A H(t-Bu) stays close to the Pt during the H_2 elimination, keeping the Pt-H(t-Bu) distance less than 2.3 Å. At 87.18 ps, the H_2 is detached and it goes away from the Pt after 87.19 ps. The H_2 rotates around the axis that penetrates the mid point of the H_2 and the Pt throughout the H_2 elimination reaction. However, the H_2 does not always rotate in the H_2 elimination. When an enough energy provided to the H_2, the H_2 is detached from the Pt atom without the significant rotation of the H_2. This process of the H_2 elimination with the contribution of a H(t-Bu) atom is a new facts revealed by the ONIOM-MD method.
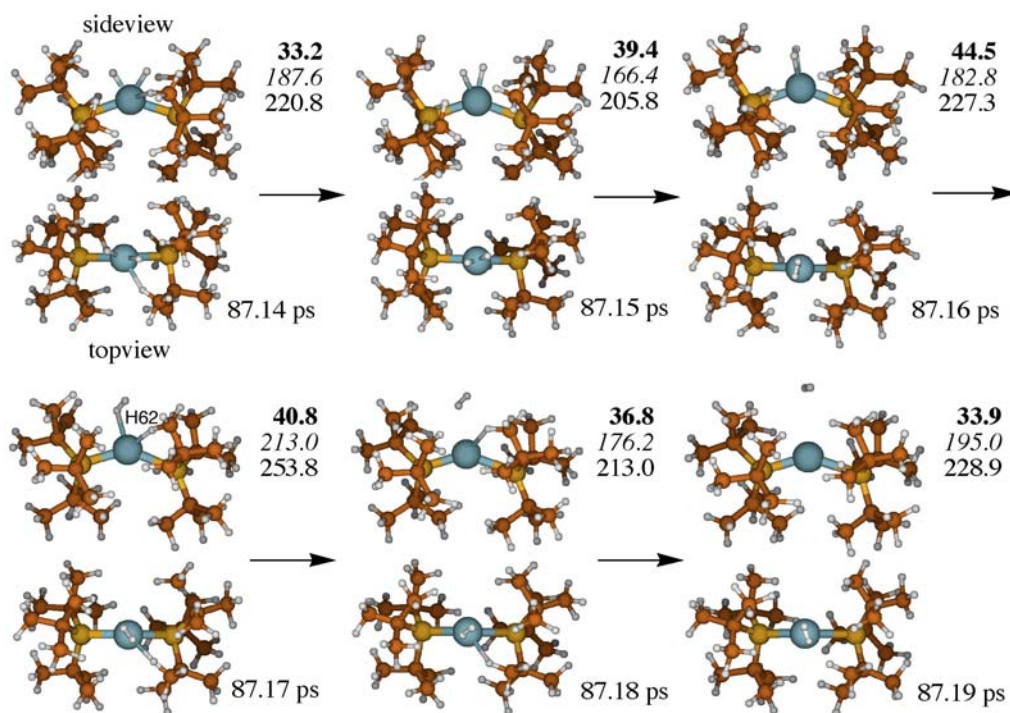
Figure 13. Snapshots of the reaction, cis-$(H)_2$Pt$[P(t-Bu_3)_2] \rightarrow H_2 + Pt[P(t-Bu_3)_2]$, in the ONIOM-MD simulation at 900 K. The values (kcal/mol) in the bold, italic, and normal type are the QM energy of the inner part, the MM energy of the outer part, and the ONIOM energy of the entire system, respectively.

The MM and ONIOM energies change randomly by their fluctuations during the H_2 elimination. On the other hand, the QM energy reaches the top of the energy mountain at 87.16 ps, where the axis of the H_2 formed on the Pt becomes perpendicular to the P2-Pt1-P3 plane. These facts indicate that the actual energy barrier exists in the QM (inner) part. The QM system overcomes an energy barrier by gaining an energy from its energy fluctuations, as shown by the fact that the top of the energy barrier is within the energy oscillation of the QM

part (see figure 14(b)). When the energy from the fluctuations concentrates on a normal mode of the H_2 elimination, the reaction proceeds, as mentioned in section 3.2. The standard deviation of the QM energy of the inner part is the largest for R=t-Bu as shown in table 2, which suggests that the reactivity is the largest for R=t-Bu. In the congested system for R=t-Bu, the inner part is strongly perturbed by the thermal motion of the bulky t-Bu having a huge energy. As a result, the energy fluctuations of the inner part increase. When the system becomes less congested after the H_2 elimination, the energy fluctuations of the inner part are reduced (table 2 and figure 14(b)).

Table 2. Standard deviation of the energy of the inner part σ_E^{QM} (kcal/mol) of cis-$(H)_2Pt(PR_3)_2$ in the ONIOM-MD simulations at various temperatures and the energy barrier of the inner part ΔE^{QM} (kcal/mol) for the reaction, cis-$(H)_2Pt(PR_3)_2 \rightarrow H_2 +$ $Pt(PR_3)_2$ (R = Me, Ph, and t-Bu), calculated by the ONIOM method

R	Standard deviation			Energy barrier	
	300 K	600 K	900 K[a]	HF level	MP2 level
Me	1.7	3.2	4.8	28.3	20.2
Ph	2.6	4.6	6.5	28.5	20.4
t-Bu	3.9	5.8	8.1/5.2	24.4	17.0

[a] The values on the left and right-hand side of the slash for R=t-Bu are those before and after the H_2 elimination, respectively.
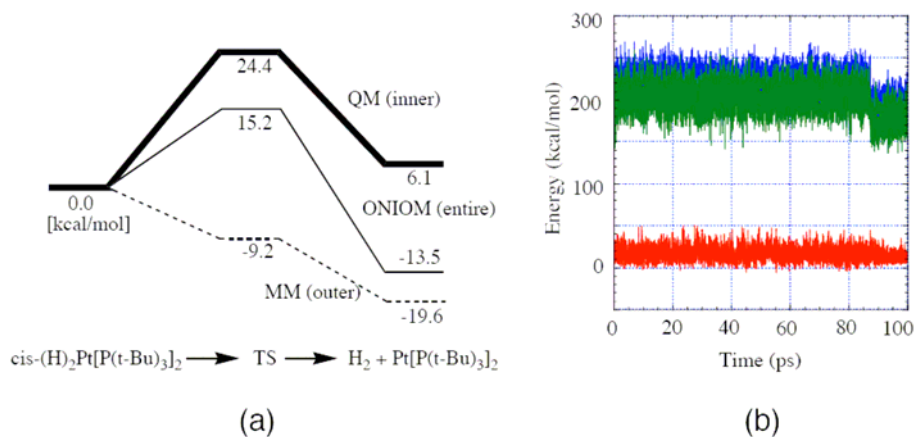
Figure 14. Change in the potential energies in the reaction, cis-$(H)_2Pt[P(t-Bu_3)_2] \rightarrow H_2 + Pt[P(t-Bu_3)_2]$, in the ONIOM calculation (a) and in the ONIOM-MD simulation at 900K (b). In (b), the color of the lines represents the potential energies as follows; blue: ONIOM energy of the entire system; green: MM energy of the outer part; red: QM energy of the inner part.

The forces added to two hydrido ligands from the substituents R are important as a driving force of the H_2 elimination reaction, as figure 13 shows that the H_2 bond is formed first before the increase in the P2-Pt1-P3 angle. Both hydrido ligands feel large forces in the case of R=t-Bu as presented in figure 15. After the H_2 elimination, these forces become zero. The magnitude of the force obviously increases in the order, t-Bu > Ph > Me.
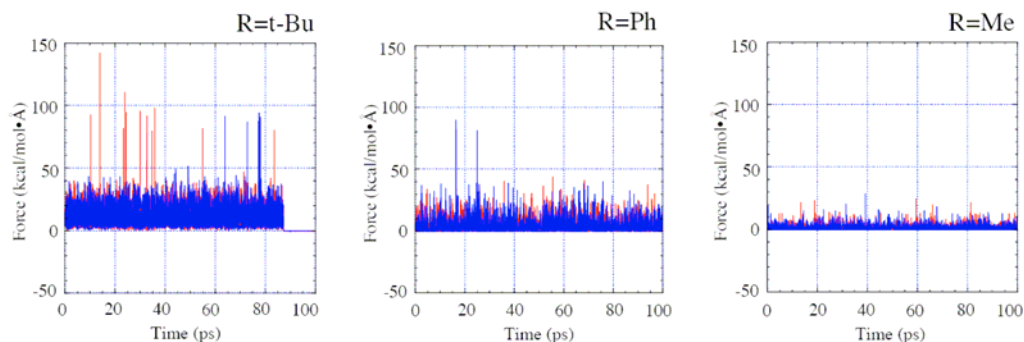
Figure 15. Change in the forces added to the hydrido ligands of the inner part from the substituents R of the outer part in the reaction, cis-$(H)_2Pt(PR_3)_2 \rightarrow H_2 + Pt(PR_3)_2$ (R=Me, Ph, and t-Bu), during the ONIOM-MD simulation at 900K. In each case, red: H4 and blue: H5.

As mentioned earlier, the inner part itself has to overcome its energy barrier to complete the reaction. After the H_2 is detached from the Pt, the large steric repulsion between two phosphine ligands is reduced by the increase in the ∠P2-Pt1-P3 angle along the downhill energy surface. The essential barrier exits in the inner part. Therefore, we have to assess the reactivity not by the energy barrier of the entire system including the outer part but by the energy barrier of the inner part. The energy required to overcome a barrier is provided from the energy fluctuations of the inner part. The reaction therefore becomes more facile, when the magnitude of the energy fluctuations of the inner part is enlarged by the dynamical environmental effects of the outer part caused by the thermal motion, as mentioned in section 3.2. The thermal motion of the bulky t-Bu having a huge energy in the congested space is a driving force of the reaction and supports to overcome the energy barrier.

The magnitude of the energy fluctuations of the inner part is different among the substituents, R=Me, Ph, and t-Bu, of the outer part at the same temperature. These difference determine the reactivity of the inner part as mentioned earlier. In this sense, not the temperature but the energy fluctuations, should be essential factors to evaluate the reaction rate. We therefore derived an equation, which connects the temperature T to the standard deviation of the energy σ_E, in order to replace the temperature T by the standard deviation of the energy σ_E in the Arrhenius' equation. The variance of the energy σ_E^2 . . is written in the following form, since we here think a canonical ensemble with a constant temperature.

$$\sigma_E^2 = \left\langle \left(E - \langle E \rangle \right)^2 \right\rangle = \left\langle E^2 \right\rangle - \left\langle E \right\rangle^2 \tag{13}$$

The average of the energy is expressed as follows.

$$\langle E \rangle = \sum_i E_i p_i \tag{14}$$

Here, the probability p_i of E_i in the state i of the system is

$$p_i = \frac{1}{Z}\exp\left(-\frac{E_i}{k_B T}\right)$$

(15)

The partition function Z is written as

$$Z = \sum_i \exp\left(-\frac{E_i}{k_B T}\right)$$

(16)

Using eq. (14), the variance of the energy is written as

$$\sigma_E^2 = \langle E^2\rangle - \langle E\rangle^2 = \frac{1}{Z}\left\{\sum_i E_i^2 \exp\left(-\frac{E_i}{k_B T}\right)\right\} - \left\{\frac{1}{Z}\sum_i E_i \exp\left(-\frac{E_i}{k_B T}\right)\right\}^2.$$

(17)

On the other hand, the specific heat $C_v = \dfrac{d\langle E\rangle}{dT}$ is calculated as follows using eq. (14).

$$\frac{d\langle E\rangle}{dT} = \frac{d}{dT}\frac{\sum_i E_i \exp\left(-\frac{E_i}{k_B T}\right)}{Z}$$

$$= \frac{1}{k_B T^2}\left\{\frac{1}{Z}\left(\sum_i E_i^2 \exp\left(-\frac{E_i}{k_B T}\right)\right) - \left(\frac{1}{Z}\sum_i E_i \exp\left(-\frac{E_i}{k_B T}\right)\right)^2\right\}.$$

(18)

Therefore, the specific heat C_v is written as

$$C_v = \frac{d\langle E\rangle}{dT} = \frac{1}{k_B T^2}\sigma_E^2$$

(19)

According to the principle of equipartition of energy, the average energy is

$$\langle E\rangle = \frac{1}{2}f k_B T$$

(20)

Here, f is the number of degree of freedom. The specific heat C_v is, thence, written in another form,

$$C_v = \frac{d\langle E\rangle}{dT} = \frac{1}{2}f k_B$$

(21)

Using eqs. (19) and (21), we obtain the following equation,

$$\frac{1}{2} f k_B = \frac{1}{k_B T^2} \sigma_E^2$$

(22)

Eq. (22) is arranged as follows.

$$T = \sqrt{\frac{2}{f}} \frac{\sigma_E}{k_B}$$

(23)

When we use eq. (23) in the Arrhenius' equation, $k = A \exp\left(-\frac{\Delta E}{RT}\right)$, we obtain

$$k = A \exp\left(-\sqrt{\frac{f}{2}} \frac{\Delta E}{\sigma_E}\right)$$

(24)

The rate constant is expressed by the standard deviation of the energy σ_E instead of the temperature T in the derived eq. (24) (Matsubara's equation). The ratio of the rate constant for the systems with the different energy fluctuations of the inner part is calculated as follows using eq. (24).

$$\frac{k_a}{k_b} = \frac{\exp\left(-\sqrt{\frac{f^{QM}}{2}} \frac{\Delta E_a^{QM}}{\sigma_{Ea}^{QM}}\right)}{\exp\left(-\sqrt{\frac{f^{QM}}{2}} \frac{\Delta E_b^{QM}}{\sigma_{Eb}^{QM}}\right)}$$

(25)

It is assumed here that the frequency factors A for two different systems are the same. The standard deviation of the energy of the inner part σ_E^{QM} and the energy barrier of the inner part ΔE^{QM} presented in table 2 were used to calculate the ratio of the rate constant using eq. (25). f is 27. The qualitative tendencies in the ratio of the rate constant for the HF and MP2 levels are quite similar as presented in table 3. The reactivity is much larger for R=t-Bu than for the other R=Me and Ph as expected. The rate constant is, for example, more than 45 times larger for R=t-Bu than for R=Ph at the MP2 level at 900 K. The rate constant increases in the order, t-Bu > Ph > Me, at each temperature.

The ratio of the rate constant is also calculated using the Arrhenius' equation as follows.

$$\frac{k_a}{k_b} = \frac{\exp\left(-\dfrac{\Delta E_a^{QM}}{RT}\right)}{\exp\left(-\dfrac{\Delta E_b^{QM}}{RT}\right)} \tag{26}$$

Since the environmental effects of the sterically congested t-Bu substituent a little reduce the energy barrier of the inner part, the reaction becomes more facile in the case of R=t-Bu. But, when we take account of the dynamical environmental effects through the standard deviation of the energy of the inner part, the reaction for the sterically congested t-Bu substituent becomes much more facile as shown in table 3. The inner part is just thought to be embedded in a bath of the outer part and is heated by the thermal motion of the sterically congested substituents of the outer part. The inner part is heated higher by 160-220 K for R=t-Bu than for R=Ph as calculated by eq. (23). This is reflected in the rate constant through the standard deviation of the energy in eq. (24). These results explicitly show the dynamical effects of the environment of the sterically congested substutuent of t-Bu on the reaction.

Table 3. Ratio of the rate constant of the reaction, cis-(H)$_2$Pt(PR$_3$)$_2$ $\rightarrow$ H$_2$ + Pt(PR$_2$)$_2$, for R=Me and Ph to that for R=t-Bu calculated at various temperatures[a]

R	Ratio 1		Ratio 2	
	HF level	**MP2 level**	**HF level**	**MP2 level**
		300 K		
Me	1.44×10^{-3}	4.66×10^{-3}	2.63×10^{-17}	9.88×10^{-13}
Ph	1.03×10^{-3}	3.33×10^{-3}	3.10×10^{-8}	2.72×10^{-6}
t-Bu	1.00	1.00	1.00	1.00
		600 K		
Me	3.79×10^{-2}	6.82×10^{-2}	3.99×10^{-8}	4.01×10^{-6}
Ph	3.21×10^{-2}	5.77×10^{-2}	6.71×10^{-4}	3.98×10^{-3}
t-Bu	1.00	1.00	1.00	1.00
		900 K		
Me	1.12×10^{-1}	1.67×10^{-1}	2.51×10^{-5}	4.30×10^{-4}
Ph	1.01×10^{-1}	1.49×10^{-1}	6.46×10^{-3}	2.19×10^{-2}
t-Bu	1.00	1.00	1.00	1.00

[a] The ratios 1 and 2 were calculated by the eq. (26) and (25), respectively, using the standard deviation of the energy of the inner part σ_E^{QM} and the energy barrier of the inner part ΔE^{QM} presented in Table 2.

4. Concluding Remarks

We have developed a QM/MM hybrid ONIOM method, to calculate the large molecular system practically, without the problem of the computational time and without losing the calculation accuracy. We recently further developed the ONIOM-molecular dynamics (MD) method integrating the ONIOM method with the molecular dynamics method to take account of the effect of the thermal motion of the environment. We first applied the ONIOM-MD method to an enzyme, citidine deaminase.

Although the reaction mechanism of citidine deaminase is being clarified, there still remain a lot of questions to be resolved to understand why citidine deaminase shows such a high catalytic activity for the deamination. From the viewpoint of improving the efficacy of the anticancer drug, further insights into the function and catalysis of the enzyme to transform the anticancer prodrug into an active form are strongly desired.

The contribution of the thermal motion of the neighboring amino acid residues environment to the catalysis is now one of subjects of interest. The ONIOM-MD simulations showed that the thermal motion of the neighboring amino acid residues perturbs the fluctuations in the geometry and energy of the substrate trapped in the active site through the steric contact. This is a 'dynamical effect' of the environment we found, which is a new concept and 'true feature' of the environmental effects. We clarified the dynamical environmental effects of the neighboring amino acid residues on the trapped substrate and successfully specified the key amino acid residues of these effects. We also revealed that the dynamical environmental effects, which enlarge the fluctuations in the energy of the substrate, are important factors controlling the reaction of the substrate. The ONIOM-MD method brought us new findings and understandings concerning the enzymatic reaction.

The dynamical environmental effects caused by the thermal motion, which was found in the pocket of the active site of the enzyme, is thought to play an important role generally in the active site of the system surrounded by a similar environment. A prototype organometallic reaction, cis-$(H)_2Pt(PR_3)_2 \rightarrow H_2 + Pt(PR_3)_2$ (R=Me, Ph, and t-Bu), is a good sample. The ONIOM-MD simulations showed that the thermal motion of the substituents R of the ligands increases the magnitude of the energy fluctuations of the active site to promote the H_2 elimination reaction. These dynamical environmental effects increase in the order, t-Bu > Ph > Me, indicating that the reactivity of cis-$(H)_2Pt(PR_3)_2$ increases in the same order. This order in the reactivity is proven by an equation derived from the Arrhenius' equation (Matsubara's equation). The snapshots of the reaction in the ONIOM-MD simulation for R=t-Bu also indicated a new feature of the H_2 elimination process.

References

[1]   N. L. Allinger, Y. H. Yuh, J.-H. Lii, *J. Am. Chem. Soc.*, **111**, 8551 (1989). J.-H. Lii, N. L. Allinger, *J. Am. Chem. Soc.*, **111**, 8566 (1989). (b) J.-H. Lii, N. L. Allinger, *J. Am. Chem. Soc.*, **111**, 8576 (1989). (c) B. R. Brooks, R. E. Bruccoleri, B. D. Olafson, D. J. States, S. Swaminathan, M. Karplus, *J. Comp. Chem.*, **4**, 187 (1983). (d) J. C. Smith, M. Karplus, *J. Am. Chem. Soc.*, **114**, 801 (1992). (e) S. J. Weiner, P. A. Kollman, D. A. Case, U. C. Singh, C. Ghio, G. Alagona, S. Profeta Jr., P. Weiner, *J. Am. Chem. Soc.*, **106**, 765 (1984). (f) S. J. Weiner, P. A. Kollman, D. T. Nguyen, D. A. Case, *J. Comp. Chem.*, **7**, 230 (1986). (g) A. K. Rappe, C. J. Casewit, K. S. Colwell, W. A. Goddard III, *J. Am. Chem. Soc.*, **114**, 10024 (1992).

[2]   N. Koga, K. Morokuma, *Chem. Rev.*, **91**, 825 (1991).

[3]   Warshel, M. Karplus, *J. Am. Chem. Soc.*, **94**, 5612 (1972).

[4]   U. C. Singh, P. A. Kollman, *J. Comp. Chem.*, **7**, 718 (1986).

[5]   M. J. Field, P. A. Bash, M. Karplus, *J. Comp. Chem.*, **11**, 700 (1990).

[6]   J. Eckert, G. J. Kubas, J. H. Hall, P. J. Hay, C. M. Boye, *J. Am. Chem. Soc.*, **112**, 2324 (1990).

[7]   H. Kawamura-Kuribayashi, N. Koga, K. Morokuma, *J. Am. Chem. Soc*., **114**, 8687 (1992).

[8]   F. Maseras, N. Koga, K. Morokuma, *Organometallics*, **13**, 4008 (1994).

[9]   T. Yoshida, N. Koga, K. Morokuma, *Organometallics*, **15**, 766 (1996).

[10] F. Masaeras, K. Morokuma, *J. Comp. Chem*., **16**, 1170 (1995).

[11] T. Matsubara, S. Sieber, K. Morokuma, *Int. J. Quantum Chem*., **60**, 1101 (1996).

[12] T. Matsubara, F. Maseras, N. Koga, K. Morokuma, *J. Phys. Chem*., **100**, 2573 (1996).

[13] S. Humbel, S. Sieber, K. Morokuma, *J. Chem. Phys*., **105**, 1959 (1996).

[14] M. Svensson, S. Humbel, K. Morokuma, *J. Chem. Phys*., **105**, 3654 (1996).

[15] M. Svensson, S. Humbel, R. D. J. Froese, T. Matsubara, S. Sieber, K. Morokuma, *J. Phys. Chem*., **100**, 19357 (1996).

[16] T. Matsubara, M. Dupuis, M. Aida, *Chem. Phys. Lett*., **437**, 138 (2007). (b) T. Matsubara, M. Dupuis, M. Aida, *J. Comput. Chem*., **29**, 458 (2008).

[17] T. Matsubara, M. Dupuis, M. Aida, *J. Phys. Chem. (B),* **111**, 9965 (2007).

[18] T. Matsubara, *J. Phys. Chem. (A),* in press (2008).

[19] S. Dapprich, I. Komaromi, K. S. Byun, K. Morokuma, M. J. Frisch, *J. Mol. Struct. (THEOCHEM),* 461-462, 1 (1999).

[20] T. Yoshida, S. Otsuka, *J. Am. Chem. Soc*., **99**, 2134 (1977). (b) J. Fornies, M. Green, J. L. Spencer, F. G. A. Stone, *J. Chem. Soc., Dalton Trans*., **1006** (1977). (c) R. S. Paonessa, W. C. Trogler, *J. Am. Chem. Soc*., **104**, 1138 (1982). (d) D. L. Packett, C. M. Jensen, R. L. Cowan, C. E. Strouse, W. C. Trogler, *Inorg. Chem*., **24**, 3578 (1985).

[21] T. Yoshida, T. Yamagata, T. H. Tulip, J. A. Ibers, S. Otsuka, *J. Am. Chem. Soc*., **100**, 2063 (1978).

[22] K. Kitaura, S. Obara, K. Morokuma, *J. Am. Chem. Soc*., **103**, 2891 (1981). (b) S. Obara, K. Kitaura, K. Morokuma, *J. Am. Chem. Soc*., **106**, 7482 (1984). (c) J. O. Noell, P. J. Hay, *J. Am. Chem. Soc*., **104**, 4578 (1982). (d) J. J. Low, W. A. Goddard III, *J. Am. Chem. Soc*., **106**, 6928 (1984). (e) J. J. Low, W. A. Goddard III, *Organimettalics*, **5**, 609 (1986).

[23] T. Vreven, K. Morokuma, *J. Comp. Chem*., **21**, 1419 (2000).

[24] K. Morokuma, *Bull. Korean Chem. Soc*., **24**, 797 (2003).

[25] M. J. Snider, S. Gaunitz, C. Ridgway, S. A. Short, R. Wolfenden, *Biochemistry*, **39**, 9746 (2000).

[26] M. J. Snider, L. Reinhardt, R. Wolfenden, W. W. Cleland, *Biochemistry*, **41**, 415 (2002).

[27] D. C. Carlow, A. A. Smith, C. C. Yang, S. A. Short, R. Wolfenden, *Biochemistry*, **34**, 4220 (1995).

[28] S. Xiang, S. A. Short, R. Wolfenden, C. W. Carter Jr., *Biochemistry*, **36**, 4768 (1997).

[29] T. Matsubara, M. Ishikura, M. Aida, *J. Chem. Inf. Model*., **46**, 1276 (2006).

[30] L. Yao, Y. Li, Y. Wu, A. Liu, H. Yan, *Biochemistry*, **44**, 5940 (2005).

Chapter 3

CONSTRAINING OPTIMIZED EXCHANGE

Marcel Swart,[a,b,c] Miquel Solà[b] and F. Matthias Bickelhaupt[a]

[a] Department of Theoretical Chemistry and Amsterdam
Center for Multiscale Modeling, Vrije Universiteit Amsterdam,
De Boelelaan 1083, 1081 HV Amsterdam, The Netherlands
[b] Institut de Química Computacional and Departament de Química,
Universitat de Girona, Campus Montilivi, 17071 Girona, Catalunya (Spain)
[c] Institució Catalana de Recerca i Estudis Avançats (ICREA),
08010 Barcelona, Catalunya (Spain)

Abstract

Several recent studies (*J. Phys. Chem. A* 2004, *108*, 5479; *J. Comput. Chem.* 2007, *28*, 2431) have shown impressive results when replacing the non-empirical PBE density functional by the empirical OPBE or OLYP functionals, i.e. replacing the PBE exchange functional by Handy and Cohen's OPTX functional. To investigate the origin of the improvements, we have placed constraints from the non-empirical PBE exchange functional on the empirical OPTX exchange functional, and tested the performance of the resulting constrained functionals for several characteristic chemical properties. The performance of the new functionals is tested for a number of standard benchmark tests, such as the atomization energies of the G2 set, accuracy of geometries for small molecules, atomic exchange energies, and proton affinities of anionic and neutral molecules. Furthermore, the new functionals are tested against a benchmark set of nucleophilic substitution S_N2 reactions, for which we have recently compared DFT with high-level coupled cluster CCSD(T) data (*J. Comput. Chem.* 2007, *28*, 1551). Our study makes clear that the performance depends critically on the number of constraints, and on the reference data to which the constrained functionals are optimized. For each of these properties studied, there is at least one functional that performs very well. Although a new promising functional ($ML_{ff}OLYP$) emerged from the set of constrained functionals that approaches coupled-cluster accuracy for geometries and performs very well for the energy profile of S_N2 reactions, there is no one of the newly constructed functionals that performs equally well for all properties.

Keywords: Density Functional Theory – Exchange functional – Geometry – Reactivity – Properties.

Introduction

Over the past twenty years, Density Functional Theory (DFT)[1-3] has become the method of choice for many investigations of chemical problems by quantum-chemistry methods. Within DFT, only the exchange-correlation energy $E_{XC} = E_X + E_C$ as a functional of the electron density $\rho(r)$ must be approximated, i.e. as $E_{XC}[\rho(r)]$. In fact, Hohenberg and Kohn[4] proved that if a suitable functional is chosen, this would give exact results. Unfortunately, they did not give the formulation for this suitable (i.e. exact) functional, for which various approximations have been proposed since then (see the "Formulation of DFT functionals" section). The first and most simple approximation (Local Density Approximation, LDA)[5-7] was derived from the uniform electron gas, and is determined completely by the density $\rho(r)$. Although this approximation works very well for physics, its performance for chemistry was less satisfactory. Therefore, also the density gradient ($\nabla\rho$) was taken into account (Generalized Gradient Approximation, GGA),[8] which indeed showed marked improvements over LDA. Later studies included not only the density gradient, but also its Laplacian ($\nabla^2\rho$) and/or the kinetic energy density (Meta-GGA, MGGA).[9] These three classes (LDA, GGA, MGGA) comprise the first three rungs on Jacob's ladder of increasing accuracy (and complexity).[10] The early GGA functionals were still not as accurate as hoped for, which also led to the inclusion of a portion of Hartree-Fock exchange in the exchange part of the functional (hybrid functionals).[11] In the fourth rung of the ladder (Hyper-GGAs, HGGA), not simply a portion but the full 100% of HF exchange will be taken into account.[12]
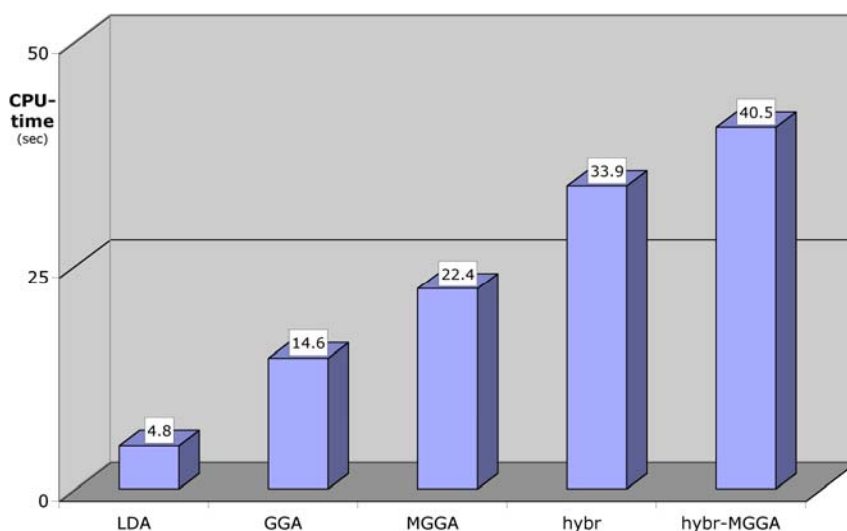
Figure 1. Computational demand (CPU-time, s) of LDA, GGA, MGGA, hybrid and hybrid-MGGA functionals for one SCF cycle for the HOF molecule with the cc-pVQZ basis.

The increase of accuracy (and complexity) comes with a price, as the computational cost increases significantly along the rungs of the ladder (see figure 1). However, because the energy depends in principle only on the density $\rho(r)$ (and its derivatives), which in turn is a

function of only 3 coordinates (x, y, z), DFT is still a much more efficient method than wavefunction (Ψ) based methods that explicitly depend on $3N_{elec}$, that is, the 3 coordinates of each of the N_{elec} electrons in the system. Moreover, because of additional enhancements to make the programs more efficient (linear scaling techniques),[13,14] the computational cost of DFT nowadays scales linearly with system size (N), in contrast to for instance the "gold standard" CCSD(T) that scales as N^7.[15] Therefore, nowadays it is already possible to treat a complete protein structure of 4728 atoms completely with DFT methods,[16] while probably the largest system studied with CCSD(T) is octane (26 atoms), which was possible only in parallel on ca. 1500 nodes.[17] However, despite the huge computational cost, the CCSD(T) method is highly popular because it is generally applicable and a very accurate method, often even more accurate than experiment.[18-20] As a result, the method is often used in benchmark studies[21-24] to give the reference data with which to compare results from e.g. DFT functionals.

One of the more promising and consistent lines of research within the formulation of DFT functionals is provided by Perdew and co-workers,[6,7,9,12,25-31] who e.g. introduced the first GGA functional. Over the past decades, they have constructed non-empirical functionals on the first three rungs: PW92 (LDA),[7] PBE (GGA),[28,32] TPSS (MGGA),[30] and semi-non-empirical hybrid functionals PBE0[33] (also known as PBE1PBE) and TPSSh[31] that contain 25% and 10% of HF exchange respectively. These functionals were constructed based (amongst others) on constraints that should be satisfied by the exchange-correlation hole,[28] which is one of the reasons why these functionals in general perform very well. However, for each of these functionals there are properties for which it does not perform very well. For instance, the PBE functional is not very accurate for the atomization energies of a set of molecules (the G2 set, see below), for which it shows a deviation of 16 kcal·mol^{-1}. Although this is only a fraction of the deviation for LDA (83 kcal·mol^{-1}),[23] it is ca. four times that of other functionals such as the highly empirical B3LYP (a hybrid functional).[34] Very soon after its publication, the PBE functional was therefore revised[35] with the atomization energies in mind. In this revPBE functional, one of the PBE constraints (see below) was lifted, which indeed improved results for the G2-set atomization energies. However, for the accuracy of geometries of a set of small molecules,[36] PBE performed significantly better, while for other properties the difference between revPBE and PBE is either insignificant or in favor of PBE. Several other modifications of the PBE functional have been proposed (RPBE,[37] mPBE,[38] xPBE[39]), which however do not show a general improvement and suffer from being highly empirical.

It seemed therefore that improvement over PBE could only be obtained by going to higher rungs on the ladder. This changed however in 2001, when Handy and Cohen[40] introduced the optimized exchange (OPTX) functional, which was fitted to minimize the difference with Hartree-Fock exchange energies for atoms (H-Ar). This difference (3.6 kcal·mol^{-1}) was indeed substantially lower than that of other popular exchange functionals like Becke88[41] (7.4 kcal·mol^{-1}) or PBEx[32] exchange (40.5 kcal·mol^{-1}; see below). When combined with the Lee-Yang-Parr (LYP)[42] correlation functional, the resulting OLYP functional was indeed shown to be a major improvement over other GGA functionals,[43] and for organic chemistry reactions it performed better than the B3LYP functional.[44] Similar good results were obtained by combining OPTX with the PBEc correlation functional (to give OPBE).[21,23,45]

The OPBE functional was tested successfully for the spin ground-state of a series of iron complexes,[45] for which early GGA functionals failed completely. The latter functionals (including PBE) showed a tendency to overstabilize low-spin states, and as a result predicted a low-spin (doublet) ground-state for an iron(III) compound $(Fe(N(CH_2\text{-}o\text{-}C_6H_4S)_3)(1\text{-Me-imidazole}))$ that was experimentally shown to be high-spin (sextet). For the vertical spin-state splittings (see figure 2 for its definition), a number of DFT functionals correctly predicted the spin ground-state, which include OPBE,[23] Becke00,[46] B3LYP,[34] TPSSh[30,47] and VS98.[48] However, a more stringent check[49,50] on the performance, by looking at the relaxed spin-state splittings (see figure 2 for its definition) for these iron complexes, revealed that only one reliable functional remained: OPBE.
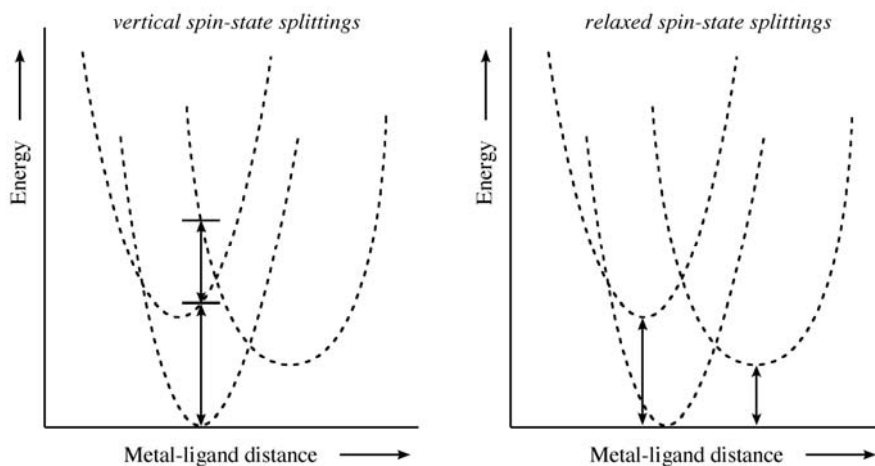
Figure 2. Vertical (left) versus relaxed (right) spin-state splittings.

In a recent study[50] by one of us, the OPBE functional has been used for a series of iron complexes, including a benchmark set $(Fe(II)(H_2O)_6^{2+}, Fe(II)(NH_3)_6^{2+}, Fe(II)(bpy)_3^{2+})$ for which high-level *ab initio* (CASPT2) data by Pierloot and co-workers[51] are available for comparison. Pierloot and co-workers also used their data to compare with Hartree-Fock (HF) and some DFT functionals, such as LDA, BP86[25,41] (GGA), PBE0[33] (hybrid) and B3LYP[34] (hybrid). These functionals all showed large deviations from the reference data,[51] of respectively 57 (LDA), 15 (BP86), 11 (B3LYP) and 9 (PBE0) kcal·mol^{-1}.[50] Moreover, the hybrid functionals B3LYP and PBE0 inadvertently predicted a high-spin (quintet) ground-state for the bipyridyl compound, which should have been low-spin (singlet). This failure of hybrid functionals can be traced directly[52] to the inclusion of a portion of HF exchange; Hartree-Fock itself predicts a high-spin ground-state for all three molecules, with a large deviation (57 kcal·mol^{-1}) from the reference CASPT2 data.

The OPBE functional gives excellent agreement[50] with the CASPT2 data for the benchmark set, from which it differs by only 1-2 kcal·mol^{-1}. Note that this is an order of magnitude smaller than those of the other DFT functionals, and falls well within the estimated accuracy (1000 cm^{-1} ≈ 3 kcal·mol^{-1}) of the CASPT2 data.[51] In the same paper,[50] a number of other difficult iron compounds have been studied that include a spin-crossover compound for which B3LYP and B3LYP* (a reparameterized form[53] of B3LYP that contains only 15% HF exchange instead of the 20% in B3LYP) were shown to fail.[54] For

all these compounds does OPBE give excellent behavior, i.e. it predicts the spin ground-state that is experimentally observed and gives metal-ligand distances that are in good agreement with experimental structures. Of particular interest[50] are two iron compounds based on pyridylmethylamine (pma) ligands, for which the mono-pma compound has a high-spin ground-state, while the di-pma compound has a low-spin ground-state. These two compounds are structurally very similar with a distorted octahedral arrangement of ligands around the iron, in which the only difference is the replacement of a chloride ligand (in mono-pma) by a pyridine ligand (in di-pma). Despite these small changes, the OPBE functional is able to correctly predict the spin ground-state, in contrast to other DFT functionals. The standard pure functionals, which overstabilize low-spin states, fail for the mono-pma compound for which they do not predict the high spin-state. Hybrid functionals, which overstabilize high spin-states due to inclusion of HF exchange, fail for the di-pma compound for which they do not predict the low spin-state. Especially noteworthy was the failure of the Minnesota M06 functionals, which were reported[55] to be the most reliable for organometallic compounds, but nevertheless failed dramatically for the spin ground-states of iron complexes.

The reliability of the OPBE functional for providing spin ground-states has been shown also by studies from other groups,[52,56-68] which also looked at other metals than iron. Furthermore, some of us have investigated[69] its performance for the spin ground-states of a number of ligands, for which experimental data are available with several first-row transition-metals in a number of oxidation states (Mn(II), Mn(III), Mn(IV), Cr(II), Co(II), Co(III), Ni(II), Ni(III), Fe(II), Fe(III)). In all these cases did OPBE correctly predict the spin ground-state.

Recently, we have investigated the influence of the basis set on the spin-state splittings,[70] which was found to be substantial. It was shown that both vertical and relaxed spin-state splittings converge rapidly with basis set size when using Slater-Type Orbitals (STOs), while the convergence is much slower for Gaussian-Type Orbitals (GTOs). The smaller GTO basis sets have in particular problems with high-spin states that are typically placed at too low energy, especially when looking at relaxed spin-state splittings. However, when using very large and demanding GTO basis sets (like NR-cc-pVTZ), the GTO series converges to the same results as obtained with the STO series. This does not occur when using basis sets that include Effective Core Potentials (ECPBs) that give results that are fundamentally different from the STO/GTO data.[70]

The good performance of the OPBE functional for the spin-states of iron complexes concurs with a recent benchmark study on the energy landscapes of bimolecular nucleophilic substitution (S_N2) reactions by us.[21] In that study, we investigated the performance of DFT functionals for the energy profile of S_N2 reactions for which reference CCSD(T) data were available in the literature. It was shown that functionals based on OPTX exchange (OPBE, OLYP) significantly improve upon early GGA functionals such as BLYP or PBE, i.e. the underestimation of reaction barriers by the latter is dramatically reduced (roughly by a factor of two). Moreover, we also investigated the geometries of the different stationary points (reactants, products, reactant complexes, product complexes, transition states), and compared the resulting structures with the CCSD(T) data. Significant improvements over standard GGA results were obtained by using the OLYP and OPBE functionals, i.e. distances from OLYP/OPBE were twice as accurate while angles were five to ten times as accurate. The overall performance for the geometry, as measured by the P_G value, is therefore ten to twenty times smaller for the more accurate OPBE (P_G value 0.04) and OLYP (P_G value 0.03)

functionals than for standard DFT functionals like BP86 (P_G value 0.34), LDA (P_G value 0.34), PBE (P_G value 0.61) or BLYP (P_G value 0.72). In fact, both OLYP and OPBE performed substantially better for the geometries than either OLAP3[71,72] (MGGA, P_G value 0.07) or mPBE0KCIS (hybrid, P_G value 0.06), which were respectively the best performing MGGA and hybrid functional for the energetics of the S_N2 reactions.[21]

In another validation study by some of us,[24] the competing elimination and substitution pathways (*anti*-E2, *syn*-E2, S_N2) were determined for $X^- + CH_3CH_2X$ (X= F, Cl) at the CCSD(T)/aug-cc-pVxZ//OLYP/TZ2P level (x=Q for F, T+d for Cl). The same geometries were used to determine the corresponding energies for a range of *ab initio* methods and DFT functionals. The reference CCSD(T) data showed the *anti*-E2 pathway to be most favorable for the fluoride reaction, while for chloride the substitution pathway is most favorable. Most DFT functionals correctly predicted the chloride pathway (apart from M06-2X), but very few GGA and MGGA functionals could correctly predict the *anti*-E2 pathway being most favorable for the fluoride reaction. The exceptions were mainly those (M)GGA functionals based on OPTX exchange (OPBE, OLYP, OLAP3). [24] The best performing GGA functional for both the overall and central barrier was again OPBE, however with a substantial mean absolute deviation (MAD) from the CCSD(T) data of 4.4 and 4.3 kcal·mol^{-1}, respectively. Similar to what was observed in the benchmark study on the energy landscapes of S_N2 reactions, these deviations show a dramatic reduction compared to early GGAs such as PBE, which showed MAD values of 11.8 and 7.5 kcal·mol^{-1}, respectively for the overall and central barrier. As the elimination transition structures involve weak interactions of the nucleophile/leaving group with the substrate (for which OPBE does not work that well, see below), part of the elevated MAD value of OPBE and OLYP might be attributed to the less satisfactory description of these by OPBE and OLYP. It should also be noted that the best performing DFT functional for the S_N2 energetics (mPBE0KCIS), now performs significantly less with MAD values close to those of OPBE.

For NMR chemical shifts, OPBE also seems to give good results,[58,59] and was in fact claimed to be the best DFT functional around,[59] often even surpassing the MP2 method, although this has recently been questioned by Truhlar and co-workers.[73] Truhlar claimed that the study by Xu and co-workers[59] was biased by leaving out ozone and PN (for which OPBE supposedly does not perform as well as for ^{13}C or ^1H NMR), but this does not explain why OPBE gives a much larger deviation for ^{13}C chemical shifts (5.8 ppm) in Truhlar's study than in the Wu study (2.3 ppm). Fact is that a different GTO basis set was used in these two studies, which might explain the observed differences. After all, NMR is a nuclear property for which a good description of the region around the nucleus is mandatory, and since GTOs do not have a cusp at the nucleus, they might not be particularly well suited for studying NMR parameters unless very large and demanding basis sets are used (see above for the enormous influence of the basis set type and size on spin-state splittings).

Despite these successes of OPBE for spin-state splittings,[45] S_N2 energy landscapes,[21] accuracy of geometries,[23] vibrational frequencies,[23] NMR chemical shifts,[59] there are also examples where it fails dramatically. The most important failings are observed for weak interactions, i.e. π-π stacking[74] and hydrogen-bonding interactions,[75] while it also does not work as well as anticipated for the proton affinities of anionic[76] and neutral[77] bases (see below). These weak interactions are especially important for biochemical systems, in particular for DNA and RNA where inter-strand hydrogen-bonding interactions and intra-strand π-π stacking interactions provide strong binding.[74]

The π-π stacking interaction remains a problematic and difficult interaction for DFT to handle,[74] which is often ascribed to the problems of DFT to describe dispersion interactions. Although it is true that empirical C/R^6 corrections[78] sometimes reduce the failings of DFT functionals, there is no causal relation between dispersion and stacking. The best example are posed by the XLYP and X3LYP functionals,[79] which were shown to perform very well for the dispersion interactions of noble-gas dimers (He_2, Ne_2). Therefore, these "best functionals available at that time" were predicted to perform equally well for π-π stacking interactions of DNA bases;[79] however, they failed badly[80] (also for spin-state splittings[49,50] and S_N2 reaction barriers[21]). Recently, some of us investigated how good or bad the DFT functionals are for π-π stacking interactions,[74] and found that there are indeed some functionals (LDA, KT1,[81] KT2,[81] BHandH[82]) that give a very good description for it. For π-π stacking OPBE and OLYP are not particularly good.[74] They even show repulsive interactions, unlike e.g. PBE that still shows attraction (although too weak).

Hydrogen-bonding interactions are in general well described by many DFT functionals, as was recently shown by some of us[75] for the H-bonding interactions in the DNA base pairs A:T and G:C. Among the functionals that perform well are PW91 and BP86, while OPBE and B3LYP underestimate H-bonding interactions. For instance for OPBE, the hydrogen-bond distances were overestimated by 0.05-0.14 Å and the corresponding energy underestimated by 9-12 kcal·mol^{-1}. We therefore concluded[74,75,83] that at present there is no DFT functional available that is simultaneously accurate for both weak (intermolecular) and strong (intramolecular) interactions, reaction barriers and spin-state splittings (to name just a few in a wide range of characteristic properties). In order to be able to study e.g. the structure and reactivity of DNA, we designed a multi-level QM/QM approach (QUILD: QUantum-regions Interconnected by Local Descriptions)[83] in which each type of interaction can be studied by that particular methodology that is appropriate for it.

Because of the emerging pattern where PBE works well for some properties, but not for others, and the impressive improvements shown by OPBE, we were interested in finding out what is the origin of the differences observed between PBE and OPBE. In other words, why does OPBE work so much better for reaction barriers and spin-state splittings, and not at all for weak interactions ? Since both functionals contain the same PBEc correlation functional, and differ only in the exchange part, it is obvious that it is determined by exchange. However, exactly which part of it ? In the design of the PBEx exchange functional,[32] Perdew and co-workers used four constraints (see below) that completely determines its formulation. The OPTX functional[40] satisfies only one of these constraints, so it is very likely that releasing the other three leads to the major improvements seen by OPBE. However, are all three important or just one or perhaps none at all ? Here, we investigate this puzzling question in two ways: (i) either by imposing the constraints on the OPTX formula; or (ii) by releasing them for the PBEx formula.

Formulation of DFT Functionals

Density functional theory methods[1-3] such as the local density approximation (LDA) and the generalized gradient approximation (GGA) describe the exchange-correlation energy in terms of the density ρ and density gradient $\nabla\rho$:

$$E_{XC}^{LDA}\left[\rho_\alpha,\rho_\beta\right]= \int d^3r \; \varepsilon_{XC}^{unif}\left(\rho_\alpha,\rho_\beta\right)$$
$$E_{XC}^{GGA}\left[\rho_\alpha,\rho_\beta\right]= \int d^3r \; f\left(\rho_\alpha,\rho_\beta,\nabla\rho_\alpha,\nabla\rho_\beta\right)$$

(1)

The expression for the exchange energy of LDA is derived from the uniform electron gas and is formulated as $C_X\cdot\rho^{4/3}$, with C_X a constant and ρ the (spin-polarized) density. Because there is no exchange taking place between electrons of opposite spin, for spin-polarized systems the exchange energy is simply the sum of the separate energies in terms of α and β density; see the spin-scaling relationship below (constraint **iv**).[32] The expression for the LDA correlation energy is a bit more involved,[5,7] and since we are focusing here on the exchange energy only, it will not be given explicitly. The formula of the GGA exchange energy can be expressed as function of the LDA exchange energy, by using an enhancement factor $F(s)$ that is expressed in terms of the reduced density gradient $s = |\nabla\rho| / 2\rho k_F$, $k_F^3=[3\pi^2\cdot\rho]$:[8]

$$E_X^{GGA} = \int d^3r \; \varepsilon_X^{unif}(\rho)\cdot F(s) \tag{2}$$

In 1996, Perdew, Burke and Ernzerhof (PBE)[32] introduced a simplification of the earlier Perdew-Wang (PW91) functional,[26] both of which contain only physical constants as parameters. Moreover, they posed[32] a set of four constraints on the exchange part of the (PBEx) functional that completely determines its expression:

i) to recover the correct uniform gas limit, the exchange functional should have an enhancement factor $F(s)$ that equals 1 (i.e. LDA) when the reduced density gradient s is zero

ii) at low values of s, i.e. for small density variations around the uniform density, the functional should have a limiting behavior that goes as $\sim 1+\mu s^2$ to cancel the correlation-GGA contribution and thus recover the LDA linear response

iii) the Lieb-Oxford bound,[10] which should be met, will be satisfied if the enhancement factor grows gradually with s to a maximum value of 1.804

iv) the exact exchange energy obeys the spin-scaling relationship:

$$E_X\left[\rho_\alpha,\rho_\beta\right]= \left(E_X\left[2\rho_\alpha\right]+ E_X\left[2\rho_\beta\right]\right)/2 \tag{3}$$

A simple expression that satisfies these four constraints is given by their chosen form for the enhancement factor[32]

$$F^{PBE}(s)=\left\lfloor A + Cs^2 \frac{1}{1+\frac{C}{B}s^2}\right\rfloor = A + B\frac{1}{1+\frac{B}{C}s^{-2}} \tag{4}$$

with A=1.0, B=0.804 and C≈0.219515. Note that the limiting behavior for both s→0 (in square brackets) and s→∞ are given in Eq. 4.

The OPTX functional by Handy and Cohen[40] satisfies only constraint **iv**, and has the following expression for the enhancement factor:

$$F^{OPTX}(s) = A + B\frac{C^2 s^4}{\left(1 + Cs^2\right)^2} = A + Bu^2 \quad ; \quad u = \frac{Cs^2}{1 + Cs^2} \tag{5}$$

with A=1.05151, B=1.538582 and C=0.364624. One of the main differences is therefore that whereas the PBEx exchange functional has s^2 as leading term, for OPTX it is s^4. One of us therefore argued in a previous validation study for the spin-states of iron complexes,[45] that this difference in leading terms could be responsible for the improvements observed for the OPBE functional. Here we will see if that assessment still holds, or if it is determined more by the constraints that are imposed on the exchange functional.

We also include a third expression for the exchange enhancement factor, which was derived from a Bayesian Error Estimate (BEEx)[84] and which is some kind of mixture between the PBE and OPTX expressions:

$$F^{BEE}(s) = A + \frac{Bs^2}{\left(1 + s\right)^2} + \frac{Cs^4}{\left(1 + s\right)^4} \tag{6}$$

with A=1.0008, B=0.1926, C=1.8962. The BEEx expression is combined with PBEc correlation.

The expression for the correlation energy in the PBE functional (PBEc) is given by the following formula:

$$E_C^{GGA} = \int d^3 r\, \rho \left[\varepsilon_C^{unif}(\rho, \zeta) + H(\rho, \zeta, t) \right] \tag{7}$$

with ζ the relative spin polarization $(\rho_{up} - \rho_{down})/\rho_{total}$, and t another dimensionless (reduced) density gradient, which depends on the spin-scaling factor ϕ and the Thomas-Fermi screening wave number k_s:

$$t = \frac{|\nabla \rho|}{2\phi(\zeta) \cdot k_s \cdot \rho} \quad ; \quad \phi(\zeta) = \frac{\left(1 + \zeta\right)^{2/3} + \left(1 - \zeta\right)^{2/3}}{2} \quad ; \quad k_s = \sqrt{\frac{4 k_f}{\pi}} \quad ; \quad k_f = \left(3\pi^2 \cdot \rho\right)^{1/3} \tag{8}$$

The function H in eq. 7 is determined by three conditions,[32] for the slowly varying limit (t→0), for the rapidly varying limit (t→∞) and uniform scaling, which are satisfied by the following ansatz:

$$H^{PBE}(\rho, \zeta, t) = \gamma \phi^3 \cdot \ln\left[1 + \frac{\beta}{\gamma} t^2 \cdot \frac{1 + A t^2}{1 + A t^2 + A^2 t^4} \right] \quad ; \quad A = \frac{\beta}{\gamma} \frac{1}{\exp\left(\frac{-\varepsilon_C^{unif}}{\gamma \phi^3}\right) - 1} \tag{9}$$

In the slowly varying limit t→0 (the term in square brackets), this is therefore slightly different than the corresponding exchange expression (see term in square brackets in eq. 4). For that reason, we implemented also the simplified expression for PBE correlation (sPBEc), with the only difference with eq. 9 in the term in square brackets:

$$H^{sPBE}(\rho,\zeta,t) = \gamma\phi^3 \cdot \ln\left[1 + \frac{\beta}{\gamma}t^2 \cdot \frac{1}{1+At^2}\right] \qquad (10)$$

Combined with the original PBEx exchange expression this makes the sPBE functional.

Benchmark Systems

We used a range of characteristic properties in order to investigate the performance of the newly obtained functionals, ranging from atomic (H-Ar) exchange energies; standard benchmark sets like G2 atomization energies, accuracy of geometries and proton affinities; weak interactions, i.e. π-π stacking interactions in DNA bases and hydrogen-bonding in small molecules; energy landscapes of S_N2 reactions; to geometric parameters of stationary points in the S_N2 reactions. Below, we report for each set where the reference data are coming from, and specific details about the reference set.

Atomic Exchange Energies for H-Ar

The atomic exchange energies from Hartree-Fock are many times used as reference values to validate or construct DFT functionals. Indeed, the OPTX functional[40] was constructed based on fitting the parameters and functional form to reproduce as best as possible the atomic exchange energies for H to Ar. In our tests on the atomic exchange energies, we compare our computed energies with the Hartree-Fock values that were taken directly from the OPTX paper.

Atomization Energies for the G2-1 and G2/97 Sets

The atomization energy of a molecule consists of its bonding energy with respect to the sum of the energies of the isolated (spin-polarized) atoms. A number of reference sets are available (such as the G2-1[85] or G2/97[86]) that are often used to compare DFT functionals. Here, we use the geometries and reference energies (ΔE_{el}) as given by Curtiss and co-workers,[1] for either the G2-1 set (55 molecules) or the G2/97 set (148 molecules).

Accuracy of Geometries for a Set of Small Molecules

Helgaker and co-workers[18,20] investigated the basis set dependence for a set of small molecules, using a number of *ab initio* methods. They observed excellent results (0.1-0.2 pm) using CCSD(T)/cc-pVxZ (x=T,Q,5) and showed an experimental error for one of the molecules.[20] Previously,[23,36] one of us used this set of molecules to test the basis set dependence and influence of the DFT functionals on the accuracy of the geometries. Early GGA functionals were shown to give deviations of ca. 1 pm,[36] while functionals containing OPTX showed somewhat smaller deviations (0.6-0.9 pm).[23] The set of molecules consists

of the following molecules: HF, H_2O, NH_3, CH_4, N_2, CH_2, CO, HCN, CO_2, HNC, C_2H_2, CH_2O, HNO, N_2H_2, O_3, C_2H_4, F_2, HOF, H_2O_2.
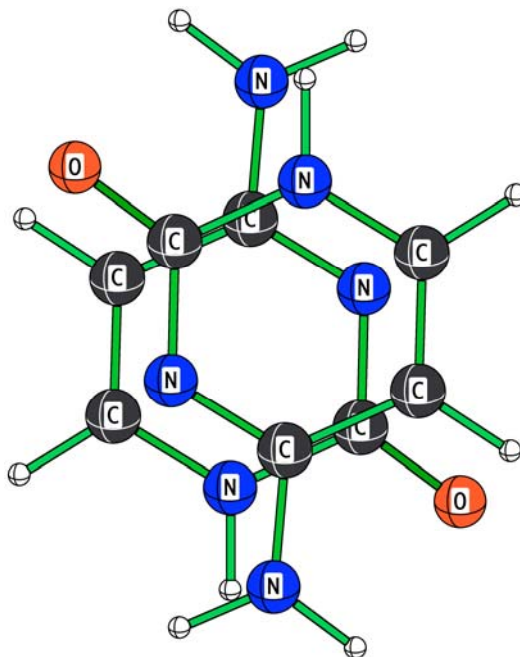
Figure 3. Geometry of 180° twisted cytosine dimer used for π-π stacking benchmark.

Proton Affinities of Anionic and Neutral Bases

The proton affinity of an anionic or neutral base B is related to the enthalpy change at 298K for the following reaction: BH → B + H ($\Delta H = -PA$). In a series of papers,[76,77,87] some of us investigated the PA values for a range of anionic and neutral bases (2nd to 6th period hydrides for group 14-18), and studied how these are affected by methyl substitution and solvation. These studies also included validation of the DFT functionals[76,77] by comparing with CCSD(T) data. Early GGA functionals like BP86 and PBE showed deviations from the CCSD(T) data of ca. 1.5 kcal·mol^{-1}, while the values for OLYP and OPBE are significantly larger (see below). The same reference geometries and energies as previously were used, and the same basis set strategy. I.e. we used the TZ2P basis for optimizing the geometry, and the QZ4P basis in the subsequent single-point energy calculation. The set of anionic bases consists of CH_3^-, $C_2H_3^-$, NH_2^-, $C_6H_5^-$, H^-, HCO^-, OH^-, CH_3O^-, $CH_3CH_2O^-$, C_2H^-, $(CH_3)_2CHO^-$, $(CH_3)_3CO^-$, F^-, SH^-, CN^-, Cl^-, Br^-,[76] while the set of neutral bases consists of NH_3, CH_2CO, H_2O, CO, CO_2, N_2.[77]

---

[1] http://chemistry.anl.gov/compmat/comptherm.htm

The π-π Stacking in DNA Bases

Recently,[74] we compared the performance of DFT functionals for π-π stacking interactions in DNA bases and analogs. Here, we take one prototypical example (stacked cytosine, see figure 3) and examine the deviation of the DFT functionals from a reference CCSD(T) value of -9.93 kcal·mol^{-1}, which was taken from ref. [88]. The vertical distance is 3.3 Å and the upper cytosine is rotated by 180° compared to the lower (around the center of mass of the upper cytosine).[88]

Hydrogen-Bonding Interactions

Sponer, Hobza and co-workers[89] proposed a set of weakly bound dimer systems that can be used to validate other methods. The geometries of the hydrogen-bonded dimer systems were mainly obtained at MP2, but for four dimers (of ammonia, water, formamide, formic acid; see figure 4) they had been obtained at the CCSD(T) level. These four were therefore used here to compare the DFT functionals with. In particular, the distances indicated in figure 4 were used for comparison with the CCSD(T)/cc-pVxZ (x=T for formic acid and formamide dimer, x=Q for ammonia and water dimer) distances.
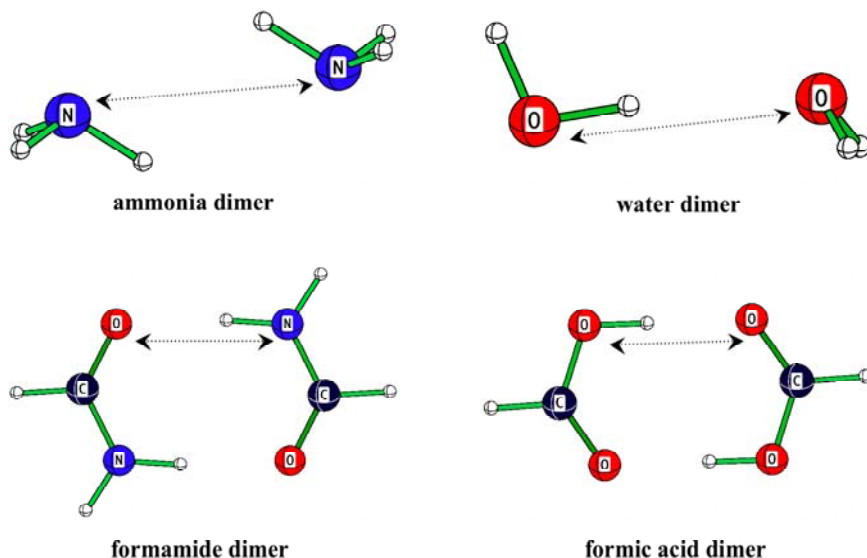
Figure 4. Geometries of the hydrogen-bonded dimers (indicated with arrows are the distances that are used for comparison with the CCSD(T) data).

Energy Landscapes of S$_N$2 Reactions

In a recent paper,[21] we reported a study on the comparison between DFT and CCSD(T) for the energy landscapes of gas-phase S$_N$2 reactions (see figure 5 for a typical energy profile). We showed that there was in general good agreement between DFT and CCSD(T) and that this coherence was better when large basis sets were used in both the CCSD(T) and

DFT. Here, we therefore look only at those reactions for which the reference data were coming from studies where CCSD(T) was used for obtaining both the energy and the geometry, and with large basis sets. In the terminology of that paper, we take only reactions **A2** to **A6** into account (see tables 1 and 2 of Ref. 21).
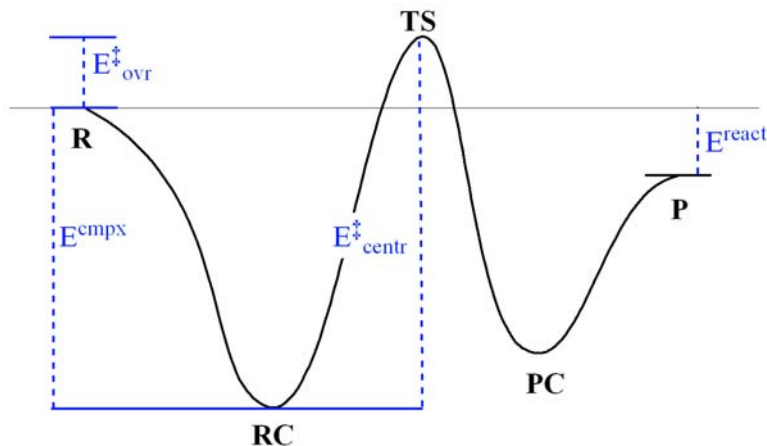
Figure 5. Energy profile for S_N2 reactions.

Structural Characterization of Stationary Points for S_N2 Reactions

Similar to the energy landscapes (see above),[21] for the structural characterization of S_N2 reactions we only look at those that were obtained using CCSD(T) with a large basis set. Therefore, the set of reactions for which the stationary points were determined by the DFT functionals (and compared to CCSD(T)) consists of the following reactions: $Cl^- + CH_3Br \rightarrow CH_3Cl + Br^-$, $F^- + CH_3Cl \rightarrow CH_3F + Cl^-$, $Cl^- + CH_3Cl \rightarrow CH_3Cl + Cl^-$, $Br^- + CH_3Br \rightarrow CH_3Br + Br^-$, $F^- + CH_3F \rightarrow CH_3F + F^-$.

Spin-State Splittings of a High-Spin Iron Compound

Previously,[45,50] we have shown that the OPBE functional works exceptionally well for spin-states of iron complexes, and we therefore include one of the typical molecules for which early GGAs were found to fail, which is the compound $Fe(N(CH_2-o-C_6H_4S)_3)(1-Me-imidazole)$. Experimentally and with OPBE, it has a high-spin sextet ground-state.

Computational Details

All DFT calculations were performed with a locally adapted version of the Amsterdam Density Functional (ADF, version 2006.01)[90,91] program developed by Baerends et al. The MOs were expanded in a large uncontracted set of Slater-type orbitals (TZ2P, QZ4P),[92] which are respectively of triple-ζ quality augmented by two sets of polarization functions, and of quadruple-ζ quality augmented by four sets of polarization functions.[91] An auxiliary set

of s, p, d, f, and g STOs was used to fit the molecular density and to represent the Coulomb and exchange potentials accurately in each SCF cycle. All energies and gradients were calculated with the local density approximation (LDA) and generalized gradient approximation (GGA) corrections added self-consistently.

Table 1. Overview of expression of exchange functionals studied (see text for further details) and Mean Absolute Deviations (kcal·mol^{-1}) against atomic exchange energies

functional	type[a,b,c]	A	B	C	MAD in E_x[d]
OPTX	optx	1.05151	1.538582	0.364624	3.73
PBEx	pbe	1.0	0.804	0.219515	40.48
BEEx	bee	1.0008	0.1926	1.8962	75.49
optimized against atomic exchange					
A_{ff}PBEx	pbe	1.0246	4.3704	0.1450	4.26
A_{fp}PBEx	pbe	1.0116	0.7924	0.2018	6.97
A_{lf}PBEx	pbe	1.0	0.7843	0.2397	8.32
A_{lp}PBEx	pbe	1.0	0.804	0.2386	8.39
A_{ff}O	optx	1.0508	1.5303	0.3687	2.94
A_{fp}O	optx	1.0416	0.7624	0.7034	5.30
A_{lf}O	optx	1.0	0.3505	2.6018	10.77
A_{lp}O	optx	1.0	0.804	1.1152	30.32
optimized against atomization energies of G2-1 set					
MP_{ff}PBEx	pbe	1.0807	1.7144	0.2497	689.72
MP_{fp}PBEx	pbe	1.0092	0.7948	0.4232	456.67
MP_{lf}PBEx	pbe	1.0	1.0446	0.2551	75.73
MP_{lp}PBEx	pbe	1.0	0.804	0.3826	315.29
ML_{ff}O	optx	1.0728	1.5124	0.4214	221.28
ML_{fp}O	optx	1.0141	0.7899	0.9191	35.65
ML_{lf}O	optx	1.0	1.2783	0.4004	380.54
ML_{lp}O	optx	1.0	0.804	0.8354	184.75
MP_{ff}O	optx	1.0890	1.4234	0.5050	416.84
MP_{fp}O	optx	1.0266	0.7774	1.0742	151.10
MP_{lf}O	optx	1.0	1.1567	0.4629	348.10
MP_{lp}O	optx	1.0	0.804	0.8680	161.63

a) pbe: $F(s) = A + B·Cs^2/(B + Cs^2)$
b) optx: $F(s) = A + B·u^2$; $u = (C·s^2)/(1 + C·s^2)$
c) bee: $A + B·s^2/(1+s)^2 + C·s^4/(1+s)^4$
d) mean absolute deviations (kcal·mol^{-1}) from Hartree-Fock atomic exchange energies for H-Ar.

The newly developed functionals are labeled (X_{ab}) according to the reference data (X) to which they were optimized and the constraints that are imposed on it (*ab*). The reference data can be either A for atomic exchange (Hartree-Fock) energies of H-Ar, or MP cq. ML for experimental molecular atomization energies of the G2-1 set; MP when obtained in combination with PBEc correlation, and ML when obtained in combination with LYPc correlation. The labeling of the constraints (*ab=ff, fp, lf, lp*) refers to the constraint at s=0 (*a=l* for LDA, constraint **i**; *a=f* for free, i.e. no constraint) and at s=∞ (*b=p* for PBE maximum of

constraint **iii**; $b=f$ for free, i.e. no constraint). For instance, A_{fp} refers to the functional optimized against atomic exchange energies, with the Perdew maximum (constraint **iii**) imposed on the enhancement factor with the LDA limit at $s=0$ not imposed (see also table 1 for the expression of the functionals).

Construction of the New Functionals

Handy and Cohen constructed their OPTX functional[40] by optimizing the atomic exchange energies of H-Ar against those from Hartree-Fock using a large basis, ending up with a deviation of 3.6 kcal·mol^{-1} between the two methods. This is significantly better than the Becke88[41] functional (7.4 kcal·mol^{-1}), or PBE[32] (40.5 kcal·mol^{-1}). In the first part of this study, we also optimize our functionals against the atomic exchange energies from Hartree-Fock, in four different combinations (see table 1 for the parameters of the exchange functionals thus obtained). The first combination ($A_{ff}O$) imposes no constraint at all, i.e. similar to the OPTX functional. Indeed we do find similar performance for the atomic exchange energies with a mean absolute deviation (MAD) of 2.9 kcal·mol^{-1} (see table 1). The slight improvement over the original OPTX functional (MAD value 3.7 kcal·mol^{-1}) probably results from our fit procedure, which might be slightly different from that of Handy and Cohen. If we now impose constraint **iii** (Lieb-Oxford bound)[32] on the enhancement factor, to give the $A_{fp}O$ functional, the MAD value for the HF exchange energies increases to 5.3 kcal·mol^{-1}. On the other hand, imposing the constraint for the LDA limit (constraint **i**), the MAD value increases to 10.8 kcal·mol^{-1}. By imposing both these constraints, the MAD value goes up to 30.3 kcal·mol^{-1} (see table 1). The smaller deviation of OPTX compared to the PBEx functional is therefore resulting directly from the enhanced flexibility of not imposing constraints on the A and C parameters. At first sight, it might seem that the improved performance is also resulting from the exchange expression of OPTX, if one compares the MAD value of $A_{lp}O$ functional (30.3 kcal·mol^{-1}) with that of PBEx (40.5 kcal·mol^{-1}). However, this is not a fair comparison since the C parameter is in PBEx fixed by constraint **ii**, while it is freely optimized in $A_{lp}O$. A better comparison is therefore made by looking at the $A_{lp}PBEx$ functional, in which the C parameter was also optimized freely. Its MAD value for the HF exchange energies (8.4 kcal·mol^{-1}) is many times smaller than that of the $A_{lp}O$ functional, which indicates in itself that the PBEx expression is "better" for exchange than the OPTX expression. In fact, the value for the C-parameter within $A_{lp}PBEx$ (0.2386) is only 9% larger than the constrained value (~0.2195). By optimizing also either the A or the B parameter, the MAD value for HF exchange energies is reduced further, but only nominally, to 8.3 kcal·mol^{-1} for $A_{lf}PBEx$ and 7.0 kcal·mol^{-1} for $A_{fp}PBEx$ (see table 1). Only by optimizing all three parameters simultaneously does a further reduction to 4.3 kcal·mol^{-1} occur, but with a limit for $s\rightarrow\infty$ (5.395) that is unrealistically high (the OPTX functional that violates both the local and integrated Lieb-Oxford bounds has a limiting behavior of "only" 2.59). Therefore, the relatively large MAD value of PBEx (40.5 kcal·mol^{-1}) for the HF exchange energies of H-Ar is largely reduced by lifting either one of constraints **i**, **ii**, or **iii**. In fact, the $A_{lf}PBEx$ functional, in which the maximum on the enhancement factor is not imposed, results in a value for the B parameter that is actually lower than the one that is set by the Lieb-Oxford bound. In other words, even though it is not constrained to satisfy the Lieb-

Oxford bound, it still does ! The downside is however that it is now no longer a non-empirical functional.

Although many exchange functionals have been obtained by comparing with atomic exchange (as Handy and Cohen did for OPTX),[40] there are also many (empirical) functionals that have been fitted to, for instance, the atomization energies of the G2-1 set.[34,38,85,93,94] Examples of the latter are, for instance, the B3PW91 functional by Becke,[11] who for the first time introduced the concept of hybrid functionals, or HCTH.[93] Therefore, we decided to also construct functionals by optimizing the parameters of the exchange expression for the atomization energies of the G2-1 set. In this second part, we therefore have to include a functional for the correlation energy, which was chosen to be the PBEc for the $MP_{ab}PBE$ and $MP_{ab}OPBE$ functionals, and LYPc for the $ML_{ab}OLYP$ functionals. It is interesting to note that for the completely free functionals ($MP_{ff}PBE$, $ML_{ff}OLYP$, $MP_{ff}OPBE$), the deviation from the LDA limit (A=1.0) is substantially larger than for the atomic functionals of the first part. For instance, the value for the A parameter increases from 1.0508 (for $A_{ff}O$) to 1.0728 ($ML_{ff}O$) or 1.0890 ($MP_{ff}O$) (see table 1), and similarly from 1.0246 for $A_{ff}PBEx$ to 1.0807 for $MP_{ff}PBEx$. Furthermore, the value for the B parameter is for the molecular functionals in this second part found to be substantially larger than the Lieb-Oxford bound (0.804), with values of 1.0446 for $MP_{lf}PBEx$, 1.2783 for $ML_{lf}O$ and 1.1567 for $MP_{lf}O$. Note that in the first part, even though the B parameter was not constrained to the Lieb-Oxford bound, it still did satisfy it. For the molecular functionals, this no longer holds.

For the molecular functionals of this second part, the mean absolute deviation (MAD) for the G2-1 set[85] ranges from 2.5 to 5.5 kcal·mol⁻¹ (see table 2). This is a major improvement over the MAD values for the combination of the atomic functionals from the first part with their respective correlation functionals, which showed MAD values from 3.1 to 14.8 kcal·mol⁻¹. It is interesting to see that for each of the three types of molecular functionals introduced here ($MP_{ab}PBE$, $ML_{ab}OLYP$ and $MP_{ab}OPBE$) that the completely free form (ab=ff) gives a significant better performance than the other three forms (ab=fp,lf,lp), which give more or less the same MAD values. This is in particular true for the $MP_{ab}PBE$ functionals, where the $MP_{ff}PBE$ functional has a MAD value of 3.1 kcal·mol⁻¹, while the other three have MAD values of 4.7-4.9 kcal·mol⁻¹, despite the very different values for the A,B,C parameters of the various molecular functionals.

The good performance of the molecular functionals does not coincide with equally good performance for the atomic exchange energies (see table 2). Apart from the $ML_{fp}OLYP$ functional, whose MAD value of 35.7 kcal·mol⁻¹ for atomic exchange is similar to that of PBEx, and the $MP_{lf}PBE$ functional, whose value of 75.7 kcal·mol⁻¹ is comparable to that of BEE, for the others a significantly larger MAD value is observed with values between 150 and 690 kcal·mol⁻¹. So it seems that by fitting to molecular properties, one is losing the accuracy for the atomic properties. We also experimented briefly by optimizing simultaneously the atomic exchange and G2-1 atomization energies (more specifically, by minimizing the product of their respective MAD values), but this basically lead to small variations on the atomic functionals of the first part and will thus not be discussed any further. The smallest deviation is observed for the $ML_{ff}OLYP$ functional.

Table 2. Mean absolute deviation (MAD) values for standard benchmark studies[a] (kcal·mol⁻¹, pm)

functional	atomic exchange	G2-1	G2/97	geom. 1st row[c]	PA anionic	PA neutrals	π-π stacking	hydrogen-bonding
basis set used	QZ4P	QZ4P	QZ4P	TZ2P	QZ4P	QZ4P	TZ2P	TZ2P
	(kcal·mol⁻¹)	(kcal·mol⁻¹)	(kcal·mol⁻¹)	(pm)	(kcal·mol⁻¹)	(kcal·mol⁻¹)	(kcal·mol⁻¹)	(pm)
PBE	40.48	7.95	16.32	0.87	1.63	1.45	7.14	2.46
sPBE	40.48	6.80	12.94	0.92	1.62	1.49	7.19	1.90
BEE	75.49	5.32	8.03	1.00	1.73	**1.17**	10.65	5.64
OPBE	3.73	4.79	8.90	0.90	5.54	3.83	15.62	28.11
OLYP	3.73	3.24	4.24	0.64	2.89	1.42	14.43	23.20
A_{ff}PBE	*4.26*	4.69	44.61	0.76	4.68	3.51	18.15	30.44
A_{fp}PBE	*6.97*	10.16	23.45	0.68	1.51	1.36	6.82	4.44
A_{1f}PBE	*8.32*	7.38	14.47	0.86	1.49	1.42	6.91	1.93
A_{1p}PBE	*8.39*	7.08	13.58	0.87	**1.48**	1.39	7.13	**1.83**
A_{ff}OLYP	*2.94*	3.10	4.23	0.65	2.87	1.40	14.41	23.55
A_{fp}OLYP	*5.30*	10.49	21.47	0.64	1.85	1.86	6.85	3.39
A_{1f}OLYP	*10.77*	14.82	29.49	0.74	7.71	5.77	0.72	8.49
A_{1p}OLYP	*30.32*	7.14	20.38	2.16	3.57	2.21	7.49	17.39
A_{ff}OPBE	*2.94*	4.66	8.41	0.90	5.49	3.82	15.59	28.53
A_{fp}OPBE	*5.30*	10.91	27.00	0.78	2.39	1.59	8.05	3.62
A_{1f}OPBE	*10.77*	14.59	34.31	0.74	4.48	3.20	**0.26**	11.21
A_{1p}OPBE	*30.32*	7.16	15.52	1.75	1.90	1.66	8.39	17.23
MP_{ff}PBE	689.72	*3.07*	**3.94**	1.01	11.94	6.16	13.38	16.75
MP_{fp}PBE	456.67	*4.77*	7.08	0.69	3.20	1.33	5.98	2.34
MP_{1f}PBE	75.73	*4.71*	7.09	1.01	1.97	1.20	9.69	7.97
MP_{1p}PBE	315.29	*4.87*	9.42	0.82	2.10	1.20	6.52	3.55
ML_{ff}OLYP	221.28	*2.51*	4.57	**0.33**	5.38	2.86	14.17	27.41
ML_{fp}OLYP	35.65	*4.42*	8.21	1.57	3.18	2.10	7.46	13.16
ML_{1f}OLYP	380.54	*3.99*	8.85	1.83	4.49	1.81	13.21	20.41
ML_{1p}OLYP	184.75	*4.61*	9.73	1.95	4.74	5.99	9.04	14.50
MP_{ff}OPBE	416.84	*3.47*	4.71	0.61	10.96	6.48	14.34	35.41
MP_{fp}OPBE	151.10	*5.09*	6.73	0.91	2.54	1.67	7.70	11.80
MP_{1f}OPBE	348.10	*5.19*	7.07	1.56	2.79	1.30	13.33	21.40
MP_{1p}OPBE	161.63	*5.47*	7.50	1.61	2.13	1.50	9.04	14.50

[a] in *italics* are the values which were used to construct the functionals in this chapter, in **bold** the functional that performs best for that particular property.

Performance of the Functionals for Standard Benchmark Studies

Apart from the atomization energies for the G2-1 set,[85] we subjected the functionals also to other standard benchmark studies, such as the atomization energies for the larger and more diverse G2/97 set,[86] the accuracy of geometries of first-row molecules,[18,20,36] proton affinities of anionic and neutral bases,[76,77] and weak interactions (π-π stacking[74,88] and hydrogen-bonding[89]).

Atomization Energies

For many functionals considered here, going from the G2-1 set[85] with small molecules to the more diverse G2/97 set[86] with medium-sized molecules results in a doubling of the MAD value. A similar pattern was observed by Perdew and co-workers[47] for the MAD values of several methods for the G2/97 and G3/3 set (that contains even larger molecules), which doubled[47] for e.g. Hartree-Fock (148.3 [G2/97] vs. 336.4 [G3/3] kcal·mol^{-1}), LDA (83.7 vs. 197.1 kcal·mol^{-1}), PBE (16.9 vs. 32.8 kcal·mol^{-1}) or B3LYP (3.1 vs. 8.4 kcal·mol^{-1}). Surprisingly,[47] the MAD values decreased for their TPSS (6.0 [G2/97] vs. 5.5 kcal·mol^{-1}) and TPSSh (4.2 vs. 3.3 kcal·mol^{-1}) functionals.

Here, we see in most cases also a doubling of the MAD value for the G2/97 set compared to that of the G2-1 set. For instance, the values for OPBE are 4.8 and 8.9 kcal·mol^{-1}, for A_{lf}PBE 7.4 and 14.5 kcal·mol^{-1}, and 4.9 and 9.4 kcal·mol^{-1} for MP_{lp}PBE, to name but a few. However, there also exceptions, both in the positive and negative sense. The MAD value for OLYP increases only from 3.2 kcal·mol^{-1} for G2-1 to 4.2 for G2/97, and that of MP_{ff}OPBE from 3.5 to 4.7 kcal·mol^{-1}. On the other hand, for A_{ff}PBE it increases from 4.7 kcal·mol^{-1} for G2-1 to 44.6 kcal·mol^{-1} for G2/97. This is probably the result of the limit for large s of this functional (see above). Although the ML_{ff}OLYP was the best performing functional for the G2-1 set, it is no longer so for the larger G2/97 set, for which a MAD value of 4.6 kcal·mol^{-1} is observed. For the G2/97 set, the best performance is shown by the MP_{ff}PBE functional, which was already second-best for the G2-1 set, with a MAD value of 3.9 kcal·mol^{-1}.

Accuracy of Geometries

Previously,[23,36] one of us investigated the accuracy of geometries of a number of early GGAs, and found the best performance for amongst others PBE (ca. 1.0 pm), while a later study[23] showed the improved performance of OPBE and OLYP (0.8-0.9 pm). Although this is still far from the accuracy obtained by the "gold standard" CCSD(T), which showed deviations of ca. 0.1-0.2 pm, it is still a major improvement over Hartree-Fock that gave deviations of 2.9 pm.[18] In comparison to the previous study,[23] where a TZP basis was used, here we use the larger TZ2P basis set. Both PBE and OLYP significantly increase their accuracy by ca. 0.3 pm, to 0.9 pm (PBE) and 0.6 pm (OLYP), while OPBE gives the same deviation as it had with the TZP basis (0.9 pm). Many of the newly developed atomic functionals provide deviations that are similar to those of OPBE and OLYP, with mean absolute deviations between 0.6 and 0.9 pm (see table 2), and few that give much larger deviations such as A_{lp}OLYP (deviation 2.2 pm) or A_{lp}OPBE (deviation 1.8 pm).

The situation is reversed for the newly developed molecular functionals, where many show larger deviations (between 1.0 and 2.0 pm), and few show deviations that are comparable to OPBE or OLYP. There is however one exception (ML$_{ff}$OLYP) that has an exceptionally good performance for the geometries of this set of small molecules. Its MAD value of 0.3 pm is by far the lowest for any DFT functional, surpasses that of MP2 and CCSD (0.5 pm),[18,20] and approaches the accuracy of the coupled cluster CCSD(T) method.

For the molecular functionals based on the OPTX expression, there is a clear correlation between the amount of constraints that are imposed and the accuracy obtained. I.e., more constraints imposed results directly in an increase of the deviation. This is not true for the molecular PBE functionals, nor for the atomic functionals. For these latter functionals, the best performance is obtained when one constraint is imposed as in A$_{fp}$PBE, A$_{fp}$OLYP, and A$_{lf}$OPBE.

Proton Affinities of Anionic and Neutral Bases

Recently,[76,77] some of use investigated the proton affinities of anionic and neutral bases for hydrides of the 2nd-6th period, and groups 14-18. These studies also involved the validation of DFT functionals for this property by comparing the DFT proton affinity values to those from CCSD(T), where available. It was shown that DFT works in general very well, and has a mean absolute deviation from CCSD(T) (and experiment) of ca 1.5 kcal·mol^{-1}. Surprisingly, the deviations were larger for OPBE and (in lesser amount) OLYP than for PBE. Here we find the same for the newly developed functionals based on the OPTX expression, which show deviations between 1.9 and 11.0 kcal·mol^{-1} for anionic bases, and between 1.3 and 6.5 kcal·mol^{-1} for neutral bases (see table 2).

Surprisingly, in many cases and for both the atomic and molecular functionals, the constrained functionals show better performance than the non-constrained (ab=ff) ones. For instance, MP$_{ff}$OPBE gives deviations of 11.0 (anionic bases) and 6.5 (neutral) kcal·mol^{-1}, while MP$_{lp}$OPBE gives values of 2.1 and 1.5 kcal·mol^{-1} respectively. The same happens for the atomic counterparts with values of 5.5/3.8 kcal·mol^{-1} for A$_{ff}$OPBE, and values of 1.9/1.7 kcal·mol^{-1} for A$_{lp}$OPBE. Therefore, there is no direct relationship between atomic exchange (or atomization energies of the G2-1 set) on one hand, and the proton affinities at the other. Or at best, there is an anti-correlation between the two sides.

Weak Interactions

One of the traditionally weak points of DFT is formed by π-π stacking interactions,[74] while hydrogen-bonding interactions are described reasonably well to very good by many functionals.[75] These trends are well shown by the PBE functional, that gives a deviation of 7.1 kcal·mol^{-1} for the π-π stacking of the 180° twisted cytosine dimer, and for a set of four hydrogen-bonded dimers gives a mean absolute deviation of 2.5 pm (see table 2). Note that PBE still predicts an attractive interaction for the π-π stacking (-2.8 kcal·mol^{-1}).

The failure of both OPBE and OLYP for weak interactions is immediately obvious from table 2, i.e. they show deviations of 15.6 (OPBE) and 14.4 (OLYP) kcal·mol^{-1} for π-π stacking. Note that this corresponds to repulsive interactions of +5.7 and +4.5 kcal·mol^{-1}

respectively. Also for hydrogen-bonding interactions are they not performing well with mean absolute deviations of 28.1 (OPBE) and 23.2 (OLYP) pm. Both functionals predict H-bond distances that are substantially larger than they should be, i.e. they severely underestimate hydrogen-bonding interactions. In a recent study on hydrogen-bonding interactions in DNA bases,[75] we already showed this failure of OPBE.

The performance of the newly developed functionals for the weak interactions shows no general trend, although all functionals without constraints imposed (ab=ff) perform badly for both π-π stacking and hydrogen-bonding interactions. For π-π stacking, these functionals show MAD values between 13.4 and 18.2 kcal·mol^{-1} (all repulsive), while for hydrogen-bonding the MAD values are between 16.8 and 35.4 pm. The functionals with one or more constraint imposed show somewhat smaller MAD values, and in some cases are the best performing functionals. For instance for π-π stacking, the A_{lf}OPBE functional has a MAD value of only 0.3 kcal·mol^{-1}, which is however not accompanied by an equally good performance for hydrogen-bonding where it shows a MAD value of 11.2 pm. The best performance for hydrogen-bonding is shown by A_{lp}PBE, with a MAD value of 1.8 pm, but in a similar fashion to A_{lf}OPBE it does not perform equally well for π-π stacking, for which it has a MAD value of 7.1 kcal·mol^{-1}.

Table 3. Deviations[a] from CCSD(T) results for S_N2 reaction energy profiles (kcal·mol^{-1})

functional	ΔE^{react}	ΔE^{cmpx}	$\Delta E^{\ddagger,centr}$	$\Delta E^{\ddagger,ovr}$	P_E
PBE	0.34	1.49	6.43	7.78	4.01
sPBE	0.68	1.48	6.54	7.45	4.04
BEE	0.32	1.44	5.92	5.61	3.32
OPBE	0.31	3.54	3.37	1.26	2.12
OLYP	0.50	2.58	4.14	1.69	2.23
A_{ff}PBE	0.23	4.09	4.95	0.92	2.55
A_{fp}PBE	0.31	1.52	6.26	7.65	3.94
A_{lf}PBE	0.34	1.55	6.53	7.99	4.10
A_{lp}PBE	0.34	1.49	6.49	7.85	4.04
A_{ff}OLYP	0.51	2.57	4.14	1.69	2.23
A_{fp}OLYP	0.50	1.67	5.04	6.32	3.38
A_{lf}OLYP	0.37	5.64	8.75	14.40	7.29
A_{lp}OLYP	0.55	1.83	5.61	7.07	3.76
A_{ff}OPBE	0.32	3.54	3.37	1.26	2.12
A_{fp}OPBE	0.31	1.56	4.27	4.47	2.65
A_{lf}OPBE	0.19	4.56	7.98	12.54	6.32
A_{lp}OPBE	0.37	1.61	4.84	5.22	3.01
MP_{ff}PBE	0.22	2.48	4.54	2.06	2.33
MP_{fp}PBE	0.32	1.97	7.28	9.26	4.71
MP_{lf}PBE	0.36	1.34	6.19	6.37	3.56
MP_{lp}PBE	0.34	1.80	7.15	8.91	4.55
ML_{ff}OLYP	0.49	2.87	3.56	1.44	2.09
ML_{fp}OLYP	0.55	1.72	5.27	6.52	3.51
ML_{lf}OLYP	0.59	2.01	5.07	3.89	2.89

Table 3. Continued.

functional	ΔE^{react}	ΔE^{cmpx}	$\Delta E^{\ddagger,centr}$	$\Delta E^{\ddagger,ovr}$	P_E
ML$_{1p}$OLYP	0.58	1.71	5.37	6.47	3.54
MP$_{ff}$OPBE	0.29	3.85	2.37	1.74	2.06
MP$_{fp}$OPBE	0.32	1.57	4.53	4.97	2.85
MP$_{1f}$OPBE	0.41	2.10	4.28	2.40	2.30
MP$_{1p}$OPBE	0.39	1.66	4.61	4.65	2.83

[a] results obtained using QZ4P basis set, in **bold** the functional that performs best for that particular property.

Performance of the Functionals for S_N2 Energy Landscapes and Structural Characterization

The performance of the functionals for the energy profile of S_N2 reactions is measured in terms of four components of the energy profile.[21] These correspond to (see figure 5): the overall reaction energy (E^{react}), the complexation energy (E^{cmpx}), the central barrier ($E^{\ddagger}_{centr}$) and the overall barrier ($E^{\ddagger}_{ovr}$). The absolute deviation from the reference CCSD(T) data for each component is obtained for each reaction, and averaged over all reactions (**A2-A6**) to give the MAD value for each component. The average of the MAD values for the four components then gives the performance for the energy profile (P_E).

Given in table 3 are the MAD values for each component and the P_E value for all functionals considered in this chapter. As already discussed previously,[21] the early GGA functionals like PBE have in particular problems with reaction barriers, which is dramatically reduced by the functionals with OPTX. For instance, the MAD value for the central barrier is 6.4 kcal·mol^{-1} for PBE, 4.1 kcal·mol^{-1} for OLYP and only 3.4 kcal·mol^{-1} for OPBE. This also influences the overall P_E performance considerably, where the value for PBE (4.0 kcal·mol^{-1}) is nearly halved for OLYP (2.2 kcal·mol^{-1}) and OPBE (2.1 kcal·mol^{-1}).

For the newly developed functionals, the best performance is obtained for those without constraints imposed (see table 3). This is in particular true for P_E and the central barrier, for which MP$_{ff}$OPBE performs best with MAD values of 2.1 and 2.4 kcal·mol^{-1} respectively, and the overall barrier, for which A$_{ff}$PBE performs best with a value of 0.9 kcal·mol^{-1}. Imposing constraints raises the MAD values of the barriers substantially, but, interestingly, at the same time lowers the MAD values for the complexation energy. The MAD values for the reaction energy seems to be hardly affected by imposing constraints or not, i.e. the MAD value for all functionals is found within the very narrow range of 0.2-0.7 kcal·mol^{-1}. The lowering of the MAD value for the complexation energy upon imposing constraints is somewhat consistent with the trend observed for the hydrogen-bonding interactions (see above), where the largest MAD value was shown by the functionals without constraints. However, imposing constraints is not in all cases favorable for the complexation energy, as is shown by e.g. the A$_{1f}$OLYP and A$_{1f}$OPBE functionals. The MAD value for the complexation energy of A$_{1f}$OLYP is more than twice as large as that of the constraint-free A$_{ff}$OLYP functional, leading to an overall P_E value of 7.3 kcal·mol^{-1}. This is the largest P_E value in this chapter, and in fact even larger than LDA, which had a P_E value of 5.6 kcal·mol^{-1} for reactions **A2-A6**.

Table 4. Deviations[a] from CCSD(T) geometries for stationary points of S_N2 reactions (Å, deg)[b]

functional	R_{all}	$R_{R,P}$	$R_{RC,PC}$	R_{TS}	θ_{all}	$\theta_{R,C}$	$\theta_{RC,PC}$	θ_{TS}	P_G
PBE	0.101	0.010	0.139	0.078	4.134	0.082	5.581	5.145	0.418
sPBE	0.092	0.012	0.139	0.050	3.842	0.106	5.577	3.375	0.353
BEE	0.037	0.012	0.041	0.042	0.921	0.076	0.754	2.771	0.034
OPBE	0.069	0.010	0.115	0.017	0.607	0.338	0.621	0.958	0.042
OLYP	0.063	0.007	0.095	0.034	0.463	**0.049**	0.396	1.317	0.029
A_{ff}PBE	0.050	0.006	0.076	0.028	0.712	0.139	0.548	2.143	0.036
A_{fp}PBE	0.031	0.005	0.038	0.032	0.993	0.071	0.819	2.988	0.031
A_{1f}PBE	0.102	0.011	0.139	0.081	4.668	0.100	5.606	8.241	0.476
A_{1p}PBE	0.092	0.011	0.139	0.050	3.933	0.102	5.603	3.836	0.362
A_{ff}OLYP	0.059	0.007	0.088	0.034	0.470	0.062	0.400	1.328	0.028
A_{fp}OLYP	0.030	0.008	0.033	0.036	0.604	0.061	0.531	1.673	0.018
A_{1f}OLYP	0.126	0.018	0.175	0.094	4.672	0.444	6.498	4.622	0.589
A_{1p}OLYP	0.151	0.036	0.187	0.145	4.525	0.598	6.211	4.514	0.683
A_{ff}OPBE	0.064	0.010	0.107	0.017	0.563	0.308	0.555	0.975	0.036
A_{fp}OPBE	**0.022**	0.009	**0.029**	0.016	0.548	0.285	0.502	1.107	**0.012**
A_{1f}OPBE	0.113	0.007	0.166	0.074	4.253	0.198	5.768	5.037	0.481
A_{1p}OPBE	0.058	0.024	0.063	0.066	0.719	0.209	0.667	1.663	0.042
MP_{ff}PBE	0.045	0.010	0.064	0.030	0.506	0.087	0.457	1.304	0.023
MP_{fp}PBE	0.113	0.018	0.147	0.101	4.547	0.498	6.254	4.645	0.514
MP_{1f}PBE	0.113	0.015	0.151	0.094	4.669	0.218	5.649	7.918	0.528
MP_{1p}PBE	0.111	0.017	0.145	0.100	5.045	0.451	6.140	8.104	0.560
ML_{ff}OLYP	0.063	**0.004**	0.097	0.034	0.357	0.069	**0.334**	0.870	0.022
ML_{fp}OLYP	0.060	0.025	0.063	0.074	1.148	0.355	1.153	2.319	0.069
ML_{1f}OLYP	0.066	0.023	0.084	0.057	0.729	0.129	0.580	2.153	0.048
ML_{1p}OLYP	0.065	0.029	0.069	0.077	1.154	0.348	1.145	2.394	0.075
MP_{ff}OPBE	0.071	0.009	0.123	**0.012**	**0.360**	0.224	0.457	**0.226**	0.026
MP_{fp}OPBE	0.039	0.012	0.045	0.044	0.478	0.057	0.436	1.255	0.019
MP_{1f}OPBE	0.053	0.015	0.076	0.031	0.534	0.167	0.432	1.441	0.028
MP_{1p}OPBE	0.047	0.019	0.055	0.046	0.482	0.057	0.445	1.249	0.023

[a] results obtained using QZ4P basis set, in **bold** the functional that performs best for that particular property
[b] more information can be found in ref. [21].

Performance of the Functionals for Structural Characterization of S_N2 Stationary Points

Similar to the energetic performance for S_N2 reactions, for the structural characterization of their stationary points we also take a look at different components,[21] and compare the DFT results for these with reference values that were obtained with CCSD(T) calculations. Specifically, we look at the bonds and angles for the reactants/products, reactant/product complexes and transition state structures. The mean absolute deviation is then taken for both the bonds and the angles, and the product of these values is then the overall performance P_G for the geometry of S_N2 reactions. Previously,[21] we already showed that not only do OPBE and OLYP improve considerably upon PBE for the overall performance for the energy, but also for the geometry. I.e., the P_G value for PBE (0.418) is dramatically reduced for both OPBE (0.042) and OLYP (0.029). Note that the values reported in this chapter are different from the previously reported values,[21] since we take only the data obtained with large basis sets into account here.

The performance of the newly developed functionals for the structural characterization of S_N2 reactions is for most cases a clear improvement over the early GGAs, and in many cases also over OLYP/OPBE. In general, the constraint-free functionals (ab=ff) perform significantly better than when constraints are imposed (see table 4). For instance, the P_G value of MP$_{ff}$PBE is small (0.02), while those of the corresponding constrained ones are very large (0.51-0.56), indeed even larger than the already substantial PBE value (0.42). This is however not true for the MP$_{ab}$OPBE functionals that have all P_G values between 0.019 and 0.028. Equally well-performing are MP$_{ff}$OLYP, MP$_{ff}$PBE and several atomic functionals. Extraordinarily good is the A$_{fp}$OPBE functional with a P_G value of only 0.012, i.e. a further reduction by around two compared to OLYP and e.g. the MP$_{ab}$OPBE functionals. This is mainly resulting from the improved description of bonds (for which it has a MAD value of 0.022 Å), and not as much the angles for which the MAD value is similar to that of e.g. OLYP/OPBE. The small MAD value for the distances is, compared to the other functionals, mainly resulting from the RC/PC complexes, for which A$_{fp}$OPBE shows a MAD value of 0.029 Å w.r.t. the CCSD(T) data, which is smaller than that of OPBE and OLYP by a factor of around three. The poorest performance is shown for the A$_{lp}$OLYP functional, with a P_G value of 0.68, which results from the poor performance for both bonds (MAD value 0.15 Å) and angles (MAD value 4.53 deg).

Taking both the P_E and P_G values into consideration, we find that there is no clear relationship between the two in general. Although there are functionals (like ML$_{ff}$OLYP and MP$_{ff}$OPBE) that improve upon OLYP and OPBE for both P_E and P_G, there are also many others that do well for one but somewhat less for the other. For instance, the best performing functional for S_N2 geometries (A$_{fp}$OPBE) is significantly less accurate for energies. Furthermore, there are many functionals (such as ML$_{fp}$OLYP) that are considerably less accurate for both S_N2 energetics and geometries.

Comparison of PBE with the Simplified PBE (sPBE) and BEE Functionals

So far we have discussed only the (non-constrained) functionals, and how the presence of these affect their performance. However, we would also like to investigate the performance of the sPBE and BEE[84] functionals. As mentioned in the section on the construction of the functionals, the sPBE functional is a simplification of the PBEc correlation functional and uses the original PBEx exchange, while the BEE was determined from a Bayesian Error Estimate[84] and is different from PBE only in the exchange part.

The performance of the sPBE functional is in many cases similar to that of the original PBE functional, both for many of the standard benchmark tests and the S_N2 benchmarks. However, there are also some tests where the simplified PBE correlation performs better than the original functional. For instance, the MAD values for the atomization energies of the G2-1 and G2/97 sets are considerably smaller for sPBE (6.8 and 12.9 kcal·mol^{-1}) than for PBE (8.0 and 16.3 kcal·mol^{-1}), see table 2. Likewise, the MAD value for the hydrogen-bonding distances is also significantly smaller for sPBE (1.9 pm) than for PBE (2.5 pm). Therefore, although for some systems the sPBE functional performs better than PBE, the improvements are not spectacular as was shown by e.g. OPBE for the reaction barriers.

The BEE functional on the other hand is significantly better than either PBE or sPBE for the atomization energies (see table 2), but at the same time significantly worse for the accuracy of geometries of the small molecules and for the weak interactions. For instance, its MAD value for π-π stacking is 10.7 kcal·mol^{-1}, and for hydrogen-bonding distances 5.6 pm, which are respectively 3.6 kcal·mol^{-1} and 3.7 pm larger than the sPBE values. For the S_N2 benchmarks, it does better than either PBE or sPBE but only marginally so, especially compared to the major improvements shown by OPBE and OLYP.

Spin-State Splittings of a High-Spin Iron Compound

It was previously shown[45,50] that the OPBE functional works exceptionally well for spin-states of iron complexes, and although we do not have CCSD(T) data to compare with, we know the experimental ground-state of the molecules. Therefore we include here as test on the newly developed functionals the calculation of the spin-state splittings of one of the typical iron compounds, i.e. Fe(N(CH$_2$-o-C$_6$H$_4$S)$_3$)(1-Me-imidazole). Experimentally, and with the OPBE functional, it has a high-spin sextet ground-state with the low-spin doublet and intermediate quartet higher in energy. Similar to what was observed for the energetics of the S_N2 reactions, the non-constrained functionals perform better than the constrained ones (see table 5). The majority of the newly developed functionals, however, do not predict the correct spin ground-state. For the ones that do, the largest separation between low- and high-spin is obtained with the MP$_{ff}$OPBE functional (17.3 kcal·mol^{-1}), while the A$_{lp}$OPBE predicts all three states at virtually the same energy.

Table 5. Spin-state splittings (kcal·mol^{-1}) for Fe(N(CH$_2$-o-C$_6$H$_4$S)$_3$)(1-Me-imidazole) (see figure 6)

functional	doublet	quartet	sextet
PBE	-4.1	-2.5	0
sPBE	-4.4	-2.7	0
BEE	-2.4	-1.6	0
OPBE	12.4	6.3	0
OLYP	7.4	4.0	0
A$_{ff}$PBE	2.2	0.9	0
A$_{fp}$PBE	-2.7	-1.7	0
A$_{1f}$PBE	-4.8	-2.8	0
A$_{1p}$PBE	-4.6	-2.8	0
A$_{ff}$OLYP	7.3	4.0	0
A$_{fp}$OLYP	2.6	1.5	0
A$_{1f}$OLYP	-16.5	-9.2	0
A$_{1p}$OLYP	-5.0	-2.6	0
A$_{ff}$OPBE	12.4	6.3	0
A$_{fp}$OPBE	7.4	3.8	0
A$_{1f}$OPBE	-11.9	-6.9	0
A$_{1p}$OPBE	-0.1	-0.2	0
MP$_{ff}$PBE	5.7	3.2	0
MP$_{fp}$PBE	-9.7	-5.2	0
MP$_{1f}$PBE	-3.9	-2.3	0
MP$_{1p}$PBE	-9.1	-4.9	0
ML$_{ff}$OLYP	10.4	5.7	0
ML$_{fp}$OLYP	-1.3	-0.6	0
ML$_{1f}$OLYP	1.4	0.5	0
ML$_{1p}$OLYP	-1.8	-1.0	0
MP$_{ff}$OPBE	17.3	9.2	0
MP$_{fp}$OPBE	2.9	1.5	0
MP$_{1f}$OPBE	6.3	2.9	0
MP$_{1p}$OPBE	2.8	1.2	0
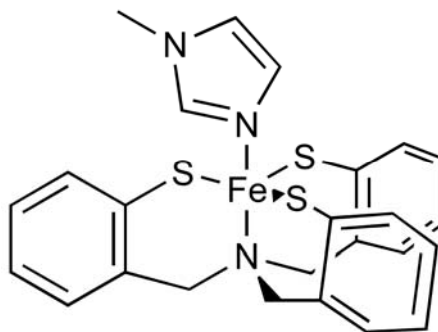
Figure 6. Iron(III) complex Fe(N(CH$_2$-o-C$_6$H$_4$S)$_3$)(1-Me-imidazole).

Conclusion

We have explored in this chapter what might be the origin of the spectacular improvements of OPBE (and OLYP) over PBE for a number of chemical properties, such as atomization energies, accuracies of geometries and reaction energy profiles. In particular, we have investigated what is the effect of the constraints that are imposed on the PBEx exchange functional, on the one hand by lifting these constraints for the PBEx functional, and on the other by imposing them on the OPTX functional. For all benchmark tests we investigated, the best performance is obtained with one of the newly developed functionals, but unfortunately there is no one that is equally good for all benchmarks.

A comparison of the performance of the $A_{lp}PBE$, $A_{lp}OPBE$ and $A_{lp}OLYP$ shows that the PBEx exchange expression is better suited for the fulfillment of the constraints than is the OPTX expression. The mean absolute deviations are in all these cases lower with the PBEx expression than with the OPTX one. However, these constrained functionals work well only for proton affinities and hydrogen-bonded systems, for the other benchmark tests are the non-constrained functionals working much better. This leads to sometimes extraordinarily good performance, for instance for the accuracy of geometries where the $ML_{ff}OLYP$ functional approaches the accuracy of CCSD(T).

The poor performance for weak interactions by OPBE and related unconstrained functionals does not result from the way how the exchange functional has been obtained. Both the newly developed atomic (e.g. $A_{ff}OPBE$) and molecular (e.g. $MP_{ff}OPBE$) functionals are particularly poor for the weak interactions, which is in some cases improved upon by imposing one (or more) constraint(s). This is especially true for the newly developed functionals based on the PBEx expression that in general do a better job for weak interactions than those based on the OPTX expression. The same is true for the proton affinities, while it is the opposite for the reaction barriers, etc. Therefore, the replacement of s^2 as leading term in the PBEx expression by s^4 in the OPTX expression is not beneficial for all systems.

Acknowledgment

References

[1]   Koch, W.; Holthausen, M. C. *A Chemist's Guide to Density Functional Theory*, Wiley-VCH, Weinheim, 2000.
[2]   Parr, R. G.; Yang, W. *Density functional theory of atoms and molecules*, Oxford University Press, New York, 1989.
[3]   Dreizler, R.; Gross, E. *Density Functional Theory*, Plenum Press, New York, 1995.
[4]   Hohenberg, P.; Kohn, W. *Phys. Rev.* 1964, 136, B864-B871.

[5]   Vosko, S. H.; Wilk, L.; Nusair, M. *Can. J. Phys.* 1980, 58, 1200-1211.

[6]   Perdew, J. P.; Zunger, A. *Phys. Rev. B* 1981, 23, 5048-5079.

[7]   Perdew, J. P.; Wang, Y. *Phys. Rev. B* 1992, 45, 13244-13249.

[8]   Perdew, J. P.; Yue, W. *Phys. Rev. B* 1986, 33, 8800-8802.

[9]   Perdew, J. P.; Tao, J. M.; Staroverov, V. N.; Scuseria, G. E. *J. Chem. Phys.* 2004, 120, 6898-6911.

[10] Perdew, J. P., in P. Ziesche, H. Eschrig (Eds.), *Electronic structure of Solids* 1991. Akademie, Berlin, 1991, p. 11.

[11] Becke, A. D. *J. Chem. Phys.* 1993, 98, 5648-5652.

[12] Perdew, J. P.; Ruzsinszky, A.; Tao, J. M.; Staroverov, V. N.; Scuseria, G. E.; Csonka, G. I. *J. Chem. Phys.* 2005, 123, 062201.

[13] Fonseca Guerra, C.; Visser, O.; Snijders, J. G.; Velde, G. T.; Baerends, E. J., in E. Clementi, G. Corongiu (Eds.), *Methods and Techniques for Computational Chemistry*, METECC-5. STEF, Cagliari, 1995, p. 303-395.

[14] Fonseca Guerra, C.; Snijders, J. G.; Velde, G. T.; Baerends, E. J. *Theor. Chem. Acc.* 1998, 99, 391-403.

[15] Gauss, J.; Stanton, J. F. *Phys. Chem. Chem. Phys.* 2000, 2, 2047-2060.

[16] Inaba, T.; Sato, F. *J. Comput. Chem.* 2007, 28, 984-995.

[17] Pollack, L.; Windus, T. L.; De Jong, W. A.; Dixon, D. A. *J. Phys. Chem. A* 2005, 109, 6934-6938.

[18] Helgaker, T.; Gauss, J.; Jørgensen, P.; Olsen, J. *J. Chem. Phys.* 1997, 106, 6430-6440.

[19] Bak, K. L.; Jørgensen, P.; Olsen, J.; Helgaker, T.; Klopper, W. *J. Chem. Phys.* 2000, 112, 9229-9242.

[20] Bak, K. L.; Gauss, J.; Jørgensen, P.; Olsen, J.; Helgaker, T.; Stanton, J. F. *J. Chem. Phys.* 2001, 114, 6548-6556.

[21] Swart, M.; Solà, M.; Bickelhaupt, F. M. *J. Comput. Chem.* 2007, 28, 1551-1560.

[22] Bento, A. P.; Solà, M.; Bickelhaupt, F. M. *J. Comput. Chem.* 2005, 26, 1497-1504.

[23] Swart, M.; Ehlers, A. W.; Lammertsma, K. *Molec. Phys.* 2004, 102, 2467-2474.

[24] Bento, A. P.; Solà, M.; Bickelhaupt, F. M. *J. Chem. Theor. Comp.* 2008, 4, 929-940.

[25] Perdew, J. P. *Phys. Rev. B* 1986, 33, 8822-8824. Erratum: Ibid. 8834, 7406.

[26] Perdew, J. P.; Chevary, J. A.; Vosko, S. H.; Jackson, K. A.; Pederson, M. R.; Singh, D. J.; Fiolhais, C. *Phys. Rev. B* 1992, 46, 6671 Ibid E 6648 (1993) 4978.

[27] Perdew, J. P.; Burke, K.; Ernzerhof, M. *Phys. Rev. Lett.* 1996, 77, 3865-3868.

[28] Perdew, J. P.; Burke, K.; Wang, Y. *Phys. Rev. B* 1996, 54, 16533-16539.

[29] Perdew, J. P.; Kurth, S.; Zupan, A.; Blaha, P. *Phys. Rev. Lett.* 1999, 82, 2544-2547.

[30] Tao, J. M.; Perdew, J. P.; Staroverov, V. N.; Scuseria, G. E. *Phys. Rev. Lett.* 2003, 91, 146401.

[31] Staroverov, V. N.; Scuseria, G. E.; Tao, J. M.; Perdew, J. P. *J. Chem. Phys.* 2003, 119, 12129-12137.

[32] Perdew, J. P.; Burke, K.; Ernzerhof, M. *Phys. Rev. Lett.* 1996, 77, 3865-3868 Erratum 3878 1396.

[33] Perdew, J. P.; Ernzerhof, M.; Burke, K. *J. Chem. Phys.* 1996, 105, 9982-9985.

[34] Stephens, P. J.; Devlin, F. J.; Chabalowski, C. F.; Frisch, M. J. *J. Phys. Chem.* 1994, 45, 11623-11627.

[35] Zhang, Y.; Yang, W. *Phys. Rev. Lett.* 1998, 80, 890.

[36] Swart, M.; Snijders, J. G. *Theor. Chem. Acc.* 2003, 110, 34-41, Erratum: ibid 111, 156.

[37] Hammer, B.; Hansen, L. B.; Norskov, J. K. *Phys. Rev. B* 1999, 59, 7413.

[38] Adamo, C.; Barone, V. *J. Chem. Phys.* 2002, 116, 5933-5940.

[39] Xu, X.; Goddard III, W. A. *J. Chem. Phys.* 2004, 121, 4068-4082.

[40] Handy, N. C.; Cohen, A. J. *Molec. Phys.* 2001, 99, 403-412.

[41] Becke, A. D. *Phys. Rev. A* 1988, 38, 3098.

[42] Lee, C.; Yang, W.; Parr, R. G. *Phys. Rev. B* 1988, 37, 785.

[43] Cohen, A. J.; Handy, N. C. *Chem. Phys. Lett.* 2000, 316, 160-166.

[44] Baker, J.; Pulay, P. *J. Chem. Phys.* 2002, 117, 1441-1449.

[45] Swart, M.; Groenhof, A. R.; Ehlers, A. W.; Lammertsma, K. *J. Phys. Chem. A* 2004, 108, 5479-5483.

[46] Becke, A. D. *J. Chem. Phys.* 2000, 112, 4020-4026.

[47] Staroverov, V. N.; Scuseria, G. E.; Tao, J.; Perdew, J. P. *J. Chem. Phys.* 2003, 119, 12129-12137.

[48] Van Voorhis, T.; Scuseria, G. *J. Chem. Phys.* 1998, 109, 400-410.

[49] Swart, M.; Ehlers, A. W.; Lammertsma, K. *in preparation* 2009.

[50] Swart, M. *J. Chem. Theory Comput.* 2008, 4, 2057-2066.

[51] Pierloot, K.; Vancoillie, S. *J. Chem. Phys.* 2006, 125, 124303.

[52] Swart, M. *Inorg. Chim. Acta* 2007, 360, 179-189.

[53] Reiher, M.; Salomon, O.; Hess, B. A. *Theor. Chem. Acc.* 2001, 107, 48-55.

[54] Reiher, M. *Inorg. Chem.* 2002, 41, 6928-6935.

[55] Zhao, Y.; Truhlar, D. G. *Theor. Chem. Acc.* 2008, 120, 215-241.

[56] Conradie, J.; Ghosh, A. *J. Chem. Theor. Comp.* 2007, 3, 689-702.

[57] Zhang, Y.-Q.; Luo, C.-L. *J. Phys. Chem. A* 2006, 110, 5096-5101.

[58] Zhang, Y.; Wu, A.; Xu, X.; Yan, Y. *Chem. Phys. Lett.* 2006, 421, 383-388.

[59] Wu, A.; Zhang, Y.; Xu, X.; Yan, Y. *J. Comput. Chem.* 2007, 28, 2431-2442.

[60] Wasbotten, I.; Ghosh, A. *Inorg. Chem.* 2006, 45, 4910-4913.

[61] Groenhof, A. R.; Ehlers, A. W.; Lammertsma, K. *J. Am. Chem. Soc.* 2007, 129, 6204-6209.

[62] Derat, E.; Kumar, D.; Neumann, R.; Shaik, S. *Inorg. Chem.* 2006, 45, 8655-8663.

[63] Romo, S.; Fernández, J. A.; Maestre, J. M.; Keita, B.; Nadjo, L.; De Graaf, C.; Poblet, J. M. *Inorg. Chem.* 2007, 46, 4022-4027.

[64] Rong, C.; Lian, S.; Yin, D.; Shen, B.; Zhong, A.; Bartolotti, L.; Liu, S. *J. Chem. Phys.* 2006, 125, 174102.

[65] Liao, M.-S.; Watts, J. D.; Huang, M.-J. *J. Comput. Chem.* 2006, 27, 1577-1592.

[66] Liao, M.-S.; Watts, J. D.; Huang, M.-J. *J. Phys. Chem. A* 2007, 111, 5927-5935.

[67] Zein, S.; Borshch, S. A.; Fleurat-Lessard, P.; Casida, M. E.; Chermette, H. *J. Chem. Phys.* 2007, 126, 014105.

[68] Conradie, J.; Ghosh, A. *J. Phys. Chem. B* 2007, 111, 12621-12624.

[69] Swart, M.; Güell, M.; Luis, J. M.; Solà, M. *Proceedings of "European Biological Inorganic Chemistry Conference - EUROBIC9"* 2008, 77-82.

[70] Güell, M.; Luis, J. M.; Solà, M.; Swart, M. *J. Phys. Chem. A* 2008, 112, 6384-6391.

[71] Proynov, E. I.; Sirois, S.; Salahub, D. R. *Int. J. Quant. Chem.* 1997, 64, 427.

[72] Grüning, M.: Density functional theory with improved gradient and orbital dependent functionals, PhD thesis, Vrije Universiteit Amsterdam, Amsterdam, 2003.

[73] Zhao, Y.; Truhlar, D. G. *J. Phys. Chem. A* 2008, 112, 6794-6799.

[74] Swart, M.; Van der Wijst, T.; Fonseca Guerra, C.; Bickelhaupt, F. M. *J. Mol. Model.* 2007, 13, 1245-1257.

[75] Van der Wijst, T.; Fonseca Guerra, C.; Swart, M.; Bickelhaupt, F. M. *Chem. Phys. Lett.* 2006, 426, 415-421.

[76] Swart, M.; Bickelhaupt, F. M. *J. Chem. Theor. Comp.* 2006, 2, 281-287.

[77] Swart, M.; Rösler, E.; Bickelhaupt, F. M. *J. Comput. Chem.* 2006, 27, 1486-1493.

[78] Grimme, S. *J. Comput. Chem.* 2004, 25, 1463-1473.

[79] Xu, X.; Goddard III, W. A. *Proc. Natl. Acad. Sci. USA* 2004, 101, 2673-2677.

[80] Cerny, J.; Hobza, P. *Phys. Chem. Chem. Phys.* 2005, 7, 1624-1626.

[81] Keal, T. W.; Tozer, D. J. *J. Chem. Phys.* 2003, 119, 3015-3024.

[82] Waller, M. P.; Robertazzi, A.; Platts, J. A.; Hibbs, D. E.; Williams, P. A. *J. Comput. Chem.* 2006, 27, 491-504.

[83] Swart, M.; Bickelhaupt, F. M. *J. Comput. Chem.* 2008, *29*, 724-734.

[84] Mortensen, J. J.; Kaasbjerg, K.; Frederiksen, S. L.; Nørskov, J. K.; Sethna, J. P.; Jacobsen, K. W. *Phys. Rev. Lett.* 2005, 95, 216401.

[85] Curtiss, L. A.; Raghavachari, K.; Trucks, G. W.; Pople, J. A. *J. Chem. Phys.* 1991, 94, 7221-7230.

[86] Curtiss, L. A.; Raghavachari, K.; Redfern, P. C.; Pople, J. A. *J. Chem. Phys.* 1997, 106, 1063-1079.

[87] Swart, M.; Rösler, E.; Bickelhaupt, F. M. *Eur. J. Inorg. Chem.* 2007, 3646-3654.

[88] Jurecka, P.; Sponer, J.; Hobza, P. *J. Phys. Chem. B* 2004, 108, 5466-5471.

[89] Jurecka, P.; Sponer, J.; Cerny, J.; Hobza, P. *Phys. Chem. Chem. Phys.* 2006, 8, 1985-1993.

[90] Baerends, E. J.; Autschbach, J.; Bérces, A.; Bo, C.; Boerrigter, P. M.; Cavallo, L.; Chong, D. P.; Deng, L.; Dickson, R. M.; Ellis, D. E.; Fan, L.; Fischer, T. H.; Fonseca Guerra, C.; Van Gisbergen, S. J. A.; Groeneveld, J. A.; Gritsenko, O. V.; Grüning, M.; Harris, F. E.; Van Den Hoek, P.; Jacobsen, H.; Van Kessel, G.; Kootstra, F.; Van Lenthe, E.; Mccormack, D. A.; Osinga, V. P.; Patchkovskii, S.; Philipsen, P. H. T.; Post, D.; Pye, C. C.; Ravenek, W.; Ros, P.; Schipper, P. R. T.; Schreckenbach, G.; Snijders, J. G.; Solà, M.; Swart, M.; Swerhone, D.; Te Velde, G.; Vernooijs, P.; Versluis, L.; Visser, O.; Van Wezenbeek, E.; Wiesenekker, G.; Wolff, S. K.; Woo, T. K.; Ziegler, T., ADF 2005.01. SCM, Amsterdam, 2005.

[91] Te Velde, G.; Bickelhaupt, F. M.; Baerends, E. J.; Fonseca Guerra, C.; Van Gisbergen, S. J. A.; Snijders, J. G.; Ziegler, T. *J. Comput. Chem.* 2001, 22, 931-967.

[92] Van Lenthe, E.; Baerends, E. J. *J. Comput. Chem.* 2003, 24, 1142-1156.

[93] Hamprecht, F. A.; Cohen, A. J.; Tozer, D. J.; Handy, N. C. *J. Chem. Phys.* 1998, 109, 6264-6271.

[94] Becke, A. D. *J. Chem. Phys.* 1997, 107, 8554-8560.

Chapter 4

TEMPERATURE INTEGRAL AND ITS APPROXIMATIONS

Junmeng Cai

Biomass Energy Engineering Research Center, School of Agriculture and Biology,
Shanghai Jiao Tong Univ., Shanghai, P.R. China

Abstract

The temperature integral, which frequently occurs in the kinetic analysis of solid-state reactions, does not have an exact analytical solution. Instead of performing the numerical integration, most of the researchers prefer to circumvent the problem by using approximate expressions.

The main aim of this chapter is to carry out a review of the known approximations for the temperature integral, to establish a ranking of those temperature integral approximations and to present some applications of the temperature integral approximations.

Temperature Integral

The reaction rate of thermally stimulated solid-state reactions can be kinetically described by the following expression:

$$\frac{d\alpha}{dt} = k(T)f(\alpha) \tag{0.1}$$

where α is the extent of reaction conversion ranging from 0 before the reaction process starts to 1 when it is over, t is the time, $k(T)$ is the reaction rate constant that describes the dependence of the reaction rate with the temperature (T), $f(\alpha)$ is the differential conversion function.

Usually, $k(T)$ is described by the Arrhenius equation:

$$k(T) = Ae^{-E/RT} \tag{0.2}$$

where A and E are the Arrhenius parameters (preexponential factor and activation energy, respectively), R is the universal gas constant.

Table 1.1. Algebraic expressions for $f(\alpha)$ for the most common mechanisms in solid-state reactions

Model	Symbol	$f(\alpha)$
Phased boundary controlled reaction	R2	$2(1-\alpha)^{1/2}$
	R3	$3(1-\alpha)^{2/3}$
Nucleation and growth (Avraml-Erofeev)	A1.5	$\frac{3}{2}(1-\alpha)[-\ln(1-\alpha)]^{1/3}$
	A2	$2(1-\alpha)[-\ln(1-\alpha)]^{1/2}$
	A2.5	$\frac{5}{2}(1-\alpha)[-\ln(1-\alpha)]^{3/5}$
	A3	$3(1-\alpha)[-\ln(1-\alpha)]^{2/3}$
	A4	$4(1-\alpha)[-\ln(1-\alpha)]^{3/4}$
One-dimensional diffusion	D1	$\dfrac{2}{\alpha}$
Two-dimensional diffusion	D2	$-\dfrac{1}{\ln(1-\alpha)}$
Three-dimensional diffusion (Jander)	D3	$\dfrac{3(1-\alpha)^{2/3}}{2[1-(1-\alpha)^{1/3}]}$
Three-dimensional diffusion (Ginstling-Brounshtein)	D4	$\dfrac{3(1-\alpha)^{1/3}}{2[1-(1-\alpha)^{1/3}]}$
Three-dimensional diffusion (Zhuralev-Lesokin-Tempelman)	D5	$\dfrac{3(1-\alpha)^{5/3}}{2[1-(1-\alpha)^{1/3}]}$
Three-dimensional diffusion (Komatsu-Uemura)	D6	$\dfrac{3(1+\alpha)^{2/3}}{2[(1+\alpha)^{1/3}-1]}$
First-order reaction	F1	$(1-\alpha)$
Second-order reaction	F2	$(1-\alpha)^2$
Third-order reaction	F3	$(1-\alpha)^3$
Prout-Tompkins	PT	$\alpha(1-\alpha)$
Reduced Šesták-Berggren function	RSB	$\alpha^m(1-\alpha)^n$

The $f(\alpha)$ function describes the dependence of the reaction rate with the reaction mechanism. Different functions have been proposed in the literature for describing the kinetic

mechanism of the solid-state reactions. These mechanisms are proposed considering different geometrical assumptions for the particles shape (spherical, cylindrical, planar) and driving forces (interface growth, diffusion, nucleation, and growth of nuclei)[1]. Some of the most common equations proposed for these reactions are included in Table 1.1. The Arrhenius parameters (A and E), and $f(\alpha)$ are sometimes called the kinetic triplet[2].

Several procedures have been proposed in the literature for the kinetic analysis of thermally stimulated solid-state reactions under different temperature evolution conditions, i.e., isothermal, nonisothermal[3]. For a nonisothermal system, a constant heating rate is often used[4]

$$\beta = \frac{dT}{dt} \tag{0.3}$$

where β is the heating rate.

For nonisothermal conditions with the linear heating program, Equation (1.1) is represented as follows

$$\frac{d\alpha}{dT} = \frac{A}{\beta} e^{-E/RT} f(\alpha) \tag{0.4}$$

By integrating Equation (1.4), we get

$$g(\alpha) = \int_0^\alpha \frac{d\alpha}{f(\alpha)} = \frac{A}{\beta} \int_0^T e^{-E/RT} dT \tag{0.5}$$

where $g(\alpha)$ is the integral conversion function.

The integral $\int_0^T e^{-E/RT} dT$ in the left hand side of Equation (1.5) is called the temperature integral or Arrhenius integral, which has no exact analytic solution and some approximations have been proposed in the literature. A ranking of the known approximations for the temperature integral is presented in the following section.

Ranking of the Temperature Integral Approximations

The temperature integral can be approximated in three different ways.

The first type of approximations, which is called the exponential – type here, is based on the following expression

$$I_{a1} = \frac{E}{R} e^{p_1 + p_2 \ln x + p_3 x} \tag{0.6}$$

where I_{a1} is the approximation for the temperature integral $\int_0^T e^{-E/RT}dT$, p_1, p_2 and p_3 are

constants, and $x=E/RT$. This type of temperature integral approximations can be found in the literature[5,6,7,8,9,10,11,12]. The parameter values of the exponential-type approximations are listed in Table 1.2.

Table 1.2. The parameter values of the exponential-type approximations

Author	Name of approximation	p_1	p_2	p_3
Dolye [5]	Doyle-1	-5.3308	0	-1.0516
Liu et al. [6]	LCSS	-5.26936572	0	-1.0516296
Tang et al. [7]	TLZW	-0.37773896	-1.894661	-1.00145033
Agherghinei [8]	Agherghinei 1	-0.679165	-1.7276	-1.01179
Agherghinei [8]	Agherghinei 2	-0.398956	-1.88582	-1.00174
Madhusudanan et al. [9]	MKN 1	-0.29758	-1.921503	-1.000953
Madhusudanan et al. [10]	MKN 2	-0.299963	-1.92062	-1.000974
Madhusudanan et al. [10]	MKN 3	-0.389677	-1.884318	-1.001928
Starink [11]	Starink 1	-0.235	-1.95	-1
Starink [11]	Starink 2	-0.312	-1.92	-1.0008
Cai and Liu [12]	CL	-0.460120828342246	-1.86847901883656	-1.00174866236974

The second type of temperature integral approximations is based on the fact that the temperature integral can be written in the following form

$$I_{a2} = \frac{RT^2}{E} e^{-E/RT} h(x) \tag{0.7}$$

where I_{a2} is the approximation for the temperature integral. The expressions of $h(x)$ are frequently rational functions of x (i.e., ratios between polynomial functions) derived from different series expansions or obtained using appropriate fitting procedures relatively to the values calculated by numerical integration in a certain range of $x[13]$. Here, this type of temperature integral approximations is called the rational fraction – type of approximations. A set of known expressions of $h(x)$ that have been used for the calculation of the temperature integral according to Equation (1.7) are given in Table 1.3.

Table 1.3. Expressions of $h(x)$

Authors	Name of approximation	$h(x)$
Doyle[14]	Doyle-2	1
Coats and Redfern[15]	Coats-Redfern	$\dfrac{x-2}{x}$
Gorbachev[16], Lee and Beck[17]	Gorbachev-Lee-Beck	$\dfrac{x}{x+2}$
van Tets[18]	van Tets	$\dfrac{x+1}{x+3}$
Wanjun et al.[19]	Wanjun-1	$\dfrac{x}{1.00198882x+1.87391198}$
Wanjun[20]	Wanjun-2	$\dfrac{x}{1.002x+1.874}$
Cai et al.[21]	Cai-1	$\dfrac{x+0.66691}{x+2.64943}$
Cai and He[22]	Cai-He	$\dfrac{0.99962x+0.60642}{x+2.56879}$
Li[23]	Li	$\dfrac{x^2-2x}{x^2-6}$
Agrawal and Sivasubramanian[24]	Agrawal-Sivasubramanian	$\dfrac{x^2-2x}{x^2-5}$

Table 1.3. Continued

Authors	Name of approximation	$h(x)$
Quanyin and Su[25]	Quanyin-Su-1	$\dfrac{x^2 - 2x}{x^2 - 5.2}$
	Quanyin-Su-2	$\dfrac{x^2 - 2x}{x^2 - 4.6}$
Urbanovici and Segal[26]	Urbanovici-Segal-1	$\dfrac{x^2 + 2x - 2}{x^2 + 4x}$
	Urbanovici-Segal-2	$\dfrac{x^2 + 3.5x}{x^2 + 5.5x + 5}$
	Urbanovici-Segal-3	$\dfrac{x^2 + 5.347x + 1.376}{x^2 + 7.347x + 10.069}$
Senum and Yang[27]	Senum-Yang-1	$\dfrac{x^2 + 4x}{x^2 + 6x + 6}$
	Senum-Yang-2	$\dfrac{x^3 + 10x^2 + 18x}{x^3 + 12x^2 + 36x + 24}$
	Senum-Yang-3	$\dfrac{x^4 + 18x^3 + 86x^2 + 96x}{x^4 + 20x^3 + 120x^2 + 240x + 120}$
Zsakó[28]	Zsakó	$\dfrac{x^4 - 4x^3 + 84x^2}{x^4 - 2x^3 + 76x^2 + 152x - 32}$
Chen and Liu[29]	Chen-Liu	$\dfrac{3x^2 + 16x + 4}{3x^2 + 22x + 30}$

Table 1.3. Continued

Authors	Name of approximation	h(x)
Órfão[30]	Órfão-1	$$\dfrac{0.995924x^2 + 1.430913x}{x^2 + 3.330657x + 1.681534}$$
	Órfão-2	$$\dfrac{0.99997x^2 + 3.03962x}{x^2 + 5.03637x + 4.19160}$$
Ji[31]	Ji-1	$$\dfrac{x^2 + 4.45239x + 0.76927}{x^2 + 6.45218x + 7.69430}$$
	Ji-2	$$\dfrac{x^2 + 16.99864x + 3.65517\ln x + 5.41337}{x^2 + 18.99977x + 3.43593\ln x + 38.49858}$$
	Ji-3	$$\dfrac{x^3 + 9.27052x^2 + 16.79440x + 1.20025}{x^3 + 11.27052x^2 + 33.33602x + 24.21457}$$
Balarin[32]	Balarin	$$\sqrt{\dfrac{x}{x+4}}$$
Cai et al.[33]	Cai-2	$$\dfrac{x + 0.25403\ln x + 0.36665}{x + 0.24598\ln x + 2.41457}$$
Cai and Liu[34]	Cai-Liu	$$\dfrac{0.999940083636437x + 0.278603058646963\ln x + 0.367233903690}{x + 0.264770161932887\ln x + 2.43832629069336}$$
Cai et al.[35]	Cai-3	$$\left(\dfrac{x\text{-}0.566552207341865}{x + 4.42348301307593}\right)^{0.400350661295612}$$

Recently, Chen and Liu[36] drawn a conclusion that the exponential – type approximations are essentially one kind of the rational fraction – type approximations with the form of $\dfrac{RT^2}{E}e^{-E/RT}\dfrac{x}{-p_2-p_3x}$. In fact, it is incorrect, which can be obtained from the following expression

$$\frac{\dfrac{E}{R}e^{p_1+p_2\ln x+p_3x}}{\dfrac{RT^2}{E}e^{-E/RT}\dfrac{x}{-p_2-p_3x}}=-x(p_2+p_3x)e^{p_1+p_2\ln x+(p_3+1)x}\neq 1 \qquad (0.8)$$

The third type of approximations is based on the fact that the temperature integral is directly correlated with the values of T and E. Gyulai and Greenhow[37] arrived at two different expressions, with a reasonable degree of approximation in the range of temperatures 400-900 K and for activation energies between 30 and 90 kcal mol^{-1}. Here, we don't consider this type of approximations due to the fact that this type is not usually used in the literature.

Evaluation of the Accuracy of the Exponential – Type and Rational Fraction – Type Approximations

To evaluate the accuracy of the exponential – type approximations for the estimation of the temperature integral, the relative deviates of the type approximations are calculated on the basis of the following expression.

$$\varepsilon_1(\%)=\frac{\dfrac{E}{R}e^{p_1+p_2\ln x+p_3x}-\displaystyle\int_0^T e^{-E/RT}dT}{\displaystyle\int_0^T e^{-E/RT}dT}\cdot 100=\frac{e^{p_1+p_2\ln x+p_3x}-\displaystyle\int_x^\infty \dfrac{e^{-x}}{x^2}dx}{\displaystyle\int_x^\infty \dfrac{e^{-x}}{x^2}dx}\cdot 100 \qquad (0.9)$$

In the above equation, the integral $\displaystyle\int_x^\infty \dfrac{e^{-x}}{x^2}dx$ doesn't have an exact analytical solution and can be numerically solved. Here the Mathematica software system has been used for the numerical calculation of the integral $\displaystyle\int_x^\infty \dfrac{e^{-x}}{x^2}dx$. The relative error percentages of the exponential – type approximations for the estimation of the temperature integral are listed in Table 1.4.

To have an immediate perception of the accuracy of each exponential – type approximation, the ranges of x associated to relative deviations lower than some selected values, mainly chosen according to the literature, are presented in Table 1.5.

Table 1.4. The relative error percentages of the exponential – type approximations for the estimation of the temperature integral

x	Doyle-1	Agherghinei I	Agherghinei II	Starink I	Starink II	MKN I	MKN II	MKN III	LCSS	TLZW	Cai-Liu
5.0	-8.735704E+01	2.152774E-01	8.108395E+00	1.587322E+01	1.214355E+01	1.341071E+01	1.328978E+01	9.277526E+00	-8.655796E+01	9.024293E+00	4.567780E+00
7.5	-7.702776E+01	-1.618687E-01	3.579168E+00	8.638489E+00	6.215797E+00	7.309475E+00	7.227807E+00	4.713874E+00	-7.557764E+01	4.158319E+00	8.916159E-01
10.0	-6.575508E+01	1.570707E-02	1.668877E+00	5.140476E+00	3.479639E+00	4.459986E+00	4.401524E+00	2.778760E+00	-6.359608E+01	2.051523E+00	-4.759958E-01
12.5	-5.436486E+01	1.319810E-01	7.560592E-01	3.162671E+00	2.010825E+00	2.903357E+00	2.860632E+00	1.842244E+00	-5.149135E+01	1.009067E+00	-9.893080E-01
15.0	-4.343871E+01	5.122642E-02	3.007945E-01	1.944338E+00	1.156463E+00	1.974549E+00	1.943269E+00	1.362187E+00	-3.988165E+01	4.634354E-01	-1.126713E+00
17.5	-3.337067E+01	-2.450562E-01	7.733055E-02	1.154914E+00	6.369178E-01	1.388511E+00	1.365886E+00	1.112243E+00	-2.918569E+01	1.756094E-01	-1.085074E+00
20.0	-2.441089E+01	-7.422294E-01	-2.257116E-02	6.283827E-01	3.141057E-01	1.004365E+00	9.884310E-01	9.840960E-01	-1.966908E+01	2.994787E-02	-9.568801E-01
22.5	-1.670002E+01	-1.416961E+00	-5.571920E-02	2.726952E-01	1.129337E-01	7.454231E-01	7.347179E-01	9.210309E-01	-1.148106E+01	-3.492601E-02	-7.894343E-01
25.0	-1.029667E+01	-2.245128E+00	-5.385337E-02	3.299252E-02	-1.038491E-02	5.669184E-01	5.603081E-01	8.914573E-01	-4.683570E+00	-5.378253E-02	-6.083024E-01
27.5	-5.199053E+00	-3.204389E+00	-3.549757E-02	-1.252711E-01	-8.275737E-02	4.413071E-01	4.378848E-01	8.770103E-01	7.255689E-01	-4.726804E-02	-4.277670E-01
30.0	-1.362216E+00	-4.274876E+00	-1.178357E-02	-2.248160E-01	-1.214032E-01	3.509375E-01	3.499598E-01	8.667100E-01	4.794435E+00	-2.806493E-02	-2.559162E-01
32.5	1.288534E+00	-5.439217E+00	1.048490E-02	-2.811187E-01	-1.376994E-01	2.841282E-01	2.849741E-01	8.538916E-01	7.602674E+00	-4.148429E-03	-9.729195E-02
35.0	2.847153E+00	-6.682317E+00	2.713029E-02	-3.050311E-01	-1.393559E-01	2.329490E-01	2.350913E-01	8.345026E-01	9.250369E+00	1.939427E-02	4.565828E-02
37.5	3.418812E+00	-7.991084E+00	3.561363E-02	-3.043487E-01	-1.317032E-01	1.919054E-01	1.948905E-01	8.061150E-01	9.849490E+00	3.930169E-02	1.717507E-01
40.0	3.113795E+00	-9.354161E+00	3.444033E-02	-2.847876E-01	-1.184853E-01	1.571292E-01	1.605627E-01	7.673331E-01	9.517402E+00	5.349438E-02	2.805739E-01
42.5	2.042955E+00	-1.076167E+01	2.279198E-02	-2.506132E-01	-1.023631E-01	1.258631E-01	1.293988E-01	7.174262E-01	8.372042E+00	6.067273E-02	3.721903E-01
45.0	3.144113E-01	-1.220503E+01	2.923915E-04	-2.050569E-01	-8.524365E-02	9.612480E-02	9.945635E-02	6.560960E-01	6.528403E+00	6.005911E-02	4.469510E-01
47.5	-1.968781E+00	-1.367672E+01	-3.314411E-02	-1.505994E-01	-6.850028E-02	6.648066E-02	6.933503E-02	5.833268E-01	4.096075E+00	5.122888E-02	5.053782E-01
50.0	-4.710180E+00	-1.517019E+01	-7.741271E-02	-8.916656E-02	-5.312321E-02	3.589206E-02	3.802448E-02	4.992855E-01	1.177587E+00	3.399755E-02	5.480909E-01

Table 1.4. Continued

x	Doyle-1	Agherghinei I	Agherghinei II	Starink I	Starink II	MKN I	MKN II	MKN III	LCSS	TLZW	Cai-Liu
52.5	-7.820925E+00	-1.667969E+01	-1.322850E-01	-2.226905E-02	-3.982409E-02	3.607825E-03	4.797678E-03	4.042565E-01	-2.132607E+00	8.344318E-03	5.757569E-01
55.0	-1.122023E+01	-1.820019E+01	-1.974543E-01	4.889805E-02	-2.911011E-02	-3.091174E-02	-3.086424E-02	2.985968E-01	-5.748661E+00	-2.564050E-02	5.890617E-01
57.5	-1.483557E+01	-1.972725E+01	-2.725662E-01	1.233819E-01	-2.133701E-02	-6.804940E-02	-6.932591E-02	1.827065E-01	-9.593500E+00	-6.779192E-02	5.886889E-01
60.0	-1.860252E+01	-2.125698E+01	-3.572397E-01	2.004178E-01	-1.674768E-02	-1.080706E-01	-1.108370E-01	5.700743E-02	-1.359872E+01	-1.178958E-01	5.753073E-01
62.5	-2.246457E+01	-2.278597E+01	-4.510819E-01	2.793883E-01	-1.550039E-02	-1.511528E-01	-1.555608E-01	-7.806980E-02	-1.770427E+01	-1.757070E-01	5.495642E-01
65.0	-2.637263E+01	-2.431119E+01	-5.536971E-01	3.597925E-01	-1.768983E-02	-1.974067E-01	-2.035959E-01	-2.220957E-01	-2.185804E+01	-2.409617E-01	5.120798E-01
67.5	-3.028458E+01	-2.582999E+01	-6.646944E-01	4.412222E-01	-2.336276E-02	-2.468930E-01	-2.549917E-01	-3.746482E-01	-2.601534E+01	-3.133868E-01	4.634459E-01
70.0	-3.416473E+01	-2.734005E+01	-7.836914E-01	5.233438E-01	-3.252985E-02	-2.996342E-01	-3.097611E-01	-5.353165E-01	-3.013827E+01	-3.927059E-01	4.042246E-01
72.5	-3.798325E+01	-2.883932E+01	-9.103173E-01	6.058836E-01	-4.517462E-02	-3.556240E-01	-3.678888E-01	-7.037036E-01	-3.419520E+01	-4.786442E-01	3.349481E-01
75.0	-4.171559E+01	-3.032601E+01	-1.044215E+00	6.886167E-01	-6.126033E-02	-4.148347E-01	-4.293391E-01	-8.794282E-01	-3.816010E+01	-5.709309E-01	2.561201E-01
77.5	-4.534197E+01	-3.179854E+01	-1.185040E+00	7.713581E-01	-8.073520E-02	-4.772222E-01	-4.940605E-01	-1.062125E+00	-4.201198E+01	-6.693022E-01	1.682161E-01
80.0	-4.884678E+01	-3.325555E+01	-1.332466E+00	8.539556E-01	-1.035364E-01	-5.427305E-01	-5.619906E-01	-1.251446E+00	-4.573434E+01	-7.735017E-01	7.168499E-02
82.5	-5.221814E+01	-3.469584E+01	-1.486179E+00	9.362837E-01	-1.295933E-01	-6.112949E-01	-6.330586E-01	-1.447059E+00	-4.931457E+01	-8.832822E-01	-3.304953E-02
85.0	-5.544738E+01	-3.611838E+01	-1.645879E+00	1.018239E+00	-1.588298E-01	-6.828445E-01	-7.071880E-01	-1.648646E+00	-5.274354E+01	-9.984055E-01	-1.455878E-01
87.5	-5.852864E+01	-3.752228E+01	-1.811283E+00	1.099738E+00	-1.911659E-01	-7.573041E-01	-7.842987E-01	-1.855909E+00	-5.601505E+01	-1.118643E+00	-2.655524E-01
90.0	-6.145845E+01	-3.890679E+01	-1.982120E+00	1.180710E+00	-2.265198E-01	-8.345959E-01	-8.643082E-01	-2.068561E+00	-5.912546E+01	-1.243775E+00	-3.925874E-01
92.5	-6.423538E+01	-4.027125E+01	-2.158132E+00	1.261100E+00	-2.648085E-01	-9.146407E-01	-9.471329E-01	-2.286332E+00	-6.207330E+01	-1.373593E+00	-5.263562E-01
95.0	-6.685971E+01	-4.161512E+01	-2.339076E+00	1.340862E+00	-3.059487E-01	-9.973585E-01	-1.032689E+00	-2.508963E+00	-6.485888E+01	-1.507896E+00	-6.665412E-01
97.5	-6.933316E+01	-4.293796E+01	-2.524718E+00	1.419959E+00	-3.498577E-01	-1.082669E+00	-1.120893E+00	-2.736210E+00	-6.748406E+01	-1.646491E+00	-8.128417E-01
100.0	-7.165857E+01	-4.423940E+01	-2.714837E+00	1.498362E+00	-3.964536E-01	-1.170494E+00	-1.211662E+00	-2.967842E+00	-6.995192E+01	-1.789197E+00	-9.649734E-01

Table 1.5. Ranges of *x* that guarantee relative deviations of the exponential – type approximations lower than the indicated values

Author	Name of approximation	Ranges of *x*			
		$|\varepsilon_1|\leq5\%$	$|\varepsilon_1|\leq1\%$	$|\varepsilon_1|\leq0.2\%$	$|\varepsilon_1|\leq0.1\%$
Dolye [5]	Doyle-1	(27.6124, 50.2449)	(30.2864, 32.1662); (44.108, 46.505)	---	---
Liu et al. [6]	LCSS	(24.871, 30.1518); (46.6327, 54.4967)	(26.6307, 27.6463); (50.1414, 51.6732)	---	---
Tang et al. [7]	TLZW	(6.87272, 146.353)	(12.5308, 85.0339)	(17.2116, 63.4639)	(18.5745, 59.1508)
Agherghinei [8]	Agherghinei 1	(2.45727, 31.5782)	(4.01806, 21.0296)	(5.03129, 17.2101)	(5.26357, 6.03834); (8.54379, 11.3665); (14.2142, 16.4899)
Agherghinei [8]	Agherghinei 2	(6.43908, 126.972)	(11.6432, 74.1889)	(15.9089, 55.0904)	(17.1414, 51.0877)
Madhusudanan et al. [9]	MKN 1	(9.38527, 181.374)	(20.0351, 95.0786)	(36.9682, 65.1352)	(44.6716, 59.5106)
Madhusudanan et al. [10]	MKN 2	(9.31836, 178.678)	(19.9062, 94.054)	(37.1561, 64.8187)	(44.9544, 59.3654)
Madhusudanan et al. [10]	MKN 3	(7.25475, 120.436)	(19.5784, 76.6602)	(57.1402, 64.6261)	(59.1661, 62.8907)
Starink [11]	Starink 1	(10.1399, 248.698)	(18.1385, 84.4425)	(23.1584, 29.2475); (45.2488, 59.9866)	(24.1941, 27.0197); (49.5763, 56.7254)
Starink [11]	Starink 2	(8.40998, 227.871)	(15.6342, 125.234)	(21.2697, 88.1449)	(22.7107, 28.4081); (42.8486, 79.6347)
Cai and Liu [12]	CL	(4.8281, 151.079)	(7.37514, 12.5984); (19.2688, 100.563)	(8.47822, 9.27041); (30.8553, 38.1122); (76.6246, 86.1527)	(8.65521, 9.04911); (32.4552, 36.0361); (79.2888, 84.0075)

Table 1.6. The relative error percentages of the rational fraction – type approximations for the estimation of the temperature integral

x	Agrawal-Sivasubramanian	Balarin	Cai-1	Cai-2	Cai-3	Cai-He	Cai-Liu	Chen-Liu
5	1.42734E+00	7.99301E-01	1.86918E-01	1.48265E-03	-2.07167E-03	1.39575E-01	-1.67456E-04	1.20754E-02
7.5	4.59150E-03	3.39416E-01	-2.16479E-02	-6.87515E-04	5.92643E-03	-2.54158E-03	-2.78892E-05	-3.73962E-03
10	-1.85066E-01	1.76331E-01	-4.67740E-02	-2.43569E-04	1.05922E-03	-1.17731E-02	-4.36013E-05	-3.58464E-03
12.5	-1.97778E-01	1.03512E-01	-4.05504E-02	1.69500E-04	-1.48443E-03	-3.55569E-03	1.47042E-05	-2.45771E-03
15	-1.77216E-01	6.60087E-02	-2.98341E-02	3.31557E-04	-2.36737E-03	4.72940E-03	4.31157E-05	-1.63249E-03
17.5	-1.52551E-01	4.46983E-02	-2.01262E-02	3.33177E-04	-2.46623E-03	1.06275E-02	4.15188E-05	-1.10119E-03
20	-1.30333E-01	3.16824E-02	-1.23256E-02	2.58371E-04	-2.23486E-03	1.43376E-02	2.55271E-05	-7.61720E-04
22.5	-1.11668E-01	2.32790E-02	-6.27882E-03	1.56862E-04	-1.88507E-03	1.64248E-02	6.27150E-06	-5.40695E-04
25	-9.62894E-02	1.76092E-02	-1.64196E-03	5.43706E-05	-1.51244E-03	1.73791E-02	-1.05685E-05	-3.93147E-04
27.5	-8.36476E-02	1.36442E-02	1.90707E-03	-3.71295E-05	-1.15824E-03	1.75612E-02	-2.28013E-05	-2.92128E-04
30	-7.32118E-02	1.07875E-02	4.62669E-03	-1.13003E-04	-8.38352E-04	1.72238E-02	-3.00899E-05	-2.21305E-04
32.5	-6.45380E-02	8.67682E-03	6.71426E-03	-1.72348E-04	-5.56935E-04	1.65415E-02	-3.29589E-05	-1.70564E-04
35	-5.72726E-02	7.08346E-03	8.31814E-03	-2.16054E-04	-3.12881E-04	1.56345E-02	-3.22555E-05	-1.33492E-04
37.5	-5.11389E-02	5.85797E-03	9.54960E-03	-2.45774E-04	-1.02925E-04	1.45858E-02	-2.88802E-05	-1.05924E-04
40	-4.59208E-02	4.89992E-03	1.04924E-02	-2.63389E-04	7.68741E-05	1.34528E-02	-2.36620E-05	-8.50939E-05
42.5	-4.14493E-02	4.14010E-03	1.12099E-02	-2.70753E-04	2.30449E-04	1.22754E-02	-1.73116E-05	-6.91258E-05
45	-3.75913E-02	3.52973E-03	1.17506E-02	-2.69569E-04	3.61429E-04	1.10812E-02	-1.04122E-05	-5.67239E-05
47.5	-3.42415E-02	3.03377E-03	1.21515E-02	-2.61342E-04	4.73036E-04	9.88905E-03	-3.42688E-06	-4.69763E-05
50	-3.13156E-02	2.62661E-03	1.24417E-02	-2.47376E-04	5.68068E-04	8.71213E-03	3.28565E-06	-3.92313E-05
52.5	-2.87459E-02	2.28922E-03	1.26434E-02	-2.28783E-04	6.48926E-04	7.55916E-03	9.45475E-06	-3.30159E-05
55	-2.64775E-02	2.00726E-03	1.27745E-02	-2.06502E-04	7.17659E-04	6.43589E-03	1.48819E-05	-2.79821E-05
57.5	-2.44654E-02	1.76980E-03	1.28490E-02	-1.81322E-04	7.76009E-04	5.34592E-03	1.94266E-05	-2.38708E-05
60	-2.26727E-02	1.56838E-03	1.28779E-02	-1.53902E-04	8.25452E-04	4.29132E-03	2.29945E-05	-2.04866E-05
62.5	-2.10690E-02	1.39642E-03	1.28701E-02	-1.24791E-04	8.67244E-04	3.27305E-03	2.55275E-05	-1.76808E-05
65	-1.96287E-02	1.24871E-03	1.28329E-02	-9.44438E-05	9.02451E-04	2.29132E-03	2.69957E-05	-1.53388E-05
67.5	-1.83305E-02	1.12114E-03	1.27721E-02	-6.32384E-05	9.31981E-04	1.34580E-03	2.73907E-05	-1.33716E-05
70	-1.71564E-02	1.01037E-03	1.26923E-02	-3.14857E-05	9.56607E-04	4.35761E-04	2.67207E-05	-1.17097E-05

Table 1.6. Continued

x	Agrawal-Sivasubramanian	Balarin	Cai-1	Cai-2	Cai-3	Cai-He	Cai-Liu	Chen-Liu
72.5	-1.60911E-02	9.13736E-04	1.25973E-02	5.57935E-07	9.76992E-04	-4.39746E-04	2.50060E-05	-1.02979E-05
75	-1.51217E-02	8.29046E-04	1.24903E-02	3.26822E-05	9.93702E-04	-1.28186E-03	2.22761E-05	-9.09250E-06
77.5	-1.42370E-02	7.54510E-04	1.23740E-02	6.47153E-05	1.00722E-03	-2.09180E-03	1.85668E-05	-8.05828E-06
80	-1.34275E-02	6.88650E-04	1.22502E-02	9.65174E-05	1.01797E-03	-2.87085E-03	1.39183E-05	-7.16691E-06
82.5	-1.26849E-02	6.30240E-04	1.21209E-02	1.27976E-04	1.02631E-03	-3.62031E-03	8.37355E-06	-6.39538E-06
85	-1.20021E-02	5.78256E-04	1.19875E-02	1.58999E-04	1.03254E-03	-4.34148E-03	1.97723E-06	-5.72488E-06
87.5	-1.13729E-02	5.31836E-04	1.18511E-02	1.89516E-04	1.03695E-03	-5.03564E-03	-5.22539E-06	-5.13994E-06
90	-1.07917E-02	4.90257E-04	1.17126E-02	2.19470E-04	1.03977E-03	-5.70401E-03	-1.31891E-05	-4.62780E-06
92.5	-1.02539E-02	4.52902E-04	1.15730E-02	2.48818E-04	1.04119E-03	-6.34781E-03	-2.18693E-05	-4.17786E-06
95	-9.75518E-03	4.19248E-04	1.14329E-02	2.77527E-04	1.04139E-03	-6.96819E-03	-3.12223E-05	-3.78128E-06
97.5	-9.29193E-03	3.88849E-04	1.12928E-02	3.05574E-04	1.04054E-03	-7.56625E-03	-4.12058E-05	-3.43064E-06
100	-8.86086E-03	3.61320E-04	1.11531E-02	3.32942E-04	1.03876E-03	-8.14305E-03	-5.17788E-05	-3.11969E-06

x	Coats-Redfern	Doyle-2	Gorbachev-Lee-Beck	Ji-1	Ji-2	Ji-3	Li	Órfão-1
5	-1.88581E+01	3.52365E+01	-3.40253E+00	7.98706E-04	3.38512E-05	-1.81324E-05	6.76562E+00	2.78497E-02
7.5	-8.88471E+00	2.42481E+01	-1.90937E+00	-1.68672E-04	-1.61899E-06	-1.88621E-05	1.99473E+00	3.30000E-02
10	-5.17581E+00	1.85302E+01	-1.22481E+00	1.35871E-04	2.89195E-05	-1.83320E-05	8.76795E-01	1.45537E-02
12.5	-3.39145E+00	1.50102E+01	-8.53293E-01	1.49710E-04	4.14740E-05	-1.69209E-05	4.66463E-01	-1.13330E-02
15	-2.39550E+00	1.26206E+01	-6.28903E-01	8.02862E-05	3.23028E-05	-1.48804E-05	2.78596E-01	-3.80986E-02
17.5	-1.78271E+00	1.08905E+01	-4.82898E-01	1.26835E-05	1.80294E-05	-1.31173E-05	1.79997E-01	-6.33712E-02
20	-1.37870E+00	9.57922E+00	-3.82529E-01	-3.46614E-05	6.61459E-06	-1.18000E-05	1.23143E-01	-8.64236E-02
22.5	-1.09822E+00	8.55073E+00	-3.10550E-01	-6.27589E-05	-5.57798E-08	-1.08402E-05	8.80084E-02	-1.07167E-01
25	-8.95519E-01	7.72226E+00	-2.57165E-01	-7.65508E-05	-2.54027E-06	-1.01206E-05	6.51059E-02	-1.25749E-01
27.5	-7.44252E-01	7.04051E+00	-2.16471E-01	-8.06707E-05	-2.03883E-06	-9.55169E-06	4.95298E-02	-1.42393E-01
30	-6.28361E-01	6.46961E+00	-1.84737E-01	-7.86091E-05	2.99871E-07	-9.07561E-06	3.85631E-02	-1.57331E-01
32.5	-5.37605E-01	5.98452E+00	-1.59511E-01	-7.27948E-05	3.57852E-06	-8.65731E-06	3.06160E-02	-1.70778E-01
35	-4.65202E-01	5.56721E+00	-1.39126E-01	-6.48555E-05	7.16356E-06	-8.27651E-06	2.47148E-02	-1.82926E-01
37.5	-4.06513E-01	5.20439E+00	-1.22416E-01	-5.58571E-05	1.06389E-05	-7.92176E-06	2.02404E-02	-1.93940E-01

Table 1.6. Continued

x	Coats-Redfern	Doyle-2	Gorbachev-Lee-Beck	Ji-1	Ji-2	Ji-3	Li	Órfão-1
40	-3.58277E-01	4.88602E+00	-1.08549E-01	-4.64843E-05	1.37505E-05	-7.58678E-06	1.67857E-02	-2.03963E-01
42.5	-3.18151E-01	4.60441E+00	-9.69125E-02	-3.71672E-05	1.63586E-05	-7.26819E-06	1.40755E-02	-2.13116E-01
45	-2.84412E-01	4.35352E+00	-8.70532E-02	-2.81675E-05	1.84007E-05	-6.96417E-06	1.19195E-02	-2.21503E-01
47.5	-2.55772E-01	4.12859E+00	-7.86264E-02	-1.96362E-05	1.98643E-05	-6.67374E-06	1.01828E-02	-2.29213E-01
50	-2.31253E-01	3.92578E+00	-7.13672E-02	-1.16521E-05	2.07686E-05	-6.39634E-06	8.76803E-03	-2.36323E-01
52.5	-2.10100E-01	3.74198E+00	-6.50694E-02	-4.24748E-06	2.11511E-05	-6.13155E-06	7.60394E-03	-2.42898E-01
55	-1.91723E-01	3.57463E+00	-5.95703E-02	2.57507E-06	2.10587E-05	-5.87904E-06	6.63730E-03	-2.48994E-01
57.5	-1.75657E-01	3.42162E+00	-5.47404E-02	8.83110E-06	2.05428E-05	-5.63844E-06	5.82794E-03	-2.54663E-01
60	-1.61530E-01	3.28118E+00	-5.04751E-02	1.45470E-05	1.96549E-05	-5.40940E-06	5.14510E-03	-2.59945E-01
62.5	-1.49042E-01	3.15182E+00	-4.66899E-02	1.97551E-05	1.84446E-05	-5.19151E-06	4.56497E-03	-2.64879E-01
65	-1.37949E-01	3.03228E+00	-4.33151E-02	2.44903E-05	1.69587E-05	-4.98436E-06	4.06894E-03	-2.69498E-01
67.5	-1.28050E-01	2.92148E+00	-4.02936E-02	2.87882E-05	1.52398E-05	-4.78748E-06	3.64229E-03	-2.73830E-01
70	-1.19180E-01	2.81849E+00	-3.75777E-02	3.26836E-05	1.33268E-05	-4.60042E-06	3.27330E-03	-2.77901E-01
72.5	-1.11201E-01	2.72252E+00	-3.51275E-02	3.62098E-05	1.12542E-05	-4.42272E-06	2.95254E-03	-2.81734E-01
75	-1.03997E-01	2.63288E+00	-3.29094E-02	3.93985E-05	9.05294E-06	-4.25391E-06	2.67238E-03	-2.85348E-01
77.5	-9.74718E-02	2.54895E+00	-3.08951E-02	4.22788E-05	6.75009E-06	-4.09354E-06	2.42659E-03	-2.88763E-01
80	-9.15420E-02	2.47021E+00	-2.90602E-02	4.48780E-05	4.36945E-06	-3.94117E-06	2.21006E-03	-2.91993E-01
82.5	-8.61375E-02	2.39619E+00	-2.73841E-02	4.72208E-05	1.93176E-06	-3.79636E-06	2.01855E-03	-2.95053E-01
85	-8.11980E-02	2.32648E+00	-2.58490E-02	4.93303E-05	-5.45013E-07	-3.65871E-06	1.84855E-03	-2.97956E-01
87.5	-7.66716E-02	2.26072E+00	-2.44394E-02	5.12271E-05	-3.04532E-06	-3.52781E-06	1.69712E-03	-3.00715E-01
90	-7.25134E-02	2.19857E+00	-2.31421E-02	5.29304E-05	-5.55579E-06	-3.40329E-06	1.56180E-03	-3.03338E-01
92.5	-6.86847E-02	2.13974E+00	-2.19455E-02	5.44573E-05	-8.06500E-06	-3.28479E-06	1.44050E-03	-3.05837E-01
95	-6.51514E-02	2.08399E+00	-2.08393E-02	5.58237E-05	-1.05632E-05	-3.17198E-06	1.33144E-03	-3.08219E-01
97.5	-6.18840E-02	2.03106E+00	-1.98148E-02	5.70436E-05	-1.30421E-05	-3.06453E-06	1.23313E-03	-3.10492E-01
100	-5.88564E-02	1.98076E+00	-1.88640E-02	5.81302E-05	-1.54948E-05	-2.96212E-06	1.14426E-03	-3.12665E-01

Table 1.6. Continued

x	Órfão-2	Quanyin-Su-1	Quanyin-Su-2	Senum-Yang-1	Senum-Yang-2	Senum-Yang-3	Urbanovici-Segal-1	Urbanovici-Segal-2
5	-2.20314E-02	2.45186E+00	-5.61431E-01	-2.35403E-01	-2.39250E-02	-3.13231E-03	-8.26600E-01	-4.26209E-02
7.5	-1.90086E-03	3.96382E-01	-7.69887E-01	-8.01761E-02	-5.21312E-03	-4.53868E-04	-2.41357E-01	4.59150E-03
10	4.18783E-05	2.55137E-02	-6.03578E-01	-3.47426E-02	-1.58300E-03	-9.93078E-05	-9.59459E-02	9.88471E-03
12.5	8.72173E-05	-6.56334E-02	-4.61022E-01	-1.74940E-02	-5.91994E-04	-2.81749E-05	-4.56984E-02	8.85185E-03
15	3.62320E-05	-8.63852E-02	-3.58382E-01	-9.76798E-03	-2.55747E-04	-9.57740E-06	-2.45403E-02	7.07248E-03
17.5	5.32920E-05	-8.62177E-02	-2.84952E-01	-5.88347E-03	-1.22886E-04	-3.72182E-06	-1.43597E-02	5.52976E-03
20	1.10532E-04	-7.97406E-02	-2.31365E-01	-3.75562E-03	-6.40864E-05	-1.60394E-06	-8.96376E-03	4.33469E-03
22.5	1.76715E-04	-7.17969E-02	-1.91316E-01	-2.51014E-03	-3.56711E-05	-7.50686E-07	-5.88545E-03	3.43236E-03
25	2.34967E-04	-6.40520E-02	-1.60702E-01	-1.74153E-03	-2.09376E-05	-3.75867E-07	-4.02449E-03	2.75126E-03
27.5	2.78458E-04	-5.70405E-02	-1.36819E-01	-1.24625E-03	-1.28443E-05	-1.99086E-07	-2.84540E-03	2.23273E-03
30	3.05691E-04	-5.08768E-02	-1.17852E-01	-9.15381E-04	-8.17891E-06	-1.10596E-07	-2.06877E-03	1.83336E-03
32.5	3.17657E-04	-4.55217E-02	-1.02549E-01	-6.87503E-04	-5.37726E-06	-6.40036E-08	-1.54026E-03	1.52194E-03
35	3.16320E-04	-4.08859E-02	-9.00300E-02	-5.26394E-04	-3.63457E-06	-3.83800E-08	-1.17043E-03	1.27613E-03
37.5	3.03877E-04	-3.68712E-02	-7.96621E-02	-4.09873E-04	-2.51692E-06	-2.37429E-08	-9.05347E-04	1.07985E-03
40	2.82420E-04	-3.33858E-02	-7.09814E-02	-3.23909E-04	-1.78063E-06	-1.50971E-08	-7.11304E-04	9.21417E-04
42.5	2.53804E-04	-3.03493E-02	-6.36420E-02	-2.59362E-04	-1.28391E-06	-9.83754E-09	-5.66615E-04	7.92243E-04
45	2.19611E-04	-2.76931E-02	-5.73820E-02	-2.10132E-04	-9.41657E-07	-6.55393E-09	-4.56943E-04	6.85943E-04
47.5	1.81156E-04	-2.53598E-02	-5.20002E-02	-1.72056E-04	-7.01302E-07	-4.45101E-09	-3.72586E-04	5.97714E-04
50	1.39523E-04	-2.33015E-02	-4.73401E-02	-1.42231E-04	-5.29599E-07	-3.08079E-09	-3.06840E-04	5.23902E-04
52.5	9.55911E-05	-2.14781E-02	-4.32785E-02	-1.18601E-04	-4.05013E-07	-2.16546E-09	-2.54986E-04	4.61697E-04
55	5.00714E-05	-1.98563E-02	-3.97172E-02	-9.96834E-05	-3.13329E-07	-1.54661E-09	-2.13643E-04	4.08918E-04
57.5	3.53547E-06	-1.84082E-02	-3.65776E-02	-8.43933E-05	-2.44977E-07	-1.11883E-09	-1.80354E-04	3.63853E-04
60	-4.35598E-05	-1.71104E-02	-3.37955E-02	-7.19269E-05	-1.93408E-07	-8.18411E-10	-1.53307E-04	3.25150E-04
62.5	-9.08507E-05	-1.59433E-02	-3.13189E-02	-6.16806E-05	-1.54074E-07	-6.05235E-10	-1.31147E-04	2.91729E-04
65	-1.38049E-04	-1.48901E-02	-2.91046E-02	-5.31963E-05	-1.23771E-07	-4.57487E-10	-1.12853E-04	2.62722E-04
67.5	-1.84929E-04	-1.39367E-02	-2.71169E-02	-4.61225E-05	-1.00197E-07	-3.45528E-10	-9.76407E-05	2.37426E-04
70	-2.31313E-04	-1.30711E-02	-2.53259E-02	-4.01867E-05	-8.16994E-08	-2.63473E-10	-8.49087E-05	2.15267E-04

Table 1.6. Continued

x	Órfão-2	Quanyin-Su-1	Quanyin-Su-2	Senum-Yang-1	Senum-Yang-2	Senum-Yang-3	Urbanovici-Segal-1	Urbanovici-Segal-2
72.5	-2.77065E-04	-1.22830E-02	-2.37065E-02	-3.51761E-05	-6.70681E-08	-2.03616E-10	-7.41867E-05	1.95776E-04
75	-3.22081E-04	-1.15634E-02	-2.22375E-02	-3.09229E-05	-5.54040E-08	-1.57655E-10	-6.51055E-05	1.78564E-04
77.5	-3.66282E-04	-1.09047E-02	-2.09009E-02	-2.72937E-05	-4.60412E-08	-1.24270E-10	-5.73727E-05	1.63307E-04
80	-4.09613E-04	-1.03004E-02	-1.96812E-02	-2.41818E-05	-3.84744E-08	-9.94646E-11	-5.07549E-05	1.49737E-04
82.5	-4.52033E-04	-9.74458E-03	-1.85651E-02	-2.15011E-05	-3.23165E-08	-7.68608E-11	-4.50647E-05	1.37627E-04
85	-4.93516E-04	-9.23230E-03	-1.75413E-02	-1.91819E-05	-2.72814E-08	-6.25283E-11	-4.01503E-05	1.26787E-04
87.5	-5.34049E-04	-8.75914E-03	-1.65999E-02	-1.71673E-05	-2.31350E-08	-4.78425E-11	-3.58880E-05	1.17054E-04
90	-5.73624E-04	-8.32124E-03	-1.57322E-02	-1.54103E-05	-1.97079E-08	-3.88385E-11	-3.21767E-05	1.08291E-04
92.5	-6.12243E-04	-7.91521E-03	-1.49308E-02	-1.38725E-05	-1.68567E-08	-2.95742E-11	-2.89332E-05	1.00380E-04
95	-6.49912E-04	-7.53805E-03	-1.41891E-02	-1.25219E-05	-1.44782E-08	-2.52966E-11	-2.60883E-05	9.32201E-05
97.5	-6.86642E-04	-7.18710E-03	-1.35013E-02	-1.13318E-05	-1.24858E-08	-2.53401E-11	-2.35847E-05	8.67246E-05
100	-7.22448E-04	-6.85999E-03	-1.28623E-02	-1.02798E-05	-1.07994E-08	-1.80815E-11	-2.13744E-05	8.08181E-05
x	Urbanovici-Segal-3	van Tets	Wanjun-1	Wanjun-2	Zsakó			
5	2.98495E-02	1.42734E+00	-1.77275E+00	-1.77480E+00	2.00170E-01			
7.5	3.56822E-03	5.81819E-01	-7.47894E-01	-7.49711E-01	2.61299E-02			
10	1.77465E-04	2.94813E-01	-3.42841E-01	-3.44515E-01	-1.14972E-01			
12.5	-2.42276E-04	1.70156E-01	-1.56262E-01	-1.57841E-01	-1.81717E-01			
15	-2.05192E-04	1.07180E-01	-6.30494E-02	-6.45612E-02	-2.01385E-01			
17.5	-1.20484E-04	7.19014E-02	-1.48458E-02	-1.63072E-02	-1.97972E-01			
20	-5.44417E-05	5.05902E-02	9.83486E-03	8.41270E-03	-1.84876E-01			
22.5	-1.10028E-05	3.69512E-02	2.15195E-02	2.01286E-02	-1.68639E-01			
25	1.57121E-05	2.78146E-02	2.57506E-02	2.43852E-02	-1.52235E-01			
27.5	3.13584E-05	2.14630E-02	2.56096E-02	2.42655E-02	-1.36906E-01			
30	3.99574E-05	1.69098E-02	2.28835E-02	2.15572E-02	-1.23085E-01			
32.5	4.41461E-05	1.35602E-02	1.86420E-02	1.73311E-02	-1.10834E-01			
35	4.56080E-05	1.10409E-02	1.35417E-02	1.22441E-02	-1.00059E-01			

Table 1.6. Continued

x	Urbanovici-Segal-3	van Tets	Wanjun-1	Wanjun-2	Zsakó			
37.5	4.54094E-05	9.10965E-03	7.99218E-03	6.70619E-03	-9.06104E-02			
40	4.42246E-05	7.60418E-03	2.25197E-03	9.76212E-04	-8.23236E-02			
42.5	4.24802E-05	6.41327E-03	-3.51539E-03	-4.78206E-03	-7.50443E-02			
45	4.04454E-05	5.45879E-03	-9.20692E-03	-1.04655E-02	-6.86337E-02			
47.5	3.82896E-05	4.68483E-03	-1.47589E-02	-1.60101E-02	-6.29710E-02			
50	3.61178E-05	4.05064E-03	-2.01332E-02	-2.13779E-02	-5.79522E-02			
52.5	3.39940E-05	3.52600E-03	-2.53089E-02	-2.65475E-02	-5.34888E-02			
55	3.19556E-05	3.08824E-03	-3.02758E-02	-3.15090E-02	-4.95058E-02			
57.5	3.00229E-05	2.72009E-03	-3.50315E-02	-3.62597E-02	-4.59394E-02			
60	2.82054E-05	2.40823E-03	-3.95781E-02	-4.08016E-02	-4.27355E-02			
62.5	2.65054E-05	2.14230E-03	-4.39209E-02	-4.51402E-02	-3.98481E-02			
65	2.49211E-05	1.91414E-03	-4.80670E-02	-4.92823E-02	-3.72380E-02			
67.5	2.34481E-05	1.71728E-03	-5.20247E-02	-5.32364E-02	-3.48716E-02			
70	2.20807E-05	1.54653E-03	-5.58028E-02	-5.70111E-02	-3.27202E-02			
72.5	2.08121E-05	1.39769E-03	-5.94103E-02	-6.06154E-02	-3.07590E-02			
75	1.96356E-05	1.26736E-03	-6.28561E-02	-6.40583E-02	-2.89665E-02			
77.5	1.85443E-05	1.15274E-03	-6.61491E-02	-6.73485E-02	-2.73244E-02			
80	1.75318E-05	1.05155E-03	-6.92976E-02	-7.04944E-02	-2.58164E-02			
82.5	1.65918E-05	9.61864E-04	-7.23097E-02	-7.35040E-02	-2.44285E-02			
85	1.57185E-05	8.82098E-04	-7.51931E-02	-7.63850E-02	-2.31485E-02			
87.5	1.49066E-05	8.10915E-04	-7.79549E-02	-7.91447E-02	-2.19657E-02			
90	1.41510E-05	7.47192E-04	-8.06021E-02	-8.17898E-02	-2.08704E-02			
92.5	1.34471E-05	6.89975E-04	-8.31410E-02	-8.43267E-02	-1.98544E-02			
95	1.27907E-05	6.38456E-04	-8.55776E-02	-8.67615E-02	-1.89103E-02			
97.5	1.21781E-05	5.91942E-04	-8.79176E-02	-8.90997E-02	-1.80314E-02			
100	1.16057E-05	5.49840E-04	-9.01663E-02	-9.13467E-02	-1.72120E-02			

The relative deviations of the rational fraction – type approximations are calculated on the basis of the following expression:

$$\varepsilon_2(\%) = \frac{\dfrac{RT^2}{E}e^{-E/RT}h(x) - \displaystyle\int_0^T e^{-E/RT}dT}{\displaystyle\int_0^T e^{-E/RT}dT}\cdot 100 = \frac{h(x) - x^2 e^x \displaystyle\int_x^\infty \dfrac{e^{-x}}{x^2}dx}{x^2 e^x \displaystyle\int_x^\infty \dfrac{e^{-x}}{x^2}dx}\cdot 100 \quad (0.10)$$

The relative error percentages of the rational fraction – type approximations for the estimation of the temperature integral are listed in Table 1.6.

Applications of the Temperature Integral Approximations

The applications of the temperature integral approximations are the estimation of the temperature integral and the determination of the activation energy[38].

The exponential – type approximations for the temperature integral are usually used in the linear integral isoconversional methods.

Inserting Equation (1.6) into Equation (1.5), one can get the following equation:

$$g(\alpha) = \frac{AE}{\beta R}e^{p_1 + p_2 \ln x + p_3 x} \quad (0.11)$$

From Equation (1.11), it follows

$$\frac{\beta}{T^{-p_2}} = \frac{A}{g(\alpha)}\left(\frac{E}{R}\right)^{p_2+1}e^{p_1 + p_3 x} \quad (0.12)$$

In general, the linear integral isoconversional methods are based on the above equation. These methods are based on Equation (1.11) in logarithmic form and leads to:

$$\ln\left(\frac{\beta_i}{T_{\alpha,i}^{-p_2}}\right) = \ln\left[\frac{A_\alpha}{g(\alpha)}\left(\frac{E_\alpha}{R}\right)^{p_2+1}\right] + p_1 + \frac{p_3 E_\alpha}{R}\frac{1}{T_{\alpha,i}} \quad (0.13)$$

where subscripts i and α designate a given value of heating rate and the degree of conversion, respectively. For α=constant, the plot $\ln\left(\dfrac{\beta_i}{T_{\alpha,i}^{-p_2}}\right)$ versus $\dfrac{1}{T_{\alpha,i}}$ should be a straight line whose slope can be used to evaluate the apparent activation energy.

The rational fraction – type approximations for the temperature integral are usually used in the model-fitting methods.

Substituting Equation (1.7) into Equation (1.5), one can obtain

$$g(\alpha) = \frac{A}{\beta} \frac{RT^2}{E} e^{-E/RT} h(x) \tag{0.14}$$

From Equation (1.14), it follows

$$\ln\left[\frac{g(\alpha)}{T^2 h(x)}\right] = \ln\left(\frac{AR}{\beta E}\right) - \frac{E}{RT} \tag{0.15}$$

When the exact mathematical form of the function $g(\alpha)$ is known, the value of the activation energy can be determined by the slope of the plot of $\ln\left[\dfrac{g(\alpha)}{T^2 h(x)}\right]$ versus $\dfrac{1}{T}$. In order to calculate the apparent activation energy, an iterative procedure must be implemented. In this method, for the first step, the value of $h(x)$ is regarded as unity, except for the first step, $h(x)$ is calculated based on the activation energy value obtained at the previous step.

Precision of Integral Methods

The integral methods are extensively used for the kinetic analysis of solid-state reactions. As the temperature integral does not have an exact analytical solution, different approximations have been proposed in the literature. A large number of approximated equations have been proposed with the objective of increasing the precision in the determination of the temperature integral, as checked from the standard deviation of the approximations with regard to the real exact value of the temperature integral.

However, the main application of these approximations for the temperature integral is the determination of the kinetic parameters, in particular the activation energy, and not the computation of the temperature integral.

Therefore, it would be interest to estimate the precision of such integral methods for the determination of the activation energy. The aim of this chapter is to perform a systematic analysis of the precision of integral methods for the determination of the activation energy.

The Precision of Integral Methods for the Determination of the Activation Energy

The integral form of the kinetic equation for solid-state reactions can be written as follows:

$$g(\alpha) = \frac{A}{\beta} \int_0^T e^{-E/RT} dT \tag{2.16}$$

where $g(\alpha)$ is the integral conversion function.

By introducing the variable $x=E/RT$, one can obtain

$$g(\alpha) = \frac{A}{\beta} \frac{RT^2}{E} e^{-E/RT} Q(x)$$ (2.17)

where

$$Q(x) = x^2 e^x \int_x^\infty \frac{e^{-x}}{x^2} dx$$ (2.18)

The $Q(x)$ function does not have an exact solution, and can be numerically calculated. The numerical values of the $Q(x)$ function as a function of the parameter x are shown in Figure 2.1. The numerical integration has been performed by means of the Mathematica software developed by Wolfram Research, Inc.
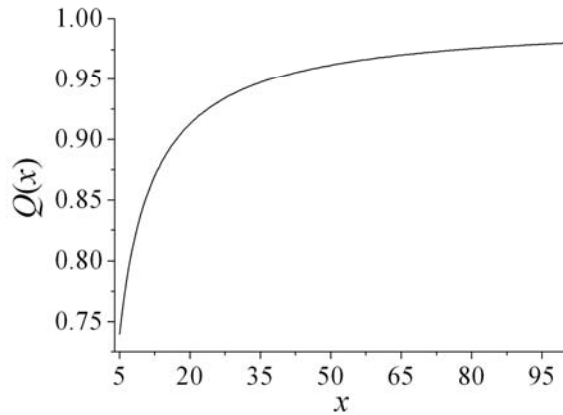
Figure 2.1. Numerical values of $Q(x)$ at various x.

If the integral methods were used for performing the kinetic analysis of solid-state reactions, the apparent activation energy, E_a, would satisfy the following equation:

$$g(\alpha) = \frac{A_a}{\beta} \frac{RT^2}{E_a} h(x_a) e^{-E_a/RT}$$ (2.19)

where the subscript a stands for the apparent values of the kinetic parameters obtained from the integral methods, $h(x)$ is the approximation for the $Q(x)$ function and $x_a=E_a/RT$.
From Equation (2.4), it follows:

$$\frac{d \ln[g(\alpha)/T^2]}{d(1/T)} = -\frac{E_a}{R}\left(1 - \frac{d \ln h(x_a)}{dx_a}\right)$$ (2.20)

The real value of the left hand side of Equation (2.5) as a function of the true activation energy, E, can be determined from Equations (2.2):

$$\frac{d \ln[g(\alpha)/T^2]}{d(1/T)} = -\frac{E}{R}\left(1 - \frac{d \ln Q(x)}{dx}\right) \tag{2.21}$$

We define the relative error of the apparent activation energy ε:

$$\varepsilon = \frac{E_a - E}{E} \tag{2.22}$$

From Equation (2.7), one can obtain

$$x_a = (\varepsilon + 1)x \tag{2.23}$$

From Equations (2.5), (2.6), (2.7) and (2.8), it follows:

$$(\varepsilon+1)\left(1 - \frac{d \ln h[(\varepsilon+1)x]}{d[(\varepsilon+1)x]}\right) = 1 - \frac{d \ln Q(x)}{dx} \tag{2.24}$$

Órfão simplified Equation (2.9) and obtained the following two equations[30]:

$$\varepsilon = \frac{d \ln h(x)}{dx} - \frac{d \ln Q(x)}{dx} \tag{2.25}$$

$$\varepsilon = (\varepsilon+1)\frac{d \ln h(x)}{dx} - \frac{d \ln Q(x)}{dx} \tag{2.26}$$

Equation (2.9) for the relative error of the apparent activation energy can't be solved by analytically solved. But for a certain x value, Equation (2.9) can be solved by some numerical technique. For this purpose, either general purposed mathematical software or a computer program developed in any programming language is used. In this chapter, the Mathematica software system has been used for the numerical calculation of Equation (2.9).

Among the existed integral methods, the most commonly used in the kinetic analysis of solid-state reactions is the integral method proposed by Coats and Redfern (here called the Coats and Redfern method)[15], although the method was proposed 50 years ago. In fact, for the original paper of Coats and Redfern, we have found about 2500 citations in the kinetic analysis of solid-state reactions (this information was obtained from the ISI web of Science database). Therefore, the precision of the Coats and Redfern method for the determination of the activation energy has been calculated and the obtained results have been given in Table 2.1.

From the results included in Table 2.1, it can be seen that the results calculated from Equation (2.9) significantly differ from the results from the other two equations presented in the paper of Órfão[30]. Therefore, the simplified Equations (2.10) and (2.11) are not proper to calculate the precision of integral methods.

**Table 2.1. The precision of the Coats and Redfern method for the determination
of the activation energy calculated from three different equations**

x	ε / %		
	Calculated by Equation (2.9)	**Calculated by Equation (2.10)**	**Calculated by Equation (2.11)**
3	26.45056	77.38702	232.16107
4	13.00869	31.82985	42.43980
5	7.15007	18.09688	20.88101
6	4.30325	11.85813	12.93614
7	2.78041	8.43406	8.94521
8	1.89837	6.33210	6.60741
9	1.35365	4.94125	5.10326
10	0.99939	3.96977	4.07156
11	0.75908	3.26275	3.33003
12	0.59029	2.73132	2.77761
13	0.46823	2.32127	2.35420
14	0.37775	1.99798	2.02205
15	0.30924	1.73840	1.75641
16	0.25640	1.52671	1.54046
17	0.21498	1.35174	1.36243
18	0.18205	1.20542	1.21385
19	0.15554	1.08178	1.08852
20	0.13395	0.97634	0.98179
21	0.11619	0.88568	0.89014
22	0.10144	0.80714	0.81083
23	0.089092	0.73866	0.74173
24	0.078675	0.67858	0.68116
25	0.069824	0.62556	0.62775
26	0.062255	0.57855	0.58041
27	0.055745	0.53667	0.53826
28	0.050113	0.49919	0.50057
29	0.045216	0.46552	0.46671
30	0.040938	0.43515	0.43619
31	0.037184	0.40767	0.40858
32	0.033876	0.38272	0.38351
33	0.030950	0.35999	0.36070
34	0.028351	0.33924	0.33986
35	0.026037	0.32024	0.32079
36	0.023967	0.30279	0.30328
37	0.022112	0.28673	0.28718
38	0.020443	0.27192	0.27232
39	0.018939	0.25823	0.25859
40	0.017579	0.24556	0.24588

Table 2.1. Continued

x	Calculated by Equation (2.9)	Calculated by Equation (2.10)	Calculated by Equation (2.11)
		ε / %	
41	0.016346	0.23379	0.23408
42	0.015225	0.22285	0.22312
43	0.014205	0.21266	0.21291
44	0.013275	0.20316	0.20338
45	0.012424	0.19428	0.19448
46	0.011644	0.18597	0.18616
47	0.010928	0.17819	0.17836
48	0.010270	0.17088	0.17104
49	0.0096631	0.16401	0.16416
50	0.0091035	0.15756	0.15769
51	0.0085864	0.15147	0.15159
52	0.0081077	0.14573	0.14584
53	0.0076640	0.14031	0.14042
54	0.0072521	0.13519	0.13529
55	0.0068692	0.13035	0.13044
56	0.0065128	0.12576	0.12584
57	0.0061807	0.12141	0.12148
58	0.0058708	0.11728	0.11735
59	0.0055813	0.11336	0.11342
60	0.0053105	0.10963	0.10969
61	0.0050570	0.10608	0.10614
62	0.0048193	0.10270	0.10276
63	0.0045963	0.099487	0.099538
64	0.0043869	0.096417	0.096466
65	0.0041900	0.093488	0.093534
66	0.0040048	0.090690	0.090733
67	0.0038303	0.088016	0.088057
68	0.0036658	0.085459	0.085497
69	0.0035106	0.083012	0.083048
70	0.0033640	0.080668	0.080702
71	0.0032255	0.078422	0.078455
72	0.0030945	0.076269	0.076300
73	0.0029705	0.074204	0.074232
74	0.0028530	0.072221	0.072248
75	0.0027416	0.070317	0.070342
76	0.0026360	0.068487	0.068511
77	0.0025357	0.066727	0.066751
78	0.0024405	0.065035	0.065057
79	0.0023500	0.063406	0.063427

Table 2.1. Continued

x	ε / %		
	Calculated by Equation (2.9)	Calculated by Equation (2.10)	Calculated by Equation (2.11)
80	0.0022639	0.061838	0.061858
81	0.0021819	0.060327	0.060346
82	0.0021039	0.058871	0.058889
83	0.0020295	0.057467	0.057484
84	0.0019586	0.056113	0.056129
85	0.0018910	0.054806	0.054821
86	0.0018264	0.053544	0.053559
87	0.0017648	0.052325	0.052339
88	0.0017059	0.051148	0.051161
89	0.0016496	0.050010	0.050022
90	0.0015957	0.048909	0.048921
91	0.0015442	0.047844	0.047856
92	0.0014948	0.046814	0.046825
93	0.0014476	0.045817	0.045827
94	0.0014023	0.044851	0.044861
95	0.0013589	0.043915	0.043925
96	0.0013172	0.043009	0.043018
97	0.0012773	0.042130	0.042139
98	0.0012389	0.041278	0.041287
99	0.0012021	0.040451	0.040460
100	0.0011667	0.039649	0.039658

References

[1] L. A. Pérez-Maqueda, P. E. Sánchez-Jiménez, J. M. Criado. Kinetic analysis of solid-state reactions: precision of the activation energy calculated by integral methods. *International Journal of Chemical Kinetics,* 2005, 37, 658-666.

[2] S. Vyazovkin, C. A. Wight. Model-free and model-fitting approaches to kinetic analysis of isothermal and nonisothermal data. *Thermochimica Acta,* 1990, 340/341, 53-68.

[3] L. A. Pérez-Maqueda, J. M. Criado, P. E. Sánchez-Jiménez. Combined kinetic analysis of solid-state reactions: a powerful tool for the simultaneous determination of kinetic parameters and the kinetic model without previous assumptions on the reaction mechanism. *Journal of Physical Chemistry A,* 2006, 110, 12456-12462.

[4] Ortega, L. A. Pérez-Maqueda, J. M. Criado. A new point of view on the evaluation of the temperature integral. *Thermochimica Acta,* 1996, 282/283, 29-34.

[5] D. Doyle. Estimation isothermal life from thermogravimetric data. *Journal of Applied Polymer Science,* 1962, 6(24), 639-642.

[6]   N. Liu, H. Chen, L. Shu, M. Statheropoulos. Error evaluation of integral methods by consideration on the approximation of temperature integral, *Journal of Thermal Analysis and Calorimetry.* 2005, 81, 99-105.

[7]   W. Tang, Y. Liu, H. Zhang, C. Wang. New approximate formula for Arrhenius temperature integral. *Thermochimica Acta.* 2003, 408, 39-43.

[8]   Agherghinei. Thermogravimetry: Empirical approximation for the "temperature integrals". *Journal of Thermal Analysis,* 1990, 36, 473-479.

[9]   P. M. Madhusudanan, K. Krishnan, K. N. Ninan. New approximation for the p(x) function in the evaluation of non-isothermal kinetic data. *Thermochimica Acta,* 1986, 97, 189-201.

[10] P. M. Madhusudanan, K. Krishnan, K. N. Ninan. New equations for kinetic analysis of non-isothermal reactions. *Thermochimica Acta,* 1993, 221, 13-21.

[11] M. J. Starink. The determination of activation energy from linear heating rate experiments: a comparison of the accuracy of isoconversion methods. *Thermochimica Acta,* 2003, 404, 163-176.

[12] J. Cai, R. Liu. Kinetic analysis of solid-state reactions: errors involved in the determination of the kinetic parameters calculated by one type of integral methods. *Journal of Mathematical Chemistry,* 2008, 43, 914-920.

[13] J. J. M. Órfão. Review and evaluation of the approximations to the temperature integral. *AIChE Journal,* 2007, 53, 2905-2915.

[14] D. Doyle. Kinetic analysis of thermogravimetric data. *Journal of Applied Polymer Science,* 1961, 5, 285-292.

[15] W. Coats, J. P. Redfern. Kinetic parameters from thermogravimetric data. *Nature,* 1964, 201, 68-69.

[16] V. M. Gorbachev. A solution of the exponential integral in the non-isothermal kinetics for linear heating. *Journal of Thermal Analysis,* 1975, 8, 349-350.

[17] T. V. Lee, S. R. Beck. A new integral approximation formula for kinetic analysis of nonisothermal TGA data. *AIChE Journal,* 1984, 30, 517-519.

[18] van Tets. Accurate determination of a modified exponential integral with special reference to thermal analysis. *Thermochimica Acta,* 1976, 17, 372-374.

[19] T. Wanjun, L. Yuwen, Z. Hen, W. Zhiyong, W. Cunxin. New temperature integral approximate formula for non-isothermal kinetic analysis. *Journal of Thermal and Calorimetry,* 2003, 74, 309-315.

[20] T. Wanjun. Letter to the editor. *AIChE Journal,* 2006, 52, ().

[21] J. Cai, F. Yao, W. Yi, F. He. New temperature integral approximation for nonisothermal kinetics. A*IChE Journal,* 2006, 52, 1554-1557.

[22] J. Cai, F. He. Reply to the editor. *AIChE Journal,* 2006, 52, 2656.

[23] H. Li. An integral approximation formula for kinetic analysis of nonisothermal TGA data. *AIChE Journal,* 1985, 31, 1036-1038.

[24] R. K. Agrawal, M. S. Sivasubramanian. Integral approximations for nonisothermal kinetics. *AIChE Journal,* 1987, 33, 1212-1214.

[25] R. Quanyin, Y. Su. New approximations of the temperature integral for nonisothermal kinetics. *Journal of Thermal Analysis,* 1995, 44, 1147-1154.

[26] Urbanovici, E. Segal. Some problems concerning the temperature integral in non-isothermal kinetics. Ⅰ. Generalities and some simple applications. *Thermochimica Acta,* 1990, 168, 71-87.

[27] G. I. Senum, R. T. Yang. Rational approximations of integral of Arrhenius function. *Journal of Thermal Analysis,* 1977, 11, 445-449.

[28] J. Zsakó. Empirical formula for the exponential integral in nonisothermal kinetics. *Journal of Thermal Analysis,* 1975, 8, 593-596.

[29] H. Chen, N. Liu. New procedure for derivation of approximations for temperature integral. *AIChE Journal,* 2006, 52, 4181-4185.

[30] J. J. M. Órfão. Review and evaluation of the approximations to the temperature integral. *AIChE Journal,* 2007, 53, 2905-2915.

[31] L. Q. Ji. New rational fraction approximating formulas for the temperature integral. *Journal of Thermal Analysis and Calorimetry,* 2008, 91(3), 885-889.

[32] M. Balarin. Improved approximations of exponential integral in tempering kinetics. *Journal of Thermal Analysis,* 1977, 12, 169-177.

[33] J. Cai, F. He, W. Yi, F. Yao. A new formula approximating the Arrhenius integral to perform the nonisothermal kinetics*. Chemical Engineering Journal,* 2006, 124, 15-18.

[34] J. Cai, R. Liu. An improved version of Junmeng-Fang-Weiming-Fusheng approximation for the temperature integral. *Journal of Mathematical Chemistry*, 2008, 43(3), 1193-1198.

[35] J. Cai, R. Liu, C. Huang. Kinetic analysis of nonisothermal solid-state reactions: determination of the kinetic parameters by means of a nonlinear regression method. *Journal of Mathematical Chemistry,* 2008, 44(2), 551-558.

[36] H. X. Chen, N. A. Liu. Approximations for the temperature integral: their underlying relationship. *Journal of Thermal Analysis and Calorimetry*, 2008, 92(2), 573-578.

[37] G. Gyulai, E. J. Greenhow. Approximation of the temperature integral in the evaluation of thermoanalytical measurements. *Thermochimica Acta,* 1973, 6, 239-244.

[38] J. M. Criado, L. A. Pérez-Maqueda, P. E. Sánchez-Jiménez. Dependence of the preexponential factor on temperature: Errors in the activation energies calculated by assuming that *A* is constant*. Journal of Thermal Analysis and Calorimetry,* 2005, 82, 671-675.

Chapter 5

DETERMINATION OF PROTEIN COARSE-GRAIN CHARGES FROM SMOOTHED ELECTRON DENSITY DISTRIBUTION FUNCTIONS AND MOLECULAR ELECTROSTATIC POTENTIALS

Laurence Leherte and Daniel P. Vercauteren

Laboratoire de Physico-Chimie Informatique
Groupe de Chimie Physique Théorique et Structurale
University of Namur (FUNDP); Rue de Bruxelles, 61;
B-5000 Namur (Belgium)

Abstract

The design of protein coarse-grain (CG) models and their corresponding interaction potentials is an active field of research, especially for solving problems such as protein folding, docking… Among the essential parameters involved in CG potentials, electrostatic interactions are of crucial importance since they govern local and global properties, *e.g.*, their stability, their flexibility…

Following our development of an original approach to hierarchically decompose a protein structure into fragments from its electron density (ED) distribution, the method is here applied to molecular electrostatic potential (MEP) functions, calculated from point charges as implemented in well-known force fields (FF). To follow the pattern of local maxima (and minima) in an ED or a MEP distribution, as a function of the degree of smoothing, we adopted the following strategy. First, each atom of a molecule is considered as a starting point (a peak, or a pit for negative potentials in a MEP analysis). As the smoothing degree increases, each point moves along a path to reach a location where the ED or MEP gradient value vanishes. Convergences of trajectories lead to a reduction of the number of points, which can be associated with molecular fragments.

Practically, to determine the protein backbone representations, we analyzed CG models obtained for an extended strand of polyglycine. The influence of the different amino acid side chains was then studied for different rotamers by substituting the central glycine residue. Regarding the determination of charges, we adopted two procedures. First, the net charge of a fragment was calculated as the summation over the charges of its constituting atoms. Second, a fitting algorithm was used to assign charges to the obtained local maxima/minima.

Applications to a literature case, a 12-residue β-hairpin peptide, are also presented. It is observed that classical CG models are more similar to ED-based models, while MEP-based descriptions lead to different CG motifs that better fit the MEP distributions.

Introduction

The design of coarse-grain (CG) models [1] and their corresponding potential functions [2] for protein computational studies is currently an active field of research, especially in solving long-scale dynamics problems such as protein folding, protein-protein docking, … For example, to eliminate fast degrees of freedom, it has been shown that one can rely on CG representations only, or on mixtures of CG and more detailed descriptions [3,4] in order to significantly increase the time step in molecular dynamics (MD) simulations. Among the parameters involved in CG potentials, the electrostatic interactions are of major importance [5] since they govern local and global properties such as their stability [6], their flexibility [7]…

Common approaches used to design a CG description of a protein consist in reducing groups of atoms into single interaction sites. For example, in reference [8], each amino acid (AA) is represented by a single spherical site, with unit or nul electric charge. The authors studied a proline-rich protein PRP-1 interacting with a mica surface using Monte-Carlo simulations. Curcó *et al.* [9] developed a CG model of β-helical protein fragments where the AAs are represented by two, three, or four blobs depending upon the AA type, in accordance with a best fitting between Monte-Carlo based all-atom and CG energies. In their work, the AAs are depicted by the amide hydrogen atom HN, the oxygen atom, the geometric center of the side chain (except for Gly), and a fourth blob whose position depends on the AA type (except for Gly, Ala, and Val). In reference [10], each AA residue is modeled using one sphere located on the geometric center of the backbone and one or two spheres located on the geometric centers of the side chain fragments (except for Gly). Differently, Pizzitutti *et al.* [11] represented each AA of a protein sequence by a charged dipolar sphere. For each AA, one CG sphere is located on the center-of-mass (c.o.m.) of the uncharged residues, while two CG spheres are assigned to the c.o.m. of the neutral part of the AA residue and to the c.o.m. of the charged part, respectively. Charged residues are Lys, Arg, Glu, Asp, and terminal AAs. The authors show that, in protein association, their model provides a good approximation of the all-atom potential if the distance between the protein surfaces is larger than the diameter of a solvent molecule.

As mentioned earlier, a CG potential can be combined with an all-atom potential. For example, Neri *et al.* [3] included a CG description, in which the potential energy is expressed as harmonic terms between close C_α and/or C_β atoms. Such elastic network representations are well-known to study the slow large amplitude dynamics of protein structures [12-15]. The small biologically relevant region of the protein is modeled using an atom-based potential while the remaining part of the protein is treated using a CG model. In this context, Heyden and Thruhlar [16] proposed an algorithm allowing a change in resolution of selected molecular fragments during a MD simulation, with conservation of energy and angular momentum. A different and relatively logic way of considering the combination between all-atom and CG potentials is to use CG as a pre-processing stage carried out to establish starting conformations for all-atom MD simulations [4].

Even when one uses an all-atom representation to model a protein structure, a reduced set of Coulomb charges can still be used. For example, Gabb *et al*. [17] reported protein docking studies where electrostatic complementarity is evaluated by Fourier correlation. Charges used in Coulomb electrostatic fields were close to unit charges and placed on a limited set of atoms. Besides the use of unit charges as in [8,11,18], an approach to assign an electrostatic charge to a fragment or pseudo-atom is to sum over the corresponding atomic charges. Extended approaches involve the assignment of dipolar and quadrupolar contributions to the CGs [19]. In this last work [19], dedicated to small molecules such as benzene, methanol, or water, the charge distribution is represented by point multipolar expansions fitted to reproduce MD simulation data. Without being exhaustive, other assignment methods consist in fitting the CG potential parameters so as to reproduce at best the all-atom potential values [9,19].

In this chapter, we present two approaches to design and evaluate CG electrostatic point charges. The first one has already been described in a previous work regarding the evaluation of the electrostatic interactions between Aldose Reductase and its ligand [20]. In that first approach, the fragment content is determined through a merging/clustering procedure of atom trajectories generated in progressively smoothed electron density (ED) distribution functions. The specific use of a Gaussian promolecular representation of an ED, *i.e*., a model where a molecule is the superposition of independent and spherical atoms, allows a fast evaluation of the ED distribution as well as their derived properties such as derivatives and integrals. In the second approach, atoms are clustered according to their trajectories defined in a smoothed molecular electrostatic potential (MEP) function. As the charge calculation approach useful in ED cases revealed to be inefficient in MEP cases, a fitting algorithm is applied to evaluate CG charges. Results are presented for the 20 AAs, first as derived from a promolecular ED representation, and second from the all-atom Amber charges reported in Duan *et al*. [21]. In this last work, the authors developed a third-generation point charge all-atom force field for proteins. Charges were obtained by a fitting to the MEP of dipeptides calculated using B3LYP/cc-pVTZ//HF/6-31G** quantum mechanical approaches in the PCM continuum solvent in a low dielectric to mimic an organic environment similar to that of the protein interior.

Finally, we will show that the CG charges obtained for each AA residue can be used to determine a CG model representation for any protein. A particular application to a literature case, a 12-residue β-hairpin HP7 [10], is described and MEP results are compared with published models.

Theoretical Background

In this section, we present the mathematical formalisms that were needed to design a protein CG representation and its point charges. First, the smoothing algorithm that is applicable to both ED and MEP functions is described. This description is followed by the mathematical expressions needed to smooth either a Gaussian-based ED distribution function, or the Coulomb electrostatic interaction function. Finally, the two approaches used to calculate CG point charges, from ED- and MEP-based CG, respectively, are detailed.

Smoothing Algorithm

An algorithm initially described by Leung *et al*. [22] was implemented to follow the pattern of local maxima in a Gaussian promolecular ED or a MEP function, as a function of the degree of smoothing. More particularly, the authors proposed a method to model the blurring effect in human vision, which is achieved (*i*) by filtering a digital image *p(x)* through a convolution product with a Gaussian function *g(x,t)*:

$$g(x,t) = \frac{1}{t\sqrt{2\pi}} e^{-x^2/2t^2}$$

(1)

where *t* is the scale parameter, and (*ii*) by assigning each data point of the resulting *p(x,t)* image to a cluster *via* a dynamical equation built on the gradient of the convoluted image:

$$x(n+1) = x(n) + h\nabla_x p(x,t)$$

(2)

where *h* is defined as the step length. We adapted this idea to three-dimensional (3D) images such as ED and MEP functions, *f*, such as:

$$\vec{r}_{f(t)} = \vec{r}_{f(t-\Delta t)} + \frac{\Delta}{f(t)}\vec{\nabla}f(t)$$

(3)

where $\vec{r}$ stands for the location vector of a point in a 3D function.

The various steps of the resulting merging/clustering algorithm are:

1. At scale *t* = 0, each atom of a molecular structure is considered as a local maximum (peak) of the ED and/or a local minimum (pit) of the MEP function. All atoms are consequently considered as the starting points of the merging procedure described below.

2. As *t* increases from 0.0 to a given maximal value t_{max}, each point moves continuously along a gradient path to reach a location in the 3D space where $\vec{\nabla}f(t) = 0$. On a practical point of view, this consists in following the trajectory of the peaks and/or pits on the ED or MEP distribution surface calculated at *t* according to Equation (3). The trajectory search is stopped when $\left|\vec{\nabla}f(t)\right|$ is lower or equal to a limit value, $grad_{lim}$. Once all peak and/or pit locations are found, close points are merged if their interdistance is lower than the initial value of $\Delta^{1/2}$. The procedure is repeated for each selected value of *t*.

If the initial Δ value is too small to allow convergence towards a local maximum or minimum within the given number of iterations, its value is doubled (a scaling factor that is arbitrarily selected) and the procedure is repeated until final convergence.

The results obtained using that algorithm are the location of the local maxima and/or minima, *i.e.*, peaks and pits, and the atomic content of all fragments, at each value of t between 0 and t_{max} [23], that can be further interpreted in terms of dendrograms as, for example, using the Web version of the program Phylodendron [24]. For information, input data were written in the adequate format using DENDRO [25], a home-made program implemented using Delphi, an object-oriented programming language that allows the representation and processing of data in terms of classes of objects.

Promolecular Electron Density Distributions

In their studies related to the Promolecular Atom Shell Approximation (PASA), Amat and Carbó-Dorca used atomic Gaussian ED functions that were fitted on 6-311G atomic basis set results [26]. A molecular or promolecular ED distribution is thus a sum over atomic Gaussian functions wherein expansion coefficients are positive to preserve the statistical meaning of the density function in the fitted structure. In the PASA approach that is considered in the present work, a promolecular ED distribution ρ_M is analytically represented as a weighted summation over atomic ED distributions ρ_a, which are described in terms of series of three squared *1s* Gaussian functions fitted from atomic basis set representations [27]:

$$\rho_a(\vec{r} - \vec{R}_a) = Z_a \sum_{i=1}^{3} w_{a,i} \left[\left(\frac{2\varsigma_{a,i}}{\pi} \right)^{3/4} e^{-\varsigma_{a,i}|\vec{r}-\vec{R}_a|^2} \right]^2 \qquad (4)$$

where $w_{a,i}$ and $\zeta_{a,i}$ are the fitted parameters, respectively, as reported at the Web address http://iqc.udg.es/cat/similarity/ASA/funcset.html. ρ_M is then calculated as:

$$\rho_M = \sum_{a \in A} \rho_a \qquad (5)$$

In the present approach to generate smoothed 3D ED functions, ρ_M is directly expressed as the solution of the diffusion equation according to the formalism presented by Kostrowicki *et al.* [28]:

$$\rho_{a,t}(\vec{r} - \vec{R}_a) = Z_a \sum_{i=1}^{3} s_{a,i} \quad \text{where} \quad s_{a,i} = \alpha_{a,i} e^{-\beta_{a,i}|\vec{r}-\vec{R}_a|^2} \qquad (6)$$

with:

$$\alpha_{a,i} = Z_a w_{a,i} \left(\frac{2\varsigma_{a,i}}{\pi} \right)^{3/2} \frac{1}{\left(1 + 8\varsigma_{a,i}t\right)^{3/2}} \quad \text{and} \quad \beta_{a,i} = \frac{2\varsigma_{a,i}}{\left(1 + 8\varsigma_{a,i}t\right)} \qquad (7)$$

where t is the smoothing degree of the ED. t can also be seen as the product of a diffusion coefficient with time or, in crystallography terms, as the overall isotropic displacement parameter [29]. Unsmoothed EDs are thus obtained by imposing $t = 0$ bohr^2.

Molecular Electrostatic Potentials

The electrostatic potential function generated by a molecule A is calculated as a summation over its atomic contributions:

$$V_A(\vec{r}) = \sum_{a \in A} \frac{q_a}{\left|\vec{r} - \vec{R}_a\right|} \tag{8}$$

A smoothed version can be expressed as:

$$V_{A,t}(\vec{r}) = \sum_{a \in A} \frac{q_a}{\left|\vec{r} - \vec{R}_a\right|} erf\left(\frac{\left|\vec{r} - \vec{R}_a\right|}{2\sqrt{t}}\right) \tag{9}$$

where the error function erf can be calculated using the analytically derivable expression [30]:

$$erf(x) = 1 - (a_1 T + a_2 T^2 + a_3 T^3 + a_4 T^4 + a_5 T^5)e^{-x^2}, \text{ with } T = \frac{1}{1 + px} \tag{10}$$

The values of the parameters p and a are: $p = 0.3275911$, $a_1 = 0.254829595$, $a_2 = -0.284496736$, $a_3 = 1.421413741$, $a_4 = -1.453152027$, and $a_5 = 1.061405429$, as reported in [30]. Equation (9) is identical to the expression found in the potential smoothing approach, a well-known technique used in Molecular Mechanics (MM) applications [31].

Calculation of Fragment Charges

Fragment charges can, *a priori*, be calculated by summing over the point charges of the atoms a leading to a given fragment F in an ED or MEP field. This approach was, for example, initially applied for the evaluation of charges in proteins [20]:

$$q_F = \sum_{a \in F} q_a \tag{11}$$

As illustrated further in the text, the charges obtained in this way differ strongly from the values obtained using a charge fitting program. That last option was thus selected, and applied through the program QFIT [32] to get fragment charges fitted from a MEP grid. In a conventional fitting procedure, grid points that are located too close or too far from the molecular structure under consideration are excluded from the calculation. The atomic van

der Waals (vdW) radii are often the reference property to select grid points under interest. However, when using smoothed MEPs, charges are located at a reduced number of positions that do not necessarily correspond to atomic positions. Therefore, the corresponding peak/pit radius, $v_{smoothed}$, was defined as follows. Let us consider a 3D spherical Gaussian function:

$$f(r) \approx e^{-ar^2} \tag{12}$$

and its smoothed version:

$$f(r,t) \approx e^{-\frac{a}{(1+4at)}r^2} \tag{13}$$

An identification of the 3D integral of expressions (12) and (13) with the volume of a sphere built on a vdW radius v, $i.e.$:

$$\int f(r)4\pi r^2 dr = \frac{4}{3}\pi v^3 \quad \text{and} \quad \int f(r,t)4\pi r^2 dr = \frac{4}{3}\pi v^3_{smoothed} \tag{14}$$

leads to the two following equalities, respectively:

$$a = \frac{\pi^{1/3}}{\left(\frac{4}{3}\right)^{2/3} v^2} \tag{15}$$

with v set equal to 1.5 Å for peaks and pits in a MEP grid, and:

$$(v_{smoothed})^3 = \frac{3}{4}\frac{\pi^{1/2}(1+4at)^{3/2}}{a^{3/2}} = (1+4at)^{3/2}v^3 \tag{16}$$

For example, at $t = 1.4$ bohr², $v_{smoothed}$ is equal to 2.036 Å, a value that is representative of low radius values that were previously associated with protein peaks observed in ED maps generated at a medium crystallographic resolution level [33]. In the present work, all MEP grids were built using the Amber point charges as reported in Duan et $al.$ [21], with a grid step of 0.5 Å. For both unsmoothed and smoothed MEP grids, fittings were achieved by considering points located at distances between 1.4 and 2.0 times the vdW radius of the atoms and peaks/pits, respectively. These two limiting distance values were selected as in the Merz-Singh-Kollman scheme [34].

In all fittings presented, the magnitude of the molecular dipole moment was constrained to be equal to the corresponding all-atom Amber value. The quality of the fittings was evaluated by two root mean square deviation ($rmsd$) values, $rmsdV$ determined between the MEP values obtained using the fitted charges and the reference MEP values, and $rmsd\mu$

evaluated between the dipolar value calculated from the fitted CG charges and the reference dipole moment of the molecular structure:

$$rmsd\mu = \sqrt{\sum_{i=x,y,z}\left(\mu_{ref} - \mu_{fit}\right)^2} \qquad (17)$$

All dipole moment components were calculated with the origin set to (0. 0. 0.).

Results and Discussions

This section is dedicated to the elaboration of protein CG models, either based on the local maxima observed in smoothed ED, or on the local maxima and minima observed in smoothed MEP functions. The two main steps of our strategy rely, first, on a CG description of the protein backbone, and then on the development of side chain CG models. Each stage involves the determination of CG locations and corresponding electrostatic point charges. The final part of the section focusses on the application of our CG model to a literature case, the 12-residue β-hairpin HP7 [10].

We have restricted our studies to several fully extended peptides made of 15 amino acids, *i.e.*, Gly_7-AA-Gly_7, with the following protonation states: Lys(+1), Arg(+1), His with protonated Nε (noted Hisε further in the text), Glu(-1), and Asp(-1). The particular choice of such peptide sequences was a compromise to ensure that *(i)* the backbone of the central AA residue can interfere with neighbors. It was indeed shown previously that molecular ED-based fragments, especially protein backbone fragments, encompass atoms from the nearest residues [20,29]; *(ii)* the interference between the central AA residue and the whole peptide structure is minimized. The concept of "interference" is solely based on the CG description obtained for various secondary structures. For example, when a α-helix is considered rather than an extended β-strand structure, atoms from the peptide backbone may merge with the side chain of the central residue. It is thus extremely difficult to define a CG model that is specific to a selected residue. We will show that the MEP-based clustering results are actually highly dependent on the peptide conformation; *(iii)* the charge on the central residue Gly8 of Gly_{15} is nul. This effect might also be obtained by considering a periodic peptide, which, up to now, is not implemented yet. For each of the pentadecapeptide studied, end residues were not charged. At first, this may sound artificial, but the presence of a large negative or positive charge in the structure strongly affects the homogeneity of the CG distribution along the peptide chain. This will be illustrated later when studying pentadecapeptide with a central charged AA residue. As also shown later, an extended structure presents an homogeneous CG distribution of a protein backbone, a specificity expected for an easy derivation of a CG model that should hopefully be transferable to any protein structure knowing its atom coordinates.

To generate all pentadecapeptides studied in this work, the simulated annealing (SA) procedure implemented in the program SMMP05 [35] was applied with dihedrals Ω, Φ, Ψ, and χ constrained to pre-defined values. The default force field (FF) ECEPP/3 [36] and SA running parameters were selected. Each SA run consisted in a first 100-step equilibration Monte Carlo (MC) Metropolis stage carried out at 1000 K. Then the procedure was continued

for 50000 MC Metropolis iterations until the final temperature, 100 K, was reached. The lowest potential energy structure generated during each run was kept.

The hierarchical decomposition of molecular structures from ED distribution functions was achieved at t values ranging from 0.0 to 3.0 bohr^2, with a step of 0.05 bohr^2. The initial value Δ_{init} was set equal to 10^{-4} bohr^2, and $grad_{lim}$ to 10^{-5} e$^-$/bohr^4. When working with MEP functions, the steepness of the MEP at the initial atom location led to the following choice of parameters: t = 0.05 to 3.0 bohr^2, Δ_{init} = 10^{-6} bohr^2, $grad_{lim}$ = 10^{-6} e$^-$/bohr^2. Computing times for pentadecapeptide Gly$_{15}$ and 12-residue HP7, on a PC Xeon 32-bit processor with a clock frequency of 2.8 GHz, are presented in table 1. It is seen that cpu times obviously increase with the number of atoms in a molecular structure but also with its packing. As Coulomb interactions are long-ranged, packing however has a limited influence on the calculation time that is required for the analysis of MEP functions.

Table 1. Calculation times (min.) for the hierarchical merging/clustering decompositions of PASA-ED and all-atom Amber MEP functions of Gly$_{15}$ and 12-residue hairpin HP7 (PDB code: 2EVQ)

	cpu time	
	ED	**MEP**
α-Gly$_{15}$	5	45
β-Gly$_{15}$	3	25
HP7	27	44
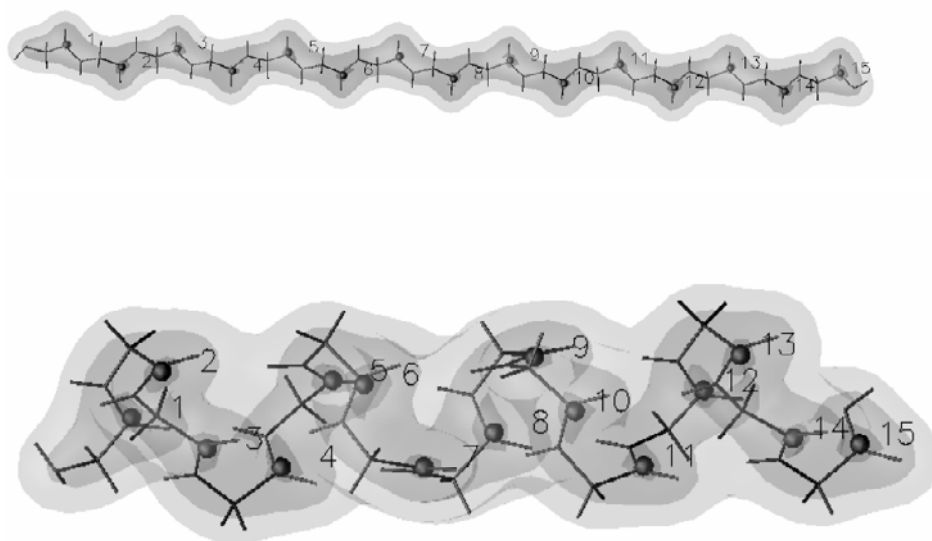
Figure 1. ED iso-contours (0.05, 0.10, 0.15 e$^-$/bohr^3) of (top) β-Gly$_{15}$ and (bottom) α-Gly$_{15}$ smoothed at t = 1.4 bohr^2. Local maxima at t = 1.4 bohr^2 were obtained using the hierarchical merging/clustering algorithm applied to the PASA ED distribution function. CG points are numbered as in table 3. Figures were generated using DataExplorer [47].
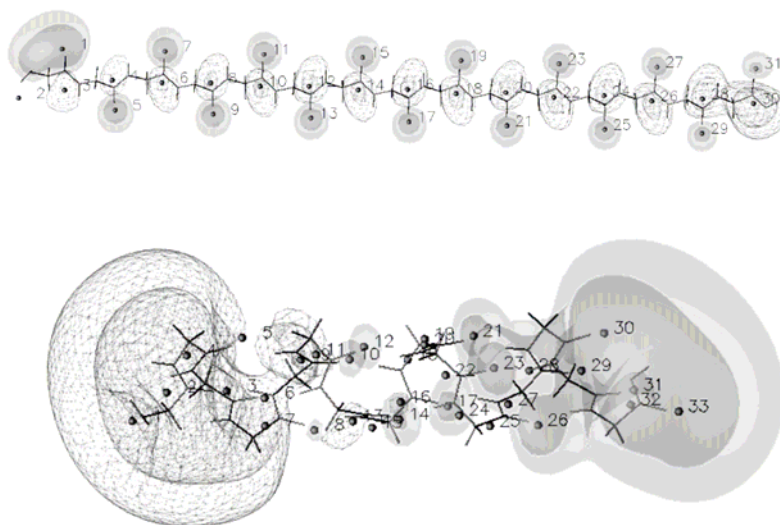
Figure 2. MEP iso-contours (plain: -0.05, -0.03 ; grid: 0.03, 0.05 e$^-$/bohr) of (top) β-Gly$_{15}$ and (bottom) α-Gly$_{15}$ smoothed at t = 1.4 bohr^2. Local maxima and minima at t = 1.4 bohr^2 were obtained using the hierarchical merging/clustering algorithm applied to the all-atom Amber MEP function. CG points are numbered as in table 2. Figures were generated using DataExplorer [47].

Protein Backbone Modeling

As announced hereabove, to maximize the interatomic distances between the backbone and side chain atoms, an extended geometry characterized by Ω = 180°, Φ = -139°, Ψ = 135° was considered. Indeed, for MEP analyses, the conformation of the peptide appeared to be extremely important on the results of the merging/clustering algorithm applied to MEP functions. This is illustrated in figures 1 and 2 that respectively depict the smoothed ED and MEP obtained at t = 1.4 bohr^2 for a β-strand and a α-helix of Gly$_{15}$. As already established before [20,29], the ED-based decomposition of the protein backbone is rather regular, consisting mainly in fragments $(C=O)_{AA}(N-C_\alpha)_{AA+1}$. The dendrograms (figure 3) resulting from the application of our hierarchical merging/clustering algorithm shows that the ED-based merging of the atoms to form fragments first occurs between the H atoms and their chemically bonded neighbors at t = 0.05 bohr^2. Then, as already shown [20,29], the C and O atoms of the backbone carbonyl groups begin to merge starting at t = 0.4 bohr^2. From 0.65 to 0.9 bohr^2, the atoms of the AA backbones merge until regular fragment structures such as $(C=O)_{AA}(N-C_\alpha)_{AA+1}$ (H atoms are not mentioned for clarity) are fully created at about t = 1.25 bohr^2. At t = 1.4 bohr^2, there still exists one peak per residue, and an *rmsd* value of 0.216 Å is observed between the coordinates of the backbone peaks and their corresponding c.o.m. (figure 4). A difference between the ED peaks of the α- and β-structures does not appear before t = 2.45 bohr^2. At that smoothing level, the close packing of the residues that occurs in the helix structure leads to a faster reduction of the number of local ED maxima (figure 5).
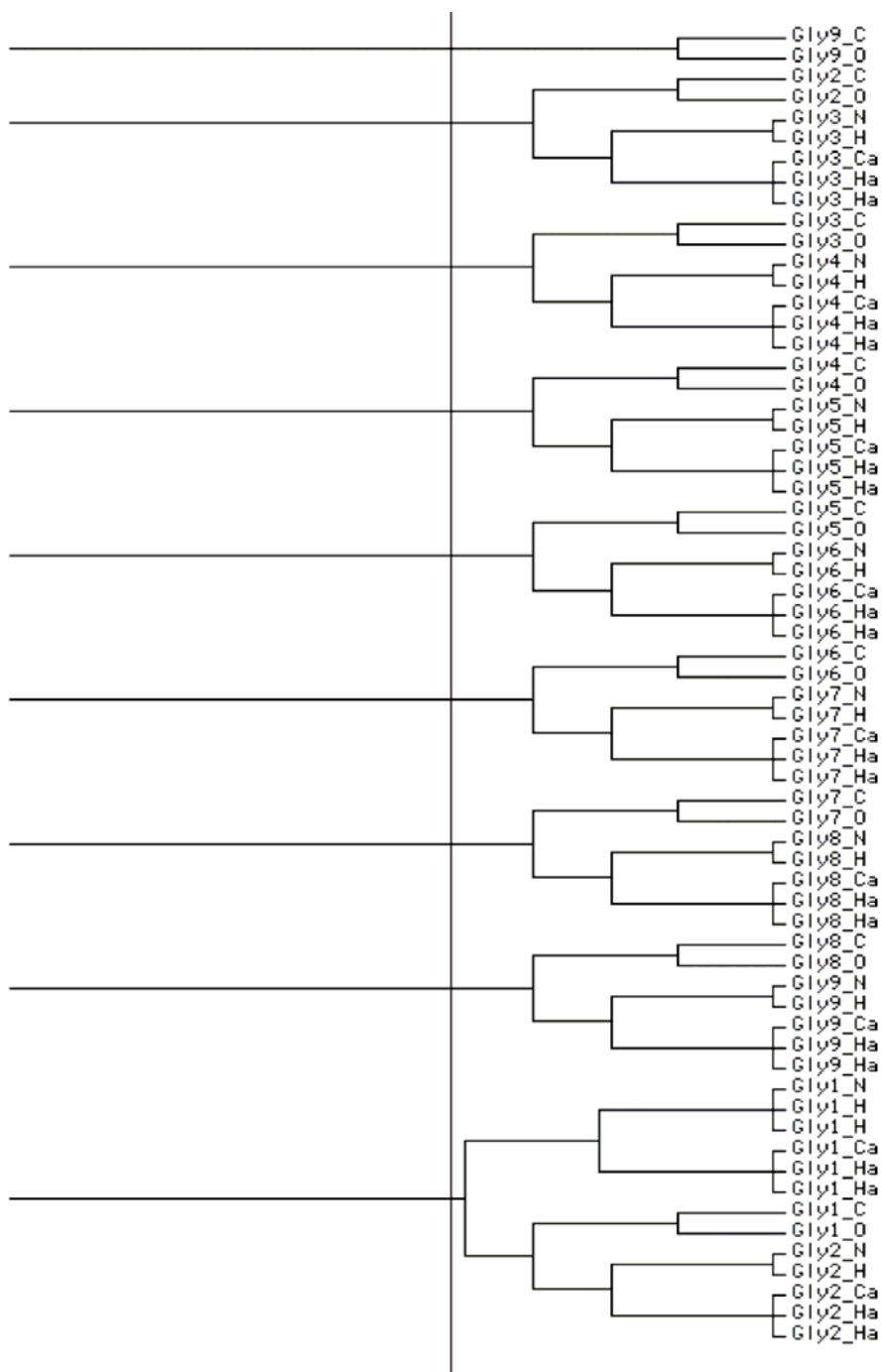
Figure 3. Dendrogram depicting the results of the hierarchical merging/clustering algorithm applied to the PASA ED distribution function of β-Gly$_{15}$. Results are displayed for the atoms of the first nine AA residues only. The vertical line locates $t = 1.4$ bohr^2.
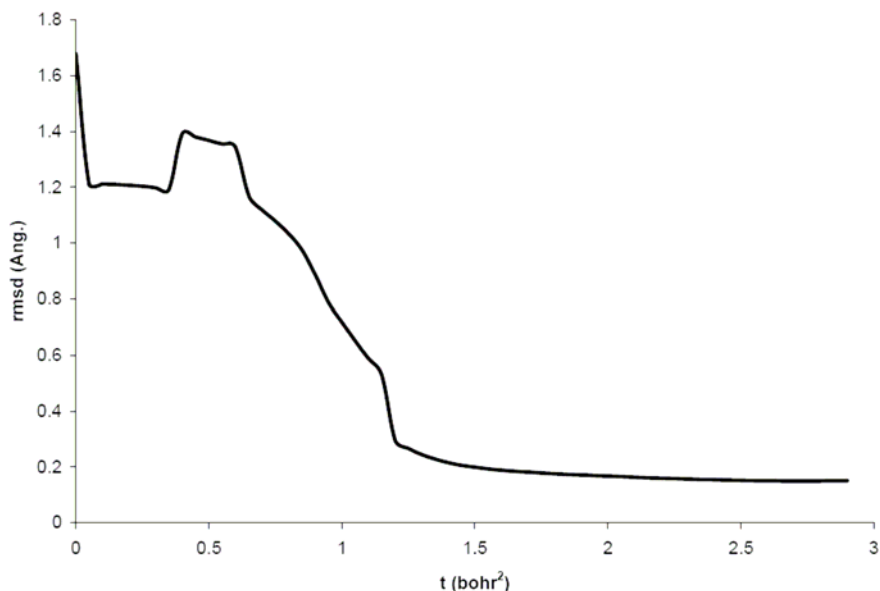
Figure 4. t-dependent $rmsd$ value calculated between the peaks observed in smoothed ED distribution functions of β-Gly$_{15}$ and their closest residue c.o.m. Local maxima were obtained using the hierarchical merging/clustering algorithm applied to the PASA ED distribution function.
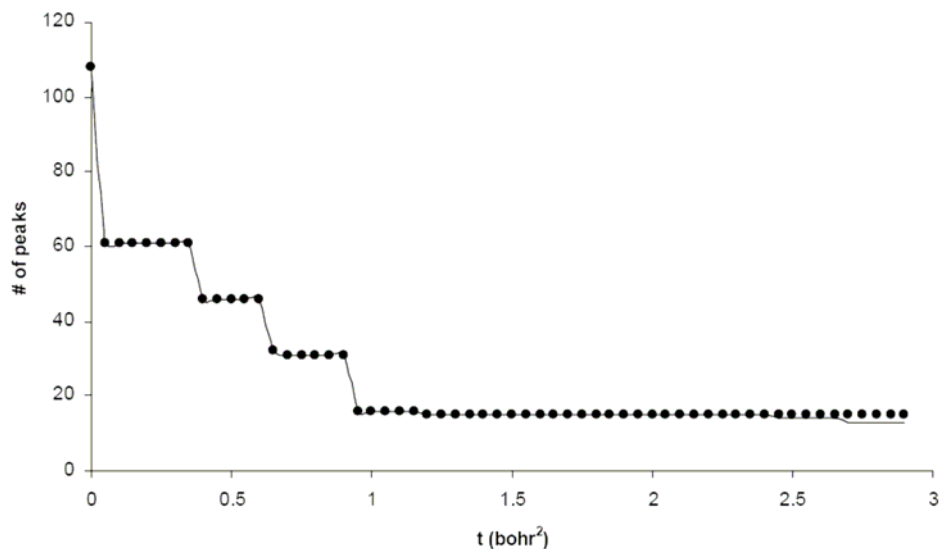
Figure 5. t-dependent number of ED peaks observed for structures α-Gly$_{15}$ (plain line) and β-Gly$_{15}$ (spheres). Local maxima were obtained using the hierarchical merging/clustering algorithm applied to the PASA ED distribution function.

As just mentioned, at $t = 1.4$ bohr^2, one observes one ED peak per residue, regardless of the secondary structure (figures 1 and 3). When a MEP function is used, results differ from the ED-based ones, and are highly dependent on the backbone conformation. The dendrogram built from the results of the merging/clustering algorithm applied to the all-atom Amber MEP

function illustrates that difference, and also shows that atoms are not necessarily merged according to their connectivity (figure 6). For example, at $t = 1.4$ bohr^2, a value selected because the number of peaks/pits does not vary significantly any longer beyond that smoothing degree, the points that are close to the O and C atoms (figure 2) are the result from the merge of the atoms (O, N, C$_\alpha$) and (H, C, H$_\alpha$, H$_\alpha$), respectively. For an easier identification of those points, the corresponding closest atom in the molecular structure is given in table 2. In the case of β-Gly$_{15}$, one interestingly observes an alternating distribution of negative and positive charges around the C=O groups, while for α-Gly$_{15}$, the dipolar character of the global structure is strongly emphasized with negative and positive charges being distributed at each end of the peptide, respectively (figure 2). Corresponding charge values, $q_{1.4}$, fitted from the MEP grids smoothed at $t = 1.4$ bohr^2, are presented in table 2. For β-Gly$_{15}$, the sign of the charges correspond to the expected dipolar distribution, *i.e.*, a positive and negative net charge close to the C and O atoms, respectively. For α-Gly$_{15}$, this expected charge distribution is observed only for residues 2, 4-7, and 15. It is thus hardly transferable from one residue to another. There are also additional charges that are close to the N atoms, with charge values being either positive (*e.g.*, point 15) or negative (*e.g.*, point 18). The information about the closest atom is thus not strictly physically significant. The *rmsd* values reflect a rather good fitting result. For example, for the α-helix structure, μ(Amber) = (-28.694, -22.761, -26.473 D) and μ(fitted) calculated with $q_{1.4}$ charges = (-29.103, -22.834, -26.672 D); for the β-strand structure, μ(Amber) = (16.369, 6.365, 3.644 D) and μ(fitted) calculated with $q_{1.4}$ charges = (16.352, 6.542, 3.720 D). Except for the residues that are close to the peptide ends, it is seen that for the extended structure, positive and negative charges are consistently located along the C=O axes, at distances of 0.83 and 0.62 Å from their closest atom. There is a greater variability of these distances in the α-helix case. As expected, the charge values depend upon the position of the residue in the peptide sequence. This variability is largely more pronounced for the α-helix case. In the β-strand structure, the charges located on the central residue, Gly8, are close to $q_{1.4} = \pm 0.196$ e$^-$ (points 16 and 17), while there is no such local dipolar distribution in the α-helix structure. Rather, in this last case, the central glycine residue leads to 3 points (points 15-17). In α-Gly$_{15}$, the positive charges are predominant between points 1 and 7, while the negative charges are predominant from point 29 to 33 (figure 7). It is also clearly seen that the charge magnitude is largely reduced at the center of α-Gly$_{15}$, while the distribution is rather homogeneous for β-Gly$_{15}$. CG charges obtained though the fitting on the unsmoothed all-atom Amber MEP grids, $q_{0.0}$, are also presented in table 2. That approach is proposed to eliminate the effect of smoothing on the charge values. Indeed, this effect may be not considered in a conventional MM calculation. The fitting is obviously less efficient but is still of a reasonable quality, especially for the β-strand structure for which *rmsdV* is equal to 1.32 kcal/mol. The dipole moment calculated over the fitted CG charges $q_{0.0}$ is equal to (16.106, 6.557, 3.732 D) and leads to a *rmsdμ* value of 0.34 D. The dipolar character of each C=O pair is characterized by charges $q_{0.0} = \pm 0.205$ e$^-$ separated by a distance of 2.65 Å. For α-Gly$_{15}$, the fitting is slightly less convincing, with *rmsdV* = 1.85 kcal/mol, while the rather good dipole moment of (-28.651, -22.796, -26.383 D) leads to *rmsdμ* = 0.11 D.
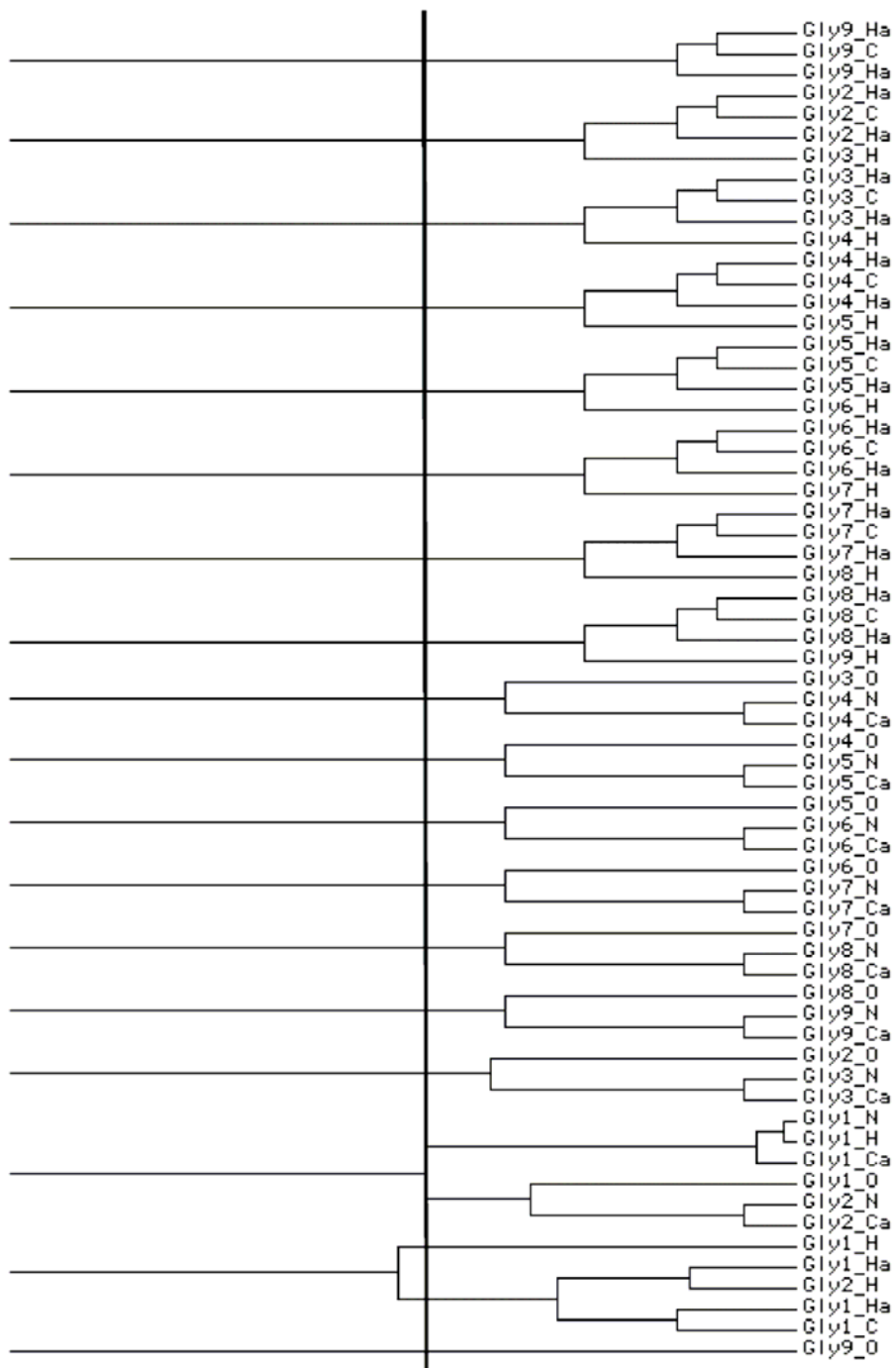
Figure 6. Dendrogram depicting the results of the hierarchical merging/clustering algorithm applied to the all-atom Amber MEP function of β-Gly$_{15}$. Results are displayed for the atoms of the first nine AA residues only. The vertical line locates $t = 1.4$ bohr^2.
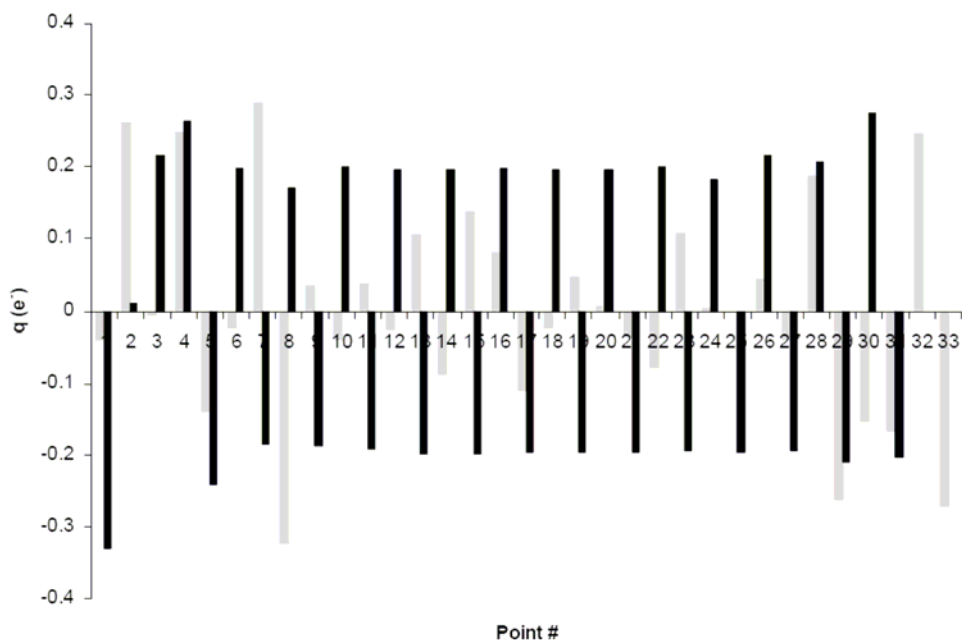
Figure 7. CG charges $q_{1.4}$ fitted from an all-atom Amber MEP grid smoothed at $t = 1.4$ bohr^2 for α-Gly$_{15}$ (grey bars) and β-Gly$_{15}$ (black bars). Local maxima and minima at $t = 1.4$ bohr^2 were obtained using the hierarchical merging/clustering algorithm applied to the all-atom Amber MEP function. Points are numbered as in table 2.

Table 2. CG charges $q_{1.4}$ and $q_{0.0}$ (in e$^-$) of Gly$_{15}$ fitted from the all-atom Amber MEP grids smoothed at $t = 1.4$ and 0.0 bohr^2, respectively, using the program QFIT. Local maxima and minima at $t = 1.4$ bohr^2 were obtained using the hierarchical merging/clustering algorithm applied to the all-atom Amber MEP function. For each point, the distance vs. the closest atom, d, is given in Å. rmsdV and rmsdμ are given in kcal/mol and D, respectively. Point numbers (#) refer to Figure 2

#	α-helix					β-strand				
	Closest atom		d	$q_{1.4}$	$q_{0.0}$	Closest atom		d	$q_{1.4}$	$q_{0.0}$
1	N	Gly1	0.768	-0.042	-0.014	O	Gly1	0.599	-0.329	-0.311
2	H	Gly3	0.973	0.261	0.216	H	Gly1	1.212	0.011	0.026
3	O	Gly1	0.681	-0.002	-0.076	Hα	Gly1	1.120	0.218	0.189
4	C	Gly2	0.899	0.246	0.307	C	Gly2	0.797	0.261	0.256
5	O	Gly2	0.598	-0.139	-0.187	O	Gly2	0.605	-0.241	-0.236
6	O	Gly3	0.560	-0.024	-0.074	C	Gly3	0.840	0.201	0.214
7	C	Gly4	0.771	0.290	0.307	O	Gly3	0.624	-0.184	-0.205
8	O	Gly4	0.524	-0.325	-0.298	C	Gly4	0.825	0.169	0.193
9	C	Gly5	0.682	0.034	0.162	O	Gly4	0.620	-0.187	-0.204
10	O	Gly5	0.507	-0.038	-0.176	C	Gly5	0.832	0.202	0.209
11	C	Gly6	0.700	0.039	0.146	O	Gly5	0.623	-0.191	-0.202
12	O	Gly6	0.499	-0.027	-0.174	C	Gly6	0.827	0.195	0.202
13	C	Gly7	0.706	0.107	0.170	O	Gly6	0.622	-0.197	-0.204
14	O	Gly7	0.492	-0.088	-0.186	C	Gly7	0.830	0.199	0.206
15	N	Gly8	0.700	0.138	0.088	O	Gly7	0.623	-0.197	-0.205

Table 2. Continued

#	Closest atom		d	$q_{1.4}$	$q_{0.0}$	Closest atom		d	$q_{1.4}$	$q_{0.0}$
		α-helix					**β-strand**			
16	C	Gly8	0.693	0.081	0.148	C	Gly8	0.828	0.197	0.205
17	O	Gly8	0.491	-0.110	-0.189	O	Gly8	0.623	-0.196	-0.205
18	N	Gly9	0.695	-0.024	0.030	C	Gly9	0.829	0.198	0.208
19	C	Gly9	0.698	0.048	0.131	O	Gly9	0.623	-0.196	-0.205
20	N	Gly10	0.691	0.005	0.066	C	Gly10	0.828	0.194	0.203
21	O	Gly9	0.499	-0.036	-0.138	O	Gly10	0.623	-0.195	-0.204
22	C	Gly10	0.716	-0.077	0.043	C	Gly11	0.829	0.204	0.210
23	O	Gly10	0.499	0.107	-0.001	O	Gly11	0.623	-0.194	-0.204
24	N	Gly11	0.675	0.005	0.039	C	Gly12	0.828	0.180	0.196
25	C	Gly11	0.747	-0.001	0.098	O	Gly12	0.623	-0.197	-0.206
26	O	Gly11	0.483	0.043	-0.050	C	Gly13	0.830	0.219	0.221
27	N	Gly12	0.678	-0.039	-0.019	O	Gly13	0.626	-0.194	-0.205
28	C	Gly12	0.824	0.186	0.209	C	Gly14	0.823	0.207	0.212
29	O	Gly12	0.581	-0.259	-0.252	O	Gly14	0.633	-0.211	-0.213
30	O	Gly13	0.619	-0.152	-0.144	C	Gly15	0.608	0.275	0.273
31	O	Gly14	0.619	-0.168	-0.159	O	Gly15	0.762	-0.205	-0.200
32	C	Gly15	0.587	0.242	0.242					
33	O	Gly15	0.648	-0.266	-0.250					
rmsdV				1.12	1.85				0.67	1.32
rmsdμ				0.46	0.11				0.19	0.34

Table 3. CG charges q_F (in e⁻) of Gly$_{15}$ obtained using Equation (11) applied to fragments determined at $t = 1.4$ bohr^2 using a hierarchical merging/clustering algorithm applied to the PASA ED distribution function. Charges $q_{1.4}$ and $q_{0.0}$ were obtained through a charge fitting algorithm using all-atom Amber MEP grids smoothed at $t = 1.4$ and 0.0 bohr^2, respectively. For each point, the distance *vs.* the closest c.o.m., d, is given in Å. *rmsdV* and *rmsdμ* are given in kcal/mol and D, respectively. Point numbers (#) refer to Figure 1

#	c.o.m.	d	q_F	$q_{1.4}$	$q_{0.0}$	c.o.m.	d	q_F	$q_{1.4}$	$q_{0.0}$
		α-helix					**β-strand**			
1	Gly1	0.253	-0.070	0.195	0.214	Gly1	0.214	-0.070	-0.184	-0.174
2	Gly2	0.239	0.001	0.195	0.172	Gly2	0.216	0.001	0.213	0.182
3	Gly3	0.238	0.001	0.285	0.276	Gly3	0.216	0.001	-0.135	-0.105
4	Gly4	0.239	0.001	-0.043	-0.053	Gly4	0.216	0.001	0.043	0.036
5	Gly5	0.239	0.001	-0.123	-0.113	Gly5	0.215	0.001	0.003	-0.001
6	Gly6	0.239	0.001	-0.108	-0.096	Gly6	0.216	0.001	0.001	0.006
7	Gly7	0.238	0.001	-0.045	-0.041	Gly7	0.216	0.001	-0.008	-0.008
8	Gly8	0.239	0.001	-0.013	-0.012	Gly8	0.216	0.001	0.017	0.014
9	Gly9	0.239	0.001	0.044	0.034	Gly9	0.216	0.001	-0.011	-0.009
10	Gly10	0.240	0.001	0.073	0.076	Gly10	0.216	0.001	0.010	0.011
11	Gly11	0.239	0.001	0.156	0.153	Gly11	0.215	0.001	-0.009	-0.009
12	Gly12	0.237	0.001	0.069	0.051	Gly12	0.216	0.001	0.034	0.027
13	Gly13	0.238	0.001	-0.235	-0.219	Gly13	0.216	0.001	-0.064	-0.051
14	Gly14	0.236	0.001	-0.146	-0.165	Gly14	0.216	0.001	0.084	0.073
15	OXT15	1.154	0.072	-0.289	-0.264	OXT15	1.234	0.072	0.020	0.023
rmsdV			17.57* 19.17**	3.59	3.97			4.43* 5.24**	4.29	5.10
rmsdμ			53.30	1.18	1.70			4.55	2.09	2.37

- Fitting achieved *vs.* all-atom Amber MEP grid smoothed at $t = 1.4$ bohr^2. **Fitting achieved *vs.* unsmoothed all-atom Amber MEP grid.

For comparison purposes, we report, in table 3, the charges q_F obtained using Equation (11) applied to the fragments observed in the PASA ED distribution function smoothed at $t = 1.4$ bohr^2. For an easier identification, each fragment is characterized by its closest residue c.o.m. except for the last peak, described with respect to the terminal oxygen atom OXT of Gly15. It is first seen that both α- and β-structures lead to identical decomposition results. As each peak consists in a glycine residue, its total charge q_F is zero (the exact value results from the atom charges reported in [21]), except for the end points which contain only a partial number of glycine atoms. We further considered those ED-based peaks as a CG model for the pentadecapeptide, and we evaluated the CG charges, $q_{0.0}$ and $q_{1.4}$, from all-atom Amber MEP grids generated at $t = 0.0$ and 1.4 bohr^2, respectively (table 3). The charges q_F determined from Equation (11) do not lead to a fitting as nice as those obtained from the MEP-based CG representations. This is especially true for the α-helix case, for which $rmsdV$ values are equal to 17.57 and 19.17 kcal/mol $vs.$ the all-atom Amber MEP grids smoothed at $t = 1.4$ and 0.0 bohr^2, respectively, and $rmsd\mu = 53.30$ D.

Protein Side Chains Modeling

Several CG representations of AA side chains were obtained by substituting the central residue Gly8 of β-Gly$_{15}$ by a selected AA in a specific conformational state. Except for AA = Gly and Ala, a number of rotamers were generated by considering the angular constraints given in table 4. These rotamers were selected according to their occurrence degree in protein structures as reported in the *Structural Library of Intrinsic Residue Propensities* (SLIRP) [37]. As already specified above, we considered the following protonation states: Lys(+1), Arg(+1), Hisε, Glu(-1), and Asp(-1). In figures 8 to 10, we present the details of the MEP-based CG representations of Asn, Arg(+1), and Glu(-1) obtained from the all-atom Amber MEP function [21], smoothed at $t = 1.4$ bohr^2. The case of Asn (figure 8) illustrates that, for a neutral residue, the number of minima and maxima may depend upon the conformation. For conformation *t,Nt*, there is only one negative charge located at the proximity of the O atom (point 17), while for the two other selected conformations, *t,Og-* and *t,Og+*, there are two additional positive charges close to the amide H atoms (points 17 and 19). For *t,Nt*, the two H atoms of the amide group are sufficiently close to the peptide backbone to be merged in the two positively charged fragments 16 and 18. In the case of Arg(+1), all four conformers showed the same characteristics, *i.e.*, three positive charges located at the neighborhood of the guanidinium group (points 17-19). The *g-,t,g-,g-* conformation is illustrated in figure 9. It is well seen that the positive charge located on the side chain strongly affects the distribution of peaks and pits at the level of the whole peptide backbone. Concerning Glu(-1), illustrated in figure 10 for the *g-,t,g-* conformation, all rotamers studied also showed a similar CG description with two negative charges facing the carboxylate O atoms (points 14 and 15). The peptide backbone CG representation is also strongly affected by the global negative charge of the residue side chain. The global influence of charged groups on the CG model of the pentadecapeptide models justifies, as mentioned earlier, the choice of studying peptides without charged end residues.
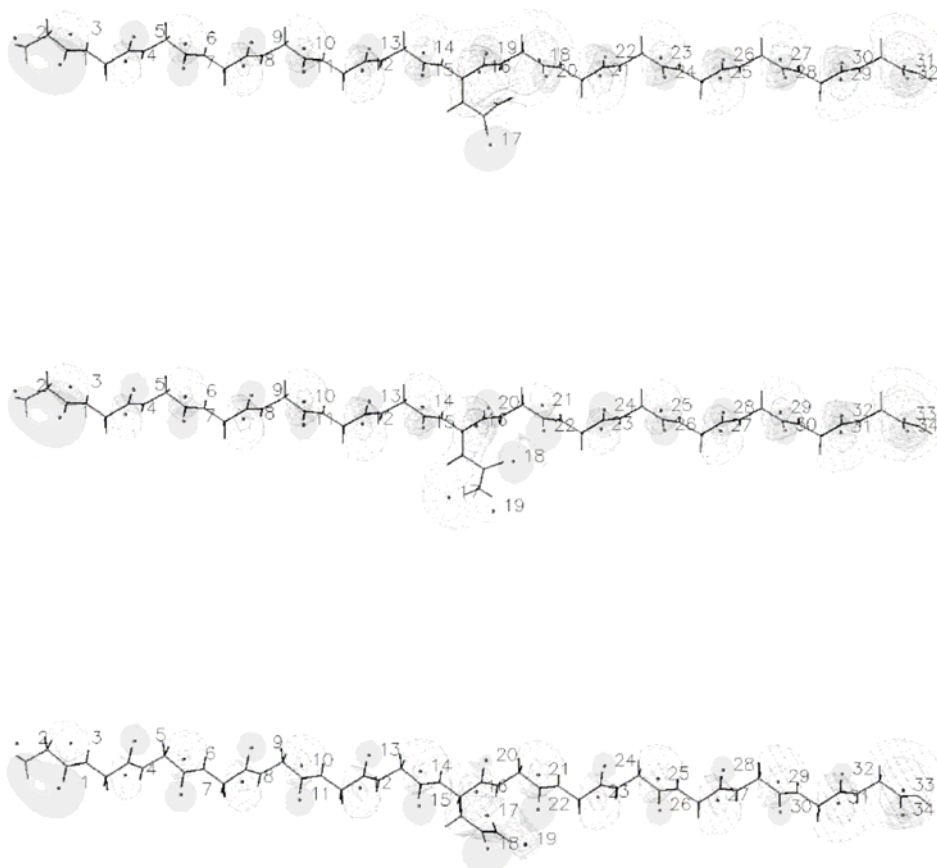
Figure 8. MEP iso-contours (plain: -0.05, -0.03 ; grid: 0.03, 0.05 e⁻/bohr) of Gly$_7$-Asn-Gly$_7$ smoothed at t = 1.4 bohr^2. Top: *t,Nt*, middle: *t,Og-*, bottom: *t,Og+* conformation. Local maxima and minima at t = 1.4 bohr^2 were obtained using the hierarchical merging/clustering algorithm applied to the all-atom Amber MEP function. Figures were generated using DataExplorer [47].
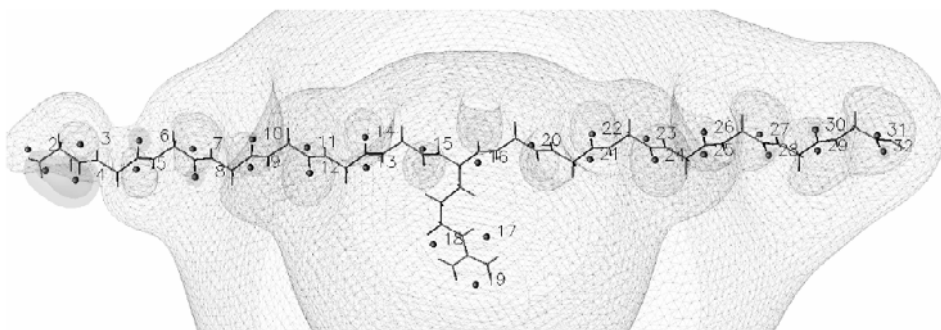
Figure 9. MEP iso-contours (plain: -0.05, -0.03 ; grid: 0.03, 0.05 e⁻/bohr) of Gly$_7$-Arg-Gly$_7$ in its *g-,t,g-,g-* conformation, smoothed at t = 1.4 bohr^2. Local maxima and minima at t = 1.4 bohr^2 were obtained using the hierarchical merging/clustering algorithm applied to the all-atom Amber MEP function. Figure was generated using DataExplorer [47].
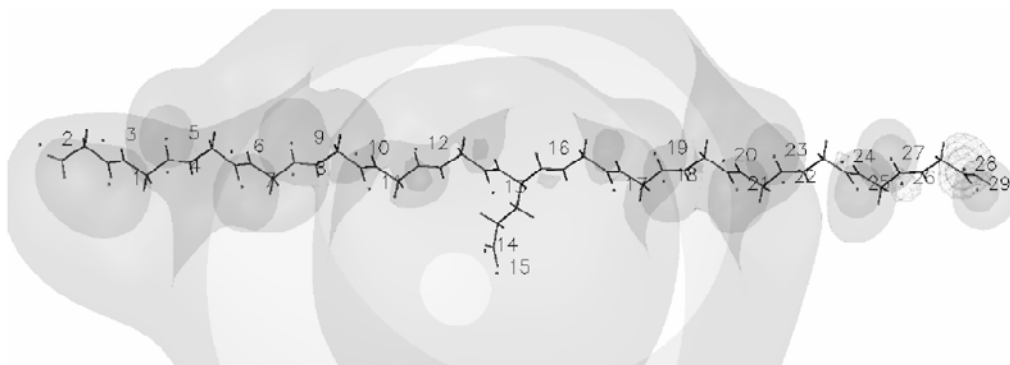
Figure 10. MEP iso-contours (plain: -0.05, -0.03 ; grid: 0.03, 0.05 e⁻/bohr) of Gly$_7$-Glu-Gly$_7$ in its *g-,t,g-* conformation, smoothed at $t = 1.4$ bohr^2. Local maxima and minima at $t = 1.4$ bohr^2 were obtained using the hierarchical merging/clustering algorithm applied to the all-atom Amber MEP function. Figure was generated using DataExplorer [47].

Table 4. Geometrical parameters and occurrence probability of the selected AA side chain rotamers. *g* and *t* stand for *gauche* and *trans*, respectively (see [37] for details)

	Conformation	χ1 (°)	χ2 (°)	χ3 (°)	χ4 (°)	Occurrence (%)
Arg	*g-, t, g-, g-*	300	180	300	300	9.5
	g-, t, g-, t	300	180	300	180	11.9
	g-, t, g+, t	300	180	60	180	12.2
	g-, t, t, t	300	180	180	180	12.2
Asn	*t, Nt*	180	0			11.1
	t, Og-	180	300			21.3
	t, Og+	180	60			23.6
Asp	*t, g+*	180	60			62.8
Cys	*g-*	300				56.3
	g+	60				15.1
	t	180				28.7
Gln	*g-, t, Nt*	300	180	0		11.2
	g-, t, Og-	300	180	300		33.2
	g-, t, Og+	300	180	60		28.6
Glu	*g-, t, g-*	300	180	120		29.9
	g-, t, g+	300	180	60		25.3
His	*g-, Ng-*	300	300			35.8
	t, Ng+	180	60			15.0
Ile	*g-, g-*	300	300			22.7
	g-, t	300	180			28.3
	g+, t	60	180			42.5
Leu	*g-, t*	300	180			65.2
	t, g+	180	60			24.1

Table 4. Continued

	Conformation	χ1 (°)	χ2 (°)	χ3 (°)	χ4 (°)	Occurrence (%)
Lys	g-, g-, t, g-	300	300	180	300	8.5
	g-, g-, t, g+	300	300	180	60	6.5
	g-, t, t, g-	300	180	180	300	21.7
	g-, t, t, g+	300	180	180	60	14.3
Met	g-, g-, g-	300	300	300		15.5
	g-, g-, t	300	300	180		11.6
	g-, t, g-	300	180	300		19.4
	g-, t, g+	300	180	60		16.4
	g-, t, t	300	180	180		15.4
Phe	g-, g-	300	300			37.8
	t, g+	180	60			31.5
Pro	g+	0				66.8
Ser	g-	300				73.1
	g+	30				24.8
Thr	g-	300				51.6
	g+	30				46.3
Trp	g-, g-	300	90			28.2
	g-, t	300	0			16.5
	t, g-	180	60			11.6
	t, g+	180	300			13.8
	t, t	180	0			11.2
Tyr	g-, g-	300	120			38.3
	t, g+	180	60			31.7
Val	g-	300				46.4
	t	180				51.9

In a further step, we determined the charge values for the CG descriptions of each AA through a fitting procedure carried out using QFIT [32] *vs.* unsmoothed MEP grids. For each of the AAs, all rotamer descriptions in terms of peaks and pits observed in all-atom Amber MEP smoothed at $t = 1.4$ bohr^2 were considered according to their occurrence probability (table 4). The peptide backbone was constrained to be modeled by a sequence of alternating negative and positive charges, $q_{0.0}$, as previously determined for β-Gly$_{15}$ (table 2), and that, even for charged residues (Arg, Lys, Glu, Asp). The exception is for the central residue under consideration, for which all charges, even the backbone ones, were free to vary during the fitting procedure, under two constraints: the molecular all-atom Amber charge and the corresponding total dipole moment. It is to be specified that, for some AA residues, the initial MEP-based peak/pit CG representation obtained for the corresponding side chain was replaced by a simpler model consisting of one of several points centered on selected atoms.

This was achieved as a first stage in the easy design of a CG protein model from its atom coordinates, *e.g.*, coordinates retrieved from the PDB [38].
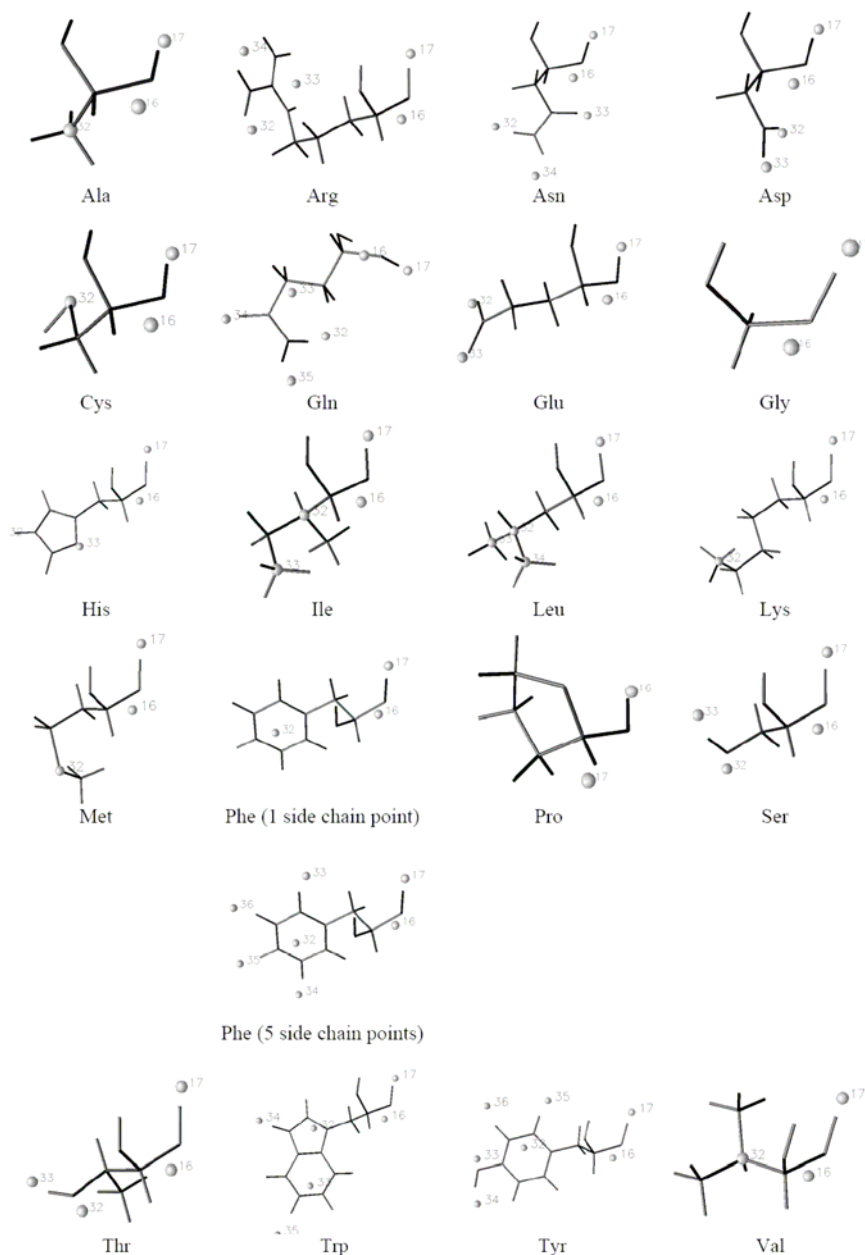
Figure 11. CG model for each of the 20 AA residues as established at $t = 1.4$ bohr^2 from the hierarchical merging/clustering algorithm applied to the all-atom Amber MEP function. CG points are numbered as in table 5. Figures were generated using DataExplorer [47].

In figure 11, we report the so-obtained original or simplified CG representations for all 20 AA residues as derived from the results of our hierarchical merging/clustering algorithm applied to the all-atom Amber MEP function, smoothed at $t = 1.4$ bohr^2. Corresponding CG

charges are reported in table 5. For all non-cyclic C-H based residues, *i.e.*, Ala, Ile, Leu, and Val, the side chain points were placed exactly on C atoms. This was chosen as an easy way to model the side chain of those specific residues in MM applications. For example, in the Ala case, the point charge that was initially observed in the all-atom Amber MEP function smoothed at $t = 1.4$ bohr^2 at a distance of 0.587 Å from Cβ (table 6) is replaced by a sphere centered exactly on atom Cβ. For the specific case of Ile, the number of peaks and pits that was initially observed in the smoothed MEP functions, depends on the conformation of the Ile side chain. More precisely, there is only one CG observed in each of the three rotamers, which is close to atom Cβ for conformations *g-,g-* and *g-,t* and close to Cδ1 for conformation *g+,t*. We thus evaluated two different models composed either of three or four points. In the case of the three-point model, the side chain CG point is located either on atom Cβ or atom Cδ1; in the case of the four-point model, the two CG points of the side chain are centered on the Cβ and Cδ1 atoms. Resulting *rmsdV* and *rmsdμ* values presented in table 6 show that the two models perform similarly in approximating the unsmoothed all-atom Amber MEP function, due to the very low charge values associated with the side chain CG points.

Similarly to the non-cyclic C-H based residues, the side chain of sulfur-containing residues, *i.e.*, Cys and Met, was modeled by a sphere placed exactly on the S atom. In the case of Cys in its *g+* conformation, there was initially an extra charge located at 1.038 Å of the H atom, which was, however, not observed in the *g-* conformation. As the charge fitting of the single structure *g+* onto the unsmoothed all-atom Amber MEP grid led to $q_H = 0.077$ e$^-$ (other output parameters were $q_O = -0.275$, $q_C = 0.360$, $q_S = -0.163$ e$^-$, *rmsdV* = 1.85 kcal/mol, *rmsdμ* = 0.44 D), we neglected the point charge q_H to generate a unique model valid for all three Cys rotamers. For Met, most of the original side chain points were very close to the S atom, below 0.28 Å (table 6), and a unique model with a sphere placed on S was built. For Lys, we also simplified the model by setting the positive charge exactly on the Nς atom. For all the other AAs, the original point locations observed in the smoothed MEP functions were kept for the charge fitting procedures. In the case of Phe, two models were evaluated (figure 11 and table 5). The first one was built from the set of CG points observed in the corresponding all-atom Amber MEP function, at $t = 1.4$ bohr^2. That model includes a point for the six-membered ring and four additional charges located close to the H atoms. This model does not reveal to be worse or better than the second one tested, consisting in a single ring point only. This is due to the very small amplitude of the H-related charges, ranging between 0.02 and 0.05 e$^-$. Indeed, the *rmsdV* values obtained for the 1- and 5-point side chain models are close to 1.5 and 1.4 kcal/mol, respectively. For *rmsdμ*, values are 0.1 and 0.3 D, respectively.

On the whole, we can also note that for hydroxyl containing residues, *i.e.*, Ser, Thr, and Tyr, there are two charges located near, but not exactly on, the O and H atoms. For the negatively charged residues, *i.e.*, Asp and Glu, each carboxylate functional group leads to two negative charges located near the O atoms. On the contrary, positively charged residues, Arg and Lys, present different behaviors. While the side chain of Lys leads to only one positive charge value, the Arg side chain is characterized by a 3-point motif, wherein each charge is almost symmetrically located on bisectors of each of the three N-C-N angles of the guanidinium group. For all these residues, distances between the CG charge and their closest atom in the molecular structure are reported in table 6.

Table 5. CG charges (in e⁻) for the AA residues obtained through a charge fitting algorithm using unsmoothed all-atom Amber MEP grids. CG locations were generated at $t = 1.4$ bohr^2 using a hierarchical merging/clustering algorithm applied to the all-atom Amber MEP function. *g* and *t* stand for *gauche* and *trans*, respectively (see [37] for details). *rmsdV* and *rmsdμ* are given in kcal/mol and D, respectively. Point numbers refer to Figure 11

	Conformation	Point 16	Point 17	Point 32	Point 33	Point 34	Point 35	Point 36	*rmsdV*	*rmsdμ*
Ala		C	O	Cβ						
		0.234	-0.236	-0.000(4)					1.77	0.66
Arg		C	O	NH-NH$_2$	NH$_2$-NH	NH$_2$-NH$_2$				
	g-,t,g-,g-								1.96	0.99
	g-,t,g-,t	0.310	-0.199	0.281	0.312	0.284			1.78	0.85
	g-,t,g+,t								1.72	0.21
	g-,t,t,t								1.67	0.30
Asn		C	O	Hδ$_{tr}$	Oδ	Hδ$_{cis}$				
	t,Nt								2.02	4.81
	t, Og-	0.371	-0.212	0.019	-0.178	0.002			2.55	3.42
	t, Og+								2.41	2.65
Asp		C	O	Oδ1	Oδ2					
	t,g+	-0.019	-0.205	-0.417	-0.358				1.58	0.64
Cys		C	O	Sγ						
	g-								1.64	0.77
	g+	0.398	-0.289	-0.103					1.92	1.46
	t								1.80	1.14
Gln		C	O	H$_{tr}$	Cγ	Oε	H$_{cis}$			
	g-,t,Nt								1.78	0.83
	g-,t,Og-	0.293	-0.289	0.167	0.001	-0.259	0.083		1.66	0.67
	g-,t,Og+								1.69	0.33
Glu		C	O	Oε1	Oε2					
	g-,t,g-	0.187	-0.270	-0.457	-0.456				1.51	0.29
	g-,t,g+								1.55	0.26

Table 5. Continued

	Conformation	Point 16	Point 17	Point 32	Point 33	Point 34	Point 35	Point 36	*rmsdV*	*rmsdμ*
Gly		C	O							
		0.205	-0.205						1.32	0.34
His		C	O	Hε	Nδ					
	g-,Ng-	0.198	-0.188	0.178	-0.184				1.54	0.23
	t,Ng+								1.58	0.39
Ile		C	O	Cβ	Cδ1					
	g-,g-	0.266	-0.283	0.019					1.47	0.51
	g-,t	0.266	-0.283	0.019					1.46	0.42
	g+,t	0.266	-0.283		0.020				1.42	0.53
Ile		C	O	Cβ	Cδ1					
	g-,g-								1.44	0.49
	g-,t	0.226	-0.280	0.068	-0.012				1.44	0.51
	g+,t								1.41	0.61
Leu		C	O	Cγ	Cδ1	Cδ2				
	g-,t	0.219	-0.245	0.062	-0.030	-0.011			1.36	0.40
	t,g+								1.36	0.58
Lys		C	O	Nς						
	g-,g-,t,g-								1.68	0.95
	g-,g-,t,g+	0.367	-0.239	0.875					1.64	1.26
	g-,t,t,g-								1.63	1.25
	g-,t,t,g+								1.68	0.92
Met		C	O	Sδ						
	g-,g-,g-								1.89	1.87
	g-,g-,t								2.15	2.06
	g-,t,g-	0.283	-0.232	-0.059					1.79	1.46
	g-,t-g+								1.80	1.55
	g-,t,t								2.02	1.67

Table 5. Continued

	Conformation	Point 16	Point 17	Point 32	Point 33	Point 34	Point 35	Point 36	*rmsdV*	*rmsdμ*
Phe		C	O	6-ring	Hδ2	Hε1	Hς	Hε2		
	g-,g-	0.263	-0.234	-0.163	0.033	0.047	0.031	0.027	1.40	0.34
	t,g+								1.40	0.30
Phe		C	O	6-ring						
	g-,g-	0.222	-0.219	-0.004					1.53	0.14
	t,g+								1.54	0.12
Pro		O	C							
	g+	-0.163	0.161						1.76	1.72
Ser		C	O	Oγ	Hγ					
	g-	0.304	-0.275	-0.173	0.153				1.50	0.45
	g+								1.65	0.62
Thr		C	O	Oγ	Hγ					
	g-	0.279	-0.247	-0.154	0.120				1.51	0.56
	g+								1.56	0.39
Trp		C	O	5-ring	6-ring	Hε1	HH			
	g-,g-	0.270	-0.210	-0.136	-0.098	0.146	0.028		1.51	0.31
	g-,t								1.54	0.27
	t,g-								1.58	0.37
	t,g+								1.54	0.43
	t,t								1.52	0.21
Tyr		C	O	6-ring	OH	HH	Hδ*	Hε*		
	g-,g-	0.267	-0.234	-0.110	-0.129	0.156	0.023	0.036	1.46	0.26
	t,g+								1.48	0.18
Val		C	O	Cβ						
	g-	0.092	-0.052	-0.051					1.62	0.66
	t								1.69	0.81

* Hδ and Hε stand on the opposite side of the O-H bond direction.

Table 6. Distances (in Å) observed between selected peaks and pits observed in all-atom Amber MEP function smoothed at $t = 1.4$ bohr^2, and their closest atom. '--' means that the peak/pit under consideration was not observed in the MEP grid of the considered rotamer

	No. of rot.	Cβ	Cγ	Cδ1	Cδ2	Sγ (Cys), Sδ (Met), Nς (Lys)		
Ala	1	0.587						
Ile	3	0.846, 0.548, --		--, --, 0.418				
Leu	2		2.645, --	0.746, --	--, 0.796			
Val	2	0.355, 0.349						
Cys	3					0.358, 0.695, 0.450		
Met	5					0.201, 0.274, 0.098, 0.100, 0.105		
Lys	4					0.510, 0.380, 0.357, 0.408		
		O	H	Oδ1 (Asp), Oε1 (Glu)	Oδ2 (Asp), Oε2 (Glu)	Cς		
						Point 32	Point 33	Point 34
Ser	2	0.659, 0.796	1.100, 1.209					
Thr	2	0.873, 0.559	0.975, 0.932					
Tyr	2	0.634, 0.627	0.907, 0.910					
Asp	1			0.330	0.363			
Glu	2			0.342, 0.337	0.331, 0.342			
Arg	4					2.282, 2.256, 2.268, 2.215	1.902, 1.964, 1.989, 1.950	2.030, 2.036, 2.036, 2.047

Table 7. CG charges (in e⁻) for the AA residues obtained from Equation (11) applied to fragments generated at $t = 1.4$ bohr^2 using a hierarchical merging/clustering algorithm applied to PASA ED distribution functions. *rmsdV* and *rmsdμ* are given in kcal/mol and D, respectively. They correspond to the mean value calculated per rotamer structure. 'BAK' stands for the backbone c.o.m. Point numbers refer to Figure 12

	BAK$_{AA-2}$	BAK$_{AA-1}$	BAK$_{AA}$	Point 8	Point 9	BAK$_{AA+1}$	*rmsdV*	*rmsdμ*
Ala	0.001	0.055	-0.058			0.001	5.19	4.27
Arg	0.001	0.020	0.081	0.899		0.001	18.60	14.68
Asn	0.001	0.002	0.022	-0.023		0.001	21.57	24.55
Asp	0.001	-0.077	-0.129	-0.793		0.001	5.70	6.78
Cys	0.001	0.038	-0.013	-0.023		0.001	30.68	21.62
Gln	0.001	0.205	-0.217	0.015		0.001	30.85	29.16
Glu	0.001	0.120	-0.194	-0.925		0.001	30.20	30.73
Gly	0.001	0.001	0.001			0.001	5.24	4.55
His	0.001	-0.100	0.062	0.039		0.001	28.98	29.95
Ile	0.001	0.123	-0.122			0.001	28.90	23.01
Leu	0.001	-0.023	-0.056	0.079		0.001	34.32	31.84
Lys	0.001	0.012	0.091	0.899		0.001	19.56	13.56
Met	0.001	0.110	-0.037	-0.073		0.001	20.87	18.31
Phe	0.001	0.030	-0.030	0.051	-0.051	0.001	29.73	24.40
Pro	0.001	0.072	-0.172	0.101		0.001	5.23	5.76
Ser	0.001	0.136	-0.169	0.033		0.001	38.75	38.52
Thr	0.001	-0.025	-0.063	0.090		0.001	37.38	34.14
Trp	0.001	0.050	0.018	-0.022		0.001	21.47	17.99
Tyr	0.001	-0.060	0.024	0.013	0.025	0.001	30.44	19.14
Val	0.001	0.029	-0.029			0.001	38.00	99.58

For comparison with the MEP-based CG representations, the same exercise was achieved using ED-based CG representations that were built from the peaks observed in PASA ED distribution functions, smoothed at $t = 1.4$ bohr^2 (figure 12). Associated charges, calculated using Equation (11), are reported in table 7. First of all, it is observed that, for a given AA, all rotamers showed the same behaviour, *i.e.,* identical hierarchical decompositions and fragment contents. A detailed description of the side chain fragments is presented in table 8. For Ala, Gly, Ile, Pro, and Val, there is no side chain peak observed. All side chain atoms have actually been merged with backbone atoms to form a fragment whose corresponding ED maximum is closer to a backbone c.o.m. For example, atoms N, Cα, and Cβ of Ala were merged with C and O of the preceding AA residue in the peptide sequence. The same occurred for Ile and Val, where a backbone fragment was formed by (CO)$_{Gly7}$ and (N-Cα-Cβ-Cγ1-Cγ2-Cδ1)$_{Ile8}$, and (CO)$_{Gly7}$ and (N- Cα-Cβ-Cγ1-Cγ2)$_{Val8}$, respectively. The backbone peak of Pro was actually associated with atoms (N-Cα-Cβ-Cγ-Cδ)$_{Pro8}$. Except for the AA under consideration and its nearest neighbor, *AA-1*, the CG model is not dependent upon the AA type, and the Gly charge remains equal to 0.001 e⁻ (table 7), the value corresponding to the total charge of a Gly residue as reported in [21]. It can also be seen that the other nearest neighbor, *AA+1*, stays unaffected by the AA type. This ED effect is thus highly local, and might be qualified as a 'shape' effect, while the electrostatic long-range influence, that is present in MEP-based results, needs to be controlled using charge constraints during the fitting procedure. To eventually evaluate the quality of charges associated with ED-based

CGs in reproducing the all-atom unsmoothed Amber MEP maps, *rmsdV* and *rmsdμ* values were calculated. They are reported in table 7 as well, and reflect the less precise reproduction of MEP and dipole values than the MEP-based CG charges.
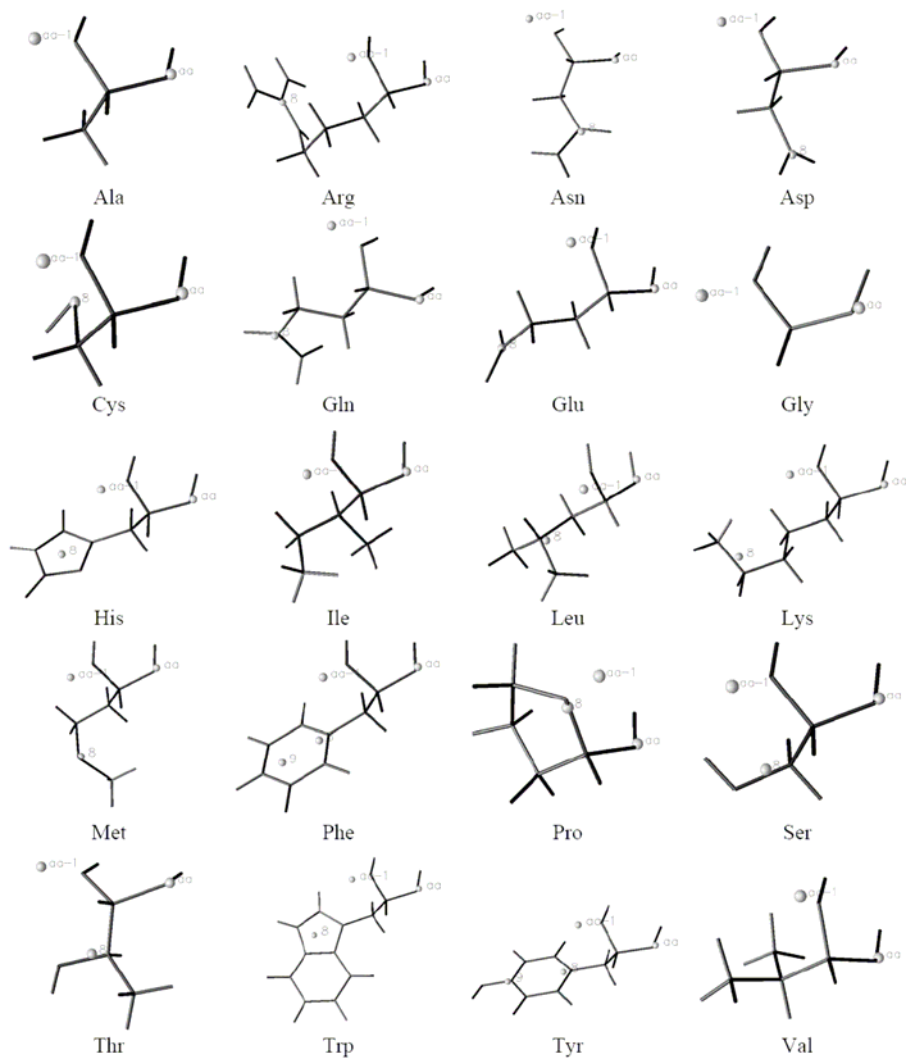
Figure 12. CG model for each of the 20 AA residues as established at $t = 1.4$ bohr^2 from the hierarchical merging/clustering algorithm applied to the PASA ED distribution function. CG points are numbered as in table 7. Figures were generated using DataExplorer [47].

Application to 12-Residue Hairpin HP7

The structure of peptide HP7 was retrieved from the PDB [38] (PDB code 2EVQ). The primary structure of that peptide is Lys-Thr-Trp-Asn-Pro-Ala-Thr-Gly-Lys-Trp-Thr-Glu (figure 13). It has a global net charge of +1.004 e$^-$ when summing over the atom charges given in reference [21]. The structure is interesting to consider as a reference structure

because a fragment-based description, as well as corresponding point charges, have been provided [10]. In that representation, each pseudo-atom is defined as the geometric center of the heavy atoms of a protein fragment.

Table 8. Atom content of the side chain ED-based fragments as obtained using a hierarchical merging/clustering algorithm, at $t = 1.4$ bohr^2. H atoms are not reported for clarity. Distances d between local ED maxima and closest side chain c.o.m. are given in Å

	Fragment content	**d**
Arg	Cγ-Cδ-Nε-Cς-(NH2)$_2$	1.182
Asn	Cβ-Cγ-Oδ1-Nδ2	0.383
Asp	Cβ-Cγ-Oδ1-Oδ2	0.426
Cys	Cβ-Sγ	0.590
Gln	Cγ-Cδ-Oε1-Nε2	0.917
Glu	Cγ-Cδ-Oε1-Oε2	0.879
His	Cγ-Nδ1-Cε1-Nε2-Cδ2	0.618
Leu	Cγ-Cδ1-Cδ2	0.115
Lys	Cδ-Cε-Nς	1.187
Met	Cγ-Sδ-Cε	0.857
Phe	Cγ-Cδ1-Cδ2	0.483
	Cε1-Cε2-Cς	1.140
Ser	Cβ-Oγ	0.070
Thr	Cβ-Oγ1-Cγ2	0.474
Trp	Cγ-Cδ1-Nε1-Cε2-Cς2-CH2-Cς3-Cε3-Cδ2	1.035
Tyr	Cγ-Cδ1-Cδ2	1.213
	Cε1-Cς-OH-Cε2	1.436

The decompositions as obtained from PASA ED and all-atom Amber MEP functions smoothed at $t = 1.4$ bohr^2 are displayed in figure 14, together with the Basdevant's CG model which is composed of 28 grains. As already mentioned above, the MEP-based results are highly dependent on the conformation of the peptide, and a MEP-based CG description obtained at $t = 1.4$ bohr^2 now consists in only 22 points. This is well below the expected number of peaks and pits, *i.e.*, 44 as will be seen later, that would be obtained if all AA residues were considered as isolated. Figure 14 illustrates the high diversity of the various CG models. In table 9, we present the charges associated with the CG representations obtained from the application of the hierarchical merging/clustering algorithm to PASA ED distribution and all-atom Amber MEP functions, smoothed at $t = 1.4$ bohr^2, compared to the effective charges reported in the literature [10]. Our charges were obtained using the program QFIT [32] *vs.* unsmoothed all-atom Amber MEP grids. The major point to mention is the very bad approximation brought by the model built on MEP CG points whose charges were simply calculated using Equation (11). Indeed, *rmsdV* and *rmsdμ* values are equal to 33.04 kcal/mol and 43.13 D, respectively. The use of a simple approximation such as Equation (11) provides better results when applied to ED-based fragments, with *rmsdV* = 12.78 kcal/mol and *rmsdμ* = 16.04 D. For that last model, we can also note that the charges obtained for the side chain peaks are identical to the values reported in table 7 for Gly7-AA-Gly7 structures. Thus, a change in the primary and secondary structures of a protein does seem to affect the backbone peaks only. When the charge fitting procedure is applied, both the 23-point ED- and 22-point

MEP-based CG models provide similar quality approximations of the all-atom unsmoothed Amber MEP grid, with, respectively, $rmsdV$ = 5.45 and 4.62 kcal/mol, and $rmsd\mu$ = 1.04 and 1.96 D.
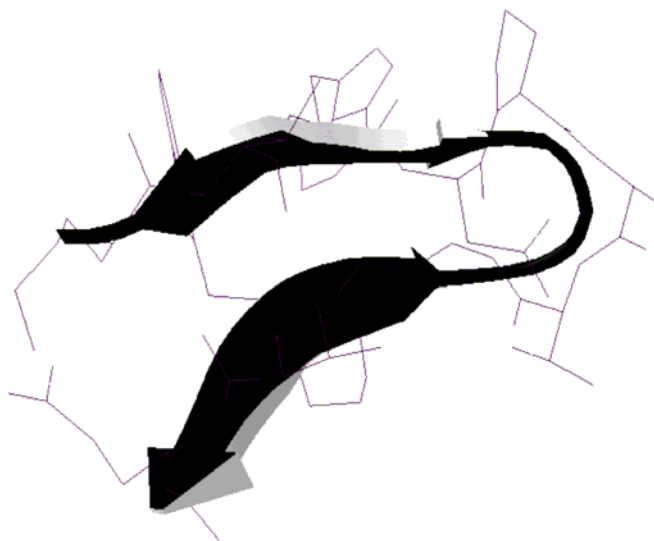
Figure 13. 3D conformation and secondary structure of the 12-residue β-hairpin peptide HP7 (PDB code 2EVQ). Figure was generated using SwissPDBViewer [48].
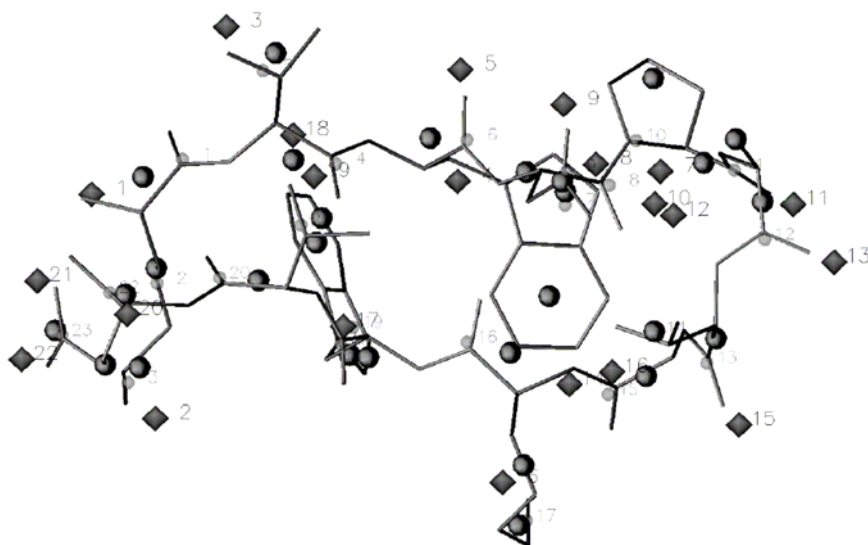
Figure 14. 3D structure of the 12-residue β-hairpin peptide HP7 (sticks) superimposed with the 22 all-atom Amber MEP point charges at t = 1.4 bohr^2 (black diamonds), the 23 PASA ED peaks at t = 1.4 bohr^2 (small grey spheres), and the 28-point Basdevant's model (large black spheres). CG points are numbered as in table 9. Figure was generated using DataExplorer [47].

Table 9. CG charges (in e⁻) for the 12-residue peptide HP7 obtained through a charge fitting algorithm using unsmoothed all-atom Amber MEP grids. CG locations were generated at $t = 1.4$ bohr^2 using a hierarchical merging/clustering algorithm applied to the PASA ED and all-atom Amber MEP functions. 'BAK' and 'SCH' stand for backbone and side chain, respectively. *rmsdV* and *rmsdμ* are given in kcal/mol and D, respectively. Charges obtained by Basdevant *et al.* [10] are reported for comparison. Point numbers (#) refer to Figure 14

Closest c.o.m.		#	[10]	[10] (Fitted)	#	ED-based CG (Eq. 11)	ED-based CG (Fitted)	Closest atom		#	MEP-based CG (Eq. 11)	MEP-based CG (Fitted)
BAK	Lys1	1	1.342	1.033	1	0.952	0.685	N	Lys1	1	1.731	0.797
SCH	Lys1	2	-0.673	-0.412	2	0.053	-0.104	Hς1	Lys1	2	1.841	0.624
SCH	Lys1	3	1.332	0.717	3	0.899	0.660	Hς1	Lys9	3	-0.602	-0.110
BAK	Thr2	4	0.353	-0.452	4	-0.059	-0.374	Oγ1	Thr2	4	0.728	-0.203
SCH	Thr2	5	-0.353	-0.170	5	0.090	-0.168	C	Trp3	5	-0.495	-0.105
BAK	Trp3	6	-0.090	0.235	6	0.019	-0.271	O	Trp3	6	1.061	0.989
SCH	Trp3	7	-0.073	0.061	7	-0.022	0.033	Hε1	Trp3	7	-0.168	0.145
SCH	Trp3	8	0.163	0.101				C	Asn4	8	0.679	0.614
BAK	Asn4	9	0.329	-0.767	8	0.093	-0.317	Oδ1	Asn4	9	-0.527	-0.319
SCH	Asn4	10	-0.329	-0.155	9	-0.023	-0.128	Hδ2	Asn4	10	0.492	0.049
BAK	Asn4				10	0.101	1.020	O	Pro5	11	-0.435	-0.252
BAK	Pro5	11	-0.375	0.270	11	-0.118	-0.265	H	Thr7	12	1.019	0.495
SCH	Pro5	12	0.375	0.298				O	Ala6	13	-0.555	-0.225
BAK	Ala6	13	-0.189	-0.570	12	-0.082	-0.131	Hγ1	Thr7	14	0.031	0.196
SCH	Ala6	14	0.189	0.367				O	Thr7	15	-0.552	-0.172
BAK	Thr7	15	-0.778	-0.435	13	-0.063	-0.641	C	Gly8	16	-0.186	-0.262
SCH	Thr7	16	0.778	0.429	14	0.090	0.470	C	Trp10	17	1.289	0.002

Table 9. Continued

Closest c.o.m.		#	[10]	[10] (Fitted)	#	ED-based CG (Eq. 11)	ED-based CG (Fitted)	Closest atom		#	MEP-based CG (Eq. 11)	MEP-based CG (Fitted)
BAK	Gly8	17	0.000	-0.277	15	0.012	-0.151	HH2	Trp10	18	-0.543	0.021
BAK	Lys9	18	0.687	1.290	16	0.095	0.895	Oγ1	Thr11	19	-0.602	0.139
SCH	Lys9	19	-0.718	-0.342	17	0.899	0.837	OXT	Glu12	20	-1.554	-0.852
SCH	Lys9	20	1.031	0.865				Oε1	Glu12	21	-0.824	-0.396
BAK	Trp10	21	0.365	-0.947	18	-0.008	-0.772	Oε2	Glu12	22	-0.824	-0.170
SCH	Trp10	22	0.093	0.538	19	-0.022	0.192					
SCH	Trp10	23	-0.458	-0.307								
BAK	Thr11	24	0.413	1.402	20	0.056	1.329					
SCH	Thr11	25	-0.413	0.023	21	0.090	-0.089					
BAK	Glu12	26	-1.194	-1.708	22	-1.123	-1.457					
SCH	Glu12	27	0.044	0.262	23	-0.925	-0.248					
SCH	Glu12	28	-0.850	-0.343								
Total charge			1.001	1.004		1.004	1.004				1.004	1.004
rmsdV			37.74	5.45		12.78	5.45				33.04	4.62
rmsdμ			23.06	1.57		16.04	1.04				43.13	1.96

In structure HP7, the two end residues are positively and negatively charged, respectively. These end charges prevent the regular carbon and oxygen CG MEP motif to appear on the residue backbones. Indeed, in figure 14 and table 9, one can observe that these two point charges are missing for most of the residues, except for Trp3 (points 5 and 6 in table 9). Thus, in order to build the backbone CG model of peptide HP7, two charges were generated for each residue backbone except for the first and the last ones. The two charges were located at distances of 0.828 and 0.623 Å, respectively from the C and O atoms, along the C=O axes. Each point was assigned a charge depending upon the AA residue type, as given in table 5. For the two Lys residues, a charge of 0.875 e$^-$ was assigned to their Nς atom. For Ala, a charge of -0.000(4) e$^-$ was set at the Cβ atom location. For the Thr, Trp, Asn, and Glu residues, a MEP-based hierarchical merging/clustering procedure was first carried out for each isolated residue, with coordinates as given in the PDB structure. This provided the location of the CG points, whose coordinates are reported in table 10. Then, charges were assigned to those points according to the values reported in table 5. This was achieved under the assumption of charge transferability between pentadecapeptide models and a protein structure. To strictly confirm this concept, a larger set of applications is however required. For Glu, a mean charge of -0.457 e$^-$ was given to each of the CG points located close to the Oε atoms. The end charges located on N$_{Lys1}$ and OXT$_{Glu12}$ were calculated as a sum over a unit charge and the corresponding C and O charges of Lys1 and Glu12, respectively. For example, the charge located on N$_{Lys1}$ was set equal to $q = 1.127$ e$^-$ = + 1.000 - 0.239 + 0.367 e$^-$. Finally, it is recalled that there is no side chain CG point for Pro and Gly. There remained a 44-point CG model for the 12-residue peptide HP7 (figure 15), with a total charge of 0.999 e$^-$. For that particular model, and with respect to the unsmoothed all-atom Amber MEP grid, the calculated *rmsdV* and *rmsdµ* values are equal to 7.34 kcal/mol and 8.89 D (table 10). In comparison, the model proposed by Basdevant *et al.* [10] does not perform correctly (table 9), with *rmsdV* = 37.74 kcal/mol and *rmsdµ* = 23.06 D; but this is most probably due to the use of a different set of atom charges, and a different parametrization of the charge fitting algorithm. An optimization of the Basdevant's model *vs.* our unsmoothed all-atom Amber MEP grid led to *rmsdV* = 5.45 kcal/mol and *rmsdµ* = 1.57 D (table 9), while an optimization of our 44-CG model *vs.* the same Amber MEP grid led to the charges reported in table 10, with *rmsdV* = 2.80 kcal/mol and *rmsdµ* = 1.11 D. The major changes brought to our model charges occurred at the level of the C atoms; indeed, the absolute differences between the model charges and their corresponding optimized values are higher than 0.30 e$^-$ at residues 3, 7, and 9-11. Other drastic changes occurred, for example, at the level of Oγ_{Thr7}, going from a charge value of - 0.154 to 0.546 e$^-$, and for Hγtr$_{Asn4}$, with a charge difference of -0.31 e$^-$. There is also an important charge re-distribution between the two Oε atoms of Glu12. In comparison, larger charge differences are observed between the original Basdevant's model and the corresponding fitted charges; most of them, *i.e.*, 17 over 28, are higher than 0.30 e$^-$ in absolute value. Backbone CG are among the points that are characterized by the largest differences, *i.e.*, Thr2, Asn4, Pro5, Lys9, Trp10, Thr11, and Glu12.
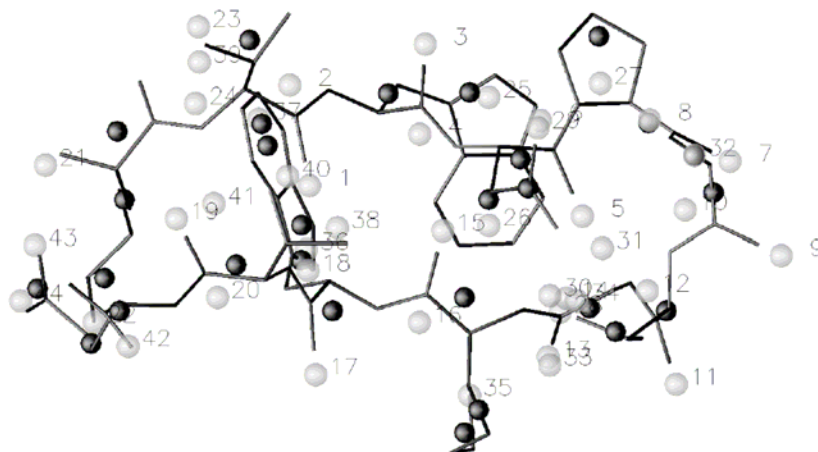
Figure 15. 3D structure of the 12-residue β-hairpin peptide HP7 (sticks) superimposed with the 44-point model built from local maxima and minima obtained for pentadecapeptides using the hierarchical merging/clustering algorithm applied to the all-atom Amber MEP function smoothed at $t = 1.4$ bohr^2 (grey spheres) and the 28-point Basdevant's model (black spheres). CG points are numbered as in table 10. Figure was generated using DataExplorer [47].

Table 10. 44-point CG model for the 12-residue peptide HP7 built from charges (in e$^-$) reported in table 5 (see text for details). *rmsdV* and *rmsdµ* are given in kcal/mol and D, respectively. Coordinates X, Y, and Z are in Å. Point numbers (#) refer to Figure 15

#	X	Y	Z	CG location	Residue	Model charges	Optimized charges
1	-3.128	1.192	-0.973	O	Thr2	-0.247	-0.120
2	-3.626	3.719	-1.710	C	Thr2	0.279	0.579
3	-0.213	4.749	-0.653	O	Trp3	-0.210	-0.254
4	-0.350	2.484	-2.079	C	Trp3	0.270	-0.049
5	3.751	0.422	-1.629	O	Asn4	-0.212	-0.125
6	2.691	2.833	-1.094	C	Asn4	0.371	0.426
7	7.470	1.805	-2.513	O	Pro5	-0.163	-0.262
8	5.439	2.844	-1.112	C	Pro5	0.161	0.083
9	8.762	-0.558	0.290	O	Ala6	-0.236	-0.261
10	6.338	0.584	0.320	C	Ala6	0.234	0.308
11	6.116	-3.794	-2.484	O	Thr7	-0.247	-0.247
12	5.388	-1.445	-1.422	C	Thr7	0.279	-0.071
13	2.889	-3.106	-5.576	O	Gly8	-0.205	-0.337
14	3.347	-1.626	-3.384	C	Gly8	0.205	0.326
15	0.230	0.059	-1.888	O	Lys9	-0.239	-0.350
16	-0.359	-2.236	-3.134	C	Lys9	0.367	0.769
17	-2.974	-3.551	-0.908	O	Trp10	-0.210	-0.270
18	-3.164	-0.934	-1.453	C	Trp10	0.270	-0.067
19	-6.482	0.356	-0.257	O	Thr11	-0.247	-0.096
20	-5.445	-1.607	1.247	C	Thr11	0.279	0.696

Table 10. Continued

#	X	Y	Z	CG location	Residue	Model charges	Optimized charges
21	-9.782	1.706	-1.460	N	Lys1	1.127	1.018
22	-8.558	-2.226	-4.238	Nς	Lys1	0.875	0.807
23	-5.926	5.187	0.580	Oγ	Thr2	-0.154	-0.225
24	-5.998	3.255	2.149	Hγ	Thr2	0.120	0.164
25	1.393	3.415	-4.851	5-ring	Trp3	-0.136	-0.054
26	1.396	0.189	-6.098	6-ring	Trp3	-0.098	-0.248
27	4.205	3.764	-5.295	Hε1	Trp3	0.146	0.162
28	3.190	-1.977	-7.552	HH	Trp3	0.028	0.033
29	2.628	2.645	2.624	Oγ	Asn4	-0.178	-0.208
30	2.929	-1.559	1.218	Hγ$_{tr}$	Asn4	0.019	-0.294
31	4.253	-0.374	3.533	Hγ$_{cis}$	Asn4	0.002	0.039
32	6.571	1.953	2.094	Cβ	Ala6	-0.000(4)	0.103
33	2.929	-3.312	-0.689	Hγ	Thr7	0.120	-0.007
34	3.603	-1.682	0.868	Oγ	Thr7	-0.154	0.546
35	0.908	-4.071	-6.309	Nς	Lys9	0.875	0.937
36	-3.204	-0.409	-5.747	5-ring	Trp10	-0.136	-0.036
37	-4.409	2.858	-5.518	6-ring	Trp10	-0.098	0.017
38	-2.424	0.132	-8.616	Hε1	Trp10	0.146	0.113
39	-5.904	4.299	-2.815	HH	Trp10	0.028	-0.189
40	-3.676	1.425	1.520	Oγ	Thr11	-0.154	-0.131
41	-5.535	0.735	2.365	Hγ	Thr11	0.120	-0.062
42	-7.699	-2.837	3.942	OXT	Glu12	-1.083	-1.036
43	-10.052	-0.302	-0.588	Oε	Glu12	-0.457	-0.774
44	-10.406	-1.697	-2.343	Oε	Glu12	-0.457	-0.347
				Total charge		0.999	1.004
				rmsdV		7.34	2.80
				rmsdμ		8.89	1.11

In conclusion, among the two models that can be easily built for HP7, *i.e.*, ED-based CG with charges assigned using Equation (11) and MEP-based CG model as described in table 5, the last one is slightly better. It is however no doubt that an optimization of the charges would drastically improve the quality of the models, but this requires an additional step that can be time-consuming for large structures. In the present work, such an optimization stage was carried out on a single rigid conformation, while the initial (non optimized) model charges implicitly involved information relative to several AA conformations (but no information relative to various secondary structures). Our present feeling is that the use of Equation (11) in combination with MEP-based CG has to be rejected at this point.

Conclusion

Following a previously described method [20,23,29] for the hierarchical merging/clustering decomposition of a molecular structure, particularly a protein structure, based on a promolecular electron density (ED) distribution function, we present an original application to molecular electrostatic potential (MEP) functions. The approaches allow to reduce the number of representative points of a molecule and assign them point charge values. The decomposition of the protein structure is achieved by following the trajectories of the atoms in progressively smoothed molecular ED or MEP functions. The present work is especially focused on the use of the all-atom Amber MEP function [21], but is readily applicable to other charge sets that are available in the literature.

Two approaches were proposed to study the electrostatic properties of a molecular model. First, for the ED-based results, the Amber atomic charges were used to calculate fragment charges. This was achieved by summing over the charges of the atoms that belong to a fragment. Second, for the MEP-based coarse grain (CG) points, a charge fitting algorithm was used to assign charges from the all-atom unsmoothed MEP. For each model, each of the 20 natural amino acid (AA) residues were studied, with the following specific protonation states: Lys(+1), Arg(+1), Hisε, Glu(-1), and Asp(-1). To generate CG models that avoid too many interaction effects, we selected, for all ED-based and MEP-based calculations, extended β-strand conformations for the molecular structures. These structures consisted in a set of pentadecapeptide Gly_7-AA-Gly_7, with various rotamers for each of the 20 AA (except Gly, Ala, Asp, and Pro).

The ED-based calculations were all achieved using ideal Gaussian-type promolecular ED distributions, without any random noise. When working with such ED distribution functions, a very interesting situation occurs at a smoothing degree t around 1.4 $bohr^2$, where the protein structure is clearly partitioned into backbone and side chain fragments. One observes one fragment for each residue backbone, mainly composed of –(C=O)-N-C_α or a derivative, and one fragment for each residue side chain, except for Gly, Ala, Ile, Pro, and Val (no fragment at all), and Tyr (two fragments). These observations are consistent with several descriptions already proposed in the literature, such as the globbic description levels of protein structures at a crystallographic resolution of about 3 Å [39] and the CG model proposed by Basdevant *et al*. [10]. Results showed to be independent on the AA residue conformation. On the contrary, the use of MEP functions provided very different decomposition results, which are hardly interpretable in terms of molecular fragments composed of chemically linked atoms, and are very sensitive to the molecular conformation. A detailed analysis was carried out at the smoothing level of 1.4 $bohr^2$, like for the ED-based results, a value beyond which there was no more drastic changes in the merging/clustering decomposition results.

Finally, the particular case of a 12-residue peptide HP7 (PDB code: 2EVQ) was studied. This structure was selected as it is deeply detailed in the literature [10] and was thus an interesting reference case. A 44-point CG model was built and evaluated in terms of its ability to reproduce all-atom MEP and corresponding dipole moment. We chose to design a CG model that already involves some simplifications for non cyclic C-H residues, sulfur-containing residues, and Lysine, with side chain CG charges placed at selected atom locations.

Further developments might include strategies to directly design CG representations for all 20 AA residues from their atomic coordinates. It is shown that without an optimization stage, our model is of a similar quality than the previously published CG model [10]; after optimization, the CG distribution is shown to provide a really better representation of the MEP and dipole moment.

Another extension of the present work resides in the evaluation of backbone charges as a function of the residue location along the protein sequence. Indeed, the CG charges of Gly_{15} models and the optimization results of the 44-point model of HP7 showed that the local charge separations observed along each C=O axis is far from being a constant.

Other perspectives to the present work are numerous. First of all, an extension to various molecular systems is needed to validate the transferability of our model. Second, the effect of the point charge set can be studied by considering other all-atom force fields such as, for example, in [40]. In this last work, a semi-empirical quantum mechanical procedure (FCPAC) was used to calculate the partial atomic charges of amino acids from 494 high-resolution protein structures. Each AA was either considered as the center of a tripeptide with the PDB geometry (free) or the center of 13 to 16 AA clusters (buried). A more general parametrization, applicable to organic molecules, peptides, and proteins, has also been presented by Arnautova *et al*. [41] in the so-called ECEPP-05 force field (FF). The partial atomic charge of multiple configurations of small molecules were obtained by fitting to the MEP calculated with the HF/6-31G* quantum mechanical approach. Other sets of atomic charges are also available. For example, Matta and Bader [42] reported charges of isolated amino acids determined through the quantum theory of atoms-in-molecules (QTAIM) and showed their transferability properties. We can also mention databases of transferable parameters to evaluate atom charges of protein structures, as, for example, designed by Lecomte *et al*. [43,44] and already used in a previous work [20]. Another set of atomic charges in the Amber-type FF family designed for proteins can be found in [45]. In that new generation united-atom force field, all hydrogen atoms bonded to aliphatic carbons in all AA are united with C except those on Cα. Polar and aromatic H are represented explicitly. Charges were obtained as in [21]. In that family of FF, we can also cite the Gromos charge sets implemented in the program GROMACS [46]. Coarser descriptions are also available, such as the one proposed by Gabb *et al*. [17] who reported protein docking studies where electrostatic complementarity was evaluated by Fourier correlation.

Finally, a resolution dependency of the CG model could be studied, with the expected behavior that, at lower smoothing levels, the efficiency of the model is expected to be better since the number of CG points and their charges would be closer to the initial all-atom MEP function.

Acknowledgments

References

[1]   Tozzini, V. *Curr. Opin. Struct. Biol*. 2005, 15, 144-150.

[2]   Nielsen, S. O.; Lopez, C. F.; Srinivas, G.; Klein, M. L. *J. Phys.: Condens. Matter* 2004, 16, R481-R512.

[3]   Neri, M.; Anselmi, C.; Cascella, M.; Maritan, A.; Carloni, P. *Phys. Rev. Lett*. 2005, 95, 218102/1-218102/4.

[4]   Colombo, G.; Micheletti, C. *Theor. Chem. Acc*. 2006, 116, 75-86.

[5]   Vizcarra, C. L.; Mayo, S. L. *Curr. Opin. Chem. Biol*. 2005, 9, 622-626.

[6]   Stigter, D.; Alonso, D. O. V.; Dill, K. A. *Proc. Natl. Acad. Sci. USA* 1991, 88, 4176-4180.

[7]   Kumar, S.; Wolfson, H. J.; Nussinov, R. *IBM. J. Res. & Dev*. 2001, 45, 499-512.

[8]   Skepö, M.; Linse, P.; Arnebrant, T. *J. Phys. Chem*. B 2006, 110, 12141-12148.

[9]   Curcó, D.; Nussinov, R.; Alemán, C. *J. Phys. Chem. B* 2007, 111, 10538-10549.

[10]   Basdevant, N.; Borgis, D.; Ha-Duong, T. *J. Phys. Chem. B* 2007, 111, 9390-9399.

[11]   Pizzitutti, F.; Marchi, M.; Borgis, D. *J. Chem. Theory Comput*. 2007, 3, 1867-1876.

[12]   Hinsen, K., Petrescu, A.-J., Dellerue, S.; Bellissent-Funel, M.-C.; Kneller, G. R. *Chem. Phys*. 2000, 261, 25-37.

[13]   Tama, F.; Gadea, F. X.; Marques, O.; Sanejouand, Y.-H. *Proteins* 2000, 41, 1-7.

[14]   Schuyler, A. D.; Chirikjian, G. S. *J. Mol. Graph. Model*. 2004, 22, 183-193.

[15]   Rader, A. J.; Chennubhotla, Ch.; Yang, L.-W.; Bahar, I. In *Normal Mode Analysis. Theory and Applications to Biological and Chemical Systems*; Cui, Q.; Bahar, I., Eds.; CRC Press: Boca Raton, FL, 2006, pp 41-64.

[16]   Heyden, A.; Truhlar, D. G. *J. Chem. Theory Comput*. 2008, 4, 217-221.

[17]   Gabb, H. A.; Jackson, R. M.; Sternberg M. J. E. *J. Mol. Biol*. 1997, 272, 106-120.

[18]   Imai, K.; Mitaku, S. *Chem-Bio. Inform. J*. 2003, 3, 194-200.

[19]   Golubkov, P. A.; Ren, P. Y. *J. Chem. Phys*. 2006, 125, 064103/1-064103/11.

[20]   Leherte, L.; Guillot, B.; Vercauteren, D.; Pichon-Pesme, V.; Jelsch, Ch.; Lagoutte, A.; Lecomte, Cl. In *The Quantum Theory of Atoms in Molecules - From Solid State to DNA and Drug Design*; Matta, C. F.; Boyd, R. J., Eds.; Wiley-VCH: Weinheim, 2007, pp 285-315.

[21]   Duan, Y.; Wu, C.; Chowdhury, S.; Lee, M. C.; Xiong, G. M.; Zhang, W.; Yang, R.; Cieplak, P.; Luo, R.; Lee, T.; Caldwell, J.; Wang, J. M.; Kollman, P. *J. Comput. Chem*. 2003, 24, 1999-2012.

[22]   Leung, Y.; Zhang, J.-S.; Xu, Z.-B. *IEEE T. Pattern Anal*. 2000, *22*, 1396-1410.

[23]   Leherte, L.; Dury, L.; Vercauteren, D. P. *J. Phys. Chem. A* 2003, 107, 9875-9886.

[24]   Gilbert, D. G. *Phylodendron, for Drawing Phylogenetic Trees*; Indiana University: Bloomington, IN, 1996; http://iubio.bio.indiana.edu/treeapp/

[25]   Dury, L. *DENDRO*; Facultés Universitaires Notre-Dame de la Paix: Namur, Belgium, 2002.

[26]   Amat, L.; Carbó-Dorca, R. *J. Chem. Inf. Comput. Sci*. 2000, 40, 1188-1198.

[27]   Amat, L.; Carbó-Dorca, R. *J. Comput. Chem*. 1997, 18, 2023-2039.

[28]   Kostrowicki, J.; Piela, L.; Cherayil, B. J.; Scheraga, H. A. *J. Phys. Chem*. 1991, 95, 4113-4119.

[29]   Leherte, L. *Acta Crystallogr. D* 2004, 60, 1254-1265.

[30] Abramowitz, M.; Stegun, I. A., Eds. *Handbook of Mathematical Functions with Formulas, Graphs, and Mathematical Tables*; Dover Publications: New York, NY, 1970.

[31] Hart, R. K.; Pappu, R. V.; Ponder, J. W. *J. Comput. Chem*. 2000, 21, 531-552.

[32] Borodin, O.; Smith, G. D. *Force Field Fitting Toolkit*; University of Utah: Salt lake City, UT; http://www.eng.utah.edu/~gdsmith/fff.html

[33] Becue, A.; Meurice, N.; Leherte, L.; Vercauteren, D. P. *Acta Crystallogr. D* 2003, 59, 2150-2162.

[34] Singh, U. C.; Kollman, P. A. *J. Comput. Chem*. 1984, 5, 129-145.

[35] Eisenmenger, F.; Hansmann, U. H. E.; Hayryan, S.; Hu, C.-K. *Comp. Phys. Comm*. 2006, 174, 422-429; http://www.smmp05.net/

[36] Nemethy, G.; Gibson, K. D.; Palmer, K. A.; Yoon, C. N.; Paterlini, G.; Zagari, A.; Rumsey, S.; Scheraga, H. A. *J. Phys. Chem.* 1992, 96, 6472-6484.

[37] Simms, A. M.; Toofanny, R. D.; Kehl, C.; Benson, N. C.; Daggett, V. *Prot. Eng. Design & Selection* 2008, 21, 369-377; http://www.dynameomics.org/

[38] Berman, H. M.; Westbrook, J.; Feng, Z.; Gilliland, G.; Bhat, T. N.; Weissig, H.; Shindyalov, I. N.; Bourne, P. E. *Nucleic Acids Res.* 2000, 28, 235-242; http://www.rcsb.org/pdb

[39] Guo, D.-Y.; Blessing, R. H.; Langs, D. A.; Smith, G. D. *Acta Cryst. D* 1999, 55, 230-237.

[40] Thomas, A.; Milon, A.; Brasseur, R. *Proteins* 2004, 56, 102-109.

[41] Arnautova, Y.A.; Jagielska, A.; Scheraga, H. A. *J. Phys. Chem. B* 2006, 10, 5025-5044.

[42] Matta, C. F.; Bader, R. F. W. *Proteins* 2003, 52, 360-399.

[43] Pichon-Pesme, V.; Lecomte, C., Lachekar, H. *J. Phys. Chem*. 1995, 99, 6242-6250.

[44] Jelsch, C.; Pichon-Pesme, V.; Lecomte, C., Aubry, A. *Acta Crystallogr. D* 1998, 54, 1306-1318.

[45] Yang, L.; Tan, C.-H.; Hsieh, M.-J.; Wang, J. M.; Duan, Y.; Cieplak, P.; Caldwell, J.; Kollman, P. A.; Luo, R. *J. Phys. Chem. B* 2006, 110,13166-13176.

[46] van der Spoel, D.; Lindahl, E.; Hess, B.; van Buuren, A. R.; Apol, E.; Meulenhoff, P. J.; Tieleman, D. P.; Sijbers, A. L. T. M.; Feenstra, K. A.; van Drunen, R.; Berendsen, H. J. C.; *Gromacs User Manual version 3.3*, 2005; http://www.gromacs.org/

[47] *OpenDX, The Open Source Software Project Based on IBM's Visualization Data Explorer*; Visualization and Imagery Solutions, Inc.; http://www.opendx.org/

[48] Guex, N.; Peitsch, M. C. *Electrophoresis* 1997, 18, 2714-2723; http://us.expasy.org/spdbv/

Chapter 6

THE EFFECT OF MOLECULAR STRUCTURE ON CONFINEMENT INSIDE THE β-CYCLODEXTRIN CAVITY

E. Alvira[*]

Departamento de Física Fundamental II;
Universidad de La Laguna; 38206 La Laguna. Tenerife. Spain

Abstract

A simulation method attempts to relate the microscopic details of a system (atomic masses, interactions between them, molecular geometry, etc.) to macroscopic properties of experimental interest (equation of state, structural parameters, etc.). The first step in performing a molecular simulation requires knowledge of the potential energy of interaction between the particles of the system, and one of the simplest methods used to obtain this treats the intermolecular energy as the sum of pairwise additive potentials (as in the force-field method). The model presented in this chapter does not consider the molecules as formed by rigid spherical particles (atoms or assemblies of atoms) but as continuum distributions of matter (without electrical charge), and this has two effects: it can be applied to many kinds of systems and extends the information on the system, relating a microscopic property (such as the interaction energy) with macroscopic properties (such as the structural parameters of the molecules). To simulate the interaction energy between β–cyclodextrin (β–CD) and molecules with different structure (cyclic, spherical and linear geometry), a model was constructed from a simple pairwise-additive Lennard-Jones potential combined with a continuum description of the cyclodextrin cavity and the guest molecule. This model reproduces the main energetic and structural features of the physisorption, in particular that guest molecule positions inside the cavity are more stable than outside the CD, as amply confirmed by molecular mechanics calculations. Therefore this model cannot explain the existence of non-inclusion complexes, and this is not a consequence of model assumptions such as rigidity of molecules or ignoring the effects of solvent. Neither does this model allow the effect of temperature to be included in the process. The aim of the present chapter is to analyse the effect of molecular structure on the mobility of the guest inside and around the β–CD, and the influence of temperature on inclusion complex formation. It was carried out by molecular dynamics, because this simulation method is based on the resolution of classical equations of

---

[*]E-mail address: malvira@ull.es

motion to determine the trajectories of the particles. From these trajectories we also determine the preferential binding site of the guest molecule and the probability of forming β−CD inclusion complex.

1. Introduction

In previous work we proposed an analytical model for the interaction energy between α-, β- and γ-cyclodextrin with guest molecules of different structure and size [1]. The intermolecular energy was then modelled by a Lennard-Jones potential which represents the attractive and repulsive interactions between all atoms and molecules in the system, and a continuum description of the cavity walls [2, 3]. The difference in molecular size was represented in that study by the potential energy parameter σ, but without including any parameter related to the structure of the guest molecules. This simple model is able to reproduce several quantitative and qualitative features of the interaction energy between cyclodextrin (CD) and atoms, and cyclic or spherical guest molecules. The adsorption energy obtained from this model is only valid when the guest centre of mass is located along the cavity axis, because for points away from it there is no analytical solution for the energy. Therefore this analytical model is inadequate to analyse the mobility of these types of molecules around β-CD and even inside the cavity, because the guest does not always move along the axis. The present chapter is a continuation and refinement of our previous model applied to the study of the physisorption of atoms and guest molecules with different structure (cyclic, spherical and linear geometry) in β-CD. Using a Lennard-Jones potential with a continuum description of the cavity walls and the guest molecule, the interaction energy is calculated for positions of the guest molecule inside and outside the β-CD, but not only along the cavity axis. In this case the interaction energy depends on the parameters of the potential and on molecular properties such as: number and distribution of atoms, composition, orientation and length of the linear molecule. This model elucidates how these factors influence the physisorption energy and contribute to forming inclusion complexes.

We also examine the influence of temperature on inclusion complex formation by means of molecular dynamics (MD), since this simulation method is based on the resolution of classical equations of motion to determine the trajectories of the particles depending on the initial conditions [4-6]. By treating the results generated in this process with statistical methods, one can obtain more detailed information about the potential parameters related to the size and composition of the guest molecule that influence formation of inclusion complexes with β−CD. In section 2 we present the theoretical methods, in section 3 their main results and in section 4 the comparison between molecular structures.

2. The Model

2.1. Expression of the Interaction Potential

The intermolecular energy W between the guest and the CD is modelled by a sum of pairwise Lennard-Jones potentials, which represents the attractive and repulsive interactions between all atoms and molecules in the system, even totally neutral ones

$$W = \sum_{i,j} V\left(\vec{r}_i, \vec{r}_j\right) \tag{1}$$

$$V\left(\vec{r}_i, \vec{r}_j\right) = 4\varepsilon_{ij}\left[\left(\frac{\sigma_{ij}}{r_{ij}}\right)^{12} - \left(\frac{\sigma_{ij}}{r_{ij}}\right)^{6}\right] \tag{2}$$

where r_{ij} characterizes the distance between each pair of atoms, i in the molecule and j in the CD. The corresponding parameters ε_{ij} and σ_{ij} are taken from the combination rules in terms of the parameters of the homopolar pairs [7, 8].

However, the essentials of the confinement effects should be preserved if we make the assumption of a continuum description of the cavity walls. We represent as W_1 the interaction energy between atoms, cyclic or spherical molecules with β-CD, and it can be calculated as:

$$W_1\left(\vec{r}_{mol}\right) = \rho_{CD} \int_S V\left(\vec{r}_{mol}, \vec{r}\right) d\vec{r} \tag{3}$$

where the guest-host interaction is represented by an average over the uniformly distributed atoms in the CD. ρ_{CD} is the superficial density of atoms in the CD cavity, $\vec{r}_{mol}$ is the position of the centre of mass of the guest molecule and $d\vec{r}$ is the differential element of surface (on the cavity) located at $\vec{r}$. The CD is considered as a truncated cone, h being the axial length ($h \approx 7$ Å), b the radius of the larger base of the cone ($b \approx 5$ Å for β-CD) and a the radius of the smaller top ($a \approx 4$ Å for β-CD) [9]. Here the Z axis is collinear with the cone axis (thus the XY plane is parallel to the cone base), and the origin of the coordinates lies at the centre of the cavity. For the conical surface we used a parametric representation [10]:

$$\vec{r}(u,v) = u\cos v\,\vec{i} + u\sin v\,\vec{j} + f(u)\vec{k} \tag{4}$$

Parameters u and v are the polar radius and angle, respectively. If $a \leq u \leq b$, then all the points located at the same distance u from the Z axis have the same coordinate $z = f(u)$ and they lie on the surface. In the case of the truncated cone, $f(u)$ is the equation of a straight line:

$$z = \alpha(b - u) \tag{5}$$

where $\alpha = \dfrac{h}{b-a}$ is its slope. In this case the element of surface is:

$$d\vec{r} = u\sqrt{1 + \left[\frac{df(u)}{du}\right]^2}\, du\, dv \tag{6}$$

where $(u,v) \in [a,b] \times [0,2\pi]$. Finally we can write:

$$W_1(\vec{r}_{mol}) = \rho_{CD} \sqrt{1+\alpha^2} \int_0^{2\pi} dv \int_a^b V(\vec{r}_{mol}, u, v) \, u \, du \qquad (7)$$

$W_1(\vec{r}_{mol})$ can be obtained as an analytical expression only when $\vec{r}_{mol}$ is located along the cavity axis, in other case it is necessary to resolve this integral with numerical methods [11]. The adsorption energy W_1 obtained from Eq. (7) for $\vec{r}_{mol} = (0,0,z_c)$ as a function of $s = \dfrac{z_c}{h}$, $q_1 = \dfrac{b}{h}$, $q_2 = \dfrac{a}{h}$ and $\beta = \alpha^2 + 1$ is [1]:

$$W_1(s) = \frac{A}{Q(s)} \left\{ \left[\sum_{i=1}^2 \frac{F_i(s)}{R_i^2(s)} \left(1 - \frac{2\sigma^{*6}}{5R_i^3(s)} \right) \right] + \frac{3\alpha\sigma^{*6}}{4Q^2(s)} \left[\sum_{i=1}^2 \frac{P_i(s)}{R_i^2(s)} \left(\frac{3}{5R_i^2(s)} + \frac{7\beta}{10Q^2(s)R_i(s)} \right) \right. \right.$$

$$\left. \left. + \frac{7\beta^2}{8Q^4(s)} \right] \right] + \frac{3\alpha}{2Q^2(s)} \left(-1 + \frac{21\beta^3\sigma^{*6}}{32Q^6(s)} \right) \left[\left(\sum_{i=1}^2 \frac{P_i(s)}{R_i(s)} \right) - \frac{\beta}{Q(s)} \left(B + \tan^{-1} \frac{s(q_1 - q_2 + \alpha) - q_1\beta}{Q^2(s) - P_1(s)P_2(s)} \right) \right] \qquad (8)$$

where $\sigma^* = \dfrac{\sigma}{h}$. Note that $0 \le s \le 1$ corresponds to the center of mass of the guest molecule inside the cavity. $B = 0$ in all cases, excepting $0.39 < s < 0.61$ for which $B = -\pi$.

$$A = \frac{294\varepsilon\sigma^{*6}}{q_1^2 - q_2^2} \qquad (9)$$

is an energy scaling factor and

$$Q(s) = s - \alpha q_1 \qquad (10)$$

$$F_1(s) = s \qquad (11)$$
$$F_2(s) = 1 - s \qquad (12)$$

$$P_1(s) = -\alpha s - q_1 \qquad (13)$$

$$P_2(s) = \alpha(s-1) + q_2 \qquad (14)$$

$$R_i(s) = F_i^2(s) + q_i^2 \quad i = 1,2 \qquad (15)$$

If we make the approximation of replacing the discrete summation by means of a continuous integration, the interaction energy W_2 between linear molecules and β-CD can be calculated as:

$$W_2(\vec{r}_{mol}) = \rho_{CD} \; \rho_{mol} \int_L d\vec{l} \int_S V(\vec{r}_l, \vec{r}) \, d\vec{r} \qquad (16)$$

where ρ_{mol} is the linear density of atoms in the guest molecule and $d\vec{l}$ is the differential of length (on the linear molecule) located at $\vec{r}_l$. The interaction energy W_2 depends on the configuration of the guest molecule (orientation and centre of mass position) represented by $\vec{r}_{mol}$.

For the linear molecule we also use a parametric representation [10]:

$$\vec{r}_l(\vec{r}_0, \theta, \varphi) = (x_0 + l\sin\theta\cos\varphi)\vec{i} + (y_0 + l\sin\theta\sin\varphi)\vec{j} + (z_0 + l\cos\theta)\vec{k} \qquad (17)$$

where $\vec{r}_0 = (x_0, y_0, z_0)$ is the position of the guest's centre of mass and the angles $(\theta, \varphi) \in [0, \pi] \times [0, 2\pi]$ define the orientation of the molecule with respect to the absolute frame (X, Y, Z). The element of length is $d\vec{l} = dl$ and $l \in \left[-\dfrac{L}{2}, \dfrac{L}{2}\right]$, where L is the length of the molecule. Finally we can write:

$$W_2(\vec{r}_0, \theta, \varphi) = \rho_{CD} \, \rho_{mol} \sqrt{1 + \alpha^2} \int_{-\frac{L}{2}}^{\frac{L}{2}} dl \int_0^{2\pi} dv \int_a^b V(\vec{r}_0, \theta, \varphi, l, u, v) \, u \, du \qquad (18)$$

$W_2(\vec{r}_0, \theta, \varphi)$ cannot be obtained as an analytical expression, it is necessary to resolve this integral with numerical methods even if $\vec{r}_0$ is located along the cavity axis. The interaction energy $W_2(\vec{r}_0, \theta, \varphi)$ depends on parameters related to the geometry of the linear molecule (defined by its length L), the composition of the guest and the distribution of atoms in it (characterized by ρ_{mol} and the parameters of the Lennard-Jones potential σ_{ij}, ε_{ij}).

When we consider the interaction energy W by the integration in Eq. (3) or (16), we are substituting the discrete atoms of the CD by a uniform distribution of mass on the cavity surface. Therefore, we can also replace the potential parameters for the different atoms belonging to the molecule $(\sigma_i, \varepsilon_i)$ and β-CD $(\sigma_j, \varepsilon_j)$ by some representative values for the composition of both systems. In order to bring out more clearly the dependence of W on the composition of the guest molecule, we do not consider the values of these parameters for β-CD and the guest separately, but represent the Lennard-Jones parameters for the interaction between the atoms of the CD and the molecule by σ and ε.

In molecular mechanics calculations of the potential energy surface where the β-CD and guest molecule are described by all their atoms, the interaction energy is determined for each position of the centre of mass $\vec{r}_0$ after minimization over the Euler angles of the guest molecule [12, 13]. In the present model, the interaction energy is minimized for different molecular orientations only for linear molecules and as we are dealing with a conical continuum geometry, for every plane Z = constant, the potential energy is the same for points (x_0, y_0) located at the same distance d from the cavity axis $\left(x_0^2 + y_0^2 = d^2\right)$. Therefore, for atoms, cyclic or spherical molecules, we characterize the guest configuration for each energy by the distance d from the cavity axis and the Z coordinate $\left(\vec{r}_{mol} = (d, z_0)\right)$. The orientation of a linear molecule is defined by the two polar angles and in this case, the potential energy is calculated for different molecular orientations (about 900) and the minimum for these values is assigned to the position $\vec{r}_0 = (d, z_0)$. However, the linear guest adopts different orientations in points located at the same distance d and Z coordinate to minimize the energy: while the polar angle formed with the cavity axis θ is the same, the value of φ is different from one point to another. Therefore, some configurations of the linear molecule ($\vec{r}_0$, θ, φ) are equivalent in that they have the same energy, for this reason we characterize the guest configuration for each energy by the centre of mass position (defined by d and the Z coordinate) and the molecular orientation (characterized only by the polar angle θ).

The potential energy is determined for different configurations of the guest $\vec{r}_{mol}$, inside and outside the CD. In each plane Z = constant, about 700 points are explored and the range of variation along the Z axis is about 11 Å. The results obtained are represented as the potential energy surfaces, penetration potentials and the inclusion complex configuration, and so their comparison with the results of the all atoms model confirms the suitability of the continuum intermolecular energy for these systems.

The curve joining the minimum potential energy for every plane Z = constant defines the penetration potential, which describes the variation in interaction energy when its path through the cavity is non-axial. The position and orientation of the guest molecule for which we obtain the absolute minimum potential energy gives the geometry of the inclusion complex.

The potential energy surfaces are represented by partitioning the variation range of the Z axis in the β-CD cavity into four parts, depending on the position of the guest molecule centre of mass near the top of the cone (region I), near the centre of the cavity (regions II and III) and near the cone base (region IV). The length of each domain is about 2 Å and the potential surface for each region is determined as the minimum energy for every point on the plane in the corresponding interval of Z.

2.2. Simulation Method

From the continuum model presented in this chapter for the interaction energy between a guest molecule and β-CD, we consider rigid non-polar guest molecules. Since continuity is assumed for the guest and the cavity, this interaction energy is not capable of reproducing the

hydrogen bonds formed by the molecule with CD. We do not consider the potential parameters for β-CD and the guest separately, but the interaction between the atoms is represented by the Lennard-Jones parameters (σ, ε), where σ defines a scale of length and ε governs the strength of the interaction.

We place the origin of the reference system at the centre of mass of the CD and the space-fixed frame over the principal axis of the β-CD. The configuration of the atom, cyclic or spherical molecule is given by the coordinates of its centre of mass, while the configuration of the linear guest includes also the molecular orientation, which is defined by the polar angles (θ, φ) formed with respect to the absolute frame (X, Y, Z). In rigid-body dynamics the molecular motion can be decomposed into two completely independent parts, translational motion of the centre of mass and rotation about the centre of mass. A basic result of classical mechanics is that the former is governed by the total force acting on the body, whereas the latter depends on the total applied torque. For a linear molecule, the angular velocity and the torque must be perpendicular to the molecular axis at all times [5, 6].

To integrate the equations of motion it is necessary to establish the initial conditions of the guest molecule: centre of mass position and translational velocity for atoms, cyclic or spherical molecules; centre of mass position, orientation and velocities (translational and rotational) for linear guests. The magnitude of the initial velocities depends on the temperature of the process, but the direction of the translational velocity in each trajectory and the initial centre of mass position are determined randomly. The simulation time for each trajectory is 1 ns with a step of 1 fs (10 fs for linear molecules with length $L < 5$ Å) and the configuration and energies (kinetic and potential) were written every 100 steps. We use an in-house program written in Fortran and the equations of motion to perform constant temperature molecular dynamics are integrated numerically using a variant of the leap-frog scheme (proposed by Brown and Clarke) [14], constraining the rotational and translational kinetic energies separately [15].

To determine the preferential binding site of the guest molecule, the number densities of presence in a volume element are calculated. We define a grid in which the distance between two consecutive points is 0.5 Å and the number of guest positions in each volume element is the resulting number density for each trajectory and for the guest [16-18]. The position probability density is calculated by dividing the number density in a volume element by the total number of centre of mass positions for the guest.

We calculate different trajectories with initial configurations of the guest on the exterior of the β-CD: near the primary (narrow end) and secondary rims (wide end) of the CD, and outside the cavity walls. However the molecule can enter the cavity and then form an inclusion complex only for certain initial positions of its centre of mass, and these positions are always near the rims of the CD and never outside the cavity walls.

The simulation is carried out for molecules with different size, length and composition, and at different temperatures.

3. Results and Discussion

3.1. Interaction Energy

The interaction energy W_1 depends on the size and composition of the atom, cyclic or spherical molecule through the potential parameters (σ, ε), and the position of its centre of mass $\vec{r}_{mol}$. In order to perform a comparative study we consider different values for the parameter σ to represent the interaction between β-CD and the guest, because ε only acts as a scaling factor on the potential energy W_1.
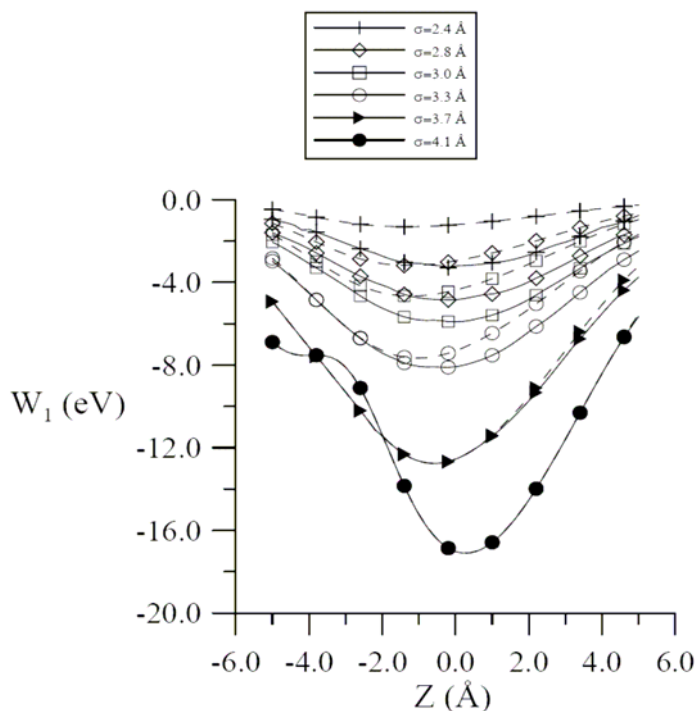
Figure 1. The penetration potential (solid curves) and the interaction energy along the cavity axis (dashed curves) for atoms, cyclic or spherical molecules with different σ and $\varepsilon = 0.006$ eV.

Figure 1 exhibits the penetration potential (solid curves) for guest molecules with different size and composition. It clearly resembles a well potential, deepening as the atomic or molecular size of the guest increases, and with small differences in the Z coordinate of the minimum values $W_{1_{min}}$ (near the cavity centre). This behaviour is similar to the well potential for the interaction between a guest molecule and CD, obtained by the sum of pairwise-additive potentials (as in molecular mechanics calculations) [19], and it means that guest molecule positions inside the cavity are more stable than outside the β-CD. Figure 1 also exhibits the interaction energy along the cavity axis (dashed curves). The two curves are seen to agree for molecules with $\sigma = 4.1$ Å, as the size of the guest decreases there are some

small differences in the energy values near the larger base of the β-CD, and for small guest molecules the penetration potential is very different from the energy on the axis because in this case the most stable molecular positions are located near the cavity walls. There are also greater differences in the values of W_1 on the potential surface as the guest increases. The centre of mass position at the minimum energy $W_{1_{min}}$ is determined by (d_{min}, z_{min}) (table 1) and it can be seen that the distance between this position and the cavity axis d_{min} depends on parameter σ by $D_{min} = 1.12\,\sigma$, $D_{min} = u(z_{min}) - d_{min}$ being the distance between the cavity walls and the molecule in the more stable configuration and $u(z_{min})$ being the cone radius at the z_{min} coordinate. Therefore, the part played by the potential parameters in the interaction energy W_1 is similar to that in the Lennard-Jones potential between a pair of atoms: ε governs the strength of the interaction and σ is related to the position of the minimum energy ($r_{min} = 1.12\,\sigma$) [7].

Table 1. The minimum energy $W_{1_{min}}$, the centre of mass position in the minimum energy (d_{min}, z_{min}) and the cone radius at the z_{min} coordinate for atoms, cyclic or spherical molecules with different σ and $\varepsilon = 0.006$ eV.

σ (Å)	$W_{1_{min}}$ (eV)	d_{min} (Å)	z_{min} (Å)	$u(z_{min})$ (Å)
2.4	−3.20	2.01	−0.2	4.48
2.8	−4.85	1.50	−0.2	4.48
3.0	−5.95	1.23	−0.4	4.46
3.3	−8.20	0.82	−0.2	4.48
3.7	−12.76	0.00	−0.6	4.43
4.1	−17.10	0.00	0.2	4.54

Figure 2a exhibits the penetration potential for linear molecules with different length and the same composition (σ = 2.7 Å, $\varepsilon = 0.006$ eV). Figure 2b shows the variation of the potential energy along the Z axis for a guest with length $L = 7$ Å and different composition. The numbers on the right-hand side on the graphs correspond to the values of the parameters used in every figure and they are related in tables 2 and 3, as well as the configurations and the energy minima. It can be observed that for every case the penetration potential resembles a well potential, which is deeper as the length or atomic size of the molecule increases. These results are similar to those obtained by the all atoms method only for molecules with length $L < 6$ Å whatever is the molecular composition [20], therefore the shape of the penetration potential for linear molecules is not a consequence of the molecular length. The centre of mass position in the minimum energy $W_{2_{min}}$ is determined by (d_{min}, z_{min}) (tables 2, 3) and it can be seen that the distance between this position and the cavity axis d_{min} is only dependent on parameter σ, with differences of about 0.1 Å. This means that for every length there is approximately the same distance between the cavity walls and the molecule

$D_{min} = u(z_{min}) - d_{min}$ in the more stable configuration, $u(z_{min})$ being the cone radius at the z_{min} coordinate, as it happens in the continuum model for the interaction between cyclic or spherical molecules and β-CD. The orientation of the molecule inside the cavity depends on the position of its centre of mass and molecular length, but for $L > 6$ Å there is no stable configuration of the guest with $\theta = 90°$, because the energy is repulsive. When the molecule is located near the cavity walls, the polar angle θ tends towards 12° for any length and composition of the guest. The configuration of the inclusion complex (the molecular orientation and position of the guest's centre of mass at the absolute minimum) (tables 2, 3) also depends on σ and L. In general, as the molecular length or atomic size increases, the most stable position of the guest's centre of mass varies from near the centre of the cavity to near the larger cone base. As regards the orientation of the guest in the inclusion complex, the maximum value of θ observed in all cases is 24° and the molecule is located parallel to the cavity axis when $\sigma \geq 4$ Å.

Table 2. Configuration of the linear molecule in the potential energy minima
$W_{2_{min}}$ ($\varepsilon = 0.006$ eV) and number of reference in figure 2a.

L (Å)	σ (Å)	d_{min} (Å)	z_{min} (Å)	θ_{min} (*deg.*)	$W_{2_{min}}$ (eV)	ref. no.
4	2.7	1.6	-0.2	24.0	-0.58	1
6	2.7	1.6	0.0	18.0	-0.81	2
7	2.7	1.6	0.0	18.0	-0.90	3
8	2.7	1.7	0.0	12.0	-0.98	4
9	2.7	1.7	0.0	12.0	-1.05	5
10	2.7	1.7	0.6	18.0	-1.14	6

Table 3. Configuration of the linear molecule in the potential energy minima
$W_{2_{min}}$ ($\varepsilon = 0.006$ eV) and number of reference in figure 2b.

L (Å)	σ (Å)	d_{min} (Å)	z_{min} (Å)	θ_{min} (*deg.*)	$W_{2_{min}}$ (eV)	ref. no.
7	2.3	2.1	0.0	18.0	- 0.60	1
7	2.5	1.8	-0.2	18.0	- 0.79	2
7	2.7	1.6	0.0	18.0	- 0.90	3
7	3.0	1.3	-0.2	12.0	- 1.23	4
7	3.5	0.4	-0.6	12.0	- 2.12	5
7	3.7	0.2	-0.4	6.0	- 2.59	6
7	4.0	0.0	0.2	0.0	- 3.20	7
7	4.3	0.0	1.4	0.0	- 3.26	8

The σ parameters selected in this work are of the same order of magnitude as pairs of atoms like C-C, C-O, O-O, etc. and the minimum interaction energy between them in the equilibrium position is $-\varepsilon$ (about -0.008 eV for such pairs) [7]. If we consider this ε value for the interaction between cyclic or spherical molecules and the cavity, the minimum energy $W_{1_{min}}$ ranges from -4.3 eV for $\sigma = 2.4$ Å to -22.8 eV for $\sigma = 4.1$ Å, therefore

the confinement in β-CD involves an intensification in the interaction, greater even for cyclic or spherical molecules than for linear ones. For instance if we apply the present model to cyclopentadiene taking into account the results obtained by a force field method [19], it can be represented by the parameters $\sigma = 3.5$ Å and $\varepsilon = 0.0004$ eV, ε being 5 times smaller than for linear molecules as acrylonitrile or methyl vinyl ketone.

Figure 3 shows the potential energy surfaces for atoms, cyclic or spherical molecules with $\sigma = 3.3$ Å, $\varepsilon = 0.006$ eV (figure 3a) and for linear guest with $L = 6$ Å, $\sigma = 2.5$ Å, $\varepsilon = 0.006$ eV (figure 3b). They are similar in the size of the regions where the energy is attractive, this feature being a consequence of the cavity geometry. The main differences in the potential energy surfaces are related to the magnitude of the energy, which is largely dependent on the molecular composition rather than its length or geometry.
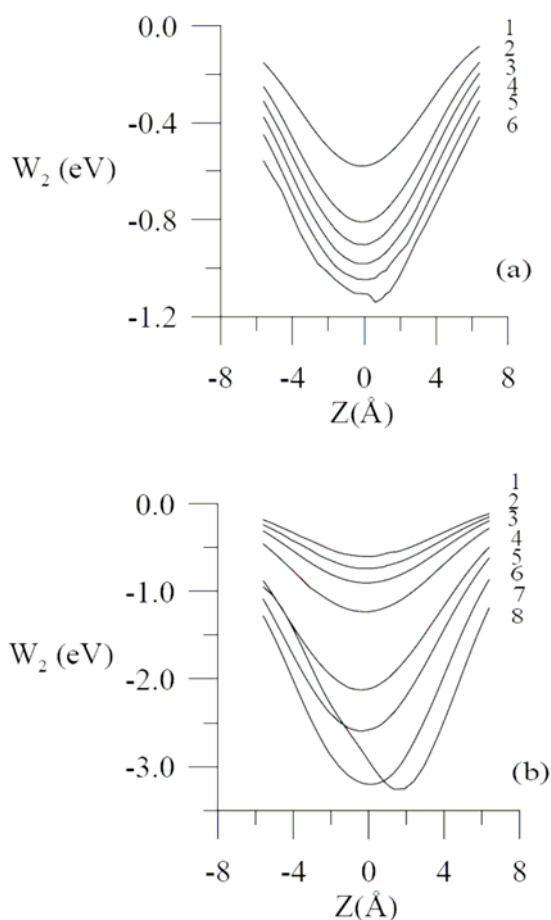
Figure 2. (a) The variation in potential energy along the Z axis for linear molecules with different length and the same composition ($\sigma = 2.7$ Å, $\varepsilon = 0.006$ eV). The numbers on the right-hand side on the graph correspond to the values of the parameters related in table 2. (b) Same as (a) for guest molecules with length $L = 7$ Å and different composition ($\varepsilon = 0.006$ eV). The numbers on the right-hand side on the graph correspond to the values of the parameters related in table 3.

The main discrepancies between the intermolecular potential presented in this chapter and the results obtained by the all atoms model derive from the position of the guest centre of mass in the configuration of the inclusion complex, because this continuum model is only able to reproduce the position in the plane Z = constant by the distance from the cavity axis instead of the (X, Y) coordinates.
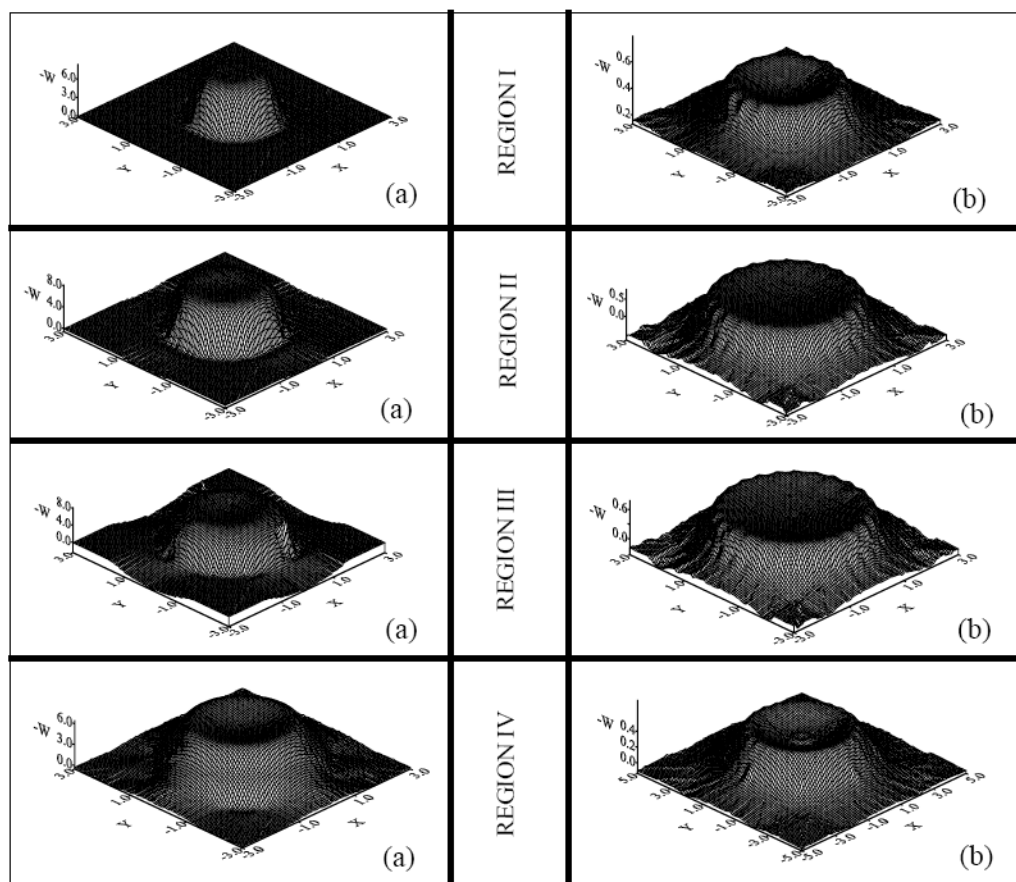
Figure 3. (a) Potential energy surfaces for atoms, cyclic or spherical molecules with $\sigma = 3.3$ Å and $\varepsilon = 0.006$ eV. (b) Same as (a) for linear molecules with length $L = 6$ Å, $\sigma = 2.5$ Å and $\varepsilon = 0.006$ eV.

3.2. Molecular Dynamics for Atoms, Cyclic or Spherical Molecules

The evolution of the guest molecule in each trajectory and the resultant average energy are different because the initial conditions determine the integration of the equations of motion. The initial velocity does not influence the number densities and the mean energy of the process, but the starting centre of mass position determines the behaviour of the guest in each process and affects decisively the probability of forming inclusion complex. When the guest initial position is located outside the cavity walls the molecule always stays on the outside of the β-CD where it does not reach a stable configuration, moving around the cavity continually or even tending to move away. During trajectories whose starting molecular

configuration is near the rims of the β-CD the guest tends to enter the cavity, remain inside forming an inclusion complex or exit from it after a period, depending on the potential parameters. However, inside the cavity the molecule does not reach a stable configuration because it is fluctuating around the most probable position $\vec{r}_p$ with an amplitude that also depends on parameters (σ, ε). This effect can be appreciated in figure 4 where the position probability for molecules with different σ and the same ε is presented, a schematic representation of the projections of the cavity in the plane has been also inserted. The range of the oscillations inside the β-CD increases as the molecular size decreases which means greater delocalization for the guest and then smaller values for the position probability. The maximum probability P_{max} and the corresponding position of the guest $\vec{r}_p = \left(d_p, z_p \right)$ are presented in table 4. It can be seen that the most probable configuration varies from near the cavity walls to the centre of the β-CD as the molecular size increases, and taking into account the method used to calculate the position probability density, we conclude that the most probable configuration of the complex in this type of molecules agrees with that of minimum energy. The mean energy for the simulation W_{mean} of different molecules is also presented in table 4. W_{mean} is greater than $W_{1_{min}}$ because the energy of every position with probability different to zero contribute to the average energy, for bigger molecules there are greater differences between the values of energy inside the β-CD and then greater differences with $W_{1_{min}}$.

Table 4. The maximum probability P_{max}, the most probable configuration of the guest $\vec{r}_p = \left(d_p, z_p \right)$ and the mean energy W_{mean} for the simulation of atoms, cyclic or spherical molecules with $\varepsilon = 0.006$ eV at temperature $T = 293$ K

σ (Å)	d_p (Å)	z_p (Å)	P_{max} (%)	W_{mean} (eV)
2.4	1.80	−0.5	2.7	−2.28
2.8	1.80	−0.5	9.1	−3.62
3.0	1.00	−0.5	25.1	−4.23
3.3	0.71	−0.5	42.1	−6.23
3.7	0.50	−0.5	68.7	−9.89
4.1	0.00	0.00	81.0	−13.20

For molecules with $\sigma \geq 3.0$ Å the parameter ε only acts as a scaling factor in W_{mean} and does not influence the position probability density. For molecules with $\sigma < 3.0$ Å ε affects the amplitude of oscillations around the most probable position: greater value of parameter implies smaller fluctuations (figure 5). The meaning of ε as strength of the interaction is also reflected in the dynamical behaviour of the system, because while the guest with $\sigma = 2.8$ Å and $\varepsilon = 0.006$ eV remain inside the cavity for all the simulation time, for

$\varepsilon = 0.003$ eV the molecule only spents inside a period (inclusion time t) after which it exits from the CD and moves away. This average inclusion time is 394 ps at 293 K and decreases as temperature increases (381 ps at 323K and 356 ps at 363K).
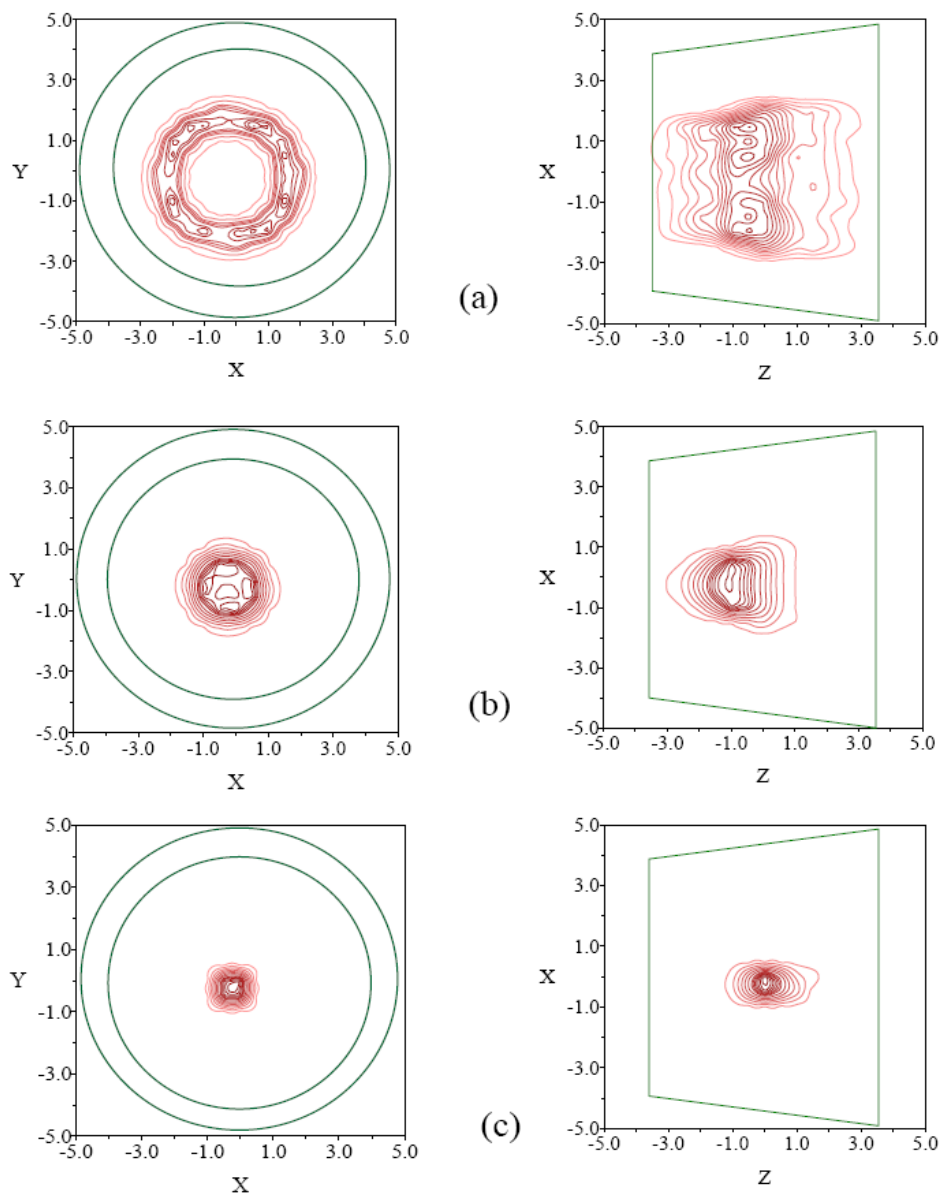
Figure 4. Projections on the XY and XZ plane of the probability density of presence for atoms, cyclic or spherical molecules with different σ, $\varepsilon = 0.006$ eV at temperature $T = 293$ K: (a) $\sigma = 2.4$ Å, (b) $\sigma = 3.3$ Å, (c) $\sigma = 4.1$ Å. A schematic representation of the projections of the cavity has been inserted in the figure.
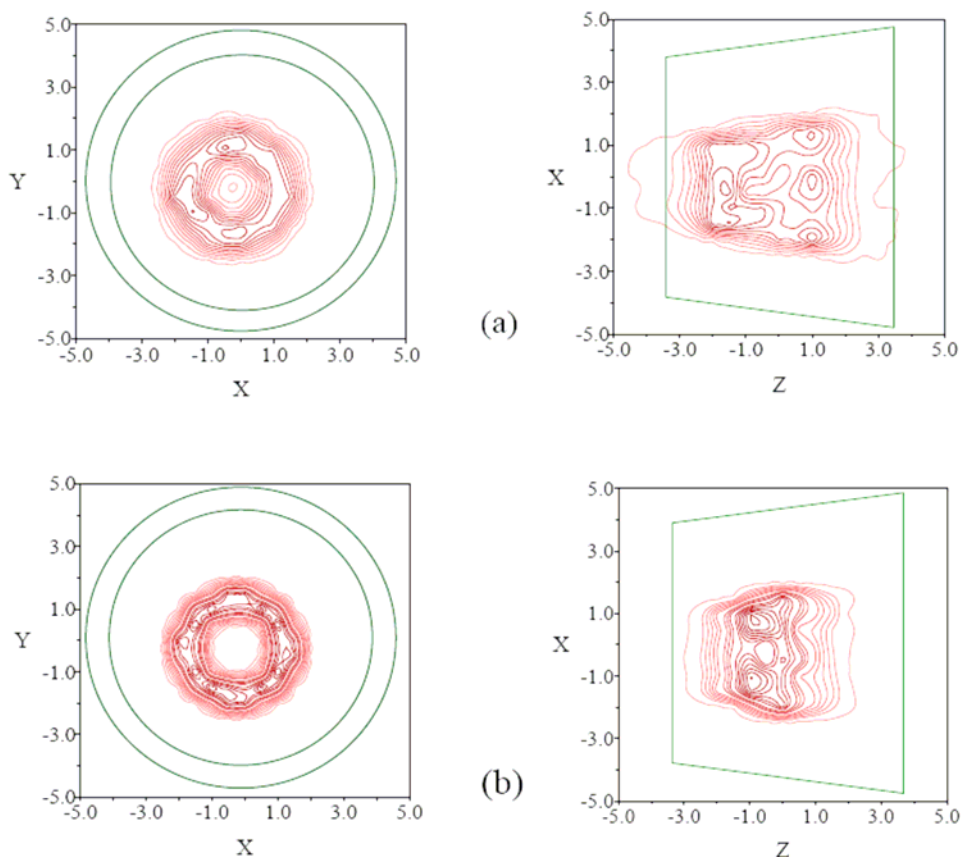
Figure 5. Projections on the XY and XZ plane of the probability density of presence for atoms, cyclic or spherical molecules with different ε, $\sigma = 2.8$ Å at temperature $T = 293$ K: (a) $\varepsilon = 0.003$ eV, (b) $\varepsilon = 0.006$ eV. A schematic representation of the projections of the cavity has been inserted in the figure.

3.3. Molecular Dynamics for Linear Molecules

In this case, the initial conditions of the guest molecule in each trajectory affect the simulation in a different way: while the molecular orientation and velocities hardly influence the number densities and the mean energy of the process, the greatest differences in these values are due to the initial position of the guest centre of mass, which also determines the behaviour of the guest in each process because it can give rise to stable or unstable configurations. In some cases the molecule moves for several ps in the trajectory until it reaches a stable configuration in which it remains for the longest period in the simulation. The complex was considered stabilized when the difference between the angles or centre of mass coordinates in two consecutive positions was lower than 0.001° and 0.01 Å respectively.

The results depend on the length L of the linear molecule but the molecular evolution is similar for $L < 5$ Å and different for lengths $L \geq 5$ Å, so we can analyse the mobility of the guest for each category:

a) On comparing the evolution of a linear molecule with length $L < 5$ Å characterized by parameters (σ, ε_1) and another with (σ, ε_2), different trajectories that always lead to the same results were found: the parameter ε did not affect the resulting position probability density and acts as a scaling factor on the average energy. Therefore the simulation was performed assuming the interaction between β-CD and guest molecule to be represented by the potential parameter σ, as in the continuum model. There are two different types of behaviour, depending on the molecular composition, and then two categories characterized by the potential parameter σ: $\sigma < 3.5$ Å and $\sigma \geq 3.5$ Å.

- $\sigma < 3.5$ Å. The mean energy in each trajectory for $L = 4.5$ Å, $\sigma = 3$ Å, $\varepsilon = 0.07$ kcal/mol at temperature $T = 293$ K is detailed in table 5 and the probability density of presence is shown in figure 6a, where a schematic representation of the projections of the cavity and the guest in the plane has been inserted. When the starting positions of the guest are near the primary (processes P1, P2, P3) and secondary rims (P4, P5, P6) of the β–CD, the linear molecule tends to move towards and remain inside it, forming a stable complex. The greatest probability of presence (about 62%) corresponds to inner positions of the guest centre of mass at 1.5 Å from the wide end of the CD, forming an angle $\theta \approx 90^{\circ}$ with the cavity axis (figure 6a). This is an inclusion complex but with a different configuration than that of minimum energy, in which the guest is located near the CD centre of mass with $\theta \approx 24^{\circ}$ and whose energy is -10.05 kcal/mol [2]. As the σ parameter increases, the guest tends to position itself nearer the wide end of the β–CD.
- $\sigma \geq 3.5$ Å. In this case the linear molecule cannot penetrate into the cavity and always remains outside the β–CD, where it can form stable non-inclusion complexes. The average energy in each trajectory for $L = 4.5$ Å, $\sigma = 4$ Å, $\varepsilon = 0.07$ kcal/mol, $T = 293$ K is shown in table 5 and the probability density of presence in figure 6b. During the processes P1, P2 or P3, the guest stays near the narrow end of the CD, forming an angle of about 90º with the cavity axis and the mean energy is higher than the trajectories P4, P5 or P6, where the most stable position is external and parallel to the wide rim of the β–CD. In this case, the guest has the same probability of forming the two complexes (about 30%) because we have considered the same number of trajectories starting from each rim of the CD.

This calculation was also carried out at temperatures $T = 323$ and 363 K and we conclude that, although the stabilization time increases with temperature, it does not affect the mean energy of the simulation or the position probability density for molecules with $L < 5$ Å.

b) For linear molecules with length $L \geq 5$ Å the molecular evolution is similar for every value of parameter σ. During trajectories P1, …, P6, the guest tends to move towards the cavity, remain inside it (forming an inclusion complex) and exit from the CD where the linear molecule can reach a stable configuration, or even tend to move away. However, the guest does not pass through the cavity in every process, it can enter and exit from the same rim of the CD during the trajectory. The time spent inside the cavity (inclusion time t) varies from

several to a hundred ps and depends on the length and composition of the guest, the temperature and initial conditions of the trajectory. Molecular dynamics calculations performed on complexes of phenol and benzoic derivatives with α–CD also suggest the guest possibly moves in and out the host on a 10-100 ps scale [21].
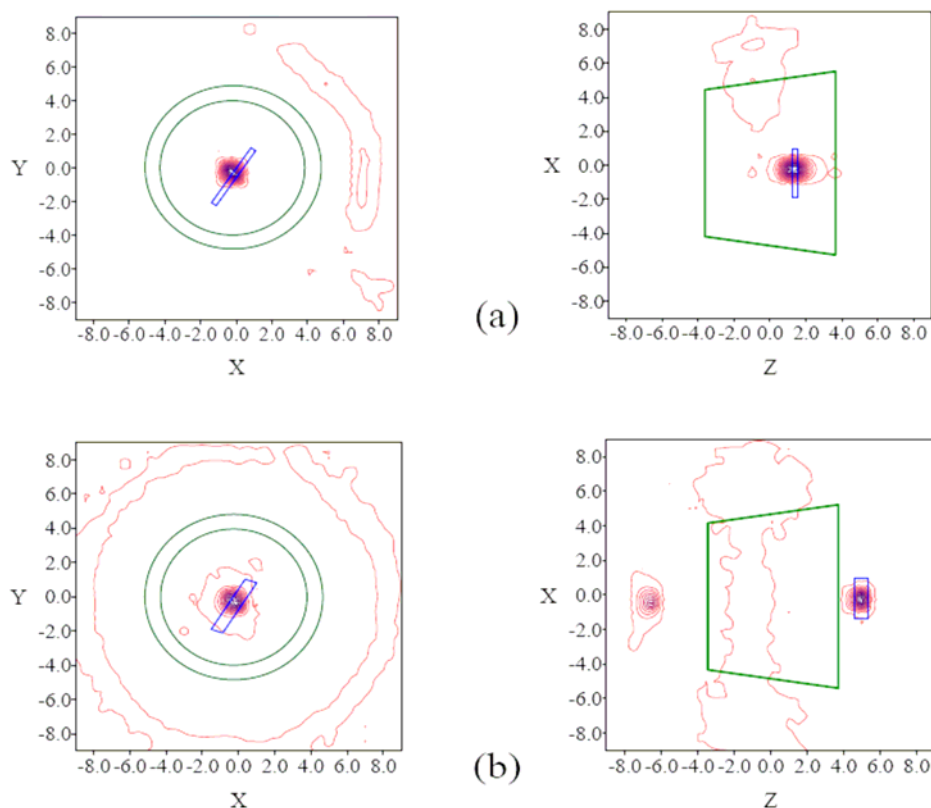
Figure 6. (a) Projections on the XY and XZ plane of the probability density of presence for linear molecules with $L = 4.5$ Å, $\sigma = 3$ Å, $\varepsilon = 0.07$ kcal/mol at temperature T = 293 K. A schematic representation of the projections of the cavity and the guest has been inserted in the figure. b) Same as (a) for linear molecules with $L = 4.5$ Å, $\sigma = 4$ Å, $\varepsilon = 0.07$ kcal/mol at temperature T = 293 K.

The inclusion time t during trajectories P1, …, P6 for $L = 7$ Å, $\sigma = 3$ Å, $\varepsilon = 0.07$ kcal/mol at temperature T = 293 K is presented in table 5. This inclusion time depends on the initial conditions and temperature of the process as it happens for cyclic or spherical molecules. The time spent by the linear guest inside the cavity t decreases as temperature rises, the differences being smaller when σ is greater (the average value of t for this molecule is 2.2 ps at T = 363 K). As can be seen, the time t is negligible compared to the simulation time (1 ns) and therefore does not influence the probability of presence, whose greatest value corresponds to positions of the guest near the cavity walls (about 8.6 %) (figure 7a). However the linear molecule does not reach a stable configuration there, on the contrary the most probable external configuration (about 7.3 %) has the guest centre of mass at 1.5 Å from the wide rim of the CD, with $\theta \approx 77°$ (figure 7a). If we consider the length of time in

trajectories P1, …, P6 as the corresponding inclusion time, the greatest probability of presence (about 20%) corresponds to outer positions of the guest centre of mass at 0.5 Å from the wide end of the CD, forming an angle $\theta \approx 64^\circ$ with the cavity axis (figure 7b), although there is another possible position near the narrow rim (about 15%).

Table 5. The mean potential energy (in kcal/mol) for the simulation of linear molecules with $\varepsilon = 0.07$ kcal/mol at temperature $T = 293$ K

Process	$L = 4.5$ Å $\sigma = 3$ Å Mean energy (kcal/mol)	$\sigma = 4$ Å Mean energy (kcal/mol)	$L = 7$ Å Mean energy (kcal/mol)	t (ps)	$\sigma = 3$ Å Mean energy (t) (kcal/mol)
P1	-6.26 ± 0.42	-5.28 ± 0.38	-3.49 ± 2.33	3.5	-10.05 ± 3.15
P2	-6.28 ± 0.37	-5.19 ± 0.34	-3.02 ± 0.85	1.9	-7.70 ± 2.95
P3	-6.32 ± 0.31	-5.14 ± 0.40	-3.52 ± 1.63	1.8	-7.36 ± 2.73
P4	-6.29 ± 0.29	-7.12 ± 0.35	-3.61 ± 0.72	4.3	-6.78 ± 1.95
P5	-6.24 ± 0.32	-7.16 ± 0.37	-2.89 ± 0.62	1.3	-6.14 ± 1.11
P6	-6.27 ± 0.39	-7.18 ± 0.43	-3.05 ± 0.41	1.1	-3.87 ± 1.10

The average energy over the simulation time for $L = 7$ Å, $\sigma = 3$ Å, $\varepsilon = 0.07$ kcal/mol at temperature $T = 293$ K is presented in table 5. The average energy over the simulation time becomes lower for linear molecules with $L \geq 5$ Å and the same composition as the molecular length increases (i. e. -4.3 kcal/mol for $L = 9$ Å, $\sigma = 3$ Å, $\varepsilon = 0.07$ kcal/mol), although always higher than $L = 4.5$ Å because those molecules tend to remain outside the cavity for most of the simulation time. The average energy over the inclusion time for a linear molecule with $L = 7$ Å, $\sigma = 3$ Å, $\varepsilon = 0.07$ kcal/mol at temperature $T = 293$ K is also presented in table 5. There is no proportional relation between the inclusion time and the mean energy of the trajectory, lower interaction energies correspond to when a larger part of the linear molecule is inside the cavity. This is also the reason for the wide differences between the mean energies of the processes. On comparing the average energy during the inclusion time for $L = 7$ and 4.5 Å, it can be concluded that the β–CD inclusion complexes formed with linear molecules of these lengths and the same composition yield lower average energies as the molecular length increases, in agreement with MM calculations. The influence of molecular relaxation on the interaction energy between β–CD and the guest is widely confirmed in molecular mechanics calculations. However, many theoretical studies carried out by rigid-body molecular dynamics have produced accurate results in accordance with experiments, depending on the simulation period. Time is therefore a decisive factor.

The dynamics simulation program used in this chapter was previously employed to investigate the enantioselectivity of equol in β–CD [18]. One of the results obtained in that study was that the guest remained inside the cavity for most of the simulation time, in agreement with experimental findings. The discrepancy with the results of the present chapter is due to the differences in potential energy, because the van der Waals contribution to the interaction energy between the chiral host and each equol enantiomer [22] is not in accordance with the continuum model of physisorption energy for those linear molecules

whose interaction with β–CD is represented by one pair of values for the Lennard-Jones parameters (σ, ε) and length $L \geq 5$ Å [2] (applied in the present chapter).
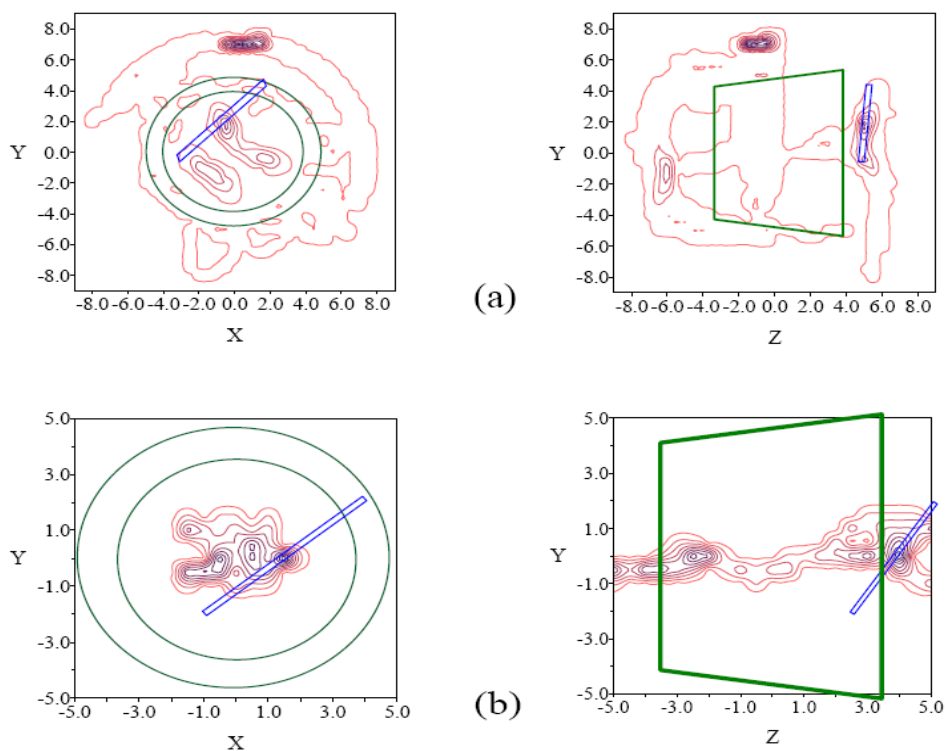
Figure 7. (a) Projections on the XY and YZ plane of the probability density of presence over the simulation time for linear molecules with $L = 7$ Å, $\sigma = 3$ Å, $\varepsilon = 0.07$ kcal/mol at temperature $T =$ 293 K. A schematic representation of the projections of the cavity and the guest has been inserted in the figure. (b) Same as (a) for the probability density of presence over the inclusion time.

4. Comparison between Molecular Structures

For each type of guest molecules the interaction energy presents some common features and also some differences. The main similarities are the following:

- The penetration potential that represents the interaction between β–CD and molecules with different size, composition and structure resembles a well potential, which is deeper as the atomic or molecular size of the guest increases.
- The role of the potential parameters in the interaction energy is similar to that in the Lennard-Jones potential between a pair of atoms: ε governs the strength of the interaction and σ is related to the position of the minimum energy ($r_{\min} = 1.12\,\sigma$).
- The confinement of the molecule in the β-CD cavity produces an enhancement of the physisorption energy seen in the interaction of a pair of atoms characterized by the

same potential parameters, greater for cyclic or spherical molecules than for linear ones

- The size of the regions where the energy is attractive (or repulsive) in the potential surfaces is consequence of the cavity geometry and the effective structural parameters of the β-CD.

For each type of guest molecule the dynamics simulation presents some common features and also some differences. The main similarities are the following:

- The molecule can enter the cavity and then form an inclusion complex only for certain initial positions of its centre of mass, and these positions are always near the rims of the CD and never outside the cavity walls.
- The trajectories of the molecules are similar: the guest tends to move towards the cavity and remain inside for the simulation or inclusion time, depending on the potential parameters.
- The inclusion time decreases as the temperature of the process increases.

The main differences are:

- Small linear molecules (length $L < 5$ Å) with $\sigma \geq 3.5$ Å cannot penetrate into the cavity, whereas cyclic or spherical molecules form stable inclusion complexes.
- The configuration of the inclusion complex formed with linear molecules does not correspond to that of minimum energy, in contrast to what happens for the other structures.

5. Conclusion

We have studied the mobility of atoms, and cyclic, spherical or linear guest molecules inside and around β–CD by molecular dynamics simulation at constant temperature. The intermolecular energy is modelled by a Lennard-Jones potential and a continuum description of the cavity walls. It is found that the variation of the potential energy along the Z coordinate (parallel to the cavity axis), resembles a well potential where the minimum energy is lower as the atomic size of the molecule increases. The distance between the cavity walls and the guest molecule in the absolute minimum energy configuration is approximately 1.12σ and ε governs the strength of the interaction. The confinement of the molecule in the β-CD cavity produces an enhancement of the physisorption energy seen in the interaction of a pair of atoms characterized by the same potential parameters (σ, ε). The attractive zones of the potential energy surfaces are related to the effective values of the β-CD cavity dimensions rather than to the guest properties.

In the dynamical study of the system we conclude that the molecule can enter the cavity and then form an inclusion complex only for certain initial positions of its centre of mass, and these positions are always near the rims of the CD and never outside the cavity walls. The probability of forming an inclusion complex increases with the size of the cyclic or spherical guest molecule. The most probable configuration of the complex formed with this type of

molecules corresponds to that of minimum energy. Linear guest molecules with length $L < 5$ Å can form inclusion and non-inclusion complexes, depending on the composition and initial position of the guest with respect to the cavity. Linear molecules with length $L \geq 5$ Å have a small probability of forming non-inclusion complexes, again depending on the composition and initial position of guest and cavity. They can form inclusion complexes for a time period which depends on the molecular properties (length and composition of the guest) as well as on the temperature and initial conditions of the trajectory. The inclusion time decreases with the temperature of the process. For atoms, and cyclic or spherical molecules the temperature of the simulation affects the time spent by the guest inside the cavity, when its interaction with β–CD is represented by parameters $\sigma < 3.0$ Å and $\varepsilon \leq 0.003$ eV.

Acknowledgments

References

[1]   Alvira, E. *Chem. Phys. Lett.* 1997, 267, 221
[2]   Alvira, E. *Chem. Phys. Lett.* 2007, 439, 252
[3]   Alvira, E. *Chem. Phys. Lett.* 2007, 439, 258
[4]   Frenkel, D.; Smit, B. *Understanding Molecular Simulation*; Academic Press: San Diego, California, 2002
[5]   Rapaport, D. C. *The Art of Molecular Dynamics Simulation*; Cambridge University Press: Cambridge, 1995
[6]   Allen, M. P.; Tildesley, D. J. *Computer Simulation of liquids*; Clarendon Press: Oxford, 1987
[7]   Hirschfelder, J. O.; Curtiss, C. F.; Bird, R. B. *Molecular theory of gases and liquids;* John Wiley and Sons: New York, 1967
[8]   Derycke, I. ; Vigneron, J. P.; Lambin, Ph. ; Lucas, A. A. ; Derouane, E. G. *J. Chem. Phys.* 1991, 94, 4620
[9]   Szejtli, J. ; Osa, T. *Comprehensive Supramolecular Chemistry*, Ed. Pergamon, Elsevier: Oxford, 1996
[10] Apostol, T. M. *Calculus*; Editorial Reverte : Barcelona, 1976
[11] Gradshteyn, I. S. ; Ryzhik, I. M. *Table of integrals, series and products*, Academic Press: New York, 1980
[12] Lipkowitz, K. B. *Chem. Rev.* 1998, 98, 1829
[13] Lipkowitz, K. B. *J. Chromatogr.* A 2001, 906, 417
[14] Brown, D.; Clarke, J. H. R. *Mol. Phys.* 1984, 51, 1243
[15] Fincham, D.; Quirke, N.; Tildesley, D. J. *J. Chem. Phys.* 1986, 84, 4535
[16] Lipkowitz, K. B.; Pearl, G.; Coner, B.; Peterson, M. A. *J. Am. Chem. Soc.* 1997, 119, 600
[17] Lipkowitz, K. B.; Coner, B.; Peterson, M. A. *J. Am. Chem. Soc.* 1997, 119, 11269

[18] Alvira, E.; Mayoral, J. A.; Garcia, J. I. *J. Incl. Phenom. Macrocycl. Chem.* 2008, 60, 1-2, 103

[19] Alvira, E.; Mayoral, J. A.; Garcia, J. I. *Chem. Phys. Lett.* 1997, 271, 178

[20] Alvira, E.; García, J. I.; Mayoral, J. A. *Recent Res. Devel. Chem. Physics.* 2000, 1, 89

[21] Van Helden, S. P.; Van Eijck, B. P.; Janssen, L. H. M. *J. Biomol. Struct. Dyn.* 1992, 9, 1269

[22] Alvira, E.; Garcia, J. I.; Mayoral, J. A. *Chem. Phys.* 1999, 240, 101

Chapter 7

Use of Error Theory in the Computational Methods Devised for Kinematic Viscosity - Temperature Correlations in Undefined Petroleum Fractions

José Alberto Maroto Centeno[*] *and Manuel Quesada-Pérez*[**]

Group of Physics and Chemistry of Linares; Departament of Physics, EPS of Linares
(University of Jaén); C/ Alfonso X el Sabio, 28, 23700 Linares, Jaén, Spain.

Abstract

Petroleum fractions are essentially complex mixtures of cyclic and non-cyclic hydrocarbons. Given the complex nature of these systems and even the difficulty of identifying the components present in such mixtures, developing a viscosity correlation accounting for all the composition details becomes a challenging task. Numerous estimation methods have been developed to represent the effect of the temperature on the viscosity of different crude oil fractions at atmospheric pressure. Most of these methods are empirical in nature since no fundamental theory exists for the transport properties of liquids. In this chapter the authors carry out both a brief review of the empirical correlations commonly used and an evaluation of their degree of accuracy. Unfortunately, the absence of information about the accuracy of the physical magnitudes used as input parameters in the correlations and the experimental data of kinematic viscosity used in the different fittings prevents a conclusive assessment of the percentage of average absolute deviation reported in the literature. Finally, the authors apply the error theory to a set of equations recently derived (and published), which has been proved to fit successfully the data of the chart of the ASTM standard D 2502-92 (reapproved 2004). This standard provides a means of calculating the mean molecular weight of petroleum oils from kinematic viscosity measurements and it is partially based on the Walter equation, that is, one of the correlations previously discussed. The use of a PC program designed in order to carry out this new analysis permits a preliminary evaluation of the errors of this ASTM standard.

---

[*] E-mail address: jamaroto@ujaen.es
[**] E-mail address: mquesada@ujaen.es

Introduction

For the development, design, planning and operation of processes in the petroleum industry, an engineer has to deal with the so-called undefined mixtures such as petroleum fractions. Petroleum fractions are essentially complex mixtures of cyclic and non-cyclic hydrocarbons. As the nature of these systems is quite complex and the identification of their components is extremely difficult to achieve a viscosity correlation accounting for all the composition details becomes a challenging task. Many estimation methods have been put forward to capture the effect of the temperature on the viscosity of different crude oil fractions at atmospheric pressure. Most of these methods are empirical in nature since no fundamental theory exists for the transport properties of liquids. In this chapter the authors carry out both a brief review of the empirical correlations commonly used and a critical survey of their degree of accuracy.

At any rate, the kinematic viscosities of these fractions are required in calculations involving mass transfer and fluid flow and, currently, there are increasing demands for accuracy in viscosity prediction techniques for implementation in computer routines. From an economical viewpoint, a reason for such demands can be clearly pointed out: Small uncertainties in the kinematic viscosity could be responsible for significant reductions in profits (up to 10%, as will be discussed later). Unfortunately, the absence of information about the accuracy of the physical magnitudes used as input parameters in the correlations and the experimental data of kinematic viscosity used in the different fittings prevents a conclusive assessment of the percentage of average absolute deviation (%AAD) reported in the literature.

As matters stand, the authors suggest the application of the error theory in this field. In fact, such theory is applied to a set of equations recently derived [1], which has been proved to fit successfully the data of the chart of the ASTM standard D 2502-92 (reapproved 2004). This standard provides a means of calculating the mean molecular weight of petroleum oils from kinematic viscosity measurements and it is partially based on the Walter equation, that is, one of the correlations previously discussed. In this way, the usefulness of the error theory in accuracy estimations is elucidated. The use of a PC program devised to carry out this new analysis permits a preliminary evaluation of the errors of this ASTM standard.

The rest of the chapter is organized as follows. First, the review on the methods for calculation of the kinetic viscosity is presented. Then, the reasons for the proposal of the error theory in accuracy estimations are briefly outlined. In next section, the error theory is applied to the mentioned ASTM standard and some results are discussed. Finally, some conclusions are highlighted.

A Review of Practical Calculation Methods for the Kinematic Viscosity of Undefined Petroleum Fractions

The relationship between kinematic viscosity and temperature for liquid petroleum fractions is of considerable importance in many engineering problems involving fluid flow and momentum transfer. The development of a generalized predictive viscosity correlation has received considerable attention from engineers and scientists working in the field of

petroleum processing and petrochemicals. Numerous calculation methods for the effect of temperature on the kinematic viscosity have been proposed. However, it is difficult to develop a theoretical or even a semitheoretical method for liquid petroleum fractions because they are exceedingly complicated undefined fluids that must be characterized to obtained relevant parameters.

This section reviews methods for the prediction and correlation of kinematic viscosity of undefined petroleum fractions, which are suited for practical engineering use. The methods reviewed were chosen because they are well known and accepted or potentially promising. The applicability and average deviations for each method are discussed too.

Amin and Maddox [2] and Beg et al. [3] proposed similar correlations based on the modification of Eyring's equation:

$$v = A\left[\exp\left(\frac{B}{T}\right)\right]$$
(1)

but with different expressions for parameters A and B, where $v = \eta / \rho$, v is the kinematic viscosity, η is the dynamic viscosity and ρ is the density. Parameters A and B should be evaluated by fitting the experimental viscosity values. Amin and Maddox [2] related A and B in equation (1) to the 50% boling point, T_b, and the Watson characterization factor, K, (dependent on the average boiling point and the specific gravity) of each crude fraction as follows:

$$\ln B = 4.717 + 0.00526\,T_b$$
(2)

$$A = 10^{-6}\,(91.8367\,T_b^{-0.175} - 29.263)\left(\frac{K}{B}\right)$$
(3)

On the other hand, Beg et al. [3] related A and B with the 50% boling point, T_b, and the API gravity, API, as follows:

$$\ln B = 5.471 + 0.00342\,T_b$$
(4)

$$A = -0.0339\,(API)^{0.188} + 0.241\left(\frac{T_b}{B}\right)$$
(5)

Moharam et al. [4] combined the double logarithmic relationship of the Walter equation [5] with the fact that the viscosity correlates well with the boiling temperature and the inverse of the absolute temperature, to develop a generalized empirical correlation to describe the kinematic viscosity-temperature behaviour in the range $50 - 550$ ºC:

$$\ln v = A\left[\exp\left(\frac{T_B}{T}\right)\gamma^B\right] + C$$
(6)

where γ is the specific gravity at 288.71 K (15.6 ºC), $A = 1.0185$, $B = T_b/305.078 - 0.55526$, $C = -3.2421$, T is in K and ν is in mm^2/s (cSt).

Dutt [6] proposed an Antoine-type correlation using the average boiling point only as an input. The equation has the form:

$$\ln \nu = A + \frac{B}{(t + C)} \tag{7}$$

where $A = -3.0171$, $B = 442.78 + 1.6452\ t_b$, $C = 239 - 0.19\ t_b$, t is in ºC and ν is in mm^2/s (cSt).

Based on Walther's equation, Mehrotra [7] proposed a correlation which has the form:

$$\log_{10} \log_{10} (\nu + 0.8) = a_1 + a_2 \log (T) \tag{8}$$

with $a_1 = 5.489 + 0.148(T_b)^{0.5}$, $a_2 = -3.7$, T and T_b are in K and ν is in mm^2/s (cSt).

Puttagunta et al. [8] proposed a relatively more accurate correlation which requires a single viscosity measurement at 37.78ºC and atmospheric pressure to make the prediction. The correlation has the form:

$$\ln \nu = \frac{b}{\left(1 + \dfrac{t - 37.78}{310.93}\right)^s} + c \tag{9}$$

where t is the temperature (ºC), $c = -0.86960$, $b = \log_{10} \nu_{37.78} - c$, being $\nu_{37.78}$ the kinematic viscosity at 37.78 ºC and $S = 0.28008\ b + 1.6180$. Nevertheless, Mehrotra showed that this viscosity correlation is essentially the Walter equation [9].

Aboul-Seoud and Moharam [10] carried out an exhaustive analysis of Mehrotra equations. As previously stated, Walther's equation was the base of the work of Mehrotra. In his work, the value of the parameter a_2 of equation (8) was set equal to -3.7 while the parameter a_1 was expressed in terms of the average boiling point. Aboul-Seoud and Moharam observed that the estimation of parameter a_1 from the boiling point alone is responsible for the deviation associated with the application of equation (8). Consequently, some trials were made to eliminate this parameter or to improve its estimation depending on the available input information.

If a single viscosity measurement is available as input parameter, the parameter a_1 of equation (8) can be eliminated and the viscosity can be estimated using the following correlation:

$$\ln \ln (\nu + 0.8) = \ln \ln (\nu_o + 0.8) + a_2 \ln \left(\frac{T}{T_o}\right) \tag{10}$$

where ν_o is the single viscosity measurements (cSt) at temperature T_o (K) and $a_2 = -3.7$.

If the specific gravity is available, together with the average boiling point, the proposed correlation has the form:

$$\ln \ln (v + 0.8) \; = \; a_1 \;\; + \;\; a_2 \, \ln (T) \tag{11}$$

with $\qquad\qquad a_1 = 4.3414 \, (T_b \, \gamma)^{0.2} + 6.6913$ and $a_2 = -3.7$.

where T_b is the 50% boiling point in (K), γ is the specific gravity and v is the kinematic viscosity in cSt.

Fang and Lei [11] extended the equation used by Amin and Maddox and Beg et al. to correlate the kinematic viscosity-temperature behaviour for several liquid petroleum fractions. The final expression takes the following form:

$$\ln \left(\frac{v}{T} \right) \; = \; 59.06 \, (t_b)^{0.1546} \, M^{0.4791} \, \frac{\rho}{T} \; - \; (18.103 + \ln M) \tag{12}$$

where the kinematic viscosity, v, is in cSt, M is the mean molecular weight of the petroleum fractions in g/mol, 50% boiling point, t_b, is in °C, T is the temperature in K and ρ is the density at T K in g/cm^3.

Since few references report the kinematic viscosity with the corresponding density and molecular weight, it is necessary to have generalized methods to predict the density and molecular weight of fractions. In this correlation, ρ and M are estimated from the following equations [12,13], respectively:

$$\rho \; = \; \left[\rho_{15.6}^2 - 1.1 \times 10^{-3} \, (t - 15.6) \right]^{0.5} \tag{13}$$

$$M \; = \; 219.05 \exp \left(0.003924 \, (t_b + 273.15) \right) \exp \left(- 3.07 \, S \right) (t_b + 273.15)^{0.118} \, S^{1.88} \tag{14}$$

where $\rho_{15.6}$ is the density (in g/cm^3) at 15.6 °C of the fraction, and $S = \rho_{15.6}/0.999024$.

From equations (12) – (14) it is evident that the kinematic viscosity of a liquid petroleum fraction at any given temperature can be predicted with only two input properties, 50% boiling point and the density at 15.6 °C.

Finally, the standard [14] ASTM D 341 – 93 (reapproved 2003) includes a kinematic viscosity-temperature chart that supplies the kinematic viscosity of a petroleum oil or liquid hydrocarbon at any temperature within a limited range, provided that the kinematic viscosities at two temperatures are known. The chart was derived with computer assistance to provide linearity over a greater range on the basis of the most reliable of modern data. The chart is based on the following general relation:

$$\log_{10} \log_{10} Z \; = \; A \; - \; B \log_{10} T \tag{15}$$

where $Z = (v + 0.7 + C - D + E - F + G - H)$, v is in cSt, T in K, A and B are constants, $C = \exp(-1.14883 - 2.65868 \, v)$, $D = \exp(-0.0038138 - 12.5645 \, v)$, $E = \exp(5.46491 - 37.6289$

v), $F = \exp(13.0458 - 74.6851\ v)$, $G = \exp(37.4619 - 192.643\ v)$ and $H = \exp(80.4945 - 400.468\ v)$.

The limits of applicability of equation (15) are listed in Table 1.

Table 1.

Z	Interval of v values (cSt)
$(v + 0.7)$	from 2.00 to 2×10^7
$(v + 0.7 + C)$	from 1.65 to 2×10^7
$(v + 0.7 + C - D)$	from 0.90 to 2×10^7
$(v + 0.7 + C - D + E)$	from 0.30 to 2×10^7
$(v + 0.7 + C - D + E - F)$	from 0.24 to 2×10^7
$(v + 0.7 + C - D + E - F + G)$	from 0.21 to 2×10^7

It is obvious that equation (15) in the simplified form $\log_{10} \log_{10} (v + 0.7) = A - B \log_{10} T$ is basically the Walter equation and permits viscosity calculations for a given fluid in the majority of practical situations. Constants A and B can be evaluated for a fluid from two data points. Kinematic viscosities for other points can be readily calculated. This standard warns on the use of equation (15): it is not useful for inter-calculations of kinematic viscosity and temperature over the full chart kinematic viscosity range. More convenient equations which agree closely with the chart scale are necessary when calculations involve kinematic viscosities smaller than 2.0 cSt.

From this brief survey of the methods available in the literature, which are summarized in Table 2, it is apparent that the methods may be categorized into two groups according to the input information required. The first contains the methods that require physical property data such as 50% boiling point and specific gravity to perform the estimation. The methods in this group are completely predictive and easy to use especially when the required input parameters are available as characterizing parameters for the liquids studied. The second group includes the methods that require one or two viscosity measurements. These methods do not require other physical properties as input data. However, they are not predictive and it is essential that considerable attention must be paid to the reference measurements as the accuracy of the estimation depends entirely on these measurements.

Table 2.

Method	Type	Equations	Input data	Year	% AAD
Amin - Madox	Predictive	1,2,3	T_b, γ	1980	37.22
Beg. et al.	Predictive	1,4,5	T_b, γ	1988	7.40
Moharam et al.	Predictive	6	T_b, γ	1995	5.54
Dutt	Predictive	7	T_b	1990	6.31
Mehrotra	Predictive	8	T_b	1995	5
Puttagunta et al.	Correlative	9	$v_{37.78}$	1992	1.59
Aboul_Seoud and Moharam	Correlative	10	v_o, T_o	1999	1.47
Aboul_Seoud and Moharam	Predictive	11	T_b, γ	1999	3.05
Fang and Lei	Predictive	12,13,14	T_b, $\rho_{15.6}$	1999	4.2
ASTM D 341 (Walter equation)	Correlative	15	v_1, v_2	2003	0.8 – 1.4

It must be clarified that the symbol %AAD in Table 2 refers to the average absolute deviation (%) which is given by:

$$\%AAD \quad = \quad \frac{1}{n} \sum_{i=1}^{n} \frac{\left| v_{i,cal} - v_{i,\exp} \right|}{v_{i,\exp}} \times 100 \qquad (16)$$

where $v_{i,cal}$ and $v_{i,\exp}$ refer to calculated and experimental values of the kinematic viscosity, respectively. Therefore, this parameter show the accuracy of the correlation analysed and is evaluated by means of the use of experimental data relative to diverse petroleum fractions. It must be emphasized that the values of %AAD showed in this work for each predictive or correlative equation were evaluated by their respective authors. This fact will be discussed in the next section.

Regarding the evaluation of the correlative methods previously mentioned, it is evident that the ASTM method has the best %AAD. In fact this is one of the methods most widely used in order to evaluate the kinematic viscosity of liquid petroleum crudes. Nevertheless, the major shortcoming of this method comes out when extrapolation is required. For the purpose of extrapolation, if the two measured values are not sufficiently far apart, experimental errors in the kinematic viscosity, and in drawing the line may seriously affect the accuracy of extrapolated points [8]. On the other hand, the methods of Puttagunta et al and Aboul_Seoud and Moharam can be successfully used if one viscosity value can be measured.

There are three predictive methods that show good values of %AAD: Aboul-Seoud and Moharam method, Fang and Lei method and Mehrotra method. It is evident that the use of two empirical parameters characterizing the petroleum liquid under study (T_b and γ in the case of Aboul-Seoud and Moharam method or T_b and $\rho_{15.6}$ in the case of Fang and Lei method) provides better results than the use one only empirical parameter (T_b in the case of Mehrotra method) since the use of two physical parameters presumably represent in a better way the nature or the composition of the fluid under study.

Further Analysis of the Calculation Methods. Use of Error Theory for the Testing of Accuracy

By reviewing the literature it can be easily proved that the authors that have worked in the field of the computational methods devised for kinematic viscosity-temperature correlations in undefined petroleum fractions have not used the same database. In fact, Mehrotra [7] wrote that it is difficult to state the accuracy and reliability with considerable certainty because the testing of most methods by the respective authors, from a common database, is limited. The majority of the authors have used old empirical data reported by Beg et al [3] and Amin and Maddox [2] which do not include data of the accuracy in the experimental values of v, T_b, and γ. In this sense, the empirical data reported by Amin and Maddox must be cautiously used because, according to Ely and Handley [15], the accuracy of most viscosity data used at this date was in the order of 5-15%. On the other hand, the database of Beg et al does not include any information about the accuracy of the experimental data of T_b and γ which were used as input parameters in their predictive equation. In

conclusion, this evident lack of information about the accuracy of both the physical magnitudes used as input parameters in the correlations and the experimental data of kinematic viscosity used in the different fittings prevents a conclusive assessment of the %AAD reported in the literature.

Apart from that, it would be necessary not only to perform a number of computer correlations in order to optimize a tentative equation but also to include physical information. In this sense, Fang and Lei [11] think that models (such as the Dutt model [6]) that use an only fitting parameter (50% boiling point) are not quite reasonable for the characterization of a petroleum fraction because the kinematic viscosities of the fractions with same boiling point range but from different crude oils are different at a given temperature. In conclusion, these authors think at least two properties are required to characterize the different petroleum fractions. Little work has been carried out in this field and the majority of authors have restricted themselves to use the equations of Eyring or Walter without carrying out any further justification about the selection of a group of fitting parameters or the mathematical function used for each fitting parameter.

In this chapter we propose the use of a useful tool, the error theory, to evaluate the real accuracy of the correlations for predicting the kinematic viscosity of liquid petroleum fractions. In general, the use of a number of input parameters x_1, x_2, ..., x_n and the evaluation of an output parameter y by means of the use of a correlation is not enough. We strongly recommend to analyse how the use of a number of input experimental parameters $x_1 \pm \Delta x_1$, $x_2 \pm \Delta x_2$, ..., $x_n \pm \Delta x_n$ influences the value of an output experimental parameter $y \pm \Delta y$ by means of the use of a correlation.

In particular, this proposal should be taken into account in the case of kinematic viscosity correlations. It has been widely reported that small changes in kinematic viscosity can have a dramatic impact on the properties of petroleum fluids [16]. In fact, the criticality of kinematic viscosity measurement prompted the petroleum industry to develop a very precise method, first published in 1937, ASTM D 445, Test Method for Kinematic Viscosity of Transparent and Opaque Liquids. Although it sounds very simple, achieving the high accuracy and precision required by the industry is an extremely formidable task. There are many factors that affect the precision of this test method. In economic terms, an error of 1 percent product viscosity that causes a blend adjustment can easily result in increasing product cost by a penny a gallon. For a large lubricant manufacturer, this can amount to $1,000,000 in lost revenue per year. If this is a 10 percent reduction in profits, then it is equivalent to throwing away 10 percent of our paycheck.

The most important factor affecting the quality of a viscosity measurement is temperature. The control of this physical magnitude is the most significant factor to obtain accurate and precise kinematic viscosity measurements. This is especially true for petroleum products as their rate of viscosity change per unit temperature is significantly greater than other products. Thus a slight variation in temperature can have a very large effect on the viscosity of a fluid. The bath temperature for the most common measurements, usually ranging from 40°C to 100°C, must be controlled within +/- 0.02°C. That is an extremely tight window and great care must be taken to achieve this control.

This previous reflection show that the use of the error theory in the evaluation of the computational methods devised for kinematic viscosity-temperature correlations in undefined petroleum fractions is not a negligible task, but an important tool for improving the accuracy and reliability of the reported %AAD.

Use of the Error Theory for the Evaluation of the Accuracy of the ASTM Standard D 2502-92 (Reapproved 2004)

In this section we apply the error theory to a set of equations recently derived [1], which has been proved to fit successfully the data of the chart of the ASTM standard D 2502-92 (reapproved 2004). This standard [17] provides a means of calculating the mean molecular weight of petroleum oils from kinematic viscosity measurements and it is partially based on the Walter equation, that is, one of the correlations previously discussed. The use of a PC program designed in order to carry out this new analysis permits a new and preliminary evaluation of the errors involved in the use of this ASTM standard.

The ASTM standard D 2502-92 (reapproved 2004) is applicable to samples with molecular weight in the range from 250 to 700 g/mol and is intended for use with average petroleum fractions. It should not be applied to oils that represent extremes of composition or posses an exceptionally narrow molecular weight range.

This standard is based on a set of equations proposed by Hirschler [18]. In order to write down tidily this set of equations it must be defined the viscosity slope factor (VSF):

$$VSF = H\left(\nu(37.78^{\circ}C)\right) - H\left(\nu(98.89^{\circ}C)\right) \qquad (17)$$

where $\nu(37.78^{\circ}C)$ and $\nu(98.89^{\circ}C)$ are the kinematic viscosities evaluated at 37.78 and 98.89ºC, respectively, and $H(\nu)$ is a function that takes the following form:

$$H(\nu) = 870 \, \log_{10} \log_{10}\left(\nu + 0.6\right) + 154 \qquad (18)$$

The mean molecular weight (MW) can be expressed in function of the previous parameters by means of the following equation:

$$MW = 180 + S \times \left[H\left(\nu(37.78^{\circ}C)\right) + 60\right] \qquad (19)$$

where S is a function which depends on VSF. Values of S were tabulated for all unit values of the VSF from 190 to 319, though in order to find an analytical form for S, Hirschler used an equation which has been recently modified by the following one proposed by Maroto and de las Nieves [1] (equation that fits with higher accuracy the tabulated values of the VSF):

$$S = 3.562 - 0.01129 \, (VSF) - 1.857 \times 10^{-5} (VSF)^2 + 6.843 \times 10^{-8} (VSF)^3 \qquad (20)$$

Maroto and de las Nieves showed that the data provided by the set of equations (17) – (20) are in excellent agreement with the ASTM chart for a viscosity index range that covers the majority of commercial oils. Finally, these authors designed a PC program in order to make the evaluation of molecular weight of petroleum oils easier for engineers and professionals. The use of this program that can be downloaded free from internet only requires the insertion of kinematic viscosity data, which remove any graphical or interpolation errors.

Nevertheless, one should keep in mind that, in this work, the authors use $\nu(37.78ºC)$ and $\nu(98.89ºC)$ as input parameter, without their corresponding uncertainties. Consequently, only *MW* can be obtained, without any additional information about its accuracy. Next, we will apply the error theory in order to obtain the equations that use $\nu(37.78ºC) \pm \Delta\nu(37.78ºC)$ and $\nu(98.89ºC) \pm \Delta\nu(98.89ºC)$ as input parameters and permit to obtain $MW \pm \Delta MW$.

To this end we must remember that the error Δy linked to the indirect measurement of a physics variable *y* depending on *n* physics variables, $x_1, x_2, \ldots x_n$, can be expressed as:

$$\Delta y = \left| \frac{\partial y}{\partial x_1} \right| \Delta x_1 + \left| \frac{\partial y}{\partial x_2} \right| \Delta x_2 + \ldots + \left| \frac{\partial y}{\partial x_n} \right| \Delta x_n \tag{21}$$

By applying equation (21) to the set of equations (17) - (20) it can be obtained that:

$$\Delta VSF = \Delta H(\nu(37.78ºC)) + \Delta H(\nu(98.89ºC)) \tag{22}$$

$$\Delta H(\nu) = \left| \frac{164.092}{(\nu + 0.6)\log_{10}(\nu + 0.6)} \right| \Delta \nu \tag{23}$$

$$\Delta MW = \left| H(\nu(37.78ºC)) + 60 \right| \times \Delta S + \left| S \right| \times \Delta H(\nu(37.78ºC)) \tag{24}$$

$$\Delta S = \left| -0.01129 - 3.714 \times 10^{-5}(VSF) + 2.05 \times 10^{-7}(VSF)^2 \right| \Delta VSF \tag{25}$$

Once the new set of equations (22) – (25) have been obtained it is necessary to look into the magnitude of the errors associated to the measurements of the kinematic viscosity in order to carry out an evaluation of the mean molecular weight of petroleum oils and, what is more, its corresponding error, $MW \pm \Delta MW$, in different experimental conditions.

The ASTM standard D 445-94 specifies a procedure for the determination of the kinematic viscosity, ν, of liquid petroleum products, both transparent and opaque, by measuring the time required by certain volume of liquid to flow under gravity through a calibrated glass capillary viscometer [19]. The result obtained from this test method is dependent upon the behaviour of the sample and is intended for application to liquids for which the shear stress and shear rates are proportional (Newtonian flow behaviour). This test requires some measure conditions to assure a high reproducibility. For example, it must be used a transparent liquid bath of sufficient depth: during the measurement any portion of the sample in the viscometer must be less than 20 mm below the surface of the bath liquid or less than 20 mm above the bottom of the bath. Also, for each series of flow time measurements, the temperature of the bath medium (usually ranging from 15 to 100ºC) must not vary by more than ± 0.02 ºC of the selected temperature over the length of the viscometer, or between the position of each viscometer, or at the location of the thermometer. Finally, it is strongly recommended the use of calibrated liquid-in-glass thermometers of an accuracy after correction of ± 0.02 ºC or better, or any other thermometric device of equal or better accuracy.

The ASTM standard D 445-94 reports on the reproducibility provided by the test, which is the difference between two single and independent results obtained by different operators working in different laboratories on nominally identical test material. The reproducibility reported by this standard is 0.65% for base oil at 40ºC and 100ºC, 0.76% for formulated oils at 40 and 100ºC and 1.8% for formulated oils at 150ºC. In the view of these data, we will assume a tentative value for Δv of 1% in the evaluation of the set of equations (22) – (25), which will permit us to obtain reliable values of $MW \pm \Delta MW$.

Figure 1 show the relative error of the mean molecular weight of the petroleum oils versus the molecular weight for four different values of the kinematic viscosity at 98.89 ºC. The data reported in this figure have been obtained by using the set of equations (17)-(20) and (22)-(25). Due to the relative complexity of this set of equations and in order to facilitate its handling we have designed a PC program which permits an easy evaluation of the molecular weight (and the error linked to it) of petroleum oils [20]. The use of this PC program, which can be downloaded free from the Internet, only requires the insertion of both the kinematic viscosity data at 37.78 and 98.89 ºC and the errors associated to these data. On the other hand, the value of the VSF is also provided by the program and can be used as a checking parameter that permits the estimation of the validity of the results obtained.
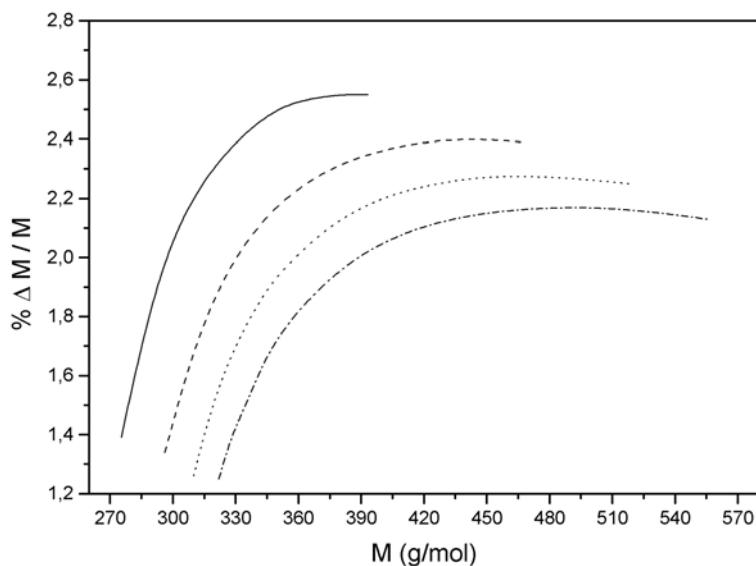
Figure 1. Error rate for the mean molecular weight of the petroleum oils versus the molecular weight for different values of the kinematic viscosity at 98.89 ºC. (———) v(98.89ºC) = 3 cSt; (— —) v(98.89ºC) = 4 cSt; (- - - - -) v(98.89ºC) = 5 cSt; (— - —) v(98.89ºC) = 6 cSt.

Figure 1 show a general increase of the error rate for the mean molecular weight of petroleum oils with increasing the mean molecular weight. Each curve is drawn at a constant value of v(98.89ºC). This increase is very sharp for low values of the mean molecular weight whereas the error rate takes an approximate constant vale for high values of the mean molecular weight. It is remarkable that the four curves have been drawn for values of the viscosity slope factor in the interval between 200 and 310 for which the set of equations (17)-(29) fit the data provided by the chart of the ASTM standard D 2502-92 (see reference [1]).

From figure 1, it is evident that the rate errors are always below 2.6 %, which seems to be a very good accuracy in the estimation of the mean molecular weight of petroleum oils. In addition, it should be stressed that figure 1 shows a general decrease of the error rate with increasing the kinematic viscosity at 98.89 ºC.

Finally, we also investigated the influence of a decrease in the accuracy of the kinematic viscosity data on the error rate for the mean molecular weight of petroleum oils. Figure 2 shows the error rate versus the molecular weight. In this case all the curves have been drawn by taking a constant value of the kinematic viscosity at 98.89ºC of 6 cSt and assuming error rates for the kinematic viscosity of 4%, 3%, 2%, 1% and 0.5%, respectively. The data plotted in figure 2 strongly warn about the sharp increase of the error rate associated to the evaluation of the mean molecular weight of petroleum oils that take places with increasing the error rate for the kinematic viscosity. Also, it is evident that only error rates for the kinematic viscosity below 2% can assure an estimation of the mean molecular weight of petroleum oils with an uncertainty below 5%.

Obviously, figures 1 and 2 only can be considered as an introductory analysis of the error rate for the mean molecular weight of petroleum oils which are linked to the application of the ASTM standard D 2502-92. In future works, a general study covering the whole range of constant values of the kinematic viscosity should be performed.
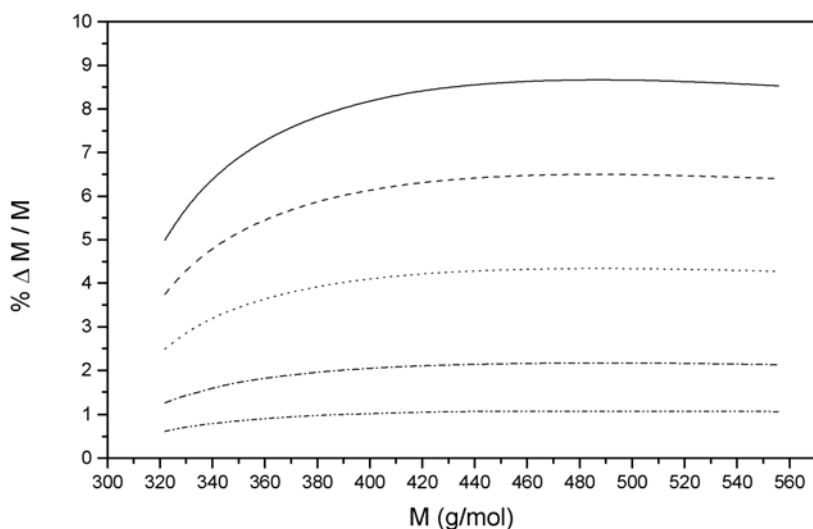
Figure 2. Error rate for the mean molecular weight of the petroleum oils versus the molecular weigh for a constant value of the kinematic viscosity at 98.89ºC of 6 cSt. (———) % $\Delta v / v$ = 4%; (— —) % $\Delta v / v$ = 3%; (- - - - -) % $\Delta v / v$ = 2%; (— - —) % $\Delta v / v$ = 1%; (— - - —) % $\Delta v / v$ = 0.5%.

Conclusion

In this chapter a brief review on the empirical correlations devised for the evaluation of the kinematic viscosity of petroleum oils and a survey of their degree of accuracy have been carried out. As the information about the uncertainty in the magnitudes used as inputs in the correlations is not usually provided, a precise calculation of the corresponding %AAD cannot

be addressed. In any case, the authors apply the error theory to a set of equations recently derived (and published), which has been proved to fit successfully the data of the chart of the ASTM standard D 2502-92 (reapproved 2004). This standard provides a means of calculating the mean molecular weight of petroleum oils from kinematic viscosity measurements. In this way, the usefulness of the error theory in this field is properly illustrated and its application to other data and relationships ((such as kinematic viscosity correlations) is strongly encouraged. Concerning the relative error of the mean molecular weight of petroleum oils, our analysis clearly shows that this error rate can depend considerably on the mean molecular weight, particularly at low viscosities.

References

[1] Maroto J.A. and de las Nieves F. J. (2007) *Petrol. Chem.* **47**(2) 87-91

[2] Amin M.B and Maddox R.N. (1980) *Hydrocarbon Process* **59**(12) 131-135.

[3] Beg S.A., Amin M.B. and Hussain I. (1988) *Chem. Eng. J.* **38** 123-136.

[4] Moharam H.M., Al-Mehaideb R.A. and Fahim M.A. (1995) *Fuel* **74** (12) 1776 - 1779.

[5] Walther C. (1931) *Erdoel und Teer* **7** 382-384.

[6] Dutt N.V.K. (1990), *Chem. Eng. J.* **45** 83-86.

[7] Mehrotra A.K. (1995) *Chem. Eng. Res. Des.* **73** 87-90.

[8] Puttagunta V.R., Miadonye A. and Singh B. (1992) *Chem. Eng. Res. Des.* **70** 627-631.

[9] Mehrotra A.K. (1994) *Ind. Eng. Chem. Res.* **33** 1410-1411.

[10] Aboul-Seoud A.L. and Moharam H.M. (1999) *Chem. Eng. J.* **72** 253-256.

[11] Fang W. and Lei Q. (1999) *Fluid Phase Equilib.* **166** 125-139.

[12] O'Donell R.J. (1980) *Hydrocarbon Process.* **59** 229-231.

[13] 1983 *API Technical Data Book – Petroleum Refining, 4th edn*. (New York: American Petroleum Institute).

[14] 2003 ASTM D 341-93 (reapproved 2003). *Viscosity-Temperature Charts for Liquid Petroleum Products*. (Philadelphia: ASTM Committee on Standards)

[15] Ely J.F. and Hanley H.J.M. (1981a) *Ind. Eng. Chem. Fundam.* **20** 323

[16] See the interesting article written by Janet L. Lane and Kenneth O. Henderson and entitled **"**Viscosity Measurement: So Easy, Yet So Difficult" which can be read in http://www.astm.org/SNEWS/JUNE_2004/lanhen_jun04.html

[17] 2004 ASTM D 2502-92 (reapproved 2004). *Standard Test Method for Estimation of Molecular Weight (Relative Molecular Mass) of Petroleum Oils from Viscosity Measurements*. (Philadelphia: ASTM Committee on Standards)

[18] Hirschler A E 1946 *J. Inst. Pet.* **32**

[19] 1994 ASTM D 445-94. *Standard Test Method for Kinematic Viscosity of Transparent and Opaque Liquids*. (Philadelphia: ASTM Committee on Standards)

[20] See http://www4.ujaen.es/~jamaroto/programs.html. This PC program is named EPEMO-PC.EXE.

Chapter 8

IMPROVEMENT TO CONVENTIONAL POTENTIAL FUNCTIONS BY MEANS OF ADJUSTABLE INTERATOMIC PARAMETERS

Teik-Cheng Lim

School of Science and Technology, SIM University (UniSIM),
535A Clementi Road, S 599490, Republic of Singapore

Abstract

Notwithstanding their simplicity, semi-empirical interatomic potential energy functions are indispensable in computational chemistry as a result of their ease of execution. With over eight decades of interatomic potential functions since the days of Lennard-Jones, numerous potential energy functions have been proposed. The potential functions developed over the decades have increased in complexities through additions of many parameters for the sake of improving the modeling accuracy. However, many established computational chemistry software still incorporate simple potential functions due to the multi-body and dynamical nature in computational chemistry. The use of highly complex potential functions would give a limited improvement in accuracy at the expense of the computational time and cost. An economical and technically feasible solution would be to retain the use of simple potential functions, but with the possibility of allowing them to readjust their properties to fit the potential energy curves of the more complex functions. This chapter discusses the techniques developed recently for attaining such purpose.

1. Introduction

Numerous interatomic and intermolecular potential energy functions have been introduced since the early days of the Lennard-Jones era [1] and subsequent early contributions [2-4]. Since then a great number of potential energy functions have been introduced for molecular [5] and solid state [6] systems. The need for more accurate potential functions for specific interactions forms the impetus for the development of newer and more complex potential functions, i.e. with more parameters to enable better flexibility for curve-fitting of spectroscopic data or *ab initio* computational results. In spite of increasingly

advanced potential energy functions introduced over the years, majority of computational chemistry packages rely on simple potential functions. For example, a number of bond-stretching potential functions in computational chemistry packages adopt the harmonic potential (e.g. [7-9])

$$U_H = \frac{1}{2}k(r-R)^2.$$ (1)

More accurate bond-stretching potential functions adopt additional terms

$$U_P = \frac{1}{2}\sum_{i=2}^{j} k_i(r-R)^i$$ (2)

where substitution of $j = 2$ reduces the polynomial form into the harmonic potential, while better accuracy is achieved when $j = 3$ [10], $j = 4$ [11-13] and $j = 6$ [14]. However the form given in Eq.(2) is unrealistic for large bond stretching due to its non-convergent characteristics. Hence the Morse potential function [2]

$$U_{Morse} = D\{1 - \exp[-\alpha(r-R)]\}^2$$ (3a)

or

$$U_M = U_{Morse} - D = D\{\exp[-2\alpha(r-R)] - 2\exp[-\alpha(r-R)]\}$$ (3b)

is utilized in some software [15-18] to cater for large bond-stretching. Likewise, the most common potential function for describing non-bonded uncharged interactions in computational chemistry packages is the Lennard-Jones (12-6) function [7,9,17]

$$U_{LJ(12-6)} = 4D\left[\left(\frac{\sigma}{r}\right)^{12} - \left(\frac{\sigma}{r}\right)^{6}\right]$$ (4a)

or

$$U_{LJ(12-6)} = D\left[\left(\frac{R}{r}\right)^{12} - 2\left(\frac{R}{r}\right)^{6}\right].$$ (4b)

An alternative potential for describing the van der Waals energy of interaction is the Exponential-6 function [8,12,14]

$$U_{X6} = A_{X6}\exp(-B_{X6}r) - \frac{C_{X6}}{r^6}$$ (5a)

or its loose form [16,17]

$$U_{X6} = D\left\{ \frac{6}{\xi - 6} \exp\left[\xi\left(1 - \frac{r}{R}\right)\right] - \frac{\xi}{\xi - 6}\left(\frac{R}{r}\right)^6 \right\} \tag{5b}$$

with the scaling factors $\xi = 13.772$ and $\xi = 12.0$ for short and long range interactions respectively, corresponding to the Lennard-Jones (12-6) potential. These scaling factors were obtained by imposing equal second order derivative

$$\left(\frac{\partial^2 U_{X6}}{\partial r^2}\right)_{r=R} = \left(\frac{\partial^2 U_{LJ(12-6)}}{\partial r^2}\right)_{r=R} \tag{6}$$

and equal limits

$$\lim_{r \to \infty} U_{X6} = \lim_{r \to \infty} U_{LJ(12-6)} \tag{7}$$

to give the short and long range scaling factors respectively. With increasing complexity and flexibility of potential energy functions, improvements to computational chemistry packages can be made by replacing the simpler potential functions with the more complex functions. However, replacement of potential functions in computational chemistry packages with more complex potentials involves extensive hard-coding on the algorithm, with slower computation speed resulting from greater number of parameters and complexity. As such it has been suggested that the accuracy associated with the more complex potentials be manifested through the simpler potentials in computational chemistry packages by allowing numerical switching of shape parameters.

2. Theoretical Framework

In recent years it has been shown that parameters from one potential function can be converted into parameters of another potential. The purposes for doing so are numerous [19]. Previous techniques for executing parameter conversions include: (a) imposition of equal force constant, i.e. equal second order derivative at the well-depth's minimum [20], (b) imposition of second and higher order derivatives at the well-depth's minimum [21], and (c) polynomial expansion with regrouping of terms [22]. A major drawback of these three techniques mentioned is the pivoting at the well-depth minimum. Although these techniques give excellent agreement for interatomic compression and small change in interatomic distance near the equilibrium bond length, discrepancies become significant generally at the range $1.2R < r < 2.4R$ due to each potential function's bond hardness or softness characteristics. Although the related potential functions' gap tend to close for $r > 2.5R$, this bridging of gap is due rather to the individual function's independently converging characteristic as $r \to \infty$.

To minimize the discrepancies between two potential functions U_1 and U_2, it has been suggested that the difference (or "error") between both potentials be minimized

$$\min(|error|) = \min\left|\oint (u_1 - U_2)\right|. \tag{8}$$

Due to the diverging nature of potential functions with diminishing interatomic distance, it is suggested that the error minimization be imposed from equilibrium $(r = R)$ to a designated interatomic distance $S > R$

$$\min(|error|) = \min\left|\int_R^S (U_1 - U_2) dr\right|. \tag{9}$$

Within the context of Hilbert space, the distance between two functions in an inner product space can be written as

$$d(U_1, U_2) = \sqrt{\int_{\Re} (U_1 - U_2)(\overline{U_1 - U_2}) dr} \tag{10}$$

where $\overline{U_1 - U_2}$ is the conjugate of $U_1 - U_2$. Hence the distance between two potential functions in an inner product space is essentially the root mean integral square

$$d(U_1, U_2) = \sqrt{\int_R^S (U_1 - U_2)^2 dr} \tag{11}$$

for the range $R < r < S$. To minimize this distance, we let the "error" magnitude be zero so that

$$\left|\int_R^S U_1 dr - \int_R^S U_2 dr\right| = 0. \tag{12}$$

To provide a physically meaningful minimization, we let the minimization be extended to complete interatomic dissociation

$$\lim_{S \to \infty} \frac{1}{S - R} \int_R^S U_1 dr = \lim_{S \to \infty} \frac{1}{S - R} \int_R^S U_2 dr \tag{13}$$

where the term $1/(S - R)$ is incorporated in order to represent the mean value of a potential energy function within the considered interatomic range, i.e.

$$U_{mean} = \frac{1}{S - R} \int_R^S U \, dr \quad ; \quad (R \le r \le S). \tag{14}$$

3. Global Versus Local Approaches

In view of the longer range for connecting potential function parameters by the energy integral approach as opposed to the second derivative approach, they are aptly referred to as the global and local approaches respectively. In order to contrast the comparative advantages of these two methodologies, two classical potential functions, namely the general Lennard-Jones function

$$U_{LJ(m-n)} = D\left[\frac{n}{m-n}\left(\frac{R}{r}\right)^m - \frac{m}{m-n}\left(\frac{R}{r}\right)^n \right] \quad ; \quad 0 < n < m \qquad (15)$$

and the general Morse function

$$U_{GM} = D\left\{ \frac{\lambda_2}{\lambda_1 - \lambda_2}\exp\left[\lambda_1 R\left(1-\frac{r}{R}\right) \right] - \frac{\lambda_1}{\lambda_1 - \lambda_2}\exp\left[\lambda_2 R\left(1-\frac{r}{R}\right) \right] \right\} \quad ; \quad 0 < \lambda_2 < \lambda_1 \qquad (16)$$

were selected as functions that are most ideal for connecting their parameters. Apart from being two of the earliest classical potentials that consist of a repulsive term and an attractive term each, these two functions possess identical functional forms for the repulsive and attractive terms. In addition, the Lennard-Jones and Morse potentials are considered "opposite" of one another due to their applications in molecular mechanics force fields as non-bonded [7,9,17] and bonded [15-18] interaction energy respectively. As such, one may expect the two potentials to exhibit large gap for intermediate and large interatomic distances if their parameters are connected based on local approach. Hence an improvement to the parameter connection for intermediate and long range interaction can be expected if the gap between the two potential functions can be effectively narrowed via the global approach. Furthermore the Morse function has also been adopted for describing van der Waals from its more usual application in covalent bond energy description. For example, Morse function has been used for describing van der Waals energy of Ne, Ar, Kr, Xe, CH_4 and N_2 by Konowalow and Hirschfelder [23], and also for non-bonded atoms of Br, C, Cl, F and H by Stelovic [24]. Ramamoorthy and Krishnamurthy [25] demonstrated that the Morse function satisfactorily quantifies both the covalent and van der Waals interaction in Pentaerythritol, while Batsanov [26] estimated the van der Waals radii of some elements using the Morse function. In addition to the use of Morse potential for describing van der Waals interaction in the fields of biomedicine, chemistry and physics (e.g. [27-29]), this potential is also adopted by the COSMIC(90) molecular force field [30] to describe the van der Waals energy of interaction. Although the use of Morse function for covalent bond energy far outweighs that for van der Waals interaction, the numerous application of this potential for quantifying the latter justifies a good connection to be made between the Morse and Lennard-Jones functions. Likewise, the Lennard-Jones function, which is synonymous to van der Waals interaction energy, has been employed for describing the 2-body interaction in condensed matter [31]. Based on the global approach, the relationship between the general Lennard-Jones and the general Morse parameters can be written as [32]

$$R\begin{Bmatrix} \lambda_1 \\ \lambda_2 \end{Bmatrix} = \frac{(m+n)(m-1)(n-1)}{m+n-1}\begin{Bmatrix} n^{-1} \\ m^{-1} \end{Bmatrix} \tag{17}$$

or

$$\begin{Bmatrix} m \\ n \end{Bmatrix} = \frac{1}{2}\begin{bmatrix} \lambda_2^{-1} & \lambda_2^{-1} \\ \lambda_1^{-1} & \lambda_1^{-1} \end{bmatrix}\left\{ \frac{g(\lambda_1,\lambda_2,R)}{\sqrt{g(\lambda_1,\lambda_2,R)\left[g(\lambda_1,\lambda_2,R)-4\left(\frac{\lambda_1\lambda_2}{\lambda_1+\lambda_2}\right)\right]}} \right\} \tag{18}$$

where

$$g(x,y,z) = x + y + xyz. \tag{19}$$

Figure 1 shows the Lennard-Jones approximation to the 2-body interaction of silicon by Biswas and Hamann [33]

$$U_{BH} = 26829.36\exp(-3.946668r) - 42.59865\exp(-1.191187r) \tag{20}$$

in electron volts. The equilibrium bond length R can be obtained from

$$\left.\frac{\partial U}{\partial r}\right|_{r=R} = 0 \tag{21}$$

such that Eq.(18) can be used to give $m = 14.4495$ and $n = 4.3612$.

Figure 2 shows the conventional Lennard-Jones function whereby $m = 2n = 12$, with the Morse parameters obtained from Eq.(17) based on global approach [32], and also by the local approach [34]

$$mn = \lambda_1\lambda_2 R^2. \tag{22}$$

Figure 3 shows the deviation, or so-called "error",

$$Error = \frac{U_{GM} - U_{GLJ}}{D} \tag{23}$$

of the Morse function whose parameters are obtained from the Lennard-Jones potential via the global and local approaches.

Similar trend is also found even among potential energy functions that are used for describing covalent bond energy. We herein show that the Rydberg potential [35,36]

$$U_{Ryd} = -D(1 + a\rho)\exp(-a\rho) \tag{24}$$

can give a better approximation to the Morse function over longer range when the global connection, rather than the local connection, is used.
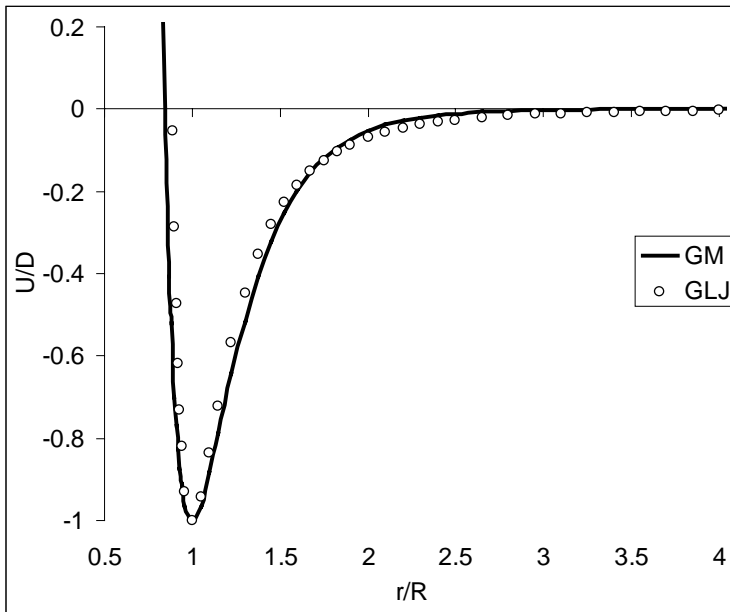
Figure 1. Lennard-Jones approximation to the generalized Morse curve based on the 2-body bonded interaction for silicon [32,33].
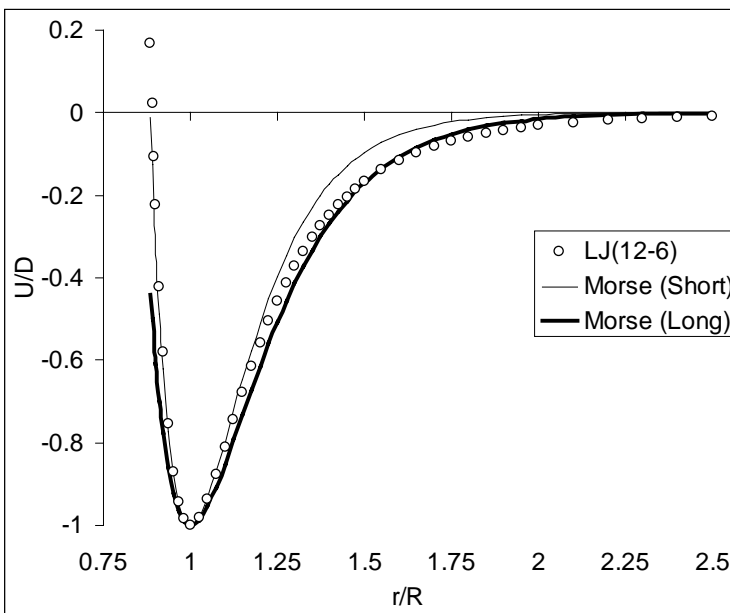
Figure 2. Comparison between the previous short range [34] and the long range [32] relations for approximating the Morse function to the LJ(12-6) energy.
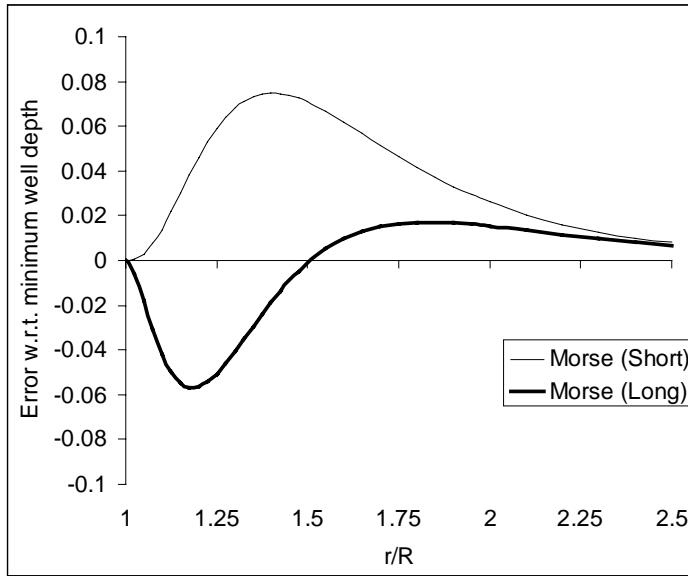
Figure 3. Comparison of dimensionless error between the LJ(12-6) with the short range [34] and long range [32] approaches.

The parameter ρ has two definitions, i.e. either

$$\rho = \frac{r - R}{R} \tag{25}$$

as in the case of 2-body portion of the Murrell-Mottram function [37], or

$$\rho = r - R \tag{26}$$

as in Murrell-Sorbie function [38]. In this chapter, we adopt the latter definition, thereby incurring an inverse length dimension to parameter a. This dimension corresponds to that of α in the conventional Morse function shown in Eq.(3b). Imposition of equal force constant (second derivative at equilibrium) and equal energy integral (from equilibrium to dissociation) gives the local and global relations as

$$\frac{a}{\alpha} = \sqrt{2} \tag{27}$$

and

$$\frac{a}{\alpha} = \frac{4}{3} \tag{28}$$

respectively [39]. Figure 4 shows the Molybdenum and Rubidium potential energy curves based on Morse potential [40], and the Rydberg curves using the local and global

approximation. The "error" is more clearly shown in figure 5, which shows the suitability of the global approach over the local approach beyond the near range.
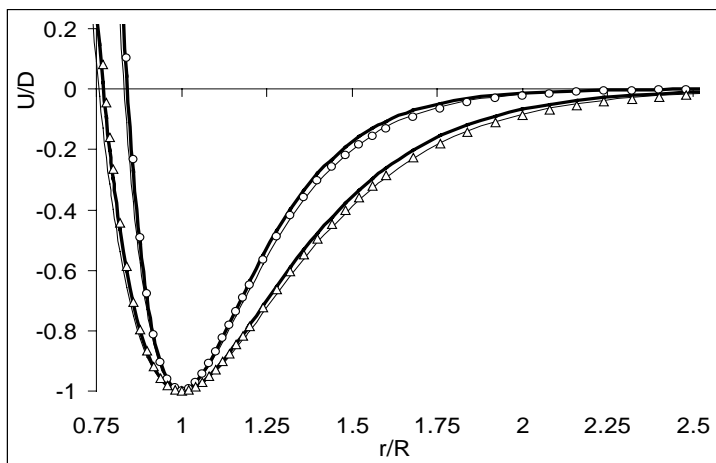
Figure 4. Morse potential energy curves for Molybdenum (circles) and Rubidium (triangles) with their corresponding Rydberg curves based on short range (thick curves) and long range (thin curves) relationships.
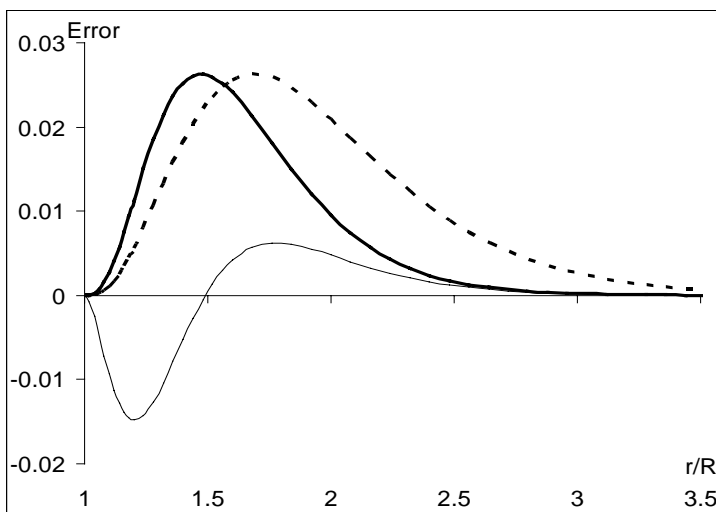
Figure 5. Error distribution of obtained Rydberg curves by short range (thick curves) and long range (thin curves) with reference to the Morse curves of molybdenum (continuous lines) and rubidium (dashed lines).

4. Application

Having shown the comparative advantage of the global approximation, we herein report five applications that can be implemented in computational chemistry algorithms with minimal hard-coding. These applications are considered in the following five sub-sections.

4.1. Scaling Factor of Exponential-6 Potential

The Exponential-6 potential, as described in Eq.(5b), is used as an alternative in some molecular force fields [16,17] . The scaling factors of $\xi = 13.772$ and $\xi = 12.0$ were therefore obtained via the imposition of Eqs.(6) and (7) for the short and long range respectively. Although the scaling factors enable good approximation to the Lennard-Jones (12-6) near equilibrium and for long range, a single switch from one scaling factor to another is undesirable due to the sudden drop in energy. This is because the Exponential-6 potential overestimates and underestimates the Lenard-Jones (12-6) potential for $\xi = 13.772$ and $\xi = 12.0$ respectively for $r > R$. To smoothen the switch, it was suggested that an intermediate scaling factor be introduced to allow two switching rather than a single switching of scaling factor. Imposition of equal energy integral, Eq.(13), on the Exponential-6 and the Lennard-Jones (12-6) function leads to

$$\xi = \frac{1}{2}\left(17 \pm \sqrt{69}\right). \tag{29}$$

Since it is required that $\xi > 6$, the upper value is selected, i.e. $\xi = 12.6533$ [41].
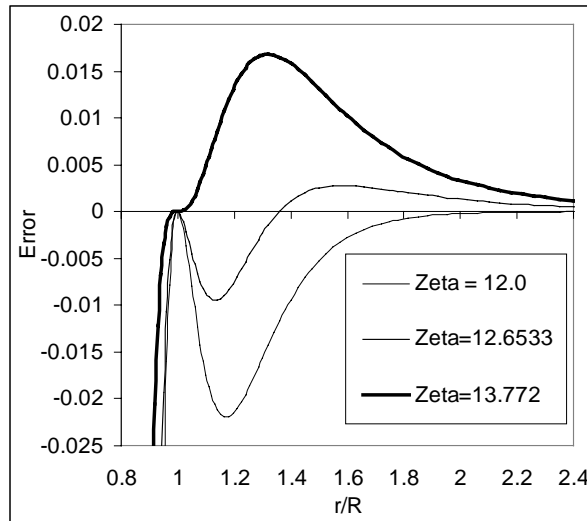
Figure 6. Error distribution of Exponential-6 function for $\xi = 13.772$ (bold curve), $\xi = 12.6533$ (thin curve) and $\xi = 12.0$ (dash curve) with respect to LJ(12-6) potential energy.

Figure 6 shows the dimensionless difference of the Exponential 6 function from the Lennard-Jones (12-6) with the use of $\xi = 13.772$, $\xi = 12.6533$ and $\xi = 12.0$. Figure 7 shows the coarse switching (i.e. from $\xi = 13.772$ to $\xi = 12.0$) and the fine switching (i.e. from $\xi = 13.772$ to $\xi = 12.6533$ and then to $\xi = 12.0$) if the switching of scaling factors are located at the interatomic distance that gives the minimum magnitude of the potential

energy difference $\left| U_{X6} - U_{LJ(12-6)} \right|$. To appreciate the benefit of double switching, it is noted that coarse switching produces a sudden drop of 3.3% while a double switching produces a drop of 1.9% from $\xi = 13.772$ to $\xi = 12.6533$ and less than 0.6% from $\xi = 12.6533$ to $\xi = 12.0$.
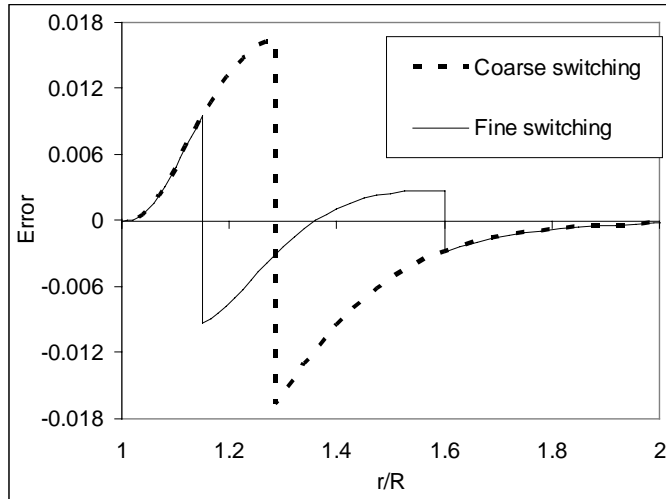
Figure 7. Error paths for single switching point using two scaling factors (dashed curve) and for double switching points using three scaling factors (continuous curve).

If the exactness at $r = R$ and $r \to \infty$ are not serious requirements, the singular use of $\xi = 12.6533$ can be used throughout to give a totally smooth Exponential-6 function, i.e. without the need for any switching of the scaling factor.

4.2. Extended Rydberg Parameters in Original Rydberg Function

While the previous sub-section deals with two commonly used potentials for describing van der Waals interaction, this sub-section considers the Rydberg and Extended-Rydberg functions, which are employed for quantifying covalent bond-stretching energy. As the name implies, the Extended-Rydberg potential incorporates additional terms to the original Rydberg function, Eq.(24), such that

$$U_{ER} = -D \left[\sum_{i=0}^{j} a_i \rho^i \right] \exp(-a_1 \rho) \quad ; \quad (a_0 = 1) \tag{30}$$

where ρ is defined by Eq.(26). The Extended-Rydberg function has been developed up to $j = 3$ for a number of diatomic molecules [42], $j = 4$ for H_2 [43] and $HgZn$ [44], $j = 8$ for $SiCl^+$ [45], and $j = 9$ for NaH [46].

In this chapter, we select the Murrell-Sorbie potential function [38]

$$U_{MS} = -D\left(1 + a_1\rho + a_2\rho^2 + a_3\rho^3\right)\exp(-a_1\rho), \tag{31}$$

which is a special case of the Extended-Rydberg potential with $j = 3$, whose parameters were made available by Huxley and Murrell [42] for a total of 71 diatomic bonds. At a glance it is easily seen that when $a_2 = a_3 = 0$, Eq.(31) reduces to the Rydberg function, thereby implying

$$a = a_1. \tag{32}$$

It is obvious that such simplistic relation is valid when $a_2 R^2 \cong a_3 R^3 \cong 0$ or when $a_1 R \gg a_2 R^2, a_3 R^3$. Applying equal force constant and equal energy integrals on the Rydberg potential and its extended form, we arrive at

$$a = \sqrt{a_1^2 - 2a_2} \tag{33}$$

and

$$\frac{2}{a} = \frac{0! a_0}{a_1^{1}} + \frac{1! a_1}{a_1^{2}} + \frac{2! a_2}{a_1^{3}} + \ldots + \frac{j! a_j}{a_1^{j+1}} \tag{34a}$$

respectively [47]. In the case of Murrell-Sorbie function, Eq.(34a) reduces to

$$a = 2\left(\frac{2}{a_1} + \frac{2a_2}{a_1^{3}} + \frac{6a_3}{a_1^{4}}\right)^{-1}. \tag{34b}$$

For convenience, the direct method, second order derivative method and the energy integral method described in Eqs.(32), (33) and (34) are termed Method 1, Method 2 and Method 3 respectively in this sub-section.

Figure 8 shows the Murrell-Sorbie and the converted Rydberg potential energy curves for NaCl and BeS. It can be seen that the Rydberg conversion based on Method 1 applies well for BeS but not NaCl even though in both cases the conditions $a_2 \approx a_3 \approx 0$ and $a_1 \gg a_2, a_3$ are not met. The explanation for this contrasting observation is best given after discussion on Method 3.

The ClF diatomic molecules potential energy curves plotted in figure 9 demonstrates the advantage of Method 2 over Method 1. For this diatom, the validity ranges are $0.95 < (r/R) < 1.05$ and $0.8 < (r/R) < 1.4$ using Method 1 and Method 2 respectively. The greater range of validity according to Method 2 is due to the imposition of equal curvature at the well-depth's minimum. Although Method 2 does not take into consideration

the parameter a_3, it is valid for ClF diatoms. This is because the terms $a_1R = 6.736$ and $a_2R^2 = 8.779$ are significantly greater than $a_3R^3 = 0.9196$ for ClF. One may expect similar validity of Method 2 for other diatoms whereby $a_1R, a_2R^2 >> a_3R^3$.
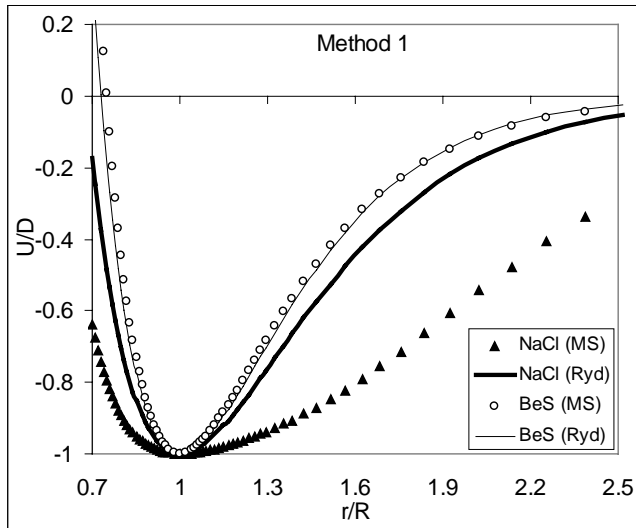
Figure 8. Comparison between Murrell-Sorbie energy (discrete points) with those of Rydberg (smooth curves) using the direct approach (Method 1) for NaCl and BeS diatomic molecules.
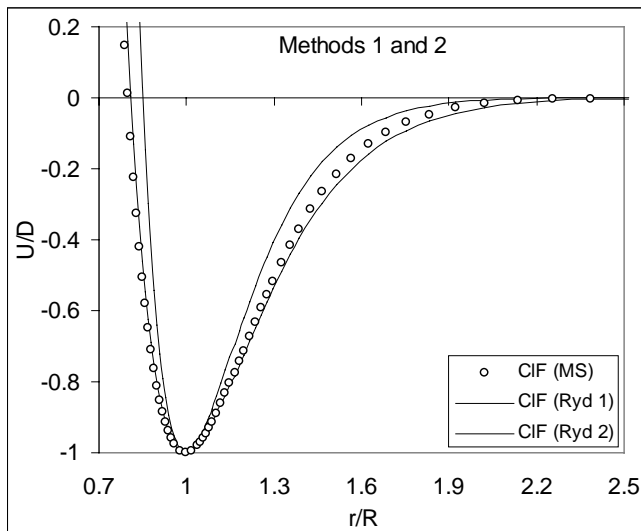
Figure 9. Comparison between Murrell-Sorbie energy (circles) with those of Rydberg using direct approach (Method 1, dashed curve) and derivative approach (Method 2, continuous curve) for ClF diatomic molecule.

What happens when the term a_3R^3 is of equal or higher order with the other two terms? To illustrate, we plot for the case of BF diatomic molecule whereby $a_1R = 4.040$, $a_2R^2 = 3.077$ and $a_3R^3 = 5.889$. Perusal to figure 10 reveals that the Rydberg function, whose parameter a follows Method 2, gives a gross overestimation in energy throughout while the same function with parameter using Method 3 exhibits very good agreement for bond stretching. This impeccable correlation is due to the imposition of equal area bounded by the potential energy curve and the bond length axis for $R \leq r \leq \infty$. With this, it is now clear why Method 1 works well for BeS but not NaCl diatoms (refer to figure 8 again). The Rydberg parameters for BeS are 2.128 and 2.127 according to Method 1 and Method 3 respectively. However, the Rydberg parameter for NaCl by Method 1 is almost twice that according to Method 3.
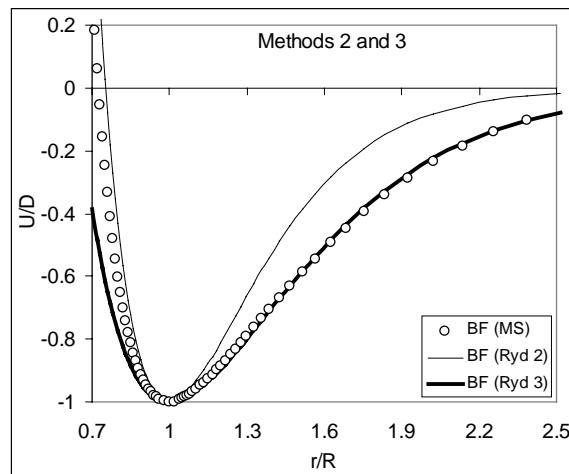
Figure 10. Comparison between Murrell-Sorbie energy (circles) with those of Rydberg using derivative approach (Method 2, fine curve) and integral approach (Method 3, bold curve) for BF diatomic molecule.

4.3. Morse and Varshni Parameter Relations

In Varshni's review [48], one of the seven potential functions introduced was of the form

$$U_{Varshni} = D\left\{1 - \exp\left[-\beta(r^2 - R^2)\right]\right\}^2. \tag{35a}$$

Perusal to Eq.(3a) shows some form of mathematical similarity between the Varshni and Morse potential functions. The Varshni potential can also be casted is an alternate form

$$U_V = U_{var\,shni} - D = D\left\{\exp\left[2\beta R^2\left(1 - \frac{r^2}{R^2}\right)\right] - 2\exp\left[\beta R^2\left(1 - \frac{r^2}{R^2}\right)\right]\right\}, \tag{35b}$$

which is comparable to Eq.(3b). An advantage of expressing in the forms shown in Eqs.(3b) and (35b) is the possibility of obtaining the energy integral from $r = R$ to $r \to \infty$. The integral is divergent when the forms given in Eq.(3a) and (35a) are used. Imposition of equal force constant and equal energy integral to the Morse and Varshni potential functions lead to [49]

$$\alpha = 2\beta R \tag{36}$$

and

$$-\frac{3}{2\alpha} = \sqrt{\frac{\pi}{8\beta}}\left[erf(\infty) - erf\left(\sqrt{2\beta}R\right)\right]\exp\left(2\beta R^2\right) - \sqrt{\frac{\pi}{\beta}}\left[erf(\infty) - erf\left(\sqrt{\beta}R\right)\right]\exp\left(\beta R^2\right). \tag{37}$$
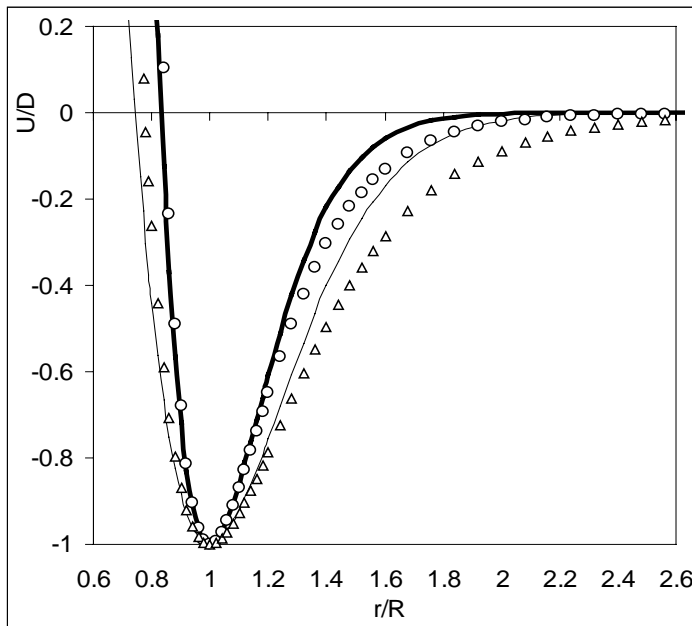
Figure 11. The Morse potential energy for molybdenum (circles) and rubidium (triangles) based on Girifalco and Wiezer [40], and the converted Varshni potential energy curves for molybdenum (bold curve) and rubidium (fine curve) based on "local" relation.

The error function

$$erf(x) = \frac{2}{\sqrt{\pi}}\sum_{n=0}^{\infty}\frac{(-1)^n x^{2n+1}}{n!(2n+1)} \tag{38}$$

can be well approximated from

$$erf(x) \approx \sqrt{1 - \exp\left[-x^2\frac{cx^2 + (4/\pi)}{cx + 1}\right]} \tag{39}$$

where

$$c = -\frac{8}{3\pi}\left(\frac{\pi-3}{\pi-4}\right). \tag{40}$$

Equations (36) and (37) show that the Morse function can be easily obtained from the Varshni parameters just as the Varshni parameter can be easily obtained from the Morse parameter using Eq.(37). To obtain the Varshni parameter from the Morse parameter using Eq.(38), i.e. based on the energy integral approach, a numerical search will need to be performed. Using the Morse parameter of molybdenum and rubidium [40], the Varshni parameter by local and global approaches can be obtained from Eqs.(36) and (37) directly and indirectly respectively. Figures 11 and 12 show the comparative advantages of the local and global approaches respectively.
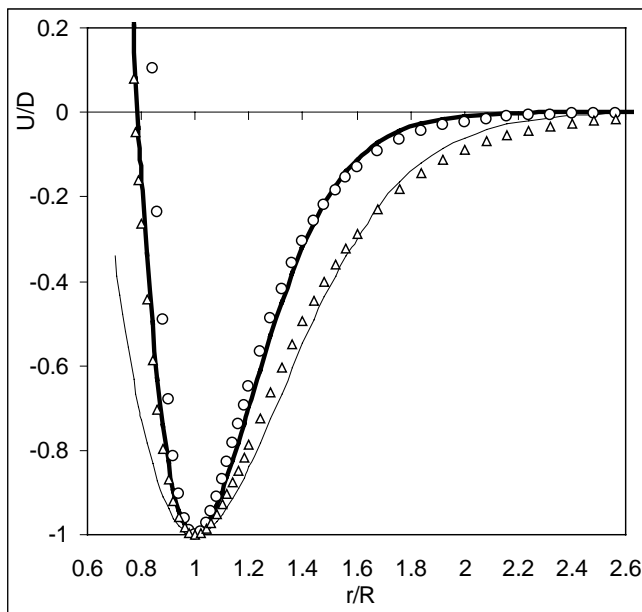
Figure 12. The Morse potential energy for molybdenum (circles) and rubidium (triangles) based on Girifalco and Wiezer [40], and the converted Varshni potential energy curves for molybdenum (bold curve) and rubidium (fine curve) based on "global" relation.

Hence it is suggested that any Varshni potential function that adopts the Morse parameters be split into two parts:

$$\frac{U_V}{D} = \exp\left[2\beta R^2\left(1-\frac{r^2}{R^2}\right)\right] - 2\exp\left[\beta R^2\left(1-\frac{r^2}{R^2}\right)\right]\begin{cases} \beta R^2 \ (local)\ ;\ r\le R \\ \beta R^2 \ (global)\ ;\ r\ge R \end{cases}. \tag{41}$$

Considering the fact that the Morse potential is more widely used in computational chemistry packages, it is more likely that the Varshni parameters be used for Morse potential in two parts [49]:

$$\alpha R = \begin{cases} 2\beta R^2 ; & r \le R \\ -\dfrac{3}{2}R\left\{\sqrt{\dfrac{\pi}{8\beta}}\big[erf(\infty) - erf\big(\sqrt{2\beta}R\big)\big]\exp\big(2\beta R^2\big) - \sqrt{\dfrac{\pi}{\beta}}\big[erf(\infty) - erf\big(\sqrt{\beta}R\big)\big]\exp\big(\beta R^2\big)\right\}^{-1} ; & r \ge R \end{cases} . \quad (42)$$

Apart from the local and global approaches described in the preceding pages, there is yet another approach for obtaining parameter relationships between both functions. By imposing equal bond stretching energy as the bond dissociates

$$\lim_{r \to \infty} U_M = \lim_{r \to \infty} U_V , \quad (43)$$

we have

$$\alpha = \beta r . \quad (44)$$

Although this relation is valid as $r \to \infty$, it appears to be of little practical value since $(U_M) = (U_V) = 0$ as the bond dissociates.

4.4. Conventional Morse Energy from General Morse Parameters

Reference to the original Morse potential, Eq.(3b), and the general Morse potential, Eq.(16), reveals that the latter can be reduced to the former (under the special case $\lambda_1 = 2\lambda_2 = 2\alpha$) but not vice versa. As such, the conventional Morse parameter can then be obtained from the general Morse function using three approaches – imposition of (a) equal force constant, (b) equal energy integral, and (c) equal attractive index – to give [50]

$$\alpha = \sqrt{\frac{\lambda_1 \lambda_2}{2}} , \quad (45)$$

$$\alpha = \frac{3}{2}\left(\frac{\lambda_1 \lambda_2}{\lambda_1 + \lambda_2}\right) \quad (46)$$

and

$$\alpha = \lambda_2 \quad (47)$$

respectively. For convenience, Eqs.(45), (46) and (47) are termed the short range, mid range and long range respectively. Equation (47) is termed long range due to the neglect of the repulsive term. It is of interest to note that the relations given in Eqs.(45) and (46) can be arrived at using a different route. Assuming a geometric progression of $\lambda_2 < \alpha < \lambda_1$, then Eq.(45) can be obtained from the indices of Eqs.(3b) and (16) on the basis of

$$2\alpha \times \alpha = \lambda_1 \times \lambda_2, \tag{48}$$

while Eq.(46) can be arrived at on the assumption of arithmetic progression of reciprocals $\lambda_1^{-1} < \alpha^{-1} < \lambda_2^{-1}$, i.e.

$$\frac{1}{2\alpha} + \frac{1}{\alpha} = \frac{1}{\lambda_1} + \frac{1}{\lambda_2}. \tag{49}$$

Supposed an arithmetic progression of $\lambda_2 < \alpha < \lambda_1$ were to be considered, i.e

$$2\alpha + \alpha = \lambda_1 + \lambda_2, \tag{50}$$

then we have

$$\alpha = \frac{\lambda_1 + \lambda_2}{3}. \tag{51}$$

It is easily seen that taking the square of Eq.(45) and dividing it with Eq.(51) leads to Eq.(46). Such direct comparison of the attractive indices of Eqs.(3b) and (16) is similar to the approach by Mayo et al [16] and Rappe et al [17] for obtaining the scaling factor of the loose form of Exponential-6 function from the Lennard-Jones potential. Although the simple comparisons lead to Eqs.(45) and (46), the valid routes to these parameter relations are nevertheless anchored by the methods described in (a) and (b) respectively. To verify the validity of the parameter relations shown in Eqs.(45), (46) and (47), the potential energy curves of the conventional Morse functions must be compared with the potential energy curve of the general Morse function. Based on the general Morse parameters ($\lambda_1 = 3.946668 \, \overset{\text{o}}{\text{A}}{}^{-1}$ and $\lambda_2 = 1.191187 \, \overset{\text{o}}{\text{A}}{}^{-1}$) in relation to the 2-body energy of Biswas and Hamann [33], the conventional Morse parameter based on the short, mid and long ranges are obtained as $\alpha = 1.533170 \, \overset{\text{o}}{\text{A}}{}^{-1}$, $\alpha = 1.372524 \, \overset{\text{o}}{\text{A}}{}^{-1}$ and $\alpha = 1.191187 \, \overset{\text{o}}{\text{A}}{}^{-1}$ respectively. The errors for these 3 approaches are shown in figure 13(a) for the short and mid range, and in figure 13(b) for long range.

In view of the comparative suitability, it is suggested that the Morse potential curve be split into 3 parts. An example corresponding to the Biswas-Hamann [33] parameters is [50]

$$U = D\left[\exp\left(-2\alpha(r-R)\right) - 2\exp\left(-\alpha(r-R)\right)\right] \begin{cases} \alpha = 1.533170 \, \overset{\text{o}}{\text{A}}{}^{-1} & ; \quad r \leq 1.231R \\ \alpha = 1.372524 \, \overset{\text{o}}{\text{A}}{}^{-1} & ; 1.232R \leq r \leq 2.654R \\ \alpha = 1.191187 \, \overset{\text{o}}{\text{A}}{}^{-1} & ; \quad r \geq 2.655R \end{cases}. \tag{53}$$
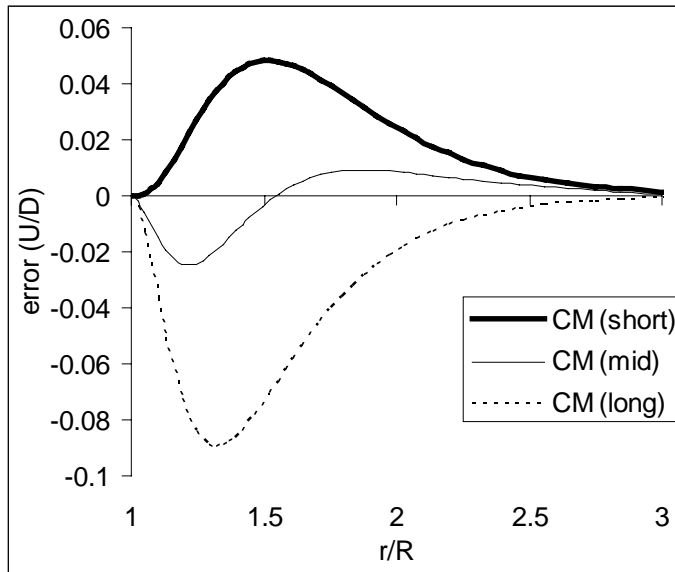
(a)
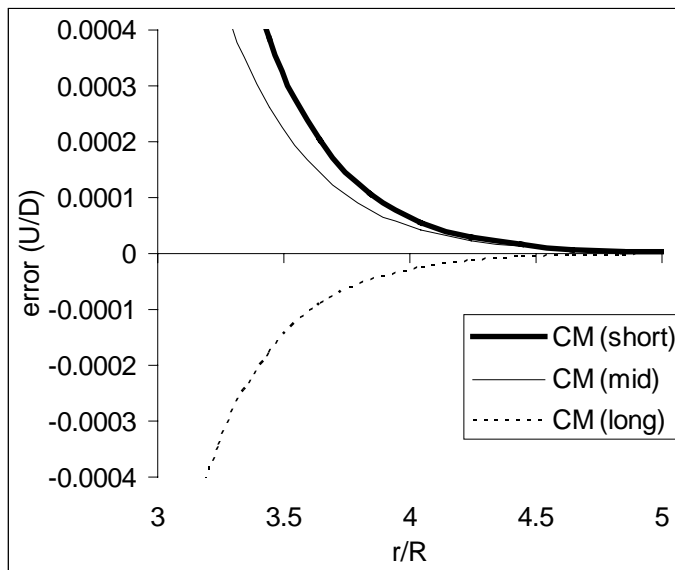
(b)

Figure 13. Discrepancies between the converted conventional Morse (CM) and the generalized Morse (GM) energy at (a) short and mid range, and at (b) long range.

   Figure 14 shows the suitability of the conventional Morse function for approximating the general Morse function (using Biswas-Hamann parameters [33]) when split into 3 parts.
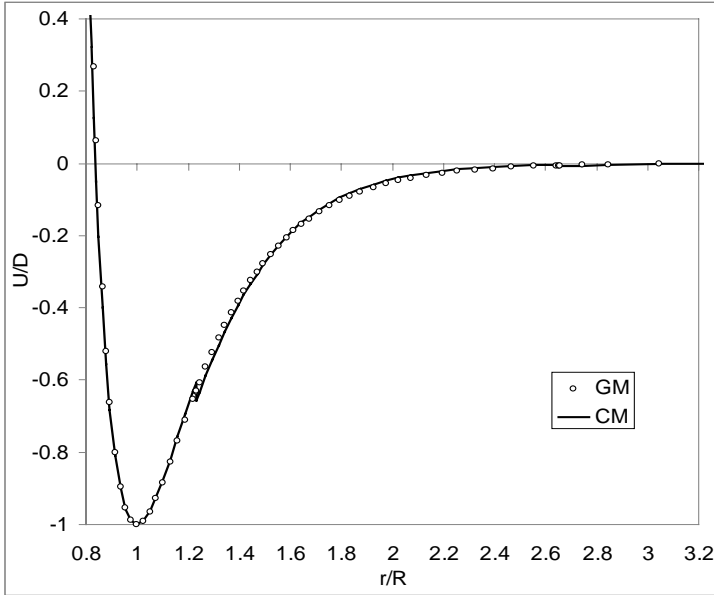
Figure 14. Approximation of a general Morse function by Biswas and Hamann [33] by splitting a conventional Morse potential into 3 parts, as described in Eq.(53).

4.5. FPDP Parameters for Morse Potential

A Four-Parameter Diatomic Potential (FPDP) function of the form

$$U_{FPDP} = D\left(\frac{e^b - d}{e^{b\frac{r}{R}} - d}\right)^2 - 2D\left(\frac{e^b - d}{e^{b\frac{r}{R}} - d}\right) \tag{54}$$

was introduced by Sun [51] and was used by Gang [52] for solving the Dirac equation. It is easily seen that when $d = 0$, the FPDP function simplifies to the Morse potential. Equating the force constants, energy integrals and limiting energy of Morse and FPDP functions lead to [53]

$$\alpha = \frac{b}{R}\left(\frac{e^b}{e^b - d}\right), \tag{55}$$

$$\alpha = \frac{3}{2}\frac{(b/R)}{e^b - d}\left[\frac{e^b + d}{d^2}\left(b - \ln(e^b - d)\right) - \frac{1}{d}\right]^{-1} \tag{56}$$

and

$$\alpha = \frac{b}{R} \quad ; \quad (d = 0) \tag{57}$$

respectively. The validity of Eq.(55) is attested for $r \approx R$ as shown in figure 15(a). However, discrepancies appear for $r > 1.5R$, and even more so for $r > 2.5R$ as evident from figure 15(b). The gap is narrowed when Eq.(56) is used, as shown in figure 16(a) and (b). A slight compromise at $r \approx R$ is not significant. When Eq.(57) is used, the compromise at $r \approx R$
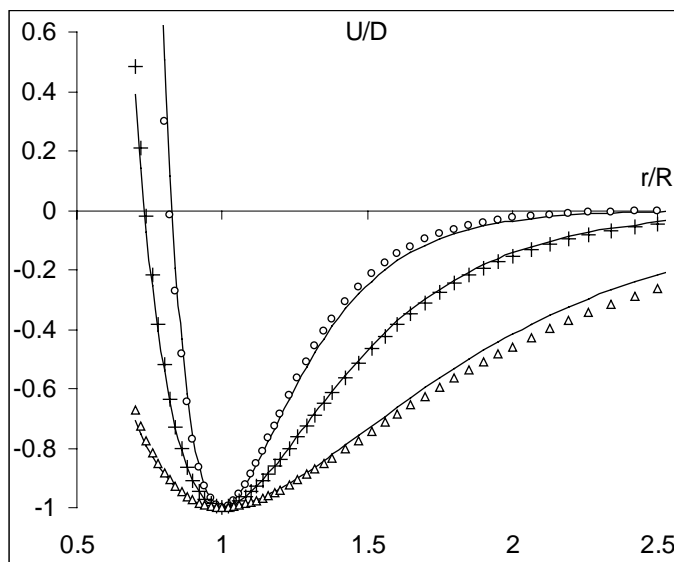
a
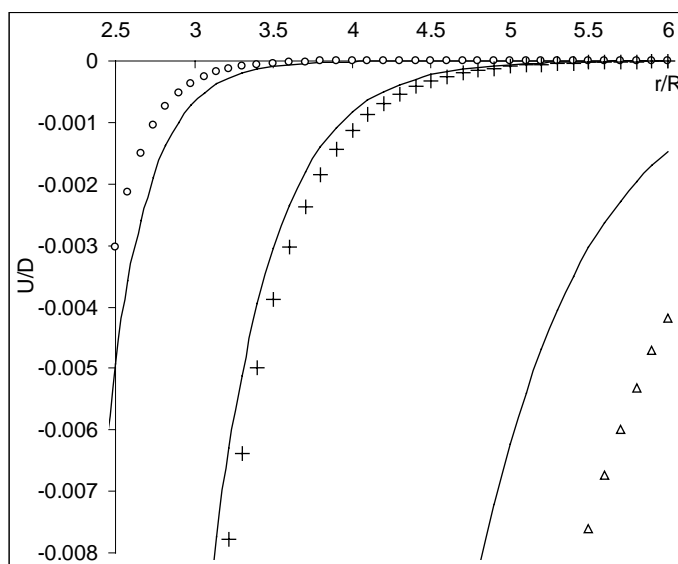
b

Figure 15. FPDP potential energy for ClCl (circles), CO (crosses), and HH (triangles) and the converted Morse potential based on near range for (a) $0.5 \leq r/R \leq 2.5$, and (b) $2.5R \leq r \leq 6.0R$.

increases as shown in figure 17(a). However, the long range relation is highly improved, as observed in figure 17(b). Hence splitting of the Morse function into 3 parts is suggested, if the FPDP parameters were to be adopted for the Morse potential used in molecular mechanics force fields. However if the energy smoothness is an essential necessity then the singular use of Eq.(56) would be sufficient.
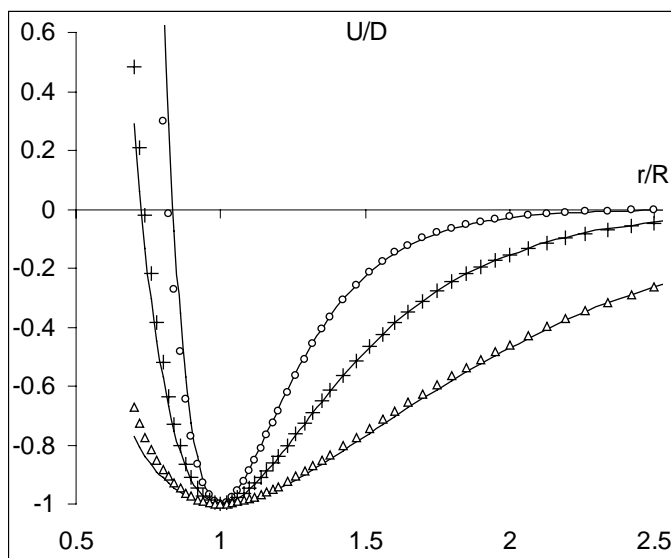
a
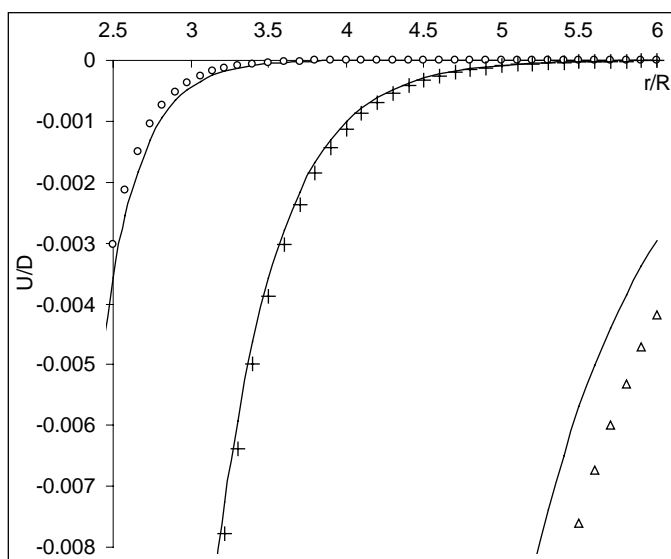
b

Figure 16. FPDP potential energy for ClCl (circles), CO (crosses), and HH (triangles) and the converted Morse potential based on mid range for (a) $0.5 \leq r / R \leq 2.5$, and (b) $2.5R \leq r \leq 6.0R$.
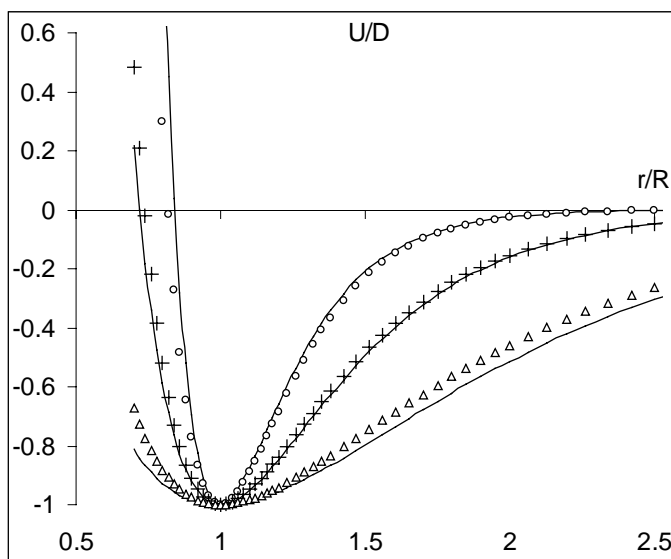
a
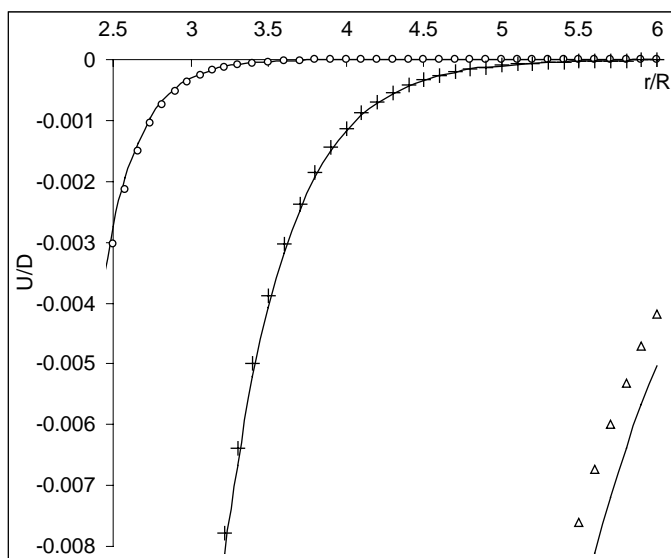
b

Figure 17. FPDP potential energy for ClCl (circles), CO (crosses), and HH (triangles) and the converted Morse potential based on far range for (a) $0.5 \leq r / R \leq 2.5$, and (b) $2.5R \leq r \leq 6.0R$.

4.6. The Linnett Potential Using Morse Parameters

The Linnett potential [4] was introduced for describing the interatomic energy of covalent bond stretching. It is of interest to note that the Linnett function complements the first 3 classical potentials of Lennard-Jones, Morse and Buckingham. With the form

$$U_L = \frac{A_L}{r^m} - B_L \exp(-C_L r), \tag{58}$$

the repulsive term of the Linnett function finds similarity with that of the Lennard-Jones potential while the attractive term is similar to that of the Morse function. The Linnett potential can also be seen to be an "anti-Buckingham" function due to its swopping of the functional forms with reference to the Buckingham potential. The use of Linnett potential for describing the covalent bond stretching is justified, even though this potential is not a common feature in computational chemistry packages presumably due to its relatively late appearance compared to other 3 classical potentials. This is because the Linnett potential correctly tends to infinity as $r \to 0$, unlike the Morse function's bond-compression, but yet resembles the Morse function for bond-stretching due to the similar functional form in the attractive term. This is in addition to the fulfillment of the other 2 conditions that a potential function must possess:

$$\left(\frac{\partial U_L}{\partial r} \right)_{r=R} = 0 \tag{59}$$

and

$$\lim_{r \to \infty} U_L = 0 . \tag{60}$$

Suppose $m = 2n$, the Linnett function can be rewritten in an equivalent form

$$U_L = D\left[\left(\frac{R}{r} \right)^{2n} - 2\exp\left[n\left(1 - \frac{r}{R} \right) \right] \right] \tag{61}$$

This ensures that the repulsive to attractive coefficient ratio is 1:2, similar to that of the conventional Morse potential. Imposing equal force constants, equal equilibrium-to-dissociation energy integral, and equal attractive indices between the Linnett and Morse potential functions, we have [54]

$$n = \frac{1}{2}\left[-1 + \sqrt{1 + (2\alpha R)^2} \right], \tag{62}$$

$$n = \frac{1}{2}\left[\left(\frac{1}{2} + \alpha R \right) + \sqrt{\left(\frac{1}{2} + \alpha R \right)^2 - \frac{8}{3}\alpha R} \right] \tag{63}$$

and

$$n = \alpha R \tag{64}$$

respectively. The Linnett parameter n obtained by Eqs.(62), (63) and (64) are herein termed the short range, mid range and long range respectively. To validate the three parameter relations, the Morse potential energy of molybdenum, iron, barium and rubidium based on the Morse parameters of Girifalco and Weizer [40] were compared with the Linnett potential, whose parameters were obtained from Eqs.(62)-(64). Figure 18 to 20 show the Morse energy of molybdenum (white circles), iron (black circles), barium (white triangles), and rubidium (black triangles), and the corresponding Linnett potential energy (smooth curves).
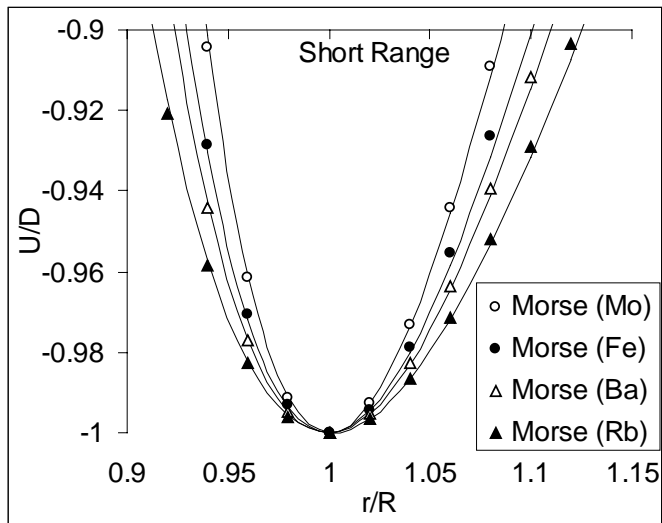
(a)
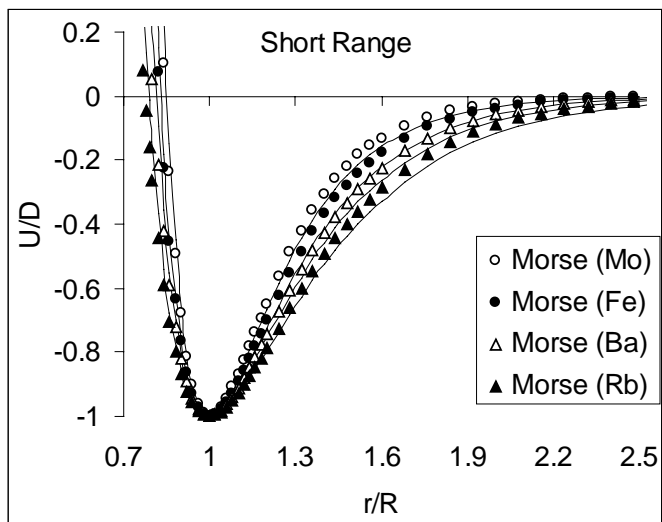
(b)

Figure 18. Plots of Morse potential energy (data points) and the converted Linnett potential energy (curves) using Eq.(62) for short range approach.

The Linnett potential with its parameter based on the short range relation, Eq.(62), gives an excellent agreement at $r \cong R$ (see figure 18(a)) with overestimation and underestimation for $r < R$ and $r > R$ respectively (figure 18(b)). The overestimation for $r < R$ is well justified since the Linnett function tends to infinity as $r \to 0$, unlike the Morse potential.
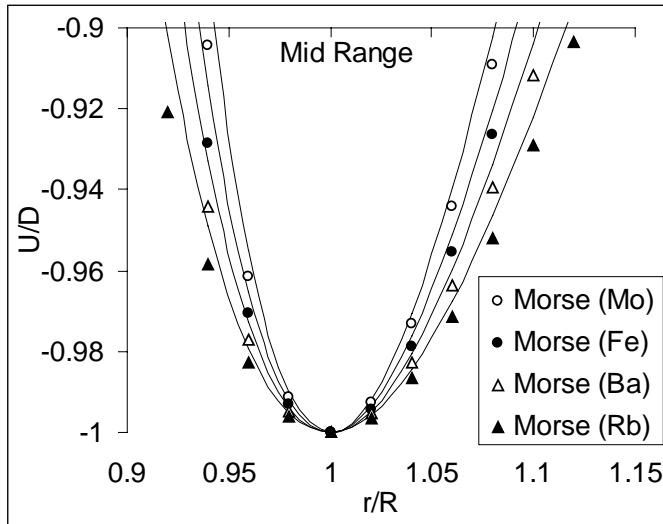
(a)
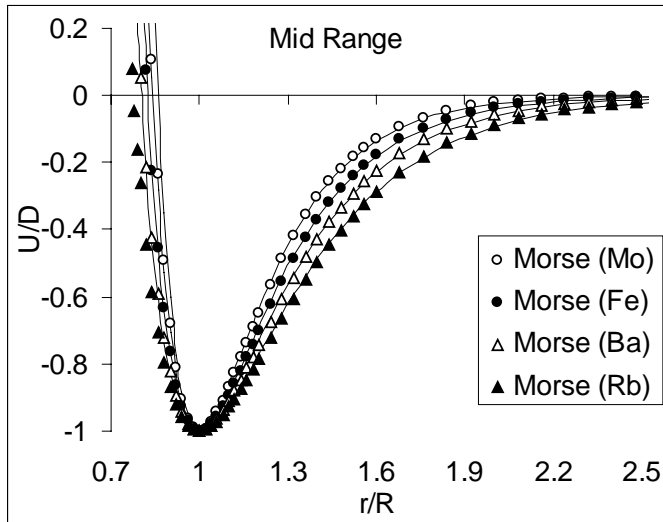
(b)

Figure 19. Plots of Morse potential energy (data points) and the converted Linnett potential energy (curves) using Eq.(63) for mid range approach.

There is a slight compromise in the case of mid range relation, as seen in figure 19(a) for $r \cong R$ and figure 19(b) for $r < R$. However the compromise is well justified due to the good agreement for $r \gg R$ (see figure 19(b)).
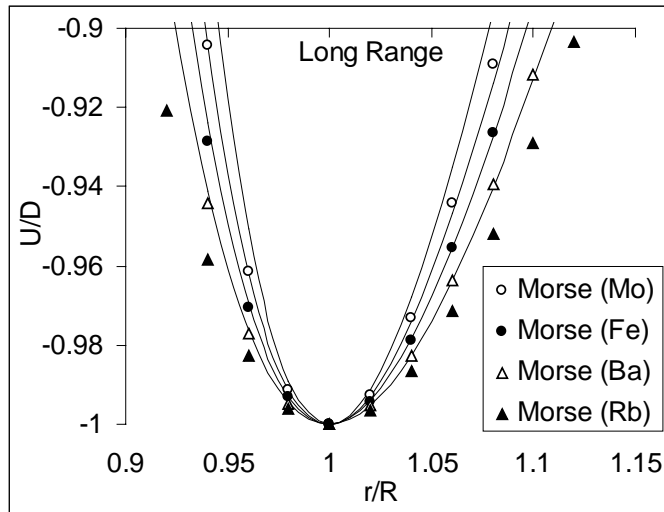
(a)
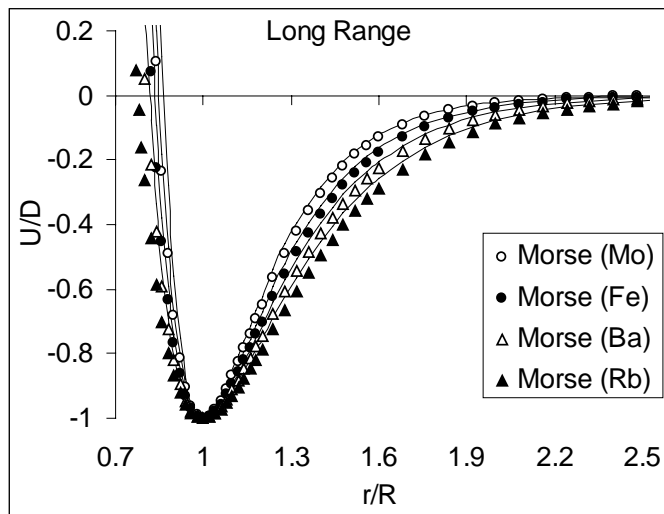
(b)

Figure 20. Plots of Morse potential energy (data points) and the converted Linnett potential energy (curves) using Eq.(64) for long range approach.

Finally, the long range relation gives the greatest extent of inaccuracy for both $r \cong R$ and $r < R$, as seen in figure 20(a) and (b) respectively. It is observable that the Linnett potential overestimates the Morse energy for the range $1.3R < r < 2.2R$. However, the agreement is very good when $r \gg R$. Since $U \approx 0$ for $r \gg R$, the good agreement for very large bond stretching would serve little practical purpose. Hence it is suggested that the use of Eqs.(62) and (63) for applying the Linnett Function is sufficient for practical purposes.

5. Conclusions

Parameter conversion allows parameters of a potential function, which have been obtained through a series of rigorous and costly experimentation and/or ab initio computation, to be converted into parameters of another potential function. The possibility of converting parameters of one potential into those of another potential paves way for enabling simple potentials in computational chemistry packages to approximate the more accurate but more complex potentials through splitting of the former into two or three parts. Parameter conversion can be made for (a) bond compression and near equilibrium bond length changes by imposing equal force constant, which is the second order derivative, (b) intermediate or mid range bond stretching by imposition of equal energy integral from equilibrium to dissociation, and (c) long range either by taking limits of the potential as the bond dissociates or by equating the indices of the attractive terms. These parameter conversions enable commercially available computational chemistry packages to be conveniently modified to attain accurate results without extensive hard-coding. By retaining the same functional forms, the computational speed remains almost the same. Hence molecular parameter conversions lead to significant improvements in the potential energy accuracy with minimal change to the computation speed.

References

[1]   J.E. Lennard-Jones, *Proc. Royal Soc. London A* **106**, 463 (1924).
[2]   P.M. Morse, *Phys. Rev*. **34**, 57 (1929).
[3]   R.A. Buckingham, *Proc. Royal Soc. London A* **168**, 264 (1938).
[4]   J.W. Linnett, *Trans. Faraday Soc.* **36**, 1123 (1940).
[5]   J.N. Murrell, S. Carter, S.C. Farantos, P. Huxley and A.J.C. Varandas, *Molecular Potential Energy Functions* (Wiley, Chichester, 1983).
[6]   S. Erkoc, *Phys. Rep.* **278**, 79 (1997).
[7]   W.D. Cornell, P. Cieplak, C.I. Bayly, I.R. Gould, K.M. Merz Jr, D.M. Ferguson, D.C. Spellmeyer, T. Fox, J.W. Caldwell and P.A. Kollman, *J. Am. Chem. Soc.* **117**, 5179 (1995).
[8]   P. Comba and T.W. Hambley, *Molecular Modeling of Inorganic Compounds*, 1st ed, (VCH, Weinheim, 1995).
[9]   W. Damm, A. Frontera, J. Tirado-Rives and W.L. Jorgensen, *J. Comput. Chem.* **18**, 1955 (1997).
[10] N.L. Allinger, *J. Am. Chem. Soc.* **99**, 8127 (1977).
[11] M.J. Hwang, T.P. Stockfisch and A.T. Hagler, *J. Am. Chem. Soc.* **116**, 2515 (1994).
[12] J.M.L. Dillen, *J. Comput. Chem.* **16**, 595 (1995).
[13] T.A. Halgren, *J. Comput Chem.* **17**, 490 (1996).
[14] N.L. Allinger, K. Chen and J.H. Lii, *J. Comput. Chem.* **17**, 642 (1996).
[15] S. Lifson, A.T. Haggler and P. Dauber, *J. Am. Chem. Soc*. **101**, 5111 (1979).
[16] S.L. Mayo, B.D. Olafson and W.A. Goddard III, *J. Phys. Chem.* **94**, 8897 (1990).
[17] A.K. Rappe, C.J. Casewit, K.S. Colwell, W.A. Goddard III and W.M. Skiff, *J. Am. Chem. Soc*. **114**, 10024 (1992).

[18] S. Barlow, A.L. Rohl, S. Shi, C.M. Freeman and D. O'Hare, *J. Am. Chem. Soc.* **118**, 7579 (1996).

[19] T.C. Lim, Relationships among parameters of molecular potential functions: Theory and applications, in *Horizons in World Physics* Vol. 252 Chemical Physics Research Trends, ed. S.V. Arnold, pp.269-318 (Nova, NY, 2007).

[20] T.C. Lim, *Chem. Phys.* **320**, 54 (2005).

[21] T.C. Lim, *Chin. J. Phys.* **43**, 43 (2005).

[22] T.C. Lim, *Chem. Phys.* **331**, 270 (2007).

[23] D.D. Konowalow and J.O. Hirschfelder, *Phys. Fluids.* **4**, 629 (1961).

[24] R. Stolevic, *J. Mol. Struct. Theochem.* **109**, 397 (1984).

[25] P. Ramamoorthy and N. Krishnamurthy, *Spectrochim. Acta A* **53**, 655 (1997).

[26] S.S. Batsanov, *Zhurnal Obshchei Khimii.* **64**, 529 (1998).

[27] D. Galanakis and C.R. Ganellin, *Bioorg. Med. Chem. Lett.* **14**, 4031 (2004).

[28] M.T.D. Cronin, N. Manga, J.R. Seward, G.D. Sinks and T.W. Schultz, *Chem. Res. Toxicol.* **14**, 1498 (2001).

[29] K. Yokoi and T. Nishikawa, *Mol. Phys.* **90**, 705 (1997).

[30] S.D. Morley, R.J. Abraham, I.S. Haworth, D.E. Jackson, M.R. Saunders and J.G. Vinter, *J. Comput.-Aided Mol. Des.* **5,** 475 (1991).

[31] Pearson, E., Takai, T., Halicioglu, T. and Tiller, W.A., *J. Cryst. Growth.* **70**, 33 (1984).

[32] T.C. Lim, *Mol. Phys.* **105**, 1013 (2007).

[33] R. Biswas and .R. Hamann, *Phys. Rev. Lett.* **55**, 2001 (1985).

[34] T.C. Lim, *Z. Naturforsch. A* **58**, 615 (2003).

[35] R. Rydberg, *Z. Phys.* **73**, 376 (1931).

[36] R. Rydberg, *Z. Phys.* **80**, 514 (1933).

[37] J.N. Murrell and R.E. Mottram, *Mol. Phys.* **69**, 571 (1990).

[38] J.N. Murrell and K.S. Sorbie, *J. Chem. Soc. Faraday Trans.* II **70**, 1552 (1974).

[39] T.C. Lim, *J. Math. Chem.* **43**, 1573 (2008).

[40] L.A. Girifalco and V.G. Weizer, *Phys. Rev.* **114**, 687 (1959).

[41] T.C. Lim, *Mol. Simul.* **33**, 1029 (2007).

[42] P. Huxley and J.N. Murrell, *J. Chem. Soc. Faraday Trans.* II **79**, 323 (1983).

[43] C.L. Yang, Y.J. Huang, X. Zhang and K.L. Han, *J. Mol. Struct. (THEOCHEM)* **625**, 289 (2003).

[44] F. Gao, C.L. Yang and T.Q. Ren, *J. Mol. Struct. (THEOCHEM)* **758**, 81 (2006).

[45] T.Q. Ren, S.L. Ding and C.L. Yang, *J. Mol. Struct. (THEOCHEM)* **728**, 159 (2005).

[46] C.L. Yang, X. Zhang and K.L. Han, *J. Mol. Struct. (THEOCHEM)* **676**, 209 (2004).

[47] T.C. Lim, *Mol. Phys.* **106**, 753 (2008).

[48] Y.P. Varshni, *Rev. Mod. Phys.* **29**, 664 (1957).

[49] T.C. Lim, *Central Eur. J. Phys.* **7**, 193 (2009).

[50] T.C. Lim, *J. Theor. Comput. Chem.* **7**, 1085 (2008).

[51] J.X. Sun, *Acta Phys. Sinica* **48**, 1992 (1999).

[52] C. Gang, *Phys. Lett.* A **328**, 116 (2004).

[53] T.C. Lim, *Internet Electronic J. Mol. Des.* **7**, 77 (2008).

[54] T.C. Lim, *MATCH Commun. Math. Comput. Chem.* **61**, 313 (2009).

Chapter 9

ORBITAL SIGNATURES AS A DESCRIPTOR OF CHEMICAL REACTIVITY: A NEW LOOK AT THE ORIGIN OF THE HIGHEST-OCCUPIED MOLECULAR ORBITAL DRIVEN REACTIONS

Teodorico C. Ramalho[*], Douglas H. Pereira, Rodrigo R. da Silva and Elaine F.F. da Cunha

Department of Chemistry, Federal University of Lavras,
Lavras-MG, 37200-000, Brazil

Abstract

We carried out Hartree-Fock (HF) and density functional theory calculations on the conjugated bases of phenols, alcohols, organic acids, and amines compounds and analyzed their acid-base behavior using molecular orbital (MO) energies and their dependence on solvent effects. Despite the well-known correlation between highest-occupied MO (HOMO) energies and pKa, we observed that HOMO energies are inadequate to describe the acid-base behavior of these compounds. Therefore, we established a criterion to identify the best frontier MO for describing pKa values and also to understand why the HOMO approach fails. The MO that fits our criterion provided very good correlations with pKa values, much better than those obtained by HOMO energies. Since they are the frontier molecular orbitals that drive the acid-base reactions in each compound, they were called frontier effective-for-reaction MOs, or FERMOs. By use of the FERMO concept, the reactions that are HOMO driven, and those that are not, can be better explained, independent from the calculation method used, since both HF and Kohn-Sham methodologies lead to the same FERMO.

1. Introduction

The calculation of gas-phase acid-base parameters has been a well-established methodology. However, the theoretical calculation of acid-base parameters, especially in solution, is a great challenge for quantum chemists [1]. The pKa and consequently the proton

affinity (PA) are the most useful acid-base parameters in aqueous solution and a lot of works have shown how PA values correlate with quantum descriptors [2-6] .

The relationships between HOMO energies and PA are often present for families of compounds, such as phenols [2]. However, for a large number of compounds, HOMO energies do not show good correlation with PA or pKa values, other quantum parameters, such as dipole moments, bond orders, atomic charges on hydrogens, and bond lengths, had to be included in multiple linear regression analysis in ordert o correlate them [3-6]. This procedure certainly weakens the familar idea that donor-acceptor reactions are driven by frontier orbital energies. In line with that, a question arises from the results: why are HOMO energies good acid-base descriptors for some compounds and not for others? A careful study is necessary to understand when HOMO energy works and when it does not because there are clear limitations to the HOMO-LUMO approach, and other concepts are needed to complement HOMO-LUMO arguments. More recently, the Frontier Effective-for-Reaction Molecular Orbital (FEMRO) concept has emerged as a powerful approach for studying this situation [7-9].

In addition to that, there is a lack of studies concerning the most common and important classes of organic compounds, alcohols and phenols, and the relationship of their acid-base behavior with their MO energies.

Molecular orbitals (MOs) and their properties such as energies and symmetries, are very useful for chemists. Since Fukui and coworkers used the frontier electron density for predicting the most reactive position in π-electron systems [10] and Hoffmann and Woodward set out orbital symmetry rules to explain several types of reactions in conjugated systems [11], the frontier MOs gained importance for the better understanding of chemical processes. Therefore, the knowledge of how MOs would control a reaction is a central key for many answers in chemistry.

Although the MOs are very important to chemists, there are some theoretical issues concerning them. The MO comes from the Hartree-Fock (HF) approximation for solving the Schrödinger equation. Because of that, in HF methods and post-HF methods (such as MP2) the MO idea is natural and their properties are widely used to explain many molecular properties and reaction mechanism [12]. However, the HF method has a problem: the lack of electron correlation. In post-HF methods the electron correlation is present, but another problem arises: the calculation time increases too much, and that type of calculation is restricted to small molecules. Because of those problems concerning HF and post-HF methods, the Density Functional Theory (DFT) became a very popular method for calculating the electronic structure of molecules, since it includes the electron correlation and the computer time spent is not as long as it is in post-HF methods.

The DFT orbitals, named Kohn-Sham (KS) orbitals, and MOs are sometimes treated as different quantum descriptors [12]. Another reason for that difference arises from the poor results given by the eigenvalues of KS orbitals in the description of the ionization potentials (IP's) of molecules (the Koopmans' theorem). Politzer and Abu-Awwad have analyzed the behavior of HF and KS orbital energies in many molecules and compared the results with the experimental IP [13], those results indicate that KS orbitals are suitable to use in qualitative MO theory and that the problem with their energies comes from the poor asymptotic behavior of the available functionals.

Thus, this work is devoted to investigate which is the best molecular orbital for describing the acid or base character for a collection of phenol and alcohol compounds in light of the FERMO concept at both Hartree-Fock and DFT levels.

2. Theoretical Approach

2.1. Computational Details

All calculations were carried out with the Gaussian 98 package [14]. Each conjugated base from all 23 compunds was fully optimized using MP2 and DFT with the B3LYP functional [15,16] employing the 6-31G(d,p) basis set. No symmetry constraint was imposed during the optimization process. No imaginary frequencies were found for the optimized geometries. Those optimized geometries were used in all subsequent calculations. MP2 single-point energy calculations were computed using the 6-31G(d,p) basis set.

To account for solvent effects from water, single-point energy calculations were performed using the polarizable continuum model (PCM) [17-19] and the conductor like screening model (COSMO) [20.21] at both DFT/mPW1PW91 and MP2 levels with 6-31G(d,p) basis set. The orbital energies from these methods were fit to a linear model with experimental PA values and the Determination coefficients (r^2) were analyzed.

The MOs figures were prepared using the Gaussian View 2.1 package [14] with a contour value of 0.020.

2.2. Orbital Choice Criteria

It is well known that Bronsted-Lowry acid-base reactions are localized phenomena, which take place between the proton and one atom (or group of atoms) in a molecule [22].. Therefore, the MO which drives those reactions must be centered in this atom or group of atoms. Thus, we carried out the investigation of these orbitals in two different ways: by looking at the orbital shapes [22] and by calculating the MO composition using the expansion coefficients.

2.3. Phenols and Alcohols

Table 1 shows the 23 Phenols and alcohols used in this work and their experimental values of the proton affinity (PA) for the reaction.

Table 1. Phenols and alcohols and their experimental proton affinity (PA) values

Número	Molecules	PA	Ref.
1	Methanol	754.3	a
2	Ethanol	776.4	a
3	Propanol	786.5	a
4	Isopropanol	793.0	a

Table 1. Continued

Número	Molecules	PA	Ref.
5	Butanol	789.2	a
6	Isobutanol	793.7	a
7	Sec-butanol	815.0	a
8	Hexanol	804.6	a
9	2,2,2-Trifluoro-ethanol	786.13	a
10	p-amino phenol	352.5	b
11	p-methoxy- phenol	350.4	b
12	p-hydroxy- phenol	350.4	b
13	p- methyl- phenol	350.3	b
14	phenol	347.5	b
15	p-terc-phenol	348.5	b
16	p-dimethylamino-phenol	351.5	b
17	p-fluoro-phenol	346.8	b
18	p-chloro- phenol	343.1	b
19	p-trifluoromethyl- phenol	337.0	b
20	p-carboxi- phenol	335.9	b
21	p-cyano- phenol	332.0	b
22	p-ethanol- phenol	333.0	b
23	p-nitro- phenol	327.8	b

a - Experimental data, in NIST Chemistry WebBook, NIST MD, 20899 (http//webbook.nist.gov).
b – ref [2].

3. Results and Discussion

3.1. HOMO and Chemical Reactivity

Some works in literature show that the HOMO energy (highest-occupied molecular Orbital) is related to the acid-base behavior of some compounds [23]. Thus, in our work, we correlated the energy values of the HOMOs with their PA values.

The correlations between the energy values of HOMO had been made with the conjugated bases of R-OH compounds and the results reported for both phenols and alcohols. From our calculations, we can observe that ionic groups (alkoxides and phenoxides) together provided very poor linear models (table 2). The exception to that conclusion was the DFT/6-311G(d,p) methodology, because we can get acceptable determination coefficients. From these data, two doubts appear: i) Can the two groups be correlated together? ii) Will the HOMO orbital be the best orbital to describe the reaction?

In order to find the answer to those questions, we separated our data in two groups: alcohols (alkoxides) and phenols (phenoxides).

Now we can analyze only the phenoxide group, whose results are presented in table 3. Whereas, the linear correlations for the HOMO in all the methodologies are good, except for the DFT/6-311G(d,p) methodology, the doubt still remains: will the HOMO be the same as the best orbital to describe the chemical reaction? In line with this, we expanded the correlations between PA and energy values for HOMO-1, HOMO-2, and HOMO-3 (table 4). From table 4, we can analyze the correlations between the energy values of each orbital and

the PA values. According to that, good correlations are also found, but none that indeed confirm which orbital really could describe the following chemical reaction:

$$R\text{-}OH \rightarrow R\text{-}O^- + H^+$$

with those correlations, it is not possible to distinguish, which orbital is the best to describe the acid/base chemical reaction. At this point, we calculated the ionization potentials for the compounds using the OVGF method (Outer Valence Green's Function) [24], in order to get more accurate energy values for the orbitals.

Table 2. Linear regression parameters for PA values vs HOMO (Phenoxide and Alkoxide Ions)

methodology	r^2	A	B
MP2/6-311G(d,p)	0.03277	552.72943	395.26751
MP2/PCM/6-311G(d,p)	0.79641	71.03561	2522.12656
MP2/cosmo/6-311G(d,p)	0.78921	1269.38595	6648.6238
DFT/ 6-311G(d,p)	0.8453	431.23953	4206.24837
DFT/PCM/6-311G(d,p)	0.74206	1800.00722	8292.4066
DFT/cosmo/6-311G(d,p)	0.74701	1805.71851	8280.34579

r^2 (linear correlation) a Angular coefficient and b Linear coefficient.

The results of the ionization potential, at HF/6-311G(d,p) level, are presented in table 5. Good correlations are obtained for all orbtials, thus it is not feasible to identify the best orbital that will describe the chemical reaction. Figure 1 shows the orbital for the molecule **21** (p-cyano-phenoxide) and **13** (p-methyl-phenoxide) using at the DFT or MP2 levels.

Table 3. Correlation between energie values of HOMO and PA for Phenoxides

methodology	r^2	a	b
MP2/6-311G(d,p)	0.96116	379.55	406.41
MP2/PCM/6-311G(d,p)	0.95824	476.00346	539.6456
MP2/cosmo/6-311G(d,p)	0.9562	479.27186	551.61192
DFT/ 6-311G(d,p)	0.77757	346.4226	259.30871
DFT/PCM/6-311G(d,p)	0.92545	440.50514	581.83915
DFT/cosmo/6-311G(d,p)	0.83005	424.3507	478.52485

r^2 (linear correlation) a Angular coefficient b Linear coefficient.

The results at all calculation levels for alkoxide ions were disappointing (table 6). It was found that none of those regressions could be considered as a linear model. Thus, for both groups (alkoxides and phenoxides), it was not possible to rationalize the acid/base behavior.

The HOMO problem arises from the influence of the aromatic π-electrons, and the solution would be finding a MO that does not have this influence. Thus, the pxpy-type MOs became a natural choice to solve this problem. Moreover, they also fit our orbital choice criterion, because they are common to all of the studied compounds and are mainly located where the reaction takes place, in the oxygen atom. From this point of view, other concepts of chemical reactivity could be useful to understand reactions that were not driven by HOMO-

LUMO properties. Recently, Silva and Ramalho proposed a simple and useful tool to explain this kind situation (the FERMO concept) [7-9].
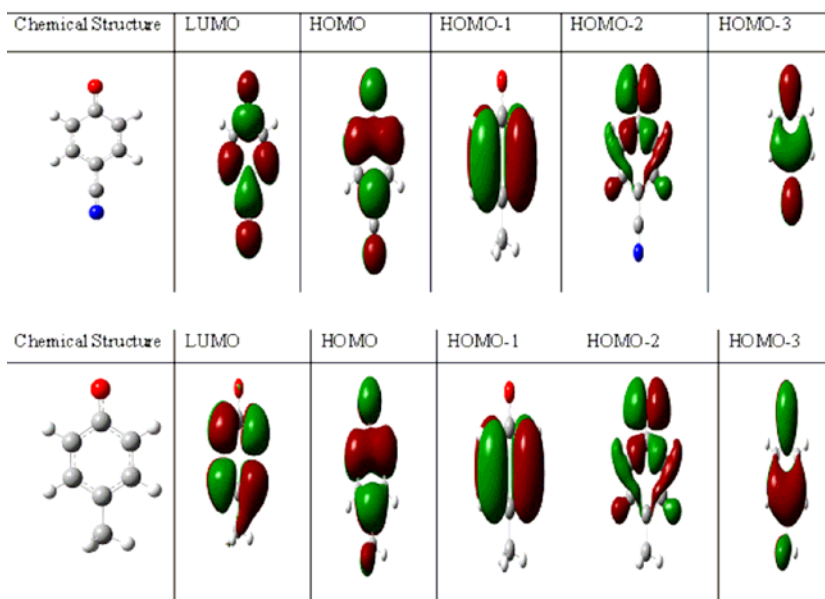
Figure 1. (A). Representation of the molecular orbital to the bases for the combined-cyano- Phenoxides and para-methyl- Phenoxides-level MP2.
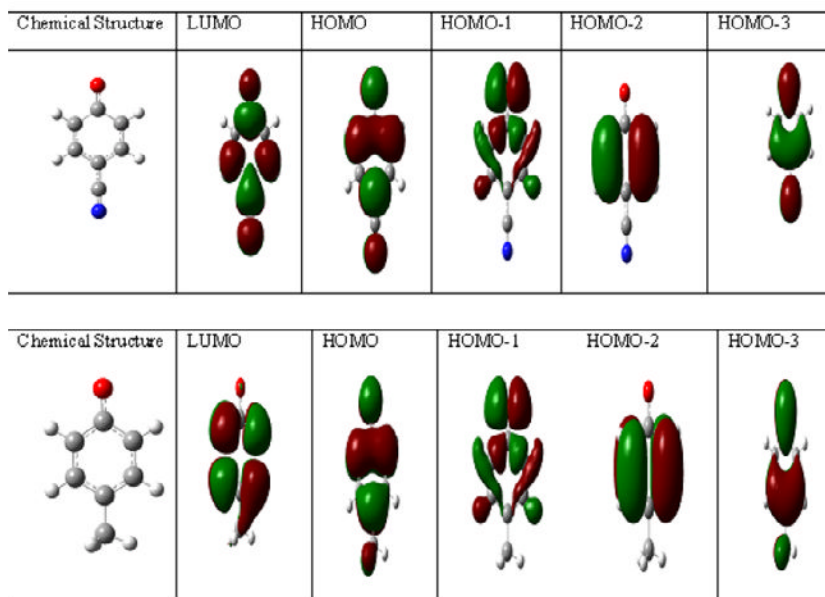
Figure 1 (B). Representation of the molecular orbital to the bases for the combined-cyano- Phenoxides and para-methyl- Phenoxides-level DFT.

Thus, based on the FERMO idea, we expanded the correlations for the other frontier orbitals (HOMO-1, HOMO-2, and HOMO-3 (table 4)). Furthermore, in the FERMO concept, MO composition and shape are taken into account to identify the MO which will actually be involved in a given reaction. A molecule could have as many FERMOs as it has reactions sites and it could be the HOMO or any other frontier MO.

Table 4. Correlation of energy of the molecular orbital LUMO,
HOMO-1, HOMO-2, HOMO-3 with the value of PA for the Phenoxides

methodology	r^2/LUMO	r^2/HOMO-1	r^2/HOMO-2	r^2/HOMO-3
MP2/6-311G(d,p)	0.92245	0.84991	0.95823	-0.24177
MP2/PCM/6-311G(d,p)	0.87934	0.93903	0.83791	0.60963
MP2/cosmo/6-311G(d,p)	0.87902	0.93903	0.83831	0.60943
DFT/ 6-311G(d,p)	0.86635	0.72088	0.93695	0.60687
DFT/PCM/6-311G(d,p)	0.9137	0.73212	0.87898	0.33447
DFT/cosmo/6-311G(d,p)	0.95701	0.68655	0.85028	-0.18095

One should keep in mind that acid/base reactions are localized. Upon analyzing the localization and the composition of the orbitals more deeply, it can be observed that there is a molecular orbital with energy quite close to the HOMO energy value and with large oxygen contribution (table 7). Thus, perhaps that orbital could better describe the acid/base behavior than HOMO. Therefore, this special orbital will be called PxPy and the HOMO orbital we will call Pz.

Nevertheless, from the data listed in table 5, another doubt appears: the HF orbital present a form (shape) identical to the orbital DFT?

Table 5. Results from the correlation of PA with the ionization potential

Orbital	r^2	A	b
Lumo	0.90563	283.35781	7.71493
Homo	0.96906	378.42357	14.28591
Homo (-1)	0.96906	378.42357	14.28591
Homo (-2)	0.97801	412.5735	13.26226
Homo (-3)	0.84199	433.69358	12.88206

r^2 (linear correlation) a Angular coefficient b Linear coefficient.

The orbital found in the methodology MP2/6-311G(d,p) is very similar to the orbitals found in the methodology DFT/ 6-311G(d,p) .These similarities also appear in other methodologies too. It is well-known that the molecular orbital is extremely sensitive to the calculation method, base set, and the solvent effect, as previously described in the literature [7-9]. According to previous works, our findings in this paper indicated that the solvent effect can be rejected for the phenol group due to the higher hydrophobic character conferred by the aromatical ring.

Figure 2 describes the PxPy orbital and HOMO of some selected molecules. It is worth noting that comparing its form (shape) with the result of the atomic composition presented in table 6, we observe that the PxPy orbital receives a larger contribution from the oxygen atom.
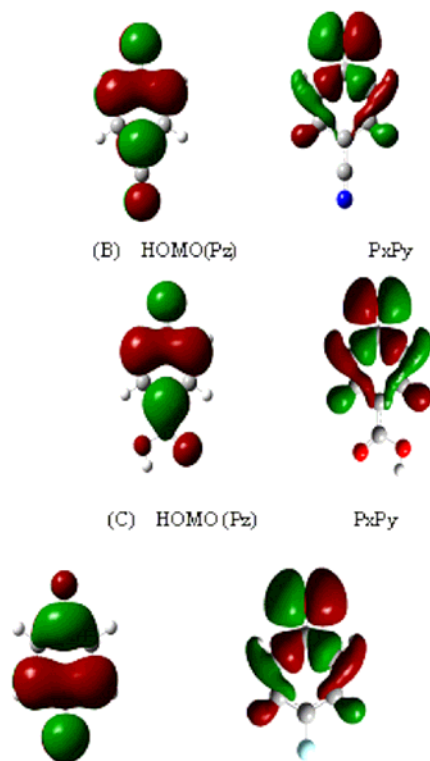
Figure 2. Representation of the molecular orbital Pz and PxPy for the combined bases p- Phenoxides - cyano-(A) p-carboxy- Phenoxides (B) and the p-Fluor- Phenoxides (C) at MP2 level.

Table 6. Correlation between energie values of HOMO and PA for Phenoxides

Metodology	r^2	a	b
MP2/6-311G(d,p)	0.45724	748.50919	-455.77741
MP2/PCM/6-311G(d,p)	0.8792	453.0908	-1680.6473
MP2/cosmo/6-311G(d,p)	0.8679	480.1635	-1530.7569
DFT/ 6-311G(d,p)	0.3002	826.35962	-422.88623
DFT/PCM/6-311G(d,p)	0.77801	493.49372	-2096.11142
DFT/cosmo/6-311G(d,p)	0.80007	533.03822	-1790.58041

r^2 (correlação linear) a coeficiente angular b coeficiente linear.

From figure 2, it is clear that the HOMO is formed mainly by the atomic Pz orbital of the oxygen, while the PxPy orbital has a high contribution of the atomic Px and Py type orbital of oxygen. A direct consequence of the different compositions of these orbitals is the position of their node planes in relation to the plane formed by hydroxyl atoms, where the HOMO presents two node planes in perpendicular orbital and the other coplanar. The PxPy orbital is perpendicular to the plane formed by the hydroxyl group. Observing the surface of the HOMO (Pz), we understand that it possesses large contribution from the π system of the aromatic ring. While the PxPy orbital is not under the influence of the π system of the phenoxide compounds, being then a frontier orbital with a high oxygen contribution. In line with that, one question arises: would it be the PxPy type orbital of the Phenoxides which governs the chemical reaction of protonation?

In spite of the results obtained for phenol and alcohol conjugated bases as independent groups, they should be considered as only one group, as they have the same acid/base group, the OH/O-. Having the same acid/base group implies that acid-base reactions will be driven by a MO common to both alkoxide and phenoxide ions. We have just shown that the HOMO is not this common orbital, since its energy cannot describe the acid-base behavior of alcohols and phenols as a single group. The question now is which MO should be used to unify them into a single group?

Analyzing the composition reported in the table 7 together with the MO shape, we can note that the best orbital to describe the chemical reaction is the PxPy orbital. In line with this expectation, we correlated their energie values with PA values in order to show which the best orbital is to describe the chemical reaction. The graphs of the correlations are reported in figure 3.

Table 7. Oxygen contribution (%) for the phenoxide and alkoxide ion using the methodology (B3LYP/6-31G(d,p)). In Blue the PxPy orbital and in Red the Pz orbital

Moléculas	HOMO	HOMO-1	HOMO-2
1	68.34	69.20	26.31
2	65.40	67.35	30.04
3	58.20	62.43	37.27
4	59.40	61.29	78.02
5	57.30	60.06	62.18
6	53.86	58.60	12.86
7	56.36	63.10	35.40
8	59.08	70.03	49.63
9	62.30	64.28	0.00
10	66.23	0.00	69.36
11	65.01	0.00	72.49
12	68.06	0.0	72.31
13	65.46	0.00	58.40
14	67.64	0.00	57.32
15	64.04	0.00	70.3
16	69.40	0.015	80.94
17	67.47	0.27	68.15
18	66.61	65.26	80.4
19	62.71	0.00	73.40
20	58.27	0.00	69.65
21	62.85	0.81	100
22	59.26	0.00	69.46
23	56.74	0.023	64.38

From the reported results of the correlation in figure 3, we can not conclude, for the phenoxide group, which orbital is preferentially reacting when analyzing only the correlation coefficients; because, interestingly, all the correlation coefficients were good. Therefore, it is

necessary to analyze the node planes, the specific forms for each orbital (Shape) and the composition to determine which orbital will govern that chemical reaction.

Based on idea that both phenol and alcohol groups have the hydroxyl group, that it is, effectively, the acid-base group (figures 4 and 5), it is interesting to note that the PxPy orbital type of the Phenoxides does not maintain a relation with the resonance effect (figure 4) because it is perpendicular to the plane of the aromatic ring. In line with that, we can consider that the PxPy orbital could be the orbital responsible for the acid/base reaction in alcohols, aliphatic and aromatic (phenols). This certainly confirms recent findings in the literature [7-9].

We got the worst results for linear correlation with the energy values of the HOMO orbital, the best correlations being those where the solvent effect is taken into consideration. In line with that, we concluded that the solvent effect for the aliphatic alcohols is significant when compared with phenol group. The orbital correlations of the PxPy with PA of the alcohols are much better as shown in table 7. Here, the solvent effect was also important.
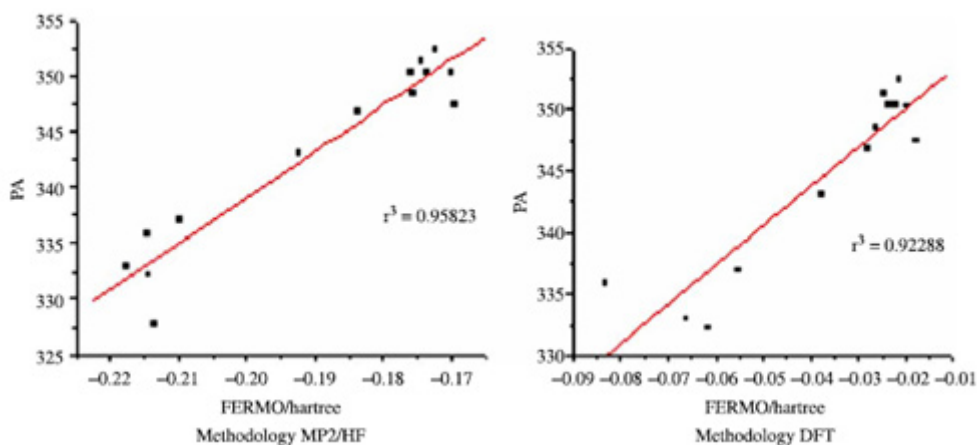
Figure 3. Graphics of the correlation energy of the PxPy orbital with methodology for AP (B3LYP/6-31G(d,p)) and (MP2/6-31G(d,p)) methodology.
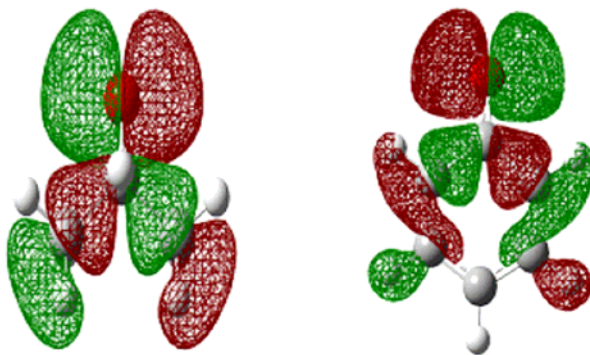
Figure 4. Comparison of the orbital HOMOs for molecules of isopropoxide Phenoxides.
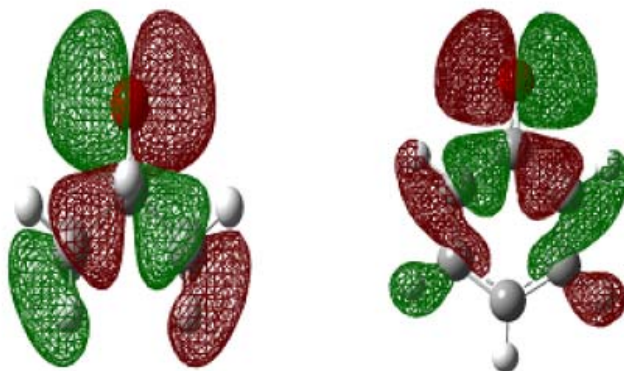
Figure 5. Comparison of the PxPy orbital for molecules of isopropoxide Phenoxides.
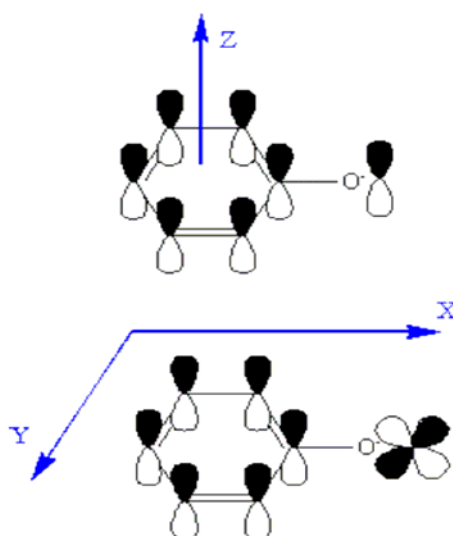
Figure 6. Molecular alignment of Pz and PxPy orbital for the Phenoxides.

3.2. The Orbital which Governs the Reaction

On the basis of the composition and localization of the orbital, it is possible to get insights about the orbital that governs the reaction of the phenoxide and alkoxide. The composition of the orbital is an important indicator for discovering the adequate orbital. The MO shape and the atomic composition are very important parameters for analyzing FERMO. Since HOMO problem arises from the influence of the aromatic π-electrons, the solution would be finding a MO that does not have this influence. Thus, the PxPy-type MOs became a natural choice to solve this problem. Moreover, they also fit our orbital choice criterion, because they are common to all of the studied compounds and are mainly located where the reaction takes place, at the oxygen atom.

It is well-known that a reaction is governed by a frontier orbital, which is not necessarily HOMO or LUMO. From this point of view, other concepts of chemical reactivity could be

useful to understand the acidity of alcohols and phenols. With the analyses performed in this work, it is possible to identify the Frontier Effective-for-Reaction Molecular Orbital (FERMO) for acid/base chemical reactions. In fact, many chemical reactions can be explained using the HOMO-LUMO arguments, however, there is a lot of them that that are not [7-9], which could easily be understood with the application of the FERMO concept. An important aspect is that the FERMO concept can be applied at HF, pos-HF or DFT level. This means that either HF or KS orbitals lead to the same conclusions on the chemical reactivity. This again brings us to the discussion on the validity of the interpretation of the KS orbitals. Thus we conclude that the FERMO concept embraces well the HOMO-LUMO argument and its exceptions.

3.3. The Effect of the Resonance

From our theoretical results and correlation coefficients between orbital energy values and PA, it was not possible to identify, with precision, the FERMO for that reaction in the phenol group. Therefore it became necessary to analyze the forms (shape) and the atomic composition of the orbital. Nevertheless, for the aliphatic alcohol group, the FERMO was easily identified mainly by the MP2/6-311G(d,p) and DFT/6-311G(d,p) methodologies, where the correlation coefficients had shown a great variation between HOMO(Pz) orbital and the PxPy orbital, which suggests that really the FERMO is the PxPy orbital. Another question that appears at this moment is: what is difference between the two compound groups. Why was the FERMO easily identified for one and not the other? To answer such a question, the energy differences (ΔE) between the HOMO and PxPy was analyzed. The results are reported in table 9.

In order to get more accurate values for the orbital energies, we calculated ionization potential with OVGF method [23,24]. From table 8, with the variation of the ionization potential energy, we observe a large energy difference between the molecular orbital PxPy and HOMO (Pz) for the phenol group, while for the aliphatic alcohol group the energy variation was much smaller. This fact is curious, because the two compound groups present the same types of orbital (figure 2). However, turning our attention to the phenol group, we can note that HOMO (Pz) has large influence from the π system and this leads to the energy increasing. In fact, the alignment between the "p" carbon orbital of the aromatic ring and the Pz atomic orbital of oxygen leads to strong interaction energy. Thus, the free electron moving from PxPy to the Pz orbital, increasing the electron population on the HOMO (pz), resulting in a good correlation between the Pz energy values and the PA results.

In literature, a good correlation between the theoretical and experimental values for **10** to **23** molecules is easily observed [2]. However, it must be noticed that the aliphatic alcohol group (alkoxides) was not studied in combination with phenols. In fact, to our knowledge the understanding of the substituent effect on the acidity of both alcohol group (phenol and aliphatic) have not been investigated so far. Using the HOMO-LUMO properties, phenoxide and alkoxide ions together provided very poor linear models. However, it is interesting to note that both groups (aliphatic and aromatic alcohols) have the same reactivity group, which is the hydroxyl group. Therefore, we could expect a similar behavior for the acid/base chemical reaction. Our data reinforce this idea, because the alkoxides and phenoxides show the same FERMO.

**Table 9. Variation between the Pz and PxPy orbital energies
(hartrees) for the values of the ionization potential**

Molecule	E_{Homo}	E_{Pxpy}	ΔEnergy
1	--	-1.721	--
2	-2.15	-2.259	0.109
3	-2.271	-2.326	0.055
4	-2.276	-2.387	0.111
5	-2.223	-2.288	0.065
6	-2.51	-2.62	0.120
7	-2.556	-2.694	0.138
8	-2.467	-2.541	0.074
9	-3.454	-3.742	0.288
10	-1.942	-4.556	2.614
11	-1.787	-4.704	2.917
12	-2.15	-4.756	2.606
13	-1.827	-4.497	2.67
14	-1.999	-4.468	2.469
15	-2.368	-4.687	2.319
16	-2.103	-4.642	2.539
17	-2.21	-4.946	2.736
18	-2.646	-5.23	2.584
19	-3.005	-5.481	2.476
20	-2.971	-5.388	2.417
21	-3.048	-5.575	2.527
22	-3.557	-6.041	2.484
23	-3.557	-6.041	2.484

4. Conclusions

In this paper, we have demonstrated that the FERMO concept can be applied to understand the acid/base behavior combining two important organic groups (alkoxides and phenoxides) in a very simple and chemically intuitive way. In fact, the use of the FERMO concept made the unification of the acid character of phenols and alcohols possible, thus showing that this is a general concept. In this way, it is not necessary to introduce too many correction terms (formulas), in order to obtain reactivity properties of compounds in solution. Also important is the independence of the results from the calculation method, as both HF and DFT MOs lead to the same FERMOs and conclusions about chemical reactivity. In principle, the FERMO can be used to understand reactions that the HOMO-LUMO [25,26] approach did and did not explain, thus making the role of MO theory in chemistry stronger.

Acknowledgments

References

[1]   W.J. Here, L. Random, P. P. Schleyer, J.A. People. *Ab Initio Molecular Orbital Theory.* 2006.
[2]   R. Vianello, Z.B. Makisié, *Tetrahedron.* **62** (2006) 3402.
[3]   O.Pytela, M. Otyepka, J. Kulhánek, E. Otyepková, T. Nevëëná, *J. Phys. Chem. A*, **107** (2003) 11489.
[4]   C. Gruber, V Buss. *Chemosphere.* **19** (1989) 15.
[5]   M.J. Citra. *Chemosphere.* **38** (1999) 191.
[6]   E. Sorino, S. Cerdán, P.Ballesteros *J. Mol. Struct. (Theochem)* **684** (2004) 121.
[7]   R.R. Da Silva, T.C. Ramalho, J.M. Santos, J.D. Figueroa-Villar *J. Phys. Chem. A* **110** (2006) 1031.
[8]   R.R. Da Silva, T.C. Ramalho, J.M. Santos, J.D. Figueroa-Villar *J. Braz. Chem. Soc.* **17** (2006) 223.
[9]   R.R. Da Silva, T.C. Ramalho, J.M. Santos *J. Phys. Chem. A* **110** (2006) 10653.
[10] K. Fukui, T. Yonezawa, H.J. Shingu, *Chem. Phys.* **20** (1952) 722.
[11] R. Hoffmann, R. Woodward*, J. Am. Chem. Soc.* **87** (1965) 395.
[12] W. Kohn, A.D. Becke, R.G. Parr*, J. Phy. Chem.* **100** (1996) 12974.
[13] P. Politzer, F. Abu-Awwad, *Theor. Chem. Acc.* **99** (1998) 83.
[14] M. J. Frisch, et al. Gaussian 98 (Revision A.11); Gaussian: Pittsburgh, 2001.
[15] A.D. Becke, *J.Chem.Phys.* **98** (1993) 5648.
[16] C. Lee, W. Yang, R.G. Parr, *Phys. Rev .B.* **37** (1988) 785.
[17] S. Miertus, E. Scrocco, J. Tomasi, *J. Chem. Phys.* **55** (1981) 117.
[18] S. Miertus, *Chem. Phys.* **65** (1982) 239.
[19] M. Cossi, V. Barone, R. Cammi, *J. Tomasi Chem. Phys. Lett.* **225** (1996) 327.
[20] Klamt, G. Schuurmann, *J. Chem. Soc.,Perkins Trans***. 2** (1993) 799.
[21] V. Barone, M. Cossi, *J. Phys. Chem. A* **102** (1998) 1995.
[22] T.C. Ramalho, E.F.F. da Cunha, R.B. de Alencastro, *J. Mol. Struct. (Theochem)* **676** (2004) 149.
[23] L.S. Cerdebaum, W. Domcke, *Adv. Chem. Phys.* **36** (1977) 206.
[24] W.V. Niessen, J. Shirmer, L. S. Cerdebaum. *Comput. Phys. Rev.* **1** (1984)57.
[25] T.C. Ramalho, E.F.F. da Cunha, F.C. Peixoto, *J. Theor. Comput. Chem***. 7** (2008) 37.
[26] E.F.F. da Cunha, R.B. de Alencastro, T.C. Ramalho, *J. Theort. Comput. Chem***. 3** (2004) 1.

Chapter 10

WAVELET BASED APPROACHES AND HIGH RESOLUTION METHODS FOR COMPLEX PROCESS MODELS

Hongmei Yao[1], Tonghua Zhang[1], Moses O. Tadé[1] and Yu-Chu Tian[2]

[1] Centre for Process Systems Computations,
Department of Chemical Engineering, Curtin University, GPO Box U1987, Perth,
Western Australia 6845, Australia
[2] School of Information Technology,
Queensland University of Technology, GPO Box 2434, Brisbane,
Queensland 4001, Australia

Abstract

Many industrial processes and systems can be modelled mathematically by a set of Partial Differential Equations (PDEs). Finding a solution to such a PDF model is essential for system design, simulation, and process control purpose. However, major difficulties appear when solving PDEs with singularity. Traditional numerical methods, such as finite difference, finite element, and polynomial based orthogonal collocation, not only have limitations to fully capture the process dynamics but also demand enormous computation power due to the large number of elements or mesh points for accommodation of sharp variations. To tackle this challenging problem, wavelet based approaches and high resolution methods have been recently developed with successful applications to a fixed-bed adsorption column model.

Our investigation has shown that recent advances in wavelet based approaches and high resolution methods have the potential to be adopted for solving more complicated dynamic system models. This chapter will highlight the successful applications of these new methods in solving complex models of simulated-moving-bed (SMB) chromatographic processes. A SMB process is a distributed parameter system and can be mathematically described by a set of partial/ordinary differential equations and algebraic equations. These equations are highly coupled; experience wave propagations with steep front, and require significant numerical effort to solve. To demonstrate the numerical computing power of the wavelet based approaches and high resolution methods, a single column chromatographic process modelled

by a Transport-Dispersive-Equilibrium linear model is investigated first. Numerical solutions from the upwind-1 finite difference, wavelet-collocation, and high resolution methods are evaluated by quantitative comparisons with the analytical solution for a range of Peclet numbers. After that, the advantages of the wavelet based approaches and high resolution methods are further demonstrated through applications to a dynamic SMB model for an enantiomers separation process.

This research has revealed that for a PDE system with a low Peclet number, all existing numerical methods work well, but the upwind finite difference method consumes the most time for the same degree of accuracy of the numerical solution. The high resolution method provides an accurate numerical solution for a PDE system with a medium Peclet number. The wavelet collocation method is capable of catching up steep changes in the solution, and thus can be used for solving PDE models with high singularity. For the complex SMB system models under consideration, both the wavelet based approaches and high resolution methods are good candidates in terms of computation demand and prediction accuracy on the steep front. The high resolution methods have shown better stability in achieving steady state in the specific case studied in this Chapter.

1. Introduction

The term "chromatography" is referred to any separation process that depends on the partition between a flowing fluid and a solid adsorbent based on the different adsorption behaviours of the mixture components. The strengths of the chromatography technique are especially manifested in the separation of isomers and natural materials. The SMB chromatography is the technical realisation of a countercurrent adsorption process, approximating the countercurrent flow by a cyclic port switching. It consists of a certain number of chromatographic columns connected in series, and the countercurrent movement is achieved by sequentially switching the inlet and outlet ports one column downwards in the direction of the liquid flow after a certain period of time. This mechanism is illustrated in the diagram in figure 1.

(a) Current switching period   (b) Next switching period
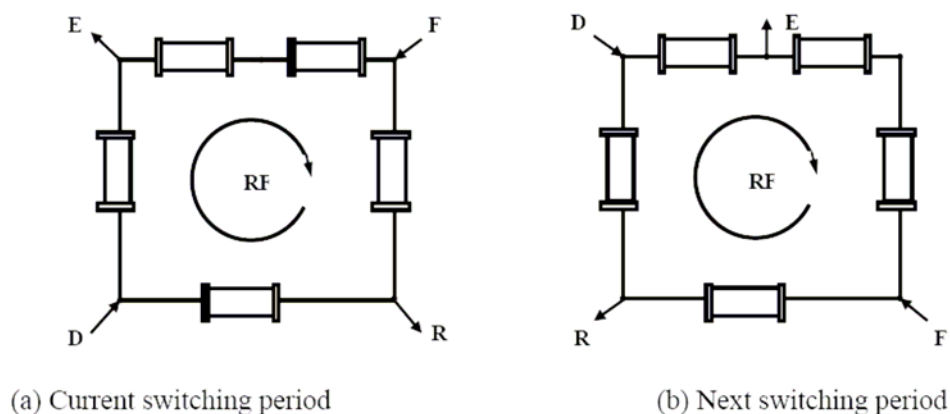
Figure 1. An SMB unit with 5 columns in 4 sections configuration of 1/2/1/1(RF: direction of fluid flow and port switching).

Simulated moving bed chromatography (SMBC) provides a viable alternative to the traditional energy-intensive separation processes, which account for a large proportion of the capital and operating cost of the process industry. Economically, a higher concentration of solute can be designed in the feed in an SMBC process, and the resulting total concentrations of the products are much higher. An SMBC process runs and produces the desired product continuously without significant operator interventions. The nature of SMB operations in fact stretches the separation column. Higher internal recirculation rate reduces the volume of the stationary phase required. The increased mass transfer driving force results in minimization of the adsorbent and eluent requirements for a given separation duty.

Increasing applications of the SMBC technology trigger a further attention in the development of numerical solution tools for improved design and effective control. Typically, a dynamic SMBC process is mathematically modelled by a set of partial differential equations (PDEs) for mass balance over the column, ordinary differential equations (ODEs) for parabolic intraparticle concentration profile and algebraic equations (AEs) for equilibrium isotherms and node mass balances. It is a distributed parameter system in which the dependent variables vary with axial position and time. The number of model equations is enlarged in folder with the number of columns involved and the components to be separated. Although for specific cases, there exist analytical solutions to a single column model, it is impossible to obtain analytical solutions for a SMB system with all the equations highly coupled.

The methods of finite difference, finite element or finite volume are traditionally employed to solve PDEs numerically. Most existing research employ the finite element method (FEM) to discretize the convection-dominated parabolic PDEs of the liquid phase and orthogonal collocation for diffusion-dominated PDEs of the solid phase (Gu, 1995). The resulting ordinary differential equation system is in general very complex and has an enormous need for computational power. Other methods developed for single column (or fixed-bed adsorption) model are not always extended for solving SMB model due to the complexity of the resulting modelling system. Effort has been made either on the development of spatial discretization technique or on the improvement of integration performance. Because some well-known stiff ODE solvers, e.g. the Gears method, can provide very good temporal performance, in this chapter, we will focus on two recently developed discretization techniques, the wavelet collocation and high resolution methods, for the numerical solution of convection-diffusion type PDEs with singularity. More details on the SMB technology development and recent advances in modelling can be found in Yao et al. (2008).

This Chapter is organised as following. In Section 2, we gave an overview on some advances in the numerical computing of sharp wave PDEs. Firstly, various adaptive grid algorithms and Upwinding schemes based on traditional finite discretization technique are summarised. Then using wavelet collocation and high resolution approach for the solution of PDEs will be reviewed. The theoretical background for the two investigated methods will be briefly introduced in Section 3. Section 4 presents a preliminary study on a single column model to investigate the performance of finite difference, wavelet collocation, and high resolution methods under a range of process parameters. Application to a real SMB chromatographic separation process will be given in Section 5.

2. Solving PDEs with Singularity

In chromatographic separation, travelling wave front possess sharp moving spatial transitions. In order to fully capture the steep front, peak, and tail, the space grid has to contain a large number of mesh points. SMB systems with more components and stiff concentration profiles require more ODEs. The large size of the ODE system is a problem due to its intensive computation when on-line optimization and real-time control are necessary. Here comes the attempt of using non-uniform grids or moving elements, such as, adaptive finite differences or moving finite elements that dynamically adapt to the changes in the solution.

2.1. Adaptive Grid Algorithm and Upwinding Scheme

Early in 1990, Furzeland (1990) conducted an evaluation and comparison of three moving-grid methods for one dimensional PDEs problem. Later in the work of Wouwer et al. (1998), five adaptive grid methods are examined.

According to Furzeland, the moving grid approach has three directions:

1. The finite-difference method proposed by Petzold (1987). It involves two steps, a moving lagrangian step and a regridding step. The moving Lagrangian step applies a stiff ODE solver to an augmented semi-discrete system, while in the regridding step a redistribution of points at the forward time level is carried out through a De Boor-type equidistribution algorithm.
2. The finite-difference method based on the ideas from Dorfi and Drury (1987). The grid movement is regularised by employing a smoothing technique in both space and time. An implicit equation is used which underlines a spatial equidistribution transformation based on an arc-length monitor function.
3. The finite-element method of Miller and co-workers (1981). It generates a system of continuous time ODEs for mesh points. Grid movement is regularised by using penalty functions.

Both finite-difference moving-grid methods are based on the equidistribution principle. The idea of the equidistribution principle is to equally distribute a given mesh function in space, placing more nodes where the spatial error is large.

Wouwer classified adaptive grid based on method of line (MOL) into two categories: the local refinement algorithms and moving grid algorithms. The former involves local addition or removal of nodes as needed, while the latter moves a fixed number of nodes to the regions of rapid solution variation. The details of the classification and test results on Burgers' equation are summarised in table 1.

Furzeland's three moving grid methods could be fitted into Wouwer's dynamic regridding algorithm. The largest difficulty with adaptive grid method is to determine the mobility of the grid (or the elements) and the accurate definition of the function when a new grid point (or element) is added between two existing grid points (or elements).

Table 1. Summary of various adaptive grid algorithms (Wouwer et al. 1998)

Adaptive Grid Algorithm		Representing Author (apart from Wouwer et al.)	Grid Placement Criterion	Test on Burgers' Equation
Local Refinement		Hu and Schiesser (1981)	Second-order derivative	Simple concept; technically complicated for implementation; substantial parameter tuning may be required
		Eigenberger and Butt (1976)	Error estimation procedure	
Moving Grid (equidistribution principle)	Static Regridding	Sanz-Serna and Christie (1986); Revilla (1986)	Equidistribute a pre-defined function based on solution curvature	Competitive with all the adaptive solvers
	Dynamic Regridding	Huang and Russell (1996)	Movement of nodes is governed by a moving mesh PDE.	Reduced nodes; robust; high computational expense (require large number of time steps)
		Blom et al. (1994)	Nonlinear Galerkin discretization ; Smoothed equidistribution principle using regularization technique of Dorfin and Drury	Very good temporal performance; robust and reliable

Another technique tracking shook or steep wave in solving PDEs is the upwinding schemes. It has been found that for reaction-convection-diffusion equations, which represent many chemical engineering problems, central difference discretization is unstable because it gives spurious oscillatory profiles (Gibbs phenomena) near the shock. Upwinding schemes are introduced to overcome the drawback from central discretization used in most of the moving mesh software. Upon which, the schemes of Essentially Non-Oscillatory (ENO) and Weighted ENO (WENO) have been developed for the discretization of first-order derivative term. The combination of moving mesh with adaptive Upwinding schemes (e.g. ENO, WENO, Flux-Limited and Piecewise Hyperbolic Method (PHM)) on uniform (Jiang and Shu, 1996; Lim et al., 2001a) or non-uniform grid (Li and Petzold, 1997) have been studied to track the rarefaction as well as the shock for problems with nonconvex flux. A review of recently developed spatial discretization methods can be found in Lim et al. (2001b). All the above mentioned upwinding schemes have been tested on convection-dominated problems with moving shock results.

2.2. Using Wavelet-Collocation Methods for Solving PDEs

Orthogonality, compact support, and multi-level structure of the basis make wavelets well-suited for approximating functions with abrupt changes, such as a shock wave or a sharp spike. In seeking numerical solution, wavelets have been used either directly as basis or for

algebraic manipulations to simplify the results using existing discretization methods (Nikolaou and You, 1994). There are two commonly used wavelet methods, the Wavelet-Galerkin and Wavelet-Collocation. In the Wavelet-Galerkin method, the solution is approximated by linear combinations of wavelets or scaling functions. The same base is used as weighting functions to calculate the unknown coefficients. In the Wavelet-Collocation method, the solution is evaluated at dyadic points by using the interpolating wavelet as the weighting function. The computations are performed in the physical space with redefined grid.

Applications of wavelet transformation to the solution of partial differential equations arising from chemical engineering processes are limited (Bindal *et al.* 2003; Briesen *et al.*, 2005). Majority of them looked at solving Burger's equation. Nikolaou and You (1994) used Daubechies' orthonormal wavelet and Chui-Wang's semi-orthogonal B-spline wavelet as basis, together with Galerkin's method to solve initial value problem and two point boundary value problems. For Burger's equation, wavelets were also compared with those using Chebyshev polynomials as the basis functions. It was pointed out that for differential equations with solutions that exhibit local irregularities, wavelets have a distinct potential.

Vasilyev et al. (1995) developed a multilevel wavelet collocation method based on the wavelet interpolation technique for solving PDEs. They suggested two different approaches to treat general boundary conditions. Their method was also tested on the one-dimensional Burger's equation with small viscosity. Comparisons with other numerical algorithms (Fourier Galerkin, Fourier pseudospectral, Chebyshev collocation, spectral element, finite difference, wavelet Galerkin) have shown the competitiveness and efficiency of the proposed method.

More recently, Cruz et al. (2001, 2002) and Liu et al. (2001) exemplified the Wavelet-Collocation application in a fixed-bed adsorption model to simulate the propagation of a concentration peak along a chromatographic column with axial dispersion and linear/nonlinear adsorption isotherm. Both adaptive grid and constant grid methods were investigated. However, applications of the wavelet technique for solving an SMB system model, which is much more complicated than a single column model, have not been found in the open literature except in our recent work (Yao et al, 2008).

2.3. The High Resolution Method

The high resolution method was originally proposed by Koren in 1993 for numerically solving advection-diffusion equations with a source term. Based on the so-called centred finite-volume discretization technique, the scheme for dealing with the one-dimensional problem was introduced first, and then it was extended to solve the multi-dimensional problem. Later, this method was introduced into chemical engineering applications by Ma et al. (2002), Gunawan et al. (2004) and Qamar et al. (2006) to solve the multi-dimensional population equations in crystallization. The numerical results obtained in the above papers show the advantage of this new scheme.

Furthermore, a modified high resolution scheme, Adaptive High Resolution Scheme, was proposed by Qamar et al. (2006) for numerically solving multi-dimensional population balance models in crystallization processes. The application of the adapted scheme demonstrates its generality, efficiency and accuracy. It is noticed that both the original high

resolution and the adaptive high resolution scheme were designed for solving the partial differential equations with Dirichlet boundary conditions.

In order to employ this powerful scheme to solve the problems arising from a much wider range of industrial processes that can be modelled by partial differential equations with other boundary conditions, Zhang et al. (2008) extended the original scheme to solve the PDEs with Cauchy or Neumann boundary conditions. They also compared the high resolution method with the wavelet based scheme for numerically solving PDEs, and concluded that the high resolution outperforms the wavelet based method for certain types of applications.

3. Background Theory

For completeness, in this section we will briefly review the wavelet collocation and high resolution methods based on the previous work of Bertoluzza et al. (1996), Koren (1993), Qamar et al. (2006) and Zhang et al. (2008).

3.1. Wavelet Based Collocation Methods

Consider the following interpolating function

$$\theta(x) = \int_{-\infty}^{+\infty} \phi(y)\phi(y-x)dy \tag{1}$$

where $\phi(x)$ is the Daubechie's wavelet with compact support $[0, L]$. It can be verified that the linear span of $\{\theta_{j,k} = \theta(2^j x - k), k \in Z\}$ forms a multiresolution analysis (MRA) and the function defined by equation (1) satisfies the interpolation properties for integer k

$$\theta(k) = \begin{cases} 1, k = 0 \\ 0, k \neq 0, k \in Z \end{cases} \tag{2}$$

In order to take advantage of the interpolating function defined by equation (1) to numerically solve differential equations, the interpolation operator

$$I_j f = \sum_k f_{j,k} \theta_{j,k}(x) \tag{3}$$

is introduced (Bertoluzza, 1994; 1996) to approximate the unknowns in the PDEs. The PDEs can then be discretized into a set of ODEs by using the dyadic points in the spatial dimension. This is the so-called interpolating wavelet based collocation method.

For the interpolation operator, we have the following error estimate, which guarantees the convergence of the numerical method.

$$\left\| f - I_j f \right\|_r \leq C 2^{-j(s-r)} \left\| f \right\|_s \tag{4}$$

To deal with boundary conditions, Bertoluzza (1996) has proposed three schemes for the construction of interpolating functions to achieve boundary interpolating operators. This is a relatively mature method for numerically solving the pure mathematical problems. However, there is only limited work addressing its application in engineering. In this chapter, we propose to simulate the Simulated Moving Bed (SMB) model by using one of his schemes, which is based on the following modified interpolation functions (Donoho, 1992)

$$\theta^l{}_{j,k} = (\theta_{j,k} + \sum_{n=-L}^{-1} a_{n,k} \theta_{j,n})$$

$$\theta^r{}_{j,k} = (\theta_{j,k} + \sum_{n=2^j+1}^{2^j+L} b_{n,k} \theta_{j,n}) \tag{5}$$

with $a_{n,k} = \prod\limits_{\substack{i=0 \\ i \neq k}}^{2M-2} \dfrac{x_n - x_i}{x_k - x_i}, b_{n,k} = \prod\limits_{\substack{i=2^j-2M+2 \\ i \neq k}}^{2^j} \dfrac{x_n - x_i}{x_k - x_i}$ and M is the number of interpolating

points in the neighbourhoods of the endpoints of the interval in question. It can be verified that the modified interpolation functions defined in Equation (5) have similar properties as the original ones. Substituting Equation (5) into Equation (3), we get the modified interpolation operator, which will be used in this chapter, as the following

$$I_j f = \sum_{k=0}^{L} f(x_k) \theta^l{}_{j,k} + \sum_{k=L+1}^{2^j-L-1} f(x_k) \theta_{j,k} + \sum_{k=2^j-L}^{2^j} f(x_k) \theta^r{}_{j,k} \tag{6}$$

Applying Equation (6) to a PDE and evaluating it at the dyadic point yields a set of ODEs. The resulting ODEs can be solved by using the time integrator scheme as will be discussed in Section 3.3.

3.2. High Resolution Method

Consider the following PDE with appropriate boundary and initial conditions,

$$\frac{\partial u}{\partial t} + \frac{\partial f(u)}{\partial x} + \beta \frac{\partial^2 u}{\partial x^2} = 0, x \in [a,b] \tag{7}$$

In wavelet collocation method, the concerned interval is discretized by using the dyadic points, which can take advantage of the interpolation property of the interpolating wavelet. For high resolution method, we will divide the interval into a number of subintervals uniformly. For instants N subintervals Ω_i. Let $d = (b-a)/N$, $x_{1/2} = a$ and $x_{N+1/2} = b$,

we have $\Omega_i = [x_{i-1/2}, x_{i+1/2}]$, $i = 1, \cdots, N$, with $x_{i-1/2} = a + (i-1)d$. Denote the approximation of the unknown u in Ω_i by y_i. Then, by using the method proposed in Qamar et al. (2006), we have

$$y_i = \frac{1}{d} \int_{x_{i-1/2}}^{x_{i+1/2}} u(x,t)dx, i = 1, \cdots, N \tag{8}$$

Substituting Equation (8) into Equation (7) gives,

$$\frac{dy_i}{dt} + \frac{1}{d}(f_{i+1/2} - f_{i-1/2}) + \frac{1}{d}\beta\left(\frac{\partial y}{\partial x}\Big|_{x_{i+1/2}} - \frac{\partial y}{\partial x}\Big|_{x_{i-1/2}}\right) = 0 \tag{9}$$

The function $f_{i+1/2}$ can be approximated by using one of the two schemes proposed in (Koren, 1993).

1) Upwinding scheme

$$f_{i+1/2} = f_i, \ i = 1, \cdots, N \tag{10}$$

2) $\kappa - $ flux interpolation scheme

$$f_{i+1/2} = f_i + \frac{1+\kappa}{4}(f_{i+1} - f_i) + \frac{1-\kappa}{4}(f_i - f_{i-1}) \tag{11}$$

$$\kappa \in [0,1], \ i = 2, \cdots, N-1$$

The function $\frac{\partial y}{\partial x}\Big|_{x_{i+1/2}}$ can be approximated by

$$\frac{\partial y}{\partial x}\Big|_{x_{i+1/2}} = \frac{y_{i+1} - y_i}{d} \tag{12}$$

Different boundary conditions will be treated for function $f_{i+1/2}$ and $\frac{\partial y}{\partial x}\Big|_{x_{i+1/2}}$ by using the methods proposed in (Koren, 1993; Zhang et al., 2008).

(1) PDEs with Dirichlet boundary conditions (Keren, 1993)
Dirichlet boundary conditions have the following format:

$$u(t,a) = u_{in} \ ; \ u(t,b) = u_{out} \tag{13}$$

On the boundary of the spatial variable, we have

$$f_{1/2} = f(u_{in}),$$ (14a)

$$f_{1+1/2} = f(\frac{y_1 + y_2}{2}),$$ (14b)

$$f_{N+1/2} = f(y_{out}),$$ (14c)

$$\frac{\partial y}{\partial x}\Big|_{1/2} = \frac{-8u_{in} + 9y_1 - y_2}{3d},$$ (14d)

$$\frac{\partial y}{\partial x}\Big|_{N+1/2} = \frac{8u_{out} - 9y_N + y_{N-1}}{3d}$$ (14e)

(2) PDEs with Cauchy boundary condition (Zhang et al., 2008)

If the boundaries are represented by the following Cauchy conditions:

$$u(t,a) + \varphi\frac{\partial u}{\partial x}\Big|_{x=a} = u_{in} \;\; ; \;\; \frac{\partial u}{\partial x}\Big|_{x=b} = u_{out}$$ (13')

Equations (14a), (14c),(14d) and (14e) will respectively become:

$$f_{1/2} = f(y(t,a)) + \frac{1}{2}(f(y_1) - f(y(t,a))),$$ (14a')

$$f_{N+1/2} = f(y_N) + \frac{1}{2}(f(y_N) - f(y_{N-1})),$$ (14c')

$$\frac{\partial y}{\partial x}\Big|_{1/2} = \frac{-8u_{in} + 9y_1 - y_2}{3d - 8\varphi},$$ (14d')

$$\frac{\partial y}{\partial x}\Big|_{N+1/2} = u_{out}$$ (14e')

where

$$y(t,a) = \frac{3du_{in} - 9\varphi y_1 + \varphi y_2}{3d - 8\varphi}$$

3.3. Time Integrator - The Alexander Method

We will use the Alexander method for the time integrator. This is a 3rd order semi-implicit Runge-Kutta method, which requires several implicit equations to be solved in series. The Alexander method has three stage equations with the order of 3. It is L-stable, implying that it not only has the whole negative half plane as stability regions, but also is capable of dampening out possible oscillation in the numerical solution even for very large negative

eigen-values. The good stability of the method makes it particularly well-suited for stiff problems. Its Butcher block looks like:

η	η	0	0
c	c- γ	η	0
1	b1	b2	η
1	b1	b2	η

where η = 0.4358665, c = (1+ η)/2, b1 = – (6 η ^{2}— 16 η + 1)/4, b2 = (6 η ^{2} – 20 η + 5)/4.

The information contained in this block can be translated into the following representations. The stage times are:

$$t_{k,1} = t_k + \eta h \,; \; t_{k,2} = t_k + ch \,; \; t_{k,3} = t_k + h \tag{15}$$

And the stage values are calculated from the equations:

$$y_{k,1} = y_k + \eta h K_1 \,; \; K_1 = f(t_{k,1}, y_{k,1})$$

$$y_{k,2} = y_k + (c - \eta) h K_1 + \eta h K_2 \,; \; K_2 = f(t_{k,2}, y_{k,2}) \tag{16}$$

$$y_{k,3} = y_k + b_1 h K_1 + b_2 h K_2 + \eta h K_3 \,; \; K_3 = f(t_{k,3}, y_{k,3})$$

The overall slope estimation is given by

$$K^* = b_1 K_1 + b_2 K_2 + \eta K_3 \tag{17}$$

Then, new point for the next time step is given as:

$$y_{k+1} = y_k + h K^* \tag{18}$$

It can be seen that Equation (16) are implicit equations. Newton's iteration method will be used as implicit equation solver to estimate each stage values. A step in the Newton iteration for the first stage estimation is:

$$y_{k,1}^{m+1} = y_{k,1}^m - (1 - \eta h \frac{\partial f}{\partial y} \bigg|_{y_{k,1}^m})^{-1} (y_{k,1}^m - y_k - \eta h f(t_{k,1}, y_{k,1}^m)) \tag{19}$$

where m is the iteration step.

4. Study on a Transport-Dispersive Plug Flow Model

Dynamic SMB model consists of two parts: the single chromatographic columns models, and the node balances model describing the connection of the columns combined with the cyclic switching. The basic structure is illustrated in figure 2. The switching operation can be represented by a shifting of the initial or boundary conditions for the single columns. After a relatively brief start-up period, the adsorption beds will reach the cyclic steady state. Normally, the cyclic steady state is determined by solving the PDE system repeatedly for each step of the cyclic process in sequence, using the final concentration profile for each step as the initial condition for the next step in the cycle.
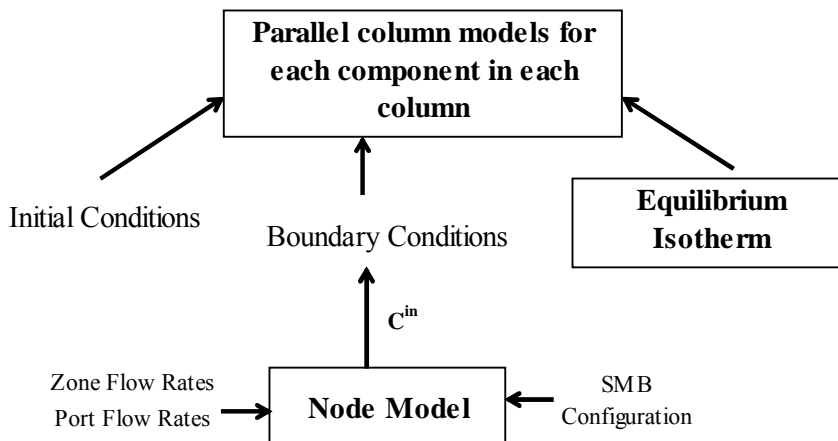
Figure 2. SMB dynamic modelling system.

Since the behaviour of the whole SMB system is determined by the equilibrium isotherm and the character of the column, the level of mathematical difficulty encountered depends significantly on the nature of equilibrium relationship, the concentration level, and the system parameters describing the column models. In this section, we will conduct a preliminary investigation on the numerical solution of a single column model with a range of key parameter, using finite difference, wavelet-collocation, and high resolution methods for spatial discretization.

As the column models for chromatography, the Transport-Dispersive Linear Driving Force (LDF) models have been widely used in modelling many adsorption processes due to their simplicity and good agreement with experimental results (Ching, 1998). LDF is the application of the first Fick's law of mass transport and is an equation of equilibrium isotherm. It offers a realistic representation of industrial processes and is shown to be a good compromise between accurate and efficient solutions of these models (Biegler et al., 2004). In this study, we will use the following typical expression of Transport-Dispersive-LDF model to describe the kinetics of each column.

$$\frac{\partial C}{\partial t} + u\,\frac{\partial C}{\partial x} = D_{ax}\,\frac{\partial^2 C}{\partial x^2} - \frac{1}{\alpha}\,\frac{\partial q}{\partial t} \qquad (20a)$$

$$\frac{\partial q}{\partial t} = k_{eff}(q^* - q) \tag{20b}$$

where $\alpha = \dfrac{\varepsilon_b}{1-\varepsilon_b}$ is the fractional void volume.

4.1. Analytical Solution for Linear Equilibrium Case

In order to evaluate the performance of different discretization methods, a simple linear equilibrium case is considered first. Under this assumption, an analytical solution is given out by Lapidus and Amundson (1952) for any time at any point in the column. In the case where equilibrium is established at each point in the bed, $q = q^*$, Equation (20a) can be transformed into:

$$\frac{\partial C}{\partial t} = \frac{1}{1+\dfrac{1}{\alpha}\dfrac{\partial q^*}{\partial C}}\left(-u\frac{\partial C}{\partial x} + D_{ax}\frac{\partial^2 C}{\partial x^2}\right) \tag{21}$$

For a linear equilibrium isotherm, $q^* = kC$, that is: $\dfrac{\partial q^*}{\partial C} = k$

If we consider a pulse injection with a concentration of C_0 and duration of t_0, and specify constant concentration as boundary conditions:

$$C(0,t) = \begin{cases} C_0 & \text{at } \begin{array}{l} t \le t_0 \\ t > t_0 \end{array} \\ 0 \end{cases} \text{ and initial conditions of: } C(x,0) = 0;$$

Using dimensionless transformation, let:

$$\tau = ut\alpha/L; \ Pe = uL/D_{ax}; \ z = x/L; \ c = C/C_0; \ \tilde{q} = q/C_0$$

Then, according to Lapidus and Amundson (1952), the model's analytical solution is:

$$c(z,\tau) = \begin{cases} H(\tau) & \text{at } \begin{array}{l} \tau \le \tau_0 \\ \tau > \tau_0 \end{array} \\ H(\tau) - H(\tau - \tau_0) \end{cases} \tag{22}$$

with

$$H(\tau) = \frac{1}{2}\left[1 + erf\left(\sqrt{\frac{\tau Pe}{4(\alpha+k)}} - z\sqrt{\frac{Pe(\alpha+k)}{4\tau}}\right) + e^{zPe}\,erfc\left(\sqrt{\frac{\tau Pe}{4(\alpha+k)}} + x\sqrt{\frac{Pe(\alpha+k)}{4\tau}}\right)\right] \tag{8}$$

where *erf*() and *erfc*() are the error and complementary error functions, respectively:

$$erf(x) = \frac{2}{\sqrt{\pi}} \int_0^x e^{-t^2} dt \; ; \; erfc(x) = \frac{2}{\sqrt{\pi}} \int_x^\infty e^{-t^2} dt$$

This solution is limited to a chromatography in an equilibrium situation with linear isotherm. Most separation processes are more complicated than this. However, it appears useful when exact solution is needed in order to compare the accuracy of solution obtained by numerical method.
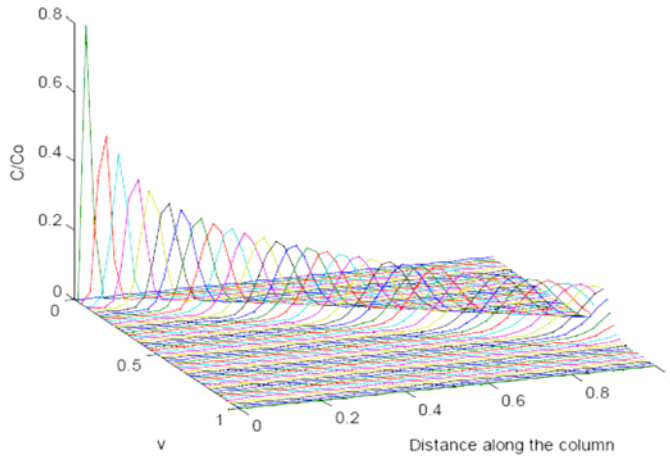
Figure 3. Analytical solution: Pe $=$ 500 , $(\alpha + k) = 20$.
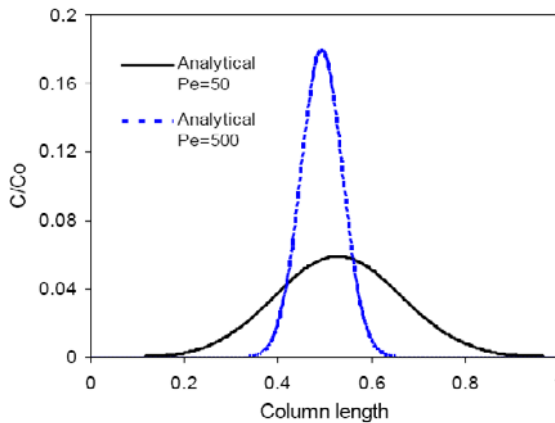
Figure 4. The effect of Peclet number for a pulse injection. $(\alpha + k) = 20, \tau = 10, \tau_0 = 0.4$.

Calculations are conducted by assuming a column with infinite extent (so the end boundary condition is not included). We will look at the concentration profiles at a column length of L. Figure 3 depicts an example of the concentration propagation along the column, which is the exact solution of this problem. Figure 4 shows the shape of the wave, at certain

time instant, for different Peclet number Pe. It is seen that the higher Pe results in a steeper wave, which directly affect the performance of different numerical solution methods. Based on this observation, we will consider three cases with Pe set as 50, 500 and 5000, respectively.

4.2. Numerical Solution - Results and Discussions

Numerical simulations have been performed using the finite difference, wavelet collocation, and high resolution methods for spatial discretization. The resulting ordinary equations using these three methods are given below.

(**1**) For the ***finite difference*** method, we use Upwind-1 for discretization. The advantage of upwinding scheme has been outlined in Section 2.1. Let $y(z, \tau) \approx C(z, \tau)$, an approximation of the concentration ratio, the resulting ODEs for each spatial mesh point are:

$$\frac{dy(z_i, \tau)}{d\tau} = \frac{1}{(\alpha + k)\Delta z}[\frac{1}{Pe\Delta z} y(z_{i+1}, \tau) - (1 + \frac{2}{Pe\Delta z}) y(z_i, \tau) + (1 + \frac{1}{Pe\Delta z}) y(x_{i-1}, \tau)] \quad (23a)$$

$$y(z_1, \tau) = \begin{cases} 1 \\ 0 \end{cases} \text{ at } \begin{matrix} \tau \leq \tau_0 \\ \tau > \tau_0 \end{matrix} \quad (23b)$$

where $i = 2 \cdots N_x$, $\Delta z = z_{i+1} - z_i$, N_x is the number of mesh points.

(**2**) To solve this problem using the ***wavelet-collocation*** method, an approximation of the concentration ratio is expressed by a compactly supported orthonormal wavelets:

$$\frac{dy(z_i, \tau)}{d\tau} = \frac{1}{\alpha + k}[\frac{1}{Pe}\sum_{j=1}^{2^J+1} y(z_j, \tau)T_{i,j}^{(2)} - \sum_{j=1}^{2^J+1} y(z_j, \tau)T_{i,j}^{(1)}] \quad (24a)$$

where, $i = 2 \cdots 2^J + 1$, $T_{i,j}^{(1)}$ and $T_{i,j}^{(2)}$ are the first- and second-order derivatives, respectively, for the interpolating function. The boundary condition imposes one more constraint in an additional equation for the first spatial point:

$$y(z_1, \tau) = \sum_{j=1}^{2^J+1} y(z_j, \tau)T_{1,j} = \begin{cases} 1 \\ 0 \end{cases} \text{ at } \begin{matrix} \tau \leq \tau_0 \\ \tau > \tau_0 \end{matrix} \quad (24b)$$

(**3**) Applying the ***high resolution*** method to the model equation gives the following ODEs:

$$\frac{dy(z_i, \tau)}{d\tau} = \frac{1}{(\alpha + k)\Delta z Pe}(\frac{\partial y}{\partial z}\Big|_{z_{i+1/2}} - \frac{\partial y}{\partial z}\Big|_{z_{i-1/2}}) - \frac{1}{\Delta z}[y(z_{i+1/2}, \tau) - y(z_{i-1/2}, \tau)] \quad (25)$$

where, $i = 1 \cdots N_z$. The expression of each component is defined in Section 3.2; and $z_{1/2}$ is the left boundary defined in Equation (13).

4.2.1. Process with Low Peclet Number ($Pe = 50$)

As shown in figure 4, at $Pe = 50$, the wave front and tail are all relatively flat. We choose finite difference and wavelet collocation methods for this study. For the trials of finite difference, the number of mesh point are chosen to be 65 (equivalent to J=6), 257 (equivalent to J=8), and 500, respectively. Figure 5 depicts the numerical solutions of the model using the finite difference method. It is seen from the figure that for low Pe, the finite-difference method can handle the problem well if the number of mesh points is sufficiently high (over 500 in this example).
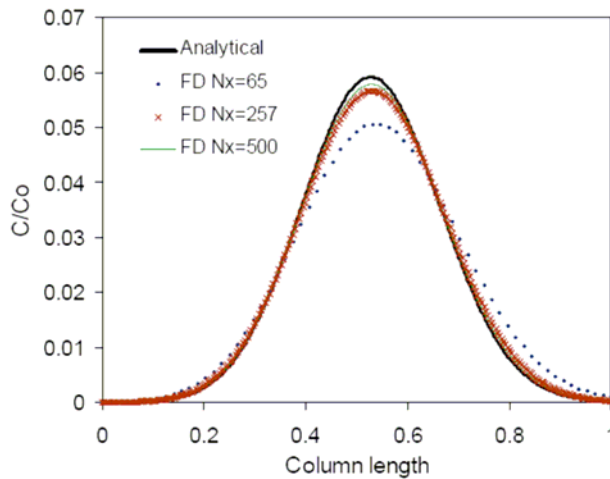
Figure 5. Numerical solutions from Finite Difference, $(\alpha + k) = 20$, $\tau = 10$, $\tau_0 = 0.4$, $Pe = 50$.

The next trials are carried out using wavelet collocation method. Simulations are conducted on the levels J = 6, 7, and 8, respectively. Such wavelet levels represent the total collocation points of 65, 129, and 257, respectively. Figure 6 is the numerical solutions. Level 7 upwards start to produce some sort of overshooting. This phenomenon is also observed by other researchers and needs further investigation. However, this could be easily avoided by choosing a higher minimum wavelet level to give acceptable numerical solutions.

For comparisons of finite difference and wavelet collocation methods, figure 7 is the absolute error between the numerical and analytical solutions. For similar degree of discretization, wavelet does show its advantage of using less collocation points to obtain a reasonable prediction. The error distributions are quite different for these two methods. For the finite difference method, the error exists at every section of the wave, e.g., front, peak and tail, especially; the peak presents the largest error. For the wavelet method, the error is located at the front and tail, but not around the peak, which is actually the turning point of the error sign. This reflects the capability of the wavelet method in capturing a steep change very well.
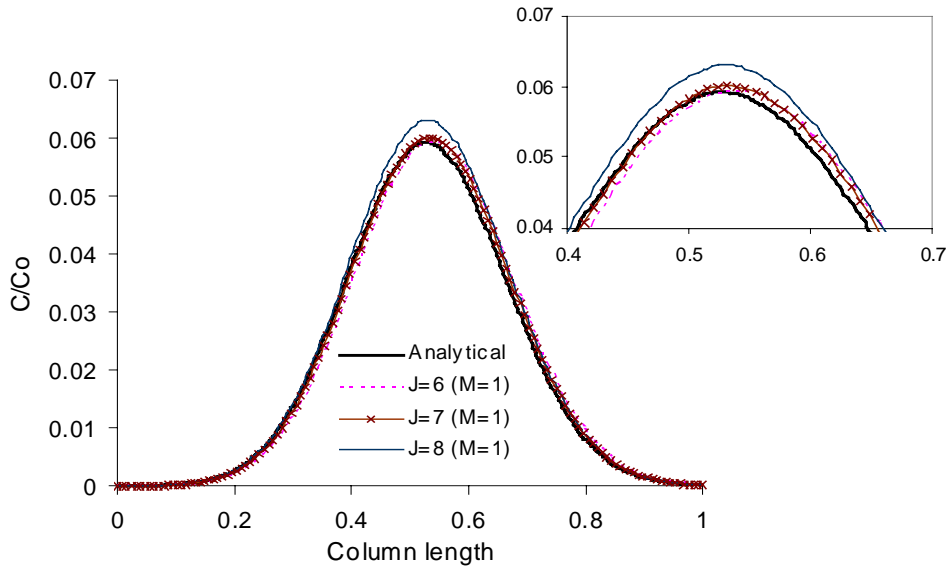
Figure 6. Numerical solutions from Wavelet Collocation, $(\alpha + k) = 20$, $\tau = 10$, $\tau_0 = 0.4$, $Pe = 50$.
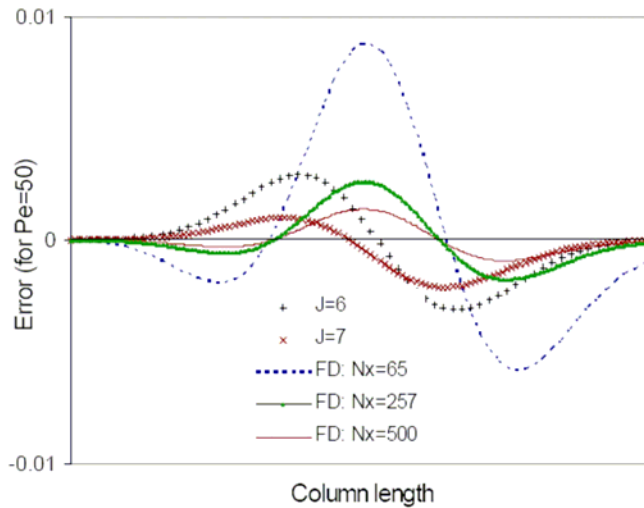
Figure 7. Comparison of prediction error. $(\alpha + k) = 20$, $\tau = 10$, $\tau_0 = 0.4$, $Pe = 50$.

4.2.2. Process with Moderate Peclet Number (Pe = 500)

In this case, we will look at all of the three methods (finite difference, wavelet collocation, and high resolution). With the increasing of steepness as a result of higher Peclet number selected, the finite difference method can no longer accurately predict the peak value (figure 8). It appears very reluctant to climb up the peak even with a large number of mesh points.

However, using wavelet-collocation method, the numerical solution catches up with this real steep change very well with J=6, 7, 8 (figure 9a). It is noticed that resolution level 8 does not displace any overshoot in this situation. However, a higher level still produces overestimation as displayed in figure 9b for J=9, and J=10, respectively.

Trials are also conducted using the high resolution method, results are shown in figure 10. When the number of mesh point increases to a certain level (e.g. 513), the high resolution method can approximate the true result very well. On the other hand, one does not need to worry about the overestimation problem arising from the wavelet approximation. It is interesting to see that the error distribution from the high resolution method (figure 11a) has adverted shape from the wavelet collocation method (figure 11b).
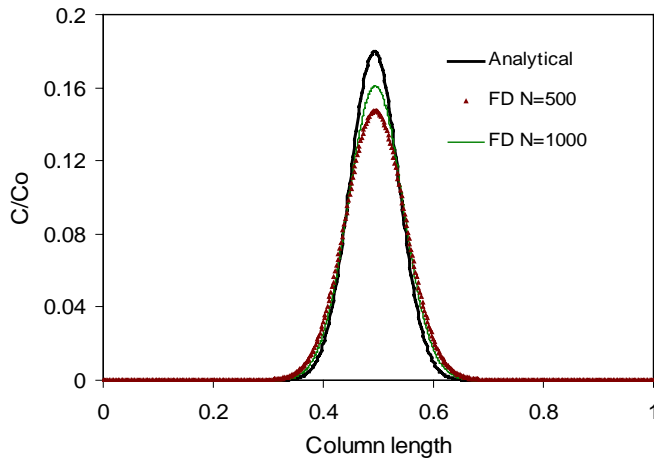
Figure 8. Numerical solutions from Finite Difference, $(\alpha + k) = 20$, $\tau = 10$, $\tau_0 = 0.4$, $Pe = 500$.

(a)   *(b)*
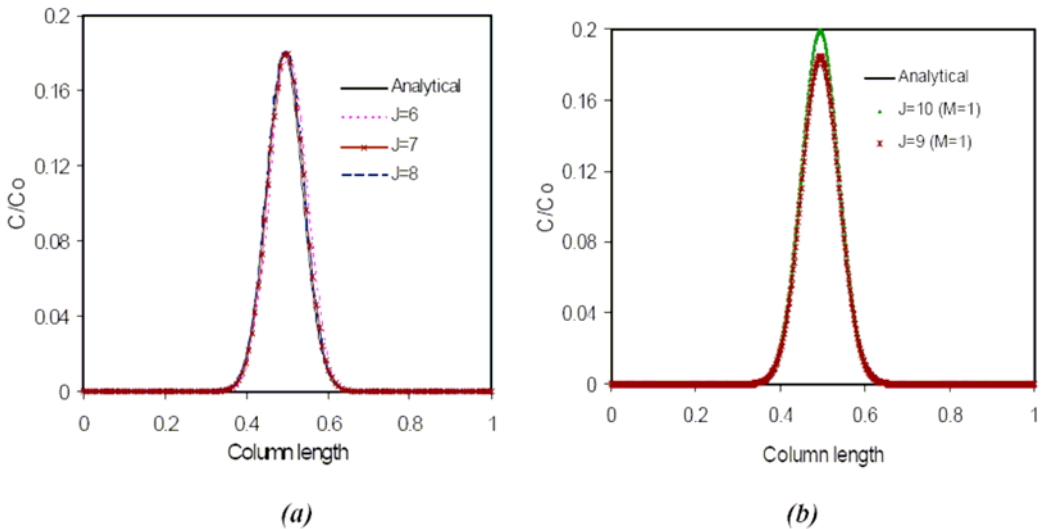
Figure 9. Numerical solutions from Wavelet Collocation, $(\alpha + k) = 20$, $\tau = 10$, $\tau_0 = 0.4$, $Pe = 500$.

The performance of PDEs solver using different spatial discretization algorithms is given in table 2. Comparisons can be made on their approximation accuracy and computing time. The numerical simulations of this paper have been conducted on a personal computer with an Intel's Pentium IV 3.00GHz processor. Wavelet has remarkable advantage against finite difference if a proper resolution level is chosen, while high resolution also produces acceptable approximation with a relatively low computational demand. Further discussion can be found in Section 6.
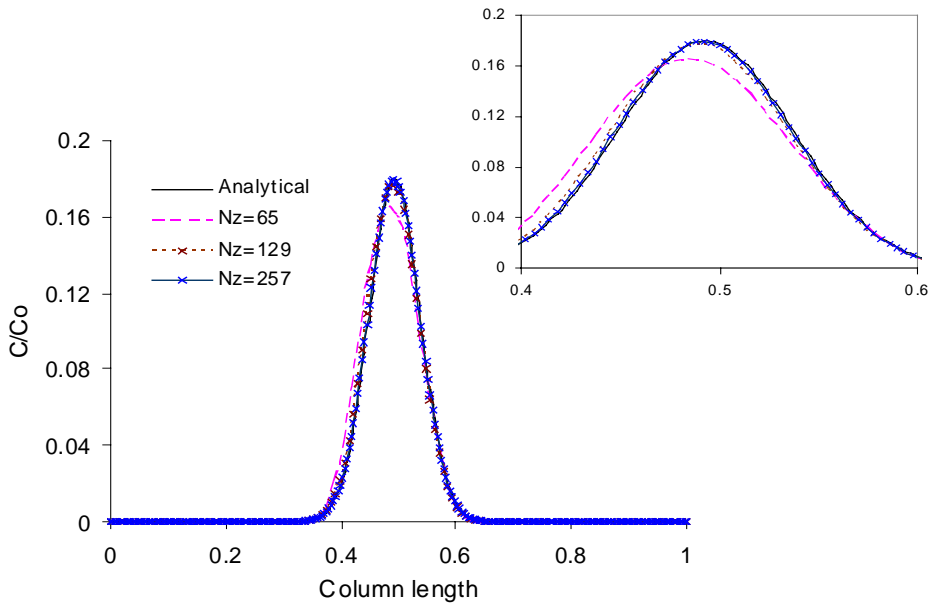
Figure 10. Numerical solutions from High Resolution $Pe = 500$.

(a)　　　　　　　　　　　　(b)
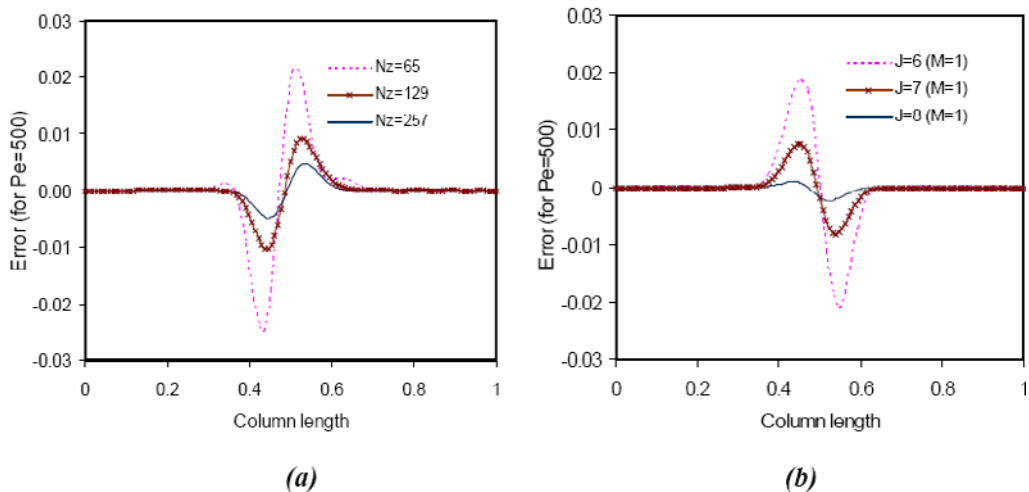
Figure 11. Error distribution from (a) High Resolution (b) Wavelet Collocation.

Table 2. Performance of discretization methods at Pe=500

Spatial Discretization		Absolute Error at Peak	CPU time* (sec)
Finite Difference	Nx=500	0.03229	106.4
	Nx=1000	0.01868	299.4
Wavelet Collocation	J=6	0.00184	2.0
	J=7	0.00000	6.9
	J=8	0.00118	37.1
	J=9	0.00458	363.4
High Resolution	Nz=65	0.01417	11.8
	Nz=129	0.00285	28.8
	Nz=257	0.00050	72.3
	Nz=513	0.00023	213.0

*the temporal mesh number is 500 for all trials on a personal computer with an Intel's Pentium IV 3.00GHz processor.

4.2.3. Process with Higher Peclet Number (Pe = 5000)

This was carried out by wavelet-collocation and high resolution methods. Finite difference method is no longer considered here because the previous case shows it is not

Table 3. Performance of discretization methods at higher Pe=5000

Spatial Discretization		Absolute Error at Peak	CPU time* (sec)
Wavelet Collocation	J=7	0.0202	6.7
	J=8	0.0040	34.0
	J=9	0.0001	322.0
High Resolution	Nz=129	0.0815	28.7
	Nz=257	0.0222	65.8
	Nz=513	0.0048	188.5

*the temporal mesh number is 500 for all trials.

a) Wavelet collocation b) High resolution.
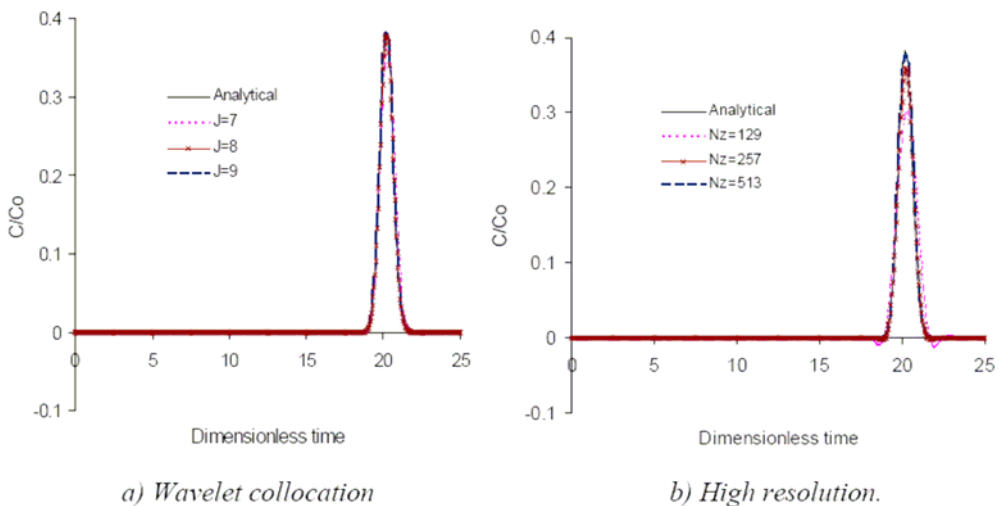
Figure 12. Calculated concentration peak at certain column position.

suitable for the model with even higher Peclet number. Comparisons are made for the concentration profile at certain point along the column length. As well as the illustration in figure 12, prediction analysis results are also tabulated in table 3. For the wavelet collocation method, the resolution level can be up to 9 without overestimation, although the cost of computation increases significantly. It is concluded that high resolution method is still a potential candidate for solving PDEs with such degree of singularity.

4.3. Discussion on the Boundary Treatment Degree in Wavelet-Collocation Method

Section 3.1 introduced the basic concept of the wavelet collocation method. The general expression of Equation (6) contains three parts. Apart from classical interpolating functions, two polynomials are defined with the degree of (2M-1) to interpolate the original problem at the left and right boundaries. The selection criterion of M is not reported in any of the previous literature. We conducted several trails for the determination of the best value of M. From figures 13, 14, and 15, it can be seen that, for this specific problem, M=1 seems to be the most reliable choice and it has been used for all our study on wavelet method.
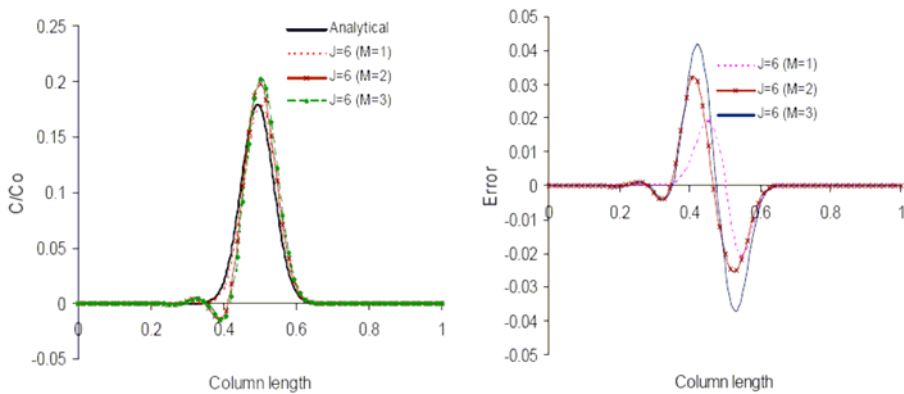
Figure 13. The effect of M on the simulation performance (J=6).
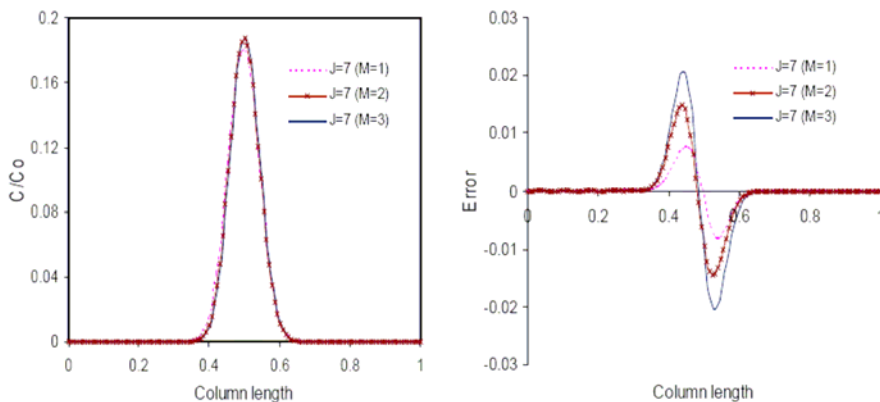
Figure 14. The effect of M on the simulation performance (J=7).
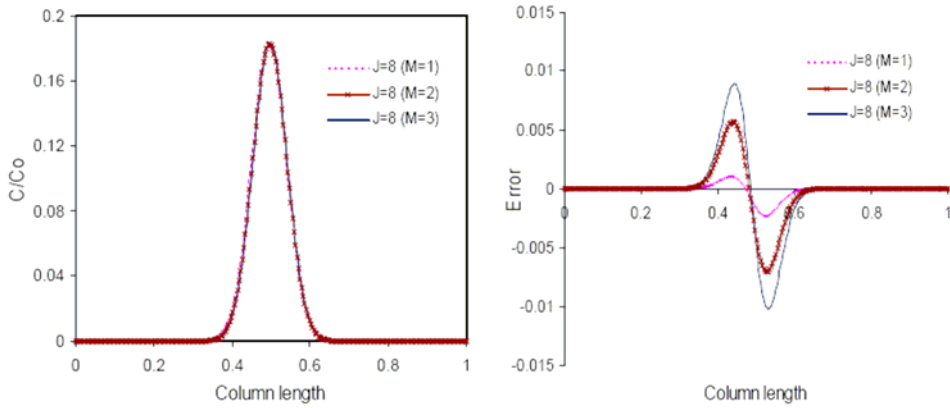
Figure 15. The effect of M on the simulation performance (J=8).

5. Application to SMBC Processes: Case Study on Bi-Naphthol Enantiomers Separation

The separation of Enantiomers of 1,1'-bi-2-naphthol in 3,5-dinitrobenzoyl phenylglycine bonded to silica gel columns reported by Pais *et al*. (1997) is taken as our case study system. The SMBCP has 8 columns with the configuration of 2:2:2:2. The schematic system is similar to that depicted in figure 1 except with 2 columns for each section.

5.1. Detailed Model Equations

- Column Model for Chromatography

The selected column model structure is the same as that described in Section 4. We will expand the model to describe this 8 columns binary separation process. The mass balance of component i in the mobile phase (or bulk-liquid phase) is,

$$\frac{\partial C_{i,j}}{\partial t} + u_j \frac{\partial C_{i,j}}{\partial x} = D_{ax} \frac{\partial^2 C_{i,j}}{\partial x^2} - \frac{1-\varepsilon_b}{\varepsilon_b} k_{eff,i}(q_{i,j}^* - q_{i,j}) \tag{26a}$$

A simple Linear Driving Force model is used to represent the overall mass transfer kinetics for the adsorption phase:

$$\frac{\partial q_{i,j}}{\partial t} = k_{eff,i}(q_{i,j}^* - q_{i,j}) \tag{26b}$$

And the equilibrium isotherms:

$$q^*_{A,j} = \frac{2.69 C_{A,j}}{1 + 0.00336 C_{A,j} + 0.0466 C_{B,j}} + \frac{0.1 C_{A,j}}{1 + C_{A,j} + 3 C_{B,j}} \tag{26c}$$

$$q^*_{B,j} = \frac{3.73 C_{B,j}}{1 + 0.00336 C_{A,j} + 0.0466 C_{B,j}} + \frac{0.3 C_{B,j}}{1 + C_{A,j} + 3 C_{B,j}}$$

where, $i = A, B$; $j = 1 \cdots 8$.

To complete the dynamic modelling system, apart from the column model described in Equation (26a) and (26b), initial conditions and boundary conditions are also essential.

$$C^{[k]}_{i,j}(0, x) = C^{[k-1]}_{i,j}(t_s, x) \quad \text{k: number of switching} \tag{26d}$$

The condition for $x = 0$ at $t > 0$ is: $\dfrac{\partial C_{i,j}}{\partial x} = \dfrac{u_j}{D_{ax}}(C_{i,j} - C^{in}_{i,j})$ (26e)

The condition for $x = L$ at $t > 0$ is: $\dfrac{\partial C_{i,j}}{\partial x} = 0$ (26f)

• The Node Model for an SMB system

The flow and integral mass balance equations at each node are summarised in table 4 according to the sketch in figure 16, under the assumptions that the dead volume by the switching devices, connecting tubes, and other parts is negligible. The operating conditions and model parameters are given in table 5.
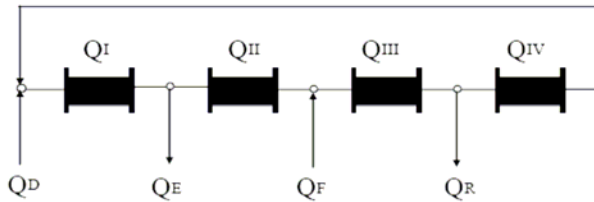
Figure 16. Flow diagram of 4 section SMB system.

Table 4. Node model

	Flow Rate Balance	**Composition Balance Eq (26g)**
Desorbent node (eluent)	$Q_I = Q_{IV} + Q_D$	$C^{in}_{i,I} Q_I = C^{out}_{i,IV} Q_{IV} + C_{i,D} Q_D$
Extract draw-off node	$Q_{II} = Q_I - Q_E$	$C_{i,E} = C^{in}_{i,II} = C^{out}_{i,I}$
Feed node	$Q_{III} = Q_{II} + Q_F$	$C^{in}_{i,III} Q_{III} = C^{out}_{i,II} Q_{II} + C_{i,F} Q_F$
Raffinate draw-off node	$Q_{IV} = Q_{III} - Q_R$	$C_{i,R} = C^{in}_{i,IV} = C^{out}_{i,III}$
Other nodes	Equal flow rates for the columns in the same zone	$C^{in}_{i,j} = C^{out}_{i,j-1}$

Table 5. System parameters and operating conditions for Bi-naphthol enantiomers separation

Symbol	Value	Symbol	Value
L (cm)	10.5	$C_{i,feed}$ (g/L)	2.9
D (cm²/min)	0.00525u	Q_F (ml/min)	3.64
ε_b	0.4	Q_I (ml/min)	56.83
$k_{eff,i}$ (min⁻¹)	6.0	Q_{II} (ml/min)	38.85
t_{switch} (min)	2.87	Q_{III} (ml/min)	42.49
		Q_{IV} (ml/min)	35.38

Thus, the SMBC model is constructed by 16 PDEs from Equation (26a), 16 ODEs from Equation (26b) and 20 AEs from Equations (26c) and (26g). All the single column models are connected in series by boundary conditions. The dominating parameters of the interstitial velocity and the inlet concentration of each column are restricted by node models. The switching operation can be represented by a shifting of the initial or boundary conditions for the single columns. This means that those conditions for each column change after the end of each switch time interval. After the cyclic steady state is reached, the internal concentration profiles vary during a given cycle, but they are identical at the same time for two successive cycles.

5.2. Numerical Simulations

As the Peclet number is close to 2000 in this application, the finite difference method will not be adopted for solving the model equations numerically due to the reason given in Section 4. Therefore, numerical simulations have been performed using both the high resolution and wavelet collocation methods for spatial discretization. The same integrator, the Alexander semi-implicit method as described in Section 3.3, is used so that the results on the effectiveness of different spatial discretization methods can be compared.

For the trials of the high resolution method, the number of mesh points along one column length has been chosen to be Nz = 17 and 33, which are equivalent to the collocation points generated by wavelet level of J = 4 and J = 5, respectively. Simulations using wavelet collocation method are conducted on the level J = 4, 5, and 6, respectively. The boundary conditions are treated using polynomial interpolation with the degree M = 1. The number of mesh points along the time axis is 5 points each switching period for all the trials. The reason for the less mesh points is that this semi-implicit integrator has built-in Newton iteration mechanism for all its three stage equations, which improves the efficiency of the scheme.

Figure 17 is the propagation of concentration profile with time.
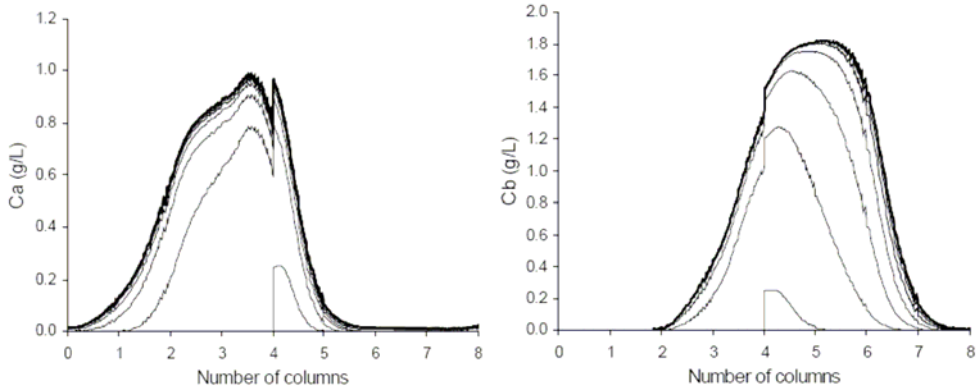
Figure 17. Propagation of concentration wave at mid of each switching.
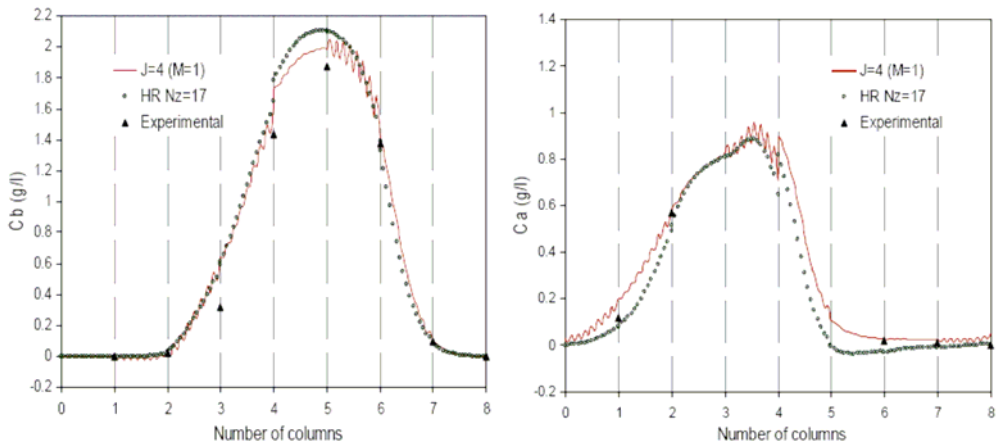
Figure 18 Concentration distributions at cyclic steady state.
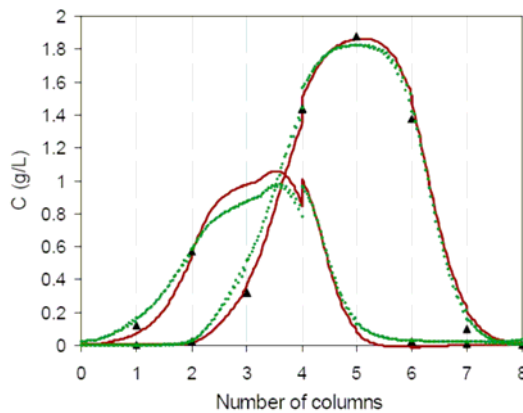
Figure 19. Concentration distribution at cyclic steady state: HR 33 line (red); Wavelet-Collocation J=5 dash line (green).

Figure 18 and figure 19 illustrate the calculated concentration distribution against experimental data, along the total columns length at the middle of 80th switching, which is

taken to be steady state. J = 4 of wavelet collocation or Nz = 17 of high resolution are not good enough to predict the real value, and furthermore, wavelet collocation presents certain degree of oscillation. However, wavelet collocation with J = 5 or high resolution with Nz = 33 produce better approximation, with high resolution has much closer results.
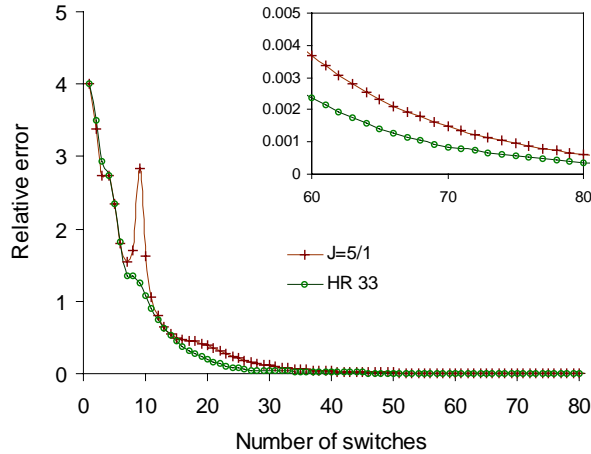
Figure 20. Comparison of relative error of prediction.

Figure 20 is the relative error defined by Minceva et al. (2003), which reflects the algorithm convergence performance. Wavelet has an abrupt point at the end of first cycle or the starting of next cycle (between 8th-9th switching). High resolution has consistent and better convergence. As far as computational cost is concerned, standing on the same number of spatial mesh points, wavelet takes less time for each switching period (16sec for J = 5) because less iteration (2) is required in the solving of Jacobi matrices. The high resolution needs 24.8sec for one switching calculation where 4 iterations are required. Nevertheless, the results from the high resolution method are much closer to the reported experimental data.

6. Concluding Remarks

This chapter has explored some upfront discretization techniques for the solution of complicated dynamic system models with sharp variations. Recently developed wavelet based approaches and high resolution methods have been successfully used for solving models of simulated moving bed chromatographic separation processes. To investigate the numerical power of proposed methods, the solution of single column chromatographic process represented by a Transport-Dispersive-Equilibrium linear model was firstly studied on the prediction of transit behaviour of wave propagation. Comparisons of the numerical solutions from finite difference, wavelet and high resolution methods with analytical solutions were conducted for a range of Peclet numbers. It has revealed that all the proposed methods work well when the PDEs system has low Peclet number, especially the upwind finite difference method, which can offer good numerical solution with reasonable computing time. The high resolution method provides an accurate numerical solution for the PDEs in question with

medium value of Pe. The wavelet collocation method is capable of catching up steep changes in the solution, and thus can be used for numerically solving PDEs with high singularity.

The advantages of the wavelet based approaches and high resolution methods are further demonstrated through applications to a dynamic SMB model for an enantiomers separation process. It shows that both of the methods are good candidates for the numerical solution of this complex model. They have provided encouraging results in terms of computation time and prediction accuracy on steep front. However, high resolution methods would be more preferable in this case because of better stability at achieving steady state and closer approximation to experimental data.

Generally, in terms of the two approaches (wavelet collocation and high resolution) mainly investigated here, wavelet based methods offers a better solution to PDEs with high singularity, however, prior knowledge of wavelet is required in order to take advantage of this kind of method. High resolution method is easy for implementation and can offer reasonable result with reasonable computing time.

However, it is suggested that wavelet based methods should be used with cautious because overestimation of wave peak is observed in our simulation results as well as in previous work. Unlike finite difference and high resolution methods, it does not follow the rule of the more points, the better approximation. The selection of wavelet resolution level is highly related to specific problem, such as, the most accurate results are from J=6 for Pe=50, J=7 for Pe=500, and J=9 for Pe=5000.

We have also noted that the selection of the value of the number of interpolating points, M, is very important since it could affect the numerical solution significantly. No report has been found on this issue so far in the open literature. Further investigation should be carried out on this subject.

Although this is a preliminary study, the results are encouraging for their applications to other complicated industrial systems. Further investigation is required into various aspects of the discussed numerical computing method to improve their capability for numerically solving difficult PDEs.

7. Nomenclature

C :	fluid phase concentration
$C_{i,j}^{in}$, $C_{i,j}^{out}$:	the concentrations of component i at the outlet or the inlet of column j.
D :	column diameter
$T_{i,j}^{(1)}$; $T_{i,j}^{(2)}$:	the first and second derivative for the autocorrelation function of scaling function
D_{ax} :	axial dispersion coefficient of the bulk fluid phase
k_{eff} :	effective fluid film mass transfer resistance
L :	column length
q :	concentration of component in the solid phase
$q*$:	equilibrium concentration in interface between two phases

Q_I, Q_{II}, Q_{III}, Q_{IV} : volumetric flow rate through the corresponding sections

Q_D :   desorbent flow rate

Q_E :   extract flow rate

Q_F :   feed flow rate

Q_R :   raffinate flow rate

t, x :   time and axial coordinates

τ, z :   dimensionless time and length

u :   interstitial velocity

t_{switch} :   switching time

ε_b :   void porosity of the mobile phase

Pe :   *Peclet number*

Acknowledgment

References

[1] Bertoluzza, S. (1996). A wavelet collocation method for the numerical solution of partial differential equations. *Applied Computers and Harmonia Analysis*, **3**, 1-9.

[2] Bertoluzza, S., & Naldi, G. (1994). Some remarks on wavelet interpolation. *Journal of computational and applied mathematics,* **13** (1), 13-32.

[3] Biegler, L. T., Jiang L., & Fox, V. G. (2004). Recent advances in simulation and optimal design of pressure swing adsorption systems. *Separation and Purification Reviews*, **33**(1), 1-39.

[4] Bindal, A., Khinast, J. G., & Ierapertritou, M. G. (2003). Adaptive multiscale solution of dynamical systems in chemical processes using wavelets. *Computers and Chemical Engineering*, **27**, 131-142.

[5] Blom, J. G., & Zegeling, P. A. (1994). Algorith 731: a moving-grid interface for systems of one-dimensional time-dependent partial differential equations. *ACM Transactions on Mathematical Software*, **20**, 194-214.

[6] Briesen, H., & Marquardt, W. (2005). Adaptive multigrid solution strategy for the dynamic simulation of petroleum mixture processes. *Computers and Chemical Engineering*, **29**(1), 139-148.

[7] Ching, C. B. (1998). Parabolic intraparticle concentration profile assumption in modeling and simulation of nonlinear simulated moving-bed separation processes. *Chemical Engineering Science*, **53**(6), 1311-1315.

[8]   Cruz, P., Mendes, A., & Magalhães, F. D. (2001). Using wavelets for solving PDEs: an adaptive collocation method. *Chemical Engineering Science*, **56**, 3305-3309.

[9]   Cruz, P., Mendes, A., & Magalhães, F. D. (2002). Wavelet-based adaptive grid method for the resolution of nonlinear PDEs. *American Institute of Chemical Engineering Journal*, **48**(5), 774-785.

[10] Donoho, D. (1992). Interpolating wavelet transform. Technical Report, Department of Statistics, Stanford University, 1992.

[11] Dorfi, E. A., & Drury, L. O. C. (1987). Simple adaptive grids for 1 - D initial value problems. *Journal of Computational Physics*, **69**, 175-195.

[12] Eigenberger, G., & Butt, J. B. (1976). A modified Crank-Nicolson technique with non-equidistant space steps. *Chemical Engineering Science,* **31**, 681-691.

[13] Furzeland, R. M. (1990). A numerical study of three moving-grid methods fro one-dimensional partial differential equations which are based on the method of lines. *Journal of Computational Physics*, **89**, 349-388.

[14] Gu, T. (1995). *Mathematical modelling and scale up of liquid chromatography*. New York: Springer.

[15] Gunawan, R., Fusman, I., & Braatz, R. D. (2004). High resolution algorithms for multidimensional population balance equations. *AIChE Journal*, **50**, 2738-2749.

[16] Hu, S. S., & Schiesser, W. E. (1981). An adaptive grid method in the numerical method of lines. In R. Vichnevetsky & R. S. Stepleman (Eds.), Advances in Computer Methods for Partial Differential Equations (pp.305-311). IMACS: North-Holland.

[17] Huang, W., & Russell, R., D. (1996). A moving collocation method for solving time dependent partial differential equations. *Applied Numerical Mathematics*, **20**, 101.

[18] Jiang, G., & Shu, C. W. (1996). Efficient implementation of weighted ENO schemes. *Journal of Computational Physics*, **126**, 202-228.

[19] Koren, B. (1993) A robust upwind discretization method for advection, diffusion and source terms, *CWI Report NM-R9308* April, Department of Numerical Mathematics.

[20] Lapidus, L., & Amundson, N. R. (1952). Mathematics of adsorption in beds. VI. The effect of longitudinal diffusion in ion exchange and chromatographic columns. *Journal of Physical Chemistry*, **56**, 984-988.

[21] Li, S., & Petzold, L. (1997). Moving mesh methods with upwinding schemes for time-dependent PDEs. *Journal of Computational Physics*, **131**, 368-377.

[22] Lim, Y., Lann, J. M., & Joulia, X. (2001). Accuracy, Temporal performance and stability comparisons of discretization methods for the numerical solution of partial differential equations (PDEs) in the presence of steep moving fronts. *Computers and Chemical Engineering,* **25**, 1483-1492.

[23] Lim, Y., Lann, J. M., & Joulia, X. (2001). Moving mesh generation for tracking a shock or steep moving front. *Computers and Chemical Engineering,* **25**, 653-633.

[24] Liu, Y., Cameron, I. T., & Bhatia, S. K. (2001). The wavelet-collocation method for adsorption problems involving steep gradients. *Computers and Chemical Engineering*, **25**, 1611-1619.

[25] Minceva, M., Pais, L.S., & Rodrigues, A. (2003). Cyclic steady state of simulated moving bed processes for enantiomers separation. *Chemical Engineering and Processing*, **42**, 93-104.

[26] Miller, K., & Miller, R. N. (1981). Moving Finite Elements. I. *SIAM Journal of numerical Analysis*, **18**, 1019-1032.

[27] Nikolaou, M., & You, Y. (1994). Chapter 7: Use of wavelets for numerical solution of differential equations. In R. Motard & B. Joseph (Eds.), *Wavelet applications in chemical engineering* (pp. 210-274). Kluwer: Academic Publisher.

[28] Pais, L. S., Loureiro, J. M., & Rodrigures, A. E. (1997). Separation of 1,1'-bi-2-naphthol Enantiomers by continuous chromatography in simulated moving bed. *Chemical Engineering Science,* **52**, 245-257.

[29] Petzold, L. R. (1987). Observations on an adaptive moving grid method for one-dimensional systems of partial differential equations. *Applied Numerical Mathematics*, **3**, 347-360.

[30] Qamar, S., Elsner, M. P., Angelov, I. A., Warnecke, G., & Seidel-Morgenstern, A. (2006). A comparative study of high resolution schemes for solving population balances in crystallization. *Computers and Chemical Engineering*, **30**, 1119-1131.

[31] Revilla, M. A. (1986). Simple time and space adaptation in one-dimensional evolutionary partial differential equation. *International Journal for Numerical Methods in Engineering*, **23**, 2263-2275.

[32] Sanz-Serna, J. M., & Christie, I. (1986). A Simple adaptive technique for nonlinear wave problems. *Journal of Computational Physics*, **67**, 348-360.

[33] Vasilyev, O. V., Paolucci, S., & Sen, M. (1995). A multilevel wavelet collocation method for solving partial differential equations in a finite domain. *Journal of Computational Physics*, **120**, 33-47.

[34] Wouwer, A. V., Saucez, P., & Schiesser, W. E. (1998). Some user-oriented comparisons of adaptive grid methods for partial differential equations in one space dimension. *Applied Numerical Mathematics*, **26**, 49-62.

[35] Yao, H. M., Tian, Y. C., & Tade, M. O. (2008). Using Wavelets for Solving SMB Separation Process Models. *Industrial & Chemical Engineering Research*, **47**, 5585-5593.

[36] Zhang, T., Tade, M. O., Tian, Y. C., & Zang, H. (2008). High resolution method for numerically solving PDEs in process engineering. *Computers and Chemical Engineering*, **32**, 2403-2408.

Chapter 11

THE STABILITY AND ANTIAROMATICITY OF HETEROPHOSPHETES AND PHOSPHOLE OXIDES

Zoltán Mucsi and György Keglevich

Department of Organic Chemistry and Technology,
Budapest University of Technology and Economics,
1521 Budapest, Hungary

Abstract

Molecular structures are often influenced by aromatic stabilization and antiaromatic destabilization effects. In spite of nearly a century's effort – from *Kekulé* 1871 to *Breslow* and *Dewar* 1965 – to synthesize cyclobutadiene, these attempts have proved to be unsuccessful [1–6]. Only theoretical chemistry was able to explain this failure by introducing the concept of antiaromaticity as a new phenomenon. The synthesis of these antiaromatic compounds has long been considered as desirable target of preparative chemistry in order to examine experimentally their species chemical properties, but only a few compounds could be prepared and studied. One of the examples may be the family of phosphole oxides exhibiting a slightly antiaromatic character [7–10]. At the same time, heterophosphetes, are of more considerable antiaromatic character and they manifest only as high energy intermediate or transition state (TS) [11–20]. In this paper, stability and thermodynamic, as well as kinetic properties of heterophosphetes and phosphole oxides are discussed.

1. Heterophosphates

Heterophosphetes (**1**), such as oxaphosphetes, thiaphosphetes and azaphosphetes, a group of four-membered β-heterocycles are structurally related to biologically active penicillin-type β-lactams and belong also to the family of the antiaromatic molecules [11–20]. The thermodynamic and kinetics aspects, as well as the electronic structures of heterophosphetes containing three different ring heteroatom moieties (Y = NH, O, S) and twelve exocyclic substituents (X = H, Me, Ph, OMe, NMe_2, SMe, F, Cl, Br, CN, OCN, SCN) were studied theoretically and experimentally [11,12].

1.1. Structure of Heterophosphates

In principle, heterophosphetes (1) may adopt two distinct conformations [11–20]. The phosphorous-heteroatom bond (P–Y) can be either equatorial (1A) or apical (1B). The situation is controlled by the apicofilicity of Y and X [21]. The interconversion of the two forms falls into the domain of pseudorotation [21–23]. Heterophosphetes 1, usually prefer undergoing a fast ring opening reaction to form the corresponding *cis* (3-I) or *trans* (3-II) isomers of β-functionalized phosphoranes as isolable products [11–20]. This equilibrium may be one of the reasons that earlier synthetic attempts to produce heterophosphetes have often failed. From a theoretical point of view, one may consider the 1B ↔ 3-I reversible transformation as a ring-chain valence tautomerism [11,12]. The saturated versions, heterophoshetanes (2) existing also as two possible conformers (2A and 2B) are more stable and in the case of Y=O are well-known as the intermediates of the Wittig reaction [24]. In contrast to 1, compound 2 never undergoes ring-opening to form 4 [11]. The overall process and structures are summarized in figure 1.
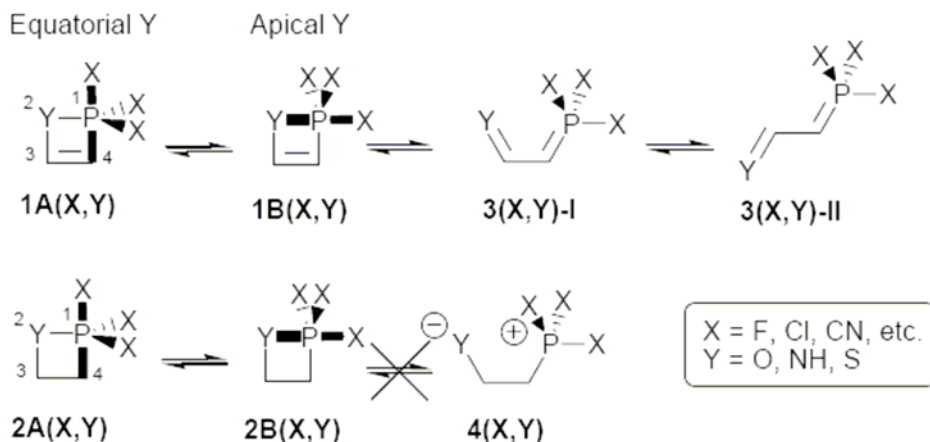
Figure 1. Structure of heterophosphetes (**1A** and **1B**) and heterophosphetanes (**2A** and **2B**) as well as their ring opened forms (**3** and **4**).
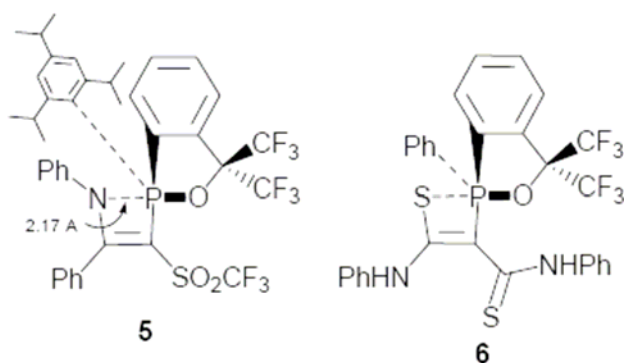
Figure 2. Heterophosphates 5 and 6 prepared.

In spite of the preparative efforts, only two compounds with the desired structure were proved to be isolable and reported in the literature (5 [25] and 6, [26] figure 2) representing the heterophosphete family. On the basis of the N···P distance of 2.170 Å, [25] compound 5 can only be regarded to have structure 1B in a broader sense. The relatively long bond distance between the P and the Y atoms is rather an ionic interaction coming from strong zwitter-ionic structure 3-I.

1.2. Synthetic Aspect of Heterophosphetes

There are many synthetic possibilities to prepare 1. From synthetic aspect, the synthesis of 1B and 3-I is equivalent, because they are linked together by a ring-chain tautomerism, therefore the successful synthesis of 1B requires a shifted equilibrium between 3-I and 1B toward 1B, meaning that 1B lies at a lower energy level than 3-I. Two possible synthetic approaches (inverse-Wittig route A and acylation C) were described for the preparation of 3-I (Scheme 1) [13,18].
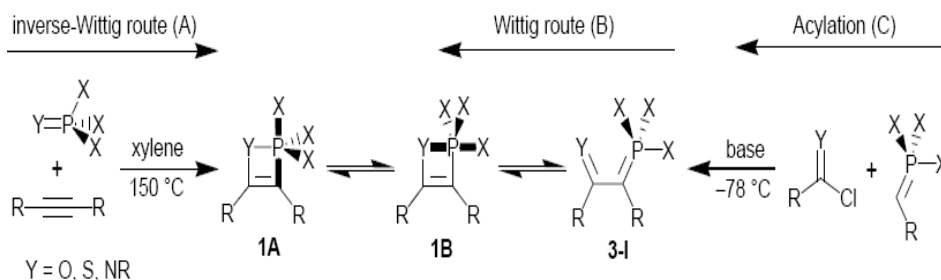
Scheme 1.

The route to produce 1B or 3-I involving an inverse-Wittig protocol was developed by the *Keglevich* group [13–17,27] (Scheme 2) and parallelly by Japanese groups [19,20,25,26,38]. In the former case, 2,4,6-trialkylphenyl cyclic phosphine oxides (7) were treated with dialkyl acetylenedicarboxylate (8) at an elevated temperature to give first 9 as an intermediate that underwent a ring-opening reaction to yield 10.
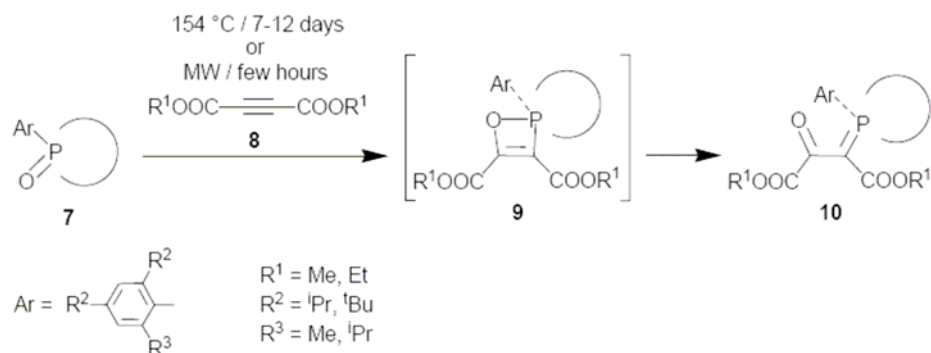
Scheme 2.

The β-oxophosphoranes (3-I) were also prepared by the acylation approach [28].

Aitken and co-workers explored the chemistry of β-oxophosphoranes, 3-I(X,O) (here 13) and elaborated a versatile synthetic method for the preparation of these compounds [29-37]. This procedure involves the acylation of phosphoranes (12) with acyl chlorides (11) (Scheme 3) [29–37].

R^1 = Ph, OMe, OEt, alkyl
R^2 = Ph, OMe, OEt, ^{t}Bu, alkyl
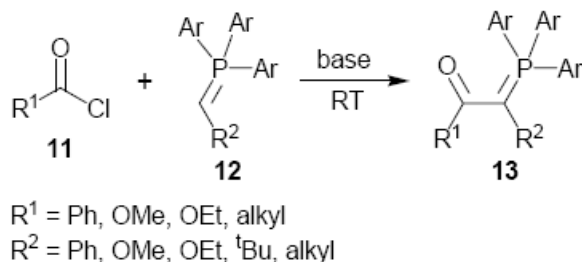
Scheme 3.

Until now, only compound 5 (Scheme 4) proved to be stable and isolable and was studied by X-ray analysis [20,25,38]. All other compounds related to structure 1B underwent a ring-opening reaction, leading to 3-I as stable products. A real equilibrium system could be observed by ^{31}P NMR spectroscopy in solution between iminophosphorane 16 and azaphosphete 5. (16) [25].
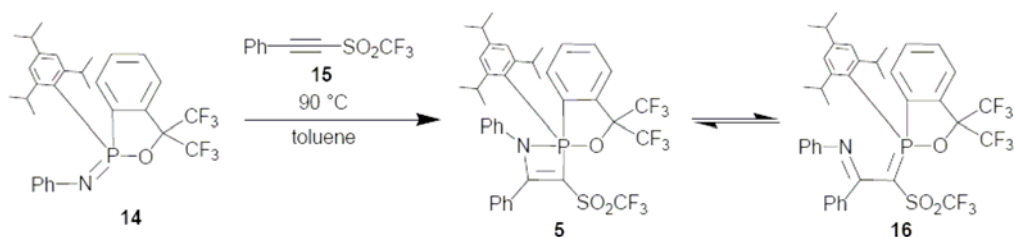
Scheme 4.

In the reaction of phosphorane/ylide 19 with aryl isothyocianates (18), a spirocyclic thiaphosphete (6) equilibrating with the corresponding β-thiophosphorane (17) was formed (Scheme 5) [38].

Ar = Ph, 1-naphtyl
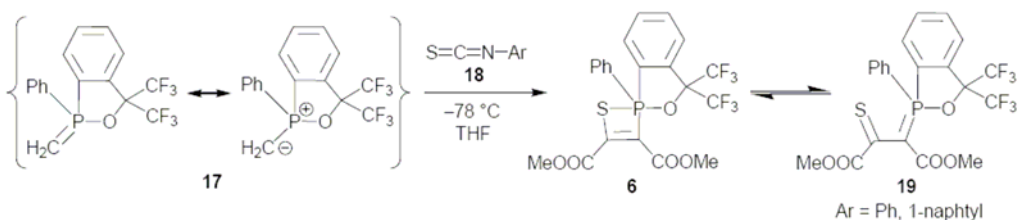
Scheme 5.

1.3. Thermodynamic and Kinetic Aspects [11,12]

The relative energetics of the four possible structures (1A, 1B, 3-I and 3-II) measure thermodynamic stability, while the two transition states 1B-TS (belonging to 1A→1B) and 3-TS (belonging to 1B→3-I) define kinetic stability. In several cases, neither 1A or 1B, nor 3-I exist, at the same time, 3-II always exists. From the point of view of thermodynamics, 3-II was used as a common reference state. Hence and the stability of 1A, 1B and 3-I can be measured and compared with respect to 3-II. Compound 3-I is expected to be isolable if ΔG(1B→3-I) is negative (the transformation is exothermic), while compound 1 is expected to be stable if the energy difference is positive (the transformation is endothermic). By examining the 3×12 3D PESs (6 representative PESs are displayed in figure 3), one can distinguish three clusters of substituents that may be classified as *Type I* (F, Cl, Br, CN, OCN, SCN), *Type II/A* (NMe$_2$, OMe, SMe) and *Type II/B* (H, Me, Ph) substituents. The effect of these clusters differs not only quantitatively, but also in the basic topology of the PESs. The existence of structures 1A, 1B and 3-I strongly depends on the type of substituents applied.

a) Electron-withdrawing groups (EWG) such as halogens, CN, OCN, and SCN belong to *Type I* substituents, which are able to stabilize both 1A and 1B to occupy distinct energy minima (figure 3A–C). The stronger EWGs yield less exothermic and more endothermic ring opening ΔG(1B→3-I) values for 1A and 1B, respectively. In the presence of strong EWGs such as CN, OCN and SCN, the minimum of 3 is annihilated and merges into 1B. As was discussed previously, in all cases, 1A lies at a higher energy level than 1B, suggesting that 1B would be more favourable from the point of view of synthesis.

b) The class of *Type II/A* substituents consists of strong electron-donating and conjugative groups (EDG) with lone electron pairs on the heteroatom of X (NMe$_2$, OMe and SMe). Substituents of *Type II/A* exhibit only 1A, 3-I and 3-II as true minima, although the ΔG(1A→3-I) and ΔG(1A→3-II) values are high and exothermic (> 100 kJ mol^{-1}). *Type II/A* substituents are unable to stabilize 1B; therefore, these structures do not represent a stationary point in the downward trend of a PES (figure 3D), but around the position of 1B, the surface is rather flat, indicating an almost a stationary point.

c) The non-conjugative H, Me and Ph groups without lone pairs belong to the *Type II/B* substituent class, which destabilizes both 1A and 1B, meaning that there are no minima for any 1B and 1A, only 1A(H,NH) and 1A(Me,NH) represent a true minima (figure 3E–F). The ring opening ΔG(1A→3-I) and ΔG(1A→3-II) values are highly exothermic (> 100 kJ mol^{-1}) (table 1). Structure 1B is positioned on a completely downward trend of a PES, without any horizontal portions.

The variation of substituents X and heteroatom Y in the heterophosphete results in dramatic changes in the "reaction profile", which is the minimal energy pathway segment (MEP) of the PES (figure4) from 1A toward 3-I.
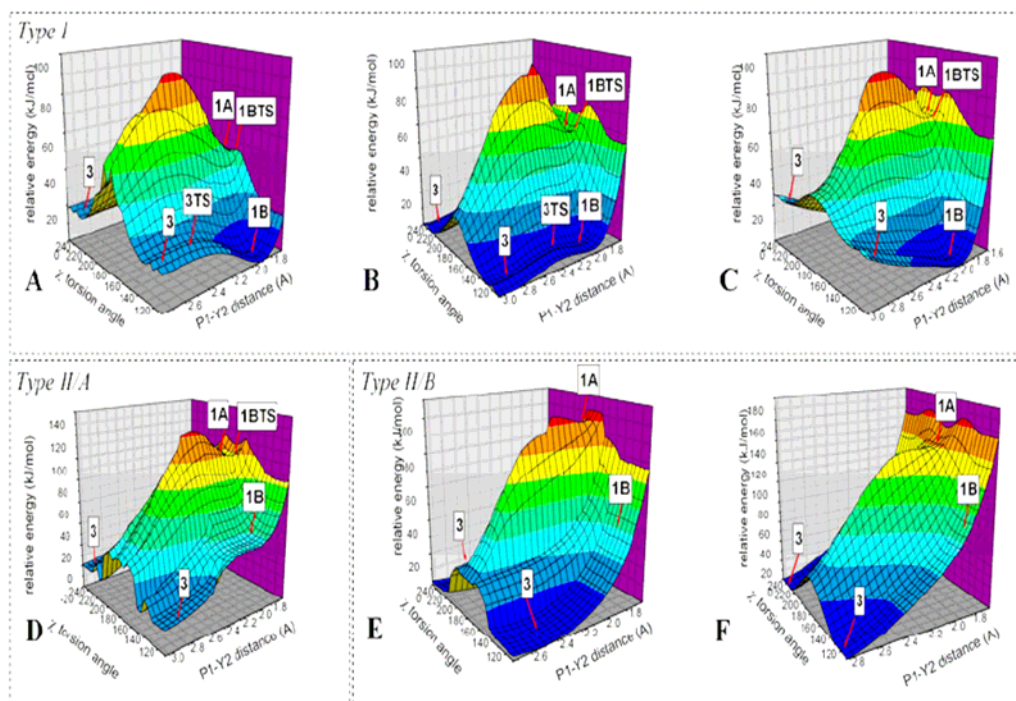
Figure 3. 3D PESs associated with Type I: X=F, Y=O (A), X=Cl, Y=O (B), X=Br, Y=O (C), Type II/A: X=OMe, Y=O (D), Type II/B: X=H, Y=O (E), X=Me, Y=O (F).

Table 1. Summary of the computed relative enthalpies for heterophosphetes. The underlined numbers indicate the global minimum of the PES based on computations carried out at B3LYP/6-311++G(2d,2p) level of theory

Type	X/Y	NH	O	S
	F	1A > 1B < 3-I < 3-II	1A > 1B < 3-I < 3-II	1A > 1B < 3-I < 3-II
Type I	Cl, Br	1A > 1B > 3-I < 3-II	1A > 1B > 3-I < 3-II	1A > 1B > 3-I < 3-II
	CN, OCN, SCN	1A > 1B < 3-II	1A > 1B < 3-II	1A > 1B < 3-II
Type II/A	OMe, NMe$_2$, SMe	1A > 3-I < 3-II	1A > 3-I < 3-II	1A > 3-I < 3-II
Type II/B	H, Me, Ph	1A > 3-I < 3-II	3-I < 3-II	3-I < 3-II

Electron-donating and conjugative groups of *Type II/A* and non-conjugative *II/B* substituents stabilize, while strong electron-withdrawing groups of *Type I* destabilize structures 3-I and 3-II (figure 5). This means that electron-donating and conjugative groups of *Type II/A* and non-conjugative groups of *Type II/B* substituents stabilize structures 3-I and 3-II to a larger extent than structure 1A, decreasing the Δ*G*(1A→3-I) and Δ*G*(1A→3-II) values (more exothermic) of this ring opening reaction. An opposite effect was recognised for *Type I* substituents. In this case, the *Type I* electron-withdrawing substituents destabilize structures

3-I and 3-II to a larger extent than structure 1A, increasing the ΔG(1A→3-I) and ΔG(1A→3-II) values of this ring opening reaction, resulting more endothermic transformations.
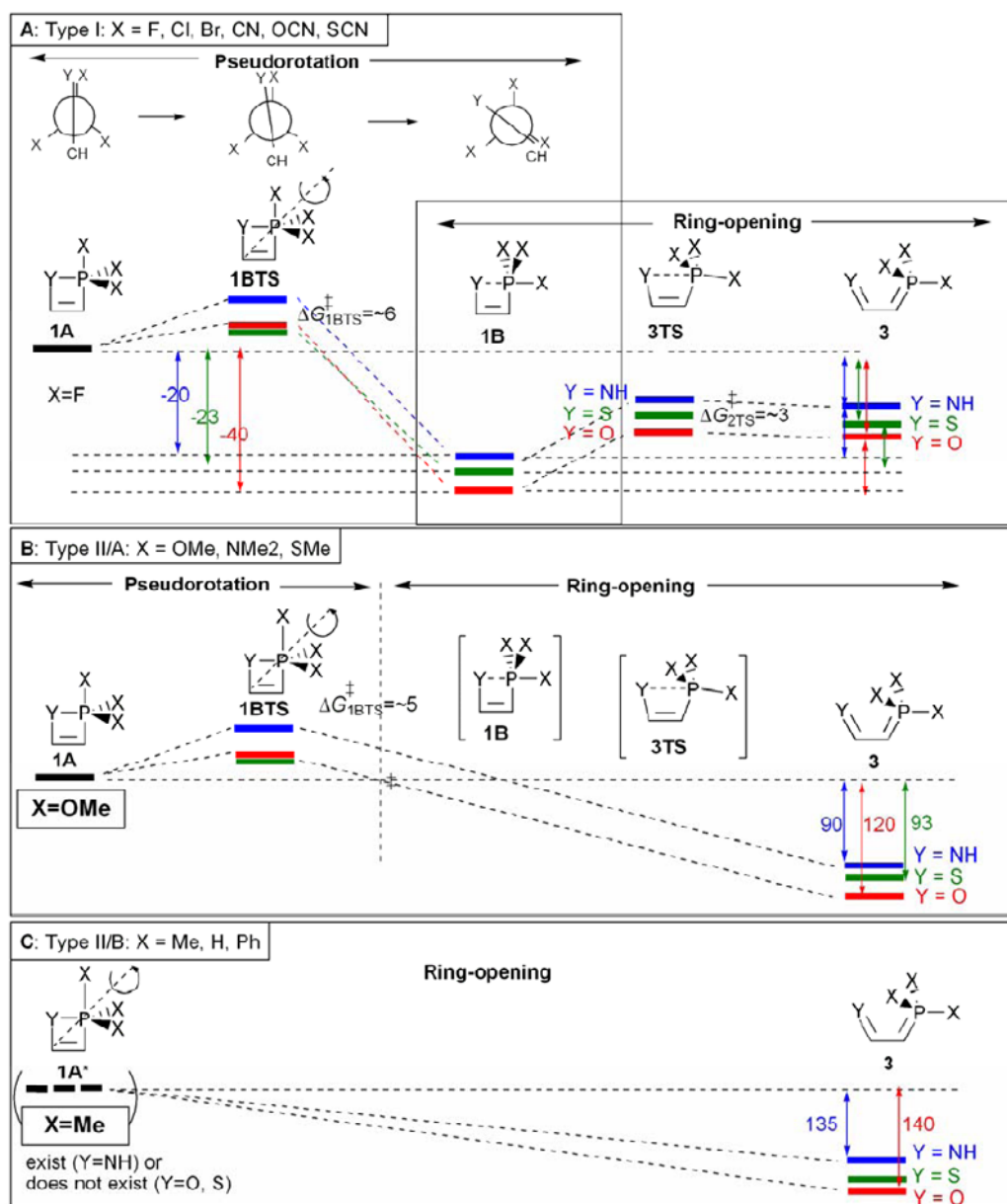
Figure 4. Schematic representations of the energy profile of the **1A → 1B → 3-I** transformation with different types of substituents denoted by X. The vertical axis is ΔG (kJ mol⁻¹), while the horizontal axis is the reaction coordinate in arbitrary units.

When both 1A and 1B exist (*Type I* substituents), the two minima are linked by pseudorotation trough χ = X$_{axial}$–P1–Y2–C3 dihedral angle from 180° to ~120° during 1A → 1B process (figure 4). The activation Gibbs free energies are rather low (ΔG$^{\neq}_{1B-TS}$ = 3–12 kJ

mol^{-1}; χ = ~172°), which means that the rate of the transformation is very fast, while the antiaromaticity decreases significantly. The greater stability of 1B and the low $\Delta G^{\neq}_{1B-TS}$ value makes the isolation of 1A kinetically impossible. The energy gap between 1B and 3-I is also rather low ($\Delta G^{\neq}_{3-TS} \approx$ 5–18 kJ mol^{-1}) due to the disappearance of the antiaromaticity. This allows a fast ring-opening reaction. From kinetic point of view, it is not possible to trap either 1A or 1B if 3-I is the thermodynamically preferred structure. However, when 1B is more stable than 3-I, 1B may be isolated. In the case of substituents of *Type II/A*, 1A represents in fact a minimum; therefore a low barrier appears for the 1A → 1B transformation ($\Delta G^{\neq}_{1B-TS} \approx$ 6–8 kJ mol^{-1} for the TS). In the case of *Type II/B* substituent due to the absence of stable 1B, the minimum energy pathway (MEP) leads, however, directly to 3-I (figure 4B). The energy profile is therefore very simple (figure 4C) due to the lack of a minimum for 1A and 1B.
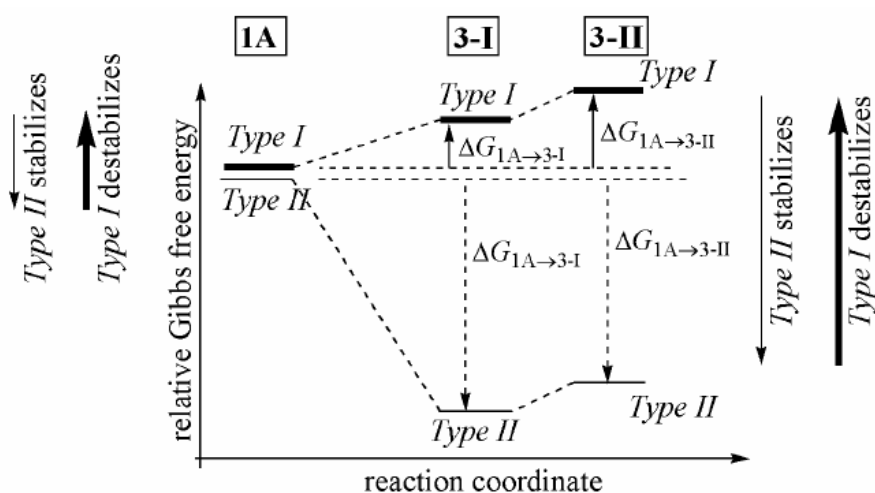
Figure 5. Proposed energy levels for 1A → 3-I → 3-II reactions for substituents of *Type I* and *Type II/A*.

1.4. Electronic Structure of Heterophosphetes [11,12]

The question then arises why the stability of the four-member ring 1 vanishes by the introduction of a double bond into the ring of 2. It is not simply a consequence of the increased ring strain due to the presence of the double bond in the four-member ring, which increase only about 20–25 kJ mol^{-1} (see the last paragraph). Furthermore, all P–Y distances are larger in both 1A and 1B by 0.05–0.1 Å than those in 2A and 2B. Moreover the structure of azaphosphetes 1(X,N) is non-planar, in contrast with the completely planar azaphosphetanes 2(X,N), due to the fact that the NH group is bent out from the plane, which refers undoubtedly to an unfavoured electronic effect. All these syndromes point to a common phenomenon, which is the significant antiaromaticity of 1. To answer the questions, what the reason for the existence of an additional destabilizing electronic effect is and what the extent of the antiaromaticity in structure 1 is, we need to examine the electronic structure.

The antiaromaticity comes from the strong conjugation between P and Y interacting with the C3=C4 double bond, which results a resonance structure (β) having a 4π electron system

for 1A and 1B [11,12]. An equatorial Y can participate in a more extensive conjugation with the P atom, therefore 1A with an equatorial Y possesses stronger antiaromaticity than 1B exhibiting an apical Y, which is rather non-conjugative (figure 6) [11,12]. The charged resonance structure (γ) for 1B is very typical. The strong antiaromaticity was observed in other non-isolable four-membered rings, such as cyclobutadiene, four-membered unsaturated lactones and unsaturated lactams.
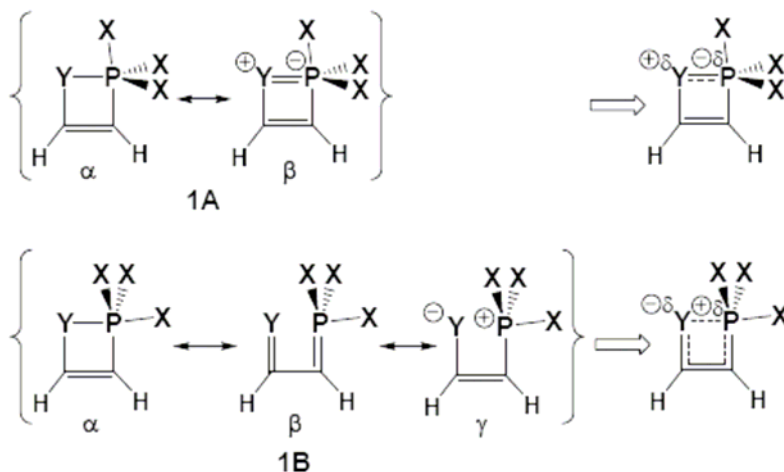
Figure 6. Resonance and the resulting structures for heterophosphetes 1A and 1B.

In the case of 1A, the overlapping orbitals comprise of three p_z AO of Y, C3 and C4, and the $(d_{xz}+d_{yz})$ AO combination of P. Therefore, this type of interaction was referred to as "heterogenic" antiaromaticity, analogous to the phenomenon of heterogenic aromaticity.
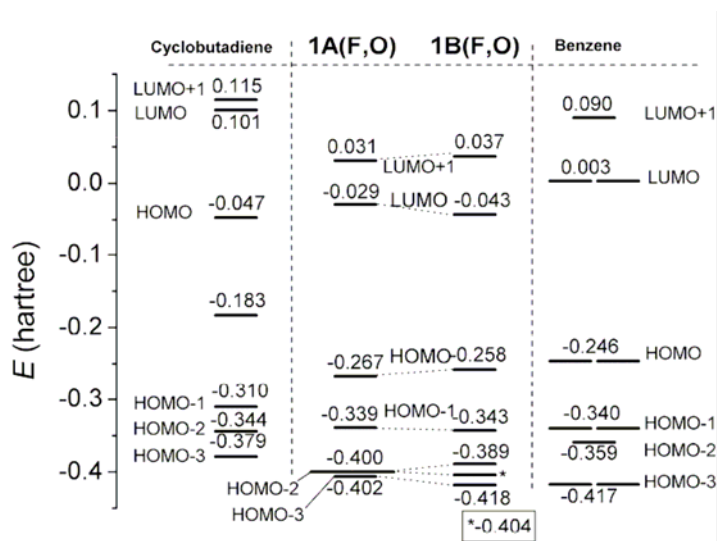
Figure 7. Schematic representation of the MO energy levels for cyclobutadiene, benzene, as well as heterophosphetes 1A(F,O) and 1B(F,O) computed at B3LYP/6-31G(d) level of theory.

The types and energies of computed molecular orbitals (MO) for 1A(F,O) and 1B(F,O) are shown in figure7 and 8. The MOs of 1A(F,O) show a significant correlation with the MOs of antiaromatic cyclobutadiene (7), e.g. the shape of the HOMO for 1A(F,O) is similar to that of the HOMO of 7, but the AO coefficients differ. During the pseudorotation of 1A to 1B, the arrangement around the P atom changes. This causes an alteration in the molecular symmetry as well, leading to different MOs, therefore the MOs of 1B(F,O) show significant differences from the MOs of 1A(F,O) and cyclobutadiene, both in the shape and the order of the energy levels (figure 7 and 8). The shapes of HOMOs in 1A(F,O) and 1B(F,O) differ markedly from each other, reflecting to the different electronic structures and molecular properties. For the sake of comparison, the MO energy levels of aromatic benzene is also shown in figure 7.
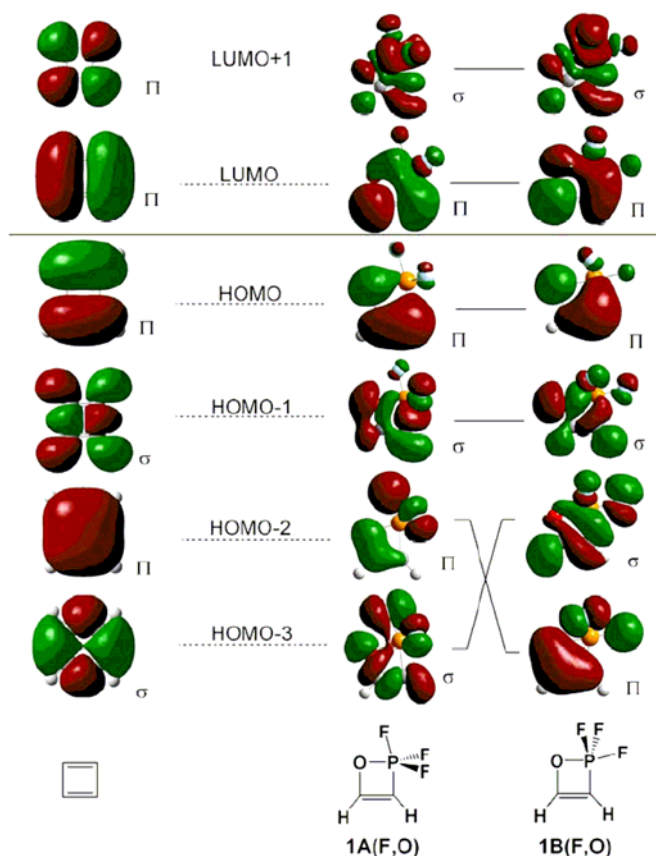
Figure 8. Schematic representation of selected molecular orbitals of cyclobutadiene, as well as heterophosphetes 1A(F,O) and 1B(F,O) computed at B3LYP/6-31G(d) level of theory.

1.5. Antiaromaticity Percentage of Heterophosphetes [11,12]

The exact description of the aromatic or antiaromatic character of ring compounds can be examined by different scales such as the HOMA index [10], NICS values [11,12] and enthalpies of homodesmic reactions, resulting in an aromatic stabilizing energy (ASE) [13]. However, the determination of the aromatic or antiaromatic character of heterophosphete 1 is

not simple by traditional means, therefore the antiaromaticity of 1 was characterized by a common and universal linear scale based on the enthalpy of hydrogenation (see ΔH_{H2} and $\Delta\Delta H_{H2}$ in figure 8) when cyclobutadiene and benzene are considered to be -100% and $+100\%$, respectively [14].

The aromaticity/antiaromaticity percentage of compounds 1A and 1B with X = F, Cl, Br, CN, OCN, SCN, OMe, NMe$_2$, SMe, H, Me, Ph and Y = O, NH, S were examined and listed in table 2 and figure 9 [11,12]. According to the linear aromaticity and antiaromaticity scale, in all cases, heterophosphetes 1A produce more exothermic ΔH_{H2} values than 1B suggesting the more significant antiaromatic character of 1A. As was predicted previously, 1A was shown to be more antiaromatic (-60% to $+1\%$) than the slightly antiaromatic or non-aromatic 1B ($-41\% - 20\%$). This sharp difference between the antiaromaticity parameters of 1A and 1B was attributed to the stronger conjugation between P and Y in 1A, than in 1B, due to the different internal molecular symmetry. Substituent X and the heteroatom Y influence significantly the degree of antiaromaticity of 1.

Table 2. Computed aromaticity/antiaromaticity percentage for heterophosphetes 1A and 1B congeners

Type	X	NH		O		S	
		1A	1B	1A	1B	1A	1B
I	F	−49.6	−14.3	−40.1	−7.3	−26.8	−4.5
	Cl	−45.1	−6.4	−34.6	5.3	−22.9	6.2
	Br	−42.2	2.5	−31.5	20.6	−20.0	10.2
	CN	−40.3	7.2	−34.1	10.2	−22.5	14.7
	OCN	−57.5	−41.5	−49.6	−20.2	−31.1	−23.7
	SCN	−45.7	−24.8	−52.2	−21.0	−32.1	−12.1
II/A	OMe	−27.3	–	−19.9	–	−30.8	–
	NMe$_2$	−4.8	–	−3.2	–	1.0	–
	SMe	−17.7	–	−17.9	–	−4.4	–
II/B	H	−20.1	–	–	–	–	–
	Me	−21.5	–	−14.8 [a]	–	–	–
	Ph[b]	–	–	–	–	–	–

[a] Stationary point with one imaginary frequencies; [b] Computed at the B3LYP/6-31++G(d,p) level of theory.

Optimized geometry parameters such as planarity, bond distance, and bond angles are also confirm the antiaromaticity discussed above, for example in 1A(X,NH) and 1B(X,NH), the N atom is not planar, as the N atom is able to alter its hybridization state from sp^2 to sp^3, decreasing the antiaromatic character that would be in the planar structure.

The antiaromaticity of 5' that covers 5 without isopropyl groups in the phenyl ring was also evaluated making use of the hydrogenation reaction, showing an extent of -7.43% antiaromaticity and meaning non-aromaticity. This is most likely due to the large P–Y bond distance (2.46 Å) that efficiently decreased the unfavourable overlapping between the two atoms involved. This supports well why this compound could be synthesized.
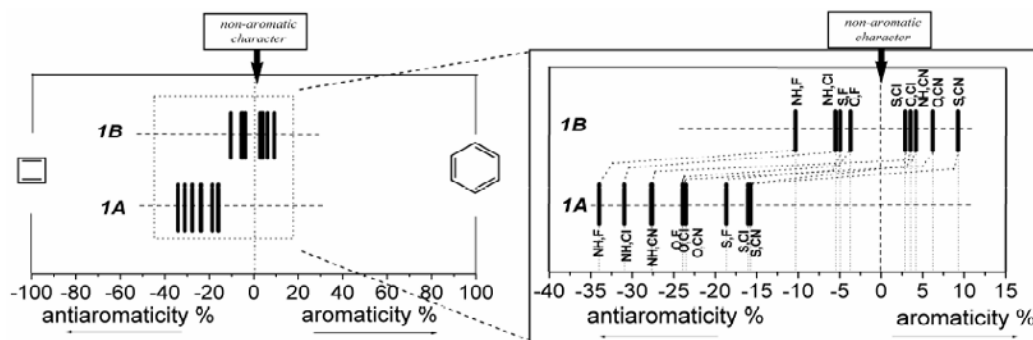
Figure 9. Computed aromaticity and antiaromaticity scale for heterophosphetes **1A** and **1B** computed at B3LYP6-311++G(2d,2p) level of theory.

The question arises, why 1A with exocyclic substituents (X) of *Type II/A* and *Type II/B* exhibits significantly lower antiaromaticity percentages, than 1A with *Type I* substituents. The less antiaromatic character of 1A with *Type II/A* and *Type II/B* X substituents may be attributed to the lone pair on X that result in an 'exoconjugation' between the X and the P atoms (figure 10). This 'exoconjugation' competes and decreases the unfavourable internal conjugation between P and Y, and lowers the "weight" of the antiaromatic resonance structure (1A-II). The opposite effect can be recognized in the case of *Type I* substituents, where the internal conjugation is increased by the strong EWG substituents due to the larger polarization of the P–Y bond, resulting in an increase in the weight of the antiaromatic resonance structure (1A-II). This effect is reflected in the P–Y atomic distances, where the shortest bond lengths can be identified in the case of *Type I* substituents as compared to 1A with substituents of *Type II/A* and *Type II/B* (figure 10). It can be also seen that the P–Y bond length in compounds 1B is systematically longer (by ~0.05Å) as compared to that in species 1A, referring to the larger degree of antiaromaticity of 1A, as compared to 1B.
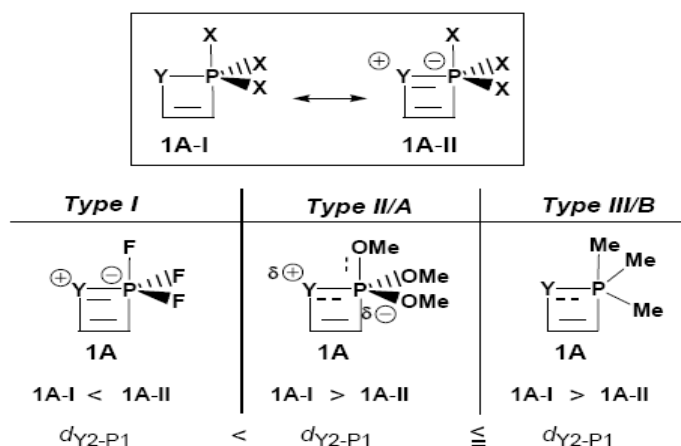
Figure 10. A schematic illustration of electronic effects exerted by exocyclic substituents (X) of Types I, II/A and II/B.

The 3D aromaticity 3D-hypersurface (figure 11) was computed for heterophosphete 1(F,O) that shows that conformation 1A is trapped in an anti-aromatic hole, while conformation 1B is on a "valley" which is neither really aromatic, nor really antiaromatic. In contrast to 1A and 1B, structure 3 is conjugated so it assumes a low value at the aromatic "hill-side".
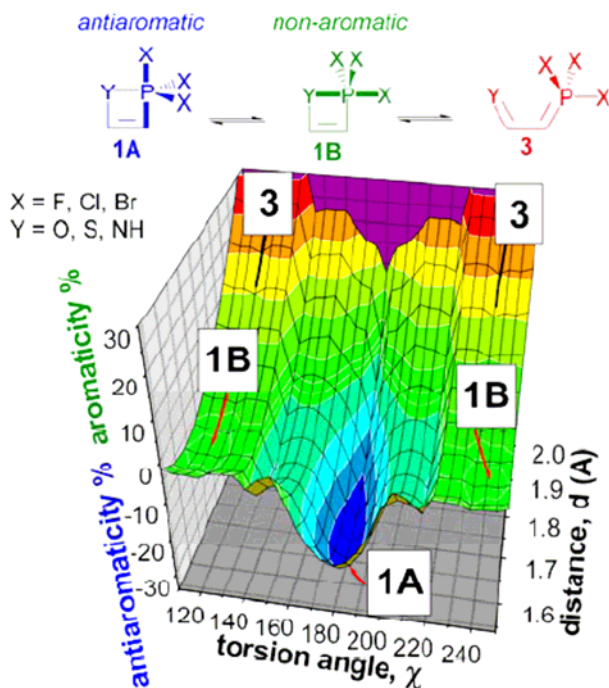
Figure 11. 3D aromaticity (positive) and antiaromaticity (negative) surface of heterophosphete **1(F,O)** as a function of selected internal geometrical parameters (χ,d).

2. Phosphole Oxides

2.1. Structure, Stability and Synthetic Aspect of Phosphole Oxides

Several studies revealed that, contrary to the stability of aromatic phospholes (20) [39–42], phosphole oxides (21) exhibit unusual instability [43,44]. Phosphole oxides (21) can be obtained by the oxidation of phospholes (20), but generally they could not be isolated, because of their instability. The phosphole oxides 21 are stabilized by a Diels-Alders [4+2] type cyclo-dimerization. The phosphole oxide dimer 22 that is a 7-phosphonorbornene derivatives formed in a regio- and stereospecific manner (Scheme 6) [43,45].

It was shown that fused phosphole derivative 23 is stable for days, but the oxidized derivative 24 is unstable, and undergoes a double-bond rearrangement under basic condition to afford 2,3-dihydrophosphole oxide 25 (Scheme 7) [9].
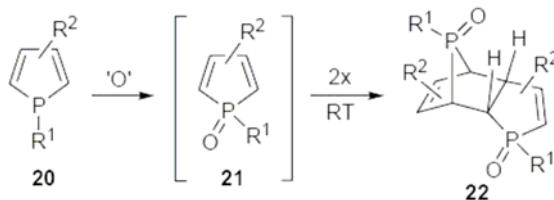
Scheme 6.
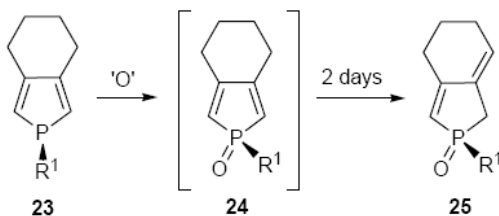
Scheme 7.

2.2. Electronic Structure and Antiaromaticity of Phosphole Oxides

It was assumed, that the instability of the phosphole oxides (21 and 24) is due to a weak antiaromaticity [9,10]. In contrast to phosphole 20 that is analogous to pyrrole (26), the antiaromaticity of phosphole oxide 21 is originated from the electron-deprived electron shell of the P atom represented by resonance structure β that is analogous with borole (27), where the empty p_z orbital allows a continuous 4π conjugation (figure 12). The ratio of resonance structures α and β results the final character of antiaromaticity [10].
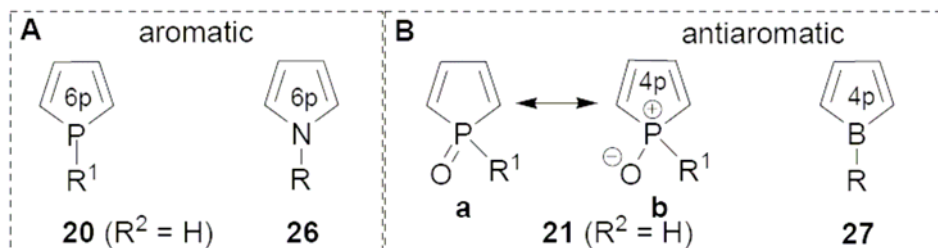
Figure 12. Electron diagram of five-membered P-, N- and B-heterocycles.

The antiaromaticity of 21 was characterized earlier by NICS values and BIRD indexes, as well. The NICS values of 21 show significant deviation from the expected values due to the shielding effect of P atom [9,10] but considering the differences between the NICS values of the aromatic 20 and antiaromatic 21 it can be concluded that they are considerable lower for 21 than expected. The calculated Bird indexes were neither too significant, but the values obtained for phosphole oxides 21 were lower than those for the phospholes (20) [10]. The antiaromaticity of 21 was confirmed by the hydrogenation approach [10,46] from which aromaticity parameters between −20% and −30% were obtained (table 3). These values strongly depended on both the R^1 and the R^2 substituents [10]. It was shown, that in case of

R^2 = Me and a large electronegative substituent on the phosphorous atom (R^1 = F and OR), the antiaromaticity of 21 increased significantly [10]. The LUMO energies of a few phosphole oxides (21) with different substituents were discussed earlier [47,48]. The driving force for the dimerisation of 21 is to vanish the antiaromaticity.

The types of computed molecular orbitals (MO) for 20', 21', 26 and 27 are shown in figure 13. The MOs and their energy levels for phosphole oxides (21') show a significant correlation with the same MOs of antiaromatic borole (27); e.g. the shape and symmetry of HOMO–1, HOMO, LUMO and LUMO+1 for 21 is very similar to the corresponding MOs of borole (27). However, the shapes and symmetries of these MOs in phosphole oxides 21' and phospholes 20' differ markedly from each other, reflecting to the different electronic structures and molecular properties. The MOs and the energy levels of phospholes 20' correlate with those of pyrrole 26.

Table 3. Computed $\Delta\Delta H_{H2}$ values (kJ mol^{-1}) and calculated aromaticity/antiaromaticity percentage of 21 (R^2=H) at the B3LYP/6-31G(d) level of theory

Y		R^1 = H			R^1 = Me	
		$\Delta\Delta H_{H2}$	%		$\Delta\Delta H_{H2}$	%
H	a	−17.12	−13.05	h	−33.31	−23.57
Me	b	−16.44	−12.60	i	−38.83	−27.15
Ph	c	−21.84	−16.12	j	−37.65	−26.39
2,4,6-triMe-phenyl	d	−23.54	−17.22	k	−43.64	−30.27
2,4,6-tri^{t}Bu-phenyl[a]	e	−12.90	−10.31	l	−13.15	−10.47
OMe	f	−24.99	−18.16	m	−47.05	−32.49
F	g	−26.54	−19.17	n	−43.13	−29.94

[a] Modelled by a 2,6-di^{t}Bu-4-Me-phenyl group.
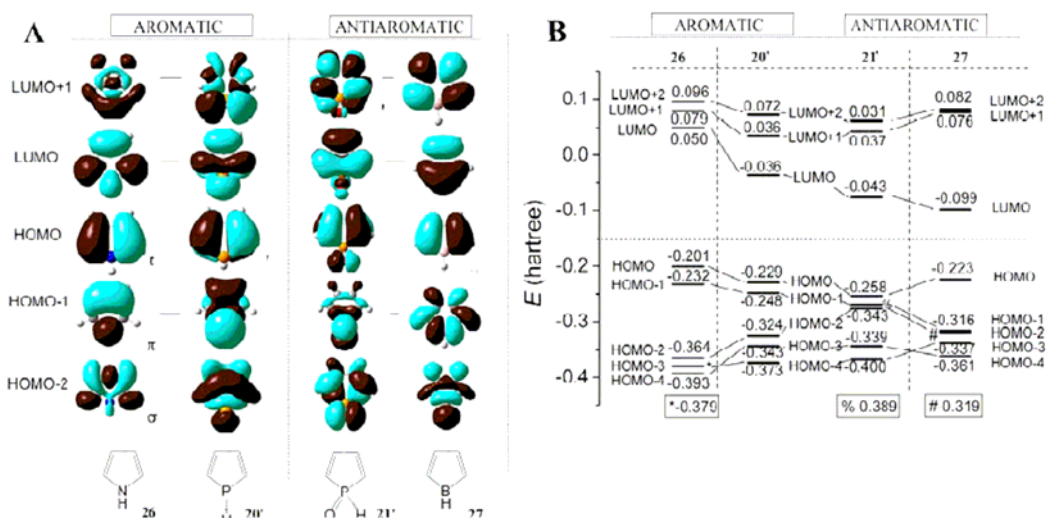
Figure 13. A: Schematic representation of selected molecular orbitals of pyrrole, phosphole (20'), phosphole oxide (21') and borole (σ' → σ-analogue; π' → π- analogue). B: Schematic representation of the MO energy levels for pyrrole, phosphole (20'), phosphole oxide (21') and borole computed at the B3LYP/6-31G(d) level of theory.

2.3. *Thermodynamic and Kinetic Aspects* **of Phosphole Oxides [10]**

In the first step, phosphole 20 is oxidized to afford phosphole oxide 21, followed immediately by a regio- and stereospecific cyclodimerization leading to 22 (figure 14). The dimerization of the unstable intermediate 21 involves a usually low or moderate energy transition state [$\Delta H_{dim}^{\neq}$ = 11.55–47.41 kJ mol^{-1}; $\Delta G_{dim}^{\neq}$ = 76.15–102.94 kJ mol^{-1}] that allows the reaction to take place at a low temperature (0–10 ºC). The large negative entropy-change values can be attributed to the bimolecular reaction, but these values may be lower in solution due to the hindered molecular translation and rotations, as compared to the gas phase situation, lowering the $\Delta G_{dim}^{\neq}$ values as well. The $\Delta H_{dim}^{\neq}$ as well as $\Delta G_{dim}^{\neq}$ values are in a relatively narrow range. Although, the energetics of the reaction explains well the process, one may outline the change in the aromaticity/antiaromaticity along with the reaction profile of the 20 → 21 → 22 transformation (figure 14), where the aromatic character of 20 is switched to antiaromatic on oxidation resulting in 21. The final product should be 22, a non-aromatic species due the four tetrahedral sp^3 C atoms in the frame discontinuing the conjugated electron system. The antiaromatic character of 21 decrease significantly the activation parameters of the dimerization of 21, as compared to the same dimerization reaction of slightly aromatic 20. The difference is *ca* 70 kJ mol^{-1} [at the B3LYP/6-31G(d) level of theory]. The disappearance of the antiaromaticity during the reaction can be considered as the main driving force, but the steric hindrance has a significant impact as well.
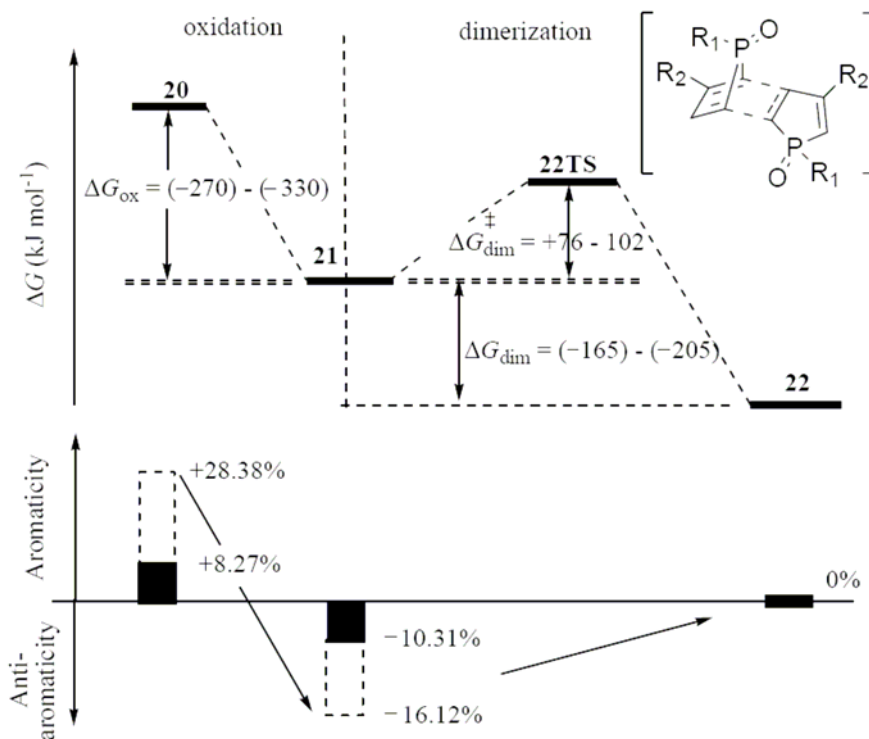
Figure 14. Reaction profile and aromaticity/antiaromaticity profile for the 20 → 21 → 22 transformation. The dashed boxes indicate the range between the minimum and maximum values computed at B3LYP/6-31G(d) level of theory.

References

[1]   De Proft, F.; Geerlings, P. *Chem. Rev.* 2001, 101, 1451–1464.
[2]   Maier, G. *Angew. Chem. Int. Ed.* 1974, 13, 425–490.
[3]   Fattahi, A.; Lis, L.; Tian, Z.; Kass, S. R. *Angew. Chem. Int. Ed.* 2006, 45, 4984–4988.
[4]   Fattahi, A.; Lis, L.; Kass, S. R. *J. Am. Chem. Soc.* 2005, 127, 13065–13069.
[5]   Minkin, V. I.; Glukhotsev, M. N.; Simkin, B. Y. *Aromaticy and Antiaromaticy: Electronic and Structural Aspects*, Wiley: New York, 1994.
[6]   Maier, G. *Angewante Chemie Int. Ed.* 1988, 27, 309–446.
[7]   Quin, L. D. *Rev. Heteroatom Chem.* 1990, 3, 39.
[8]   Keglevich, G.; Tőke, L.; Böcskei, Zs.; Harmat, V. *Heteroatom Chem.* 1997, 8, 527–531.
[9]   Nyulászi, L.; Hollóczki, O.; Lescop, C.; Hissler, M.; Réau, R. *Org. Biomol. Chem.* 2006, 4, 996–998.
[10] Mucsi, Z.; Keglevich, G. *Eur. J. Org. Chem.* 2007, 4765–4771.
[11] Mucsi, Z.; Körtvélyesi, T.; Viskolcz, B.; Csizmadia, I. G.; Novák, T.; Keglevich, G. *Eur. J. Org. Chem.* 2007, 1759–1767.
[12] Mucsi, Z.; Viskolcz, B.; Hermecz, I.; Csizmadia, I. G.; Keglevich, G. *Tetrahedron* 2008, 64, 1868–1878.
[13] Keglevich, G.; Forintos, H.; Körtvélyesi, T. *Cur. Org. Chem.* 2004, 8, 1245–1261.
[14] Keglevich, G.; Körtvélyesi, T.; Forintos, H.; Lovas, S. *J. Chem. Soc., Perkin Trans.* **2**. 2002, 1645–1646.
[15] Keglevich, G.; Forintos, H.; Körtvélyesi, T.; Tőke, L. *J. Chem. Soc., Perkin Trans.* **1**. 2001, 1–3.
[16] Keglevich, G.; Körtvélyesi, T.; Forintos, H.; Vaskó, Á. Gy.; Vladiszlav, I.; Tőke, L. *Tettrahedron* 2002, 58, 3721–3727.
[17] Keglevich, G.; Dudás, E.; Sipos, M.; Lengyel, D.; Ludányi, K. *Synthesis* 2006, 8, 1365–1369.
[18] Mucsi, Z.; Csizmadia, I. G. *Cur. Org. Chem.* 2008, 12, 83–96.
[19] Uchiyama, T.; Fujimoto, T.; Kakehi, A.; Yamamoto, I. *J. Chem. Soc., Perkin Trans.* **1**. 1999, 1577–1580.
[20] Kano, N.; Xing, J. H.; Kawa, S.; Kawashima, T. *Tetrahedron Lett.* 2000, 41, 5237–5241.
[21] Smith, D. J. H. In Barton, D. (Ed.), *Comprehensive Org. Chem.* Vol. 2, Pergamon, Oxford, 1979, Ch. 10.4, 1233–1256.
[22] Vansteenkiste, P.; van Speybroeck, V.; Verniest, G.; De Kimpe, N.; Waroquier, M. *J. Phys. Chem.* 2007, 111, 2797–2803.
[23] Altman, J. A.; Yates, K.; Csizmadia, I. G. *J. Am. Chem. Soc.* 1976, 98, 1450–1454.
[24] Vedejs, E.; Marth, C. F. *In Phosphorus-31 NMR Spectral Properties in Compound Characterization and Structural Analysis*, Quin L. D.; Verkade, J. G. (Eds.), VCH, New York, 1994, Ch. 23, p. 297.
[25] Kano, N.; Kikuchi, A.; Kawashima, T. *Chem. Commun.* 2001, 2096–2097.
[26] Kawashima, T.; Iijima, T.; Kikuchi, A.; Okazaki, R. *Phoshorus, Sulfur, Silicon* 1999, 144–146 and 149–152.
[27] Keglevich, G.; Forintos, H.; Szelke, H.; Tamás, A.; Vaskó, Á. Gy.; Kovács, J.; Körtvélyesi, T.; Kollár, L.; Tőke, L. *Phoshorus, Sulfur, Silicon* 2002, 177, 1681–1684.

[28] Keglevich, G.; Forintos, H.; Ujvári, A.; Imre, T.; Ludányi, K.; Nagy, Z.; Tőke, L. *J. Chem, Res*. 2004, 432–434.

[29] Aitken, R. A.; Hérion, H.; Janosi. A.; Raut, S. V.; Seth, S.; Shannon, I. J.; Smith, F. C. *Tetrahedron Lett*. 1993, 34, 5621–5622.

[30] Aitken, R. A.; Hérion, H.; Janosi. A.; Karodia, N.; Raut, S. V.; Seth, S.; Shannon, I. J.; Smith, F. C. *J. Chem. Soc., Perkin Trans 1* 1994, 2467–2472.

[31] Aitken, R. A.; Horsburgh, C. E. R.; McCreadie, J. G.; Seth, S. *J. Chem. Soc., Perkin Trans* **1** 1994, 1727–1732.

[32] Aitken, R. A.;Cooper, H. R.; Mehrotra, A. P. *J. Chem. Soc., Perkin Trans* **1** 1996, 475–483.

[33] Aitken, R. A.; Atherton, J. I. *J. Chem. Soc., Perkin Trans* **1** 1994, 1281–1284.

[34] Aitken, R. A.; Hérion, H.; Horsburgh, C. E. R.; Karodia, N.; Seth, S. *J. Chem. Soc., Perkin Trans* **1** 1996, 485–489.

[35] Aitken, R. A.; Balkovich, M. E.; Bestmann, H. J.; Clem, O.; Gibson, S.; Gros, A.; Kumar, A.; Röder, T. *Synlett* 1999, 1235–1236.

[36] Aitken, R. A.; Al-Awadi, N. A.; Balkovich, M. E.; Bestmann, H. J.; Clem, O.; Gibson, S.; Gros, A.; Kumar, A.; Röder, T. *Eur. J. Org. Chem.* 2003, 840–847.

[37] Aitken, R. A.; Karodia, N.; Lightfoot, P. *J. Chem. Soc., Perkin Trans* **2** 2000, 333–340.

[38] Kano, N.; Xing, J.H.; Kikuchi, A.; Kawashima, T. *Heteroatom Chem.* 2001, 12, 282–286.

[39] Keglevich, G. In Attanasi, O.A.; Spinelli, D. (Eds.), *Targets in Heterocyclic Systems*, Italian Society of Chemistry, 2002, Vol. 6, p. 245.

[40] Keglevich, G.; Böcskei, Zs.; Keserű, G. M.; Újszászy, K.; Quin, L. D. *J. Am. Chem. Soc.* 1997, 119, 5095–5099.

[41] Quin, L. D.; Keglevich, G.; Ionkin, A.S.; Kalgutkar, R.; Szalontai, G. *J. Org. Chem.* 1996, 61, 7801–7807.

[42] Keglevich, G., Quin, L. D., Böcskei, Zs.; Keserű, G. M., Kalgutkar, R.; Lahti, P. M. *J. Organomet. Chem.* 1997, 532, 109–116.

[43] Quin, L. D. *The Heterocyclic Chemistry of Phosphorus*, Wiley-Interscience, New York, 1981, Ch. 2, p. 79.

[44] Quin, L. D. *Heteroatom Chem.* 1991, 2, 359.

[45] Keserű, G. M.; Keglevich, G. *J. Organomet. Chem.* 1999, 586, 166–170.

[46] Mucsi, Z.; Viskolcz, B.; Csizmadia, I. G. *J. Phys. Chem A*. 2007, 111, 1123–1132.

[47] Hay, C.; Hissler, M.; Fischmeister, C.; Rault-Berthelot, J.; Toupet, L.; Nyulászi, L.; Réau, R. *Chem. Eur. J.* 2001, 7, 4222–4236.

[48] Delaere, D.; Nguyen, M. T.; Vanquickenborne, L. G. *J. Phys. Chem. A* 2003, 107, 838–846.

Chapter 12

A MODERN TOOL TO EVALUATE THE SOLVENT EFFECT ON ORGANIC SYSTEMS

Boaz Galdino de Oliveira[*]

Departamento de Pharmaceutical Sciences,
Federal University of Pernambuco
50740-521, Recife – PE, Brazil

1. Introduction

1.1. Available In Silico Procedures: Continuum and Discrete Methods

The description of the solvent effects through the *in silico* procedures can be realized by using continuum and discrete models. Based on the classic works of Born, Onsager and Kirkwood, the continuum models became an important tool in the study of the solvent effects in several chemical process. In its formalism, the insertion of the solute into a arbitrary cavity modelled by overlap spheres and the description of the solvent as a dielectric unleashed a popular growth of the continuum models. All this methodologic advance provided the development of many other current implementations, such as PCM and COSMO, which have been used successfully in the study of many molecular systems. However, the description of solvent as a dielectric yields some limitations, i.e. the underestimates of specific interactions between solvent and solute, in particular hydrogen bonds.

So, the limitation of the continuum methods into describe efficiently specific interactions can be supplied through the application of discrete methods, such as the Molecular Dynamics (MD) and the Monte Carlo (MC) simulation. These methods treat the solvent molecules explicitly by wrapper at solute molecule, providing then concise details about the liquid structure. As an overview, the MD has its fundament based in the Maxwell-Boltzmann theory, wherein the solvation properties are obtained through the resolution of Newtonian equations related to kinetic of the elements (molecules, atoms or ions) that composes the subject system. On a counterpart, the MC was developed in terms of the Gibbs

---

[*] E-mail address: boazgaldino@gmail.com

thermodynamics postulates and the observables properties are obtained into an isothermal or isobaric ensemble through the statistical analysis according with the algorithm projected by Metropolis and co-workers.

Indeed, MD and MC are able methods to reproduces an important question, that is the excessive number of configurations related to the solvent within the process to soak the solute. This advantage can be counterproductive due the high computational demand used to describe all possible Free of Degrees (FD) of the solvent. For instance, if treats 200 water molecules explicitly, it is obtained 1.800 FD. Although for ethyl ether and 1-octanol, the number of FD are higher, 9.000 and 16.200 respectively. Other important point that can hinder the applicability of the discrete models is the proper necessity of the intermolecular interaction potentials calibrated for the interaction between solute-solvent and solvent-solvent, although it is important to emphasize that these kinds of potentials are very difficult to be determined. Moreover, the description of the solvent around the solute request other special attention concerning to the initial configurations of the solvent, which depends of a previous optimization procedure to get the corresponding structures at the minimum of the potential energy surface. However, a classic alternative to build adequately hydration structures can be obtained simply performing purely *ab initio* calculations. In spite of the considerable computational demand used, for instance, in case of Hartree-Fock calculations with Pople's polarization split valence basis sets, the SCF procedure request previously a good configurational adjust of the water molecules around the solute molecule.

2. AGOA Methodology

Considering the limitations of the continuum methods to describe specific interactions between solvent-solute, as well as the high computational demand of MD and MC formalisms, Hernandes *et al* have developed and presented a new model to describe the solvent effects through the hydration clusters generation. This procedure is called AGOA and its implementation is based on the analysis of the Molecular Electrostatic Potential (MEP) of the solute molecule. To formulate such methodology, it was presumed that the electronic and nuclear distribution of any chemical system generates an electrostatic potential, which can be calculated according to the Coulomb's law as follow:

$$U = \sum_{A=1}^{N_{nuc}} \frac{Z_A}{\vec{r} - \vec{R}_A} \quad + \quad \sum_{i>j}^{N_{ele}} \frac{\psi * \psi}{\vec{r}_{ij}} \tag{1}$$

The first term correspond to the nuclear configurations, ($\vec{R}_A$) and charge (Z_A), whereas the second is related to the $\psi*\psi$ electronic density distribution. Once the MEP 3D-grid has been calculated and solute overlap points have been excluded, the AGOA program performs a search to find the points in the grid corresponding to the largest negative and positive values of the MEP. The neighboring points are used to estimate the MEP gradient, since the water dipole moment can be oriented parallelly or antiparallelly in reference to the largest gradient vector. Thereby, it is defined the positions of the hydrogen atoms of the water molecule, as summarized in flow-chart of the AGOA procedure (see scheme 1).
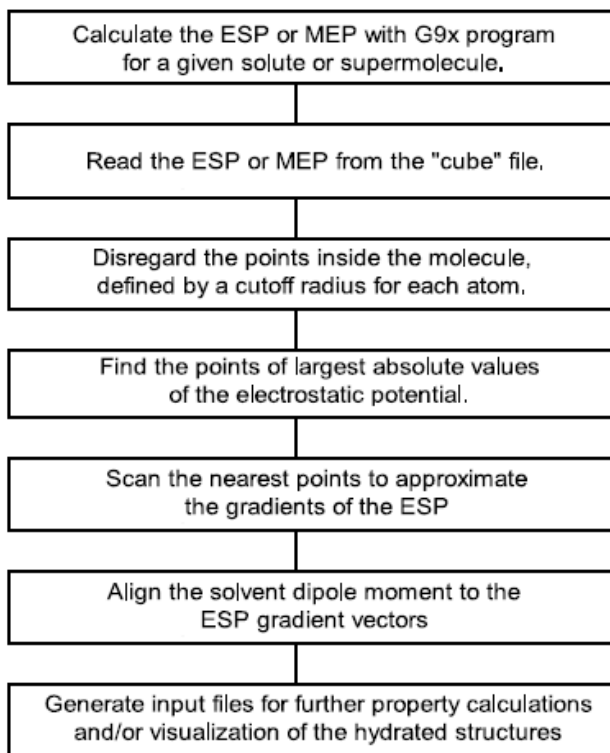
Scheme 1. The algorithm for the AGOA procedure.

In according with the default cutoff radii, AGOA excludes the points of MEP 3D-grid that are inside the volume defined by the solute molecule. Considering that the solvent can be described by distribution of qi punctual charges, the electrostatic interaction energy (E) can be evaluated according to the equation (2):

$$E = \sum U.q_i \tag{2}$$

Thereby, the interaction energy between solvent-solute is high or low in the respective points of maximum or minimum of the potential electrostatic potential. This condition is used to locate the water molecules not in function to the punctual charges, but using its proper $\vec{\mu}$ dipole moment. Thus, according to the equation (3), the hydration energy can be evaluated through the orientation of the water dipole moment with the ∇U electrostatic potential gradient of a three-dimensional (3-D) grid that contains qi points, wherein the dipole moment is parallel or anti-parallel whether the MEP is minimum or maximum, respectively.

$$E_{H_2O} = -\vec{\mu}\,\nabla U \tag{3}$$

In the description of the solvent effects, the AGOA methodology uses the TIP4P (*Transferible Intermolecular Potential 4 Points*) model. This model is formed by four interaction sites centered in the three atoms of the water molecule (oxygen and hydrogen) more one additional center 0.15 Å far from oxygen, as can be seen in the figure 1. Although

there are other models to simulate the solvent effects, such as TIP3P, TIPS and TIP5P, but the TIP4P is widely known due its efficiency into reproduce precisely the position and orientation of the water molecules during the computational simulation process.
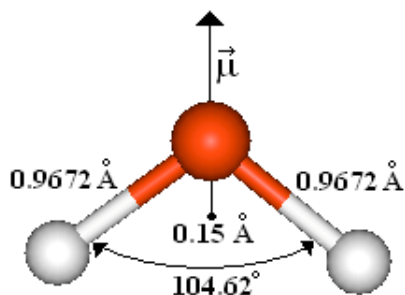
Figure 1. Water molecule TIP4P model.

3. Applications of AGOA Methodology

3.1. Indolic Ring Solvation

The AGOA procedure was validated successfully by applying it in analysis of hydration clusters for *anti* and *syn* conformational isomers of the 1-phenyl-β-carbonile indole derivative, also known as 1-phenyl-β-carboline molecule, see figure 2.
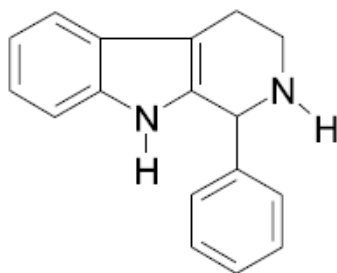
Figure 2. 1-phenyl-1, 2, 3, 4-tetrahydro-carboline or 1-phenyl-β-carboline.

This molecule belongs to a class of compounds with high antimicrobial activity. Moreover, it is well-known their spectroscopic and biological properties are highly dependent upon the hydration process. In this sense, several high level theoretical studies have been performed for this indole-water system, which suggest that the water molecule can interact with the π-electrons of the indole ring. Thus, the MEP 3D-grid for the *anti* conformer of the 1-phenyl-β-carboline is presented in figure 3.
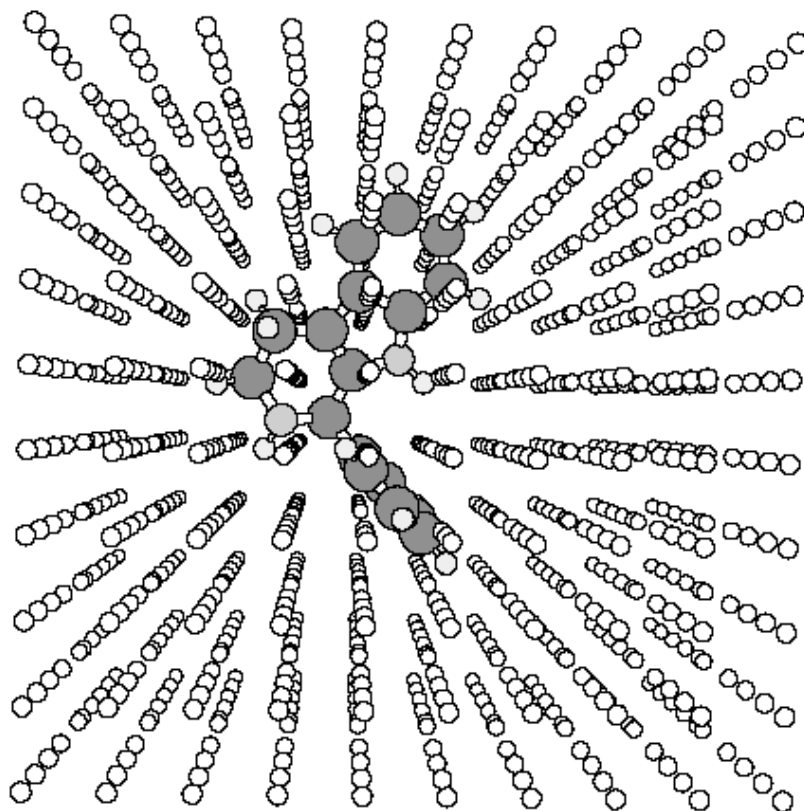
Figure 3. 3D grid of the calculated electrostatic potential for the *anti* conformer.

It is worthwhile noticing that through this MEP procedure, hydration clusters that includes the interaction of the water molecule with the β-electrons of the indolic ring are yielded. This compound presents *syn* and *anti* conformations, which describes the relative position of the phenyl group with respect to the hydrogen atom bonded to the nitrogen atom of the pyperidine. So, the solvent effects on both *syn* and *anti* conformations have been studied by the AGOA procedure, whose hydration clusters are displayed in figure 4 (**1**)-(**2**), whereas the values of the hydration energies calculated from AM1 method are listed are illustrated in figure 5.

This result is very encouraging since previous studies of the indole-water systems required high level *ab initio* calculations to yield such a hydration structures. These hydration structures were also used as the initial guess for a partial geometry optimization of the water molecules (AGOA-OPT) with the AM1 method, which is depicted in Figure 6 (**3**)-(**4**).

As expected, the solute-water interaction energies ΔE^H are larger with the AGOA-OPT procedure, since it allows for inter and intramolecular relaxation of the water molecules. However, this result seems to be an artifice of the AM1 method, which usually yields unrealistic hydration structures and hydration energies. In addition, this AGOAOPT procedure lacks convergence of the interaction energy with respect to the number of water molecules added. It also lacks a consistent *anti*/*syn* energy relationship according to the hydration of each conformer. In contrast, the AGOA procedure yielded convergent results for the solute-water interaction energy ΔE^H as well as a consistent relationship between the

energies of the *anti* and *syn* conformers. As a result, it can be seen that the hydration is important for the relative stabilization of the conformers, and that the *syn* conformer is consistently more stable than the *anti* one. For comparison, the (**3**)-(**4**) hydration structures of these conformers obtained with the AGOA-OPT procedure are illustrated in figure 7. These unrealistic results yielded by the optimization with the AM1 are also a consequence of simulating the solvent effects by a finite cluster, and since in the bulk these solvent molecules would be strongly interacting with the remaining water molecules present in the liquid, it should decrease the solute-solvent interaction energy ΔE^H.
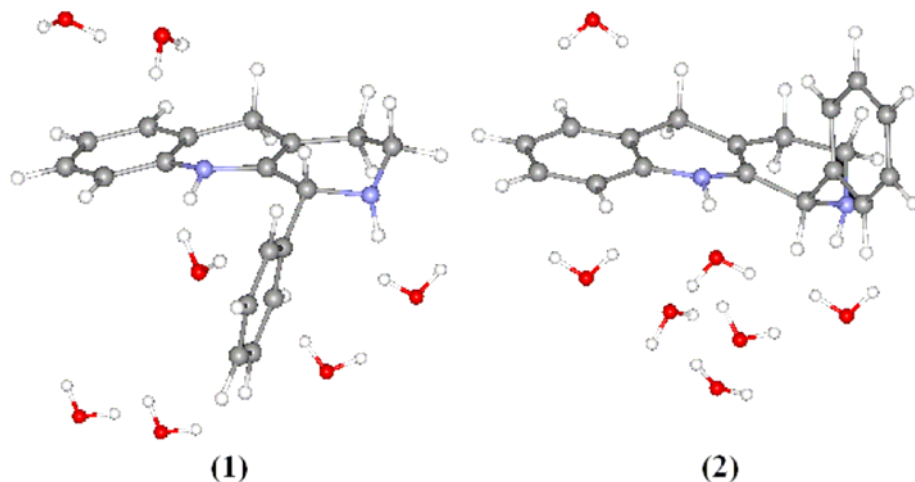
Figure 4. The (1)-(2) hydration structures of the *anti* conformers using the AGOA.
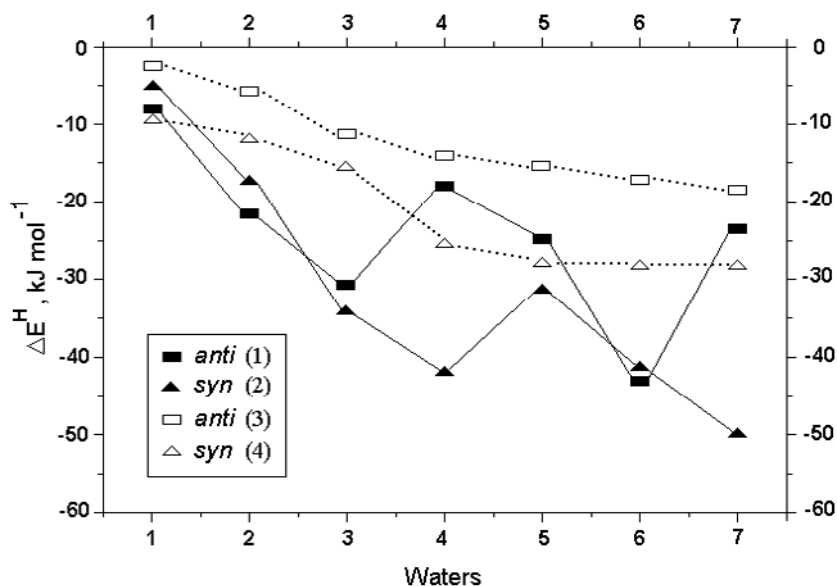
Figure 5. The solute-water hydration energy ΔE^H as a function of the water molecules.
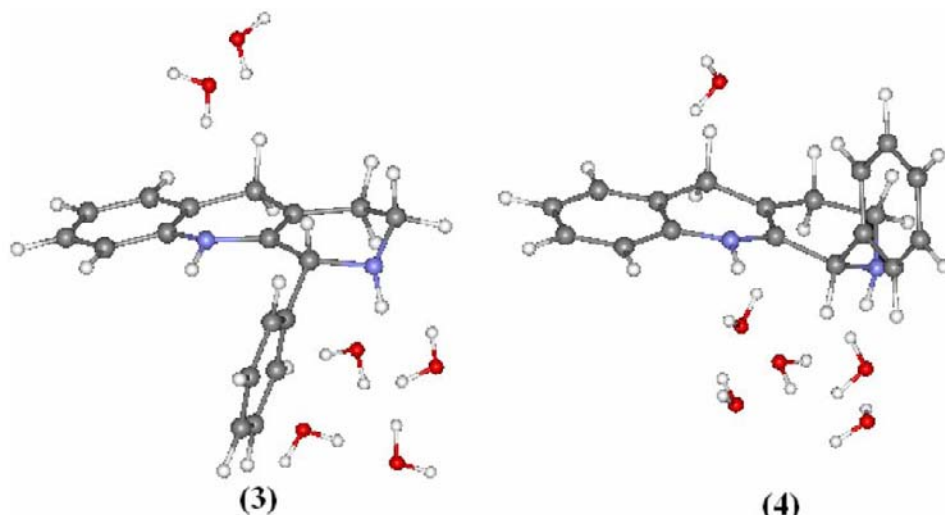
Figure 6. The (3)-(4) hydration structures of the *anti* conformers using the AGOA-OPT.

Consequently, it thus seems very difficult to correctly represent the solute in solution using these optimized cluster models in vacuum. However, the AGOA procedure, without the geometry optimization, provides realistic results, including the interaction with the β-electrons of the indole ring system. The importance of these results is related to the fact that it was necessary to employ high level *ab initio* methods (MP2/DZP) in order to describe these water-indole β-electrons interactions, which are promptly provided by the AGOA procedure using the MEP from the AM1 method.
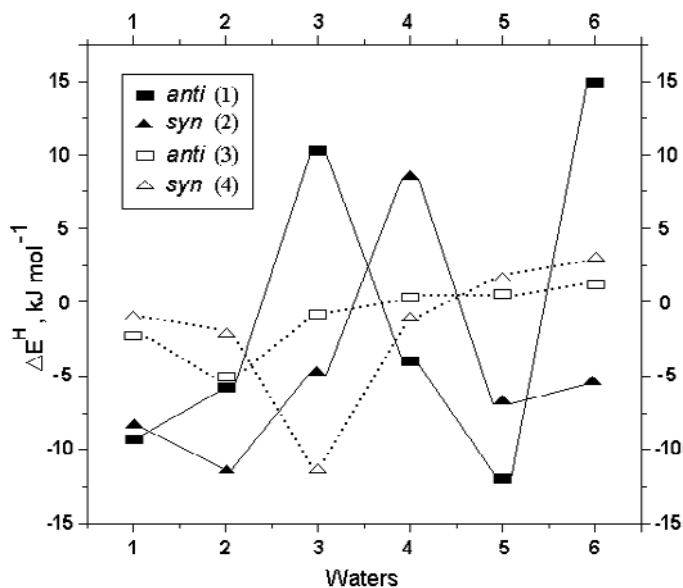
Figure 7. The solute-water hydration energy ΔE^H as a function of the number of water molecules.

3.2. Alkoxydes Solvation

Alcohol and water are considered a system of molecular properties of interest in physics, chemistry and biology. In the midst of several sources known, the solubility of alcohols is a vital parameter to better comprehend the chemical behavior of these molecules. As a brief overview, the solubility of alcohols in water decrease gradually in concordance at growth of the number of alkyl groups in the molecule. Thereby, long alcohol chains are chemically similar to alkanes, so how more extensive the alcohol hydrophobic fragment, minor its aqueous solubility. Although the lone pairs of the oxygen become the alcohols a basic specie, the electronegativity of the oxygen also capacitate itself to accumulate a negative charge, providing an asymmetric distribution of the electronic density which polarize the O—H hydroxyl bond in way such that the hydrogen can acquires a partial positive charge, converting then the alcohols into acid entities. This ambiguous behavior is very important to understand the most varied reaction types, for instance, the well established acid/base equilibrium of the methanol in aqueous medium. In this reaction, the methanol produces an alkoxide ion so-called methoxy (CH_3O^-), as can be seen in scheme (2).

$$CH_3OH \xrightarrow{H_2O} CH_3O^- + H^+ \tag{2}$$
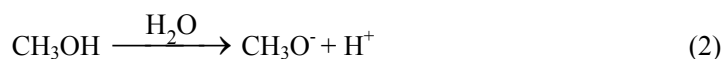
Not only in reference to the methanol, but under this environment other alcohols such as ethanol, iso-propanol and tert-butanol can naturally to form their correspondent alkoxide ions. These anions are considered as bi-functionary substances, in other words, alkoxide ions can act nucleophilically to production of molecular ether, as well as can act as catalytic bases in the fabrication of silicon compounds, reactions wherein the presence of the water solvent is important variable within the success/failure of the process. However, the acidity of aliphatic alcohols determines their stabilities in aqueous solution in order to methanol less stable (pKa = 15.5), passing by ethanol (pKa =15.9) and iso-propanol (pKa = 17.1), until the more stable tert-butanol (pKa = 17.2). In terms of proper acid/base equilibrium, the same behavior is expected to the correspondent conjugate anionic bases, which are featured in figure 8.
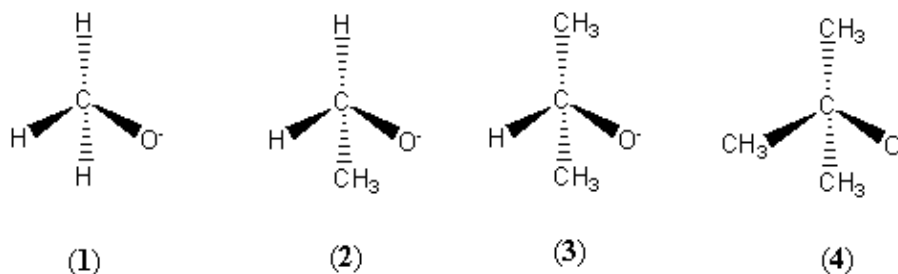
Figure 8. Methoxy (1), ethoxy (2), iso-propoxy (3) and tert-butoxy (4) alkoxide anions.

Although it is well documented several studies of alcohols solvation by applying discrete methods, the proposal to examine the stability of conjugate basis in agreement with the acid/base theory must be worthwhile, once the stability of the alkokides follows the order (1) > (2) > (3) > (4). Such evaluation will be focused in the description of the solvent effects through the energetic quantification of the interactions between the alkoxide:water. For

AGOA, it does not describe the thermodynamic behavior or even similar properties, but generate hydration clusters that characterize specific interactions between solute and solvent at low computational cost without restriction to the any theoretical method. Thus, the 3-D grids for the (1), (2), (3) and (4) alkoxides can be visualized in figure 9.
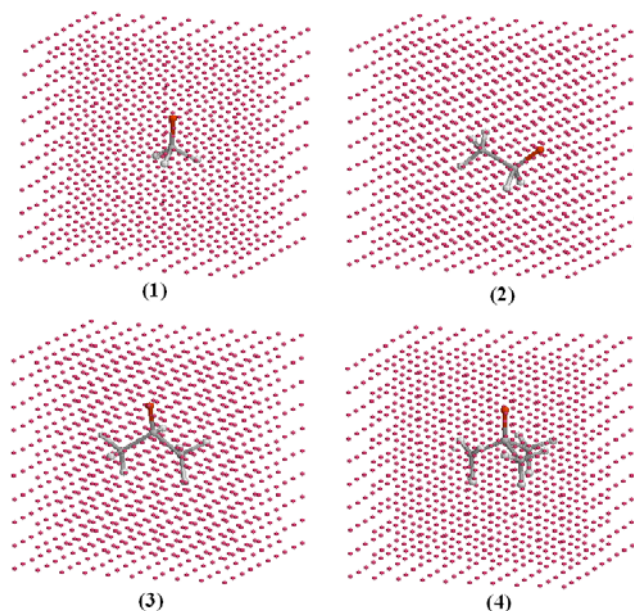
Figure 9. MEP 3D-grid of the (1), (2), (3) and (4) alkoxides.
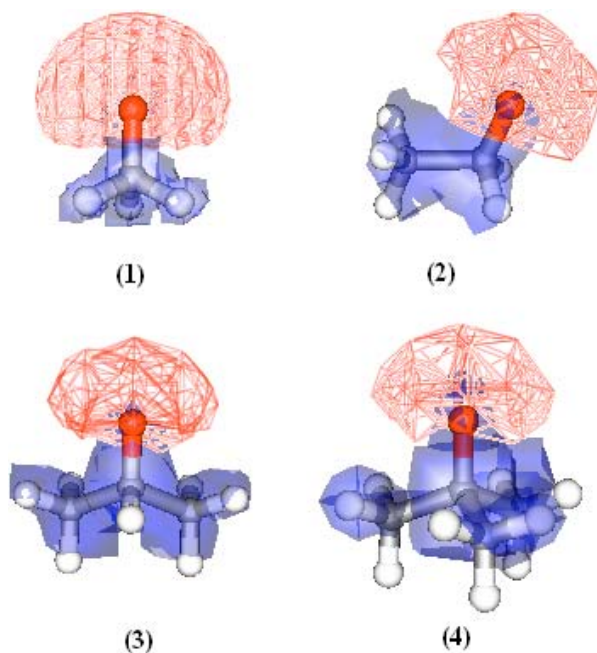
Figure 10. Transparent (+0.25 a.u.) and meshed (-0.25 a.u.) MEP isosurfaces for the (1), (2), (3) and (4) alkoxides.

These grids must contains a minima amount of points that involves the whole solute molecule where their regions of maximums and minimums of electrostatic potential can be adequately represented. In other words, depending on the size and the form of solute, AGOA allows the complete variability of this grid, as much in x, y and z dimensions, number of MEP points or even though in the space among them. The electrostatic potential of the (1), (2), (3) and (4) anionic species can be visualized in the figure 10.

Thus, AGOA selects the adequate number of water molecules for characterization the hydration clusters. For the (1), (2), (3) and (4) alkoxides, the SASA values computed were 163.80 Å, 201.21 Å, 232.0 Å e 256.9Å and the number of water molecules suggested were 10, 12, 14 and 16 respectively, as can be observed in the figure 11. These hydration clusters shows that the hydrogen atoms of the water molecules are aligned in parallel to the gradient of the electrostatic potential, forming then an interaction such as hydrogen bonding, wherein the values for R^H hydration distances were obtained from single-point B3LYP/6-311++G(d,p) calculations. Clearly, the number of water molecules suggested by AGOA to solvate the alkoxides can be undoubtedly the typical representation of the water molecules population in the first solvent shell at MEP of -0.25 a.u.
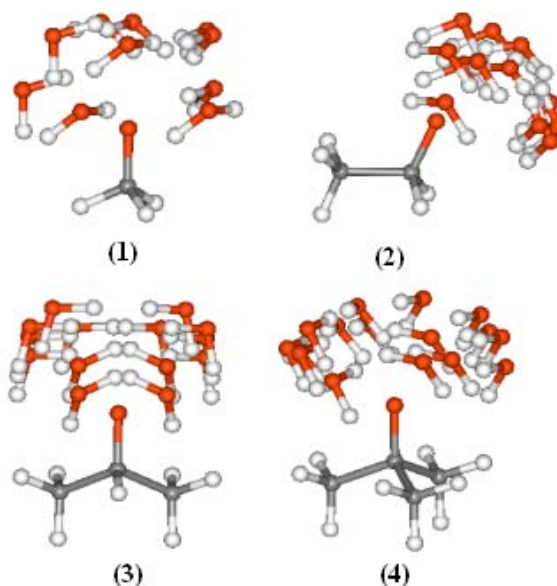
Figure 11. Hydration clusters for the (1), (2), (3) and (4) alkoxides.

In similar way to MD and MC, which provide spatial configurations (rotation and translation) of N elements with values of mechanical observables whose arithmetic media are used to calculate and evaluate subject properties, the medium value of the $\overline{R}^H$ hydration distances can be considered an entail that describes the strength of the solute-solvent interaction, whose values for the (1), (2), (3) and (4) alkoxides are 2.1334 Å, 2.2050 Å, 2.2495 Å and 2.3000 Å, which are graphically illustrated in figure 12. Indeed, these hydration distances indicates a stronger interaction for the methoxy and consequently decrease in order to ethoxy, iso-propoxy and tert-butoxy anions in fully concordance to the acidity values to the correspondent alcohols.
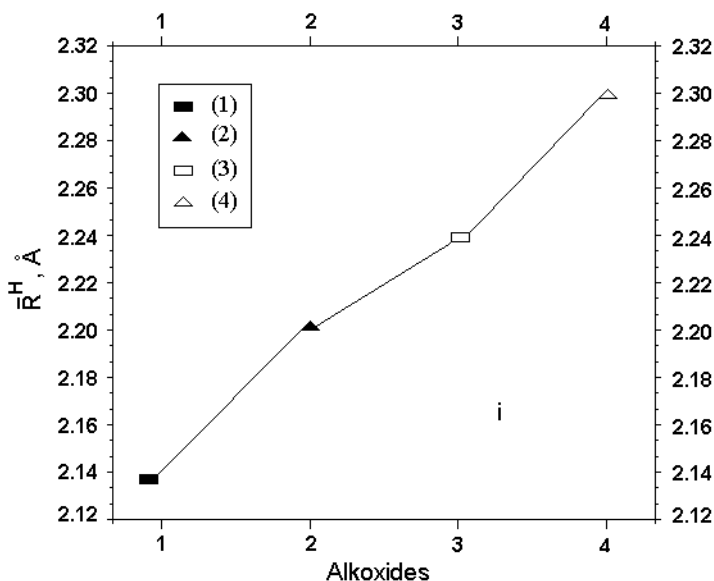
Figure 12. Plot graph of the medium values of the hydration distance for the (1), (2), (3) and (4) alkoxides.

However, the generation of the hydration clusters and their $\overline{R}^H$ values were determined by adjusted standard cutoff radii implemented into the AGOA program, whose values for the H, C, N, O, P, S, F, Cl and Br atoms are 1.3 Å, 2.00 Å, 2.00 Å, 2.00 Å, 2.00 Å, 2.00 Å, 1.80 Å, 1.90 Å and 2.20 Å, respectively. So, MEP points delimited outside by these values are dismissed by AGOA because only the MEP region defined by these cutoff radii is considered physically enough to generate the hydration clusters. However, it is worth notice that the AGOA cutoff radii can be modified according the exigency of the size and shape of hydrated molecule. In electronic terms, the single-point calculations from structures built by AGOA provided the values of the hydration energies ΔE^H. Of course that each ΔE^H value was appraised by BSSE approach and, in corroborating with the medium values for the distances, the medium of the hydration energies $\Delta\overline{E}^H$ also can suggest a panorama about the behavior of the (1), (2), (3) and (4) alkoxides in aqueous phase, as illustrated in figure 13.

In general, we can observe that all $\Delta\overline{E}^H$ values are higher than then van der Waals interaction type (~8 kJ mol^{-1}), as well as highest as typical hydrogen boding energy in biological systems (~35 kJ mol^{-1}). Prominently, the values of the hydration energies provides a systematic stabilization in follows order (1) > (2) > (3) > (4), wherein is evidenced satisfactorily the experimental acidity of the correspondent alcohols in aqueous phase in order to methanol, ethanol, iso-propanol and tert-butanol, respectively. For these alkoxides, however, due the lower pKa value of the correspondent alcohol, the methoxy is the more stable and hence the most solvated ion. Otherwise, the tert-butanol has three alkyl groups (CH$_3$—) within its molecular structure, what leads to a high pKa value and hence at lowest hydration energies for this anion, describing it as the less stabilized conjugate basis.
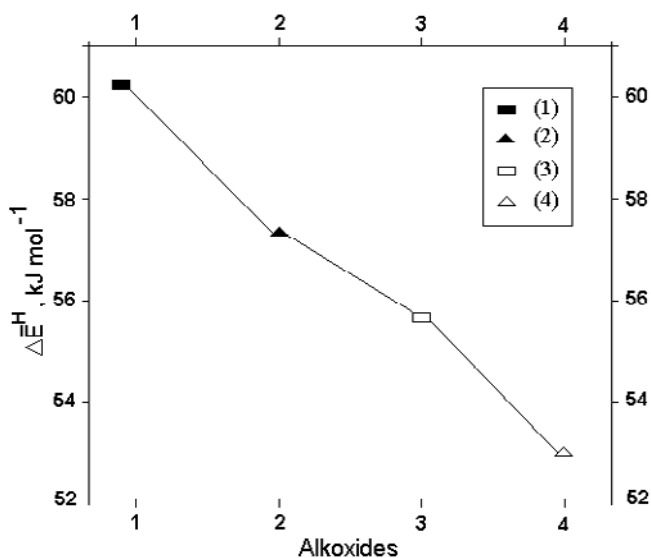
Figure 13. Plot graph of the medium values of the hydration energies $\Delta\overline{E}^{H}$ for the (1), (2), (3) and (4) alkoxides.

On contrary to the traditional discrete methods used to simulate the solvent effect wherein the computational demand is sensibly high, AGOA generate hydration clusters instantaneously, something like few seconds. To idealize the computational economy yielded by AGOA, for study the solvent effects in methanol, ethanol, iso-propanol and tert-butanol by using MC simulation for instance, are necessaries 500.000 random configurations. Obviously, depending from computational display used, this kind of discrete calculations can dispose hours or even days of processing to solely obtains the structures that correspond to the first solvation shell. In fact, this is amazing whether comparer the flexibility of the AGOA methodology, once that its unique mathematic argument concern to the analysis of the solute electrostatic potential which is the primordial physical criterion for determination of the molecular energy stabilization.

3.3. Ammoniums Solvation

The AGOA hydration clusters for the (**1**), (**2**), (**3**), and (**4**) ammonium cations are pictured in figure 14. These water molecules represents the first solvation shell, wherein can be easily seen that the orientation of the oxygen atoms of the water molecules are directly aligned with the ammonium positive MEP or hydrogen atoms.

The 14, 15, 18, and 20 water molecules used to simulate the hydration clusters of these cations are in accordance with the default options of the AGOA methodology. Furthermore, $\Delta\overline{E}^{H}$ medium values of the corrected hydration energies were also calculated and these are illustrated graphically in figure 15.
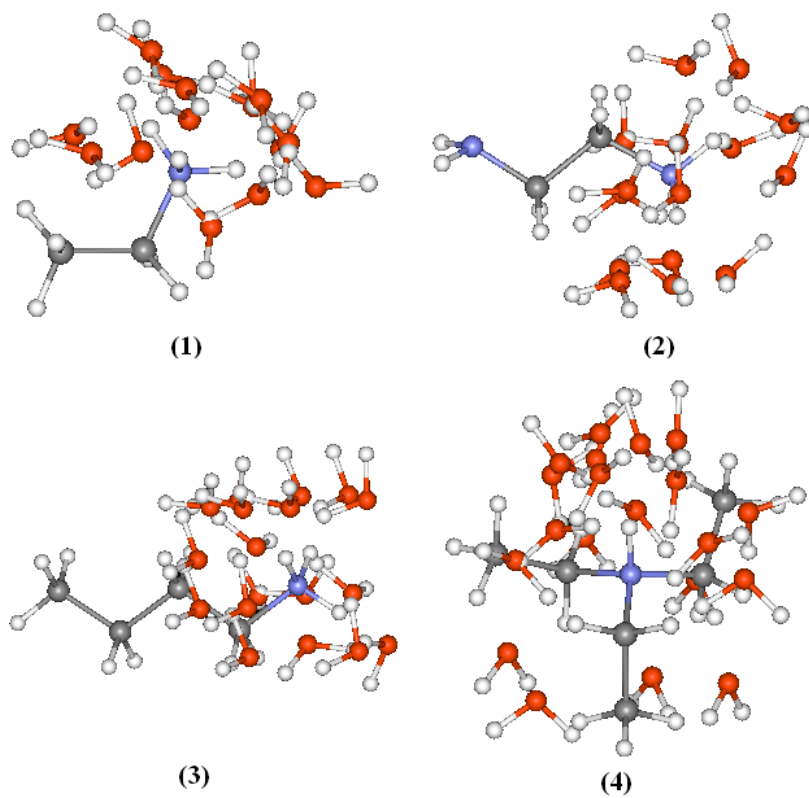
Figure 14. AGOA hydration clusters of the (1), (2), (3), and (4) cations.
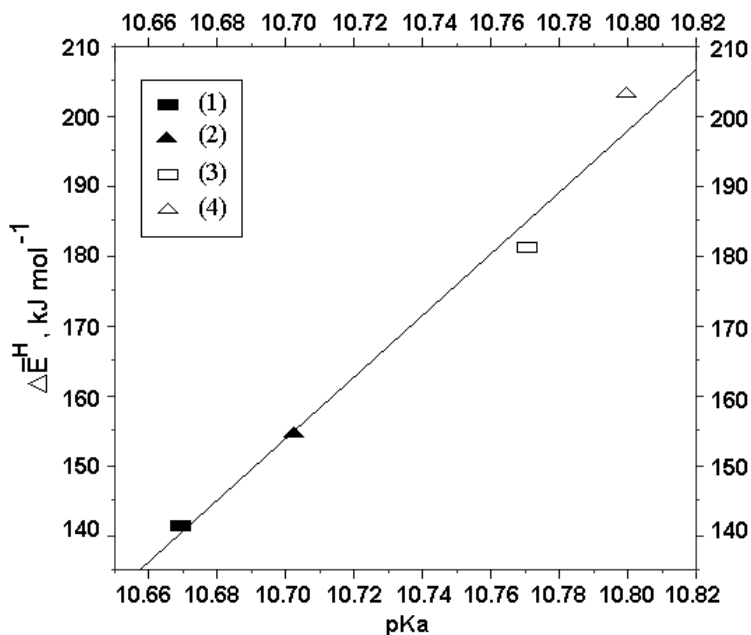
Figure 15. Relationship between the $\Delta\overline{E}^H$ medium hydration energies and the correspondent pKa values of the (1), (2), (3), and (4) cations using the AGOA procedure.

The $\Delta\overline{E}^H$ values of 141.73 kJ mol^{-1}, 153.7 kJ mol^{-1}, 178.70 kJ mol^{-1} and 202 kJ mol^{-1} suggest systematic stabilization of the ammoniums as follows (**1**) < (**2**) < (**3**) < (**4**). It is quite similar to alkoxides, by which these hydration energies are also higher than van der Waals interactions (8 kJ mol^{-1}), as well as being compatible with biological hydrogen binding energies (35 kJ mol^{-1}). Moreover, it can also be observed that there is a direct relationship between the $\Delta\overline{E}^H$ results and the pKa values of 10.67, 10.70, 10.77 and 10.80 of the respective (**1**), (**2**), (**3**), and (**4**) cations. Although our recent studies have revealed that the acid/base equilibrium of alkoxides is accurately evaluated using the AGOA methodology, the results presented above are precisely the reverse, if the volumes of protonated amines alone are taken into consideration. Owing to the lower pKa value for ethylaminium, this cation should be the most solvated species, but its hydration energy of 141.73 kJ mol^{-1} is the lowest. On the other hand, the tri-ethylaminium has three alkyl groups in its structure, which leads to a high pKa value and, consequently, low values of hydration energies for this cation would be expected. Unfortunately, the AGOA result indicates that tri-ethylaminium has the highest hydration energy (202 kJ mol^{-1}). In this context, then, the AGOA methodology does not satisfactorily describe the solvation effect of the (**1**), (**2**), (**3**) and (**4**) ammoniums. As a result the AGOA-OPT procedure does in fact need to be carried out.
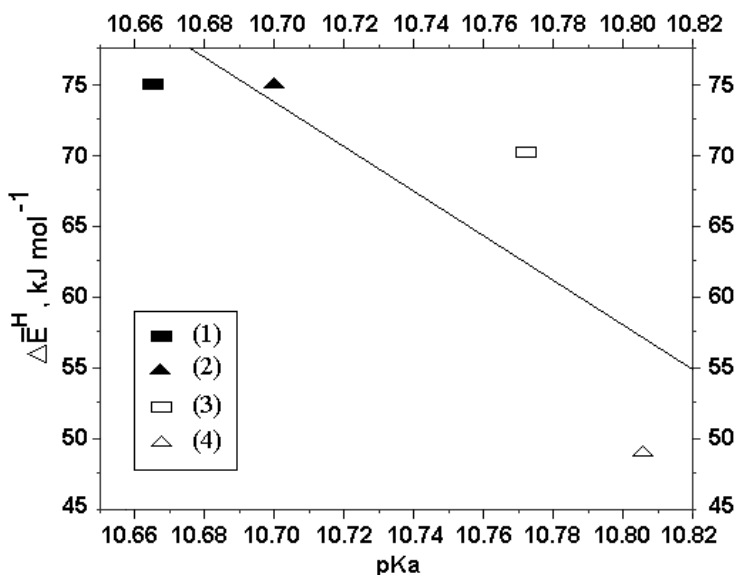
Figure 16. Relationship between the medium hydration energies $\Delta\overline{E}^H$ and the correspondent pKa values of the (1), (2), (3), and (4) cations using the AGOA-OPT procedure.

AGOA-OPT consist of a re-optimization of the geometry for each dimer (solute-solvent) obtained using the AGOA calculations. It is expected that, by taking into account the quantum method used to carried out the AGOA-OPT procedure, the results obtained would present a realistic range for the (**1**), (**2**), (**3**), and (**4**) systems. Different from the AGOA methodology, the hydration energies obtained from AGOA-OPT are now in accordance with the experimental acidity of the cations (**1**) (75.12 kJ mol^{-1}) and (**4**) (47.40 kJ mol^{-1}), as can be seen in figure 16. In fact, the most (**4**) and the least (**1**) voluminous cations present the lowest and highest hydration energies, respectively. However, as the acid-base equilibrium in an

aqueous media depends on the intrinsic and solvent effects, the observed experimental values are the result of a combination of both effects. Then, as cation (**4**) is less solvated than (**1**), the effect of the solvent is not strong enough to overcome the intrinsic effect.

References

Tomasi, J.; Mennuci, B.; Roberto, C. *Chem. Rev.* 2005, 105, 2999-3094.

Allen, M.P.; Tildesley, D.J. *Computer Simulation of Liquids*, Clarendon Press, Oxford, 1987.

Hernandes, M.Z.; da Silva, J.B.P.; Longo, R.L. *J. Braz. Chem. Soc.* 2002, 13, 36-42.

Oliveira, B.G.; Araújo, R.C.M.U.; Carvalho, A.B.; Ramos, M.N.; Hernandes, M.Z.; Cavalcante, K.R. *J. Mol. Struct. (THEOCHEM)* 2006, 802, 91-97.

Oliveira, B.G.; Vasconcellos, M.L.A.A. *J. Theo. Comp. Chem.* 2007, 6, 399-412.

Oliveira, B.G.; Vasconcellos, M.L.A.A.; Leite, L.F.C.C.; *J. Mol. Struct. (THEOCHEM)* 2008, 860, 13-17.

Costa, P.R.R.; Ferreira, V.F.; Esteves, P.M.; Vasconcellos, M.L.A.A. *Ácidos e Bases em Química Orgânica*; Bookman, Porto Alegre, Brazil, 2005.

Brauman, J.I.; Blair, L.K. *J. Am. Chem. Soc.* 1968, 90, 6561-6562.

Hernandes, M.Z.; Longo, R.L. *J. Mol. Model.* 2006, 11, 61-68.

Chapter 13

A MORPHOLOGICAL APPROACH TO THE OFFSET CURVE PROBLEM

Antomio Jimenno

Department of Computer Technology and Computation,
Alicante Univ., Alicante, Spain

Abstract

Offsets are one of the most important problems in Computational Geometry. They can be used in many fields, such as geometric modelling, CAD/CAM and robot navigation. Although some efficient algorithms have been developed to solve this problem, their lack of generality makes them efficient in only a limited number of cases.

Our aim is to propose a model that applies methods and concepts used in mathematical morphology paradigms to solve the problem of general offset curves.

Presented in the work there is a method for offsetting any kind of curve at any distance, constant or not. As a consequence, we will obtain a geometrical abstraction which will provide solutions to typically complex problems.

The resulting method avoids any constraint in curve shape or distance to the offset and obtains valid and optimal trajectories, with a low temporal cost of O(n•m), which is corroborated by the experiments. It also avoids some precision errors that are present in the most popular commercial CAD/CAM libraries.

The use of morphology as the base of the formulation avoids self intersections and discontinuities and allows the system to obtain general offsets to free-form shapes without constraints. Most numerical and geometrical problems are also avoided. Obtaining a practical algorithm from the theoretical formulation is straightforward, as it will be shown with the application of the method to an algorithm to obtain tool paths for contour-parallel pocketing. The resulting procedure is simple and efficient.

The work has been divided into next parts:

Introduction provides the reader with background information on existing offset methods and their associated problems in offset computation. The new concept of general offset is also introduced.

Second section develops the morphological system resulting from applying the conventional morphological model to *which the feature of primitives ordering has been added. The new model, called DTM model,* owns features for order establishment of morphologic primitives. The use of morphology as the base of the formulation allows the system to obtain general offsets to free-form shapes without constraints. A computational

model which enables the morphological operations defined in the DTM to be carried out is also developed. Its existence makes the new model (DTM) operative and permits its efficiency to be checked through testing.

Morphologic primitives are translated into *offset computation* and are applied to real machining tests in order to probe the correct behaviour of the model. The proposed model has been successfully implemented in a commercial CAD/CAM system specialised in shoe last making. Finally, some illustrative examples are shown.

Conclusion and discussion part summarizes this investigation and offers recommendations for future work.

1. Introduction

Offsets, also called general parallels, are one of the most important problems in Computational Geometry. They can be used in many fields, such as geometric modelling, CAD/CAM and robot navigation. For instance, offsetting is essential for tool path generation in NC machining, for defining tolerance regions in several disciplines such as robotics or for constructing skeletons or medial axes of geometric models.

Offset curves are defined as the locus of the points which are at a constant distance d along the normal from the generator or target curve [Maekawa, 1999]. In a more formal way, let $C(t)=(C_x(t),C_y(t))$ be a curve defined in a space *R* for parameter *t*, and a representation space R^2, designed on a plane (e.g. XY plane). Its offset $C_d(t)$ with constant distance *d* is defined as [Elber, 1997; Li, 1998]:

$$C_d(t) = C(t) + d \cdot N(t) \qquad \text{(Exp. 1.1)}$$

where $N(t)$ is the unit normal vector of $C(t)$, defined as follows:

$$N(t) = \frac{(C_y'(t), -C_x'(t))}{\sqrt{C_x'(t)^2 + C_y'(t)^2}} \qquad \text{(Exp. 1.2)}$$

If $C(t)$ is a parametric curve its condition of regularity guarantees that the derivative $C'(t)=(C_x'(t),C_y'(t))\neq(0,0)$, so $N(t)$ is well defined to any curve $C(t)$ that fulfils this condition. Specifically, Bézier and BSpline curves (which are the most common curves in CAD) easily fulfil this condition, so the offset curve can be obtained in this case, because every Bézier or BSpline curve is regular if there is no point whose derivative is 0. If the derivative is 0, the curve can be divided at this point following any known method [Farin, 1993].

This formulation is mathematically elegant but it has some drawbacks. The most important one is the fact that the root in the denominator of expression 1.2 makes the offset of curve $C(t)$ not polynomial or rational in general, even when $C(t)$ is. There exist some special curves whose offsets are rational. These special cases include straight lines and circles, as well as a class of curves called Pythagorean hodographs [Farouki, 1990]. However, offsets to BSpline curves, the standard in most CAD systems, are not rational in general. For this reason, nowadays approximation methods are the practical solution to curve offsetting in most cases.

Some methods for approximating the offset have been proposed and they can be divided into two large sets: algorithms based on discretization, and analytic algorithms. The first set

algorithms present problems with precision and, sometimes, with efficiency. The analytic algorithms are less versatile, because they cannot solve every case and they can be invalid.

Offset curves may self-intersect locally (when the offset distance is greater than the minimum radius of curvature in the concave regions) or globally (when the distance between two points on the curve reaches a local minimum). They can also have discontinuities in convex regions. So, an essential task for any approximation is to avoid the discontinuities and detect all self-intersections and trim the offset curve in a correct way (figure 1.1).
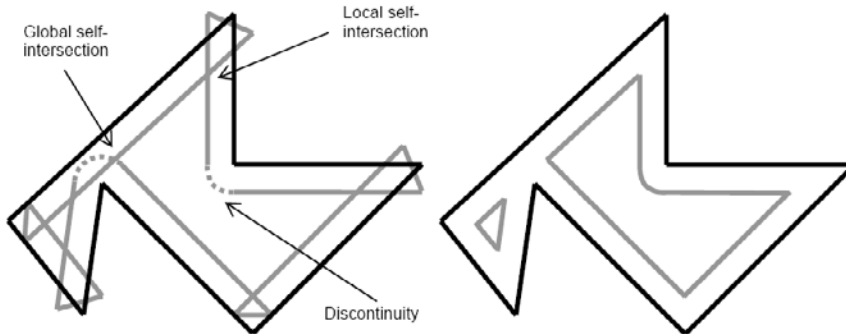
Figure 1.1. Raw offset of a curve, with local and global self-intersections and discontinuities (left), and offset after trimming self-intersections and avoiding the discontinuities (right).

Most offset approximation methods use a divide and conquer approach that exploits the subdivision property of the target curve. They fix a tolerance and iteratively fit an approximation curve, measuring the accuracy, and subdividing the problem into smaller problems if the approximation error is larger than the tolerance. In [Elber, 1997] an interesting comparison of some of these offsetting methods can be found: control polygon-based methods, interpolation methods and circle approximation methods. Qualitative and quantitative comparisons of several techniques are done, using the number of control points generated as a measure of the efficiency of the offset approximation, always within a prescribed tolerance. In general, the least squares based methods perform very well. However, for simple curves (quadratic curves, for instance) the simplest methods are the best. Anyway, none of these techniques avoid the problem of local and global self-intersections.

Other authors prefer series approximation based methods. In [Li, 1998], Legendre series are used to approximate the offset curve thanks to their good convergence properties. The main drawbacks of this approach are that discontinuities must be considered as a special case, and that self-intersections are produced. From the point of view of computation, the transformation of the Legendre offset to a useful BSpline is the bottleneck of the method.

Pair-wise offset approach consists of generating an offset segment for each element of the target curve. As a result, a raw offset-curve is constructed by closing the gaps with trimming arcs. Finally all pair-wise self-intersections and invalid loops are detected and removed. In [Choi, 1999] an algorithm is presented for offsetting a closed curve having no islands. In this case, all local invalid loops are removed before constructing the raw offset curve by invoking a pair-wise interference-detection test. The resulting raw offset curve contains only global invalid loops, and it is subjected to a sweep-line algorithm to find all self-intersections. Finally, global invalid loops are removed by invoking the pair-wise interference-detection test again.

Some other techniques use distance maps. In [Elber 2003], a distance map is derived analytically so that the local and global self-intersections in offsets of freeform curves are detected and eliminated. Nevertheless, small loops might still exist and a further process may be used to detect and eliminate them.

All the methods that may produce self-intersections need a postprocess to eliminate the loops. The self-intersection problem can be handled through two main approaches to detect the local and global intersections: line-segments intersections and sweep-line [EL-Midany, 2002]. The intersection detection and the loop removal steps are, unfortunately, time consuming and prone to numerical errors.

Another important approach is using Voronoi diagrams of the boundary [O'Rourke, 1993; Lambregts, 1996; Held, 1998; Jeong, 1999]. The techniques based on the Voronoi diagram use this diagram to construct a distance map and to obtain some topological information of the curve to trim the offset, so that self-intersections are avoided. These kinds of methods are robust but, as drawbacks, they are mainly suitable for a limited range of curve shapes and they can have numerical errors and a high computational cost.

As a result of all the aforementioned methods, the main problems involved in offset techniques are: self-intersections, discontinuities, lack of generality, inadequate precision, numerical errors and low efficiency. Besides, the offset is only defined for constant distance (expression 1.1), so there are some problems that are unapproachable. For instance, in tool path generation for NC machining, these offsets are useful only for one radius tools (i.e. spherical, cylindrical and conical) and are not valid for more complex tools (toroidal, rectangular, "free-form" tools). A new concept, general offset curves, is needed.

Similarly as offset curves, general offset curves can be defined as the locus of the points which are at a distance given by any function along the normal from the generator curve. Given a parametric curve $C(t)$ and any function $D(t)$, the general offset is defined as:

$$C_D(t) = C(t) + D(t) \cdot N(t) \qquad \text{(Exp. 1.3)}$$

$D(t)$ can be viewed as a distance function that provides the distance from the curve to the offset at a given parameter value t. If $D(t)$ is a constant function, the result is the classical definition of an offset curve.

General offset curves, are not rational in a general case, for the same reasons as the classical offset curves. Moreover, the new term introduced to evaluate de distance, makes their calculation even more difficult.

General offset are intimately related with envelopes. For instance, simplification envelopes, introduced by [Cohen 96], are a generalization of offset surfaces. They are used, in this case, to generate minimal approximations of polygonal objects. The use of general offsets (or simplification envelopes, as they are called in [Cohen 96]), generates approximations that are guaranteed not to deviate from the original representation by more than a user-specifiable amount while preserving global topology.

Another related concept are roulettes [Eells 1992]. For example, a Sturm´s roulette is the locus of the centre of a conic section as the section rolls on a line. A Delaunay's roulette it the locus of the focus of a conic section as the section rolls on a line. This two roulettes can be formulated as two general offsets where function $D(t)$ is defined, respectively, as the distance from the centre or from the focus of the conic section to its boundary.
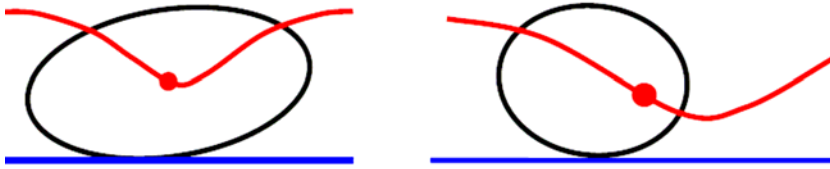
Figure 1.2. Example of Sturm's roulette (left) and Delaunay's roulette (right) of an ellipse.

From a practical point of view, the uses are several. For instance, in robot navigation, an important strategy is wall following. In this case, a security region parallel to the walls must be established. Nevertheless, the security distance can be variable depending on several factors: for instance, in narrow corridors, the distance can be smaller. The distance can also be adapted to optimize the robot path, for minimizing the centrifugal and centripetal forces, as well as the inertia or the speed of the robot [Ciccimaro, 1998]. Another possibility is increasing the distance offset as the robot speed increases, to avoid wall crashes due to odometry errors and object avoidance. From a different point of view, robots, in general, have not a circular shape. Therefore, to maintain a security area, the robot trajectory can be traced at a different distance to the walls for different orientations (figure 1.3).
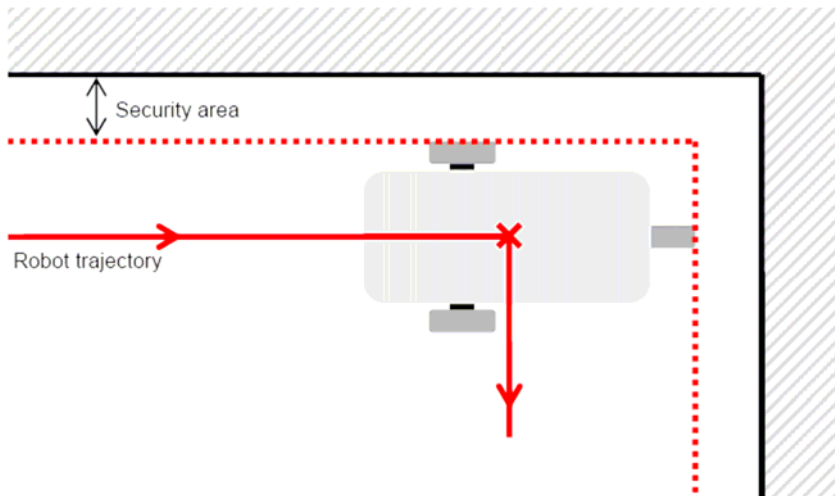
Figure 1.3. The distance from robot trajectory to walls depends on the orientation.

In shoe or textile pattern design, the calculation of offsets is very useful. The hem or margin of a shoe or a garment pattern is in fact an offset. Nevertheless, this margin is usually dependent on the curvature and other factors. General offsets can be used to model the hems, using D(t) to obtaine wider or narrower margins.

Another important field of use for offset curves is machining pieces using an NC machine. The main problem is the so called *tool compensation*, that is, calculating the path that the tool must follow to machine a given curve. The compensated trajectory is an offset curve. However, the classical definition of offset curve is only valid for one radius tools, since the distance to the target curve is always constant. The introduction of a general offset definition would allow the use of rectangular, elliptical or any geometry tools. For instance,

some moulds are machined by means of torical tools with the rotating axe parallel to the surface; in this special case two radii are implied in the machining process (figure 1.4).
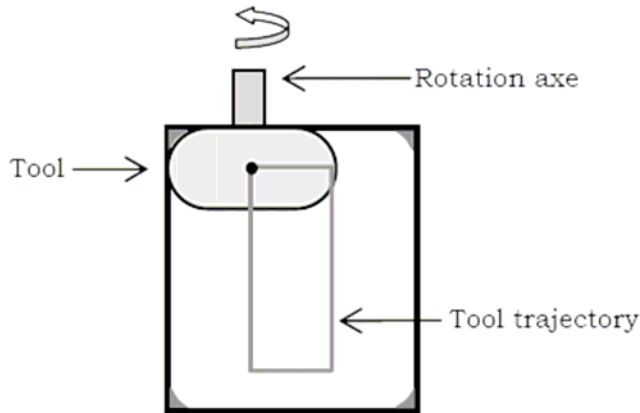
Figure 1.4. Experiment in two dimensions. Shaded regions will not be machined. On the left, a morphological erosion for a toroidal tool (two radii implied). On the right, the classical offset for a spherical tool.

Motivated initially by the manufacturing machining process, a Deterministic Topological Model was presented in [Jimeno, 2004]. Based on this model, presented in this paper, there is a new algorithm for general offsetting that avoids or solves the problems mentioned above. Due to the fact that it is defined morphologically (an object, the structuring element, defines another object, the offset), operators avoid the problem of self-intersections by its own definition. It is a versatile and general process, useful for every curve shape and structuring element and highly efficient and precise. Once the offset calculation is presented, an application a machining problem is shown.

2. Determinist Topological Model

In order to model the manufacturing machining process it is necessary to provide a conceptual framework which will permit definition of the parts as tools, and which will be equipped with operations that carry out the cutting process using the tool when it moves on a substratum base, following a specific trajectory.

The model presented in this section uses the definitions and operations established in the paradigm of Mathematical Morphology [Matheron, 1975] as it demonstrates properties which can be assimilated in the machining process. In particular, it permits the specification of parts and tools using set of points and it also has operations which describe geometric cutting processes and reconstruction such as erosion and dilation respectively.

The idea is for objects to be described as surfaces and for sweeping criteria to be proposed, as this is the intuitive conceptual model of machining and using this proposal, both parts and tools will be modelled.

The morphological operation is not subject to temporal constrictions as its primitives act on sets and as a result, produce new sets without a path order being established on their elements. These orders are necessary when the operation is transferred to physical processes such as

machining, due to the fact that the sequencing permits a definition of the trajectory. For this reason a refinement is established which will permit an order to be associated with each morphological primitive. The sequencing of the primitives will add a determinist component to the model which will be used to describe the performance of the tools in motion.

The Determinist Topological Model (DTM) arose as a consequence of the adaptation of the morphological paradigm to the description of machining processes. However, its use is not restricted to this field. In fact, the aim of this work is using it to describe a solution of the offset curve problem.

2.1. General Structure

The DTM morphological system is based on the model proposed by mathematical morphology, specifying morphological operations inherited from it, which are conditioned by determinist impositions of optimising trajectories. This system may be defined by the following

$$MTD = \langle MM, OP_{TP} \rangle \qquad \text{(Exp. 2.1)}$$

in which:

Table 2.1. Description of components of the Determinist Topological Model

MM	Represents the framework of conventional mathematical morphology. It defines objects and operations which transform them.
OP_{TP}	Represents a specialisation of a subset of morphological operations with which a trajectory path is associated

Figure 2.1 shows the main elements of the proposed model.
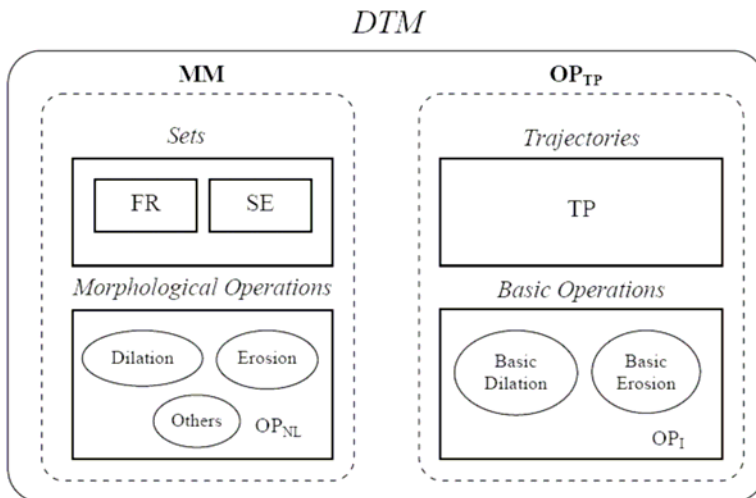
Figure 2.1. Main components of the Determinist Topological Model.

2.2. Morphological Framework

In similar manner to mathematical morphology a complete reticule is defined which will be formed by the subsets of *E*, that is, the parts of *E (P(E))*, with the partial order relation $\subseteq$, with *E* being the Euclidean n-dimensional space, $E \equiv R^n$, the same as that used for representing images in the continuous domain, although, in this case homomorphism *(E,{0,1}^{n})* is considered for binary images or *(E,N^n)* for grey level images.

The morphological framework of the Determinist Topological Model is modelled with the expression (2.2).

$$MM = \langle SE, FR, OP_{NL} \rangle$$
(Exp. 2.2)

in which:

Table 2.2. Description of the Morphological Framework components

SE	Represents the family of structuring elements by means of which the morphological operations are carried out.
FR	Represents the set of frontier objects on which a morphological operation will be carried out.
OP$_{NL}$	A set of morphological operations which modify the set of frontier objects using structuring elements.

The previous definitions are taken from the paradigm of classic mathematical morphology[1] Nevertheless in the DTM some clarifications need to be made in respect of the nature of the sets which make up the topological model.

The elements to be considered in *E* will simply be geometric points $p \in R^n$, of coordinates *(p$_1$, p$_2$,..., p$_n$)*. The *P(E)* sets may in this way have a non determinist nature, considering them simply as a collection of points, or either determinist, when they may be obtained based on a parameterised geometric function of the type expressed in (2.3).

$$
\begin{aligned}
&f_i{:}R \rightarrow R \\
&f(R^n) : R^n \rightarrow R^n \\
&f(r_1, r_2, ..., r_n) = (f_1(r_1), f_2(r_2), ..., f_n(r_n))
\end{aligned}
$$
(Exp. 2.3)

The definition which appears in the equation (2.4) is taken directly from the morphological paradigm and determines a set of points based on a centre *x*.

$$B_x = \{b + x : b \in B\}$$
(Exp. 2.4)

The model defined will be used with two types of sets, addressing their topological function.

---

[1] Convention definitions of mathematical morphology may be found in [Serra, 1982].

On one hand the structuring set type will be established as that which makes up the topology of an object.

The family of structuring elements *SE* is determined by those objects which have as their centre the origin of coordinates of Euclidean space, that is:

$$SE = \{B_x : x = o\} \qquad \text{(Exp. 2.5)}$$

Furthermore, the family of frontier objects *FR* will be considered. These objects are those on which morphological operations are carried out.

An object *X* of centre *c* will also comprise a set of points defined as:

$$X_c = \{o + c : o \in X\} \qquad \text{(Exp. 2.6)}$$

In this model structuring objects and elements shall be considered closed and compact, that is, they shall not be considered to have possible gaps or islands. As a result of this restriction, the topological information of these objects is found within their boundaries. From here on frontier (or boundary) which characterises the object shall be considered instead of the whole which, according to this model, will not entail any loss of generality.

The function *Fr* is defined, which relates a set with its frontier, so that all the points of the object which belong to its boundary are obtained (in [Nikopoulos, 1997] the use is already established of the surfaces for representing sets of points for mathematical morphology).

$$Fr(X) : X \to Y / Y \subseteq X \qquad \text{(Exp. 2.7)}$$

In the Determinist Topological Model the frontier functions will establish a relation on the elements of the set considered. For example, the two dimensional boundary of a figure may be represented through the function of the curve which constitutes its boundary, with its domain being that expressed in (2.7).

In this way the family of frontier FR sets of the Euclidean space is defined as the set of all the frontiers of the sets belonging to that space.

$$FR = \{Fr(X), X \in P(R^n)\} \qquad \text{(Exp. 2.8)}$$

The function which enables points to be recovered from a set from which their boundary has been extracted shall be termed *In(C)* and shall be formed by the set of all points situated inside the boundary:

$$In(C) = \{p \in X, C = Fr(X)\} \qquad \text{(Exp. 2.9)}$$

The family of operations which act on the sets is very extensive within the mathematical morphology. In the DTM all of these have been grouped under the name of non linear operations (OP_{NL}). This paper places special emphasis on two of these: erosion and dilation.

2.3. Operations with Trajectory

An extension of some common morphological operations shall be defined, such as erosion and dilation, to which the order of obtaining points for the final set will be added. Specifically, the two operations mentioned constitute the basis of the remainder of the filtering operations in the mathematics morphology, thus the extension of its definition shall cover all the morphological operations in the Determinist Topological Model.

In the DTM the set of operations with trajectory are defined according to the expression (2.10).

$$OP_{TP} = \langle TP, OP_I \rangle \qquad \text{(Exp. 2.10)}$$

where:

Table 2.3. Description of the components of the set of operations with trajectory

TP	Represents a set of parametric homogenous transformations that will result in a trajectory path movement for the selected operation.
OP_I	Set of instantaneous elemental morphological operations

The proposal consists of breaking down each morphological operation into a succession of basic steps or operations. The new operation in the Determinist Topological Model will be formed by the successive application of these operations to which a transformation will be associated. This transformation will be applied to the frontier object and will depend on consecutive values of a real variable, which represents an ordered sequencing of positions of the object in space.

The transformations will establish an order in the execution or application of morphological primitives.

2.3.1. Parametric Homogenous Transformations

This section establishes a mechanism for defining trajectories or paths on objects in the Determinist Topological Model. Based on the principles of mathematical morphology, an extension is established on the basis of a family of functions of real variables using a set of homogenous transformations. The model will only use transformation matrices resulting from matrix compositions which carry out rotations and translations.

$$T^n = \left\{ \begin{bmatrix} a_{11} & a_{12} & \cdots & a_{1n} & 0 \\ a_{21} & a_{22} & \cdots & a_{2n} & 0 \\ \vdots & \vdots & & \vdots & \vdots \\ a_{n1} & a_{n2} & \cdots & a_{nn} & 0 \\ a_{(n+1)1} & a_{(n+1)2} & \cdots & a_{(n+1)n} & 1 \end{bmatrix}, a_{ij} \in R \right\} \qquad \text{(Exp. 2.11)}$$

Let T^n be the set of homogenous transformation matrices with the dimension $n+1$. Taking the form of T^n the function of real variable $\Gamma_n(r)$ is defined, which represents a parameterisation on the elements of T^n.

$$\Gamma_n : R \to T^n$$

$$\Gamma_n(r) \equiv \begin{bmatrix} f_{11}(r) & f_{12}(r) & \cdots & f_{1n}(r) & 0 \\ f_{21}(r) & f_{22}(r) & \cdots & f_{2n}(r) & 0 \\ \vdots & \vdots & & \vdots & \vdots \\ f_{n1}(r) & f_{n2}(r) & \cdots & f_{nn}(r) & 0 \\ f_{(n+1)1}(r) & f_{(n+1)2}(r) & \cdots & f_{(n+1)n}(r) & 1 \end{bmatrix}$$

(Exp. 2.12)

A point p of coordinates $(p_1, p_2,..,p_n)$ of the vectorial space R^n will be extended to the vectorial space R^{n+1} using as coordinates $(p_1, p_2,..,p_n,1)$. Multiplying that point p by a transformation matrix of T^n, a new point p' shall be obtained on the vectorial space R^{n+1} with coordinates $(p'_1, p'_2,..,p'_n,1)$ to which shall correspond a point $p'=(p'_1, p'_2,..,p'_n)$ of the vectorial space R^n.

$$p' = p \cdot \Gamma_n(r) = \begin{pmatrix} p_1 f_{11}(r) + p_2 f_{21}(r) + \ldots + p_n f_{n1}(r) + f_{(n+1)1}(r) \\ p_1 f_{12}(r) + p_2 f_{22}(r) + \ldots + p_n f_{n2}(r) + f_{(n+1)2}(r) \\ \vdots \\ p_1 f_{1n}(r) + p_2 f_{2n}(r) + \ldots + p_n f_{nn}(r) + f_{(n+1)n}(r) \\ 1 \end{pmatrix}^T$$

(Exp. 2.13)

The function of vector-matrix product is extended to the elements of a set O. For this purpose the function $\bullet$ is defined which obtains the set of transformations of the elements of the original set.

$$\bullet : FR \times T^n \to FR$$
$$O' = O \bullet \Gamma_n(r) = \left\{ p \cdot \Gamma_n(r), p \in O, r \in [0 \ldots 1] \right\}$$

(Exp. 2.14)

Due to the fact that such transformations only make rotations and translations, the resulting set will not suffer any distortions. As a result, the operation maintains the form of the set although it changes its position in the representation space. The parametric values r are normalised, thus the set of possible positions defining a homogenous parametric transformation is ordered on the basis of such parameter with initial position $\Gamma_n(0)$ and final position $\Gamma_n(1)$.

Figure 2.2 shows the relation of the *TP* set of transformations within the general framework of the Determinist Topological Model. The parametric transformations T^n are used for prior conversion of the frontier elements FR using the function $\bullet$. The resulting set is used to carry out determinist morphological operations through reiterated application of elemental operations.
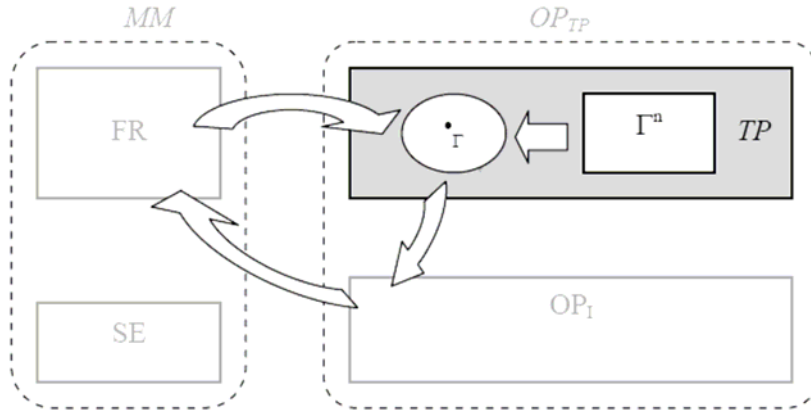
Figure 2.2. A frontier object is transformed successively by an orderly application of a sequence of elemental operations.

2.3.2. Instantaneous Basic Operation

In conventional mathematical morphology, the operation of transformation of objects is defined as a succession of operations which act on their component elements [Serra, 1982]. There is no order of application established for these elemental or basic operations. Subsequently, a basic morphological operation is defined deriving from elemental operations which carry out the morphological erosion and extension which, however, differs from these in that it includes a parameter that indicates its position within the complete set of elemental operations. The operation has been defined as *instantaneous* due to the fact that it is linked to a concrete value of parametric space in which the transformations of Γ_n are defined and it only obtains a point of the same as result.

The basic instantaneous operation has the following domain:

$$OP_{\Gamma(k)} : T^n \times SE \times FR \times R^n \to R^n \qquad \text{(Exp. 2.15)}$$

where $\Gamma(k)$ is a homogenous transformation obtained by means of application of the normalised parametric value k on the function Γ_n. *SE* represents the family of structuring elements of the space R^n with its centre in the origin of coordinates; *FR*, the family of frontier objects; and R^n, a family of dimension vectors n.

In descriptive terms, this operation obtains the centre of the structuring element when this touches, following the direction marked by a vector $\vec{v}$, a frontier object which has been previously transformed.

Formally:

$$X \, OP_{\Gamma_n(k)} \, B = p \in R^n : p = dist_{\vec{v}}(B, X \bullet \Gamma_n(k)) \cdot \vec{v} \wedge B_p \cap X \neq \varnothing$$

$$B \in SE, X \in FR, \Gamma_n(k) \in T^n, \vec{v} \in R^n \qquad \text{(Exp. 2.16)}$$

where $dist_v$ is a function which shall be defined later in order to determine the minimum distance between the set X and B in the direction determined by a vector $\vec{v}$. For this reason, the translation B_p will lead to the structuring element when it touches the object X, so that $B_p \cap X \neq \varnothing$.

Graphically:
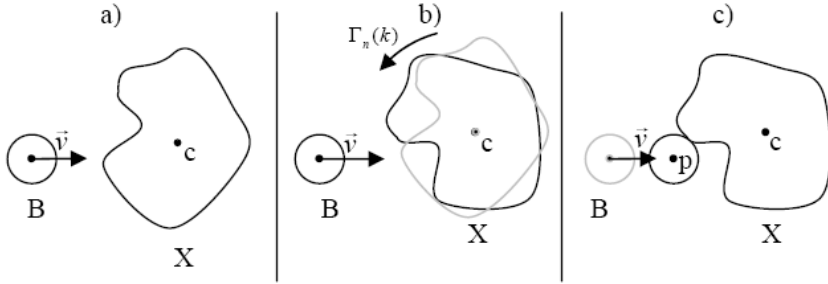
Figure 2.3. Geometric description of the basic instantaneous operation a) initial situation b) transformation of the object X c) Application of the distance function.

By way of example, figure 2.3 shows the application of the basic instantaneous operation on an object X as a succession of three phases:

a. Represents the initial situation of the elements involved. The structuring element B is centred on the origin of coordinates and the object X with centre situated in c.
b. In this situation a homogenous transformation is applied on the elements of X. On this occasion such transformation corresponds to a rotation round point c.
c. Having transformed the object, the distance is calculated between this and the structuring element in the direction indicated by the vector $\vec{v}$. The result of the operation is represented by the point p.

Definition of the Function Dist$_v$

As has been indicated above, this function expresses the distance existing between the two sets of the Euclidean space in the direction which determines a given vector.
In formal terms:

$$dist_{\vec{v}}(B, X) = \min(d_{\vec{v}}(b, X)), \forall b \in B$$

$$dist_{\vec{v}} : SE \times FR \rightarrow R \qquad \text{(Exp. 2.17)}$$

where the function $d_{\vec{v}}$ determines the distance existing between any point p of the space and a determined object X in the direction indicated by the vector $\vec{v}$. Geometrically it is defined by the Euclidean distance existing between p and the closest point obtained as the intersection

of the line defining the vector and which passes through that point and the object X. This function may be expressed in the following manner:

$$d_{\vec{v}}(p,X) = \begin{cases} \overline{pp'}, & Int(r_{p\vec{v}},X) \neq \varnothing, \forall q \neq p' \in Int(r_{\vec{v}},X), \overline{pp'} \leq \overline{pq} \\ +\infty, & Int(r_{p\vec{v}},X) = \varnothing \end{cases} \quad \text{(Exp. 2.18)}$$

where $Int(r_{pv},X)$ represents the set of points of intersection between the line that passes through p with direction $\vec{v}$ (represented as $r_{p\vec{v}}$) and the set X. the figure 2.4 shows an example of application of these functions.
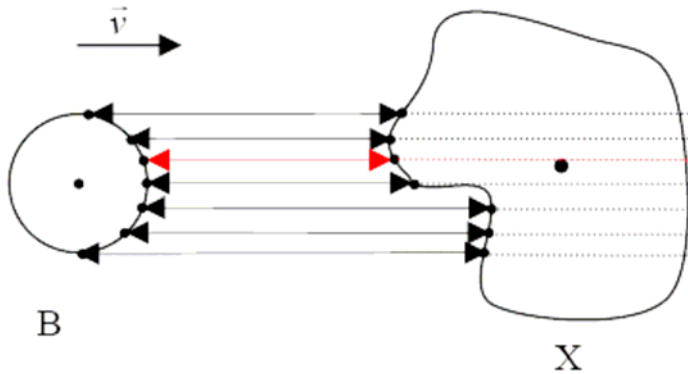
Figure 2.4. Calculation of the function $dist_v$ between the objects B and X. The calculation of successive $d_{\vec{v}}$ appears as a black line, and the red line depicts the result of the distance function.

The family DIS_V is defined as the set of all the possible functions of minimum distance:

$$DIS_V = \{dist_{\vec{v}}(B,X), \forall B \in SE, \forall X \in FR\} \quad \text{(Exp. 2.19)}$$
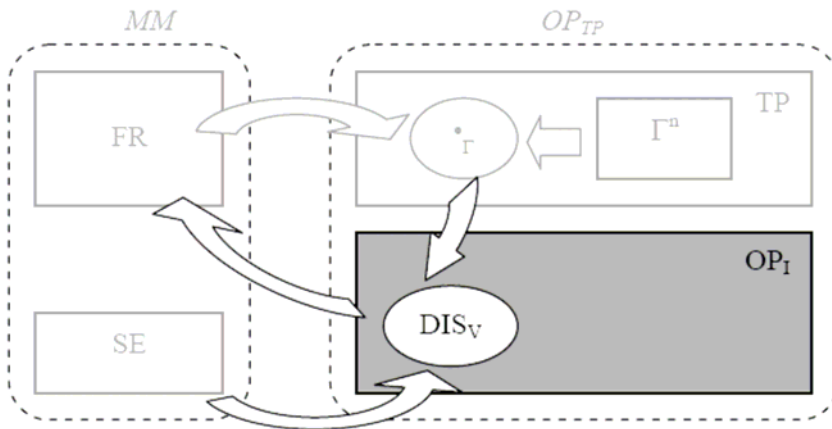
Figure 2.5. The application of the minimum distance function on a transformation of a frontier object and a structuring element constitutes the kernel of the basic instantaneous operation in the DTM.

Figure 2.5 shows how DIS_V constitutes the basic element for carrying out a basic instantaneous operation. The reiterated application of this on the set of all the possible parametric values will give rise to the complete morphological operation. This operation is associated to a relation of order established by the transformation Γ, obtaining as a result a new frontier set of FR. In the following section this type of complete operation shall be detailed.

2.3.3. DILATION with Trajectory

The dilation operation in mathematical morphology is defined by the expression:

$$X \oplus B = \left\{ x \in R^n, B_x \cap X \neq \varnothing \right\} \qquad \text{(Exp. 2.20)}$$

In descriptive terms, this operation may be defined as the place for the positions of the centre of the structuring element B when it touches the set X [Serra, 1982]. In the context of this model, in which the objects are represented by their frontier, it is interesting to define the frontier of the dilation operation as those places which occupy the centre of a structuring element which exclusively touches the frontier of a set X, that is, without invading its interior (2.21).

$$Fr(X \oplus B) = \left\{ x \in R^n, B_x \cap X \neq \varnothing \wedge B_x \cap In(X) = \varnothing \right\} \qquad \text{(Exp. 2.21)}$$

It is precisely the previous definition which will permit the use of the basic instantaneous operation in order to be able to carry out the dilation operation. The result is a set of points, each of these, obtained by repeated application of basic instantaneous real variable parameter operations

The operation *instantaneous dilation* is defined as a step in the morphological dilation:

$$\oplus_{\Gamma(k)}$$

$$X \oplus_{\Gamma(k)} B = X\ OP_{\Gamma(k)}\ B = p \in R^n : B_p \cap X \neq \varnothing \wedge B_p \cap In(X) = \varnothing \qquad \text{(Exp. 2.22)}$$

Taking as a starting point the basic instantaneous operation (2.16) a new operation is defined conditioned on the fact that the structuring element does not intersect the interior of set X. This condition is necessary as the calculation of the associated distance function should be determined so that the structuring element is situated in the external edge of object X.

Dilation with trajectory as the set of points obtained by repeated application of the instantaneous dilation $\oplus_{\Gamma(k)}$ for real domain *[0..1]*. The trajectory should ensure that the geometric place of all the centres of the structuring element which touch X from the exterior. The operation is defined as the union of all possible instantaneous operations in (2.23).

$$X \oplus_{\Gamma} B = \bigcup_{k \in [0..1]} (X \oplus_{\Gamma(k)} B) = \left\{ y \in R^n : B_y \cap X \neq \varnothing \wedge B_y \cap In(X) = \varnothing \right\} \qquad \text{(Exp. 2.23)}$$

Comparing the expression of dilation with trajectory (2.23) with the frontier of the morphological dilation (2.21) it is trivial to check the equality between the two sets. If the real variable k covers the whole distance, as a result the frontier of the complete dilation of the object will be obtained, as all the centres of the structuring element will have been obtained when it touches the object, making the frontier of the morphological and determinist definition coincide. With the frontier of the dilation being a subset thereof the ratio appearing in the expression (2.24) is obtained.

$$X \oplus_{\Gamma} B = Fr(X \oplus B) \subseteq X \oplus B \qquad \text{(Exp. 2.24)}$$

The dilation with trajectory permits the order for obtaining points of the final set to be controlled. Having defined the relation of partial order $\leq$ as R, an ordered succession of parametric values of k on the interval *[0..1]* will cause the ordered obtaining of centres of the structuring element according to the movement defined by the homogenous transformation Γ.

Another possibility which permits the model, and which is not considered in classic mathematical morphology, is being able to obtain ordered subsets of primitives provided that an incomplete trajectory is established for the interval (local primitive) ,or either a discretisation of the real variable in its trajectory (discrete primitive). In this case it is trivial due to expressions (2.23) and (2.21) arriving at the conclusion that an incomplete dilation is a subset of the morphological dilation.

Figure 2.6 shows an example of dilation with a two dimensional trajectory in which it has taken as a structuring element a circle and is compared with conventional morphological dilation.
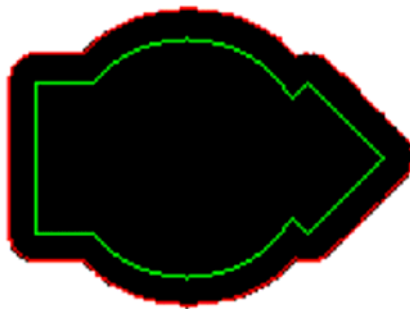
Figure 2.6. Comparison of morphological dilation (in black) and dilation with trajectory (red line) of the object the boundary of which is shown in green.

2.3.4. EROSION with Trajectory

The erosion operation in mathematical morphology may be defined according to the equation (2.25).

$$X \odot B = \left\{ y \in R^n, B_y \subseteq In(X) \right\} \qquad \text{(Exp. 2.25)}$$

A descriptive interpretation of the operation may be defined as the place of the positions of the centre of the structuring element B when it touches the set X [Serra, 1982]. For objects which do not contain islands, the erosion boundary is defined by the centres of the structuring element when this touches the interior edge of the object.

$$Fr(X \odot B) = \left\{ y \in R^n : B_y \subseteq In(X) \land B_y \cap X \neq \varnothing \right\} \qquad \text{(Exp. 2.26)}$$

In the light of the previous definition it is possible to use the basic instantaneous operation in order to be able to carry out the erosion operation. Each point of the final set will be obtained by means of repeated application of basic instantaneous operations of real variable parameter.

Similarly to the manner in which the dilation was carried out, *instantaneous erosion* is defined as a step of morphological erosion:

$$X \odot_{\Gamma(k)} B = X \, OP_{\Gamma(k)} \, B = p \in R^n : B_p \cap X \neq \varnothing \land B_p \subseteq In(X) \quad \text{(Exp. 2.27)}$$

Using the basic instantaneous operation, a new operation has been created which adds the condition that the structuring element is included in the original set. This condition is necessary as the calculation of the associated distance function should be determined in such a way that the structuring element is situated on the interior edge of the object X. If it is not possible to situate the structuring element within the X set (for example, when the size is X is less than that of B) then, the step of erosion cannot be applied, and thus no points are obtained.

Erosion with trajectory is defined as the set of points obtained by repeated application of the instantaneous erosion $\odot_{\Gamma(k)}$ for real domain *[0..1]*.

$$X \odot_{\Gamma} B = \bigcup_{k \in [0..1]} (X \odot_{\Gamma(k)} B) = \left\{ y \in R^n : B_y \cap X \neq \varnothing \land B_y \subseteq In(X) \right\} \quad \text{(Exp. 2.28)}$$

The homogenous parametric transformation Γ should ensure an interior trajectory through the object X in the normalised space *[0..1]*. If the real variable *k* covers the whole interval, as a result the frontier of the complete erosion of the object will be obtained, as all the centres of the structuring element will have been obtained when it touches the object. In a similar manner to the case of dilation by (2.28) and (2.26) it is deduced that the frontier of morphological erosion and erosion with trajectory will coincide. In general the following is completed:

$$X \odot_{\Gamma} B = Fr(X \odot B) \subseteq X \odot B \qquad \text{(Exp. 2.29)}$$

Figure 2.7 shows a two dimensional example of erosion by trajectory and morphological erosion.

As occurred with the dilation operation, erosion with trajectory permits control of how the points of the final set are obtained. Having defined the relation of partial order $\leq$ as R, an ordered succession of parametric values of k on the interval *[0..1]* will cause the ordered obtaining of centres of the structuring element, according to the movement defined by the homogenous transformation Γ.
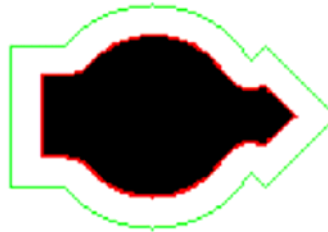
Figure 2.7. Comparison of morphological erosion (in black) and erosion with trajectory (red line) of the object the boundary of which is shown in green.

A result from which it is simple to deduce using (2.28) that a partial erosion (when it does not completely cover the parametric space of k) will constitute a subset of the complete erosion.

Characteristics of Operations with Trajectory

Given that the result of the operations with trajectory coincide with the boundary of the primitive morphologies when the homogenous transformation determines a complete path on the boundary of the objects on which it is applied, and since they are a consequence of the final result of the operation and not the manner in which it is obtained, the properties which, in mathematical morphology, are associated with these operations continue to be maintained. Specifically, the properties of duality, extensiveness, commutability, growth and separatability, [Serra, 1992] continue to be maintained in the primitives with trajectory, provided that the characteristics of inclusion and membership of sets is made inside the boundaries described by erosion and dilation with trajectory.

In addition to the properties inherited from the morphology, operations with trajectory present characteristics which permit operations to be carried out which are not considered in conventional morphology. The breakdown into basic operations, and the association of each of these with a different homogenous transformation, enables the structuring element to be situated, with respect to the object in different positions and orientations. In mathematical morphology the structuring element does not vary its orientation throughout the operation; in fact, the operation is considered as a translation of the same onto the original object. In the Determinist Topological Model this behaviour corresponds to a particular case of transformation in which the structuring element does not vary its initial orientation throughout the operation. If this restriction is not followed, it is possible to carry out dilation or erosion operations in which the structuring elements have different positions and orientations in respect of the objects on which the morphological operation is applied.

Figure 2.8 shows an example of an application of a morphological operation in the Determinist Topological Model. In this example, the structuring element (a square with 30 side pixels) varies its orientation according to how far it traces the boundary of the original object (a square of 80 side pixels traced in green) so that the front face of the structuring element always points to the centre of the original object. The result of the classic morphological operation is shown in black in which there is no change of orientation in the structuring element. The variation characteristic of the element is interesting for emulating a certain type of real morphological behaviour.
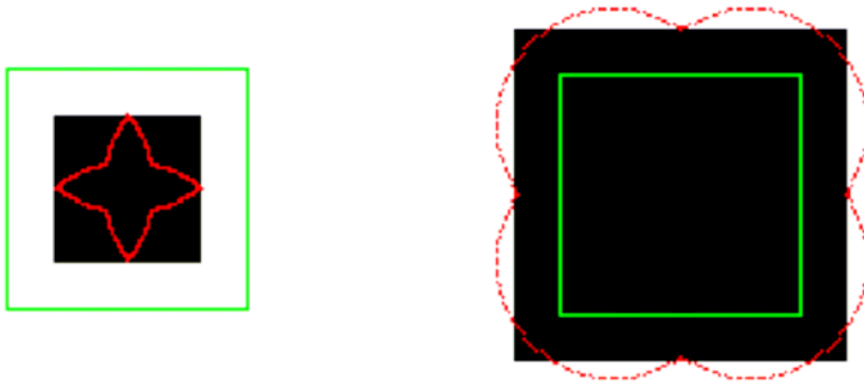
Figure 2.8. Different morphological operations in the DTM using variable orientation for a square structuring element. On the left erosion and on the right dilation (results shown in red).

2.4. Computational Model for the DTM

This section presents and evaluates a model which permits morphological operations in accordance with the Determinist Topological Model so that the contents resumed below may be developed.

- *Definition of the model* Based on the aforementioned definitions, a generic algorithmic method is created for resolving morphological operations. On the basis of this model, an initial analysis is carried out of the most complex functions and various alternatives are examined.
- *Study of the efficiency of the model* At this point the advantages and disadvantages of this computational model are analysed with respect to others, morphological operations are carried out which show correction of the model and they are compared in computational terms with other methods.
- *Refinements* A study on inherent parallelism reveals that its use is possible on platforms which permit parallel computation, which leads to a drop in temporal levels. The parts of the algorithm which are most complex in computational terms are analysed and various alternatives are proposed for improving temporal efficiency of the algorithm to the determent of its spatial cost.

2.4.1. Definition of the Computational Model

There are two basic elements in the Determinist Topological Model: the parametric transformations (*TP)* and the basic instantaneous operation (*OP$_I$*). Both configure the basis of the operations with trajectory as any of them translates to a successive application of basic instantaneous operations on different transformations of the object. Below, a computational model is presented which carries out a basic operation of the DTM based on a specific parametric transformation.

```
 1: for each f∈FR do
 2:    t=0
 3:    while t<=1 do
 4:       f'=f•Γ(t)
 5:       d =distᵥ(f',SE)
 6:       SECentre=ComputeCentre(d,Γ(t))
 7:       AddFT(SECentre)
 8:       Increment(t)
 9:    endwhile
10: endfor
```

Figure 2.9. Generic computational model based on DTM.

The algorithm shown in figure 2.9 is proposed as a successive search for minimals which are stored in a list of results (line 7). This list, comprising different centres of the structuring element, shall constitute the set of points which will form the result of a morphological operation with trajectory in the Determinist Topological Model.

For each frontier object which makes up the FR set of the DTM, a homogenous transformation $\Gamma(t)$ which is successively applied and which situates the object at a specific point in space (line 4 of figure 2.9). The function $dist_v$ calculates the minimum distance between the structuring element and the transformed object, always in the direction indicated by the vector *v* (line 5 of figure 2.9).

Finally, with the minimum distance found and the transformation applied, the position of the central point of the structuring element is determined by means of the *ComputeCentre* function, (line 6 of figure 2.9). The computation is expressed in the equation (2.30) and is obtained in an analytical manner due to the application of the inverse of the parametric transformation $\Gamma^{-1}(t)$.

$$c_{\Gamma(t)} = (c_{EE} + dist_{\vec{v}} \cdot \vec{v}) \cdot \Gamma^{-1}(t) \qquad \text{(Exp. 2.30)}$$

From the computational point of view, the function $dist_v$ is that which shows greater complexity. Below this is analysed in detail.

2.4.2. Calculation of the Function of Minimum Distance

The function $dist_v$ constitutes the most important element of the basic instantaneous operation. Its calculation is made by means of obtaining the minimum distance between objects associated to a directing vector *v*.

The flexibility of the model, which permits working with both the geometric descriptions of points of the Euclidean space, and the non-ordered subsets of the same, permits the introduction in the computational model of different mechanisms for calculating that function.

The Function Dist$_v$ for Geometric Objects

If the geometric representation of the objects is obtained, the calculation of this function consists of obtaining the mathematical function which determines the distance between them in the direction indicated by the directing vector. As a general analytical method, the calculation of the minimum of the previous function may be used which will be carried out through the first derivative from that function.

The difficulty of finding the distance function depends on the geometric nature of the objects in question. If the objects are too complex in their definition, the search for the analytical solution proposed previously may lead to a resolution of a non linear system of equations. This type of system usually poses difficulties in computation and, on occasion, it is only possible to obtain an approximate solution by means of a high cost in temporal terms. Conversely, if the objects can be described in a simple formulation, it is possible to find an analytical solution to the aforementioned problem. This fact will enable exact calculations (as methods of approximation are no longer used) and reduced computation times.

Examples will be shown in which it is possible to find an analytical solution to this problem. For the sake of clarity, the calculation shall be restricted to 2 dimensional spaces and shall assume, as directing vector, the positive direction of the X axis (it is always possible to find a rotation transformation which any vector brings to the X axis, thus this ultimate hypothesis does not presuppose a loss of the generality of the problem).

Distance Polygon – Polygon

The problem of calculating the minimum distance between two given polygons is simplified if each of these is considered as a collection of concatenated and closed segments in the two dimensional space.

Effectively, when $p_{\square n}$ and $q_{\square m}$ are two polygons of n and m sides respectively. In order to maintain a compact form in the notation, the first point of a segment is used to represent that segment.

$$
\begin{aligned}
p_{\square n} &= \left\{ \overline{p_1 p_2}, \overline{p_2 p_3}, ..., \overline{p_{n-1} p_n}, \overline{p_n p_1} \right\} = \left\{ \overline{p_1}, \overline{p_2}, ..., \overline{p_{n-1}}, \overline{p_n} \right\} \\
q_{\square m} &= \left\{ \overline{q_1 q_2}, \overline{q_2 q_3}, ..., \overline{q_{m-1} q_m}, \overline{q_m q_1} \right\} = \left\{ \overline{q_1}, \overline{q_2}, ..., \overline{q_{m-1}}, \overline{q_m} \right\}
\end{aligned}
\qquad \text{(Exp. 2.31)}
$$

The minimum distance function between the aforementioned polygons will be the minimum possible between any pair of segments of the two polygons. Using the equations of minimum distances between segments, would obtain an analytical solution to the problem posed. This solution would be determined by the following equations (2.32):

$$d_{\overline{pq}} = \min\left(d_{\overline{p}}(q_1), d_{\overline{p}}(q_2), d_{\overline{q}}(p_1), d_{\overline{q}}(p_2)\right)$$

(Exp. 2.32)

$$d_{\square nm} = \min(d_{\overline{p_i q_j}}), \forall i \in [1..n], \forall j \in [1..m]$$

Distance Polygon – Circle

In similar manner to the previous case, the computation of the distance between any polygon and a circle centred in the origin is simple. For this purpose it is only necessary to make reiterated use of the functions which calculate the minimum distance between a segment and a circle which appear defined in (2.33).

$$d'_{c\overline{p}}(s) = 0$$

$$s = \begin{cases} \dfrac{r \cdot |p_{1x} - p_{2x}| \cdot SIGN(p_{1y} - p_{2y}) - p_{1y} \cdot \sqrt{p_{1x}^2 - 2 \cdot p_{1x} \cdot p_{2x} + p_{1y}^2 - 2 \cdot p_{1y} \cdot p_{2y} + p_{2x}^2 + p_{2y}^2}}{\sqrt{p_{1x}^2 - 2 \cdot p_{1x} \cdot p_{2x} + p_{1y}^2 - 2 \cdot p_{1y} \cdot p_{2y} + p_{2x}^2 + p_{2y}^2} \cdot (p_{2y} - p_{1y})} \\[2em] \dfrac{r \cdot |p_{1x} - p_{2x}| \cdot SIGN(p_{1y} - p_{2y}) + p_{1y} \cdot \sqrt{p_{1x}^2 - 2 \cdot p_{1x} \cdot p_{2x} + p_{1y}^2 - 2 \cdot p_{1y} \cdot p_{2y} + p_{2x}^2 + p_{2y}^2}}{\sqrt{p_{1x}^2 - 2 \cdot p_{1x} \cdot p_{2x} + p_{1y}^2 - 2 \cdot p_{1y} \cdot p_{2y} + p_{2x}^2 + p_{2y}^2} \cdot (p_{1y} - p_{2y})} \end{cases}$$

$$d_{c\overline{p}} = \begin{cases} \left. \begin{cases} d_{c\overline{p}}(s), 0 < s < 1 \\ d_{c\overline{p}}(0), s \le 0 \\ d_{c\overline{p}}(1), s \ge 1 \end{cases} \right\} |p_{1y}| \le r \vee |p_{2y}| \le r \vee p_{1y} \cdot p_{2y} < 0 \\[2em] \infty, |p_{1y}| > r \wedge |p_{2y}| > r \end{cases}$$

(Exp. 2.33)

The minimum distance function for a polygon with n sides would be defined by the equation (2.34).

$$d_{\square nc} = \min(d_{c\overline{p_i}}), \forall i \in [1..n]$$

(Exp. 2.34)
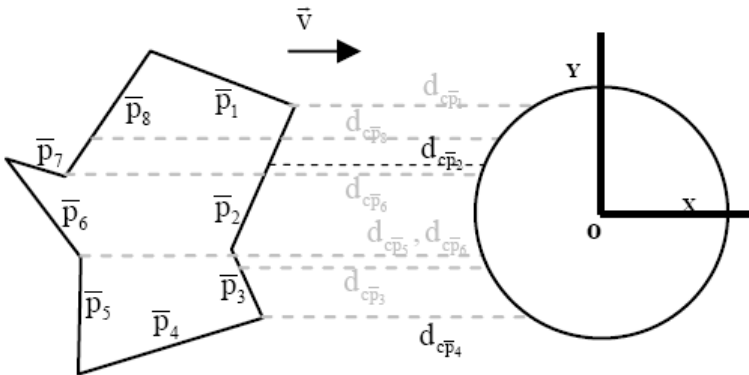
Figure 2.10. Calculation of the minimum distance function between a polygon and a circle.

In the two previous examples, an analytical solution to the problem of calculation of the minimum distance has been obtained. Furthermore the solution shall be exact and

independent of the size of the objects. Since the geometric space has not be discretised, the basic instantaneous operation may continue to be computed without needing to make use of spaces and discrete methods, which translates into the calculation of continuous morphological primitives.

When an analytical solution exists (as occurs in the cases presented previously) the computational cost of the algorithm which calculates the basic instantaneous operation will depend exclusively on the number of the objects treated *(f)* and the values of the trajectory considered *(t)*, , as the minimum distance will be computed in constant time. Thus, this will have a greater limit expressed as O(t.f).

Although it is possible to use methods of resolving non linear systems, there is another alternative for carrying out the calculation of the *dist_v* function which, furthermore, does not depend on the geometric complexity of the objects. The idea is based on considering the objects as mere collections of points of the Euclidean space. In the following section this alternative will be proposed.

The Function Dist_v for Sets of Points

When the geometric objects are considered as a set of points in space, the calculation of the distance function is simplified, due to the fact that only distances need to be computed, in the direction of the directing vector, between any two pairs of points in both objects.

Considering the objects as sets of points obviates the need to have recourse to their geometry, which is only used to enable selection of elements of the set. The model shown in figure 2.11 covers both objects, analysing all the possible combinations between pairs of points in this way obtaining the minimum distance.

```
 1: t=0
 2: while t<=1 do
 3:   MinDistance=∞
 4:   for each f∈FR do
 5:     for each p∈f do
 6:         p'=p•Γ(t)
 7:         for each q∈SE do
 8:            d =d_v(p',q)
 9:         endfor
10:         if d<MinDistance then MinDistance=d endif
11:     endfor
12:   endfor
13:   SECentre=ComputeCentre(MinDistance,Γ(t))
14:   AddFT(SECentre)
15:   Increment(t)
16: endwhile
```

Figure 2.11. Computational model of the DTM for sets of points.

In view of the previous model, the distance function will be defined only between pairs of points in the Euclidean space. The expression (2.35) shows such function for a three dimensional space, taking the axis X as directing vector. In this case the auxiliary function *dr* was used which determines the distance between a point *q* and the line formed by the point *p* and the director vector *(1,0,0)*.

$$d_{p_{xyz},q_{x'y'z'}} = \begin{cases} |x-x'| & , dr(r_{p\bar{x}^+},q) \leq \lambda \\ \infty & , dr(r_{p\bar{x}^+},q) > \lambda \end{cases} \qquad \text{(Exp. 2.35)}$$

The function defined in the previous expression has a formulation which introduces a high level of temporal complexity in the model, as the accuracy of the calculation resides in the number of points analysed for both objects. The greater the number of points, the greater will be the accuracy of the calculation, although this will also increase the computation time.

Furthermore, it is necessary to guarantee the solidity of the discretised object; for this purpose, an area of influence will be established around each point of the object with radio known as λ. The choice of this value does not preclude complications, as the solidity of the discretised object must be guaranteed. Figure 2.12 shows how the result of the minimum distance may change based on an insufficient separation value (case a).
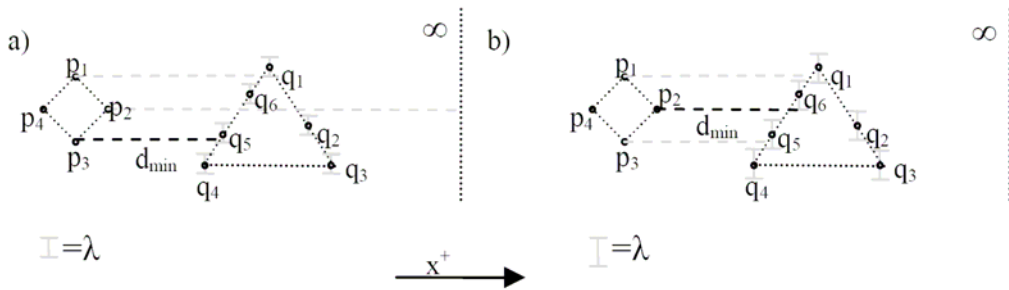
Figure 2.12. Calculation of the minimum distance function between two discretised polygons for two different λ values.

The asyntotic limit for the calculation model of the algorithm in figure 2.11 will be given by the expression O(t.f.n.m), where *n and m* constitute the maximum number of points selected for geometric objects treated and the structuring element respectively. Since this is a case of spatial discretisation, the size of the objects will influence the accuracy and, therefore the time it takes to obtain a solution.

The Function Dist$_v$ of Mixed Calculation

The main disadvantage of the solution by calculation of the distance between points resides in its high computational cost along with the inaccuracy of the calculation. Conversely, it has the advantage that it is completely independent from the geometric complexity of the object. It is possible to use a hybrid algorithmic scheme in which only one of the two objects, the structuring element, is considered, defined by means of a geometric function. This decision is based on the fact that object usually has a more simple structure in morphology.

In formal terms, the function of mixed calculation is defined as a special case of the function of minimum distance introduced in (2.17), in that the calculation is made on the structuring element instead of on the object:

$$dist_{\vec{v}}(B, X) = \min\left(d_{\vec{v}}(x, B)\right), \forall x \in X \qquad \text{(Exp. 2.36)}$$

where the function d_v determines the distance existing between any point p of the space and a determined structuring element B, in the direction indicated by the vector v. It is geometrically defined by the Euclidean distance existing between p and the closest point obtained as the intersection of the line defining the vector and which passes through point p and the object in question. This function may be expressed in a manner similar to that used in (2.18) taking into account that the points involved belong to object X considered:

$$d_{\vec{v}}(p, X) = \begin{cases} \overline{pp'}, & Int(r_{p\vec{v}}, X) \neq \varnothing, \forall q \neq p' \in Int(r_{\vec{v}}, X), \overline{pp'} \leq \overline{pq} \\ +\infty, & Int(r_{p\vec{v}}, X) = \varnothing \end{cases} \qquad \text{(Exp. 2.37)}$$

where $Int(r_{p\vec{v}}, X)$ represents the set of points of intersection between the straight which passes through p in direction $\vec{v}$ ($r_{p\vec{v}}$) and the set X. Figure 2.13 shows an example of the application of these functions.

For this model, the object X will be that which is considered as a structuring element since, as mentioned above, it presents a simpler structure in morphological casuistics. In actual fact, this simplicity will permit the function to have an analytical and simple solution to the problem of the geometric intersection between a straight and the structuring element chosen for the morphological operation.
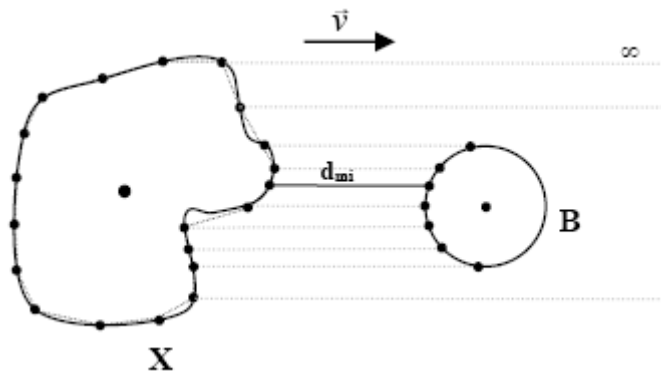
Figure 2.13. Calculation of the function $dist_v$ between the objects B (structuring element) and X (discretised object). The dotted line represents the calculation of successive d_v, the straight line, and the result of the distance function.

Figure 2.14 contains the algorithm which uses the mixed calculation model: computation of the minimum distance value is carried out between lines 4 and 10 of the model. The computational weight falls on function d_v, which is responsible for finding the intersection between the structuring element and a straight formed by the selected point p' and the director vector v.

The computational cost of this model has, in asynthotic terms, and in the worst of all cases, a temporal complexity of **O(t.f.n)**, with *n* being the maximum number of points considered for discretisation of the geometric objects.

```
 1: t=0
 2: while t<=1 do
 3:   MinDistance=∞
 4:   for each f∈FR do
 5:     for each p∈f do
 6:         p'=p•Γ(t)
 7:         d =d_v(p',SE)
 8:         if d<MinDistance then MinDistance=d endif
 9:     endfor
10:   endfor
11:   SECentre=ComputeCentre(MinDistance,Γ(t))
12:   AddFT(SECentre)
13:   Increment(t)
14: endwhile
```

Figure 2.14. Computational model of the DTM with mixed calculation of the minimum distance.

Due to the fact that there is a discretisation factor in the model, this will be associated implicitly with an error in calculation of the minimum distance at which the structuring element is found. The error will depend on the actual geometry of the element and the maximum distance existing between neighbouring points of the discretised object. The literature contains numerous methods which will permit a representative set of points to be obtained from a geometric object, given a maximum separation value between neighbouring points [Farin, 1993].

As an example, figure 2.15 shows the geometric representation of the error calculation committed by considering a discretised polygon and a circle as structuring element. In this case the error committed will be given as the expression (2.38).

$$R^2 = \left(\frac{D}{2}\right)^2 + \left(R-e\right)^2 \rightarrow e = R - \sqrt{R^2 - \left(\frac{D}{2}\right)^2}, R \geq \frac{D}{2} \qquad \text{(Exp. 2.38)}$$

where *D* represents the distance between neighbouring points and R the radius of the structuring element. For informative purposes it could be stated that given a maximum discretisation distance of 2mm and an SE with a 40 mm radius according to the expression (2.38) a calculation error of 0.0125 mm. would be obtained.

When analysing table 2.4 in terms of effectiveness, the best option is the geometric method, as it offers accuracy in calculation and a cost which depends only on the number of objects involved in the computation. Since in this method there is no discretisation, it also has the added advantage of its generality, as it operates on spaces with continuous definition. Nevertheless, the advantages of this method are based mainly on the existence of an analytical solution to the problem. When this solution does not exist, or when it is computationally unviable, only iterative approximating methods should be employed which will introduce a new order of complexity in the algorithm and inaccuracy in calculation of the solution.
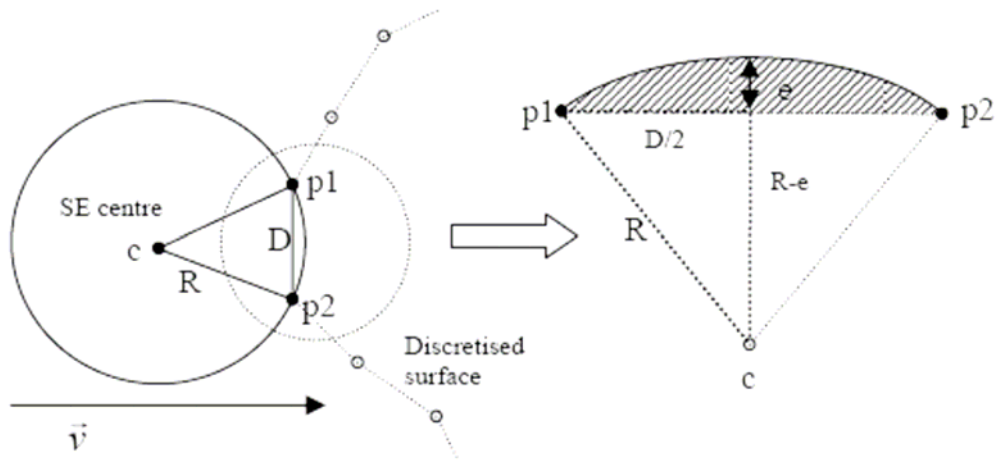
Figure 2.15. Calculation of the error produced by discretisation of a polygon under a circular structuring element.

The mixed method provides a good alternative, as although it introduces inaccuracy through discretisation of the object, the calculation of the intersection between a straight and object, of a more simple nature due to its structuring element, has an analytical solution. In this research this method will be chosen as it does not depend on the geometric formulation of the object in question leading to more generic solutions (in reality it will only depend on the geometry of the structuring element). Nevertheless, it is necessary to indicate that the continuous method should be taken into account in those cases in which the geometry of the objects which intervene in the calculation permit the analytical computation of the function $dist_v$.

Table 2.4. Characteristics of minimum distance calculation methods

Model	Continuous		Discrete		Mixed	
Elements	OBJs	EEs	OBJs	EEs	OBJs	EEs
Type	GEO	GEO	PTO	PTO	PTO	GEO
Cost"O"	O(t·n)*		O(t·f·n·m)		O(t·f n)	
Accuracy	**Accurate***		**Low**		**Medium**	
Space	Cont.	Cont.	Discr.	Discr.	Discr.	Cont.

(*) Cost and accuracy in the event that there is an analytical solution to the problem.

2.4.3. Study of the Efficiency of the Computational Model

In this section various morphological operations will be carried out on diverse objects and structuring elements, using a specific instantiation of the Determinist Topological Model. The objective is to analyse the efficiency of the model on a computer with sequential structure and compare it to traditional methods of application of morphological primitives.

The tests carried out restrict, in this section, the space of two dimensions. Although the model does not restrict the spatial dimension, the 2 dimensional field has been chosen due to its facility of representation, as well as for obtaining results comparable to the methods applied in mathematical morphology for treatment of images.

The morphological operations used in these experiments will be *dilation* and *erosion;* both constitute the base on which the more complex morphological operations will be carried out. Figure 2.16 shows the algorithm which makes the dilation/erosion of images.

```
1: for each image point i do
2:  for each SE point e do
3:    ComputeMaximum(i+e); // Dilation
4:    ComputeMimimum(i+e);  // Erosion
5:  endfor
6: endfor
```

Figure 2.16. Sequential algorithm for calculation of the dilation/erosion of an image.

On this point it is necessary to state that the results of times which will be shown may indicate the efficiency of the Determinist Topological Model with respect to other algorithms, although comparison cannot be direct as the nature of the objects and representation space of this model is completely different from that of the algorithms used in morphology for treatment of images.

Table 2.5 summarises the main differences between the methods to be compared. In classical mathematic morphology, the calculation is made on a complete image, that is, the morphological operation does not distinguish whether or not the pixels belong to a specific object or not, it simply applies a calculation operation of maximum in a neighbourhood environment. In the Determinist Topological Model, it is necessary to differentiate between the objects given in the space, as each one of these has a different geometric representation. Furthermore, this representation defines the frontier of the object and not its interior. The characteristics of the DTM will cause the same result for objects with or without islands. Another important difference is the representation of the structuring element; whereas in traditional morphology it is treated as a set of points (which is discretised for the case of operating with images), the DTM considers the geometric function of the points which make up their frontier, without it being necessary to carry out a discretisation thereof.

Table 2.5. Characteristics of the algorithms based on classical mathematical morphology (MM) and DTM of morphological computation

	MM on images	DTM of mixed calculation on 2D
Application space	Finite set of pixels as discretisation of the Euclidean space	Euclidean space 2D
Objects	Based on a complete image	Discrete representation of the boundary of each object
EEs	Set of pixels	Geometric representation of the frontier
Method	On each pixel it operates in a neighbourhood environment defined by the SE	The minimum distance of the SE centre is calculated in a $\vec{v}$ direction on a *t* trajectory
Result	Erosion/ dilation as set of pixels.	Frontier points of the Erosion/Expansion operation

Finally, the result obtained by the classic morphological model will be a complete image, that is, there will be no distinction between objects and gaps. There will be a result in the DTM for each object treated, which will comprise the frontier of each morphological operation with trajectory.

2.4.4. Experiments

In order to evaluate the two previous models, given the difficulty in making a comparison, due to the differences from the perspective of definition, it was decided to develop a new model in the Determinist Topological Model which will permit use of the same input domain as the model based on the classic mathematical morphology. The changes introduced are described below:

Input/Output Domain

In order to ensure that the algorithms are comparable, both should be based on the same input data and should produce results in a same domain. In this respect it was decided to use a set of two dimensional points for the algorithms. An image formed by a set of pixels will therefore constitute its scope of application. This conditioning factor has only supposed a restriction on the Determinist Topological Model which will define objects as sets of positions in the form $(x, y) \in \mathbb{Z}x\mathbb{Z}$.

Representation of Objects

In the model explained in this work, there is a need to differentiate objects individually, as these will be addressed one by one in computing the minimum distance function. In the experiments carried out, only one object per image was taken into account so it is not necessary to make that distinction. Furthermore, in the DTM only the frontier set of points of that object is considered and therefore, in order to locate that frontier, it will be necessary to apply a method for obtaining the boundary points of an image.

Since the number of points to be treated by the classic morphological model does not distinguish whether these belong to the object or not, it was decided to carry out two different variations of this method (hereinafter MM1 and MM2 designed to balance this disadvantage of treating a greater amount of input data than the Determinist Topological Model;

- In the MM1, the morphological operation will only carried out on the pixels which are the object of the image, that is, those which have a value "one". In this way they will not expand or erode the gaps (zeros) therein.
- The second variation, known as MM2 only carries out the operation on the image pixels which are considered to be the boundary of the object, so that it has exactly the same input field as the DTM. Although this method may serve as a reference for comparative purposes, it should be noted that its result will not coincide with that obtained by means of a morphological dilation as calculated by the MM1.

Structuring Element

For methods which use the classic mathematical morphology, the structuring element is no more than another subset of pixels. In these experiments a circle of a specific radius was considered. Both the MM1 and the MM2 will apply as neighbourhood environment the set of positions defined by the area of the circle as shown in figure 2.17.

The Determinist Topological Model is based on the geometric definition of the boundary of the structuring element which, in this case, will have the form $(x-c_x)^2+(y-c_y)^2=r^2$, corresponding to a circumference centred on point (c_x,c_y) of radius r.
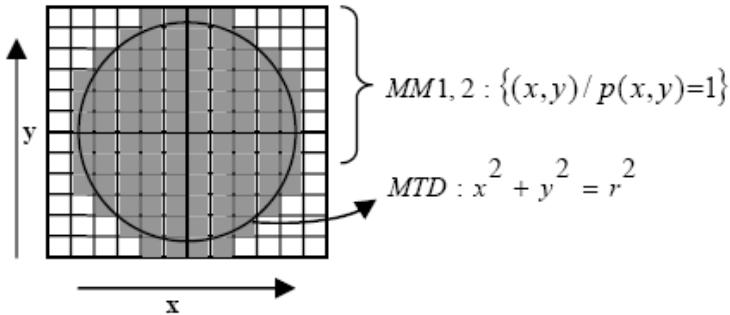
Figure 2.17. Differences in the interpretation of the structuring element between the DTM and the MM1 and MM2 algorithms.

Compared Algorithms

Table 2.6 shows a pseudo-code of algorithms on which the experiments were carried out. The information on the object boundary ($Fr(X)$) is necessary for algorithms based on the Determinist Topological Model and MM2 and for this reason in the experiments the calculation time was accounted for.

Table 2.6. Different morphological algorithms carried out in a dilation operation. In the lower part the associated computational cost

MM1	MM2
1: for each p∈X do	1: for each p∈Fr(X) do
2: for each e∈SE do	2: for each e∈SE do
3: Image(p+e)=1;	3: Image(p+e)=1;
4: endfor	4: endfor
5: endfor	5: endfor
O(p.e)	O(Fr(X).e)

Mixed calculation DTM
1: t=0
2: while t<=1 do
3: MinDistance=∞
4: for each p∈Fr(X) do
5: p'=*Rotate*(p,t*360)
6: d =d_v(p', $x^2+y^2=r^2$) // Minimum distance circle-point.
7: if d<MinDistance then MinDistance=d endif
8: endfor
9: SECentre=*ComputeCentre*(MinDistance,t)
10: *AddFT*(SECentre)
11: *Increment*(t)
12: endwhile
O(t.Fr(X))

The chosen trajectory for the experiments with DTM was implemented using a parametrised rotation matrix using an angular value, in sexagesimal degrees, of *360*t*. For each value this parameter will produce a rotation of the point of the object considered at that moment.

Tests on Images

Various tests and experiments were carried out in order to obtain the calculation time under different input conditions. Both the size of the object and that of the structuring element were varied, as these are the parameters which intervene in the morphological operation.

The models were evaluated on a state-of-the art Pentium processor.
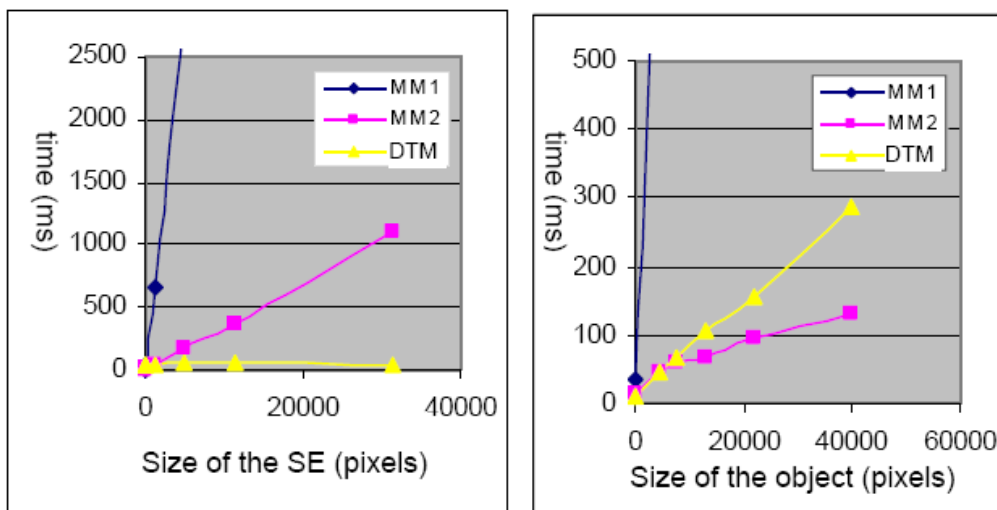
Figure 2. 18. Morphological dilation tests On the left, influence of the size of the structuring element On the right, influence on the size of the object.

Figure 2.18 shows the behaviour of the algorithms resulting from the size variation of the structuring element and the size of the object respectively, with the complementary parameter remaining fixed. The conclusion drawn from these graphs is the practical independence shown by the Determinist Topological Model given size variations in the structuring element; a logical consequence due to the use of its geometric representation instead of its content, as occurs with MM1 and MM2. The difference between MM2 and MM1 arises from that fact that the former only processes the pixels of the object boundary and so its temporal level descends an order of magnitude with respect to MM1.

With regard to the size variation of the object, in this experiment the DTM gives worse results than MM2 which is greater than MM1. Since the MM2 works only on the object boundary, the difference with the DTM arises from the size chosen for the *SE*, if this size is sufficiently small, the MM2 will employ less time than the DTM as it has a simpler computational logic (see table 2.6). The radius of the structuring element chosen for this test was 10 pixels, which is equivalent to an area of 81 points. In order to ascertain the effect of the increase of the structuring element on a set of object sizes, the experiments described below were carried out.
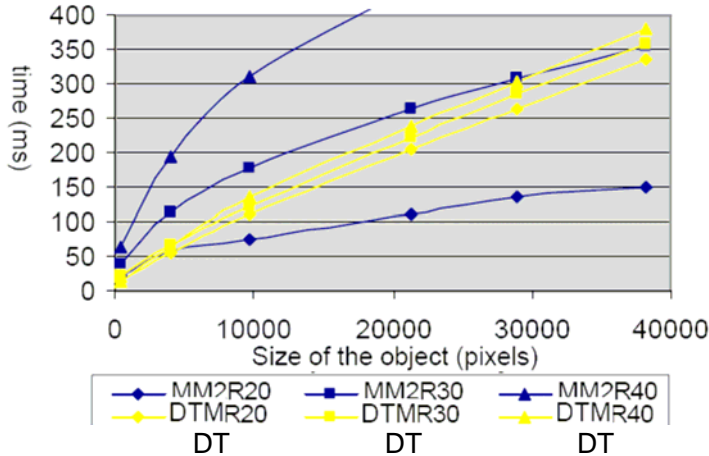
Figure 2.19. Morphologic dilation. Comparative study between the MM2 and the DTM models for SE sizes of 20, 30 y 40 pixels.

Figure 2.19 shows that there is a slight increase in computation time in the Determinist Topological Model when the size of the structuring element is increased, although this variation is minimal compared to the morphological methods studies. The reason for this increase is in the number of pixels of the object under which the distance function is defined. If the size of the *SE* increases, this number is greater, which causes the need to make new calculations on the new points.
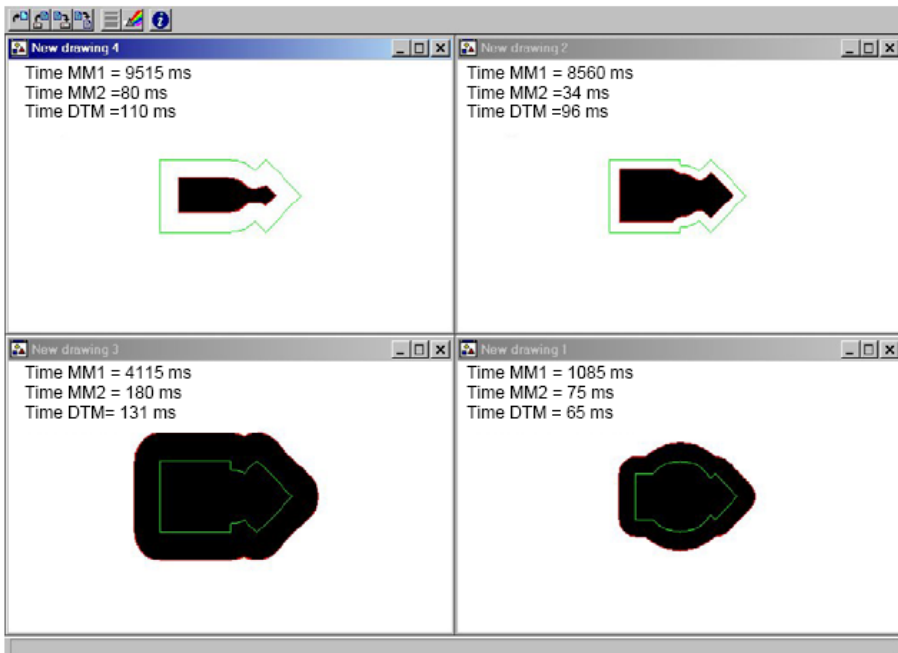
Figure 2.20. Morphological dilation and erosion Results of various morphological operations which have served as a basis for the experiments In the upper part, two erosions and in the lower part two expansions The boundary of the original object is depicted in green and the result of the MM1 operation in black, with the DTM result in red.

Figure 2.20 shows the various results of application of the morphological operation. Specifically, it may be seen how the DTM obtains the frontier of the morphological operation made by the MM1.

To summarise, it may be concluded that the Determinist Topological Model offers an effective alternative to traditional methods for computing morphological primitives. This alternative is further justified if the number of points of the objects and of the structuring elements is high. Due to the fact that the number of the set points is directly related to the dimension of the space in which the object and the structuring element are defined, the importance of the DTM is made more relevant when the dimension in the representation space is increased (3D, 4D etc). In the two dimensional space, the application of the DTM may be justified for high resolution images to which large size operators are applied.

2.4.5. Refinements for the Model

Computational models based on mathematical morphology have been subject to continuous revisions and improvements since their scope of application deviated towards the field of computer vision for applications in real time. Thus, at the present time there are various alternatives which increase the efficacy of the basic morphological model (MM1) analysed in the previous section.

Below further details of the study of the computational model are provided. New principles and properties will derive from this study and will introduce a series of refinements to the original model. The purpose is to ensure that those refinements will serve as a basis for future optimisations which increase the efficacy of morphological operations made using the Determinist Topological Model.

Principle of Achievability

The DTM carries out morphological operations following the boundary of objects, reaching its frontier and storing the position of the centre of the structuring element. For the trajectory value t, a function of minimal distance is calculated on all the points of the object boundary. Nevertheless, provided that the trajectory and the size of the SE permit, it is possible for there to be boundary points which are never reached by the SE in the direction of the directing vector (see figure 2.22) or, which is the same thing, those for which the minimum distance function returns ∞ as a result. Under the principle of *achievability* the points of the object for which the distance function is designed are grouped within a specific value of trajectory t. this set is defined for a specific object X as:

$$A_{\Gamma,\vec{v}}(t,X) = \left\{ p \in X : d_{\vec{v}}(p',EE) \neq \infty, p' = p \bullet \Gamma(t) \right\} \qquad \text{(Exp. 2.39)}$$

$$A_{\Gamma,\vec{v}}(t,X) = X$$

with a simple modification it is possible to transform the Determinist Topological Model so that it only takes into account those boundary points grouped under this principle. In the worst of cases , in which case it is not possible to reduce the "**O**" cost of the algorithm; however, a slight improvement will be attained in the average case.

Visibility Criterion

Another idea relating to the principle of attainability is that of only considering points which are not concealed behind other points of the boundary. This idea is related to algorithms representing three dimensional objects (*backculling*) and has also been used in improving algorithms for tracing machining trajectories [Wallner, 2000]. Obviously, the idea has some purpose when the boundary of the object is considered to be continuous (defined by means of geometric functions or by joining consecutive points). The criterion takes into account the points which normally form an angle of less than 90º with the directing vector (see figure 2.21). On average, around 50% of the boundary points will be eliminated under the criterion expressed in the equation (2.40).

$$B_{\Gamma,\vec{v}}(t,X) = \left\{ p \in X : \sphericalangle(\vec{N}(p'),\vec{v}) \le \frac{\pi}{2}, p' = p \bullet \Gamma(t) \right\} \qquad \text{(Exp. 2.40)}$$
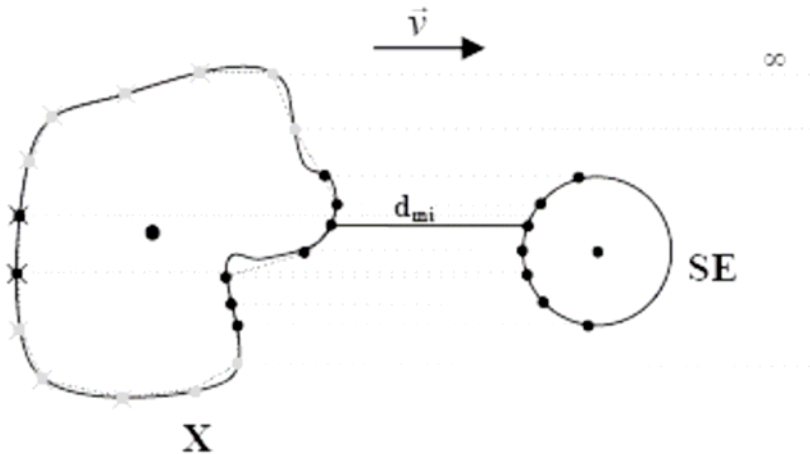
Figure 2.21. Optimisation of the DTM The points in black of the object X belong to *A(t,X)*. The points marked with a cross would be eliminated by means of backculling.

Vicinity Range

The trajectory, in the Determinist Topological Model was based on a set of homogenous parametric transformations. These trajectories define a path on the frontier of the object. This path is continuous due to use of the parameter *t*, that is, values close to *t*, will place the structuring element in close positions. This fact, together with the geometric continuity offered by the boundaries of objects permits the points obtaining minimum distances under two neighbouring trajectory points will also be close together. On the basis of this criterion it is possible to define a vicinity range of δ which ensures that the point of minimum distance for the parameter *t* is found in a vicinity of the minimum point for a value, immediately previous to *t* ó *t-Δ*. The selection of this value δ will depend on the geometry of the object and the structuring element, with the possibility of using heuristics to determine its value. The equation (2.41) defines the set of points found in the vicinity range for a specific value of

trajectory *t*. As support for the definition of V, the function *C(t)* is used which represents the set of points of an object X closest to the structuring element, that is, those which are situated at a minimum distance from the structuring element which indicates the function $dist_v$ for a value of trajectory *t*.

$$C_{X,\bar{v}}(t) = \left\{ p \in X : d_{\bar{v} \bullet \Gamma(t)}(p, EE) = dist_{\bar{v} \bullet \Gamma(t)}(EE, X) \right\}$$

$$V_{\Gamma,\bar{v}}(t, X) = \left\{ p \in X : \left| p - q \right| \leq \delta, \quad q \in C_{X,\bar{v}}(t - \Delta) \right\}$$

(Exp. 2.41)

Factor δ means the continuity possessed by an object in a specific path. A high value means that the boundary is very irregular along the trajectory (for example, a star) and conversely, a small factor would indicate a high regularity in the position occupied by the frontier elements of the object, for example, a circle). It is possible to use heuristics which estimate the value of the factor for a specific type of object and trajectory. The problem raised by the use of those heuristics is that of their efficiency. The more complicated it is to obtain the value, the less the computational reduction will be. Nevertheless, it would be possible to characterise certain types of geometry and trajectories in order to obtain a specific range of vicinity which includes a class of problems.
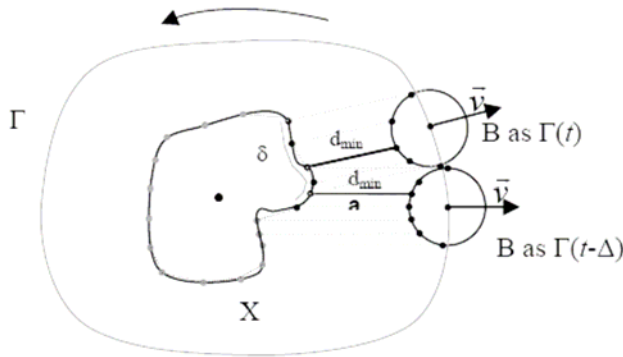
Figure 2.22. Refinement of the DTM using the criterion of vicinity. The points in black of the object X belong to V(t,X).

Parallelisation of the Model

As has been extracted from [Jonker, 1992] and [Pujol, 2000], the main contributions in mathematical morphology to the efficiency of filtering algorithms has been based on parallelism and segmentation of operations which have instrumentalised primitive morphologies on architectures which are well adapted to the type of parallelism applied.

Parallelisation of the DTM computational model is possible. The key for making this refinement possible is the independence of the *t* trajectory values. A minimum distance calculation corresponds to each parametric trajectory value. Figure 2.23 shows a possible parallelisation of the DTM. In this type of problem is the costs of communication are not considered, it is possible to obtain a level in the worst possible of cases of *O(t/n Fr(X))*, with

n being the number of processors in which the primitive is carried out, although the real existence of communication will limit the maximum number of processors.

```
 1: Send(Fr(X),p₀,p₁, ..., pₙ₋₁)
 2: In parallel t=proc*n;
 3: In parallel while t<(proc+1)/n do
 4:   MinDistance=∞
 5:    for each p∈X do
 6:       p'=p•Γ(t)
 7:       d =dᵥ(p',SE)
 8:       if d<MinDistance then MinDistance=d endif
 9:    endfor
10:   SECentre=ComputeCentre(MinDistance,Γ(t))
11:   AddFT(SECentre)
12:   Increment(t)
13: endwhile
14: In parallel if proc<>0 then Send(FT,p₀)
15: if proc==0 then ReceiveAndGather(FT,e)
```

Figure 2.23. Parallel computational model of the DTM. The *proc* variable refers to the current processor. The *n* variable contains the number of processors of the system, so that $0 \leq proc \leq n-1$.

3. Morphological Offset Calculation

The classical morphologic paradigm is based on set theory. Thus, most operations are indeterministic, defined over elements of a set. Nevertheless, the DTM model introduces two interesting features that make the definition of a morphological offset calculation possible: only the boundaries of the sets are considered to calculate the morphological operations and the use of instantaneous basic operation applied successively introduces an order relation. The order of the morphology operation is important because it will allow the method to represent the offset as a trajectory. The other important consideration is that the interest is only on the boundary of operations, since both shapes and offsets are curves, and the inner space is not of interest for this purpose.

The offsetting method that is presented here is suitable for any kind of curve. Specifically, we use parametric cubic curves, which are one of the most general models, and as such are very popular in CAD/CAM applications.

Back to the morphological operations, is trivial to observe that the operations Fr(X⊕B) and Fr(XΘB) correspond, respectively, with the outer and inner offset of the shape generated by the frontier of X at a distance given by the radius of a circular structuring element B. Red curves in Figures 2.6 and 2.7 could represent, therefore, the outer and inner offsets of a given curve represented by the green line. In both cases, the black part corresponds to the classical operation result.

3.1. Morphological Offset Definition

In this section, the instant basic operator defined previously is applied in order to define the morphological offset.

Using the instant basic dilation, the morphological outer offset of an X shape is defined as the set of points resulted from the repeated and ordered application of the instant basic dilation, for the normalized k range [0..1]. Analogously, the morphological inner offset of an X shape is the set of points obtained after the repeated and ordered application of the instant basic erosion, also for the normalized k range [0..1]. It is trivial to confirm that the offsets correspond to the operations of dilation and erosion with trajectory.

Trajectory-based erosion and dilation, by means of homogeneous transformations which are compounded by translations and rotations, could orientate the structuring element in any position on the object boundary. This feature is not supported by classical operations where the structuring element remains in the same position, but it is necessary to generalize the concept of offset. For instance, when it is used for machining purposes, the structuring element orientation corresponds to the tool orientation.

Moreover, the definitions of instant operations and the establishment of an order relation between the frontier points allow the generalization of the offset at a variable distance. If the distance if set as a function of the parameter t, the obtaining of a general offset is straightaway: the structuring element radius must be changed for each instant operation.

3.2. Morphological Offset Computation

The algorithm (as described in [Molina, 2007]) becomes simple if the concepts of morphologic erosion and dilation are applied as defined above. First of all, the curve is discretized in a set of ordered points p along the length of the curve using a step s. For every point we compute the structuring element centre position (p') that touches that point in a perpendicular direction (v_p) from the shape outside (for outer offset) or inside (for inner offset). That centre p' will be valid if the structuring element placed at p' does not collide with the curve C. Here can be introduced the concept of generalized offset, using a different structuring element for each point.

Obtaining a discrete model for computing the tool path means a loss of precision. On the other hand, the algorithm becomes simpler and faster when a discrete model is used since there are no critical or singular situations. A discrete model of more or less definition can represent every curve. The proper step values will depend on the complexity of the curve.

A pseudo code algorithm is presented below:

```
1:  for every pᵢ ∈ C do
2:      pᵢ' = ObtainSECentre(pᵢ,vₚᵢ);
3:      if not CollideSE(pᵢ',C) then AddTrajectory(pᵢ')
4:  endfor
```

Figure 3.1. Basic pseudo-code algorithm for the morphological offset.

If a point *p* presents a discontinuity in first derivative, we generate a swept of new vectors in order to cover the gap (see figure 3.2). The swept is obtained displacing the structuring element on a circular path around the point of discontinuity. This path is covered in discrete steps, so that a new set of centres is obtained. From that new set we also compute more possible valid structuring element centres, using the same test as before.
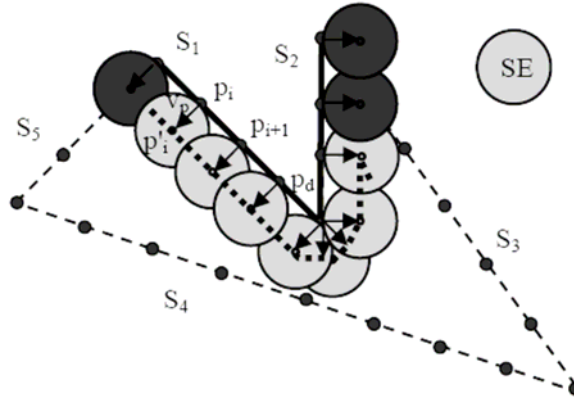
Figure 3.2. Analysis of s_1 and s_2 segments of shape C. Shaded SE positions are discarded due to shape collision. Note that discontinuity at pd is solved by a vector swept generation.

3.3. Algorithm Cost

Computational cost is analysed in this section in terms of the problem size for the algorithm introduced in the algorithm in figure 3.1. The operator used is O to determine an upper limit of the computation cost.

The basic algorithm consists in one external loop and two main function calls. The external loop is used to access every point of the shape. Let's call n the number of points that represent the shape C once it has been discretized. If we use a constant step factor s and the total length of C is L, then n will be L/s points.

The function *ObtainSECentre* computes the centre of the structuring element when it touches a point p in the direction addressed by the v_p vector. So, this function depends of the SE geometry. For simple SEs as circles, rectangles, triangles, and so on, the function can be evaluated at constant time, we call this cost ct. Expression 3.1 shows this function for a circle tool with R in radius.

$$SECentre(p, \overrightarrow{v_p}) = p + R.\overrightarrow{v_p}$$

(Exp. 3.1)

Next function, called *CollideSE(p',C),* returns true if the SE centred in the p' point is not completely inside the shape C and otherwise returns false. In order to evaluate this condition, this function computes the intersection of the SE geometry and the C shape. The cost of this function depends on the C representation. For the experiments we have discretized the shape into a set of contiguous segments that represents the shape within a defined maximum error. Then, every segment is tested (at a constant time), if a segment produces two or more intersections in the SE geometry then function returns true. Note that, in this case, discretization of C shape will be not the same that the previous one that we use to determine centre positions in shape. For shapes with a high degree of co linearity the number of segments will be reduced slightly. Let's call m that number of segments. From experience we obtain $m \ll n$.

The last expression in expression 3.2 shows the quadratic equation used to determine the intersection between a circle centred at origin and a 2D segment defined between the (x_1,y_1) and (x_2,y_2) points for a normalized t range $[0..1]$. As a conclusion, a double solution for t variable in the range $[0..1]$ will cause a true return in the function CollideSE, otherwise the next segment will be analysed.

Segment function:
$$x = x_1 + (x_2 - x_1) \cdot t$$
$$y = y_1 + (y_2 - y_1) \cdot t$$
$$t \in [0..1]$$

Circle function:
$$x^2 + y^2 = R^2$$

Segment-Circle intersection equation on t:
$$\left(x_1 + (x_2 - x_1) \cdot t\right)^2 + \left(y_1 + (y_2 - y_1) \cdot t\right)^2 = R^2$$

(Exp. 3.2)

Finally, the third function, called *AddTrajectory*, appends the new p' centre to the list of successful centres at a constant time, so is not consider for evaluating cost purposes.

We analyse the whole algorithm in order to obtain an upper limit for the computational cost. Expression 3.3 evaluates the cost:

$$\lim_{n,m \to \infty}\left(n \cdot (ct + m)\right) = O(n \cdot m)$$

(Exp. 3.3)

3.4. Morphological Offset for Machining

General morphological offset can have a wide field of use. An important one is the problem of machining pieces using an NC machine as addressed in [Molina, 2008].

In this case, the most important advantage of using morphological offset is the fact that the focus can be done on the machining process itself, without technological considerations. A machining process could be described as the definition of an object (the shape) by means of another object (the tool). This idea is clearly related to a morphological operation, where the shape could be represented as a set X, and the tool could be modelled by a structuring element B.

From the point of view of machining purposes, no specific structuring element geometry is given, that is, this method works for any structuring element geometry. In other words, the concept of offset (classically related to one radius tools) is here generalized, so even rectangular, elliptical or any geometry offset could be obtained. This is particularly useful to no standard pocketing, where other geometry tools are used (i.e. top piece moulds for heels in shoe making are made by means of torical tools with the rotating axe attacking parallel to the surface, in this special case two radii are implied in the machining process. See left side of figure 3.3).
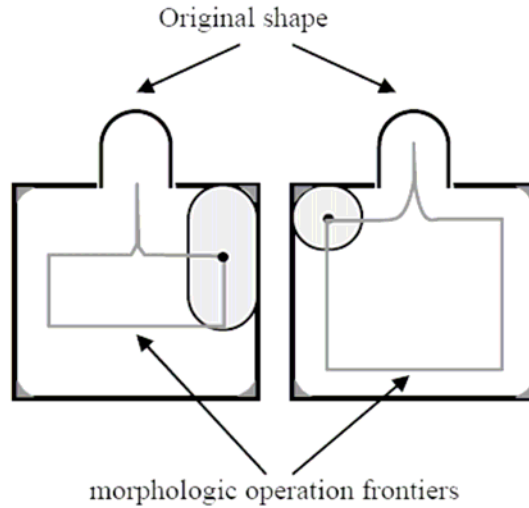
Figure 3.3. Experiment in two dimensions. Shaded regions will not be machined. On the left, a morphological erosion for a toroidal tool (two radii implied). On the right, the classical offset for a spherical tool.

A first problem is the tool compensation, that is, calculating the trajectory that the tool must follow to machine a given curve. The compensated trajectory is, exactly, the offset curve. In this way, we could look at figure 3.4 and observe a morphologic dilation of the shape using a circle as a structuring element (*SE*). The compensated trajectory or offset corresponds to the dilation boundary.
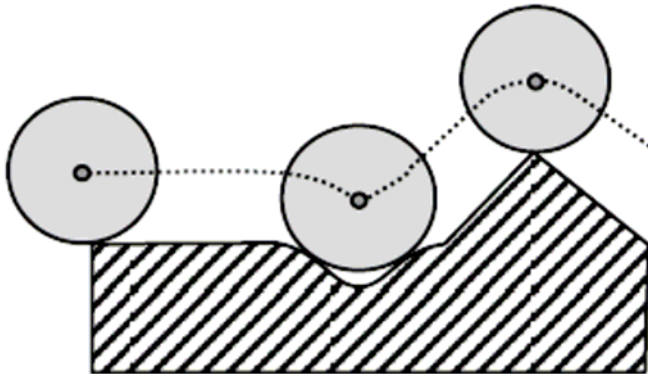
Figure 3.4. Morphologic dilation of a shape using a circle as structuring element.

A similar idea was described in order to obtain pencil tracing trajectories. The process, called virtual digitizing [Jimeno, 2001], defines a tool movement over the part surface as a mechanical digitizer does, virtually touching an object. The virtual digitizing method, restricted to z-maps representations and one radius tools, was also extended to NURBS surfaces used in shoe last machining [Jimeno 2004].

A third problem is the contour pocketing. In this case, the interior of a given curve must be cast. The method is a recursive algorithm that obtains successive interior general

offsets to a given shape (which can be a single or a multiple curve). The base case of the recursion takes place when the offset to the current curve does not exist, because the tool is too large to machine such a curve. In the general case, the algorithm is called recursively for every curve and the resulting offset is added to the final path. Due to the morphological notation, even when there are islands, the algorithm works correctly. In figure 3.5 the operation of the algorithm and the recursion tree are shown. In this figure, let O be the shape to be machined and let I_1 be an island. A first offset curve O_1 is obtained and it is used to recursively compute the offset again. As a consequence of this computation and due to the shape of the curve, three offset curves O_{11}, O_{12} and O_{13} are obtained now. These new curves are recursively offset, until the base case is reached. The recursion tree shows the order of the recursion calls.

An important aspect to control is which sections of the path must be followed at security height. This control is very complex in the recursive method. We alternatively propose an iterative method that uses a stack to simulate the recursions. The iterative version allows us to control the security height and to improve the efficiency of the method.

The stack is used to store the calculated offsets, unstacking and adding them to the list of paths when the curve does not have offsets any further. This case is the same as the base case in the recursive algorithm, so unstacking simulates the procedure of going back in the recursion.

We also use a Boolean flag in the curves, whose value is true when we must continue obtaining new parallels to the curve and false when every parallel is already calculated. We can simulate the recursion tree and identify which points must be machined at security height by using the Boolean flags.
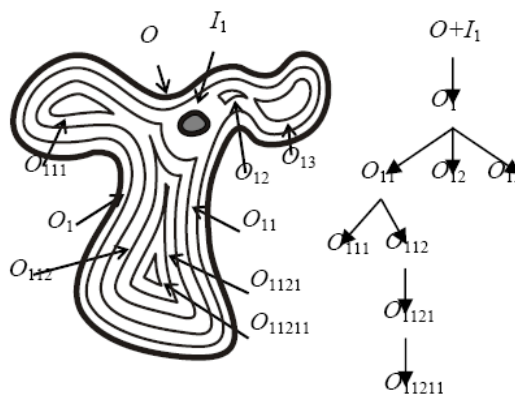
Figure 3.5. Recursive algorithm for contour pocketing. The recursion tree can be easily simulated by a stack.

A pseudo code algorithm is presented below. Let O be the shape to be machined, I be a set of islands and Offset (O,I) a function that calculates the offset of the curve O that includes the set of islands I. This function returns a set of offsets.

```
 1: repeat
 2:    S = Offset(O,I);
 3:    if S ≠ ∅ then
 4:      for every sᵢ ∈ S do
 5:         sᵢ.flag = true;
 6:         Stack (sᵢ);
 7:      endfor
 8:    else
 9:      O = Unstack;
10:      if not O.flag then AddPointAtSecurityHeight;
11:      while not O.flag do
12:        AddTrajectoryToList (O);
13:        O = Heap;
14:        if not O.flag then O = Unstack;
15:      endwhile
16:    endif
17:    O = Heap;
18:    O.flag = false;
19: until EmptyFlag;
```

Figure 3.6. Basic Basic pseudo-code iterative algorithm for contour pocketing.

3.5. Experiments for Offset Computation

We present some experiments to prove four main properties of the morphological approach: generality, validity, optimality and efficiency.
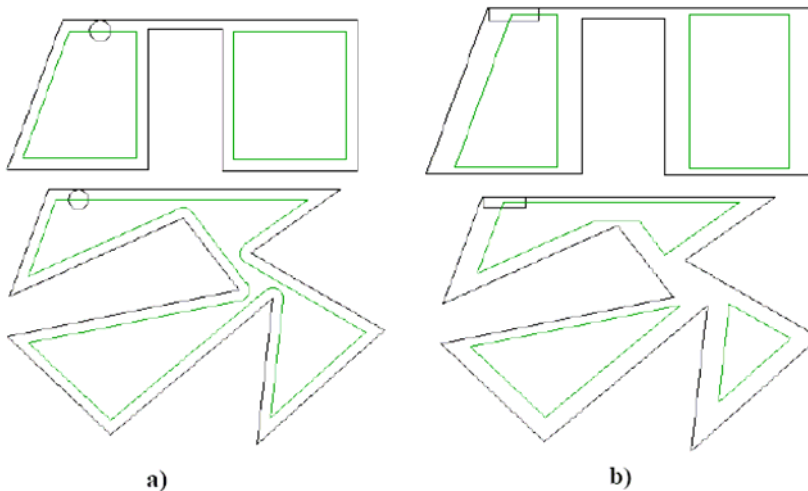
Figure 3.7. Offset of curves using the morphological approach. a) Offset with a one radius tool (e.g. spherical tool). b) Offset with a rectangular tool.

Generality is one of the main advantages of the morphological approach. This feature is referred to as the lack of any constraint in object or tool shape. By definition, no constraint is set up. In figures 3.7 and 3.8 some cases are shown. For instance, no standard pocket machining in shoe making includes cylindrical (figure 3.8b) or torical (figures 3.3 and 3.4) tools attacking the surface with the rotation axe parallel to material.
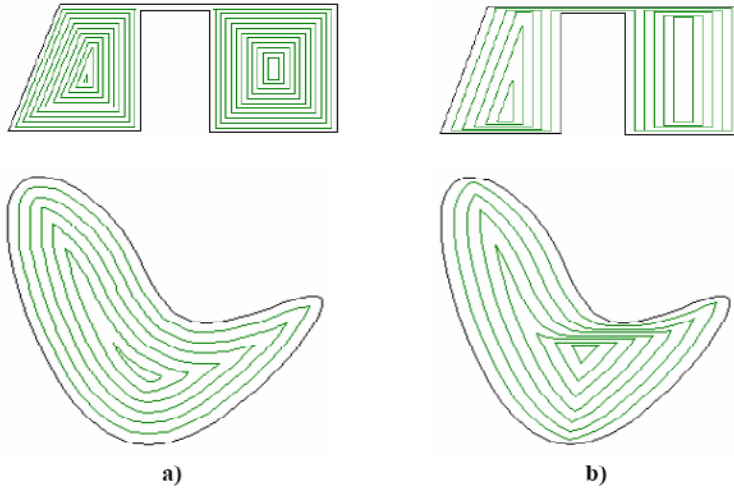
Figure 3.8. Contour pocketing using the morphological approach. a) Pocketing with a one radius tool (e.g. spherical tool). b) Pocketing with a rectangular tool.

From another point of view, generality is also achived by making possible the obtaining of general offset. For instance, in figure 3.9, some examples of general offsets are shown, using as distance function $D(t)=sin(t)$ and $D(t)=k{\cdot}t$.

Figure 3.9. Examples of general offsets. On the left, generic sine offset; at middle and right side, proportional generic offsets.
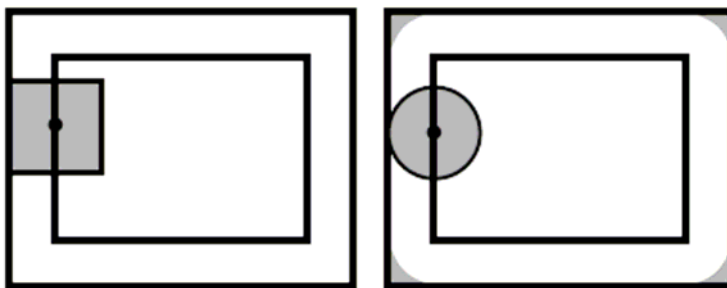
Figure 3.10. Contour pocketing using a free form tool and a one radius tool. Shaded regions will not be machined. On the left, the shape is machined correctly. On the right, some regions are not machined because of the use of a one radius tool.
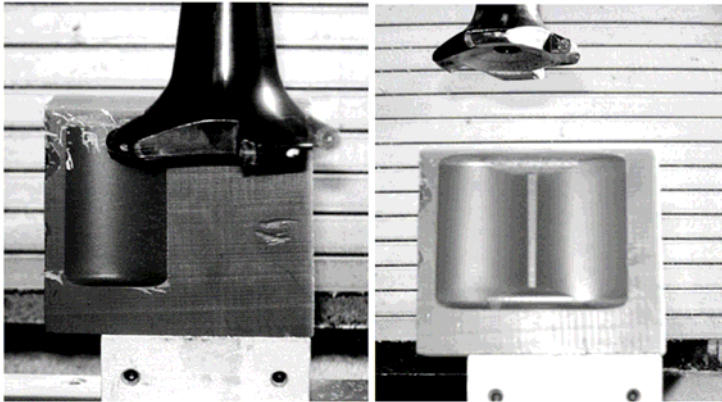
Figure 3.11. A torical tool with the rotating axe attacking parallel to the surface. In this case, the tool can be considered as having two radii.

   Validity and optimality are consequences of generality. As there are no constraints in tool shape, it can be selected to correctly fit the object shape. As a result, it is easier to obtain a valid and optimal trajectory. For example, in figure 3.10 the shape cannot be correctly machined with a classical one-radius tool (some regions are not machined). However, a free form tool as proposed can correctly machine it and, so, would allow us to obtain a valid shape. Moreover, the use of several radii tools is very convenient to obtain optimal trajectories, that is, shorter tool paths that allow the system to machine the shape in a shorter time (see figures 3.3 and 3.11).

   Validity is also achieved from the perspective of the correctness of the trajectory. One of the most powerful features of the morphological method is the fact that it is a formalization of the offset definition, instead of a geometrical or numerical method that approximates this definition. This is a very important feature, because geometrical or numerical problems are avoided. As a result, we can state that the morphological approach, from the theoretical point of view, allows us to obtain valid trajectories. From a practical perspective, it is easy to obtain an algorithm to implement the method, as we have shown above.
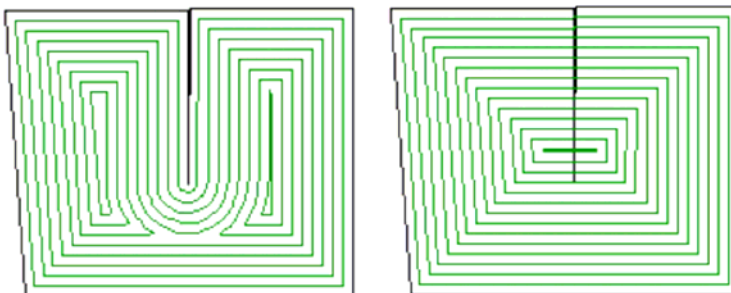
Figure 3.12. Contour pocketing using the morphological approach (left) and the commercial library (right). The library does not detect the two segments that are almost parallel.

   The presented method has been compared with one of the most popular libraries, which is in fact the standard in commercial CAD/CAM systems. Although it is a very good library, it has some precision errors. Specifically, it fails when the angle between two consecutive

segments is too close to 2π. The morphological method does not have this kind of problem, due to the fact that intersections, angles and other geometrical operations are not included in the definition of the formal method. Results are compared in figure 3.12.

Finally, some experiments have been done to prove the cost of the morphological method. In the previous section we defined *n* as the number of points that represent a given shape C once it has been discretized, and *m* the number of segments used to detect collisions. To prove that the cost of the morphological approach is $O(n \cdot m)$ (expression 3.2), we present a set of 50 experiments. Table 3.1 shows the results for 10 of the experiments, representing several kinds of shapes including all the geometrical cases (local and global self-intersections and discontinuities). It shows that, as we stated in the previous section, $m << n$.

Table 3.1. Results for a sample of 10 experiments, n is the number of segments after discretization, m is the number of segments used to detect collisions and t is the time in milliseconds used to obtain the offset

m	n	t
102	2370	31
158	5620	141
198	4772	156
200	3943	140
190	3071	109
161	2461	79
181	5772	172
296	10516	500
391	9702	609
444	6009	531
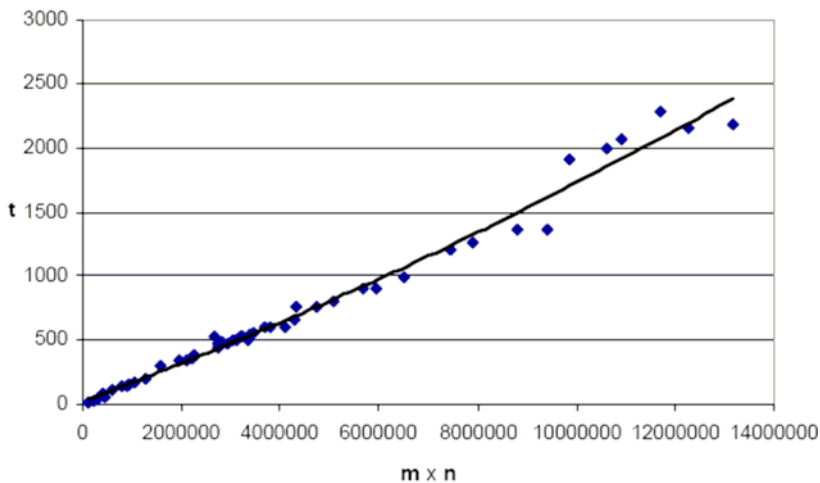
Figure 3.13. Results for a sample of 50 experiments. Time of execution (t) compared with the product of n and m: t is linearly dependent of n × m.

Figure 3.13 shows the results of the 50 experiments (including those in table 3.1), comparing $n \times m$ with the execution time in milliseconds. The time is very clearly related to $n \times m$, so it proves that the theoretical cost $O(n \cdot m)$ is corroborated by the experiments.

Conclusions

During the course of this chapter a specialisation of the formalism proposed by mathematical morphology has been created which has been termed Determinist Topological Model. This specialisation consists of specifying a model which will permit morphological operations to be used which are subject to a particular order or path. In this way the determinism appears explicitly linked to the morphological concept and it is possible to use it to describe trajectories on objects.

The new model redefines the operations of mathematical morphology as a composition of successive basic or elemental operations on which an order is established. In this way the new model proposes the possibility of carrying out partial morphological operations when an ordered path, yet incomplete, path is made of the objects defined.

Each basic operation in a Determinist Topological Model situates the structuring element in a specific position and orientation in the space of representation. This characteristic, which is not considered by the conventional morphological model, permits a whole new range of possibilities as it is possible to carry out operations which implicitly produce a variable orientation of the structuring element.

In particular, the *dilation with trajectory* operation performs an exact offset computation over the selected object.

This section has presented a computational model which enables the morphological operations defined in the Determinist Topological model to be carried out. Its existence makes the new model (DTM) operative and permits its soundness to be checked through testing.

From a study of the temporal costs associated with this computational model, it may be deduced that the calculation method does not grow exponentially with the dimension of the structuring element, as occurs with the methods based on mathematical morphology. This result is of interest in carrying out morphological operations on high density images of points or objects with more than two dimensions, as it is in these cases that traditional methods pose the greatest problems, offering temporal results which would be prohibitive with conventional computers.

The model is sufficiently general in nature to process information either continuously or discretely. Therefore, it may be used on continuous fields of application, such as functions of real variables, surfaces and continuous curves; without having to resort to prior discretisation.

A study on the properties of the computational model raises the possibility of some refinements to it which would improve its efficiency. These include the range of vicinity and the principle of attainability. The former would reduce the temporal complexity of the model in an order of magnitude, and the latter would permit implementation on platforms operating in parallel.

The new proposed model (DTM) is based on the description of trajectory-based morphological operations, that is, a topological system resulted from the application of the conventional morphological model to which the feature of primitive ordering has been added. The proposed operations account for the problems present in the manufacturing processes derived from the tool machining. The implementation of the new morphological primitives, now machining operations, performed in the actual manufacturing process for validation. As a result, a new formalism to define and obtain generalized offsets is presented. This new

formulation, based on morphology, avoids the main problems of the traditional methods, such as self intersections, discontinuities and lack of generality. Specifically, the main features of our method are:

The use of morphology as the base of the formulation avoids certain problems by its own definition: self intersections and discontinuities do not exist in our approach, so they do not have to be treated in any way.

The object to be machined and the tool are free-form shapes, so the method is general and versatile, useful for every pocket shape and tool without any constraint.

As free form tools can be used, we can obtain optimal paths to get correct objects by just choosing the best fitting tool.

The method is based on very simple and accurate calculations, so most numerical and geometrical problems are avoided.

Obtaining the practical algorithm from the theoretical formulation is straightforward, as it has been shown in section 2.4. The resulting procedure is simple and efficient.

We are now working on adapting the formulation approach to three dimensional machining. The method could be especially useful in 5-axis machining. However, the computing cost of the algorithm could be a bottle neck for three dimensions due to the high discretization effect. An extra effort must be made to improve and optimize the algorithm efficiency in 3D.

There are other morphological operations such as dilations, openings, closures etc. which could be useful in the machining domain. We are interested in demonstrating their utility and efficiency for surface reconstruction or trajectory optimization.

References

[Choi, 1999] Choi, B.K., Park, S.C. A pair-wise offset algorithm for 2D point-sequence curve. *Computer-Aided Design* **31**, pp. 735-745, 1999.

[Chuang, 2004] Chuang, J.J., Yang, D.C.H. A laplace-based spiral contouring method for general pocket machining. *ASME International Mechanical Engineering Congress and Exposition (IMECE2004)*, Anaheim (California), Paper No. 2004-6138, 2004

[Ciccimaro, 1998] Ciccimaro, D.A., Everett, H.R., Gilbreath, G.A., Tran, T.T. An Automated Security Response Robot. *SPIE Proc.* 3525: Mobile Robots XIII and Intelligent Transportation Systems, pp 50-61, Boston, Massachusetts, 1-5 November 1998.

[Cohen, 1996] Cohen, J., Varshney, A., Manocha, D., Turk, G., Weber, H., Agarwal, P., Brooks, F., Wright, W. Simplification envelopes. *International Conference on Computer Graphics and Interactive Techniques*, pp. 119 – 128, 1996.

[Eells, 1992] Eells, J. *Harmonic Maps: Selected Papers of James Eells and Collaborators*. World Scientific, 1992.

[Elber, 1997] Elber, G., Lee, I.K., Kim, M.S. Comparing Offset Curve Approximation Methods. *IEEE Computer Graphics & Applications*, **17**(3), pp. 62-71, 1997.

[Elber, 2003] Elber, G. Trimming Local and Global Self-intersections in Offset Curves Using Distance Maps. Lecture Notes in Computer Science. *Mathematics of Surfaces*, vol. 2768/2003, pp. 213-222, 2003.

[EL-Midany, 2002] EL-Midany, T.T., Elkeran, A., Tawfik, H. Sweep-Line Algorithm and Its Application to Spiral Pocketing. *International Journal of CAD/CAM*, **2**(1), pp. 23-38, 2002.

[Farin, 1993] Farin, G. Curves and Surfaces for Computer Aided Geometric Design. A Practical Guide. *Academic Press*, Inc. 1993.

[Farouki, 1990] Farouki, R.T., Sakkalis, T. Pythagorean hodographs. *IBM Journal of Research and Development archive*, vol. 34 , issue 5, pp. 736 – 752, September 1990.

[Held, 1998] Held, M. Voronoi Diagrams and Offset Curves of Curvilinear Polygons. *Computer-Aided Design*, **30**(4), pp. 287-300, 1998.

[Jeong, 1999] Jeong, J., Kim, K. Generating Tool Paths for Free-Form Pocket Machining Using z-Buffer-Based Voronoi Diagrams. *International Journal of Advanced Manufacturing Technology,* **15**, pp. 182-187, 1999.

[Jimeno, 2001] Jimeno, A., García, J., Salas, F. Shoe lasts machining using Virtual Digitising. *International Journal of Advanced Manufacturing Technology*, **17**(10), pp.744-750, 2001.

[Jimeno, 2004] Jimeno, A., Maciá, F., García-Chamizo, J. Trajectory-based morphological operators: a morphological model for tool path computation". *Proc. Internacional conference on algorithmic mathematics & computer science*, AMCS 2004, Las Vegas (USA), 2004.

[Jonker, 1992] Jonker, P. P. *Morphological Image Processing: Architecture and VLSI design.* Kluwer Technische Boeken BV, Deventer, 1992.

[Jung, 1991] Jung W. Park, Yun C. Chung, Bo Hyoung Kim, Byoung Kyu Choi. Pencil Curve Tracing via Virtual Digitizing. *Proc. of IFIP CAPE Conference*, pp.97-104, 1991.

[Lambregts, 1996] Lambregts, C.A.H., Delbressine, F.L.M., de Vries, W.A.H., van der Wolf, A.C.H. An efficient automatic tool path generator for 2 ½ D free-form pockets. *Computers in Industry*, **29**(3), pp. 151-157, 1996.

[Li, 1998] Li ,Y.M., Hsu, V.Y. Curve offsetting based on Legendre series. *Computer-Aided Geometric Design*, **15**, pp. 711-720, 1998.

[Maekawa, 1999] Maekawa, T. An overview of offset curves and surfaces. *Computer-Aided Design*, **31**, pp. 165-173, 1999.

[Matheron, 1975] Matheron, G. *Random Sets and Integral Geometry*. John Wiley & Sons, New York, 1975.

[Molina, 2007] Molina-Carmona, R.; Jimeno, A.; Rizo-Aldeguer, R. Morphological Offset Computing for Contour Pocketing *Journal of Manufacturing Science and Engineering-Transactions of The Asme.*, vol. 129 (2), pp. 400-406, (2007)

[Molina, 2008] Molina–Carmona, R.; Jimeno, A.; Davia, M. "Contour pocketing computation using mathematical morphology" *, International Journal of Advanced Manufacturing Technology* , vol. 36, pp. 334–342, (2008)

[Nikopoulos, 1997] Nikopoulos, N., Pitas, I. An Efficient Algorithm for 3D Binary Morphological Transformations with 3D Structuring Elements of Arbitrary Size and Shape. *Proceedings of 1997 IEEE Workshop on Nonlinear Signal and Image Processing (NSIP'97)*.1997.

[Nikopoulos, 1997] Nikopoulos, N., Pitas, I. An Efficient Algorithm for 3D Binary Morphological Transformations with 3D Structuring Elements of Arbitrary Size and Shape. *Proc. 1997 IEEE Workshop on Nonlinear Signal and Image Processing (NSIP'97)*, 1997.

[O'Rourke, 1993] O'Rourke, J. *Computational Geometry in C*. Cambridge University Press, Cambridge, UK, 1993.

[Park, 2001] Park, S.C., Choi, B.K. Uncut free pocketing tool-paths generation using pair-wise offset algorithm. *Computer-Aided Design*, **33**, pp. 739-746, 2001.

[Pujol, 2000] Pujol, F. A., García-Chamizo, J. M. et al. DSP Implementations of Morphological Filtering: Application to Path Planning Problems. *Proceedings of the 11th Portuguese Conference on Pattern Recognition*, pp. 353-357, Oporto, 2000.

[Serra, 1982] Serra, J. *Image Analysis and Mathematical Morphology*. Academic Press, London, 1982.

[Serra, 1992] Serra, J., Vincent, L. An Overview of morphological filtering. *Circuits Systems Signal Process*, vol. 11, no. 1, pp. 47-108, 1992

[Vincent, 1991] Vincent, L. Morphological transformations of binary images with arbitrary structuring elements. *Image Processing*, **22**(1), pp. 3-23, 1991.

[Wallner, 2000] Wallner, J., Pottmann, H. On the geometry of sculptured surface machining. *Curve and Surface Design*, Vanderbilt University Press, pp. 417-432, 2000.

[Wang, 1996] Wang, Y. Intersection of offsets of parametric surfaces. *Computer-Aided Geometric Design,* **13**, pp. 453-465, 1996.

Chapter 14

A New Computational Chemistry and Complex Networks Approach to Structure-Function and Similarity Relationships in Protein Enzymes

Riccardo Concu[1,2,3], Gianni Podda[2], Eugenio Uriarte[3], Francisco J. Prado-Prado[3], Miguel A. del Río Vazquez [4], and Humberto González-Díaz[,1]*

[1] Department of Microbiology and Parasitology, Faculty of Pharmacy, University of Santiago de Compostela, Santiago de Compostela, 15782, Spain.
[2] Dipartimento Farmaco Chimico Tecnologico, Facoltà di Farmacia, Universitá Degli Studi di Cagliari, Cagliari 09124, Italy.

Abstract

Dobson and Doig (D and D) reported an important but somehow complicated non-linear model for alignment-free prediction of 3D-structures of enzymes opening the search of simpler Computational Chemistry models. In this work we have used Markov Chain Models (MCM) to calculate electrostatic potential, hydrophobic interactions (HINT), and van der Waals (vdw) interactions in 1371 protein structures (essentially the D and D data set). Next, we developed a simple linear model that discriminates 73.5% of enzyme/no-enzyme proteins using only one electrostatic potential while the D and D reaches 80% of accuracy with a non-linear model based on more than 30 parameters. We both analyzed ROC and constructed Complex Networks for the first time in order to study the variations of the three fields in enzymes. Finally, we illustrated the use of the model predicting drug-target enzymes and antibiotic enzymes (enzybiotics). In closing, this MCM allowed fast calculation and comparison of different potentials deriving accurate protein 3D structure-function relationships and protein-protein Complex networks obtained in a way notably simpler than in the previous way.

---

[*] E-mail address: gonzalezdiazh@yahoo.es; Tel: +34-981-563100; Fax: +34-981 594912; Faculty of Pharmacy, USC, Spain (Correspondence to: H. González-Díaz).

List of Abbreviations

SVM   Support Vector Machine
PDB   Protein Data Bank
CN   Complex Network
HINT   Hydrophobic interaction
MCM   Markov Chains Model
LDA   Linear Discriminant Analysis

Introduction

Several facts hinder the prediction of protein function using computational methods based on sequence alignment. In fact, Bioinformatics methods based on sequence alignment may generally fail in cases of low sequence homology between the query and the template sequences deposited in the data base.[1] The lack of function annotation (defined as biological function)[2] for the sequences deposited in databases and used as templates for function prediction, constitutes another weakness of alignment approaches. For instance, in a significant work, Dobson and Doig (D and D)[3] illustrated protein prediction as enzymatic or not from spatial structure without resorting to alignments. They used 32 protein features and a non-linear support vector machine (SVM) to classify more than 1000 proteins with accuracy above 70 to 80%.[4,5] Nowadays we assist at the growing importance of enzymatic proteins in many fields like bio-technologies,[6] enzyme-target drugs,[7] search of new enzybiotics[8] (antimicrobial enzymes) and others.

Considering the growing importance of proteins in these and other fields, we think the prediction of enzymatic proteins is very important. Recently, a group of researchers has published a review[9] on the growing importance of machine learning methods for predicting protein functional class, independent of sequence similarity. In this review the authors make reference to many papers on the topic [10-16] These methods often use the input 1D sequence numerical parameters, specifically defined to seek sequence-function relationships[17-25]. Alternatively, some authors generalized molecular indices which were classically used on small molecules in order to describe protein sequences, such as the generalization of Broto–Moreau indices by Caballero and Fernández *et al.*[26]. On the other hand, many authors have introduced 2D or higher dimension representations of proteins or DNA sequences prior to the calculation of numerical parameters [27-32]. We discussed many of these methods in a recent in-depth review of current topics on medicinal chemistry and bioinformatics.[33]

In any case, all these methods, even aligned independently, are based ultimately on sequence and not on protein 3D structure. In our opinion, 3D Quantitative Structure-Activity Relationships (3D-QSAR)[34-36] methodology, usually applied to small-sized molecules, may become an alternative to sequence methods for 3D-Structure-Function predictions in proteins. A major factor for the future will be necessarily the database growth of

experimentally determined protein structures, through structural genomics projects.[37] In this context, the ability to predict protein function from the experimentally determined 3D structure is becoming increasingly important as the number of resolved structures is growing more rapidly than our capacity to study this function.[38] Some authors have introduced and/or used 2D or 3D parameters for this kind of alignment-independent annotation of protein function[39] and have combined them with Machine Learning methods as in the case of the D and D model and others.[40]

The energetics of biopolymer folding involves free energy, electrostatic, van der Waals (vdW), and/or other terms and it is of high importance in the Biophysics branch of Proteins research[41-45] as it determines the folded structure and finally the function. Thus, the use of 3D QSAR models, dependent of structural parameters based on vdW, Electrostatic, and other molecular potentials is a promising way for the prediction of protein function and the development of new methods incorporating these factors becomes a very important goal.[46,47] For instance, Hou and Zhang *et al.* [48] proposed the use of an energetic decomposition analysis to characterize domain-peptide interactions and the molecular interaction energy components, including vdW, electrostatic, and desolvation energy between residue pairs on the binding interface. In some cases some of these interactions (for instance hydrophobic or vdW) dominate the rest of them[49-50]; thence, the use of fast methods that allow investigation in different fields is of major importance.

Markov Chain Models (MCM) of model-based interactions; for instance the Monte Carlo method has been used in Protein Science to predict important protein interactions.[51] The MARkovian CHemicals IN SIlico DEsign (MARCH-INSIDE 1.0) approach [52] is a MCM [53] of the intra-molecular movement of electrons that has been applied to the computational design of small-sized drugs. In previous studies, we extended this method to perform fast calculation of 2D and 3D alignment independent structural parameters based on molecular vibrations in RNA secondary structures[54], or electrostatic potential,[55,56] and vdW interactions [57,58] in proteins. Currently the method was renamed as MARkov CHains INvariants for SImulation and DEsign (MARCH-INSIDE 2.0) [59] describing more adequately the broad uses of this method. A very recent review published on Proteomics 2008[60] illustrates the necessity of giving general formulae for different kind of molecular fields by incorporating other important factors such as hydrophobic interaction field (HINT), making possible to develop comparative studies and determine the influence of the different fields over biological function. In this work, we give for the first time general MCM formulae in order to calculate local average of 3D-potentials considering neighbor amino acids at different distance including: Electrostatic $e_k(R)$, van der Waals $v_k(R)$, and HINT field $h_k(R)$ and develop 3D-QSAR prediction of enzymes. We used 1371 proteins (689 enzymes and 682 non-enzymes), essentially the same data used by D and D. We calculated three types of total and local potentials for four regions of protein structure (core, inner, middle, and surface). The simplest model we found was able to classify 73.5% of proteins (similar to D and D models)[3] using only one electrostatic potential; the model was carried out using a Linear Discriminant Analysis (LDA).[61] We built up some models performing the cut-off value without a significant increase of the model accuracy; the subsequent step was to build a complex network (CN)[62] to study the relationship between the proteins connected in the network. Finally, we performed a test by applying the LDA model to some proteins and we obtained very encouraging results that support our theory and our method. In closing, the use of MCM allows us to perform fast calculation and comparative study of different types of

potentials and investigate protein structure-function relationships. The advantages in this sense are similar to Comparative Molecular Field Analysis (CoMFA) studies on small-sized drugs.[63]

Material and Methods

Markov Chain Model (MCM)

The method uses as a source of macromolecular descriptors the stochastic matrices $^1\Pi_f$ built up as a squared matrices (n × n), where n is the number of amino acids (aa) in the protein or nucleotides in the nucleic acid sequence. The subscript f points to the type of molecular force field. The used stochastic matrices may encode any potential field including the more common fields: a) short-term vibration field ($\Psi = \nu$, $f_j = \nu_j$) with stochastic matrix $^1\Pi_{vib}$, b) electrostatic (f = e, $f_j = \varphi_j$) with $^1\Pi_e$, c) van der Waals (f = v, $f_j = _j$) with $^1\Pi_{vdw}$, or d) HINT (f = h, $f_j = _j$) with $^1\Pi_h$. In order to extend the method we consider a hypothetical situation where every j^{th}-aa has general potential f_j at an arbitrary initial time (t_0). All these potentials can be listed as elements of the vector $^0\varphi_f$. It can be supposed that, after this initial situation, all the aa interact with the energy $^1_{ij}$ with every other aa_j in the protein. For the sake of simplicity, a truncation function α_{ij} is applied in such a way that a short-term interaction takes place in a first approximation only between neighbouring aa ($\alpha_{ij} = 1$). Otherwise, the interaction is banished ($\alpha_{ij} = 0$)[58]. Neglecting direct interactions between distant aa in $^1\Pi_f$ does not avoid the possibility of potential interaction propagation between those aa within the protein backbone in an indirect manner. Consequently, in the present model, long-range interactions are possible (not forbidden) but estimated indirectly using the natural powers of $^1\Pi_f$. The use of MCM theory allows a simple and fast model to calculate the average values of π_k, considering indirect interaction between any aa_j and the other aa_i after previous interaction of aa_j with other k neighbour amino acids.[53] As follows, we give the general formula for any potential and specific formulae as well:

$$^f\pi_k(o) = \sum_{j=1 \in o}^{n \in o} {}^k p_{jj} = Tr\left({}^k\mathbf{\Pi}_f\right)_{\in o} = Tr\left(\left({}^1\mathbf{\Pi}_f\right)^k\right)_{\in o}$$

(1)

$$^e\pi_k(o) = \sum_{j=1 \in o}^{n \in o} {}^k p_{jj} = Tr\left({}^k\mathbf{\Pi}_e\right)_{\in o} = Tr\left(\left({}^1\mathbf{\Pi}_e\right)^k\right)_{\in o}$$

(1a)

$$^h\pi_k(o) = \sum_{j=1 \in o}^{n \in o} {}^k p_{jj} = Tr\left({}^k\mathbf{\Pi}_h\right)_{\in o} = Tr\left(\left({}^1\mathbf{\Pi}_h\right)^k\right)_{\in o}$$

(1b)

$$^v\pi_k(o) = \sum_{j=1 \in o}^{n \in o} {}^k p_{jj} = Tr\left({}^k\mathbf{\Pi}_v\right)_{\in o} = Tr\left(\left({}^1\mathbf{\Pi}_v\right)^k\right)_{\in o}$$

(1c)

where, in the symbols $^f\pi_k(o)$ used in the equations have the following elements: π indicates that we are using an spectral moment of the stochastic matrix, the letter f represents the type

of potential (e,h, or v), k is the topological distance between the amino acids considered and the letter (o) between brackets indicates the orbit of amino acids considered in the calculation. [78] In other words, c, i, m and s are called orbits (O) and constitute specific groups or collections of amino acids placed at the protein core (c), inner (i), middle (m) or surface region (s). In figure 1 we represented a protein with its orbits (i correspond to core, ii to inner, iii to middle, and iv to surface). The orbit diameters, as a percentage of the longer distance according to the charge centre, are between 0 and 25 for orbit c, between 26 and 50 for orbit i, between 51 and 75 for orbit m, between 76 and 100 for orbit s.[64]
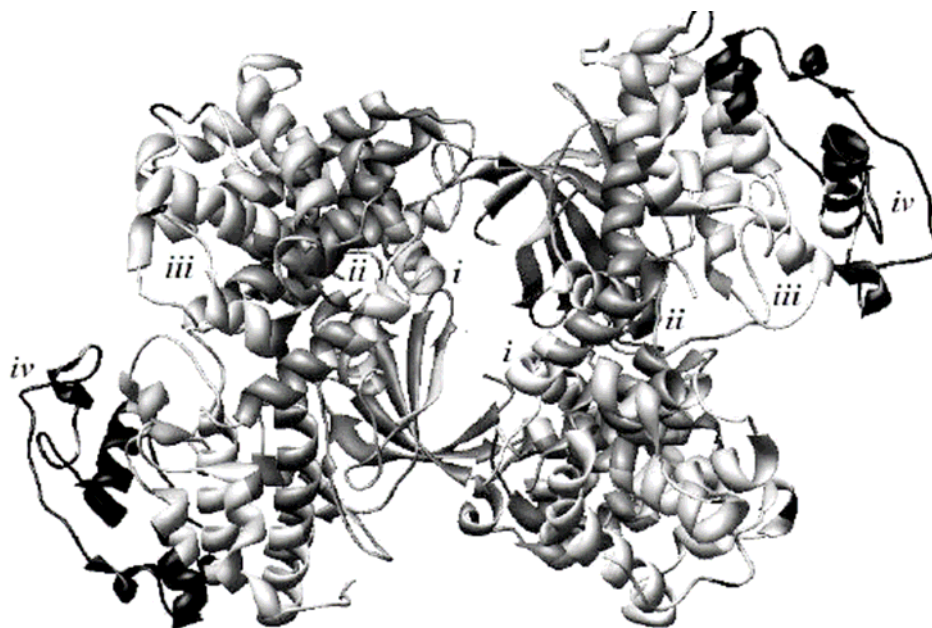
Figure 1. Illustration of the protein orbits or regions.

In particular, the evaluation of such expansions for k = 0 gives the initial average unperturbed electrostatic potential (e_0); for k = 1 the short-range potential (e_1), for k = 2 the middle-range potential (e_2), and for k = 3 the long-range one. This expansion is illustrated for the tripeptide Ala-Val-Trp (AVW):

$$\pi_0(e) = Tr\left(\begin{bmatrix} {}^1p_{AA} & {}^1p_{AV} & 0 \\ {}^1p_{VA} & {}^1p_{VV} & {}^1p_{VW} \\ 0 & {}^1p_{WV} & {}^1p_{WW} \end{bmatrix}^0\right) = Tr\begin{bmatrix} 1 & 0 & 0 \\ 0 & 1 & 0 \\ 0 & 0 & 1 \end{bmatrix} = 3$$

(2a)

$$\pi_1(e) = Tr\left(\begin{bmatrix} {}^1p_{AA} & {}^1p_{AV} & 0 \\ {}^1p_{VA} & {}^1p_{VV} & {}^1p_{VW} \\ 0 & {}^1p_{WV} & {}^1p_{WW} \end{bmatrix}\right) = {}^1p_{AA} + {}^1p_{VV} + {}^1p_{WW}$$

(2b)

$$\pi_2(e) = Tr\left(\begin{bmatrix} {}^1p_{AA} & {}^1p_{AV} & 0 \\ {}^1p_{VA} & {}^1p_{VV} & {}^1p_{VW} \\ 0 & {}^1p_{WV} & {}^1p_{WW} \end{bmatrix} \cdot \begin{bmatrix} {}^1p_{AA} & {}^1p_{AV} & 0 \\ {}^1p_{VA} & {}^1p_{VV} & {}^1p_{VW} \\ 0 & {}^1p_{WV} & {}^1p_{WW} \end{bmatrix}\right) = Tr\begin{bmatrix} {}^2p_{AA} & {}^2p_{AV} & {}^2p_{AW} \\ {}^2p_{VA} & {}^2p_{VV} & {}^2p_{VW} \\ 0 & {}^2p_{WV} & {}^2p_{WW} \end{bmatrix} = {}^2p_{AA}+{}^2p_{VV}+{}^2p_{WW}$$

(2c)

$$\pi_k(e) = Tr\left(\begin{bmatrix} {}^1p_{AA} & {}^1p_{AV} & 0 \\ {}^1p_{VA} & {}^1p_{VV} & {}^1p_{VW} \\ 0 & {}^1p_{WV} & {}^1p_{WW} \end{bmatrix} \cdot \begin{bmatrix} {}^1p_{AA} & {}^1p_{AV} & 0 \\ {}^1p_{VA} & {}^1p_{VV} & {}^1p_{VW} \\ 0 & {}^1p_{WV} & {}^1p_{WW} \end{bmatrix} \cdots \left(\begin{bmatrix} {}^1p_{AA} & {}^1p_{AV} & 0 \\ {}^1p_{VA} & {}^1p_{VV} & {}^1p_{VW} \\ 0 & {}^1p_{WV} & {}^1p_{WW} \end{bmatrix}\right)_{k-2}\right) = Tr\begin{bmatrix} {}^kp_{AA} & {}^kp_{AV} & {}^kp_{AW} \\ {}^kp_{VA} & {}^kp_{VV} & {}^kp_{VW} \\ {}^kp_{WA} & {}^kp_{WV} & {}^kp_{WW} \end{bmatrix} = {}^kp_{AA}+{}^kp_{VV}+{}^kp_{WW}$$

(2d)

In order to carry out the calculations referred to in equations (1) for any kind of potential and detailed in (2a), (2b), (2c) and (2d), for electrostatic potential the elements (${}^1p_{ij}$) of ${}^1\Pi_f$ and the absolute initial probabilities ${}^Ap_k(j)$ were calculated as follows[65] (see for instance, equations 3 and 4 for the general case; 3a and 4a for the particular electrostatic potential case, or 3b and 4b for the vdW case).

$$^1p_{ij} = \frac{\alpha_{ij} \cdot E_{ij}}{\sum\limits_{m=1}^{\delta+1} \alpha_{im} \cdot E_{im}} = \frac{\alpha_{ij} \cdot \psi_j(w_i, w_j, d_{ij})}{\sum\limits_{m=1}^{\delta+1} \alpha_{im} \cdot \psi_j(w_i, w_j, d_{ij})} = \frac{\alpha_{ij} \cdot \varphi_j}{\sum\limits_{m=1}^{\delta+1} \alpha_{im} \cdot \varphi_m}$$

(3)

$$^1p_{ij} = \frac{\alpha_{ij} \cdot E_{ij}}{\sum\limits_{m=1}^{\delta+1} \alpha_{im} \cdot E_{im}} = \frac{\alpha_{ij} \cdot \dfrac{q_i \cdot q_j}{d_{ij}}}{\sum\limits_{m=1}^{\delta+1} \alpha_{im} \cdot \dfrac{q_i \cdot q_m}{d_{im}}} = \frac{\alpha_{ij} \cdot q_i \cdot \dfrac{q_j}{d_{ij}}}{q_i \cdot \sum\limits_{m=1}^{\delta+1} \alpha_{im} \cdot \dfrac{q_m}{d_{im}}} = \frac{\alpha_{ij} \cdot \dfrac{q_j}{d_{ij}}}{\sum\limits_{m=1}^{\delta+1} \alpha_{im} \cdot \dfrac{q_m}{d_{im}}} = \frac{\alpha_{ij} \cdot \varphi_j}{\sum\limits_{m=1}^{\delta+1} \alpha_{im} \cdot \varphi_m}$$

(3a)

$$^1p_{ij} = \frac{\alpha_{ij} \cdot E_{ij}}{\sum\limits_{m=1}^{\delta+1} \alpha_{im} \cdot E_{im}} = \frac{\alpha_{ij} \cdot \left(\dfrac{a_j}{d_{ij}^{12}} - \dfrac{b_j}{d_{ij}^{6}}\right)}{\sum\limits_{m=1}^{\delta+1} \alpha_{im} \cdot \left(\dfrac{a_m}{d_{ij}^{12}} - \dfrac{b_m}{d_{ij}^{6}}\right)}$$

(3b)

where, w_i are the weights or parameters of the amino acid related to the specific potential field and f is a non-negative potential function of w and d. For instance, q_i and q_j are the electronic charges, and a_j and b_j are the vdW field parameters the ith-aa and the jth-aa, and neighbourhood relationship (truncation function $\alpha_{ij}= 1$) was turned on if these amino acids are connected by a peptidic hydrogen bond or $d_{ij}< d_{cut-off}= 5$ Å. [66] In this sense, truncation of the molecular field is usually applied to simplify all the calculations in large biological systems [67]. The distance d_{ij} is the Euclidean distance between the Cα atoms of the two amino acids and d_{0j} is the distance between the amino acid and the centre of the protein charge. Both kinds of distances were derived from the x, y, and z coordinates of the amino acids collected from the protein PDB files.[68] All calculations were carried out with our in-house software MARCH-INSIDE.[58] All water molecules and metal ions were removed for calculation.

LDA Study

We started training some models using all variables for any class of potential in order to train and find some good models. After this first step we trained the models with the LDA forward stepwise;[69] subsequently some models were carried out with only one variable each time, these variables are the same we have found training the model using the forward stepwise analysis. After this, using the Randic method,[70] we orthogonalized all the variables with respect to the best variables we found, in order to investigate the models and the variable means with great detail. All the models are carried out with the software STATISTICA 6.0®,[71] license acquired by our research group. Using STATISTICA 6.0® we made the orthogonalization protocol because we saw that our variables were collinear. All the variables included in the model were standardized in order to be brought onto the same scale. Subsequently, a standardized linear discriminant equation that allows comparison of their coefficients was obtained.[72] The square of Mahalanobis's distance (D^2) and Wilk's (λ) statistic ($\lambda = 0$ perfect discrimination, being $0 < \lambda < 1$) were examined in order to assess the discriminatory power of the model. [73]

CN Study

In order to perform the enzyme activity with a network approach we carried out the following steps:

1   First, we calculated the molecular descriptors included in the QSAR equation for 1371 proteins selected using the MARCHINSIDE® software.
2   We calculated the scores of enzyme activity for each of the 689 enzymatic proteins against all the non-enzymatic protein studied here, by substituting the molecular descriptors into the QSAR equation, using the Microsoft Excel[74] application.
3   Using Microsoft excel again, we transformed the distance matrix into a Boolean matrix. The elements of this matrix are equal to 1 either if two proteins have a high correlation or they are very close [short distance (1 2 Pearson r)]. The cut-off value used was chosen in order to have the entire network with a number of disconnect protein equal to 0. The line command used in Excel to transform the distance matrix into a Boolean matrix was: f= if (D3 = F1, 0, if (ABS(0.02*($E3 - F$2)) > E1, 0, 1)). In this function: D3 and F1 are references to the heads of rows and columns of the matrix; $E3 and F$2 are references to the elements in the distance matrix; and E1 is an absolute reference to a cut-off value cell. It allows transforming distance into Boolean values and it equals the main diagonal elements to 0, avoiding loops in the future network. The Boolean matrix was saved as a .txt format file
4   Next, renaming the.txt file as a .mat file we read it with the software CentiBin.[75] Using CentiBin we can not only represent the network but also highlight all enzymes (nodes) connected and in fact calculating many parameters including node degree, average node degree, density of the network, and some others.
5   CentiBin software was used to generate one random network by the Erdos–Renyi random algorithm.

Data Bases of Enzybiotics and Enzyme Targets

The database extracted from PDB to test the model with enzybiotics and enzyme-target drugs were 109 and 54 proteins, respectively. For the database recovery on the enzyme target drugs, a search through the EC numbers[76] retrieved in a table on the article of Robertson et al. was first carried out; in the web page of the IUMB Enzyme Nomenclature 54 of 71 enzyme, reported in the above-named article, had a direct link to the web page of the PDB where the molecules could be downloaded. For the enzybiotics database we made a simple research on the PDB with the lysine phage key word; the result was 109 enzymes of this enzyme class. The subsequent step was to calculate the potential of all the molecules through the MARCH-INSIDE using the same parameters, like cut-off value, used to calculate the protein in the model.

Results and Discussion

LDA Models

In this study we used MCM to calculate average non-interacting (e_0, v_0, h_0), short-range (e_1, v_1, h_1), middle-range (e_2, v_1, h_1), and long-range electrostatic, vdW, and HINT interactions (e_k, v_k, $h_k > 3$) in different regions for 689 proteins. All the PDB files with the 3D protein structures [77] and their classification into enzymes or non-enzymes were taken from the literature [4,5]. The aforementioned descriptors were subsequently used to carry out a LDA with a random training subset of proteins in order to classify each one as enzyme or non-enzyme. The best model found was:

$$Enzyme-score = 0.02 \times {}^e\pi_2(t) - 0.64$$

$$N = 823 \qquad \lambda = 0.86 \qquad F = 118.60 \qquad p < 0.001$$

$$\tag{4}$$

where, in the symbols ${}^e\pi_k(o)$ used in the equations have the following elements: π indicates that we are using an spectral moment of the stochastic matrix, the letter e represents the electrostatic potential, k is the topological distance between the amino acids considered and the letter (o) between brackets indicates the orbit of amino acids considered in the calculation.[78] In equation (1) the value N = 823 is the number of proteins used to train the model, which were randomly selected out of the first 1370. The statistical parameters of the above equation were also shown including Wilk's statistic (λ), Fischer Ratio (F) and significance level (p-level).[79] The model can classify correctly 294 out of 414 enzymes in the train series with a 71.01% accuracy level, 198 out of 275 in the validation series with a 72.00% accuracy level, 492 out of 689 in a training + validation series with a 71.41% accuracy level, and 251 out of 344.5 the average accuracy level was 72.86%; this accuracy was obtained using a linear model based on the electrostatic potential with only 1 protein feature. In addition to this model we found two more models based on the van der Waals and Hint potential, with a very good accuracy; both models have a 74.8% accuracy level. In table 1 we report some other models obtained using the Electrostatic, van der Waals, and HINT

spectral moment and the combination of the three potentials; in this table we can observe that there is a good model obtained with every potential.

Table 1. Summary of the LDA-QSAR models

Potential [a]	VS[b]	p[c]	Vars[d]	Variables in the model[e]	NE[f]	E[f]	T[f]
D and D	SVM		52	---	---	---	77
D and D	SVM		36	---	---	---	80.9
E	STD	0.56	30	All	75.1	74.0	74.5
E	FWD	0.55	2	$^e\pi_2(t), {}^e\pi_4(t)$	73.3	75.9	74.6
E	STD	0.55	1	$^e\pi_4(t)$	75.4	70.1	72.7
E*	STD	0.55	1	$^e\pi_2(t)$	75.5	71.4	73.5
V	STD	0.59	30	All	74.0	74.7	74.4
V	FWD	0.56	2	$^v\pi_4(t), {}^v\pi_3(t)$	75.1	73.1	74.1
V	STD	0.55	1	$^v\pi_3(t)$	75.7	73.7	74.7
V	STD	0.55	1	$^v\pi_4(t)$	75.7	73.9	74.8
H	STD	0.58	30	All	77.3	72.4	74.8
H	FWD	0.56	2	$^h\pi_4(t), {}^h\pi_3(t)$	75.7	73.1	74.4
H	STD	0.55	1	$^h\pi_3(t)$	76.0	73.6	74.8
H	STD	0.55	1	$^h\pi_4(t)$	76.0	73.6	74.8
E+V	STD	0.58	60	All	75.4	74.7	75.1
E+V	FWD	0.56	2	$^v\pi_4(t), {}^v\pi_3(t)$	75.1	73.1	74.1
E+V	STD	0.56	4	$^e\pi_2(t), {}^e\pi_4(t), {}^v\pi_4(t), {}^v\pi_3(t)$	77.7	75.6	76.7
E+H	STD	0.58	60	All	78.0	74.3	76.1
E+H	FWD	0.56	5	$^h\pi_5(t), {}^h\pi_4(t), {}^h\pi_3(t), {}^e\pi_5(t), {}^e\pi_3(t)$	75.5	73.6	74.5
V+H	STD	0.59	60	All	73.6	72.9	72.9
V+H	FWD	0.56	2	$^h\pi_4(t), {}^h\pi_3(t)$	75.7	73.1	74.4
V+H	STD	0.57	4	$^v\pi_4(t), {}^v\pi_3(t), {}^h\pi_4(t), {}^h\pi_3(t)$	74.3	76.6	75.5
E+V+H	STD	0.57	90	All	78.4	72.7	75.6
E+V+H	FWD	0.57	5	$^e\pi_5(t), {}^e\pi_3(t), {}^h\pi_5(t), {}^h\pi_4(t), {}^h\pi_3(t)$	72.4	75.6	74.0
E+V+H	STD	0.56	6	$^e\pi_2(t), {}^e\pi_4(t), {}^v\pi_4(t), {}^v\pi_3(t) \ h \ ^h\pi_4(t), {}^h\pi_3(t)$	76.7	75.2	75.9

[a] Fields investigated: E =electrostatic; V =Van der waals; H = Hint;
[b] VS = Variable Selection technique FWD= forward stepwise; STD= standard;
[c] p = prior probability of the model to classify a protein as enzyme;
[d] Number of variables in the model
[e] Fields notation: *e*=electrostatic; *v*=Van der waals; *h*=Hint;
[f] Accuracy values (%) NE= no-enzymes; E= Enzymes; T= Total.

In order to investigate the results obtained with the LDA models we have orthogonalized the most important variables we found, by studying the results of the various models we have obtained. At the orthogonal transformation we trained some models with the same process and the same variables as those of the LDA model; the results we found were very interesting because after the orthogonalization process we did not find models that confirm the good results we obtained after the process. Our best models with these new protein features had a 58.3% average accuracy, with only one van der Waals variable, and 56.2% with only one Hint variable. In table 2 we report some other models obtained with the new protein features.

Table 2. Summary of the LDA models with the orthogonalized variable

Potential [a]	VS[b]	p[c]	Vars[d]	Variables in the model[e]	NE[f]	E[f]	T[f]
D and D	SVM		52	---	---	---	77
D and D	SVM		36	---	---	---	80.9
One-potential models							
E	STD	0.56	30	All	75.1	74	74.5
E	FWD	0.55	2	$^e\pi_2(t)$, $^e\pi_4(t)$	73.3	75.9	74.6
E	STD	0.55	1	$^e\pi_4(t)$	75.4	70.1	72.7
E	STD	0.55	1	$^e\pi_2(t)$	75.5	71.4	73.5
V	STD	0.59	30	All	74	74.7	74.4
V	FWD	0.56	2	$^v\pi_4(t)$, $^v\pi_3(t)$	75.1	73.1	74.1
V	STD	0.55	1	$^v\pi_3(t)$	75.7	73.7	74.7
V	STD	0.55	1	$^v\pi_4(t)$	75.7	73.9	74.8
H	STD	0.58	30	All	77.3	72.4	74.8
H	FWD	0.56	2	$^h\pi_4(t)$, $^h\pi_3(t)$	75.7	73.1	74.4
H	STD	0.55	1	$^h\pi_3(t)$	76	73.6	74.8
H	STD	0.55	1	$^h\pi_4(t)$	76	73.6	74.8
Two-potential models							
E+V	STD	0.58	60	All	75.4	74.7	75.1
E+V	FWD	0.56	2	$^v\pi_4(t)$, $^v\pi_3(t)$	75.1	73.1	74.1
E+V	STD	0.56	4	$^e\pi_2(t)$, $^e\pi_4(t)$, $^v\pi_4(t)$, $^v\pi_3(t)$	77.7	75.6	76.7
E+H	STD	0.58	60	All	78	74.3	76.1
E+H	FWD	0.56	5	$^h\pi_5(t)$, $^h\pi_4(t)$, $^h\pi_3(t)$, $^e\pi_5(t)$, $^e\pi_3(t)$	75.5	73.6	74.5
V+H	STD	0.59	60	All	73.6	72.9	72.9
V+H	FWD	0.56	2	$^h\pi_4(t)$, $^h\pi_3(t)$	75.7	73.1	74.4
V+H	STD	0.57	4	$^v\pi_4(t)$, $^v\pi_3(t)$, $^h\pi_4(t)$, $^h\pi_3(t)$	74.3	76.6	75.5
Three-potential models							
E+V+H	STD	0.57	90	All	78.4	72.7	75.6
E+V+H	FWD	0.57	5	$^e\pi_5(t)$, $^e\pi_3(t)$, $^h\pi_5(t)$, $^h\pi_4(t)$, $^h\pi_3(t)$	72.4	75.6	74
E+V+H	STD	0.56	6	$^e\pi_2(t)$, $^e\pi_4(t)$, $^v\pi_4(t)$, $^v\pi_3(t)$ h $^h\pi_4(t)$, $^h\pi_3(t)$	76.7	75.2	75.9

[a] Fields investigated: E =electrostatic; V =Van der waals; H = Hint;
[b] VS = Variable Selection technique FWD= forward stepwise; STD= standard;
[c] p = prior probability of the model to classify a protein as enzyme;
[d] Number of variables in the model
[e] Fields notation: *e*=electrostatic; *v*=Van der waals; *h*=Hint;
[f] Accuracy values (%) NE= no-enzymes; E= Enzymes; T= Total.

LDA-CN Models

We can use the CNs to derived and/or select new structural indices for Computational Chemistry studies. For instance, taking into consideration the structure of the CN given a cut-off value we can calculate the average of the difference between the spectral moments of a protein (i) and all its neighbors (j) in the CN, the number of neighbors is the node degree of the proteins (δ_i). This kind of difference parameter $^f\Delta_k(o)$ derived from the CN give information on how far the protein deviates from the parameters presented by their neighbors in the CN. Considering that in all the models presented here the more important spectral moments are of type total we calculated differences indices only for total spectral moments

and omit the t in the notation of the difference indices from now on $^f\Delta_k(t) = {}^f\Delta_k$. The general formula and some examples of particular formulas used in this work appear at follows:

$$^f\Delta_k(o) = \frac{1}{n}\sum_{k=1}^{\delta_i}\left({}^f\pi_k(o)_i - {}^f\pi_k(o)_j\right)$$

(5)

$$^e\Delta_5 = \frac{1}{n}\sum_{k=1}^{\delta_i}\left({}^e\pi_5(t)_i - {}^e\pi_5(t)_j\right)$$

(5a)

$$^v\Delta_1(o) = \frac{1}{n}\sum_{k=1}^{\delta_i}\left({}^v\pi_1(t)_i - {}^v\pi_1(t)_j\right)$$

(5b)

In table 3 we report our investigation about these features; moreover we report the values of the average node degree, the isolated protein in the network, the percentage of the isolated and some other values we used subsequently to analyze the complex network.

Table 3. Summary of the cut-off scanning for different networks

Field[a]	E		V* vs. V				H* vs. H			
cut-off	δ[b]	u[c]	δ*	u*	δ	u	δ*	u*	δ	u
0.1	1	1005	2	61	0	1300	114	3	0	1296
0.2	1	768	3	50	0	1260	429	1	0	1255
0.3	3	382	3	46	0	1216	195	0	0	1213
0.4	4	216	3	43	0	1192	269	0	0	1181
0.5	5	185	15	38	0	1156	167	0	0	1150
0.7	5	130	34	44	1	1098	167	0	0	1092
0.9	6	107	93	30	1	1055	167	0	1	1049
1	8	89	111	29	1	1038	167	0	1	1033
2	11	36	183	14	2	746	167	0	2	732
2.1	11	33	165	13	2	712	167	0	2	697
2.2	11	33	173	11	2	661	167	0	2	660
2.3	11	31	148	10	2	631	167	0	2	611
2.4	11	31	155	10	3	586	167	0	3	572
2.5	11	30	167	8	3	533	167	0	3	520
2.6	11	28	172	8	3	525	167	0	3	472
2.7	11	27	172	8	3	505	167	0	3	436
2.8	11	24	187	7	3	461	167	0	3	416
2.9	11	22	202	5	3	439	167	0	3	400
3	13	14	217	6	4	407	167	0	4	390
5	116	2	346	0	5	202	167	0	5	171
6	119	1	332	0	5	145	167	0	5	140
6.5	80	1	340	0	5	137	167	0	5	131
10	267	0	304	0	6	87	167	0	6	86
50	167	0	167	0	74	1	167	0	72	1
60	167	0	167	0	100	0	167	0	100	0

[a] Field: Indicates the type of potential used to derive the network E: Electrostatic, V: van der Waals, and H: HINT, [b] δ is the average node degree and [c] u the number of nodes that remain unconnected for a given cut-off value, the symbols δ* and u* have the same meaning but the * indicates that we used a QSAR model with orthogonal variables to construct the CN.

We apply this method on the variables before and after the procedure of orthogonalization and then we train some models using the same method applied for the LDA models we have just mentioned. After this process we did not obtain considerable improvement of our model, none of the new variables could improve our first model. In table 4 we report all the models carried out with these new variables and with the same method we used to train the other LDA models. We can easily observe in the table that only by the combination of some variables, we get similar results to the model we have just reported.

Table 4. Summary of the QSAR and QSAR+CN models obtained before and after orthogonalization

Potential [a]	VS[b]	Before [c]	T [c]	After [d]	T[* e]
D and D	SVM	---	77	---	---
D and D	SVM	---	80.9	---	---
E	STD	All	71.7	Same	71.7
E	FWD	$^e\pi_2(t)$, $^e\Delta_5$, $^e\Delta_1$	71.9	Same	71.9
E	STD	$^e\pi_2(t)$	73.5	Same	73.5
E	STD	$^e\Delta_5$	62.1	Same	62.1
E	STD	$^e\Delta_4$	67.5	Same	67.5
V	STD	All	74.4	Same	69.3
V	FWD	$^v\pi_4(t)$, $^v\Delta_5$, $^v\Delta_1$	74.3	$^v\Delta_1{}^*$	70.4
V	STD	$^v\pi_4(t)$	74.8	Same	58.3
V	STD	$^v\Delta_5$	64.7	---	---
V	STD	$^v\Delta_1$	66.9	---	---
H	STD	All	74.5	All	59.9
H	FWD	$^h\pi_4(t)$, $^h\Delta_5$, $^h\Delta_1$	75.3	$^h\Delta_1{}^*$	60.0
H	STD	$^h\pi_4(t)$	74.8	Same	56.2
H	STD	$^h\Delta_5$	66.4	Same	
H	STD	$^h\Delta_1$	66.1	Same	
E+V	STD	All	73.6	All	67.0
E+V	FWD	$^v\pi_4(t)$, $^v\Delta_5$, $^v\Delta_1$, $^v\Delta_4$, $^v\Delta_2$	74.1	$^e\Delta_2$, $^e\Delta_2$, $^v\Delta_1{}^*$	65.8
E+V	STD	$^v\Delta_5$, $^v\Delta_1$, $^v\Delta_4$, $^v\Delta_2$	67.5	Same	
E+H	STD	All	73.7	All	72.1
E+H	FWD	$^h\pi_4(t)$, $^e\Delta_5$, $^h\Delta_1$, $^e\Delta_2$, $^e\Delta_4$, $^e\pi_4(t)$, $^h\Delta_3$	75.1	$^e\pi_4(t)$, $^v\pi_4(t)$, $^e\Delta_5$	73.9
V+H	STD	---	75.3	Same	58.7
V+H	FWD	$^e\Delta_5$, $^h\Delta_1$, $^e\Delta_2$, $^e\Delta_4$, $^h\Delta_3$	75.1	$^h\Delta_1{}^*$, $^v\Delta_1{}^*$	63.7
V+H	STD	$^h\Delta_1$, $^e\Delta_5$, $^e\Delta_4$, $^h\Delta_3$	71.8	Same	
E+V+H	STD	---	74.9	Same	71.55
E+V+H	FWD	$^h\pi_4(t)$, $^e\Delta_5$, $^h\Delta_1$, $^v\Delta_4$, $^v\Delta_3$, $^e\Delta_2$	75.9	$^e\pi_2(t)$, $^h\pi_4(t)$, $^e\Delta_5$, $^v\Delta_1{}^*$	72.21

[a] Fields investigated: E =electrostatic; V =Van der waals; H = Hint;
[b] VS = Variable Selection technique FWD= forward stepwise; STD= standard;
[c] Variables in the model and Total Accuracy % values before (T) and after (T[*]) orthogonalization.

CN Topology

We build our complex network with our most important variables before and after orthogonalizing them; these variables are the most important for electrostatic, van der Waals, and Hint. We compare the network, built with the electrostatic variable, with one random network; the other network built with the van der Waals and Hint variables are compared before and after the orthogonalizing process. The network used to compare the network

Table 5. Effect of the Randic's orthogonalization on Complex Networks topology

Electrostatic	value	TI [a]	value	Erdos Renyi
	689	n	689	
	36862	m	21454	
	877136	W	907100	
	4	D	3	
	1.85	Dist	1.91	
	0.155	C	0.091	
van der Waals	**value**	**TI**	**value**	**van der Waals [b]**
	689	n	689	
	25033	m	37533	
	899706	W	907100	
	3	D	2	
	1.8980	Dist	1.9136	
	0.106	C	0.158	
HINT	**value**	**TI**	**value**	**HINT [b]**
	689	n	689	
	25135	m	26358	
	899510	W	895430	
	4	D	3	
	1.8976	Dist	1.8890	
	0.106	C	0.111	
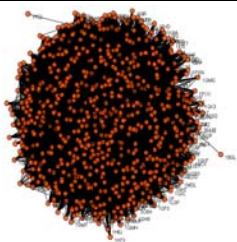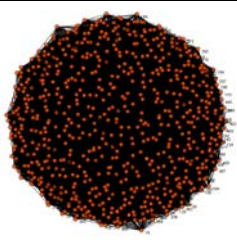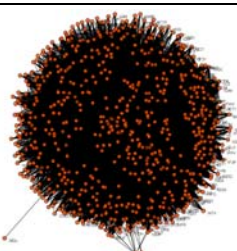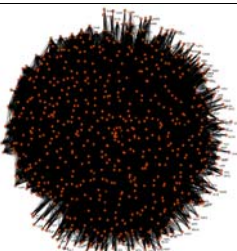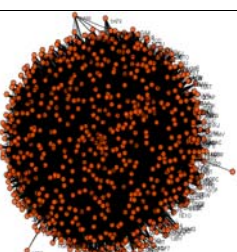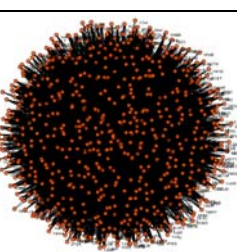
[a] The TIs used are number of nodes (n), number of edges (m), Wiener index (W), diameter (D), node degree (d), topological distance (Dist).
[b] Complex Networks based on a QSAR equation that has been transformed by means of the Randic's orthogonalization procedure.

constructed with the electrostatic variable was the Erdos Renyi random network.[80-81] All the networks were built including only the enzymatic proteins, 689 edges, because by this method we were searching a correlation between the protein and a similar activity, and because the centibin, the program we used to build the networks, was not performed to work with a large database like ours. Before, we had used different continuous and dummy measures of network topology such as the number of nodes (n), the number of edges (m), the

network density or Clustering coefficient (C) the diameter (D, longest path), the Wiener index (W).[75, 82, 83] In table 5 we report all the networks and all the measures we used to study the network. The network density was calculated with the formula 4.[84]

$$C = \frac{m}{\binom{n}{2}} = \frac{m}{\dfrac{n!}{(n-2)!-2!}} = \frac{2 \cdot m}{n^2 - n} \tag{6}$$

In the equation (6), m is the number of edges and n the number of nodes. In the complex network theory, the density is a probability too and it is used to calculate the average of node connection. All these data at the topological distance in the complex network theory define a small world network; a small world network is defined as a network where most nodes are not neighbors but most nodes can reach each other by a small number of hops or steps.

Some Possible Applications

After the development and the optimization of the QSAR models and CNs we decided to test their applicability. For this we took as a reference two important articles that illustrated the important applications that enzymes have in modern biology, especially in the therapeutic field. Referring to the articles about drug-target enzymes (enzymes acting as molecular targets of marketed drugs)[76] and enzybiotics (enzymes acting as antibacterial or, in general, as antimicrobial drugs).

Application to Enzyme-Targeted Drugs

Enzymes offer unique opportunities for drug design that are not available for cell surface receptors, nuclear hormone receptors, ion channels, transporters, and DNA. In a recent article, by Akesson and al., we found a review on the variety of inhibition mechanisms for enzyme-targeted drugs, and on the establishment of an enzyme target database for drugs currently marketed in the United States. According to an analysis of the FDA Orange Book, there are 317 marketed drugs that work by inhibiting an enzyme.[7] Despite that the objective of this work is to propose a new and innovative method for prediction of enzymes, we consider important to mention some important implications that such a method can have, especially considering the numerous applications that the enzymes have had lately in the biological and medical field. We insert 54 enzymes in the model in a prediction series and we obtained very good results, our model was able to predict correctly 52 out of 54 enzymes (96.29%), otherwise we calculate the average Accuracy 60.93%. In table 6 we report all these data and the PDB id for each enzyme used in this calculation. We think this result corroborates our investigation model, our theory and opens new ways and new application fields based on the computational chemistry theory.

Table 6. Classification of the drug-target enzymes

PDB ID	p[a]	PDB ID	p	PDB ID	p
1KNI	0.58	1SSY	0.61	2HUL	0.59
1LGU	0.58	1SWY	0.70	2HUM	0.63
1LGW	0.58	1SWZ	0.67	2IGC	0.60
1LGX	0.58	1SX2	0.70	2IXU	0.65
1LI2	0.58	1SX7	0.71	2IXV	0.65
1LI3	0.58	1T6H	0.59	2J8F	0.66
1LI6	0.58	1T8A	0.59	2J8G	0.65
1LPY	0.58	1T8F	0.58	2NTG	0.59
1LW9	0.60	1T8G	0.58	2NTH	0.59
1LWG	0.59	1T97	0.68	2O4W	0.60
1LWK	0.58	1XEP	0.68	2O7A	0.58
1OV5	0.58	1XJT	0.53	2O79	0.58
1OV7	0.58	1XJU	0.67	2OE4	0.58
1OVH	0.58	1XOV	0.60	2OE7	0.58
1OVJ	0.58	1ZUR	0.60	2OE9	0.58
1OVK	0.58	1ZWN	0.59	2OEA	0.58
1OWY	0.58	1ZYT	0.60	2OTY	0.72
1OWZ	0.58	2A4T	0.60	2OTZ	0.59
1OYU	0.61	2ANV	0.56	2OU0	0.72
1P2L	0.60	2ANX	0.57	2OU8	0.59
1P2R	0.60	2B6T	0.59	2OU9	0.60
1P3N	0.59	2B6W	0.58	2Q9D	0.60
1P5C	0.71	2B6X	0.58	2Q9E	0.63
1P6Y	0.60	2B6Y	0.59	2QAR	0.60
1P7S	0.58	2B6Z	0.58	2RAY	0.59
1P36	0.60	2B7W	0.62	2RAZ	0.73
1P37	0.60	2B7X	0.62	2RB0	0.59
1P46	0.59	2B70	0.59	2RB2	0.59
1P56	0.59	2B72	0.58	2RBN	0.70
1P64	0.59	2B73	0.59	2RBO	0.73
1PQD	0.59	2B74	0.59	2RBP	0.70
1PQI	0.60	2B75	0.59	2RBQ	0.72
1PQJ	0.59	2CUU	0.60	2RBR	0.72
1PQK	0.68	2F2Q	0.71	2RBS	0.72
1PQM	0.60	2F32	0.60	2RH1	0.59
1PQO	0.59	2F47	0.59	1SSW	0.59

[a] p is the probability by which the Electrostatic LDA-QSAR model recognizes this 3D-structure.

Application to Enzybiotics

In a recent review Villa T.G. *et al.* [8] revised the importance of enzybiotics highlighting some important points. The discovery and development of antibiotics was one of the greatest medical achievements in the 20th century and allowed the control of many diseases caused by microorganisms. Nevertheless, it is necessary to search constantly for new therapeutic tools in the continuing fight against disease-causing microorganisms and this probably leads us to today's concept of enzybiotics. Although microorganism-degrading enzymes have been known since the beginning of the last century, their use was soon forgotten because of the widespread use of antibiotics. As referred above, the term "enzybiotic" is a hybrid word from "enzyme" and "antibiotic" and refers to phages: that is, a type of virus that attack and lyses bacteria and that can potentially help us to fight against bacterial diseases. If the concept of enzybiotic is extended to antifungal enzymes, an enormous potential in the struggle against microorganism-due diseases may become available in the foreseeable future. [8, 85, 86.]

As in the case of enzyme target drugs, we introduced the lysine phage enzymes in the model and carried out one with a prediction series only for the enzybiotics, where we found very good results also: the model, the same reported above with only 1 variable, was able to predict correctly all the 109 enzymes (100%); otherwise, we calculated the average of the highest probability of the classification, as for the enzyme target drugs, with a 61.22% result. All these data and the PDB id of the proteins are reported in table 7.

Table 7. Classification of Enzybiotics

PDB ID	p [a]	PDB ID	p
12CA	0.70	1CQE	0.58
1A0H	0.65	1DBT	0.65
1A14	0.39	1E9X	0.60
1A1Q	0.59	1EZF	0.59
1A2N	0.62	1FDS	0.60
1A30	0.53	1FFY	0.65
1A31	0.62	1FIQ	0.62
1A4L	0.59	1GNX	0.59
1A4U	0.63	1GOS	0.70
1A5K	0.60	1GZA	0.55
1A7T	0.61	1H1D	0.55
1AB4	0.64	1IOV	0.60
1AC0	0.60	1ITQ	0.58
1AD1	0.58	1IWC	0.52
1AI9	0.67	1J36	0.65
1AIQ	0.69	1JS3	0.68
1AK5	0.60	1OBB	0.55
1AKN	0.66	1SP9	0.61
1AMY	0.64	1TAZ	0.59
1ARO	0.66	1TOH	0.60
1AV8	0.59	1XKT	0.60

Table 7. Continued

PDB ID	p [a]	PDB ID	p
1BD0	0.63	2ACE	0.57
1BU7	0.63	2ANY	0.73
1C2T	0.65	2C3C	0.67
1C4K	0.59	2Q7M	0.69
1C5M	0.39	2VEU	0.67
1CEF	0.55	3C61	0.62

[a] p is the probability by which the Electrostatic LDA-QSAR model recognizes this 3D-structure.

Conclusions

The spectral moments of MCM could be used to calculate and compare different potentials in protein Structure-Function Relationship studies. In particular, we introduced a method in order to distinguish enzymes from non-enzymes with average 3D electrostatic potentials, which are notably simpler than the previous model reported by D and D. We can use this QSAR to derive Complex Networks to study the behavior of these molecular fields on enzymes.

Acknowledgments

References

[1]   Cozzetto, D.; Tramontano, A., Relationship between multiple sequence alignments and quality of protein comparative models. *Proteins.* 2005, 58, (1), 151-7.
[2]   Iliopoulos, I.; Tsoka, S.; Andrade, M. A.; Enright, A. J.; Carroll, M.; Poullet, P.; Promponas, V.; Liakopoulos, T.; Palaios, G.; Pasquier, C.; Hamodrakas, S.; Tamames, J.; Yagnik, A. T.; Tramontano, A.; Devos, D.; Blaschke, C.; Valencia, A.; Brett, D.; Martin, D.; Leroy, C.; Rigoutsos, I.; Sander, C.; Ouzounis, C. A., Evaluation of annotation strategies using an entire genome sequence. *Bioinformatics.* 2003, 19, (6), 717-26.
[3]   Dobson, P. D.; Doig, A. J., Distinguishing enzyme structures from non-enzymes without alignments. *J. Mol. Biol.* 2003, 330, (4), 771-83.

[4] Dobson, P. D.; Doig, A. J., Predicting enzyme class from protein structure without alignments. *J. Mol. Biol.* 2005, 345, (1), 187-99.

[5] Dobson, P. D.; Cai, Y. D.; Stapley, B. J.; Doig, A. J., Prediction of protein function in the absence of significant sequence similarity. *Curr. Med. Chem.* 2004, 11, (16), 2135-42.

[6] Akesson, M.; Dufour, M.; Sloan, G. L.; Simmonds, R. S., Targeting of streptococci by zoocin A. *FEMS Microbiol. Lett.* 2007, 270, (1), 155-61.

[7] Robertson, J. G., Mechanistic basis of enzyme-targeted drugs. *Biochemistry.* 2005, 44, (15), 5561-71.

[8] Veiga-Crespo, P.; Ageitos, J. M.; Poza, M.; Villa, T. G., Enzybiotics: a look to the future, recalling the past. *J. Pharm. Sci.* 2007, 96, (8), 1917-24.

[9] Han, L.; Cui, J.; Lin, H.; Ji, Z.; Cao, Z.; Li, Y.; Chen, Y., Recent progresses in the application of machine learning approach for predicting protein functional class independent of sequence similarity. *Proteomics.* 2006, 6, (14), 4023-37.

[10] Lin, H. H.; Han, L. Y.; Zhang, H. L.; Zheng, C. J.; Xie, B.; Chen, Y. Z., Prediction of the functional class of lipid binding proteins from sequence-derived properties irrespective of sequence similarity. *J. Lipid Res.* 2006, 47, (4), 824-31.

[11] Cui, J.; Han, L. Y.; Cai, C. Z.; Zheng, C. J.; Ji, Z. L.; Chen, Y. Z., Prediction of functional class of novel bacterial proteins without the use of sequence similarity by a statistical learning method. *J. Mol. Microbiol. Biotechnol.* 2005, 9, (2), 86-100.

[12] Lin, H. H.; Han, L. Y.; Cai, C. Z.; Ji, Z. L.; Chen, Y. Z., Prediction of transporter family from protein sequence by support vector machine approach. *Proteins.* 2006, 62, (1), 218-31.

[13] Han, L. Y.; Cai, C. Z.; Ji, Z. L.; Cao, Z. W.; Cui, J.; Chen, Y. Z., Predicting functional family of novel enzymes irrespective of sequence similarity: a statistical learning approach. *Nucleic Acids Res.* 2004, 32, (21), 6437-44.

[14] Han, L. Y.; Cai, C. Z.; Ji, Z. L.; Chen, Y. Z., Prediction of functional class of novel viral proteins by a statistical learning method irrespective of sequence similarity. *Virology.* 2005, 331, (1), 136-43.

[15] Cai, C. Z.; Han, L. Y.; Ji, Z. L.; Chen, Y. Z., Enzyme family classification by support vector machines. *Proteins.* 2004, 55, (1), 66-76.

[16] Han, L. Y.; Cai, C. Z.; Lo, S. L.; Chung, M. C.; Chen, Y. Z., Prediction of RNA-binding proteins from primary sequence by a support vector machine approach. *RNA.* 2004, 10, (3), 355-68.

[17] Cai, Y. D.; Zhou, G. P.; Chou, K. C., Predicting enzyme family classes by hybridizing gene product composition and pseudo-amino acid composition. *J. Theor. Biol.* 2005, 234, (1), 145-9.

[18] Chou, K. C., Using amphiphilic pseudo amino acid composition to predict enzyme subfamily classes. *Bioinformatics.* 2005, 21, (1), 10-9.

[19] Chou, K. C., Prediction of protein cellular attributes using pseudo-amino acid composition. *Proteins.* 2001, (Erratum: ibid., 2001, Vol. 44, 60) 43, (3), 246-55.

[20] Wang, S. Q.; Yang, J.; Chou, K. C., Using stacked generalization to predict membrane protein types based on pseudo-amino acid composition. *J. Theor. Biol.* 2006.

[21] Xiao, X.; Shao, S.; Ding, Y.; Huang, Z.; Chou, K. C., Using cellular automata images and pseudo amino acid composition to predict protein subcellular location. *Amino Acids.* 2006, 30, (1), 49-54.

[22] Cai, Y. D.; Chou, K. C., Predicting membrane protein type by functional domain composition and pseudo-amino acid composition. *J. Theor. Biol.* 2006, 238, (2), 395-400.

[23] Chou, K. C.; Cai, Y. D., Predicting protein quaternary structure by pseudo amino acid composition. *Proteins.* 2003, 53, (2), 282-9.

[24] Cai, Y. D.; Chou, K. C., Predicting membrane protein type by functional domain composition and pseudo-amino acid composition. *J. Theor. Biol.* 2005.

[25] Chou, K. C.; Cai, Y. D., Prediction of membrane protein types by incorporating amphipathic effects. *J. Chem. Inf. Model.* 2005, 45, (2), 407-13.

[26] Caballero, J.; Fernandez, L.; Abreu, J. I.; Fernandez, M., Amino Acid Sequence Autocorrelation vectors and ensembles of Bayesian-Regularized Genetic Neural Networks for prediction of conformational stability of human lysozyme mutants. *J. Chem. Inf. Model.* 2006, 46, (3), 1255-68.

[27] Liao, B.; Ding, K., Graphical approach to analyzing DNA sequences. *J. Comput. Chem.* 2005, 26, (14), 1519-23.

[28] Liao, B.; Xiang, X.; Zhu, W., Coronavirus phylogeny based on 2D graphical representation of DNA sequence. *J. Comput. Chem.* 2006, 27, (11), 1196-1202.

[29] Randic, M.; Balaban, A. T., On a four-dimensional representation of DNA primary sequences. *J. Chem. Inf. Comput. Sci.* 2003, 43, (2), 532-9.

[30] Aguero-Chapin, G.; González-Díaz, H.; Molina, R.; Varona-Santos, J.; Uriarte, E.; Gonzalez-Diaz, Y., Novel 2D maps and coupling numbers for protein sequences. The first QSAR study of polygalacturonases; isolation and prediction of a novel sequence from Psidium guajava L. *FEBS Lett.* 2006, 580, (3), 723-30.

[31] Zupan, J.; Randic, M., Algorithm for coding DNA sequences into "spectrum-like" and "zigzag" representations. *J. Chem. Inf. Model.* 2005, 45, (2), 309-13.

[32] Agüero-Chapin, G.; Gonzalez-Diaz, H.; Molina, R.; Varona-Santos, J.; Uriarte, E.; Gonzalez-Diaz, Y., Novel 2D maps and coupling numbers for protein sequences. The first QSAR study of polygalacturonases; isolation and prediction of a novel sequence from Psidium guajava L. *FEBS lett.* 2006, 580 723-730.

[33] González-Díaz, H.; Vilar, S.; Santana, L.; Uriarte, E., Medicinal Chemistry and Bioinformatics − Current Trends in Drugs Discovery with Networks Topological Indices. *Curr. Top Med. Chem.* 2007, 7, (10), 1025-39.

[34] Paula, S.; Tabet, M. R.; Keenan, S. M.; Welsh, W. J.; Ball, W. J., Jr., Three-dimensional structure-activity relationship modeling of cocaine binding to two monoclonal antibodies by comparative molecular field analysis. *J. Mol. Biol.* 2003, 325, (3), 515-30.

[35] Verma, R. P.; Hansch, C., An Approach towards the quantitative structure-activity relationships of caffeic acid and its derivatives. *Chembiochem.* 2004, 5, (9), 1188-95.

[36] Klabunde, T.; Hessler, G., Drug design strategies for targeting G-protein-coupled receptors. *Chembiochem.* 2002, 3, (10), 928-44.

[37] Baker, E. N.; Arcus, V. L.; Lott, J. S., Protein structure prediction and analysis as a tool for functional genomics. *Appl. Bioinformatics.* 2003, 2, (3 Suppl), S3-10.

[38] Shindyalov, I. N.; Bourne, P. E., A database and tools for 3-D protein structure comparison and alignment using the Combinatorial Extension (CE) algorithm. *Nucleic Acids Res.* 2001, 29, (1), 228-9.

[39] Estrada, E.; Uriarte, E.; Vilar, S., Effect of Protein Backbone Folding on the Stability of Protein-Ligand Complexes. *J. Proteome Res.* 2006, 5, 105-111.

[40] Fernández, M.; Caballero, F.; Fernández, L.; Abreu, J. I.; Acosta, G., Classification of conformational stability of protein mutants from 3D pseudo-folding graph representation of protein sequences using support vector machines. *Proteins.* 2008, 70, (1), 167-175.

[41] Camacho, C. J.; Gatchell, D. W., Successful discrimination of protein interactions. *Proteins.* 2003, 52, (1), 92-7.

[42] Gong, X. Q.; Chang, S.; Zhang, Q. H.; Li, C. H.; Shen, L. Z.; Ma, X. H.; Wang, M. H.; Liu, B.; He, H. Q.; Chen, W. Z.; Wang, C. X., A filter enhanced sampling and combinatorial scoring study for protein docking in CAPRI. *Proteins.* 2007, 69, (4), 859-65.

[43] Mottamal, M.; Zhang, J.; Lazaridis, T., Energetics of the native and non-native states of the glycophorin transmembrane helix dimer. *Proteins.* 2006, 62, (4), 996-1009.

[44] Camacho, C. J.; Ma, H.; Champ, P. C., Scoring a diverse set of high-quality docked conformations: a metascore based on electrostatic and desolvation interactions. *Proteins.* 2006, 63, (4), 868-77.

[45] Tramontano, A.; Macchiato, M. F., Probability of coding of a DNA sequence: an algorithm to predict translated reading frames from their thermodynamic characteristics. *Nucleic Acids Res.* 1986, 14, (1), 127-35.

[46] Roy, M.; Chavez, L. L.; Finke, J. M.; Heidary, D. K.; Onuchic, J. N.; Jennings, P. A., The native energy landscape for interleukin-1beta. Modulation of the population ensemble through native-state topology. *J. Mol. Biol.* 2005, 348, (2), 335-47.

[47] Piacenza, M.; Grimme, S., Van der Waals interactions in aromatic systems: structure and energetics of dimers and trimers of pyridine. *Chemphyschem.* 2005, 6, (8), 1554-8.

[48] Hou, T.; Zhang, W.; Case, D. A.; Wang, W., Characterization of Domain-Peptide Interaction Interface: A Case Study on the Amphiphysin-1 SH3 Domain. *J. Mol. Biol.* 2008.

[49] Xiang, Z.; Honig, B., Extending the accuracy limits of prediction for side-chain conformations. *J. Mol. Biol.* 2001, 311, (2), 421-30.

[50] Karanasios, E.; Simader, H.; Panayotou, G.; Suck, D.; Simos, G., Molecular determinants of the yeast Arc1p-aminoacyl-tRNA synthetase complex assembly. *J. Mol. Biol.* 2007, 374, (4), 1077-90.

[51] Liu, Y.; Beveridge, D. L., Exploratory studies of ab initio protein structure prediction: multiple copy simulated annealing, AMBER energy functions, and a generalized born/solvent accessibility solvation model. *Proteins.* 2002, 46, (1), 128-46.

[52] González-Díaz, H.; Torres-Gomez, L. A.; Guevara, Y.; Almeida, M. S.; Molina, R.; Castanedo, N.; Santana, L.; Uriarte, E., Markovian chemicals "in silico" design (MARCH-INSIDE), a promising approach for computer-aided molecular design III: 2.5D indices for the discovery of antibacterials. *J. Mol. Model.* 2005, 11, (2), 116-23.

[53] González-Díaz, H.; Uriarte, E., Proteins QSAR with Markov average electrostatic potentials. *Bioorg. Med. Chem. Lett.* 2005, 15, (22), 5088-94.

[54] González-Díaz, H.; de Armas, R. R.; Molina, R., Markovian negentropies in bioinformatics. 1. A picture of footprints after the interaction of the HIV-1 Psi-RNA packaging region with drugs. *Bioinformatics.* 2003, 19, (16), 2079-87.

[55] Gonzalez-Diaz, H.; Molina, R.; Uriarte, E., Recognition of stable protein mutants with 3D stochastic average electrostatic potentials. *FEBS Lett.* 2005, 579, (20), 4297-301.

[56] Ramos de Armas, R.; González-Díaz, H.; Molina, R.; Uriarte, E., Markovian Backbone Negentropies: Molecular descriptors for protein research. I. Predicting protein stability in Arc repressor mutants. *Proteins.* 2004, 56, (4), 715-23.

[57] González-Díaz, H.; Saiz-Urra, L.; Molina, R.; Santana, L.; Uriarte, E., A Model for the Recognition of Protein Kinases Based on the Entropy of 3D van der Waals Interactions. *J. Proteome Res.* 2007, 6, (2), 904-908.

[58] González-Díaz, H.; Saiz-Urra, L.; Molina, R.; Gonzalez-Diaz, Y.; Sanchez-Gonzalez, A., Computational chemistry approach to protein kinase recognition using 3D stochastic van der Waals spectral moments. *J. Comput. Chem.* 2007, 28, (6), 1042-1048.

[59] Cruz-Monteagudo, M.; González-Díaz, H.; Borges, F.; Dominguez, E. R.; Cordeiro, M. N., 3D-MEDNEs: An Alternative "in Silico" Technique for Chemical Research in Toxicology. 2. Quantitative Proteome-Toxicity Relationships (QPTR) based on Mass Spectrum Spiral Entropy. *Chem. Res. Toxicol.* 2008, doi:10.1021/tx700296t.

[60] González-Díaz, H.; González-Díaz, Y.; Santana, L.; Ubeira, F. M.; Uriarte, E., Proteomics, networks and connectivity indices. *Proteomics.* 2008, 8, 750-778.

[61] González-Díaz, H.; Gia, O.; Uriarte, E.; Hernadez, I.; Ramos, R.; Chaviano, M.; Seijo, S.; Castillo, J. A.; Morales, L.; Santana, L.; Akpaloo, D.; Molina, E.; Cruz, M.; Torres, L. A.; Cabrera, M. A., Markovian chemicals "in silico" design (MARCH-INSIDE), a promising approach for computer-aided molecular design I: discovery of anticancer compounds. *J. Mol. Model.* 2003, 9, (6), 395-407.

[62] González-Díaz, H.; Prado-Prado, F. J.; Santana, L.; Uriarte, E., Unify QSAR approach to antimicrobials. Part 1: Predicting antifungal activity against different species. *Bioorg. Med. Chem.* 2006, 14 5973–5980.

[63] Caballero, J.; Saavedra, M.; Fernández, M.; González-Nilo, F. D., Quantitative Structure–Activity Relationship of Rubiscolin Analogues as δ Opioid Peptides Using Comparative Molecular Field Analysis (CoMFA) and Comparative Molecular Similarity Indices Analysis (CoMSIA) *J. Agric Food Chem.* 2007, 55, (20), 8101-8104.

[64] Freund, J. A.; Poschel, T., Stochastic processes in physics, chemistry, and biology. In *Lect. Notes Phys.* Springer-Verlag: Berlin, Germany, 2000.

[65] Drawid, A.; Gerstein, M., A Bayesian system integrating expression data with sequence patterns for localizing proteins: comprehensive application to the yeast genome. *J. Mol. Biol.* 2000, 301, (4), 1059-75.

[66] Saiz-Urra, L.; González-Díaz, H.; Uriarte, E., Proteins Markovian 3D-QSAR with spherically-truncated average electrostatic potentials. *Bioorg. Med. Chem.* 2005, 13, (11), 3641-7.

[67] Lehar, J.; Zimmermann, G. R.; Krueger, A. S.; Molnar, R. A.; Ledell, J. T.; Heilbut, A. M.; Short, G. F., 3rd; Giusti, L. C.; Nolan, G. P.; Magid, O. A.; Lee, M. S.; Borisy, A. A.; Stockwell, B. R.; Keith, C. T., Chemical combination effects predict connectivity in biological systems. *Mol. Syst. Biol.* 2007, 3, 80.

[68] von Grotthuss, M.; Plewczynski, D.; Ginalski, K.; Rychlewski, L.; Shakhnovich, E. I., PDB-UF: database of predicted enzymatic functions for unannotated protein structures from structural genomics. *BMC Bioinformatics.* 2006, 7, 53.

[69] Santana, L.; Uriarte, E.; González-Díaz, H.; Zagotto, G.; Soto-Otero, R.; Mendez-Alvarez, E., A QSAR model for in silico screening of MAO-A inhibitors. Prediction, synthesis, and biological assay of novel coumarins. *J. Med. Chem.* 2006, 49, (3), 1149-56.

[70] Randic´, M., Orthogonal molecular descriptors. *New J. Chem.* 1991, 15, 517-525.

[71] Hill, T.; Lewicki, P., *STATISTICS Methods and Applications. A Comprehensive Reference for Science, Industry and Data Mining*. StatSoft: Tulsa, 2006 Vol. 1, p 813.

[72] Kutner, M. H.; Nachtsheim, C. J.; Neter, J.; Li, W., Standardized Multiple Regression Model. In *Applied Linear Statistical Models*, Fifth ed.; McGraw Hill: New York, 2005; pp 271-277.

[73] Liu, W. M.; Chou, K. C., Prediction of protein structural classes by modified mahalanobis discriminant algorithm. *J. Protein Chem.* 1998, 17, (3), 209-17.

[74] Microsoft.Corp. *Microsoft Excel.* 2002.

[75] Koschützki, D. *CentiBiN Version 1.4.2*, 2006.

[76] EC number, I. E. N. http://www.chem.qmul.ac.uk/iubmb/enzyme/

[77] Ivanisenko, V. A.; Pintus, S. S.; Grigorovich, D. A.; Kolchanov, N. A., PDBSite: a database of the 3D structure of protein functional sites. *Nucleic Acids Res.* 2005, 33, (Database issue), D183-7.

[78] González-Díaz, H.; Pérez-Castillo, Y.; Podda, G.; Uriarte, E., Computational Chemistry Comparison of Stable/Nonstable Protein Mutants Classification Models Based on 3D and Topological Indices. *J. Comput. Chem.* 2007, 28, 1990-1995.

[79] Casanola-Martin, G. M.; Marrero-Ponce, Y.; Khan, M. T.; Ather, A.; Khan, K. M.; Torrens, F.; Rotondo, R., Dragon method for finding novel tyrosinase inhibitors: Biosilico identification and experimental in vitro assays. *Eur. J. Med. Chem.* 2007, 42, (11-12), 1370-1381.

[80] Kleinberg, J. M., Navigation in a small world. *Nature.* 2000, 406, (6798), 845.

[81] Kleinberg, J.; Lawrence, S., Network analysis. The structure of the Web. *Science.* 2001, 294, (5548), 1849-50.

[82] Tsaparas, P.; Marino-Ramirez, L.; Bodenreider, O.; Koonin, E. V.; Jordan, I. K., Global similarity and local divergence in human and mouse gene co-expression networks. *BMC Evol. Biol.* 2006, 6, 70.

[83] Spirin, V.; Mirny, L. A., Protein complexes and functional modules in molecular networks. *Proc. Natl. Acad. Sci. U.S.A.* 2003, 100, (21), 12123-8.

[84] Boccaletti, S.; Latora, V.; Moreno, Y.; Chavez, M.; Hwang, D. U., Complex networks: Structure and dynamics. *Physics Reports.* 2006, 424, 175-308.

[85] Biziulevicius, G. A.; Biziuleviciene, G.; Kazlauskaite, J., A list of enzyme preparations covered by the term enzybiotics should not be restricted to bacteriophage-encoded peptidoglycan hydrolases (lysins). *J. Pharm. Pharmacol.* 2008, 60, (4), 531-2.

[86] Hermoso, J. A.; Garcia, J. L.; Garcia, P., Taking aim on bacterial pathogens: from phage therapy to enzybiotics. *Curr. Opin. Microbiol.* 2007, 10, (5), 461-72.

Chapter 15

A New Density Functional Method for Electronic Structure Calculation of Atoms and Molecules

Amlan K. Roy [*]
Division of Chemical Sciences,
Indian Institute of Science Education and Research (IISER),
Block HC, Sector III, Salt Lake, Kolkata-700106, India

Abstract

In recent years, density functional theory (DFT) has emerged as one of the most successful and powerful approaches in electronic structure calculation of atoms, molecules and solids, as evidenced from burgeoning research activities in this direction. This chapter concerns with the recent development of a new DFT methodology for accurate, reliable prediction of many-electron systems. Background, need for such a scheme, major difficulties encountered, as well as their potential remedies are discussed at some length. Within the realm of non relativistic Hohenberg-Kohn-Sham (HKS) DFT and making use of the familiar LCAO-MO principle, relevant KS eigenvalue problem is solved numerically. Unlike the commonly used atom-centered grid (ACG), here we employ a 3D cartesian coordinate grid (CCG) to build atom-centered localized basis set, electron density, as well as all the two-body potentials directly on grid. The Hartree potential is computed through a Fourier convolution technique via a decomposition in terms of short- and long-range interactions. Feasibility and viability of our proposed scheme is demonstrated for a series of chemical systems; first with homogeneous, local-density-approximated XC functionals followed by non-local, gradient- and Laplacian-dependent functionals. A detailed, systematic analysis on obtained results relevant to quantum chemistry, are made, *for the first time*, using CCG, which clearly illustrates the significance of this alternative method in the present context. Quantities such as component energies, total energies, ionization energies, potential energy curve, atomization energies, etc., are addressed for pseudopotential calculations, along with a thorough comparison with literature data, wherever possible. Finally, some words on the future and prospect of this method are mentioned. In summary, we have presented a new CCG-based *variational* DFT method for accurate, dependable calculation of atoms and molecules.

---

[*]E-mail address: akroy@iiserkol.ac.in, akroy@chem.ucla.edu

1. Introduction

With continuous rapid advances in sophisticated methodologies, techniques, algorithms as well as ever-increasing growth of powerful computers, attempts to study electronic *structure, properties* of atoms, molecules, solids, clusters by direct *ab initio* solution of many-body Schrödinger equation has received an enormous amount of stimulus in the past several decades. The great challenge of solving this equation for realistic systems has opened up whole new avenues in chemistry, as, in almost all cases, no *exact* analytic solution could be obtained (except in a small number of simple cases); hence recourse must be taken to approximate methods. Obviously, the ultimate goal is to achieve an accuracy obtained in the best experimental result using optimal computational resources. Now it is no more an unrealistic contemplation to think of highly accurate quantum mechanical calculations of molecules having 100 electrons or more, and quantum chemistry has been a full-fledged, firmly established discipline for some time now.

Apart from the ground-state electronic structure (in terms of wave functions and densities), a theoretician ought to be able to tackle a multitude of other important aspects, such as excited states, spectroscopic term values, oscillator strengths for transitions, fine and hyperfine structure of energy levels due to relativistic corrections to Hamiltonian and so on. Molecular case, however, poses more overwhelming and spectacular challenges; for in addition to the physical properties mentioned (applicable to atoms as well), one has also needs to address a host of certain unique *chemical* properties specific to them. For example, a molecule has a well-defined "geometry", which requires specification of various bond lengths, angles etc. Some other quantities of interest include, for example, force constants for stretching, bending (molecular vibration), energy needed to break a particular bond or to dissociate the molecules into fragments, nature of interaction between molecules, chemical reactions which may occur when they come into close proximity (synthetic and decomposition pathways), absolute and relative interaction energies, dipole and higher multipole moments, cross section for collision with other particles, stability of such a system (through second derivatives of energy with respect to the spatial coordinates, the Hessian matrix), the properties revealed by various modern spectroscopic methods (including electron spin resonance, nuclear magnetic resonance, nuclear quadrupole resonance, photoelectron spectroscopy, ro-vibrational spectroscopy, electronic spectroscopy) etc.

Demands on the theory is no less severe. Considering the fact that energy required to break a bond is roughly of the order of 5 eV, while total electronic energy may be thousands of times higher, estimation of dissociation energy as a difference of two such large quantities, is clearly a non-trivial exercise. Furthermore, the elegant methods of angular momentum applicable to atomic systems can no longer be used for general polyatomic molecules which, in general, lack symmetry. Besides, we are interested in both static and dynamic situations. In all cases, the computer time and resources dramatically increase with system size in consideration. Thus a whole echelon of formalisms, ranging from highly accurate to very approximate, strive to achieve the best trade-off between accuracy and computational cost. The former *ab initio* method is feasible only for relatively smaller systems, as these are based entirely on theory from first principles. The other, often less accurate and less reliable, empirical or semi-empirical methods usually employ experimental results to approximate some elements of the underlying theory. All these fall into the

general gamut of modern computational chemistry. A large number of excellent reviews, textbooks, monographs are available on the subject. Some of the recent ones are given here [1, 2, 3, 4, 5, 6, 7, 8, 9, 10, 11, 12].

Two distinct lines of attack may be visualized. In the "conventional" approaches (rooted in early works of Slater [13] on atoms, molecules), direct approximate solution of Schrödinger equation is sought through carefully designed variational wave functions with the aid of most powerful computers available. In the indirect, second line of development, calculation of wave function is avoided by deriving expressions for observable themselves, namely electron density, giving birth to the versatile and popular density functional theory (DFT) [14, 15, 16, 17, 18, 19, 20, 21, 22, 23, 24]. Last few decades have witnessed a proliferation of DFT-based methodologies for electronic calculations of a broad range of systems including atoms, molecules, condensed phases, materials science, etc. With diverse advancements in computer technology, this allows larger systems of physical and chemical interest to be approached than are ordinarily accessible within the domains of traditional methods, and this continues to grow at a steady pace. An overwhelming variety of important challenging problems are addressed ranging from to study properties of doped fullerene superconductor or a solid semiconductor; structure, modeling and docking of a peptide; catalytic properties of a zeolite or a surface layer; predict, design reaction pathways leading to the desired pharmaceutical product; electronic as well as spin-dependent (spintronic) transport properties of molecules; modeling of intermolecular forces and potential energy surfaces at the molecular level, etc. An extensive amount of successful applications have been made to a varied range of molecular studies as well; such as prediction of physicochemical properties like equilibrium geometries, harmonic vibrational frequencies, polarizabilities, hyperpolarizabilities, dissociation energies, stability, transition states, weak interactions like H-bonds, reaction pathways, etc. Indeed it is no more an overstatement that today's electronic structure calculations of materials is principally dominated by DFT, so much so that it has now become an indispensable tool for any large-scale calculations demanding high accuracy. The conspicuous success lies in its unique ability to strike a balance between quantitative accuracy, efficient computational resource in conjunction with readily interpretable, conceptual simplicity. This is possible because the perennial problem of many-body electron correlation is dealt with indirectly, but satisfactorily, through introduction of a fictitious *non-interacting* system having *same* ground state density of the *real* system concerned. The three-dimensional, physically realizable, single-particle electron density (in contrast to the complicated, complex-valued, many-body wave function in traditional wave function-based approaches; a function of 3N space and N spin coordinates) takes centrestage. A major crux of the problem is now transferred in finding the elusive, yet-to-be-found, all-important exchange-correlation (XC) density functional, whose exact form still remains unknown; hence must be approximated. For small molecules while DFT can be seen as an *alternative* to the conventional *ab initio* methods such as full configuration interaction (CI), many-body perturbation theory or coupled cluster approaches, for electronic structure calculations of larger complicated molecules (having chemical, physical, biological interest), DFT has an edge over these methods. So far this appears to be the most practical route in terms of accuracy and efficiency.

This chapter focuses on an in-depth account of work done by me in past three years or so on stationary atomic and molecular ground states, where relativistic effects are chemically

insignificant; therefore allowing us to use the nonrelativistic time-independent Kohn-Sham (KS) equation. Adiabatic partitioning of the system's wave functions into electronic and nuclear portions are tacitly assumed within Born-Oppenheimer approximation; thus electronic part can be separated from nuclear counterpart. We propose an alternative to the most commonly used and popular approach of the so-called atom-centered grid (ACG), by using a much simpler cartesian coordinate grid (CCG) to obtain electronic structure of atoms, molecules. The pertinent KS equation is solved by linearly expanding the desired molecular orbitals (MO) in terms of a set of known localized, atom-centered basis set within an LCAO-MO approximation. Analytical, one-electron *ab-initio* pseudopotentials (expressed in terms of a sum of Gaussian functions) represent core electrons, whereas energy-optimized truncated Gaussian basis sets are used for valence electrons. It is demonstrated that our obtained self-consistent eigenvalues, eigenfunctions (and other properties derived from them) are highly accurate, reliable and produce practically identical results as those obtained from their ACG counterparts. Illustrative results are given for a number of local and global properties (such as energy components, potential energy surface, etc.) to assess, establish the efficacy and relevance of our approach for a modest set of chemical species using both local, non-local XC density functionals.

2.   The Methodology

2.1.   A Brief Review of DFT

This subsection gives an overview of DFT to the extent of summarizing only the essential ingredients as needed for our future discussion. By no means it is a review, because it is not needed as already there exists an extensively large number of excellent articles covering numerous aspects of the theory; moreover it is impossible to keep pace with the innumerable amount of work that has been published on the subject. Application area are diverse starting from atoms to condensed matter to computational material science. For more detailed exposition, references [14, 15, 16, 17, 18, 19, 20, 21, 22, 23, 24] may be consulted.

The important idea of expressing part or all of the energy of a many-electron system as functional of single-particle electron density has its root in seminal works of Thomas-Fermi-Dirac as early as in 1927. The kinetic energy and exchange energy can be approximated as explicit functionals of electron density; idealized as non-interacting electrons in a homogeneous gas with density equal to the local density at any given point,

$$E_{TFD}[\rho(\mathbf{r})] = C_F \int \rho(\mathbf{r})^{5/3} \, \mathrm{d}\mathbf{r} + \int \rho(\mathbf{r})v(\mathbf{r}) \, \mathrm{d}\mathbf{r} - C_x \int \rho(\mathbf{r})^{4/3} \, \mathrm{d}\mathbf{r} + \frac{1}{2} \int \int \frac{\rho(\mathbf{r})\rho(\mathbf{r}')}{|\mathbf{r} - \mathbf{r}'|} \, \mathrm{d}\mathbf{r}\mathrm{d}\mathbf{r}',$$
(1)

where $C_F = \frac{3}{10}(3\pi^2)^{2/3}$, $C_x = \frac{3}{4}(\frac{3}{\pi})^{1/3}$ correspond to the local approximations to kinetic energy and exchange energy respectively in first and third terms in the right hand side. The second and last terms refer to nuclear-electron attraction and classical electrostatic Hartree repulsion respectively. While the stunning simplicity of replacing complicated many-body Schrödinger equation by a *single* equation in terms of electron density *alone* is conspicuously appealing, underlying approximations are too crude and inaccurate to offer any prac-

tical applications in modern quantum chemistry; also the essential physics and chemistry is missing (e.g., it fails to explain shell structure in atoms and molecular binding [25]).

Insurmountable difficulties are encountered to approach such a problem beyond gross levels of Thomas-Fermi model. Consequently DFT was lost into oblivion until 1964, when it got a rebirth in the landmark works of Hohenberg-Kohn-Sham [26, 27]. It was placed on a rigorous theoretical foundation thenceforth. Following an astonishingly simple proof, Hohenberg-Kohn theorem states that for a many-electron system, external interacting potential $v(\mathbf{r})$ is completely determined (within a trivial constant) by $\rho(\mathbf{r})$. Since the Hamiltonian is thus fully defined uniquely, it immediately follows that ground-state wave function and all other properties of such a system can be obtained from $\rho(\mathbf{r})$ alone. Further, they proved the existence of a *universal functional*, $F_{HK}[\rho]$, for *any* valid well-behaved external potential, whose global minimum leads to exact ground-state energy and the density which minimizes this functional corresponds to exact density,

$$
\begin{aligned}
E_v[\rho] &\equiv F_{HK}[\rho] + \int v(\mathbf{r})\rho(\mathbf{r})\mathrm{d}\mathbf{r} \ \geq E_v[\rho_0] \qquad (2)\\
F_{HK}[\rho] &= \langle \Psi | T + V_{ee} | \Psi \rangle.
\end{aligned}
$$

Here Ψ denotes ground-state wave function associated with ρ, $E_v[\rho_0]$ is ground-state energy of the Hamiltonian with external potential $v(\mathbf{r})$, ρ_0 is its ground-state density, V_{ee} denotes two-particle interaction energies including both classical and non-classical effects.

While Hohenberg-Kohn theorem physically justifies earlier works of Thomas-Fermi and others to employ $\rho(\mathbf{r})$ as a central variable to describe a many-electron system, it is a *proof of existence* only. All it asserts is that there is a unique mapping between ground-state density and energy, in principle; but it keeps mute on furnishing any information on the construction of such a functional. Although $\rho(\mathbf{r})$ is sufficient, the relation is subtle, intricate, and how to extract any set of general properties from it, remains unknown. Another important disconcerting feature is that minimization of $E_v[\rho]$ is, in general, a tough numerical task. Actual calculations are still as hard as before; there is absolutely no clue on what kind of approximations to be used for unknown functionals. In effect, no visible progress could be discerned for realistic calculations (no simplification over MO theory), and hence it is of not much help in quantum chemistry, because the final step still constitutes solution of Schrödinger equation, which is prohibitively difficult. Another awkward dilemma arises in density variation principle, which holds true only for *exact* functionals. Thus, in contrast to conventional wave-function-based approaches, where, e.g., Hartree-Fock (HF) or Configuration interaction wave functions are strictly variational, within the rubric of Hohenberg-Kohn DFT, energy delivered by a trial functional has absolutely no physical meaning whatsoever.

In a breakthrough work, Kohn and Sham, in order to alleviate these outstanding difficulties, introduced the concept of a hypothetical *non-interacting* reference system having *same* overall ground-state density as our real interacting system. This Hamiltonian can now be expressed as sum a of one-electron operators, has eigenfunctions that are Slater determinants of individual one-electron eigenfunctions and has eigenvalues that are sum of one-electron eigenvalues. This realization of a non-interacting system, built from a set of one-electron functions (orbitals) came from an observation that conventional orbital-based approaches such as HF or so fares better in this regard. Thus a major chunk of actual kinetic energy

can now be recovered fairly accurately as a sum of individual electronic kinetic energies. The residual, often small, contribution (T_c) is merged with the non-classical contributions to electrostatic repulsion, whose *exact* form is also unknown,

$$\begin{aligned} F[\rho] &= T_s[\rho] + J[\rho] + E_{xc}[\rho] \\ E_{xc}[\rho] &= (T[\rho] - T_s[\rho]) + (V_{ee}[\rho] - J[\rho]) = T_c[\rho] + (V_{ee}[\rho] - J[\rho]). \end{aligned} \tag{3}$$

Here the subscript in T_s denotes independent-particle kinetic energy of a non-interacting system, $V_{ee}[\rho]$ signifies two-particle repulsion energy while $J[\rho]$ the classical part of $V_{ee}[\rho]$, $E_{xc}[\rho]$ refers to XC energy. Kohn-Sham (KS) orbital equations, in their canonical form, are written as follows (henceforth atomic units implied, unless otherwise mentioned),

$$\left[-\frac{1}{2}\nabla^2 + v_{eff}(\mathbf{r}) \right] \psi_i(\mathbf{r}) = \epsilon_i \psi_i(\mathbf{r}) \tag{4}$$

$$v_{eff}(\mathbf{r}) = v(\mathbf{r}) + \int \frac{\rho(\mathbf{r}')}{|\mathbf{r} - \mathbf{r}'|}\, \mathbf{dr}' + v_{xc}(\mathbf{r}). \tag{5}$$

Here $v_{eff}(\mathbf{r})$ is the effective potential and $v(\mathbf{r})$ gives the external potential due to nuclei or any other external field (assumed to be spin-independent). It is noteworthy that although working equations of KS DFT are very similar to those of HF theory, the most profound difference between them lies in that KS theory incorporates the intriguing, delicate electron correlation effects rigorously; thus, it is, in principle, capable of yielding *exact* Schrödinger energy, which is certainly not the case for latter.

2.2. LCAO-MO Ansatz of DFT

As already hinted, minimization of the explicit functional is not normally the most efficient and recommended path towards an actual working DFT. A far more attractive practical route is through KS equation, that owes its success and popularity, interestingly, partly due to the fact that it does not work solely in terms of particle density, but rather brings back an orbital picture into the problem. Hence, in essence, formally it seems to appear like a single-particle theory. Nevertheless many-body effects are incorporated *in principle*, exactly.

In some straightforward implementation, the so-called real-space method [28], instead of expanding wave functions in a suitably chosen, predetermined basis set, latter are normally sampled in a real-space grid, usually through either of the following three representations, such as finite difference (FD), finite element or wavelets. In all these cases, however, relevant discrete differential equations produce highly structured, banded, sparse matrices. This representation has advantages that the potential operator is diagonal in coordinate space; also Laplacian is nearly local (that makes them good candidates for linear-scaling approaches) and these are easily amenable to domain-decomposition parallel implementation. Moreover, Hartree potential can be found using highly optimized FFTs or real-space multigrid algorithms. Some of the earliest successful works along this direction were by [29, 30, 31], where a basis-set-free, fully numerically converged, FD approach was adopted for solution of self-consistent eigenvalue problems encountered in atomic, molecular cases, with reasonably good accuracy. Thereafter, a polyatomic numerical integration scheme was

devised, whereby the actual physical domain was partitioned into a collection of single-centre components having radial grids centered at each nucleus. While these results rekindled hope of employing grid-based methods for full-scale atomic and molecular studies in quantum chemistry, they lacked the highly desirable scalability and efficiency requirement essential for any large-scale calculation. Later, instead of above mentioned atom-centered grids, high-order real-space pseudopotential method was used for relatively larger systems in uniform cartesian coordinates [32, 33]. In a uniform orthogonal 3D mesh containing grid points (x_i, y_j, z_k), mth order expansion of Laplacian operator, within an FD approximation, can be expressed as follows (h denotes grid spacing and m is a positive integer),

$$\left[\frac{\partial^2 \psi}{\partial x^2}\right]_{x_i, y_j, z_k} = \sum_{-m}^{m} C_m \psi(x_i + mh, y_j, z_k) + O(h^{2m+2}). \tag{6}$$

As it is known, this approximation is valid in the limit of $h \to 0$ (i.e., finer grid structure). However, our common experience suggests that to obtain physically meaningful and sufficient accuracy, orders higher than second are most often necessary. FD methods have been applied to a number of interesting *ab initio* self-consistent problems including clusters and other finite systems [32, 33, 34, 35, 36]. Standard iterative processes are noticeably less efficient on finer messes, however, and multigrid methods have been proposed to accelerate the self-consistent iteration procedure [37, 38]. They have been used in conjunction with adaptive grids to enhance the resolution [39, 34]. Numerical convergence is controlled by only a few parameters like grid spacing, domain size, order of representation, etc.

Some of the major limitations of this method are that they are (i) non-variational and (ii) dimension of Hamiltonian matrix is unmanageably large. The parallel, *basis-set* approach, however, dominates quantum chemistry community and a plethora of physical, chemical, biological applications have been made to study energetics, dynamics, reaction mechanisms, etc., encompassing an astoundingly wide range of interesting systems. This is advantageous since it gives an opportunity to exploit the enormous advances made in previously developed techniques within the context of basis-set solutions of wave function-based methodologies (such as HF, for example). The so-called linear combination of atomic orbitals (LCAO) ansatz is by far the most practical, popular and convenient computational route for iterative solution of molecular KS equation. Denoting the one-electron KS operator in parentheses of Eq. (4) by $\hat{f}^{KS}$, one can cast KS equation in following operator form,

$$\hat{f}^{KS} \psi_i = \epsilon_i \psi_i. \tag{7}$$

The above operator differs from Fock operator $\hat{f}^{HF}$ used in connection to HF theory in that former includes non-classical many-body exchange-correlation effects, v_{xc} exactly (as a functional derivative with respect to charge density, $v_{xc}[\rho] = \delta E_{xc}[\rho]/\delta \rho$), whereas latter does not account for any correlation effects. This represents a fairly complicated system of coupled integro-differential equation (kinetic energy is given by a differential operator, whereas the Coulomb contribution by an integral operator), whose solution yields the desired KS MOs $\{\psi_i\}$. Numerical procedures for solution of this equation are much too demanding. Computationally the most efficient way is to linearly expand unknown KS MOs

in terms of a K known basis functions $\{\phi_\mu, \mu = 1, 2, \cdots, K\}$,

$$\psi_i = \sum_{\mu=i}^{K} C_{\mu i}\phi_\mu, \quad i = 1, 2, \cdots, K \tag{8}$$

in a manner analogous to the LCAO-MO scheme employed in Roothaan-Hartree-Fock method. For a complete set $\{\phi_\mu\}$ with $K = \infty$, above expansion is exact and any complete set could be chosen, in principle. However, for realistic computational purposes, one is invariably restricted to a finite set; thus it is of paramount importance to choose functions $\{\phi_\mu\}$ such that the approximate expansion reproduces KS orbitals as accurately as possible. Now, inserting Eq. (8) in (7), multiplying the resulting equation from left with arbitrary basis function ϕ_μ, integrating over space, followed by some algebraic manipulation, leads to, in close analogy to HF case, following compact matrix equation,

$$\mathbf{F}^{KS}\mathbf{C} = \mathbf{S}\mathbf{C}\epsilon. \tag{9}$$

Here, $\mathbf{S}$ and $\mathbf{F}$ denote $K \times K$ real, symmetric overlap and total KS matrices respectively; eigenvector matrix $\mathbf{C}$ contains unknown expansion coefficients $C_{\mu i}$ whereas orbital energies ϵ_i are embedded in the diagonal matrix ϵ. Note that through the introduction of a basis set, original problem of optimizing a complicated, highly nonlinear integro-differential equation is now transformed into a linear one, which could be easily solved efficiently, accurately by using standard techniques of linear algebra. Individual elements of KS matrix are given as,

$$\begin{aligned} F_{\mu\nu}^{KS} &= \int \phi_\mu(\mathbf{r}) \left[h^{\text{core}} + v_{HXC}(\mathbf{r})\right] \phi_\nu(\mathbf{r})\mathrm{d}\mathbf{r} = H_{\mu\nu}^{\text{core}} + \langle\phi_\mu(\mathbf{r})|v_{HXC}|\phi_\nu(\mathbf{r})\rangle \tag{10} \\ &= H_{\mu\nu}^{\text{core}} + J_{\mu\nu} + V_{\mu\nu}^{XC}, \end{aligned}$$

where $H_{\mu\nu}^{\text{core}}$ denotes bare-nucleus Hamiltonian matrix (including kinetic energy plus nuclear-electron attraction) and accounts for one-electron energies; $v_{HXC}(\mathbf{r})$ determines all two-electron potentials including classical Coulomb repulsion as well as the non-classical XC potential. For certain choices of $\{\phi_\mu\}$ (such as Gaussian bases), one-electron matrix elements can be fairly easily computed analytically using well-tested algorithms. $J_{\mu\nu}$ signifies the matrix elements corresponding to classical Hartree repulsion term, which is expressed in terms of electron density which takes the following form within LCAO approximation,

$$\rho(\mathbf{r}) = \sum_{i=1}^{N} \sum_{\mu=1}^{K} \sum_{\nu=1}^{K} C_{\mu i} C_{\nu i} \phi_\mu(\mathbf{r})\phi_\nu(\mathbf{r}). \tag{11}$$

The remaining term, $V_{\mu\nu}^{XC}$ represents matrix element of XC contribution and constitutes the most difficult step of the whole process.

2.3.   Basis Set and Pseudopotential

Design and choice of an appropriate basis set for a particular problem is a very crucial step in molecular calculation. Stunningly large volumes of work have been done towards their construction as well as effects on various physicochemical properties. Broadly speaking, there are two major considerations besides accuracy: (a) reduction of number of functions in the expansion (b) ease and efficiency of the computation of relevant integrals. At the

onset, it is anticipated that basis set requirement for wave function-based and density-based approaches should be quite different. In the former, MOs generate approximate wave function, while in latter scenario, orbitals enter in to the picture indirectly as a tool to generate charge density. Ever since the inception of LCAO-MO procedures in quantum chemistry, a significantly large number of versatile, elegant, flexible basis sets have been developed in context of molecular calculation (for a variety of situations such as HF method, correlated post-HF methods, ground and excited states, weakly interacting systems, diffused systems such as anions etc). This remains to be a very tricky and delicate problem, at best, because as yet, there is no universal molecular basis set applicable for all methods or chemical systems of interest. Many decent reviews are available [2, 5, 8, 11] on this topic and thus our current disposition pertains only to the point as needed for our future discussion.

Some commonly used basis functions are: for periodic systems (e.g., solids), plane wave whereas for non-periodic systems (e.g., molecules, clusters), atom-centered localized basis sets such as Slater type orbitals (STO), Gaussian type orbitals (GTO), numerical radial functions, linear muffin-tin orbitals, delta functions, etc. Combination of basis sets have also been devised; e.g., in a Gaussian and augmented plane wave approach [40, 41], KS MOs and electron charge densities are expanded in Gaussian and an auxiliary augmented plane wave basis sets respectively. However, amongst all these, GTOs have gained maximum popularity over others and have remained the most preferred option for long time (also used in this work) chiefly due to their computational advantages offered for various multicenter one- and two-electron integrals involved (efficient analytical algorithms can be employed for these). STOs, on the other hand, although, were, at first used as a natural choice, for they correspond to atomic orbitals of H atom (and hence offer a better qualitative description of molecular orbitals), were later disfavored because of difficulty in evaluating the aforementioned integrals (no analytical routes are known and recourse must be taken to numerical techniques). Cartesian GTOs are typically written as,

$$\phi(\zeta, n_x, n_y, n_z; x, y, z) = N x^{n_x} y^{n_y} z^{n_z} \ e^{-\zeta r^2}. \tag{12}$$

In the above equation, N denotes normalization constant, while ζ, the orbital exponent, characterizes compactness (large ζ) or diffuseness (small ζ) of the function. Functions with $\lambda = n_x + n_y + n_z = 0, 1, 2, \cdots$, are referred to as $s, p, d, \cdots$, respectively, with λ being closely related to total angular momentum quantum number. It is easy to approximate the shape of an STO function by summing up a number of GTOs with different exponents and coefficients. However, usually one needs about three times as many GTOs than STO functions to achieve a certain desired accuracy. This dilemma is resolved by employing the so-called *contracted* GTOs consisting of a fixed linear combination (i.e., same coefficients and exponents) of the *primitive* functions, ϕ_p,

$$\phi_\mu^{\text{CGF}}(\mathbf{r} - \mathbf{R_A}) = \sum_{p=1}^{L} d_{p\mu} \phi_p(\zeta_{p\mu}, \mathbf{r} - \mathbf{R_A}). \tag{13}$$

Here L corresponds to the length of contraction, $d_{p\mu}$ is contraction coefficient, "p" symbolizes primitive functions while "CGF" stands for contracted Gaussian functions. Gaussian primitives are often optimized from atomic calculations (ideally HF or CI, etc.) variationally until lowest total energy of the atom achieved; there are also cases where they are explicitly optimized through KS scheme using XC functionals of homogeneous electron gas.

However, interestingly, basis sets originally designed for wave function-based methodologies apparently work fairly well, as fortunately it turns out that, for most of the common important properties (like energy, equilibrium geometry, etc.), the results are fairly insensitive with respect to the way exponents and coefficients in a basis set have been determined. This gives us a pleasant opportunity for it validates the use of basis sets, primarily designed for wave function based methods, within the rubric of DFT, with reasonable confidence.

Now it is well known that many-electron HF or KS equation could be much simplified by dividing electrons into core and valence categories. Inner-shell electrons, being strongly bound to the nucleus (forming the so-called "inert" core and thus to a good approximation, retain an atomic-like configuration), play less significant role in chemical binding and most of the chemical properties can almost completely be accounted for by taking care of valence shells only. In essence, this facilitates to replace the strong Coulomb potential of nucleus and tightly bound core electrons by an effective potential (smoother, non-local) acting on the valence electrons. Under these circumstances, our desired KS equation in presence of pseudopotential could be rewritten as,

$$\left[-\frac{1}{2}\nabla^2 + v_{ion}^p(\mathbf{r}) + v_H[\rho](\mathbf{r}) + v_{xc}[\rho](\mathbf{r})\right]\psi_i(\mathbf{r}) = \epsilon_i\psi_i(\mathbf{r}), \tag{14}$$

where v_{ion}^p denotes ionic pseudopotential for the system,

$$v_{ion}^p = \sum_{R_a} v_{ion,a}^p(\mathbf{r} - \mathbf{R_a}). \tag{15}$$

Here, $v_{ion,a}^p$ is the ion-core pseudopotential associated with atom A, situated at R_a; $v_H[\rho](\mathbf{r})$ describes the classical electrostatic interaction among valence electrons, while $v_{xc}[\rho](\mathbf{r})$ represents non-classical part of the many-electron Hamiltonian.

A host of different pseudopotentials have been developed by many workers over the years, such as empirical, *ab initio*, norm-conserving, ultrasoft, etc., [42, 43, 44, 45, 46, 47, 9]. This work uses the *ab initio* effective core potentials developed by [48, 49], where total potential is expressed in terms of projection operators, $P_l = |l\rangle\langle l|$, as,

$$U(r) = U_L(r) + \sum_{l=0}^{L-1} [U_l(r) - U_L(r)]\, P_l. \tag{16}$$

In this equation, U_l identifies numerical effective core potentials for each l. For computational conveniences, an analytic form for $U(r)$ is obtained by fitting,

$$\begin{aligned} r^2\left[U_l(r) - U_L(r)\right], & \qquad l = 0, 1, \cdots, L-1, \\ r^2\left[U_l(r) - N_c/r\right], & \qquad l = L, \end{aligned} \tag{17}$$

to a Gaussian of the form $\sum_k d_k r^{n_k} e^{-\zeta_k r^2}$. Here, L signifies the lowest angular momentum not represented in core, N_c is number of core electrons and $n_k = 0, 1, 2$.

2.4.   Computational Considerations

In this subsection we discuss various practical problems encountered in dealing with the solution of a molecular KS equation within the basis-set framework. Before we get

into mind-boggling details, it is noteworthy to mention, on the outset, that formally HF calculation scales as N^4, while KS calculations do so no worse than N^3, where N stands for number of basis functions. Clearly, this is better than HF by a factor of N and significantly better than other traditional correlated methods. This N^4 originates from the total number of two-electron repulsion integrals (proportional to N^4) in the HF case. However later it has been argued that well-implemented HF or KS programs for large systems, in effect, scale as N^2 only, if one takes consideration of the fact that a vast majority of these two-electron integrals are essentially zero due to negligible overlap among basis functions involved.

A very widely used LCAO-MO-based DFT procedure [50] introduces an *auxiliary* basis set (in addition to the one used for MO expansion) to fit (often some variation of least square technique) some of the computationally intensive terms to reduce the integral evaluation overhead significantly, making this an N^3 process. Some of the earliest notable works in this direction [51, 52, 53] proposed following expansion for electron density and XC potential in terms of auxiliary basis sets, f_i and g_j respectively as,

$$\rho(\mathbf{r}) \quad \approx \quad \tilde{\rho}(\mathbf{r}) = \sum_i a_i f_i(\mathbf{r}) \tag{18}$$

$$v_{xc}(\mathbf{r}) \quad \approx \quad \tilde{v}_{xc}(\mathbf{r}) = \sum_j b_j g_j(\mathbf{r}),$$

where tildes identify fitted quantities and $\{a_i\}, \{b_j\}$ are the fitting coefficients. The latter are determined by minimization of either the following straightforward function,

$$Z = \int [\rho(\mathbf{r}) - \tilde{\rho}(\mathbf{r})]^2 \mathrm{d}\mathbf{r}, \tag{19}$$

or Coulomb self-repulsion of residual density. Both, of course, are subject to the constraint that normalization of this fitted density gives total number of electrons. Originally, this technique was first suggested in the context of STOs [54] and later extended to GTOs [51]. Typically XC potentials are calculated in real-space; corresponding matrix elements are evaluated by some analytical means.

While the above fitting procedure has witnessed tremendous success in explaining many chemical phenomena within DFT, it suffers from some serious discomfitures. Firstly, there are many different flavors of fitting techniques (variational as well as non-variational) available which remains a primary source of inconsistency among various implementations; also constraints imposed on density and XC fitting are different, thus aggravating the problem. Second, number of electrons is not automatically conserved in fitted density; neither does it reproduce true multipole moments exactly. Another important shortcoming of this scheme is that this greatly complicates analytic derivative theories. Last, but not the least, it is worth mentioning that, the historical motivation for development of fitting method arose primarily due to the lack of efficient, good-quality integral methods at that time. However thereafter, a plethora of work was reported by various workers on multi-center molecular integrals (see [55] for a review); thus once seemingly daunting task of integration evaluation, although even now poses a major efficiency issue, has found many attractive, elegant, high-quality, manageable and satisfactory approximations. As expected, however, the appeal of fitting method somehow dwindled with time, especially after the emergence of numerous highly accurate efficient quadrature schemes.

Solution of our desired KS equation always involves mathematically non-trivial integrals. Unlike the exchange integrals of HF theory which can be analytically calculated for Gaussians basis sets, unfortunately, XC functionals (by virtue of their complicated approximate algebraic forms) in DFT require computation of integrals, for which, as yet, there is no easy analytic route available and almost invariably must only be done by numerical methods. One of the most successful, popular and generic schemes (so-called atom-centered grid (ACG)), is due to [56]. In this case, a 3D molecular integrand is partitioned into single-center discrete, overlapping atomic "cells". For an arbitrary integrand $F(\mathbf{r})$, this decomposition gives the value of integral I, as,

$$I = \int F(\mathbf{r})\mathrm{d}\mathbf{r} = \sum_A^M I_A. \tag{20}$$

Here, the sum runs over all M nuclei present in the system, and $I_A = \int F_A(\mathbf{r})\mathrm{d}\mathbf{r}$ denotes single-center atomic contributions in it. Atomic integrands, F_A are chosen such that when summed over all the nuclei M, they should return our original function,

$$\sum_A^M F_A(\mathbf{r}) = F(\mathbf{r}). \tag{21}$$

The individual components $F_A(\mathbf{r})$ are finally constructed from original integrand through some sufficiently well-behaved weight functions, $F_A(\mathbf{r}) = w_A(\mathbf{r})F(\mathbf{r})$. Thus each of the atomic subintegrations can be carried out using standard mono-centric numerical techniques. Once F_As are determined, the corresponding integrals I_A are subsequently computed on grid as follows (assuming polar coordinates, which is the commonest choice in literature),

$$I_A = \int_0^\infty \int_0^\pi \int_0^{2\pi} F_A(r, \theta, \phi) r^2 \sin\theta \, \mathrm{d}r \, \mathrm{d}\theta \, \mathrm{d}\phi \approx \sum_p^P w_p^{\mathrm{rad}} \sum_q^Q w_q^{\mathrm{ang}} F_A(r_p, \theta_q, \phi_q), \tag{22}$$

where w_p^{rad}, w_q^{ang} signify radial, angular weights respectively with P, Q points (total number of points being $P \times Q$). Usually angular part is not further split into separate θ, ϕ contributions, as surface integrations on a sphere can be done numerically quite easily accurately by the help of available highly efficient algorithms.

Judicious choice and determination of proper weight functions involve certain amount of mathematical subtlety and requires both scientific as well as artistic skill. Detailed account on this and various other related issues can be found in following references [56, 57, 58]. A number of elegant and clever prescriptions have been proposed for both radial as well as angular integrations, depending on the particular quadrature scheme and mapping functions. Some of the most promising choices for former are: Gauss-Chebyshev quadrature of second kind, Chebyshev quadrature of first and second kind, Gaussian quadrature, Euler-MacLaurin formula, numerical quadrature [57, 58, 59, 60, 61], etc. For angular integrations, there is some sort of consensus that octahedral Lebedev grid [62, 63, 64] is possibly the most efficient and satisfactory. Numerically 3D integration of molecular integrands have also been achieved based on a division of space and applying product Gauss rule for subsequent integration of resulting regions [65]. A variational integration mesh

[66], depending on the position of individual atoms in three different regions of space, *viz.,* atomic spheres, excluded cubic region and interstitial parallelepiped, has been reported as well. In another development [67], an automatic numerical integrator capable of generating adaptive molecular grid depending on size and shell structure of a given basis set, was also suggested.

The above observation clearly points out that LCAO-MO-based KS DFT calculations of molecules have largely been done through ACG. Very little attempt has been made to test other grids in this occasion. Of particular interest is the much simpler cartesian co-ordinate grid (CCG). To our knowledge, virtually no results are available to judge their performance. In a Fourier Transform Coulomb method [68], molecular integrations have been approached by separating Gaussian shell pairs into "smooth" and "sharp" categories. Of late, a multiresolution technique has also been proposed, where a connection between CCG and ACG is made via a divided-difference polynomial interpolation scheme, which virtually translates the electron density and gradients from former to latter [69]. Our primary objective here is to report the development of a new, successful DFT methodology [70, 71] which utilizes CCG. This has been shown to produce highly accurate dependable results for small to medium sized atoms/molecules using Gaussian basis set. For a series of atoms and molecules, results offered were almost identical to those obtained from other existing reliable calculations available (especially those involving ACG). Atom-centered basis functions, electron densities, MOs, as well as Hartree and XC potentials all are directly built up on a real uniform 3D Cartesian grid simulating a cubic box (although nonuniform grids could be used for this purpose, and we are currently engaged into it),

$$r_i = r_0 + (i-1)h_r, \quad i = 1, 2, \cdots, N_r; \quad \text{for } r \in \{x, y, z\}, \tag{23}$$

where h_r, N_r signify the grid spacing and total number of grid points respectively ($r_0 = -N_r h_r/2$). Electron density in this grid is then simply given by,

$$\rho(\mathbf{r}) = \sum_i^N |\psi_i(\mathbf{r})|^2 = \sum_{\mu=1}^K \sum_{\nu=1}^K P_{\mu\nu} \, \phi_\mu(\mathbf{r}) \, \phi_\nu(\mathbf{r}). \tag{24}$$

Here $P_{\mu\nu}$ represents an element of the density matrix.

Now we turn our focus on to a discussion on calculation of classical electrostatic repulsion potential in the grid. For finite systems, possibly the simplest and crudest means to compute $v_H(\mathbf{r})$ consists in a direct numerical integration, which, in many occasions show sluggish performance, and in general, remains feasible only for relatively smaller systems. However the most successful and favorite route is through a solution of corresponding Poisson equation. An alternate accurate and efficient technique utilizes conventional Fourier convolution method and several of its variants [72, 73]; this has been immensely successful in the context of molecular modeling in recent years,

$$\begin{aligned} \rho(\mathbf{k}) &= \text{FFT}\{\rho(\mathbf{r})\} \\ v_H(\mathbf{r}) &= \text{FFT}^{-1}\{v_H^c(\mathbf{k})\rho(\mathbf{k}). \end{aligned} \tag{25}$$

Here $\rho(\mathbf{k})$ and $v_H^c(\mathbf{k})$ represent Fourier integrals of density and Coulomb interaction kernel, respectively, in the grid. The former is customarily obtained from a discrete Fourier

Table 1. Energy components and total number of electrons (in a.u.) for Cl$_2$ compared with reference values at $R = 4.20$ a.u., for various grids.

	$N_r = 32$			$N_r = 64$		$N_r = 128$		$N_r = 256$	Ref. [78]
Set	A	B	C	D	E	F	G	H	
h_r	0.3	0.4	0.2	0.3	0.4	0.1	0.2	0.1	
$\langle T \rangle$	11.00750	11.17919	11.18733	11.07195	11.06448	11.18701	11.07244	11.07244	11.07320
$\langle V_t^{ne} \rangle$	−83.43381	−83.68501	−83.70054	−83.45722	−83.44290	−83.69988	−83.45810	−83.45810	−83.45964
$\langle V_t^{ee} \rangle$	32.34338	31.22265	31.22885	31.00981	31.00306	31.22832	31.01000	31.01000	31.01078
$\langle V \rangle$	−39.42376	−40.79570	−40.80503	−40.78074	−40.77317	−40.80489	−40.78144	−40.78144	−40.78219
$\langle E_{el} \rangle$	−40.08293	−41.28318	−41.28437	−41.37545	−41.37535	−41.28455	−41.37566	−41.37566	−41.37566
$\langle E \rangle$	−28.41626	−29.61651	−29.61770	−29.70878	−29.70868	−29.61789	−29.70900	−29.70900	−29.70899[1]
N	13.89834	13.99939	13.99865	14.00002	14.00003	13.99864	14.00000	13.99999	13.99998

transform of its real-space value by standard FFT quite easily. Evaluation of the latter, however, is a non-trivial task because of the presence of singularity in real space and demands caution. In our current communication, this is overcome by applying a decomposition of the kernel into long- and short-range interactions, reminiscent of the commonly used Ewald summation technique in condensed matter physics,

$$v_H^c(\mathbf{r}) = \frac{\text{erf}(\alpha r)}{r} + \frac{\text{erfc}(\alpha r)}{r} \equiv v_{H_{\text{long}}}^c(\mathbf{r}) + v_{H_{\text{short}}}^c(\mathbf{r}), \tag{26}$$

where erf(x) and erfc(x) correspond to the error function and its complements respectively. Short-range Fourier integral can be calculated analytically whereas the long-range contribution can be obtained directly from FFT of real-space values. There are several other routes as well available for classical repulsion as needed in the large-scale electronic structure within KS DFT framework. For example, in the fast multipole method, near-field contributions are handled explicitly, while the far-field is treated through a clustering of spatial cells, whereas the field itself is expressed by a multipole expansion. Another efficient route employs a multigrid method within real-space formalism (such as finite difference or finite element). More thorough account on this topic is covered in the review [28].

Now a few words on the construction of respective one- and two-body matrix elements is in order. All the one-electron integrals like overlap, kinetic-energy, nuclear-attraction integral, pseudopotential integral as well as their respective matrix elements are completely identical to those encountered in standard GTO-based HF calculation; they are performed by following standard recursion algorithms [74, 75, 76]. In absence of any analytical method, respective two-electron matrix elements in the real-grid are computed through direct numerical integration,

$$\langle \phi_\mu(\mathbf{r}) | v_{HXC}(\mathbf{r}) | \phi_\nu(\mathbf{r}) \rangle = h_x h_y h_z \sum_{\text{grid}} \phi_\mu(\mathbf{r}) v_{HXC}(\mathbf{r}) \phi_\nu(\mathbf{r}). \tag{27}$$

The matrix eigenvalue problem is accurately and efficiently solved using standard LAPACK routines [77] following usual self-consistent procedure to obtain KS eigenvalues and eigenfunctions, from which total energies and/or other quantities can be calculated. In all the results presented in next section, convergence of three quantities, *viz.,* (i) potential (ii) total energies and (iii) eigenvalues has been monitored. Tolerance of 10^{-6} a.u., was employed for (ii), (iii), while 10^{-5} a.u., for (i).

3.   Results and Discussion

At first, we will examine the stability and convergence of our calculated nonrelativistic ground-state energies as well as individual energy components for a representative molecule, Cl_2 with respect to grid parameters (8 Sets are given), in Table I, at an internuclear distance 4.20 a.u., for LDA XC potential. These are to compared with the widely used GAMESS [78] quantum chemistry program, with same XC functional, basis set and effective core potential. The homogeneous electron-gas correlation of Vosko-Wilk-Nusair (VWN) [79] is employed in all LDA calculations. The Hay-Wadt (HW) valence basis set, used in this work, has the orbital split into inner and outer components (described by two and one primitive Gaussians respectively). Total integrated electron density, N is given as well. Reference total energies obtained from "grid" and "grid-free" DFT are quoted; former using a default "army" grade grid with Euler-McLaurin quadratures for radial integration and Gauss-Legendre quadrature for angular integrations. Grid-free approach [80, 81], on the other hand, utilizes a resolution of identity to simplify molecular integrals over functionals rather than in quadrature grids. Most appealing feature of such a method is that it enables one to bypass any error associated with a finite grid; however that usually requires an auxiliary basis set to expand the identity itself, which also suffers from inherent weakness of incompleteness. First we note that, our maximum deviation in energy and N with respect to reference values is observed in Set A, mainly because our box length is insufficient to capture all important interactions present. At Set B, with an increase in spacing, box gets enlarged and all these quantities get significantly bettered than in Set A. Notice that Sets C and F both produce very similar results for all quantities including N, which is expected intuitively, as they both cover same box length. As Set B also corresponds to same box size as the above two Sets, results are again comparable; however, component energies and N show slight deviations. Sets D, E give all energy quantities as well as N in very good agreement with reference values. For further verification, some calculations are also performed in relatively larger finer grids F, G, H. From above discussion it is easily concluded that Sets D, E, G, H are our four best results, while Sets D, E are sufficiently accurate for all practical purposes. More detailed discussion on this (for Cl_2, HCl) could be found in [70].

Now a thorough comparison was made for computed eigenvalues for Cl_2 (at $R = 4.20$ a.u.) and HCl (at $R = 2.40$ a.u.) for several grid sets [70]. These either completely match or show an absolute maximum deviation of only 0.0001 a.u., for all sets, except E, where the same becomes 0.0007 a.u. Figure I shows the potential energy curve for Cl_2 and HCl, for 4 Sets. Total energies for both these molecules are given in [70], for $R = 3.50 - 5.00$ (Cl_2) and $R = 1.60 - 3.10$ (HCl), at intervals of 0.1 a.u. [71]. Clearly they faithfully reproduce reference energies for the entire range of R. For Cl_2, Set D energy values are quite well (higher by only 0.0001 a.u.) up to $R = 4.00$ a.u., and after that shows a gradual tendency to deviate. Even then the maximum discrepancy is quite small (0.0007 a.u. for $R = 5.00$). Sets G and I ($N_r = 128, h_r = 0.3$) either completely match with reference values or show deviations of only 0.0001 a.u. Computed energies are always found to be above reference values except in two occasions ($R = 4.00$ and 4.30 for Set G). Excepting two R values, Set G gives exact quantitative agreement with reference results. For HCl also, very good agreement is observed for all three sets with reference values, with Set D performing best.
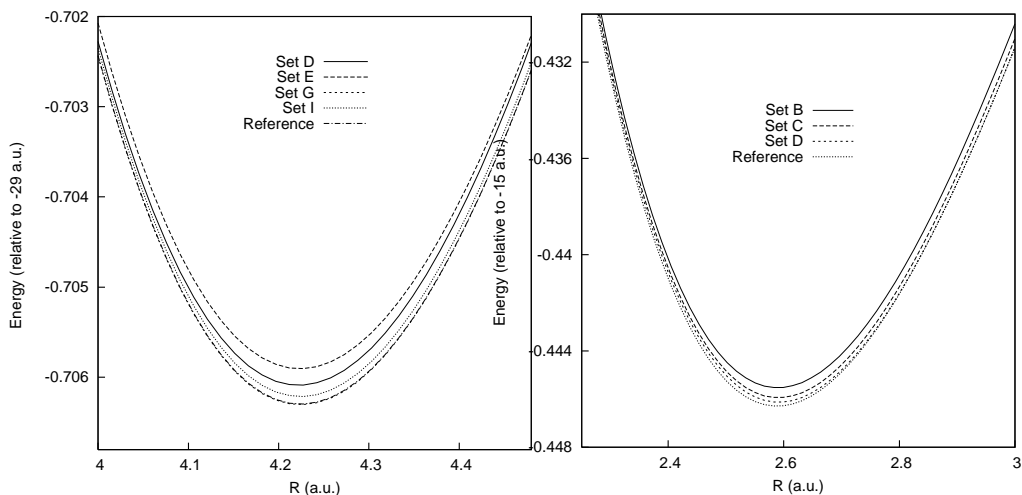
Figure 1. Cl$_2$(left panel) and HCl(right panel) potential energy curves for different grid sets.

Table 2. Kinetic energy, $\langle T \rangle$, potential energy, $\langle V \rangle$, total energy, E, and N for selected atoms and molecules (in a.u.) within LDA. PW=Present Work.

System	$\langle T \rangle$		$-\langle V \rangle$		$-\langle E \rangle$		N	
	PW	Ref. [78]	PW	Ref. [78]	PW	Ref. [78]	PW	Ref. [78]
Na$_2$	0.14507	0.14499	0.52800	0.52791	0.38292	0.38292	1.99999	2.00000
P	2.35430	2.35334	8.73501	8.73404	6.38070	6.38071	5.00000	4.99999
Br	4.22038	4.22011	17.28157	17.28131	13.06119	13.06120	7.00000	6.99967
PH$_3$	4.08953	4.08953	12.27387	12.27383	8.18434	8.18430	8.00000	7.99965
SiH$_2$Cl$_2$	13.95036	13.94989	48.78729	48.78685	34.83693	34.83696	19.99999	20.00015

Now that the stability and reliability of our current method is established, in Table II, we assess its performance for a representative set of atoms and molecules, within the LDA approximation, in terms of energy components and N. Henceforth, in this and all other tables presented in this work, all experimental geometries are taken from [82]. Set E grid is used for all these calculations, which was found to be quite satisfactory for Cl$_2$, HCl. These are ordered with increasing N. Reference grid-DFT results are quoted for direct comparison. Excellent agreement is observed once again, for all of them, as expected. For LDA results on a more extended set of atoms and molecules, see [70].

So far we have discussed only LDA results. It is well-known that local density functionals suffer from a number of serious problems. Hence it is essential to use more accurate functionals for practical calculations. Note that E_{xc} accounts for two separate contributions in terms of two differences, *viz.,* (i) between classical and quantum mechanical electron repulsion (ii) between kinetic energies of fictitious non-interacting system and actual systems concerned. In practice, most functionals do not make explicit attempts to incorporate this second portion. Since exact functionals are not available as yet, a host of fairly accurate, sophisticated, elaborate approximate functionals have been devised with varying degrees of complexity over the years. These have been found to be quite valuable for a broad range of chemical problems (see, for example, [83, 84, 85, 86, 87, 88, 89, 90, 91, 92, 93], for

Table 3. Variation of BLYP energy components as well as N with respect to grid parameters for Cl_2 and HCl. Quantities are in a.u.

Set	Cl_2 ($R = 4.2$ a.u.)			HCl ($R = 2.4$ a.u.)		
	A	B	Ref. [78]	A	B	Ref. [78]
N_r	64	128		64	128	
h_r	0.3	0.2		0.3	0.2	
$\langle T \rangle$	11.21504	11.21577	11.21570	6.25431	6.25464	6.25458
$\langle V_t^{ne} \rangle$	−83.72582	−83.72695	−83.72685	−37.29933	−37.29987	−37.29979
$\langle V_t^{ee} \rangle$	31.07572	31.07594	31.07594	12.63884	12.63903	12.63901
$\langle V \rangle$	−40.98344	−40.98434	−40.98424	−21.74382	−21.74417	−21.74411
$\langle E_{el} \rangle$	−41.43506	−41.43524	−41.43522	−18.40618	−18.40620	−18.40620
$\langle E \rangle$	−29.76840	−29.76857	−29.76855[1]	−15.48951	−15.48953	−15.48953[2]
N	14.00006	14.00000	13.99998	8.00002	8.00000	8.00000

some representative candidates). Commonly used functionals typically use gradient and/or Laplacian of density–the so-called generalized gradient approximation (GGA); there is also a class of orbital-dependent functionals, such as optimized effective potential approach; yet another category combines orbital-dependent HF and an explicit density functional falling in to the variety of "hybrid functionals". At this stage, we wish to extend the scope of applicability of our method by incorporating at first, gradient corrected XC functionals (popular non-local Becke exchange [83] and Lee-Yang-Parr (LYP) correlation [84]) are used, for illustration. For practical implementional purposes, however, an alternative equivalent form [94], containing only first derivative has been used for LYP correlation functional. This demonstrates feasibility and viability of our current scheme in the context of non-local XC functionals which would be necessary for future chemical applications. Following [95], gradient-dependent functionals can be treated without evaluating density Hessians by using a finite-orbital basis expansion. To this end, XC contributions of KS matrix is written in following working form,

$$F_{\mu\nu}^{XC\alpha} = \int \left[\frac{\partial f}{\partial \rho_\alpha} \chi_\mu \chi_\nu + \left(2 \frac{\partial f}{\partial \gamma_{\alpha\alpha}} \nabla \rho_\alpha + \frac{\partial f}{\partial \gamma_{\alpha\beta}} \nabla \rho_\beta \right) \cdot \nabla(\chi_\mu \chi_\nu) \right] d\mathbf{r} \qquad (28)$$

where $\gamma_{\alpha\alpha} = |\nabla \rho_\alpha|^2$, $\gamma_{\alpha\beta} = \nabla \rho_\alpha \cdot \nabla \rho_\beta$, $\gamma_{\beta\beta} = |\nabla \rho_\beta|^2$ and f is a function only of local quantities ρ_α, ρ_β and their gradients. Non-local functionals are implemented using the Density Functional Repository program [96].

A comparison of our calculated BLYP ground-state energy components and N with respect to variations in grid parameters are given in Table III, for Cl_2 and HCl at internuclear distances 4.2 and 2.4 a.u respectively. To make a test of our convergence, a series of calculations were performed which produced very similar conclusions as reached in for LDA XC-case. From these numerical experiments, results for two selected sets are presented here, which is sufficient to illustrate the relevant points. Reference theoretical results of [78] have been quoted once again, for comparison, employing same basis set, effective core potential within grid method). Some extra calculations in different grids were also done for a decent number of molecules to monitor performance of calculated energies as well as other quantities with respect to radial and angular grid, *viz.*, (i) $N_r, N_\theta, N_\phi = 96, 36, 72$ (ii)

Table 4. Comparison of BLYP negative eigenvalues (in a.u.) of Cl_2, HCl with reference values.

MO Set	Cl_2 ($R = 4.2$ a.u.)			MO	HCl ($R = 2.4$ a.u.)		
	A	B	Ref. [78]		A	B	Ref. [78]
$2\sigma_g$	0.8143	0.8143	0.8143	2σ	0.7707	0.7707	0.7707
$2\sigma_u$	0.7094	0.7094	0.7094	3σ	0.4168	0.4167	0.4167
$3\sigma_g$	0.4170	0.4171	0.4171	$1\pi_x$	0.2786	0.2786	0.2786
$1\pi_{xu}$	0.3405	0.3405	0.3405	$1\pi_y$	0.2786	0.2786	0.2786
$1\pi_{yu}$	0.3405	0.3405	0.3405				
$1\pi_{xg}$	0.2778	0.2778	0.2778				
$1\pi_{yg}$	0.2778	0.2778	0.2778				

$N_r, N_\theta, N_\phi = 128, 36, 72$, in addition to the default grid ($N_r, N_\theta, N_\phi = 96, 12, 24$). Three integers here denote number of integration points in r, θ, ϕ directions respectively. Overall, very similar results were obtained from these sets. For example, out of a total of 17 atoms and molecules, total energies remained unchanged up to 5th decimal place for 8 species, while in remaining cases, very slight deviations were observed among them; the largest in total energy being 0.00064 a.u. for Na_2Cl_2 (for all others this remains below 0.00007). However, passing from default grid to (ii) gradually improves N. Quantities considered are those same as those in Table I, *viz.,* kinetic (T), total nucleus-electron attraction (V_t^{ne}), total two-electron potential (V_t^{ee}), total potential (V), electronic (E_{el}), total energy (E) and N. Evidently, once again, calculated results show excellent agreement with literature values, as found earlier in LDA case. For obvious reasons, Set B results are expected to be better than A; this does happen, but only marginally. Cl_2 shows this effect slightly more pronounced than that for HCl. Set B total energies show absolute deviations of 0.00002 and 0.00000 a.u. respectively for Cl_2 and HCl. For all practical purposes, Set A is adequate enough for both of them. Note that reference *grid-free* and *grid*-DFT energies differ substantially from each other.

As in the LDA case, now our calculated orbital energies for Cl_2, HCl are compared with reference eigenvalues within BLYP XC functional [71] in Table IV. In this occasion too, both molecules produce highly satisfactory agreement with literature values. Sets A and B results match *completely* for *all* orbital energies except the lone case of 3σ levels for both (with absolute deviation being only 0.0001 a.u.). Now, a thorough comparison of our computed total energies of Cl_2 ($R = 3.5 - 5.0$ a.u.) and HCl ($R = 1.5 - 3.0$ a.u.) for BLYP XC functional was made, as in LDA case, for a broad range of internuclear distance, with intervals of 0.1 a.u. [70]. It is quite gratifying that, for both molecules, Sets A and B results practically coincide on reference values for the *entire* range of R. Cl_2 gives a maximum absolute deviation of 0.0001 a.u. with Set B and 0.0002 a.u. (only in 2 instances) with Set A. However, for HCl, the two corresponding deviations remain well below 0.0001 a.u. For further details, see [71].

Table V reports various energy components as well as N for selected atoms, molecules calculated using BLYP XC functional (ordered in terms of increasing N as we descend the table). Calculated component energies show very similar agreements with reference values

Table 5. Comparison of BLYP energy components (in a.u.) and N for selected atoms, molecules with reference grid-DFT results. PW=Present Work.

System	$\langle T \rangle$		$-\langle V \rangle$		$-\langle E \rangle$		N	
	PW	Ref. [78]	PW	Ref. [78]	PW	Ref. [78]	PW	Ref. [78]
Mg	0.24935	0.24935	1.06017	1.06017	0.81082	0.81083	1.99999	1.99999
Br	4.27022	4.27043	17.36122	17.36148	13.09100	13.09105	7.00000	6.99999
$MgCl_2$	11.75947	11.75999	42.54049	42.54103	30.78102	30.78104	16.00004	15.99999
SiH_2Cl_2	14.14948	14.14945	49.04463	49.04461	34.89515	34.89516	19.99999	20.00000

as noted in previous tables and are thus omitted to avoid repetition. Atomic calculations were performed using $N_r = 64, h_r = 0.4$, whereas for molecules $N_r = 128, h_r = 0.3$, was used. Overall, present results agree with reference values excellently. Out of 5 atoms and 10 molecules, in 5 occasions, total energies are identical as those obtained from reference theoretical method; maximum absolute deviation in total energy remains well below 0.0013%. Results for more atoms and molecules are given in [71].

Finally Table VI gives a comparison of calculated $-\epsilon_{\text{HOMO}}$ (in a.u.) and atomization energies (in kcals/mole) with experimental results [97] for select 7 molecules at their experimental geometries [82], for both LDA and BLYP XC functionals. Since reference theoretical results from [78] are practically identical to ours (as anticipated from previous discussion), they are omitted here. An asterisk in experimental atomization energies denote 298°K values; otherwise they imply 0°K values. Ionization energies are also reported for another exchange functional, for the following reason. It may be remembered that simple LDA or GGA XC potentials suffer from improper asymptotic *long-range* behavior. Stated otherwise, whereas ground-state total energies of atoms, molecules, solids are estimated quite satisfactorily through these functionals, unfortunately ionization energies obtained from these functionals are typically off by 30-50% of experimental values. Furthermore, these functionals provide a rather poor description of higher-lying excited states. At this stage, we note that a fundamental, primary objective of our proposed methodology is to extend its scope and applicability towards dynamical studies of atoms and molecules (particularly under the influence of strong high-intensity laser field through multi-photon ionization, high-order harmonic generation, photoionization, photoemission, photodissociation, etc.) via TDDFT, that can potentially exploit the remarkable advances already made in basis-set based DFT approaches in the past decades. This has been a highly fertile, fascinating area of research for more than a decade, for they (i) possess a wealth of information about many important, fundamental physical and chemical phenomena (often counter-intuitive) occurring in such systems (ii) could lead to diverse practical applications in various branches of science, engineering (iii) pose enormous complications and challenges for both experiment and theory (some representative references are, for example, [98, 99, 100, 101, 102, 103]). Of late, activity in this field has dramatically increased, as evident from an enormous number of sophisticated experimental and theoretical works reported in the literature. Theoretically, while there exists a few approaches to deal with such systems (mostly within single active electron or frozen-core approximation), dependable *ab initio* calculations have been very much limited for atoms and even more for molecules, so much so that accurate calculations of even H_2 molecule is a significantly challenging task, not to speak of polyatomic molecules, in general. Moreover whereas remarkable advance-

ments has been made for atomic case, molecular situation, nowadays, is in its embryonic stage only. Our long term goal is to formulate a general non-perturbative TDDFT-based formalism for dynamical studies of such species using an LCAO-MO prescription for solution of the TDKS equation, rather than a grid-discretization of molecular KS equation, as has been traditionally employed.

A necessary prerequisite for such dynamical studies is that both ionization energies as well as higher levels be approximated more accurately. The modified Leeuwen-Baerends (LB) potential [104, 105], $v_{xc\sigma}^{LB\alpha}(\alpha, \beta : \mathbf{r})$, which contains two empirical parameters, seems to be a very good choice in this game (see, for example, [106], and the references therein). This is conveniently written as,

$$v_{xc\sigma}^{LB\alpha}(\alpha, \beta : \mathbf{r}) = \alpha v_{x\sigma}^{LDA}(\mathbf{r}) + v_{c\sigma}^{LDA}(\mathbf{r}) + \frac{\beta x_\sigma^2(\mathbf{r})\rho_\sigma^{1/3}(\mathbf{r})}{1 + 3\beta x_\sigma(\mathbf{r})\ln\{x_\sigma(\mathbf{r}) + [x_\sigma^2(\mathbf{r}) + 1]^{1/2}\}} \quad (29)$$

Here σ signifies up, down spins and last term containing gradient correction bears some resemblance with the exchange energy density functional of [83], $x_\sigma(\mathbf{r}) = |\nabla\rho_\sigma(\mathbf{r})|[\rho_\sigma(\mathbf{r})]^{-4/3}$ is simply a dimensionless quantity, $\alpha = 1.19, \beta = 0.01$. The desired long-range property is satisfied properly, i.e., $v_{xc\sigma}^{LB\alpha}(\mathbf{r}) \to -1/r, r \to \infty$. Ionization energies obtained from LBVWN (LB exchange, VWN correlation) combination of XC functionals are presented in column 4 to demonstrate its noticeable superiority over LDA or BLYP counterpart. It is clear that, for all these species considered, LDA ionization energies are consistently lower than corresponding BLYP values, whereas LBVWN values are substantially lower and presumably more accurate (this feature will be very important for TDDFT calculations in future which requires accurate higher-lying states) than both these two functionals. Now, computed LDA, BLYP, atomization energies are also compared with experimental results (including zero-point vibrational correction and relativistic effects) in columns 6,7, which shows considerable deviation from experimental results. Surprisingly, LDA results are apparently better than their BLYP counterparts, in several occasions. However this observation should not be taken too optimistically to favor the former over the latter, for there could be some cancellation of errors in LDA case. Moreover, several other factors, such as use of more appropriate pseudopotential, basis set, etc., should be taken into consideration. Large deviations are observed in atomization energies, which could be also due to the above factors. However, such discrepancies are not so uncommon in DFT, even in more elaborate and extended basis sets within all-electron calculation as well (see, for example, [107]). In any case, this is an evolving process and does not directly interfere with the main objective of this work.

4. Future and Outlook

We have demonstrated the plausibility and feasibility of simple CCGs in atomic/molecular domain within the context of Gaussian-based LCAO approach to DFT. For a modest number of atoms, molecules, this has been found to be extremely accurate and dependable; producing practically identical results with those obtained from other grid-based/grid-free quantum chemistry programs available in the literature. Atom-centered localized basis set, MOs, two-body potentials have been constructed on a 3D cubic box directly. Illustrative results have been presented for local and non-local XC density functionals. Classical Hartree potential was obtained through a Fourier convolution technique,

Table 6. Negative HOMO energies, $-\epsilon_{HOMO}$ (in a.u.) and atomization energies (kcals/mol) for a cross-section of molecules. LDA, LBVWN (LB+VWN), BLYP results are compared with experiment [97]. An asterisk indicates 298°K values. Otherwise, 0°K results are given.

Molecule	$-\epsilon_{HOMO}$ (a.u.)				Atomization energy (kcals/mol)		
	LDA	BLYP	LBVWN	Expt. [97]	LDA	BLYP	Expt. [97]
Al_2	0.1407	0.1400	0.2371	0.1984	22.92	21.42	37.0
HI	0.2518	0.2432	0.3824	0.3817	82.82	72.07	45.8*
SiH_4	0.3188	0.3156	0.4624	0.4042	339.43	312.02	302.6
S_2	0.2007	0.2023	0.3443	0.3438	56.75	52.47	100.8
$SiCl_2$	0.2514	0.2448	0.3909	0.3804	190.40	155.11	202.7
P_4	0.2712	0.2575	0.3964	0.3432	200.77	142.99	285.9
PCl_5	0.2825	0.2722	0.4397	0.3748	246.22	145.33	303.2

accurately and efficiently in the real grid. No auxiliary basis set was invoked and Hay-Wadt-type pseudopotentials was used to describe core electrons. The method has been overwhelmingly successful in predicting static properties, such as total energy and component energies, HOMO energies, potential energy curves, orbital energies, atomization energies. The results were found to be variationally bounded.

This works provides the necessary springboard to explore the possibility of investigating real-time dynamical studies of many-electron systems which constitutes one of our next immediate future objective. In particular, our interest lies in the laser-atom/molecule interactions in intense/superintense regime, which are inherently non-perturbative, non-linear phenomena. Although a number of theoretical methods have been developed for their studies, TDDFT seems to be the most promising among them. Within TDDFT, however, only real-space methods have been employed in a number of such problems with some success. However, to our knowledge, no attempt has been made so far to exploit a Gaussian-based DFT approach (which has been so profoundly successful for a multitude of static problems over the past several decades) in real-time dynamical regime. The overwhelming success of this work, as illustrated here, encourages to venture into such an undertaking and it is hoped that this will be equally fruitful in our future dynamical studies. Incorporation of LB exchange potential was a necessary first step in developing a basic workable solution for this. Introduction of more appropriate pseudopotentials devoted to density functional methods as well as more elaborate, extended, sophisticated basis sets would be highly desirable and worthwhile. Application of this method to other interesting chemical problems such as weakly bonded systems including H-bonded molecules, clusters and larger systems would further consolidate its success. A systematic analogous investigation of its performance on all-electron systems would also be interesting.

Acknowledgment

References

[1] D. R. Yarkony (Eds). *Modern Elecronic Structure Theory*. World Scientific, Singapore, 1995.

[2] A. Szabo and N. S. Ostlund. *Modern Quantum Chemistry*. Dover, New York, 1996.

[3] J. Simons and J. Nichols. *Quantum Mechanics in Chemistry*. Oxford University Press, New York, 1997.

[4] W. Kohn. *Rev. Mod. Phys.*, **71**:1253, 1999.

[5] P. Jorgensen T. Helgaker and J. Olsen. *Modern Electronic Structure Theory*. John Wiley, New York, 2000.

[6] D. C. Young. *Computational Chemistry: A practical Guide for Applying Techniques to Real-World Problems*. John Wiley, New York, 2001.

[7] E. Lewars. *Computational Chemistry: Introduction to the Theory and Applications of Molecular and Quantum Mechanics*. Kluwer Academic, Netherlands, 2003.

[8] C. J. Cramer. *Essentials of Computational Chemistry: Theories and Models*. John Wiley, New York, 2004.

[9] R. M. Martin. *Electronic Structure: Basic Theory and Practical Methods*. Cambridge University Press, Cambridge, UK, 2004.

[10] E. O. Hoffman. *Progress in Quantum Chemistry Research*. Nova Science, New York, 2007.

[11] F. Jensen. *Introduction to Computational Chemistry*. John Wiley, New York, 2007.

[12] M. P. Kaisas (Eds). *Quantum Chemistry Research Trends*. Nova Science, New York, 2007.

[13] J. C. Slater. *Quantum theory of Atomic Structure, Vols. 2*. McGraw-Hill, New York, 1960.

[14] N. H. March and B. M. Deb (Eds). *The Single Particle Density in Physics and Chemistry*. Academic Press, London, 1987.

[15] R. G. Parr and W. Yang. *Density Functional Theory of Atoms and Molecules*. Oxford university Press, New York, 1989.

[16] R. O. Jones and O. Gunnarsson. *Rev. Mod. Phys.*, **61**:689, 1989.

[17] D. P. Chong (Eds). *Recent Advances in Density Functional Methods*. World Scientific, Singapore, 1995.

[18] J. M. Seminario (Eds). *Recent Developments and Applications of modern DFT*. Elsevier, Amsterdam, 1996.

[19] D. Joulbert (Eds). *Density Functionals: Theory and Applications*. Springer, Berlin, 1998.

[20] J. F. Dobson, G. Vignale, and M. P. Das (Eds). *Density FunctionalTheory: Recent Progress and New Directions*. Plenum, New York, 1998.

[21] W. Koch and M. C. Holthausen. *A Chemist's guide to Density Functional Theory*. John Wiley, New York, 2001.

[22] R. G. Parr and K. D. Sen. *Reviews of Modern Quantum Chemistry: A Celebration of the Contributions of Robert G. Parr*. World Scientific, Singapore, 2002.

[23] C. Fiolhais, F. Nogueira, and M. Marques. *A Primer in Density Functional Theory*. Springer, Berlin, 2003.

[24] N. I. Gidopoulos and S. Wilson. *The Fundamentals of Electron Density, Density Matrix and Density Fucntional Theory in Atoms, Molecules and the Solid State*. Springer, Berlin, 2003.

[25] E. Teller. *Rev. Mod. Phys.*, **34**:627, 1962.

[26] P. Hohenberg and W. Kohn. *Phys. Rev. B*, **136**:864, 1964.

[27] W. Kohn and L. J. Sham. *Phys. Rev.*, **140**:A1133, 1965.

[28] T. L. Beck. *Rev. Mod. Phys.*, **72**:1041, 2000.

[29] L. Laaksonen, D. Sundholm, and P. Pyykko. *Int. J. Quant. Chem.*, **27**:601, 1985.

[30] A. D. Becke. *Int. J. Quant. Chem.*, **23**:599, 1989.

[31] S. R. White, J. W. Wilkins, and M. P. Teter. *Phys. Rev. B.*, **39**:5819, 1989.

[32] J. R. Chelikowsky, R. N. Troullier, and Y. Saad. *Phys. Rev. Lett.*, **72**:1240, 1994.

[33] J. R. Chelikowsky, R. N. Troullier, K. Wu, and Y. Saad. *Phys. Rev. B.*, **50**:11355, 1994.

[34] N. A. Modine, G. Zumbach, and E. Kaxiras. *Phys. Rev. B.*, **55**:10289, 1995.

[35] Y.-H. Kim, M. Staedele, and R. M. Martin. *Phys. Rev. A.*, **60**:3633, 1999.

[36] I.-H. Lee, Y.-H. Kim, and R. M. Martin. *Phys. Rev. B.*, **61**:4397, 2000.

[37] E. L. Briggs, D. J. Sullivan, and J. Bernholc. *Phys. Rev. B.*, **52**:R5471, 1995.

[38] E. L. Briggs, D. J. Sullivan, and J. Bernholc. *Phys. Rev. B.*, **54**:14375, 1996.

[39] F. Gygi and G. Galli. *Phys. Rev. B.*, **52**:R2229, 1995.

[40] G. Lippert, J. Hutter, and M. Parinello. *Theor. Chem. Acc.*, **103**:124, 1999.

[41] M. Krack and M. Parinello. *Phys. Chem. Chem. Phys.*, **2**:2105, 2000.

[42] D. R. Hamann, M. Schluter, and C. Chiang. *Phys. Rev. Lett.*, **43**:1494, 1979.

[43] G. B. Bachelet, D. R. Hamann, and M. Schluter. *Phys. Rev. B.*, **25**:2103, 1982.

[44] D. Vanderbilt. *Phys. Rev. B.*, **41**:7892, 1990.

[45] N. Troullier and J. L. Martins. *Phys. Rev. B.*, **43**:1993, 1991.

[46] M. C. Payne, M. P. Teter, D. C. Allan, T. A. Arias, and J. D. Joannopoulos. *Rev. Mod. Phys.*, **64**:1045, 1992.

[47] C. Hartwigsen, S. Goedecker, and J. Hutter. *Phys. Rev. B.*, **58**:3641, 1998.

[48] W. R. Wadt and P. J. Hay. *J. Chem. Phys.*, **82**:284, 1985.

[49] P. J. Hay and W. R. Wadt. *J. Chem. Phys.*, **82**:299, 1985.

[50] J. Andzelm and E. Wimmer. *J. Chem. Phys.*, **96**:1280, 1992.

[51] H. Sambe and R. H. Felton. *J. Chem. Phys.*, **62**:1122, 1975.

[52] B. I. Dunlap, J. W. D. Connolly, and J. R. Sabin. *J. Chem. Phys.*, **62**:1122, 1979.

[53] B. I. Dunlap, J. W. D. Connolly, and J. R. Sabin. *J. Chem. Phys.*, **71**:3396, 1979.

[54] E. J. Baerends, D. E. Ellis, and P. Ros. *Chem. Phys.*, **2**:41, 1973.

[55] P. M. W. Gill. *Adv. Quant. Chem.*, **25**:141, 1994.

[56] A. D. Becke. *J. Chem. Phys.*, **88**:2547, 1988.

[57] C. W. Murray, N. C. Handy, and G. J. Laming. *Mol. Phys.*, **78**:997, 1993.

[58] O. Treutler and R. Ahlrichs. *J. Chem. Phys.*, **102**:346, 1995.

[59] M. M. Mura and P. J. Knowles. *J. Chem. Phys.*, **104**:9898, 1996.

[60] P. M. W. Gill, B. G. Johnson, and J. A. Pople. *Chem. Phys. Lett.*, **209**:506, 1993.

[61] R. Lindh, P.-A. Malmqvist, and L. Gagliardi. *Theor. Chem. Acc.*, **106**:178, 2001.

[62] V. I. Lebedev and Zh. Vychisl. *Mat. Mat. Fiz.*, **15**:48, 1975.

[63] V. I. Lebedev and Zh. Vychisl. *Mat. Mat. Fiz.*, **16**:293, 1976.

[64] V. I. Lebedev and A. L. Skorokhodov. *Russ. Acad. Sci. Docl. Math.*, **45**:587, 1992.

[65] P. M. Boerrigter, G. Te. Velde, and E. J. Baerends. *Int. J. Quant. Chem.*, **33**:87, 1988.

[66] M. R. Pederson and K. A. Jackson. *Phys. Rev. B*, **41**:7453, 1990.

[67] M. Krack and A. M. Koster. *J. Chem. Phys.*, **108**:3226, 1998.

[68] L. Fusti-Molnar and P. Pulay. *J. Chem. Phys.*, **117**:7827, 2002.

[69] J. Kong, S. T. Brown, and L. Fusti-Molnar. *J. Chem. Phys.*, **124**:094109, 2006.

[70] A. K. Roy. *Int. J. Quant. Chem.*, **108**:837, 2008.

[71] A. K. Roy. *Chem. Phys. Lett.*, **461**:142, 2008.

[72] G. C.Martyna and M. E. Tuckerman. *J. Chem. Phys.*, **110**:2810, 1999.

[73] P. Minary, M. E. Tuckerman, K. A. Pihakari, and G. J. Martyna. *J. Chem. Phys.*, **116**:5351, 2002.

[74] S. Obara and A. Saika. *J. Chem. Phys.*, **84**:3963, 1986.

[75] L. E. McMurchie and E. R. Davidson. *J. Chem. Phys.*, **26**:218, 1978.

[76] L. R. Kahn, P. Baybutt, and D. G. Truhlar. *J. Chem. Phys.*, **65**:3826, 1976.

[77] E. Anderson, Z. Bai, C. Bischof, S. Blackford, J. Demmel, J. Dongarra, J. Du Croz, A. Greenbaum, S. Hammarling, A. McKenney, and D. Sorensen. *LAPACK Users' Guide (3rd Ed.)*. SIAM, Philadelphia, 1999.

[78] M. W. Schmidt, K. K. Baldridge, J. A. Boatz, S. T. Elbert, M. S. Gordon, J. H. Hensen, S. Koseki, N. Matsunaga, K. A. Nguyen, S. J. Su, T. L. Windus, M. Dupuis, and J. A. Montgomery. *J. Comput. Chem.*, **14**:1347, 1993.

[79] S. H. Vosko, L. Wilk, and M. Nusair. *Chem. Phys. Lett.*, **58**:1200, 1980.

[80] Y. C. Zheng and J. Almlof. *J. Chem. Phys.*, **214**:397, 1993.

[81] K. R. Glaesemann and M. S. Gordon. *J. Chem. Phys.*, **108**:9959, 1998.

[82] R. D. Johnson III (Eds.). *NIST Computational Chemistry Comparisons and Benchmark Database, NIST Standard Reference Database, Number, Release 14*. NIST, Gaithersburg, MD, 2006.

[83] A. D. Becke. *Phys. Rev. A*, **38**:3098, 1988.

[84] C. Lee, W. Yang, and R. G. Parr. *Phys. Rev. B*, **37**:785, 1988.

[85] J. P. Perdew and Y. Wang. *Phys. Rev. B*, **45**:13244, 1992.

[86] A. D. Becke. *J. Chem. Phys.*, **107**:8554, 1997.

[87] M. Filatov and W. Thiel. *Mol. Phys.*, **91**:847, 1997.

[88] F. A. Hamprecht, A. J. Cohen, D. J. Tozer, and N. C. Handy. *J. Chem. Phys.*, **109**:6264, 1998.

[89] E. Proynov, H. Chermette, and D. Salahub. *J. Chem. Phys.*, **113**:10013, 2000.

[90] C. Adamo and V. Barone. *J. Chem. Phys.*, **116**:5933, 2002.

[91] A. D. Boese and N. C. Handy. *J. Chem. Phys.*, **116**:9559, 2002.

[92] J. Toulouse, A. Savin, and C. Adamo. *J. Chem. Phys.*, **117**:10465, 2002.

[93] J. Tao, J. P. Perdew, V. N. Staroverov, and G. E. Scuseria. *Phys. Rev. Lett.*, **91**:146401, 2003.

[94] B. Miehlich, A. Savin, H. Stoll, and H. Preuss. *Chem. Phys. Lett.*, **157**:200, 1989.

[95] J. A. Pople, P. M. W. Gill, and B. G. Johnson. *Chem. Phys. Lett.*, **199**:557, 1992.

[96] Quantum Chemistry Group. *Density Functional Repository*. CCLRC Daresbury Laboratory, Daresbury, Cheshire, UK, 0000.

[97] H. Y. Afeefy, J. E. Liebman, in P. J. Linstrom S. E. Stein, and W. G. Mallard (Eds). *NIST Chemistry Webbook, NIST Standard Reference Database, Number 69*. NIST, Gaithersburg, MD, 2005.

[98] T. Brabec and F. Krausz. *Rev. Mod. Phys.*, **72**:545, 2000.

[99] Th. Udem, R. Holzwarth, and T. W. Hansch. *Nature (London)*, **416**:233, 2002.

[100] H. Stapelfeldt and T. Seideman. *Rev. Mod. Phys.*, **75**:543, 2003.

[101] A. Baltuska, Th. Udem, M. Uiberacker, M. Hentschel, E. Goulielmakis, Ch. Gohle, R. Holzwarth, V. S. Yakolev, A. Scrinzi, T. W. Hansch, and F. Krausz. *Nature (London)*, **421**:611, 2003.

[102] J. H. Posthumus. *Rep. Prog. Phys.*, **67**:623, 2004.

[103] Ch. Gohle, Th. Udem, M. Herrmann, J. Rauschenberger, R. Holzwarth, H. A. Schuessler, F. Krausz, and T. W. Hansch. *Nature (London)*, **436**:234, 2005.

[104] R. van Leeuwen and E. J. Baerends. *Phys. Rev. A*, **49**:2421, 1994.

[105] P. R. T. Schipper, O. V. Gritsenko, S. J. A. van Gisbergen, and E. J. Baerends. *J. Chem. Phys*, **112**:1344, 2001.

[106] S. I. Chu. *J. Chem. Phys*, **123**:062207, 2005.

[107] M. Cafiero. *Chem. Phys. Lett.*, **418**:126, 2006.

Chapter 16

ADDITION THEOREMS FOR MULTI-CENTER INTEGRALS OVER EXPONENTIAL TYPE FUNCTIONS

Rachid Ghomari[1,2], *Abdelati Rebabti*[1,3], *Ahmed Bouferguene*[1]
and Hassan Safouhi[1]
[1]Campus Saint Jean/Univ. Of Alberta, 8406 - 91 Street,
T6C 4G9, Edmonton, Canada
[2] Dept. de Chimie Univ. Abou Bakr Belkaid,
Tlemcen, Algeria
[3] Dept. de Chimie, Univ. Chouaib Doukali,
El Jadida, Maroc

Abstract

Infinite series are probably one of major tools that was elaborated in the early days of modern mathematics for the purpose of answering practical and theoretical questions. In chemistry and physics, infinite series in terms of spherical harmonics, also known as multipole expansions, are routinely used to solve a variety of problems particularly those with spherical symmetry, *eg.* an electron moving in the field created by a fixed nucleus. The present review addresses a specific application of spherical harmonics, namely the so-called two-range addition theorems. Such mathematical constructs essentially allow one to expand a function $f(\mathbf{r}+\mathbf{a})$ in terms of $Y_l^m(\theta_{\mathbf{r}}, \phi_{\mathbf{r}})$ hence leading to a separation of the angular and radial parts of the variable $\mathbf{r}$. In fact such a problem is very common in quantum chemistry where it is used to express a given charge distribution as a sum of multipolar contributions and multicenter integrals over Exponential Type Functions (ETFs) are just one of many such problems. As a consequence and in order to illustrate the mechanics behind the two-range addition theorems, we will use the case of multicenter integrals over ETFs as working example. In addition to numerical algorithms, symbolic computation which is perfectly geared to obtain analytical expressions, we will purposely address in some detail the convergence of the multipole expansion, in the context of multicenter integrals, since this aspect is often overlooked by researchers.

1. Introduction

In order to understand the fundamentals of chemical phenomena, it is essential to track the dynamics and the magnitude of electronic charge interactions since electrons are the known to be major actors in chemistry. From a theoretical standpoint, these interactions may computed using first principle based models at the foundation of which one finds the so-called multicenter integrals. In fact, the starting point of theoretical and computational chemists is the Schrödinger equation which can be solved exactly only for one-electron systems, *eg.* the hydrogen atom, the molecular ion H_2^+. Unfortunately to make the leap from these limited cases to those with practical interest, one must introduce several approximations, *eg.* the Linear Combination of Atomic Orbitals (LCAO) [1], whose sole purpose is to ease the mathematical difficulties. This in turn, makes it possible to obtain approximate solutions from which chemical properties (energetics, kinetics) can be calculated. Here, it is important to mention that despite the approximate nature of the solutions, their accuracy has dramatically increased over the years mainly due to the increase in computer power and availability. It is in this very context that Exponential Type Functions (ETFs) have re-emerged as a possible tool which has the potential of improving the accuracy of ab initio procedures. In fact, the benefit of using ETFs in quantum chemistry is, nowadays, considered common knowledge among chemists since the work on the hydrogen atom was already hinting towards the use of exponentially decreasing orbitals as the basis of quantum chemical modeling. In this respect and since the Schrödinger equation cannot be solved exactly for multi-electron systems, scientists were compeled to uncover as much information as possible regarding such solutions. Two major aspects were brought to light; on the one hand the exact solutions must possess a cusp [2] at the origin, that is the nucleus, and on the other hand they must decrease exponentially [3]. A later investigation conducted by Silverstone and Handy [4] went beyond the mathematical properties of the wavefunctions and showed that a physical property such as the Hartree-Fock energy must also decrease asymptotically as $\exp[-2(-2\epsilon_j)^{1/2}r]$ in which ϵ_j is the energy of the j-th spin orbital. All the above arguments have been used by many scientist to build a case for the defense of STFs. Unfortunatelly, as is the case for many research areas, practical issues sometimes put severe limitations on the use of concepts which theoretically are well founded. ETFs fall within this category since even though they exhibit the right properties, the evaluation of multi-center integrals involving these functions is extremely demanding in terms of computer time. It is this reason that pushed the pioneers of modern quantum chemistry away from ETFs and by the same token opened an unprecedented success for Gaussian Type Functions (GTFs) [5]. Of course, GTFs were specifically chosen because of the so-called multiplication theorem [5,6 (p. 154)] which can be found in most introductory textbooks to modern computational chemistry.

A product of two 1s GTFs centered on two arbitrary points defined by their location vector $\mathbf{a}$ and $\mathbf{b}$ is a new 1s GTF that is related to the initial functions as,

$$\exp\left(-\alpha_1\|\mathbf{r}-\mathbf{a}\|^2\right)\exp\left(-\alpha_2\|\mathbf{r}-\mathbf{b}\|^2\right)=\exp\left(-\frac{\alpha_1\,\alpha_2}{\alpha_1+\alpha_2}\,\|\mathbf{a}-\mathbf{b}\|^2\right)$$

$$\times\,\exp\left[-(\alpha_1+\alpha_2)\,\left\|\mathbf{r}-\frac{\alpha_1\mathbf{a}+\alpha_2\mathbf{b}}{\alpha_1+\alpha_2}\right\|^2\right] \quad (1)$$

Clearly the right hand side is, to within a constant, a GTF centered on a point defined by the location vector $(\alpha_1 \mathbf{a} + \alpha_2 \mathbf{b})/(\alpha_1 + \alpha_2)$.

As mentioned above, because of their correct behavior on the nucleus and farther away, ETFs are expected to accurately describe chemical properties calculated in the neighborhood of the nuclei, *eg.* nuclear magnetic resonance, and at large distance as is the case for inter-molecular interactions. Here, it is worth reminding that in the case of GTFs, a common work around commnly used to improve the accuracy of the calculated properties is simply to increase the size of the basis set. The viability of this procedure can, however, be severely questioned in practice by those who like to correct the shortcomings of the Self Consistent Field procedure by means of a Configuration Interaction treatment. Indeed, for C.I calculations, the size of the sample space is paramount since not only this affects the requirement in terms of memory but more importantly the speed of the computation. In this respect (and once again owing to their correct behavior) the ETFs are more attractive than GTFs since it will take fewer ETFs than GTFs to describe a molecular system to the same accuracy. Obviously, the configuration space will be smaller with ETFs!

Evaluation of multicenter integrals remains a challenging problem in computational chemistry. Over the past few decades, a rich mathematical apparatus was developed with the hope of obtaining efficient numerical algorithms. These technique can be categorized into (1) addition theorems, (2) integral transform based methods and (3) others (for the lack of a more suitable description), *cf.* figure (1.).
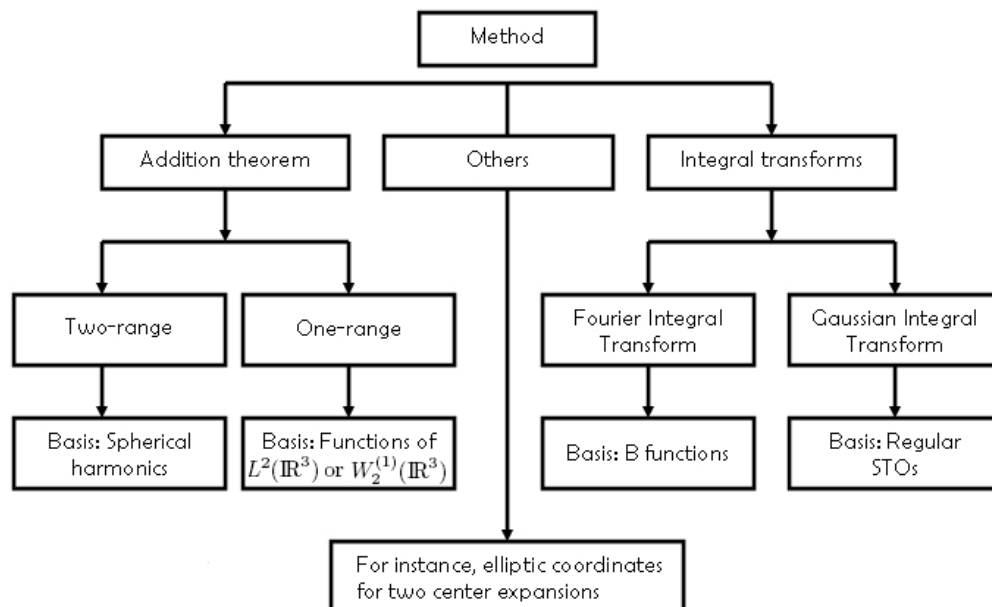
Figure 1. Overview of most widely used method for the evaluation of multicenter integrals over Exponential Type Functions. When applicable, the figure also provide the most suitable or widely used basis.

1. Addition theorems: In essence these techniques rely on infinite series expansions in order to separate the integration variable $\mathbf{r}$ from the molecular geometric parameters. Perhaps the most widely known two-range addition in chemistry and physics is the so-called Laplace expansion allowing the variables $\mathbf{r}$ and $\mathbf{a}$ occurring in the Coulomb potential $1/\|\mathbf{r} - \mathbf{a}\|$ to be separated,

$$\frac{1}{\|\mathbf{r} - \mathbf{a}\|} = \sum_{l=0}^{+\infty} \frac{[\min(a,r)]^l}{[\max(a,r)]^{l+1}} \sum_{m=-l}^{l} Y_l^m(\theta_{\mathbf{r}}, \phi_{\mathbf{r}}) \; [Y_l^m(\theta_{\mathbf{a}}, \phi_{\mathbf{a}})]^* \qquad (2)$$

where $\theta_{\mathbf{u}}$ and $\phi_{\mathbf{u}}$ denote the azimuthal and polar angles of the vector $\vec{u}$. As for the term Y_l^m and $[Y_l^m]^*$ they respectively represent the spherical harmonic and its complex conjugate (the full definition will be given in the next section). Clearly, the above expansion has two different forms according to whether $r < a$ or $r > a$ hence the nomenclature "two-range addition theorem" [7–27].

The second type of addition theorems, known as one-range [28–35], are generally derived by considering an expansion over a complete orthonormal set of functions $\{\psi_{n,l}^m(\mathbf{r})\}$ with respect to an inner product of Hilbert space $L_2(\mathbb{R}^3$ of square summable functions. As a result, for any given function $\Phi(\mathbf{r} - \mathbf{a}) \in L_2(\mathbb{R}^3)$, we can write,

$$\Phi_{n,l}^m(\mathbf{r} - \mathbf{a}) = \sum_{n',l',m'} C_{n',l',m'}(\mathbf{a}) \, \Psi_{n',l'}^{m'}(\mathbf{r}) \quad \text{with} \quad C_{n',l',m'}(\mathbf{a}) = \left\langle \Psi_{n',l'}^{m'}(\mathbf{r}) | \Phi(\mathbf{r} - \mathbf{a}) \right\rangle \quad (3)$$

According to this definition, the expansion coefficients depend solely on the geometric parameter $\mathbf{a}$. Two major types of functions $\Psi_{n,l}^m(\mathbf{r})$ have been used in the past,

(a) Used by Hylleras [36], Shull and Lowdin [28, 29] and later on by Filter and Steinborn [30],

$$\Lambda_{n,l}^m(\zeta, \mathbf{r}) = \mathcal{N}_{n,l}(\zeta) \, \exp(-\zeta r) \, L_{n-l-1}^{2l+2}(2\zeta r) \, \mathcal{Y}_l^m(2\zeta\mathbf{r}) \qquad (4)$$

$$\text{with} \quad \mathcal{N}_{n,l}(\zeta) = (2\zeta)^{3/2} \sqrt{\frac{(n-l-1)!}{(n+l+1)!}}$$

(b) As reported previously [37], completeness in $L^2(\mathbb{R}^3)$ is not sufficient for a set of functions to be suitable for quantum mechanics. Indeed, if one considers the so-called sturmians,

$$\Phi_{n,l}^m(\zeta, \mathbf{r}) = \mathcal{N}_{n,l}(\zeta) \, \exp(-\zeta \, r) \, L_{n-l-1}^{2l+1}(2\zeta r) \, \mathcal{Y}_l^m(2\zeta\mathbf{r}) \qquad (5)$$

$$\text{with} \quad \mathcal{N}_{n,l} = (2\zeta)^{3/2} \sqrt{\frac{(n-l-1)!}{2n\,(n+l)!}}$$

one can prove that they form a complete orthonormal set in $L_{1/r}^2(\mathbb{R}^3)$. However, as was discussed by Weniger [37, 38], the latter is not suitable for quantum mechanics problems. On the other hand, and since Sturmians are also complete with respect to the inner product $\zeta^2 - \nabla^2$ they form a complete orthonormal set in the Sobolev space $W_2^{(1)}(\mathbb{R}^3)$ which makes their use in acceptable candidates for atomic and molecular physics applications.

2. Integral transforms: The other major alternative to infinite series expansions that was explored for the purpose of evaluating multicenter integrals over ETFs is based on integral transformations. Two important transforms have been extensively documented in the literature: the Fourier [39–45] and the Gaussian [46–52] integral transforms.

In the present work, we will review the addition theorem method and show its applications in the context of multicenter integrals over ETFs. This project has been motivated by two major aspects. On the one hand, addition theorems and especially those involving spherical harmonics are very useful in a variety of areas of chemistry and physics, *eg.* electron scattering, potential calculations. On the other hand, some theoretical aspects, particularly those related to convergence, are often overlooked by researchers. This can be penalizing because the leading algorithms may end up time consuming.

2.   The Two-range Addition Theorem: Mathematical Apparatus

An exponential type function centered on a point defined by the location vector $\mathbf{a}$ is generally defined as,

$$\chi_{n,l}^{m}(\zeta, \mathbf{r} - \mathbf{a}) = \mathcal{P}_{n,l}(\|\mathbf{r} - \mathbf{a}\|) \, \exp(-\zeta \|\mathbf{r} - \mathbf{a}\|) \, Y_l^m\left(\theta_{\mathbf{r}-\mathbf{a}}, \phi_{\mathbf{r}-\mathbf{a}}\right) \tag{6}$$

where $\mathcal{P}_{n,l}(\|\mathbf{r} - \mathbf{a}\|)$ is a polynomial whose degree is a function of the quantum numbers n and l. As for the term $Y_l^m(\theta, \phi)$ it corresponds to the spherical harmonic of degree l and order m. Under the Condon-Shortley convention [53], spherical harmonics are defined as,

$$Y_l^m(\theta, \phi) = i^{m+|m|} \sqrt{\frac{2l+1}{4\pi} \frac{(l-|m|)!}{(l+|m|)!}} \, P_l(\cos\theta) \, e^{i\,m\,\phi} \tag{7}$$

where $P_l(\cos\theta)$ is the associated Legendre function which according to Rodrigues formula [54 (p. 94),55 (p. 768)] may be written as,

$$P_l^m(z) = (1-z^2)^{|m|/2} \left(\frac{d}{dz}\right)^{|m|} P_l(z) = (1-z^2)^{|m|/2} \left(\frac{d}{dz}\right)^{l+|m|} \left[\frac{(1-z^2)^l}{2^l \, l!}\right] \tag{8}$$

Although spherical harmonics are widely used in quantum mechanics, they may be difficult to handle when deriving formulas involving derivatives such is the case for tensor definitions and shift operators. As a consequence, Weniger recommends the use of solid spherical harmonics which in the cartesian representation corresponds to homogeneous polynomials in the variable $x \times y \times z$ [56, 57]. Solid spherical harmonics are defined as,

$$\mathcal{Y}_l^m(\mathbf{r}) = \|r\|^l \, Y_l^m(\theta_{\mathbf{r}}, \phi_{\mathbf{r}}) \tag{9}$$

Among the advantages of solid spherical harmonics is their addition theorem which can be put in the following form [58],

$$\mathcal{Y}_l^m(\mathbf{r} - \mathbf{a}) = 4\pi \, (2l+1)!! \sum_{l'=0}^{l} \sum_{m'=-l'}^{l'} \frac{\langle l\,m|l'\,m'|l-l'\,m-m'\rangle}{(2l'+1)!! \, [2(l-l')+1]!!} \, \mathcal{Y}_{l'}^{m'}(\mathbf{r}) \, \mathcal{Y}_{l-l'}^{m-m'}(\mathbf{a}) \tag{10}$$

where the double factorial is defined as $(2n + 1)!! = \prod_{q=0}^{n} (2q + 1) = (2n + 1)!/[2^n \, n!]$ whereas the symbol $\langle l_1 \, m_1 | l_2 \, m_2 | l_3 \, m_3 \rangle$ denotes the Gaunt coefficient [55, 59] which is defined as,

$$\langle l_1 \, m_1 | l_2 \, m_2 | l_3 \, m_3 \rangle = \int_{\theta=0}^{\pi} d\theta \int_{\phi=0}^{2\phi} d\phi \; \left[Y_{l_1}^{m_1}(\theta, \phi) \right]^* \, Y_{l_2}^{m_2}(\theta, \phi) \, Y_{l_3}^{m_3}(\theta, \phi) \quad (11)$$

For practical purposes, it is important to remind the reader that for the Gaunt coefficients to be non-zero the following constraints must be fulfilled,

$$\langle l_1 \, m_1 | l_2 \, m_2 | l_3 \, m_3 \rangle \; \neq \; 0 \quad \Longleftrightarrow \quad \begin{cases} |l_1 - l_2| \leq l_3 \leq |l_1 + l_2| \\[2mm] l_1 + l_2 + l_3 \text{ is even} \; \Longleftrightarrow \; l_3 \text{ varies by steps of two} \\[2mm] m_3 = m_1 - m_2 \end{cases}$$
$$(12)$$

More complicated properties of these coefficients may be found several specialized references [59–67]. In what follows, we will focus on deriving a two-range addition theorem for Slater Type Orbitals (STOs) [68], which can be considered as a special case of equation (6). In fact, to derive such a theorem, it is usually a good idea to define an STO as the derivative of a Yukawa potential with respect to the screening constant, that is,

$$\begin{aligned} \chi_{n,l}^m(\mathbf{r} - \mathbf{a}) \; &= \; \mathcal{N}(n, \zeta) \, \|\mathbf{r} - \mathbf{a}\|^{n-l-1} \, \exp(-\zeta \, \|\mathbf{r} - \mathbf{a}\|) \, \mathcal{Y}_l^m(\mathbf{r} - \mathbf{a}) \\[3mm] &= \; \mathcal{N}(n, \zeta) \left[\left(-\frac{\partial}{\partial \zeta} \right)^{n-l} \underbrace{\frac{\exp(-\zeta \|\mathbf{r} - \mathbf{a}\|)}{\|\mathbf{r} - \mathbf{a}\|}}_{\text{Yukawa Potential}} \right] \mathcal{Y}_l^m(\mathbf{r} - \mathbf{a}) \quad (13) \end{aligned}$$

where $\mathcal{N}(n, \zeta) = (2\zeta)^{n+1/2}/\sqrt{(2n)!}$ is a normalisation factor. At this point, we can introduce the Gegenbauer addition theorem which allows the variable $\mathbf{r}$ and the parameter $\mathbf{a}$ occurring in Yukawa potential to be separated [69, pp. 218,219],

$$\frac{\exp(-\zeta \|\mathbf{r} - \mathbf{a}\|)}{\|\mathbf{r} - \mathbf{a}\|} = \frac{1}{\sqrt{a \, r}} \sum_{\lambda=0}^{+\infty} (2\lambda + 1) \underbrace{\mathbf{I}_{\lambda+1/2}(\zeta \rho_<) \, \mathbf{K}_{\lambda+1/2}(\zeta \rho_>)}_{\text{BCLF} \, : \, \mathcal{A}_{\lambda+1/2}^0(\zeta, a, r)} \, P_l\left(\frac{\mathbf{a} \cdot \mathbf{r}}{a \, r} \right) \quad (14)$$

where $\rho_< = \min(a, r)$ and $\rho_> = \max(a, r)$. The term $\mathcal{A}_{\lambda+1/2}^0(\zeta, a, r)$ is known as the Barnett-Coulson/Löwdin (BCLF) function which can be defined recursively as,

$$\begin{cases} \mathcal{A}_{\lambda+1/2}^0(\zeta, a, r) \; = \; \mathbf{I}_{\lambda+1/2}(\zeta \, \rho_<) \, \mathbf{K}_{\lambda+1/2}(\zeta \, \rho_>) \\[3mm] \mathcal{A}_{\lambda+1/2}^n(\zeta, a, r) \; = \; (-\partial/\partial\zeta)^n \, \mathcal{A}_{\lambda+1/2}^0(\zeta, a, r) \end{cases} \quad (15)$$

in which $\mathbf{I}_\nu(z)$ and $\mathbf{K}_\nu(z)$ represent the Bessel functions of the first and second kind. And, since the index ν is half integral both Bessel functions can be represented, according to [70,

p. 80] in closed forms as,

$$
\begin{aligned}
\mathbf{I}_{\lambda+1/2}(z) &= \frac{1}{\sqrt{2\pi z}} \sum_{p=0}^{\lambda} \frac{(\lambda+p)!}{p!\,(\lambda-p)!} \; \frac{(-1)^p \exp(z) - (-1)^{\lambda} \exp(-z)}{(2z)^p} \\
\mathbf{K}_{\lambda+1/2}(z) &= \sqrt{\frac{\pi}{2z}} \sum_{q=0}^{\lambda} \frac{(\lambda+q)!}{q!\,(\lambda-q)!} \; \frac{\exp(-z)}{(2z)^q}
\end{aligned}
\tag{16}
$$

Such closed forms might be advantageous in some cases since multicenter integrals can be evaluated analytically hence providing a framework allowing a variety of mathematical properties to be investigated. Note that emphasis was purposely put on the analytical aspects since for numerical purposes, a closed form is not necessarily synonymous of algorithmic stability. Combining equations (10) and (13), one can write a general two-range addition theorem for an arbitrary STO,

$$
\chi_{n,l}^m(\zeta, \mathbf{r} - \mathbf{a}) = \frac{1}{ar} \left[\sum_{\lambda=0}^{+\infty} (2\lambda+1)\, \mathcal{A}_{\lambda+1/2}^{n-l}(\zeta, a, r)\, P_\lambda \left(\frac{\mathbf{a} \cdot \mathbf{r}}{a\,r} \right) \right]
$$
$$
\left[\sum_{l'=0}^{l} \sum_{m'=-l'}^{l'} \frac{\langle l\,m|l'\,m'|l-l'\,m-m'\rangle}{(2l'+1)!!\,[2(l-l')+1]!!} \; \mathcal{Y}_{l'}^{m'}(\mathbf{r})\, \mathcal{Y}_{l-l'}^{m-m'}(\mathbf{a}) \right]
\tag{17}
$$

Although the above expression may be simplified a little, we prefer introducing the appropriate simplifications when multicenter integrals are addressed. Before closing this paragraph, it is extremely important to point out that even though the addition theorem (17) involves the BCLF of order $n-l$ that is, $\mathcal{A}_\lambda^{n-l}(\zeta, a, r)$, all we need in fact is $\mathcal{A}_{\lambda+1/2}^0(\zeta, a, r)$ and $\mathcal{A}_{\lambda+1/2}^1(\zeta, a, r)$. Indeed, any given STO can be represented as,

$$
\chi_{n,l}^m(\zeta, \mathbf{r} - \mathbf{a}) = \mathcal{N}(n,\zeta) \underbrace{\|\mathbf{r}-\mathbf{a}\|^{n-l-2\lfloor (n-l)/2\rfloor} \exp(-\zeta\|\mathbf{r}-\mathbf{a}\|)/\|\mathbf{r}-\mathbf{a}\|}_{\text{Infinite expansion}}
$$
$$
\underbrace{\|\mathbf{r}-\mathbf{a}\|^{2\lfloor (n-l)/2\rfloor}\, \mathcal{Y}_l^m(\mathbf{r}-\mathbf{a})}_{\text{Finite expansion}}
\tag{18}
$$

where the symbol $\lfloor z \rfloor$ denotes the integer part of z. As can be seen the terms labeled as "Infinite expansion" have one of the following forms,

$$
\begin{cases}
\exp(-\zeta\|\mathbf{r}-\mathbf{a}\|)/\|\mathbf{r}-\mathbf{a}\| &: \quad \text{If } (n-l) \text{ is even.} \quad \text{This requires } \mathcal{A}_{\lambda+1/2}^0(\zeta, a, r) \\
\exp(-\zeta\|\mathbf{r}-\mathbf{a}\|) &: \quad \text{If } (n-l) \text{ is odd.} \quad \text{This requires } \mathcal{A}_{\lambda+1/2}^1(\zeta, a, r)
\end{cases}
\tag{19}
$$

2.1. Convergence Analysis

A very important aspect that is paramount to investigate whenever infinite series are used for numerical computation is the convergence of the expansions in which such series

occur. Multicenter integrals, to the exception of overlap and electron-nuclei integrals, describe the Coulombian interaction between two-charge distributions and can, generally, be represented as

$$\left\langle \rho_1(\mathbf{r}_1) \left| \frac{1}{\|\mathbf{r}_1 - \mathbf{r}_2\|} \right| \rho_2(\mathbf{r}_2) \right\rangle = \int_{\mathbf{r}_1} \int_{\mathbf{r}_2} \rho(\mathbf{r}_1) \frac{1}{\|\mathbf{r}_1 - \mathbf{r}_2\|} \rho(\mathbf{r}_2) \, d\mathbf{r}_1 \, d\mathbf{r}_2 \qquad (20)$$

where $\rho(\mathbf{r})$ stands for an electronic density. Clearly, when the above interaction is evaluated by means of a two-range addition theorem, the Coulomb potential is generally expanded by means of the so-called Laplace addition theorem, that is,

$$\frac{1}{\|\mathbf{r}_1 - \mathbf{r}_2\|} = \sum_{l=0}^{+\infty} \frac{[\min(r_1, r_2)]^l}{[\max(r_1, r_2)]^{l+1}} P_l \left(\frac{\mathbf{r}_1 \cdot \mathbf{r}_2}{r_1 \, r_2} \right) \qquad (21)$$

Consequently, we shall start this section by focusing on the convergence properties of the above multipole expansion of the Coulomb potential. For this purpose, it is appropriate to recall a few fundamental theorems that will be very useful in subsequent analyses. More detailed discussions may be found in a review paper by Weniger [71] and more recently in a book by Brezenski and Redivo-Zaglia [72]. Let $S = \sum_{k=0}^{+\infty} a_k$, be a convergent series, whose limit is s, and let ρ be the ratio which is defined as,

$$\lim_{n \to +\infty} \frac{S_{n+1} - s}{S_n - s} = \rho \qquad (22)$$

in which S_n denotes the partial sum of S and such that $S_n = \sum_{k=0}^{n} a_k$. According to Wimp [73] (p. 6 and 41), the series S converges linearly if $0 < |\rho| < 1$ and logarithmically if $\rho = 1$. What this means in practice is that, linearly convergent series can be evaluated by a brute force scheme in which terms are simply added together. Although this might be inefficient, the corresponding computational time may still be within reasonable bounds. Conversely, for logarithmically convergent series, a brute force summation algorithm is likely to be worthless. In this respect, one of the most cited logarithmically convergent series is the Riemann function $\zeta(1) = \sum_{k=1}^{+\infty} 1/k$, for which the summation of the first million terms yields 14.3927, hence giving a false impression of convergence. This, of course, is incorrect since one can easily show that $\zeta(1)$ is divergent. Consequently, for extremely slowly converging (or diverging) series, the so-called convergence accelerators become an absolute necessity in practice. If the term a_n of a series $S = \sum_{k=0}^{+\infty} a_k$ has a Poincaré type asymptotic expansion, that is,

$$a_n = \lambda^n \, n^\Theta \left[\alpha_0 + \frac{\alpha_1}{n} + \frac{\alpha_2}{n^2} + \ldots \right] \quad \text{with} \quad \begin{cases} \alpha_0 \neq 0 \\ n \to +\infty \end{cases} \qquad (23)$$

then the series S converges linearly for $|\lambda| < 1$ and logarithmically if $\lambda = 1$ and $\Re(\Theta) < -1$. In contrast to the definition (2.1.), the above theorem is very useful, from a practical standpoint, since it does not require the knowledge of the limit s in order to determine whether S is linearly or logarithmically convergent. At this point, the concepts of linear and logarithmic convergence can be abstract in the mind of the practitioners of quantum chemistry. Therefore, we illustrate these concepts through a simple example that will help

illustrate the difficulties. For this purpose, let r_n be the residual between the limit of the series to be summed and its n-th partial sum, that is, $r_n = s - S_n$. Using this new notation, equation (22) will be represented as,

$$\rho_n = \frac{r_{n+1}}{r_n} \quad \text{where } \rho_n < 1 \quad \text{to ensure convergence} \tag{24}$$

Now, using the above equation we can estimate the number of terms p to be computed in order to gain an extra significant digit. Indeed, assuming that equation (24) is approximately constant for large values of n, that is for n greater than some threshold value N. We can therefore write,

$$\frac{r_{n+1}}{r_n} = \tilde{\rho}, \quad \text{for} \quad n > N \quad \Longrightarrow \quad \begin{cases} r_{N+p} &=& \tilde{\rho} \times r_{N+p-1} \\ r_{N+p} &=& \tilde{\rho} \times \tilde{\rho} \times r_{N+p-2} \\ \dots &=& \dots\dots \\ r_{N+p} &=& \underbrace{\tilde{\rho} \times \tilde{\rho} \times \dots \times \tilde{\rho}}_{\tilde{\rho}^p} \times r_N \end{cases} \tag{25}$$

The last of the above equation, $r_{N+p} = \tilde{\rho}^p \, r_N$, can now be used to estimate the extra number of terms p needed to gain an extra significant digit. This, in fact, corresponds to a reduction of the numerator by a factor of 10 (at least),

$$r_{N+p} = \tilde{\rho}^p \, r_N \;\leq\; 0.1 \, r_N \;\Longrightarrow\; p \;\geq\; -\frac{1}{\log_{10} \, \tilde{\rho}} \tag{26}$$

A plot of $\tilde{\rho}$ as a function of $\tilde{\rho}$ shows the immense computational challenge we encounter when a direct summation procedure is used to estimate the limit of a logarithmically convergent series. Now that, the reader has a more practical (and visual) idea about the concepts of
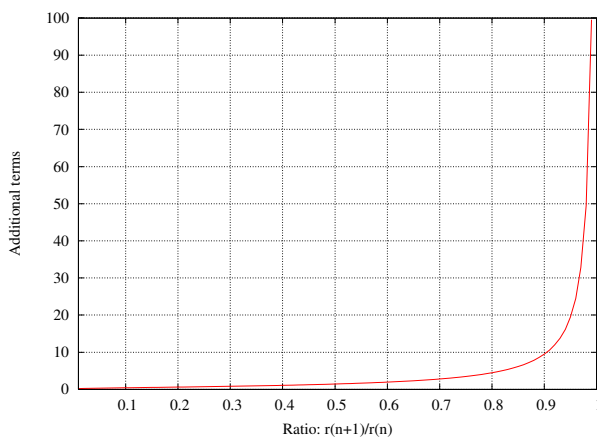
Figure 2. An estimate of the number of terms required to gain an extra significant digit.

linear and logarithmic convergence, let us go back to the Coulomb potential and determine what type of convergence the multipole expansion is exhibiting. The term of order n can

easily be written,

$$a_n = \frac{[\min(r_1, r_2)]^n}{[\max(r_1, r_2)]^{n+1}} P_n(\cos\theta) \sim \left[\frac{\min(r_1, r_2)}{\max(r_1, r_2)}\right]^n P_n(\cos\theta) \tag{27}$$

A special case of the above equation is obtained when the vectors $\mathbf{r}_1$ and $\mathbf{r}_2$ are parallel in which case $P_n(\cos\theta) = (\pm 1)^n$. In such a case, the radial part of the term a_n is represented asymptotically as $\lambda^n(1)$ in which $\lambda = \min(r_1, r_2)/\max(r_1, r_2) < 1$ when $r_1 \neq r_2$. In virtue of theorem (2.1.) we conclude that for $r_1 \neq r_2$, the multipole expansion of the Coulomb potential is linearly convergent when $\mathbf{r}_1$ and $\mathbf{r}_2$ are parallel.

2.1.1. Convergence Analysis of Multicenter Integrals over STFs in the Two-Range Addition Theorem Approach

The convergence analysis of the Coulomb potential is more of a classroom example than anything else. To make things more interesting, the following is devoted to the analysis of the convergence of multicenter integrals over STFs when these are evaluated in the framework of the two-range addition theorem. For this purpose, let us start by considering the case of the three-center nuclear attraction integrals which, for the sake of simplicity, will involve only ns orbitals,

$$
\begin{aligned}
\mathfrak{I} &= \left\langle \chi^0_{n_1,0}(\alpha, \mathbf{r} - \overrightarrow{OA}) \left| \frac{1}{\|\mathbf{r} - \overrightarrow{OC}\|} \right| \chi^0_{n_2,0}(\beta, \mathbf{r} - \overrightarrow{OB}) \right\rangle \\
&= \left\langle \chi^0_{n_1,0}(\alpha, \mathbf{r}) \left| \frac{1}{\|\mathbf{r} - \mathbf{c}\|} \right| \chi^0_{n_2,0}(\beta, \mathbf{r} - \mathbf{b}) \right\rangle
\end{aligned}
\tag{28}
$$

in which O is an arbitrary origin whereas the points A, B and C are the respective locations of the three centers (nuclei). To obtain the rightmost term, it suffices to change the origin of the coordinates from O to A which, by the same token, allow us to introduce two new vectors $\mathbf{b} = \overrightarrow{AB}$ and $\mathbf{c} = \overrightarrow{AC}$. At this point, the integral defined above can be expanded in terms of spherical harmonics by combining the addition theorem (17) and the multipole expansion of the Coulomb potential. This leads,

$$\mathfrak{I} = \frac{\mathcal{N}_1 \, \mathcal{N}_2}{\sqrt{b}} \sum_{\lambda=0}^{+\infty} \left\langle r^{n_1-1} \exp(-\alpha\, r) \left| \frac{r_<^\lambda}{r_>^{\lambda+1}} \right| \frac{1}{\sqrt{r}} \left(-\frac{\partial}{\partial\beta}\right)^{n_2} \mathrm{I}_{\lambda+1/2}(\beta\rho_<)\, \mathrm{K}_{\lambda+1/2}(\beta\rho_>) \right\rangle P_\lambda\left(\frac{\mathbf{b}\cdot\mathbf{c}}{b\,c}\right) \tag{29}$$

where $r_< = \min(r, c)$, $r_> = \max(r, c)$, $\rho_< = \min(r, b)$ and $\rho_> = \max(r, b)$. Based of the definitions of $r_<$, $r_>$, $\rho_<$ and $\rho_>$, the above integral can be split into three contributions,

$$\mathfrak{I} = \frac{\mathcal{N}_1 \, \mathcal{N}_2}{\sqrt{b}} \sum_{\lambda=0}^{+\infty} \left[\mathcal{R}_\lambda + \mathcal{R}'_\lambda + \mathcal{R}"_\lambda\right] \, P_\lambda\left(\frac{\mathbf{b}\cdot\mathbf{c}}{b\,c}\right) \tag{30}$$

in which $\mathcal{R}_\lambda$, $\mathcal{R}'_\lambda$ and $\mathcal{R}"_\lambda$ are respectively defined as,

$$
\mathcal{R}_\lambda = \frac{1}{c^{\lambda+1}} \int_0^{\min(b,c)} r^{n_1+\lambda+1/2} \exp(-\alpha r) \left(-\frac{\partial}{\partial\beta}\right)^{n_2} \left[\mathbf{I}_{\lambda+1/2}(\beta r)\, \mathbf{K}_{\lambda+1/2}(\beta b)\right] dr
$$

$$
\mathcal{R}'_{\lambda,b<c} = \frac{1}{c^{\lambda+1}} \int_b^c r^{n_1+\lambda+1/2} \exp(-\alpha r) \left(-\frac{\partial}{\partial\beta}\right)^{n_2} \left[\mathbf{I}_{\lambda+1/2}(\beta b)\, \mathbf{K}_{\lambda+1/2}(\beta r)\right] dr
$$

$$
\mathcal{R}'_{\lambda,c<b} = c^\lambda \int_c^b r^{n_1-\lambda-1/2} \exp(-\alpha r) \left(-\frac{\partial}{\partial\beta}\right)^{n_2} \left[\mathbf{I}_{\lambda+1/2}(\beta r)\, \mathbf{K}_{\lambda+1/2}(\beta b)\right] dr
$$

$$
\mathcal{R}"_\lambda = c^\lambda \int_{\max(b,c)}^{+\infty} r^{n_1-\lambda-1/2} \exp(-\alpha r) \left(-\frac{\partial}{\partial\beta}\right)^{n_2} \left[\mathbf{I}_{\lambda+1/2}(\beta b)\, \mathbf{K}_{\lambda+1/2}(\beta r)\right] dr
$$

$$(31)$$

in which the integral $\mathcal{R}'_\lambda$ has two different definition according to whether $b < c$ or $c < b$. Having defined explicitly the basic building blocks of the infinite series (30), the next step that will take us closer to an understanding of its convergence requires the determination of the Poincaré representation of $\mathcal{R}_\lambda$, $\mathcal{R}'_\lambda$ and $\mathcal{R}"_\lambda$. For this purpose, it would be expedient to first setup the poincaré representation of the BCLF $\mathcal{A}^{n_2}_{\lambda+1/2}(\beta, b, r)$ which occurs in all the integrals. In fact, for large values of λ, it can be shown that when $\rho_< \neq \rho_>$ such functions can be represented asymptotically as,

$$
\left(-\frac{\partial}{\partial\beta}\right)^{n_2} \mathbf{I}_{\lambda+1/2}(\beta\,\rho_<)\, \mathbf{K}_{\lambda+1/2}(\beta\,\rho_>) \sim (-1)^{\lfloor n_2/2\rfloor} \frac{n_2!}{(2\beta)^{n_2}} \left(\beta\sqrt{|b^2-r^2|}\right)^{2\lfloor(n_2+1)/2\rfloor}
$$

$$
\times \frac{(\rho_</\rho_>)^{\lambda+1/2}}{2(\lambda+1/2)^{\lfloor(n_2+1)/2\rfloor+1}} \sum_{p=0}^{\lfloor n_2/2\rfloor} (-1)^p \frac{1}{(\lfloor n_2/2\rfloor-p)!\,(n_2-2\lfloor n_2/2\rfloor+2p)!} \frac{\left(\beta\sqrt{|b^2-r^2|}\right)^p}{(\lambda+1/2)^p} (32)
$$

Obviously to within a constant the leading term of the above asymptotic representation, as $\lambda \to +\infty$, can be written as,

$$
\mathcal{A}^{n_2}_{\lambda+1/2}(\beta, b, r) \sim \mathcal{K}\, \frac{(\rho_</\rho_>)^\lambda}{(\lambda+1/2)^{\lfloor(n_2+1)/2\rfloor+1}} \tag{33}
$$

where $\mathcal{K}$ is a constant independent of λ. As mentioned previously, the above expansion is only valid for values of $\rho_<$ and $\rho_>$ such that $\rho_< \neq \rho_>$. For the special case where $\rho_< = \rho_>$, the leading term of the asymptotic representation of the BCLF $\mathcal{A}^{n_2}_{\lambda+1/2}(\beta, b, r)$ can be written as,

$$
\mathcal{A}^{n_2}_{\lambda+1/2}(\beta, b, r) \sim \mathcal{K}'\, \frac{1}{(\lambda+1/2)^{2\lfloor(n+1)/2\rfloor+1}} \tag{34}
$$

in which $\mathcal{K}'$ is once again a constant not depending on λ. Since BCLFs are in fact the terms of the infinite series (17), we can use equations (33) and (34) conclude that for an s orbital, the series representation (17) converges linearly when $\rho_< \neq \rho_>$ (*cf.* Eq. 33) and logarithmically on the cusp, that is $\rho_< = \rho_>$ (*cf.* Eq. 34).

Now that we have determined the asymptotic representations of BCLFs, it is time to address the convergence issues of multicenter integrals over STOs. From the introductory paragraph of this section, the reader can easily surmise that one-electron integrals constitute the first case that we intend to analyse. However, to keep the length of this review within reasonable bounds, we chose to consider only the most difficult case, *i.e.* three-center nuclear attraction integrals. In fact, what makes these integrals important is the fact that within

the framework of the Density Functional Theory (DFT), such integrals are the most difficult constructs that need to be calculated for molecular structure determination. Consequently, we believe that the analysis presented in this review can be very helpful for those interested in methods development for DFT.

Using the asymptotic forms of BCLFs determined in (33) and (34), we are now in a position to determine the leading term of the Poincaré representations of the radial integrals defined in equation (31),

$$
\begin{aligned}
\mathcal{R}_\lambda &\sim \mathcal{K} \, \frac{[\min(b,c)/\max(b,c)]^\lambda}{(\lambda+1/2)^{\lfloor(n_2+1)/2\rfloor+2}} \\[2mm]
\mathcal{R}'_{\lambda, b<c} &\sim \mathcal{K}' \, \frac{[\min(b,c)/\max(b,c)]^\lambda}{(\lambda+1/2)^{\lfloor(n_2+1)/2\rfloor+2}} \\[2mm]
\mathcal{R}''_{\lambda+1/2} &\sim \mathcal{K}'' \, \frac{[\min(b,c)/\max(b,c)]^\lambda}{(\lambda+1/2)^{\lfloor(n_2+1)/2\rfloor+2}}
\end{aligned}
\tag{35}
$$

where $\mathcal{K}$, $\mathcal{K}'$ and $\mathcal{K}''$ are constants independent of λ. From the above equation, we can easily see that for large values of λ, the element of the series expansion (30) can be expressed in a unified form as,

$$
a_\lambda \sim \text{Some constant} \times \frac{[\min(b,c)/\max(b,c)]^\lambda}{(\lambda+1/2)^{\lfloor(n_2+1)/2+2\rfloor}} \times P_\lambda\left(\frac{\mathbf{b}\cdot\mathbf{c}}{b\,c}\right) \qquad \text{with } \lambda \to +\infty \tag{36}
$$

Using the above asymptotic expansion in connection with theorem (2.1.), we can easily conclude that the infinite series in equation (30) should converge linearly for $b \neq c$ and logarithmically for $b = c$.

For two electron integrals, things are rather complicated namely because of the variety of multicenter that might occur. A useful approach that helps to classify such constructs relies on graph theory,

For two electron integrals, we chose to address the case of the three-center hybrid integral. This choice is motivated since it illustrate a combination of a single center potential with a two-center distribution; in addition its expansion using the tools developed above leads to a single infinite integral (as is also the case for two-center exchange integrals). Three-center hybrid integrals are defined as,

$$
\mathcal{I} = \left\langle \chi^{m_1}_{n_1,l_1}\left(\alpha_1, \mathbf{r}_1 - \overrightarrow{OA}\right) \chi^{m_3}_{n_3,l_3}\left(\alpha_3, \mathbf{r}_2 - \overrightarrow{OB}\right) \left| \frac{1}{\|\mathbf{r}_1 - \mathbf{r}_2\|} \right| \chi^{m_2}_{n_2,l_2}\left(\alpha_2, \mathbf{r}_1 - \overrightarrow{OA}\right) \chi^{m_4}_{n_4,l_4}\left(\alpha_4, \mathbf{r}_2 - \overrightarrow{OC}\right) \right\rangle
\tag{37}
$$

To simplify the above definition, let us apply a translation which makes the center A as the new origin. This yields,

$$
\mathcal{I} = \left\langle \chi^{m_1}_{n_1,l_1}\left(\alpha_1, \mathbf{r}_1\right) \chi^{m_3}_{n_3,l_3}\left(\alpha_3, \mathbf{r}_2 - \mathbf{b}\right) \left| \frac{1}{\|\mathbf{r}_1 - \mathbf{r}_2\|} \right| \chi^{m_2}_{n_2,l_2}\left(\alpha_2, \mathbf{r}_1\right) \chi^{m_4}_{n_4,l_4}\left(\alpha_4, \mathbf{r}_2 - \mathbf{c}\right) \right\rangle
\tag{38}
$$

in which $\mathbf{x} = \overrightarrow{OX} - \overrightarrow{OA} = \overrightarrow{AX}$. Since the atomic orbitals related to particle (1) are centered on the same center, it is clear that the corresponding distribution can be expressed

Table 1. Graph representation of two-electron integrals and the corresponding nomenclature

Descriptive graph	Nomenclature	Descriptive graph	Nomenclature
	Two-center Coulomb integrals		Three center hybrid integrals
	Two-center hybrid integrals		Three center exchange integrals
	Two-center exchange integrals		Four center integrals
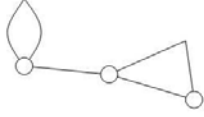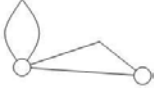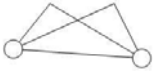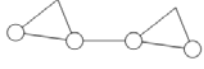
as a linear combination of STOs,

$$\chi_{n_1,l_1}^{m_1}(\alpha_1, \mathbf{r}_1)\, \chi_{n_2,l_2}^{m_2}(\alpha_2, \mathbf{r}_1) = \frac{\mathcal{N}(n_1, \alpha_1)\, \mathcal{N}(n_2, \alpha_2)}{\mathcal{N}(n_1 + n_2 - 1, \alpha_1 + \alpha_2)}$$

$$\sum_{l_3=|l_1-l_2|}^{l_1+l_2}{}'' \langle l_1\, m_1 \mid l_2\, m_2 \mid l_3\, m_2 - m_1 \rangle\, \chi_{n_1+n_2-1,l_3}^{m_2-m_1}(\alpha_1 + \alpha_2, \mathbf{r}_1) \tag{39}$$

where the symbol $\sum''$ means that the running index in the summation symbol is incremented by steps of 2. Because of the above property, instead of analysing the full definition as given by (38), we will rather consider a simplified version which is defined as,

$$\mathcal{I} = \left\langle \chi_{n_3,l_3}^{m_3}(\alpha_3, \mathbf{r}_2 - \mathbf{b}) \left| \frac{\chi_{n,l}^{m}(\alpha, \mathbf{r}_1)}{\|\mathbf{r}_1 - \mathbf{r}_2\|} \right| \chi_{n_4,l_4}^{m_4}(\alpha_4, \mathbf{r}_2 - \mathbf{c}) \right\rangle \tag{40}$$

Using the Laplace expansion for the Coulomb potential and performing the integration over $\mathbf{r}_1$ yields the following,

$$\mathcal{I} = \frac{4\pi}{2l+1}\, \mathcal{N}(n, \alpha) \left\langle \chi_{n_3,l_3}^{m_3}(\alpha_3, \mathbf{r}_2 - \mathbf{b}) \left| \mathcal{V}_l(r_2)\, Y_l^m(\theta_{\mathbf{r}_2}, \phi_{\mathbf{r}_2}) \right| \chi_{n_4,l_4}^{m_4}(\alpha_4, \mathbf{r}_2 - \mathbf{c}) \right\rangle_{\mathbf{r}_2} \tag{41}$$

where the symbol $\langle \ldots \rangle_{\mathbf{x}}$ is the usual bra-ket notation made more explicit by showing the integration variable to prevent any confusion. As for $\mathcal{V}_l(r_2)$, it is the radial part of the potential created by a single center distribution and is defined as,

$$\mathcal{V}_l(r_2) = \frac{1}{r_2^{l+1}} \int_0^{r_2} r_1^{n+l+1} \exp(-\alpha\, r_1)\, dr_1 \; + \; r_2^l \int_{r_2}^{+\infty} r_1^{n-l} \exp(-\alpha\, r_1)\, dr_1 \tag{42}$$

Since particle number (2) is described by a two-center distribution, we can apply the addition theorem given in equation (17). Of course to simplify matters we will restrict ourselves

to using s-type orbitals. Hence, for large s-type orbitals we have,

$$\mathcal{I} = \frac{(4\pi)^{3/2}}{\sqrt{b\,c}}\,\mathcal{N}(n,\alpha)\,\mathcal{N}(n_3,\alpha_3)\,\mathcal{N}(n_4,\alpha_4)$$

$$\times \sum_{\lambda_3=0}^{+\infty}\left\langle \frac{1}{\sqrt{r_2}}\,\mathcal{A}_{\lambda_3+1/2}^{n_3}(\alpha_3,b,r_2)\left|\,\mathcal{V}_l(r_2)\,\right|\frac{1}{\sqrt{r_2}}\,\mathcal{A}_{\lambda_4+1/2}^{n_4}(\alpha_3,c,r_2)\right\rangle_{r_2}\,P_{\lambda_3}\left(\frac{\mathbf{b}\cdot\mathbf{c}}{b\,c}\right) \quad (43)$$

As in the case of the three-center nuclear attraction integral, an obvious special case of the above equation can readily be obtained if one assumes that the vectors $\mathbf{b}$ and $\mathbf{c}$ are parallel or anti-parallel. In such a case, the values of the Legendre polynomials are $P_{\lambda_3}[\cos(\widehat{\mathbf{b},\mathbf{c}})] = (\pm 1)^{\lambda_3}$. From this point, the next step is to determine the Poincaré representation of the terms of the infinite series (43). Because of the intrinsic conditions in the *two-range* addition theorem (17), the above equation represents in fact the sum of three integrals defined over the intervals, $[0,\min(b,c)]$, $[\min(b,c),\max(b,c)]$ and finally $[\max(b,c),+\infty)$. To illustrate how the Poincaré representation is obtained within each of these intervals, we will provide a detailed analysis in the case of the radial integral $\mathcal{R}_1$, that is the integral over $[0,\min(b,c)]$. For the others, we will limit ourselves to provide only the leading term of the Poincaré representation from which the appropriate conclusion can be drawn. To within a constant, the integral $\mathcal{R}_1$ is defined as,

$$\mathcal{R}_1 = \int_0^{\min(b,c)}\mathcal{A}_{\lambda_3+1/2}^{n_3}(\alpha_3,b,r_2)\,\mathcal{V}_0(r_2)\,\mathcal{A}_{\lambda_3+1/2}^{n_4}(\alpha_4,c,r_2)\,r\,dr \quad (44)$$

Now, using the leading term of the Poincaré asymptotic representations of the BCLFs occurring in the above integrals yields,

$$\mathcal{R}_1 \sim \mathcal{K}_1\,\frac{1}{[\min(b,c)]^{\lambda_3+1/2}\,[\max(b,c)]^{\lambda_3+1/2}}\,\frac{1}{(\lambda_3+1/2)^{\lfloor(n_3+1)/2\rfloor+\lfloor(n_4+1)/2\rfloor+2}}$$

$$\int_{r_2=0}^{r_2=\min(b,c)}r_2^{2\lambda+3}\,\mathcal{V}_0(r_2)\,dr_2 \quad (45)$$

To start our derivation of the Poincaré asymptotic representation of $\mathcal{R}_1$ and for the sake of completeness, we propose to begin by giving the expression of the potential $\mathcal{V}_0(r_2)$ (although this can be found is a variety of calculus textbooks) [74, Eq. 3.351],

$$\begin{aligned}\mathcal{V}_0(r_2) &= \frac{1}{r_2}\int_0^{r_2}r_1^{n+1}\,\exp(-\alpha\,r_1)\,dr_1 \;+\; \int_0^{r_2}r_1^{n-l}\,\exp(-\alpha\,r_1)\,dr_1\\[2mm] &= \frac{(n+1)!}{\alpha_2^{n+2}}\frac{1}{r_2} - \frac{(n+l)!}{\alpha_2^{n+2}}\frac{\exp(-\alpha\,r_2)}{r_2}\sum_{q=0}^{n+l}\frac{(\alpha\,r_2)^q}{q!}\\[2mm] &\quad + \frac{n!}{\alpha^{n+1}}\,\exp(-\alpha\,r_2)\sum_{q=0}^{n}\frac{(\alpha\,r_2)^q}{q!}\end{aligned} \quad (46)$$

Next, let us derive the asymptotic representation for large values of n of the integral $\int_0^R r^n\,\exp(-\alpha\,r)\,dr$ since this quantity will be encountered several times in the convergence analysis of $\mathcal{R}_1$, $\mathcal{R}_2$ and $\mathcal{R}_3$. In fact the usual integration technique is to apply the

"by-part" integration technique in which $U = r^n$ and $dV = \exp(-\alpha r)\,dr$. The result is a closed analytical similar to the first two terms in equation (46). However, in order to obtain the asymptotic representation for the integral in question, when n is large, we set $U = \exp(-\alpha r)$ and $dV = r^n\,dr$ and once again integrate by part. As a result we obtain,

$$
\int_0^R r^n \exp(-\alpha\,r)\,dr = \frac{R^{n+1}}{n+1}\,\exp(-\alpha\,R)
$$
$$
\left[1 + \frac{\alpha R}{n+2} + \frac{(\alpha R)^2}{(n+2)(n+3)} + \ldots + \frac{(\alpha R)^M}{(n+2)(n+3)\ldots(n+M+1)}\right]
$$
$$
+ \frac{\alpha^M}{(n+1)(n+2)\ldots(n+M+1)} \int_0^R r^{n+M+1}\,\exp(-\alpha r)\,dr \tag{47}
$$

For the integral on the right hand side, we can easily construct its upper bound since we the integrand is a non negative function within the interval $[0, R]$,

$$
\text{Since } \alpha\,r \geq 0, \quad \exp(-\alpha\,r) \leq 1 \quad \implies \quad r^{n+M+1}\,\exp(-\alpha\,r) \leq r^{n+M+1} \tag{48}
$$

where M is a cutoff index conveniently chosen based on the accuracy needed to be achieved. Using the above property in connection with equation (47), we can write the following when n is large,

$$
\int_0^R r^n \exp(-\alpha\,r)\,dr \ \sim \ \frac{R^{n+1}}{n+1}\,\exp(-\alpha\,R)
$$
$$
\left[1 + \frac{\alpha R}{n+2} + \frac{(\alpha R)^2}{(n+2)(n+3)} + \ldots + \frac{(\alpha R)^M}{(n+2)(n+3)\ldots(n+M+1)}\right] \tag{49}
$$

To validate the above asymptotic expansion, it is instructive to provide some numerical data that are obtained for large values of n such that $\alpha R \ll n$.

Clearly, the values listed in table (2) provides a numerical support for the validity of the asymptotic representation given in equation (49). In the sequel and for the sake of simplifying the analysis, we will keep only the leading term of (49) since for asymptotic analysis this generally suffices. Thus, going back to the definition of $\mathcal{R}_1$ (45) we obtain the following after some algebra,

$$
\mathcal{R}_1 \sim \mathcal{K}_1 \left[\min(b,c)\right]^2 \left[\frac{(n+1)!}{\alpha^{n+2}} - \frac{(n+1)!}{\alpha^{n+2}}\,\exp(-\alpha\,\min(b,c)) \sum_{q=0}^{n+1} \frac{[\alpha\,\min(b,c)]^q}{q!\,[1 + q/(2\lambda_3 + 3)]} \right.
$$
$$
+ \frac{n!}{\alpha^{n+1}}\,\min(b,c)\,\exp(-\alpha\,\min(b,c)) \sum_{q=0}^{n} \frac{[\alpha\,\min(b,c)]^q}{q!\,[1 + (q+1)/(2\lambda_3 + 3)]} \left.\right]
$$
$$
\times \left[\frac{\min(b,c)}{\max(b,c)}\right]^{\lambda_3 + 1/2} \frac{1}{(2\lambda_3 + 3)\,(\lambda_3 + 1/2)^{\lfloor(n_3+1)/2\rfloor + \lfloor(n_4+1)/2\rfloor + 2}} \tag{50}
$$

Clearly for large values of λ_3, the above representation can easily be cast in a form similar to that given in theorem (2.1.), that is,

$$
\mathcal{R}_1 \sim \mathcal{K}_1' \left[\frac{\min(b,c)}{\max(b,c)}\right]^{\lambda_3} \lambda_3^{-\lfloor(n_3+1)/2\rfloor - \lfloor(n_4+1)/2\rfloor - 2} \tag{51}
$$

Table 2. Numerical validation of the asymptotic representation of the finite integral $\displaystyle\int_0^R r^n \exp(-\alpha\, r)\, dr$ **for which** $\alpha = 1.5$, $R = 2$.

n	Exact value	Leading term	$M = 1$	$M = 2$	$M = 3$	$M = 4$	$M = 5$
100	1.28761448155023(27)	1.2497545960421 2.94(-02)	1.2865120841610 8.56(-04)	1.2875826906111 2.47(-05)	1.2876135734894 7.05(-07)	1.28761445585738 1.99(-08)	1.28761448083006 5.59(-10)
200	8.08067113456499(56)	7.96067007686009 1.49(-02)	8.07889785027881 2.19(-04)	8.08064505875297 3.23(-06)	8.08067075299524 4.72(-08)	8.08067112900854 6.88(-10)	8.08067113448447 9.96(-12)
300	6.80635134848264(86)	6.73874082535306 9.93(-03)	6.80568195937974 9.83(-05)	6.80634474288496 9.71(-07)	6.80635128351166 9.55(-09)	6.80635134784569 9.36(-11)	6.80635134847641 9.14(-13)
400	6.46031269475044(116)	6.41210230539757 7.46(-03)	6.45995381513934 5.56(-05)	6.46031002985206 4.13(-07)	6.46031267501082 3.06(-09)	6.46031269460459 2.28(-11)	6.46031269474937 1.66(=13)

In which $\mathcal{K}_1'$ is a constant independent of λ_3. In the case of $\mathcal{R}_2$, the calculation is straightforward since the corresponding asymptotic representation can be written as,

$$
\begin{aligned}
\mathcal{R}_2 \quad \sim \quad & \mathcal{K}_2 \, \frac{1}{(\lambda + 1/2)^{\lfloor (n_3+1)/2 \rfloor + \lfloor (n_4+1)/2 \rfloor + 2}} \\
& \int_{\min(b,c)}^{\max(b,c)} \left[\frac{\min(b,c)}{r_2} \right]^{\lambda_3 + 1/2} \left[\frac{r_2}{\max(b,c)} \right]^{\lambda_3 + 1/2} \mathcal{V}_0(r_2) \, r^2 \, dr \\
\sim \quad & \mathcal{K}_2' \, \underbrace{\left[\int_{\min(b,c)}^{\max(b,c)} r_2^2 \, \mathcal{V}_0(r_2) \, dr_2 \right]}_{\text{Independent of } \lambda_3} \left[\frac{\min(b,c)}{\max(b,c)} \right]^{\lambda_3} \\
& \lambda_3^{-\lfloor (n_3+1)/2 \rfloor - \lfloor (n_4+1)/2 \rfloor - 2}
\end{aligned} \tag{52}
$$

Since the integral over r_2 does not depend on λ_3, it can be included as part of the leading constant. As a result, and without any further calculations, we notice that the above Poincaré asymptotic representation is shaped in a form similar to what's needed to apply theorem (2.1.). As for the term $\mathcal{R}_3$ which occurs as part of the radial integral of the three-center hybrid integrals (43), it can be written after substituting for the BCLFs the leading term of their Poincaré asymptotic representation,

$$
\begin{aligned}
\mathcal{R}_3 \quad \sim \quad & \mathcal{K}_3 \, \frac{[\min(b,c)]^{\lambda_3 + 1/2} \, [\max(b,c)]^{\lambda_3 + 1/2}}{(\lambda_3 + 1/2)^{\lfloor (n_3+1)/2 \rfloor + \lfloor (n_4+1)/2 \rfloor + 2}} \int_{\max(b,c)}^{+\infty} r^{-2\lambda_3 + 1} \, \mathcal{V}_0(r_2) \, dr_2 \\
\sim \quad & \mathcal{K}_3 \left[\frac{(n+1)!}{\alpha^{n+2}} - \frac{(n+1)!}{\alpha^{n+2}} \exp[-\alpha \, \max(b,c)] \sum_{q=0}^{n+1} \frac{[\alpha \, \max(b,c)]^q}{q! \, [1 - q/(2\lambda_3 - 1)]} \right. \\
& \left. + \frac{n!}{\alpha^{n+1}} \, \max(b,c) \, \exp[-\alpha \, \max(b,c)] \sum_{q=0}^{n} \frac{[\alpha \, \max(b,c)]^q}{q! \, [1 - (q+1)/(2\lambda_3 + 1)]} \right] \\
& \times \left[\frac{\min(b,c)}{\max(b,c)} \right]^{\lambda_3 + 1/2} \frac{1}{(\lambda_3 + 1/2)^{\lfloor (n_3+1)/2 \rfloor + \lfloor (n_4+1)/2 \rfloor + 2}}
\end{aligned} \tag{53}
$$

And once again, the above asymptotic representation can easily by re-written in a form similar to that required for the application of theorem (2.1.),

$$
\mathcal{R}_3 \sim \mathcal{K}_3' \left[\frac{\min(b,c)}{\max(b,c)} \right]^{\lambda_3} \lambda_3^{-\lfloor (n_3+1)/2 \rfloor - \lfloor (n_4+1)/2 \rfloor - 3} \tag{54}
$$

in which $\mathcal{K}_3'$ is a term independent of λ_3. At this point, we clearly notice that the Poincaré asymptotic representations of the radial integral $\mathcal{R}_1$, $\mathcal{R}_2$ and $\mathcal{R}_3$ have a common leading term that is $[\min(b,c)/\max(b,c)]^{\lambda_3} \lambda_3^{\lfloor (n_3+1)/2 \rfloor + \lfloor (n_4+1)/2 \rfloor + 3}$. As a result, applying theorem (2.1.) allows one to conclude that when $b \neq c$, that is $\min(b,c) < \max(b,c)$, the convergence of the infinite series (43) is linear. In contrast this convergence becomes loga-

rithmic for $b = c$ hence leading us to conclude that under such a condition one must not use a direct summation procedure for the evaluation of the three-center hydrid integral (43).

3. Numerical Evaluation

From the previous paragraph, we have shown that under special circumstances, the use of the two-range addition theorem to evaluate multicenter integrals over STOs can lead to logarithmically convergence series. This of course makes it practically impossible to rely on simple algorithms for their evaluation. Fortunately, the problem of logarithmically convergent series occurs in a variety of problems be it in physical sciences or in pure mathematics. And because of this, it has attracted so much attention which led to a rich literature and along with this some powerful algorithms geared specifically for the summation of such series. In this work, we will mainly use two of what is considered as the most powerful and versatile procedures for the acceleration of infinite series, namely, the Levin u [75–78] transformation and the Wynn ϵ algorithm [79]. The popularity of the latter and its relevance to Padé approximants has even led to generic implementations that can be found in a variety of general purpose mathematical libraries, C06BAF (NAG) [80], IN-LAP/DINLAP (IMSL) [81]. For the evaluation of multicenter integrals, the first issue that needs to be addressed is the evaluation of the BCLFs since these terms enter every series expansion built on the two-range addition theorem.

3.1. Numerical Evaluation of Barnett-Coulson/Löwdin Functions

BCLFs can be evaluated by a variety of techniques. Jones has previously used closed analytical forms which were shown to be unstable because of two features which when combined together inevitably lead to a drastic loss of significance. To examine this issue let us write the closed form of the BCLF $\mathcal{A}^0_{\lambda+1/2}(\zeta, a, r)$ using Jones **C**-matrix representation,

$$\frac{\mathcal{A}^0_{\lambda+1/2}(\zeta, a, r)}{\sqrt{ar}} = (-1)^\lambda \frac{\zeta}{2} \sum_{i=0}^{\lambda} \sum_{j=0}^{\lambda} \mathbf{C}^0_\lambda(i,j) \, (\zeta\rho_<)^{i-\lambda-1} \, (\zeta\rho_>)^{j-\lambda-1} \, H_i(\zeta, a, r)$$

(55)

in which $H_i(\zeta, a, r)$ is a function defined as,

$$H_i(\zeta, a, r) = \exp\left(\zeta\rho_>\right) \left[(-1)^i \exp\left(\zeta\rho_<\right) - \exp\left(-\zeta\rho_<\right)\right]$$ (56)

As for the term $\mathbf{C}^0_\lambda(i,j)$, it represents a matrix of integer numbers such that,

$$\mathbf{C}^0_\lambda(i,j) = \frac{(\lambda-i)!}{2^{\lambda-i}} \frac{(\lambda-j)!}{2^{\lambda-j}} \begin{pmatrix} \lambda \\ i \end{pmatrix} \begin{pmatrix} 2\lambda-i \\ \lambda \end{pmatrix} \begin{pmatrix} \lambda \\ j \end{pmatrix} \begin{pmatrix} 2\lambda-j \\ \lambda \end{pmatrix}$$ (57)

Table 3. Two-range addition theorem applied to the $1s$ orbital, $\zeta = 3.5$, $a = 4$, $\cos(\widehat{\mathbf{r}, \mathbf{a}}) = 1$

λ	$r = 1.0$		$r = 2.5$		$r = 4.0$	
	Negative part	Positive part	Negative Part	Positive Part	Negative part	Positive part
5	-1.0516135013(-5)	3.7158903043(-5)	-4.7119126878(-3)	7.7242621259(-3)	-2.8534065951(+0)	3.1465934049(+0)
10	-1.1356633439(-5)	3.8889225279(-5)	-9.0055027740(-3)	1.3813438872(-2)	-9.8228840223(+0)	1.0343782644(+1)
15	-1.1364222411(-5)	3.8900664191(-5)	-1.0516946082(-2)	1.5705971262(-2)	-2.1008985999(+1)	2.1657680668(+1)
20	-1.1364248879(-5)	3.8900698218(-5)	-1.0846698238(-2)	1.6087733465(-2)	-3.6387414519(+1)	3.7112585481(+1)
30	-1.1364248938(-5)	3.8900698288(-5)	-1.0910296642(-2)	1.6157751432(-2)	-7.9678365176(+1)	8.0488301491(+1)
40			-1.0911488958(-2)	1.6159006799(-2)	-1.3965574270(+2)	1.4051092396(+2)
50			-1.0911506289(-2)	1.6159024683(-2)	-2.1630842590(+2)	2.1719157410(+2)
60			-1.0911506510(-2)	1.6159024909(-2)	-3.0963228062(+2)	3.1053438605(+2)
100			-1.0911506513(-2)	1.6159024912(-2)	-8.4961298475(+2)	8.5055368192(+2)
200					-3.3662649188(+3)	3.3672350812(+3)
300					-7.5495932982(+3)	7.5505733685(+3)
400					-1.3399590814(+4)	1.3400575853(+4)
500					-2.0916255988(+4)	2.0917244012(+4)
Sum	2.7536449350(-5)[†]	2.7536449350(-5)[‡]	5.2475183992(-3)[†]	5.2475183990(-3)[‡]	1.0000000000[†]	9.8802400000(-1)[‡]

[†] Exact value of the $1s$ orbital, $\exp(-\zeta|\mathbf{r} - \mathbf{a}|)$

[‡] Two-range expansion, *cf.* equation (17)

Table 4. Applying the epsilon algorithm to the two-range expansion of the unnormalized $1s$ **orbital** $\exp(\zeta|\mathbf{r} - \mathbf{a}|)$ **with** $\zeta = 6.473$, $a = r = 4.043$ **and** $\cos(\widehat{\mathbf{r}, \mathbf{a}}) = 0$.

n	$\epsilon_0^{(n)} = S_n$	$\epsilon_2^{(n)} = \Delta^2$ †	$\epsilon_{22}^{(n)}$
	$\ldots$	$\ldots$	$\ldots$
		0.87359826765917957186	0.85303416902442378142
30	0.35492851303740599779		0.87735214169438363894
		0.85638751220470603565	0.89155775620814097356
31	0.36692865767280399913		0.89709390427704151874
		0.84282782264848708729	0.89910641383940196554
32	0.37863365232861858840		0.89994299975246699987
		0.83211456764152286573	0.90020698388759544083
33	0.39004412624131380623		0.89957179539431583803
		0.82365248236128637802	0.89636665025726549386
34	0.40116203070272818609		0.88470617356862636087
		0.81699226838470187549	0.83372124259869021957
35	0.41199042037906212214		2.05226482485654820620
		0.81178891279666021337	1.04067038356126526680
36	0.42253326123213194178		0.99971888094617188481
		0.80777350920394048096	0.98901407427213483543
37	0.43279526266484355853		1.00002951968762153170

†Convergence accelerated series using Aitken's Δ^2.

Table 5. Three-center hybrid integrals using normalized Slater orbitals. The present values correspond to the linear molecule LiCCH, the geometrical parameters of which are Li (0,0,0), C (3.55,0,0), C' (5.8196,0,0), and H (7.8284,0,0). Lengths are in a.u. Numbers in parentheses denote powers of 10.

Integral	ζ_1	ζ_2	ζ_3	ζ_4	$\epsilon_{20}^{(n)}$	I[†]
$\langle 1s^{C'}\, 1s^{H}|1s^{C}\, 1s^{C}\rangle$	7.96897	0.45441	5.23090	5.23090	0.188877949(-01)	0.188877949(-01)
$\langle 1s^{C'}\, 1s^{H}|1s^{C}\, 2s^{C}\rangle$	7.96897	0.45441	5.23090	1.16782	0.275256680(-02)	0.275256680(-02)
$\langle 1s^{C'}\, 1s^{H}|1s^{C}\, 2p_z^{C}\rangle$	7.96897	0.45441	5.23090	1.25572	0.484256051(-03)	0.484256051(-03)
$\langle 1s^{C'}\, 1s^{H}|2p_z^{C}\, 3d_z^{C}\rangle$	7.96897	0.45441	2.72625	2.01591	0.477576604(-02)	0.477576604(-02)
$\langle 2s^{C'}\, 1s^{H}|1s^{C}\, 1s^{C}\rangle$	1.16782	0.45441	5.23090	5.23090	0.231915790(+0)	0.231915790(+00)
$\langle 2s^{C'}\, 1s^{H}|1s^{C}\, 2p_z^{C}\rangle$	1.16782	0.45441	5.23090	1.16782	0.335758750(-01)	0.335758750(-01)
$\langle 2s^{C'}\, 1s^{H}|1s^{C}\, 1s^{C}\rangle$	1.16782	0.45441	5.23090	1.25572	0.318914301(-02)	0.318914301(-02)
$\langle 2s^{C'}\, 1s^{H}|2p_z^{C}\, 3d_z^{C}\rangle$	1.16782	0.45441	2.72625	2.01591	0.247693208(-01)	0.247693208(-01)
$\langle 2s^{C'}\, 1s^{H}|1s^{Li}\, 1s^{Li}\rangle$	1.16782	1.33761	2.43309	2.43309	0.752720784(-01)	0.752720787(-01)
$\langle 2s^{C'}\, 1s^{H}|1s^{Li}\, 2s^{Li}\rangle$	1.16782	1.33761	2.43309	0.45000	0.778234078(-02)	0.778234081(-02)
$\langle 2s^{C'}\, 1s^{H}|2s^{Li}\, 2s^{Li}\rangle$	1.16782	1.33761	0.45000	0.45000	0.713495636(-01)	0.713495640(-01)
$\langle 2s^{C'}\, 2s^{C}|1s^{Li}\, 1s^{Li}\rangle$	1.16782	1.16782	4.51769	4.51769	0.150148075(+0)	0.150148075(+0)
$\langle 2s^{C'}\, 2s^{C}|2s^{Li}\, 2s^{Li}\rangle$	1.16782	1.16782	0.85000	0.85000	0.143404295(+0)	0.143404295(+0)

[†] Comparison values calculated with ALCHEMY II package.

Table 6. Selected three-center nuclear attraction integrals in the case of a linear HCN molecule whose geometry is such that $d(H,C) = 2.0143$ and $d(N,H) = 4.1934$. Numbers in parentheses represent powers of 10.

Atomic orbitals			Integral	DEXC	This work	ALCHEMY[a]	DTEST[b,c]
1 : (H)	1 s	[1.24]	$\langle 1\|2\rangle$	5	2.945496054(-2)	2.945496054(-2)	2.945494454(-2)
2 : (C)	1 s	[5.67]	$\langle 1\|3\rangle$	11	1.606646078(-1)	1.606646041(-1)	1.606645937(-1)
3 : (C)	2 s	[1.61]	$\langle 1\|4\rangle$	7	-1.163866018(-1)	-1.163866018(-1)	-1.163865846(-1)
4 : (C)	$2p_0$	[1.56]	$\langle 2\|6\rangle$	2	3.710041454(-5)	3.710041454(-5)	3.710152495(-5)
5 : (C)	$2p_1$	[1.54]	$\langle 2\|7\rangle$	6	2.695528880(-2)	2.695528880(-2)	2.695532230(-2)
6 : (N)	1 s	[6.66]	$\langle 2\|8\rangle$	6	-4.621491513(-2)	-4.621491513(-2)	-4.621497451(-2)
7 : (N)	2 s	[1.94]	$\langle 3\|6\rangle$	2	1.408177370(-2)	1.408177370(-2)	1.408441969(-2)
8 : (N)	$2p_0$	[1.92]	$\langle 3\|7\rangle$	3	1.467233406(-1)	1.467233406(-1)	1.467232649(-1)
9 : (N)	$2p_1$	[1.80]	$\langle 3\|8\rangle$	4	-1.530415963(-1)	-1.530415963(-1)	-1.530415938(-1)
			$\langle 5\|9\rangle$	4	1.009914329(-1)	1.009914329(-1)	1.009914330(-1)

"This work": Values obtained after accelerating the initial series expansion using the ϵ algorithm. Column DEXC represents the number of exact digits obtained after the summation of 17 terms of the original series. The values listed in the column referred to as "This work" correspond to the term $\epsilon_{16}^{(16)}$.

[a] See Ref. [82].

[b] DTESTThese values were obtained using the so-called Legendre Mobius quadrature (LRM) [83] method for which the parameters are: LRM 90 I 30,20; 1(-6) I 20, 16; 1(-7) 110, 10; 1(-8).

[c] See Ref. [84].

Table 7. Three-center nuclear attraction integrals and comparison values for linear and non-linear systems. The orbitals are assumed to be on the Z axis and separated by a distance a while the center C is defined by its vector c. Calculations are carried out following the same protocol as in table (6). Numbers in parentheses represent powers of 10.

Geometry	Integral	This work	Rico *et al*[a]	DTEST[b]
$a = 3$, **c**(3,4,5)	$\langle 2p_x[4.0]\|3d_{xz}[3.0]\rangle$	-3.020076721(-3)	-3.02007672(-3)	-3.028935052(-3)
$a = 5$, **c**(3,4,5)	$\langle 2p_x[4.0]\|3d_{xz}[3.0]\rangle$	-2.587578890(-5)	-2.58757860(-5)	-2.600519879(-5)
$a = 5$, **c**(0,0,7)	$\langle 2p_x[4.0]\|3d_{xz}[3.0]\rangle$	-2.818653000(-5)	-2.81865700(-5)	-2.818654096(-5)
$a = 5$, **c**(-2,5,4)	$\langle 2s\ [3.0]\|2p_z\ [3.0]\rangle$	-1.333583172(-3)	-1.33359600(-3)	-1.333586292(-3)
$a = 5$, **c**(-3,6,5)	$\langle 2s\ [3.0]\|2p_z\ [3.0]\rangle$	-1.045218434(-4)	-1.04521917(-4)	-1.045222323(-4)
$a = 5$, **c**(-4,7,6)	$\langle 2s\ [3.0]\|2p_z\ [3.0]\rangle$	-8.531955275(-5)	-8.53195579(-5)	-8.531988486(-5)
$a = 2$, **c**(0,0,9)	$\langle 2s\ [4.0]\|1s\ \ [1.0]\rangle$	-2.630240914(-2)	2.63024091(-2)	2.630314167(-2)
$a = 5$, **c**(0,0,9)	$\langle 2s\ [4.0]\|1s\ \ [1.0]\rangle$	1.538280150(-3)	1.53828015(-3)	1.538316674(-3)
$a = 8$, **c**(0,0,9)	$\langle 2s\ [4.0]\|1s\ \ [1.0]\rangle$	7.945638156(-5)	7.94563790(-5)	7.945820427(-5)

[a]Ref. [25]
[b]Ref. [84]

Table 8. Three center nuclear attraction integrals computed using the two-range addition theorem. The atoms are located on the vertices of an equilateral triangle having the coordinates: (0, 0, 0), (0, 0, 2.51900) and (2.18152, 0, 1.25950). All calculations are performed using the protocol described for table (6).

	Integral			This work	DTEST[a]
1 :	$1s$	[5.67]	$\langle 1\|5 \rangle$	2.32034676(-5)	2.32032039(-5)
2 :	$2s$	[1.61]	$\langle 2\|5 \rangle$	2.03634967(-2)	2.03634671(-2)
3 :	$2p_0$	[1.56]	$\langle 3\|5 \rangle$	3.59413007(-2)	3.59412561(-2)
4 :	$2p_1$	[1.54]	$\langle 4\|5 \rangle$	-4.89157390(-4)	-4.89113961(-4)
			$\langle 2\|6 \rangle$	1.94935000(-1)	1.94934928(-1)
			$\langle 3\|6 \rangle$	2.05267819(-1)	2.05268243(-1)
			$\langle 4\|6 \rangle$	-4.32821200(-2)	-4.32821990(-2)
5 :	$1s$	[5.67]	$\langle 1\|7 \rangle$	-3.59413680(-2)	-3.59412561(-2)
6 :	$2s$	[1.61]	$\langle 2\|7 \rangle$	-2.05268214(-1)	-2.05268243(-1)
7 :	$2p_0$	[1.56]	$\langle 3\|7 \rangle$	-1.66713873(-1)	-1.66713808(-1)
8 :	$2p_1$	[1.54]	$\langle 4\|7 \rangle$	4.60773136(-2)	4.60772924(-2)

[a]Ref. [84]

The above definition clearly shows that the elements of the matrix $\mathbf{C}_\lambda^0(i, j)$ are all integers which makes Jones approach suitable for computer algebra systems since it allows highly accurate benchmarks to be generated. As for higher order BCLFs we write according to equation (15),

$$\frac{\mathcal{A}_{\lambda+1/2}^n(\zeta, a, r)}{\sqrt{ar}} = \sum_{\mu=0}^{\lambda+n} \sum_{\nu=0}^{\lambda+n} \mathbf{C}_\lambda^n(\mu, \nu) \ (\zeta\rho_<)^{\mu-\lambda-1} \ (\zeta\rho_>)^{\nu-\lambda-1} \ H_\mu(\zeta, a, r) \qquad (58)$$

where the $\mathbf{C}_\lambda^n$ matrix is related to $\mathbf{C}_\lambda^0$ as described by the following equation,

$$\mathbf{C}_\lambda^n(i, j) = \sum_{p=0}^{n} \sum_{q=\max(0, i-\lambda, p-j)}^{\min(p, i, \lambda+p-j)} \left(\begin{array}{c} n \\ p \end{array} \right) \left(\begin{array}{c} p \\ q \end{array} \right) (2\lambda - i - j + p + 1)_{n-q} \ \mathbf{C}_\lambda^0(i, j) \quad (59)$$

in which $(x)_n$ stands for the Pochhammer symbol which is related to the Γ function as, $(x)_n = \Gamma(x+n)/\Gamma(x)$. To illustrate the problem of loss significance mentioned above, we use an unnormalized $1\,s$ orbital as a working example.

From the values listed in table (3), we notice that as we approach the cusp, the effect due to loss of significance inflates which leads to less accurate results. In addition and as predicted by our the analysis presented in the previous section, the convergence of the infinite series (17) deteriorates since it is was shown to be logarithmic. To remedy the difficulties inherent to direct summation procedures, the most expedient option relies on a suitable convergence accelerator.

3.2. Shank's Transformation

Previously, the convergence analysis of the infinite series representations of the two-range expansions of the three-center nuclear attraction and hybrid integrals was performed assuming the nuclei were aligned hence allowing to write $P_\lambda(\cos \theta) = (\pm 1)^\lambda$. Of course, for non linear systems, such a simplification cannot be used and this leads to infinite that cannot be categorized as linearly or logarithmically convergent. In such cases, it was noticed that Wynn's ϵ algorithm outperforms Levin's u transformation. In order to shed some light on this matter, we go back to the series analyzed in this work and as mentioned above we notice they all involve Legendre polynomials $P_\lambda(\cos \theta)$. For an arbitrary angle θ, that is $\theta \neq 0, \pi$, the asymptotic representation of a Legendre polynomial can be written (for $\lambda \to +\infty$) as,

$$P_\lambda(\cos \theta) \sim \frac{1}{\sqrt{\lambda} \sqrt{\pi \ \sin(\theta)}} \ (\cos \left[(\lambda + 1/2)\theta \right] + \sin \left[(\lambda + 1/2)\theta \right]) \qquad (60)$$

where $0 < \theta < \pi$. Clearly, Legendre high order Legendre polynomials behave asymptotically as a Fourier series. As a result, we may conclude beforehand that the difficulties that will be encountered during the convergence acceleration of the series (21), (30) and (43) are similar to those occurring when dealing with Fourier series. And, in this context only very few accelerators can be successfully used; the ϵ algorithm belongs to the class of accelerators that can be used on Fourier series since its kernel includes special Fourier series

of the form,

$$\sum_i \left[B_i(\theta) \, \cos(\beta_i \theta) + C_i(\theta) \, \sin(\beta_i \theta) \right] \, \exp(w_i \, \theta) \tag{61}$$

According to the above discussion, it is most advisable to implement the ϵ convergence accelerator as part of the algorithms geared towards the evaluation of multicenter integrals whenever these are evaluated by means of the two-range addition theorem. And, because the ϵ accelerator is central to such procedures, it is advisable to outline briefly its foundations.

Perhaps, the first and oldest convergence accelerating transformation, which can be shown to be a special case of the ϵ algorithm, is the so-called Aitken Δ^2 process. This method is often introduced in introductory numerical analysis courses as a means to speed up the convergence of Newton's algorithm for finding the roots of a function. Aitken's algorithm proceeds by transforming the initial sequence $\{S_n\}_{n=0,1,\ldots}$ whose limit is s into a new sequence denoted by $\{e(S_n)\}_{n=0,1,\ldots}$ which is constructed as,

$$e_1(S_n) = \frac{S_n \, S_{n+1} - S_n^2}{S_{n+2} - 2S_{n+1} + S_n} \qquad n = 0, 1, \ldots \tag{62}$$

Of course, in the context of infinite series the term S_n corresponds to the n-th partial sum (*cf.* Sec. (2.1.), Def. (2.1.)). If the sequence $\{S_n\}_{n=0,1,\ldots}$ satisfies the linear equation $a_0(S_n - s) + a_1(S_n - s) = 0$ in which $a_0 + a_1 \neq 0$, it follows that $e(S_n) = s$ for $n > N$ where N is some large index. The aim of Shanks' transformation is essentially a generalization of the Aitken's process. Indeed, for any convergent sequence $\{S_n\}_{n=0,1,\ldots}$ satisfying the linear difference equation,

$$\begin{cases} \displaystyle\sum_{i=0}^{k} a_i \, (S_{\mu+i} - s) = 0 \qquad \mu = n, n+1, \ldots, n+k \\[2mm] \text{subjected to the condition} \quad \displaystyle\sum_{i=0}^{k} a_i \neq 0 \end{cases} \tag{63}$$

Obviously, the above equation can be written more explicitly as,

$$\begin{cases} a_0 & + & a_1 & + & \ldots & + & a_k & = & 1 \\ a_0 S_n & + & a_1 S_{n+1} & + & \ldots & + & a_k S_{n+k} & = & s \\ a_0 S_{n+1} & + & a_1 S_{n+2} & + & \ldots & + & a_k S_{n+k+1} & = & s \\ \vdots & & \vdots & & & & \vdots & & \vdots \\ a_0 S_{n+k} & + & a_1 S_{n+k+1} & + & \ldots & + & a_k S_{n+2k} & = & s \end{cases} \tag{64}$$

After few linear combinations of the equations occurring in the above system, we are able

to express the limit s of the sequence as,

$$
s = e_k(S_n) = \frac{\begin{vmatrix} S_n & S_{n+1} & \ldots & S_{n+k} \\ \Delta S_n & \Delta S_{n+1} & \ldots & \Delta S_{n+k} \\ \vdots & \vdots & \ddots & \vdots \\ \Delta S_{n+k-1} & \Delta S_{n+k} & \ldots & \Delta S_{n+2k-1} \end{vmatrix}}{\begin{vmatrix} 1 & 1 & \ldots & 1 \\ \Delta S_n & \Delta S_{n+1} & \ldots & \Delta S_{n+k} \\ \vdots & \vdots & \ddots & \vdots \\ \Delta S_{n+k-1} & \Delta S_{n+k} & \ldots & \Delta S_{n+2k-1} \end{vmatrix}}
\tag{65}
$$

in which ΔS_n stands for the difference $S_{n+1} - S_n$. Clearly, from the above we can obtain the working formula of Aitken's Δ^2 process as,

$$
\begin{aligned}
\Delta^2 &= \frac{\begin{vmatrix} S_n & S_{n+1} \\ \Delta S_n & \Delta S_{n+1} \end{vmatrix}}{\begin{vmatrix} 1 & 1 \\ \Delta S_n & \Delta S_{n+1} \end{vmatrix}} = \frac{S_n\,\Delta S_{n+1} - S_{n+1}\,\Delta S_n}{\Delta S_{n+1} - \Delta S_n} \\
&= \frac{S_n\,\Delta S_{n+1} - S_{n+1}\,\Delta S_n}{\Delta^2 S_n} = \frac{S_n\,S_{n+2} - S_{n+1}^2}{S_{n+2} - 2S_{n+1} + S_n}
\end{aligned}
\tag{66}
$$

in which the higher order difference operator Δ^2 which can be expressed recursively $\Delta^2 S_n = \Delta(\Delta S_n)$. From a practical standpoint, the solution proposed by Shanks (65) is extremely limited since it requires the evaluation of determinants for which numerical procedures are very unstable. To circumvent this difficulty, that is not evaluating Shanks determinants, Wynn introduced what is known as the ϵ algorithm which is defined recursively as,

$$
\begin{cases}
\epsilon_{-1}^{(n)} = 0, \qquad \epsilon_0^{(n)} = S_n & n = 0, 1, 2, \ldots \\[2mm]
\epsilon_{k+1}^{(n)} = \epsilon_{k-1}^{(n)} + \dfrac{1}{\epsilon_k^{(n+1)} - \epsilon_k^{(n)}} & k, n = 0, 1, 2, \ldots
\end{cases}
\tag{67}
$$

And once again, if the rules of the ϵ algorithm listed in the above equation are written for $k = 1$, the working formula of Aitken's Δ^2 process immediately follows.

4.   Conclusion

In this work, we have provided the details of the procedure that can be used to analyse the convergence of multipole expansions as they occur in the context of multicenter integrals over STOs. It is important to note, however, that although the relevant proofs were illustrated using multicenter integrals, the same concepts can still be applied to other problems which are solved by means of multipole expansions. In the case of three-center nuclear attraction and three-center hybrid integrals, it was shown that the corresponding two-range infinite expansions converge logarithmically when the centers are the vertices of an equilateral triangle and linearly otherwise. As a result, the use of convergence accelerators is

paramount to keep the computational time within reasonable bounds. Of course, prior to applying these algorithms, one needs to generate the terms of the series to be accelerated. In this respect, it is crucial to elaborate an efficient procedure for the evaluation of large order BCLFs.

Acknowledgements

References

[1] C. C. J. Roothaan, *Rev. Mod. Phys.* **23**, 69 (1951).

[2] T. Kato, *Commun. Pure. Appl. Math* **10**, 151 (1957).

[3] S. Agmon, *Analyse Mathémathique et Applications* **1**, 1 (1988).

[4] N. C. Handy, M. T. Marron, and H. J. Silverstone, *Phys. Rev* **180**, 45 (1969).

[5] S. F. Boys, *Proc. Roy. Soc.* **A200**, 542 (1950).

[6] A. Szabo and N. Ostlund, *Modern quantum chemistry*, Mc Graw-Hill Publishing Company, New York, first (revised) edition, 1989.

[7] A. S. Coolidge, *Phys. Rev.* **42**, 189 (1932).

[8] P.-O. Löwdin, *Arkiv Mat. Fys. Astr.* **35 A**, 9 (1947).

[9] M. P. Barnett and C. A. Coulson, *Phil. Trans. Roy. Soc.* **243**, 221 (1951).

[10] M. P. Barnett, In Alder et al. [85], pages 95–153.

[11] E. O. Steinborn and E. Filter, *Theor. Chim. Acta.* **38**, 247 (1975).

[12] E. O. Steinborn and E. Filter, *Theor. Chim. Acta.* **38**, 273 (1975).

[13] R. R. Sharma, *Phys. Rev. A* **13**, 517 (1976).

[14] M. A. Rashid, *J. Math. Phys.* **22**, 271 (1981).

[15] M. A. Rashid, International Conference on ETO Multicenter Integrals, Tallahasse, 1981, In Weatherford and Jones [86], pages 61–78.

[16] H. W. Jones and C. A. Weatherford, *Int. J. Quantum Chem. Symp.* **12**, 483 (1978).

[17] H. W. Jones, *International Conference on ETO Multicenter Integrals, Tallahasse, 1981*, In Weatherford and Jones [86], pages 53–59.

[18] H. W. Jones, *Phys. Rev. A* **38**, 1065 (1988).

[19] H. Jones and J. Jain, *Int. J. Quantum Chem. Symp.* **30**, 1257 (1996).

[20] J. D. Talman, *J. Chem. Phys.* **84**, 6879 (1986).

[21] N. Suzuki, *J. Math. Phys.* **25**, 1133 (1984).

[22] N. Suzuki, *J. Math. Phys.* **31**, 2314 (1990).

[23] N. Suzuki, *J. Math. Phys.* **33**, 4288 (1992).

[24] J. F. Rico, R. López, and G. Ramírez, *J. Chem. Phys.* **91**, 4204 (1989).

[25] J. F. Rico, R. López, and G. Ramírez, *J. Chem. Phys.* **91**, 4213 (1989).

[26] A. Bouferguene and D. Rinaldi, *Int. J. Quantum Chem.* **50**, 21 (1994).

[27] A. Bouferguene and M. Fares, *Int. J. Quantum Chem.* **51**, 345 (1994).

[28] H. Shull and P.-O. Löwdin, *J. Chem. Phys.* **23**, 1392 (1955).

[29] P.-O. Löwdin, *Adv. Phys.* **5**, 96 (1956).

[30] E. Filter and E. O. Steinborn, *J. Math. Phys.* **21**, 2725 (1980).

[31] T. Yamaguchi, *Phys. Rev. A* **27**, 646 (1983).

[32] E. J. Weniger and E. O. Steinborn, *Phys. Rev. A* **29**, 2268 (1984).

[33] I. Guseinov, *J. Chem. Phys.* **65**, 4718 (1976).

[34] I. Guseinov, *Phys. Rev. A* **31**, 2851 (1985).

[35] I. Guseinov, *Phys. Rev. A* **37**, 2314 (1988).

[36] E. Hylleraas, *Z. Phys.* **54**, 347 (1929).

[37] E. J. Weniger, *J. Math. Phys.* **26**, 276 (1985).

[38] E. J. Weniger and E. O. Steinborn, *J. Math. Phys.* **30**, 774 (1989).

[39] F. P. Prosser and C. H. Blanchard, *J. Chem. Phys.* **36**, 1112 (1962).

[40] R. A. Bonham, J. L. Peacher, and H. L. Cox, *J. Chem. Phys.* **40**, 3083 (1964).

[41] E. Filter and E. O. Steinborn, *J. Math. Phys.* **19**, 79 (1978).

[42] E. J. Weniger and E. O. Steinborn, *J. Chem. Phys.* **78**, 6121 (1983).

[43] H. P. Trivedi and E. O. Steinborn, *Phys. Rev. A* **27**, 670 (1983).

[44] E. J. Weniger, J. Grotendorst, and E. O. Steinborn, *Phys. Rev. A* **33**, 3688 (1986).

[45] E. J. Weniger and E. O. Steinborn, *Theoret. Chim. Acta* **73**, 323 (1988).

[46] I. Shavitt and M. Karplus, *J. Chem. Phys.* **36**, 550 (1962).

[47] M. Karplus and I. Shavitt, *J. Chem. Phys.* **38**, 1256 (1963).

[48] I. Shavitt, The gaussian function in calculations of statistical mechanics and quantum mechanics, In Alder et al. [85], pages 1–45.

[49] C. Kern and M. Karplus, *J. Chem. Phys.* **43**, 415 (1965).

[50] J. F. Rico, J. J. Fernandez, I. Ema, R. Lopez, and G. Ramirez, *Int. J. Quantum Chem.* **78**, 83 (2000).

[51] J. F. Rico, J. J. Fernandez, R. Lopez, and G. Ramirez, *Int. J. Quantum Chem.* **78**, 137 (2000).

[52] I. Shavitt and M. Karplus, *J. Chem. Phys*. **43**, 398 (1965).

[53] E. U. Condon and G. H. Shortley, *The Theory of Atomic Spectra*, Cambridge University Press, Cambridge, 1970.

[54] H. W. Hobson, *The Theory of Spherical and Ellipsoidal Harmonics*, Cambridge University Press, Cambridge, 1931.

[55] G. Arfken and H. Weber, *Mathematical Methods for Physicists*, Academic Press Inc., Orlando, Florida, fourth edition, 1995.

[56] E. J. Weniger, *Int. J. Quantum Chem.* **76**, 280 (2000).

[57] E. J. Weniger, *Int. J. Quantum Chem.* **90**, 92 (2002).

[58] E. O. Steinborn and K. Ruedenberg, *Adv. Quantum Chem.* **7**, 1 (1973).

[59] E. J. Weniger and E. O. Steinborn, *Comput. Phys. Commun.* **25**, 149 (1982).

[60] B. I. Dunlap, *Phys. Rev. A* **66**, 032502 (2002).

[61] B. I. Dunlap, *J. Chem. Phys.* **118**, 1036 (2003).

[62] B. I. Dunlap, *Comput. Phys. Commun.* **165**, 18 (2005).

[63] H. H. H. Homeier and E. O. Steinborn, *J. Mol. Struct. (THEOCHEM)* **368**, 31 (1996).

[64] H. Mavromatis and R. Alassar, *Appl. Math. Lett.* **12**, 101 (1999).

[65] D. Sébilleau, *J. Phys. A*. **31**, 7157 (1998).

[66] Y. Xu, *Math. Comput.* **65**, 1601 (1996).

[67] Y. Xu, *J. Comput. Phys.* **139**, 137 (1998).

[68] J. C. Slater, *Phys. Rev.* **36**, 57 (1930).

[69] W. Magnus, F. Oberhettinger, and R. P. Soni, *Formulas and Theorems for the Special Functions of Mathematical Physics*, Springer-Verlag, New York, 1966.

[70] G. N. Watson, *A Treatise on the Theory of Bessel Functions*, Cambridge University Press, Cambridge, second edition, 1944.

[71] E. J. Weniger, *Comput. Phys. Rep.* **10**, 189 (1989).

[72] C. Brezinski and M. Redivo Zaglia, *Extrapolation methods*, North Holland, Amsterdam, 1991.

[73] J. Wimp, *Sequence Transformations and their Applications*, Academic Press Inc., New York, 1981.

[74] I. S. Gradshteyn and I. M. Ryzhik, *Table of Integrals, Series and Products*, Academic Press Inc., Orlando, Florida, 1980.

[75] D. Levin, *Int. J. Comput. Math.* **B3**, 371 (1973).

[76] H. H. H. Homeier, *J. Comput. Appl. Math.* **122**, 81 (2000).

[77] J. Čížek, J. Zamastil, and L. Skála, *J. Math. Phys.* **44**, 962 (2003).

[78] E. J. Weniger, *J. Math. Phys.* **45**, 1209 (2004).

[79] P. Wynn, *SIAM J. Numer. Anal.* **3**, 91 (1966).

[80] Numerical Analysis Group, NAG Central Office, Oxford, U.K., *The NAG FORTRAN Library, Mark 14*, 1991.

[81] International Mathematical and Statistical Library Inc., Houston, Texas, *IMSL/MATH FORTRAN Library, Mark 1.1*, 1990.

[82] M. Yoshimine, B. H. Lengsfield, P. S. Bagus, McLean, and B. Liu, *Alchemy II*, International Business Machines Inc., 1990, From MOTECC-90.

[83] E. O. Steinborn and H. H. H. Homeier, *Int. J. Quantum Chem. Symp.* **24**, 349 (1990).

[84] H. H. H. Homeier and E. O. Steinborn, *Comput. Phys. Commun.* **77**, 135 (1993).

[85] B. Alder, S. Fernbach, and M. Rotenberg, editors, volume 2, New York, 1963, Academic Press.

[86] C. A. Weatherford and H. W. Jones, editors, *International Conference on ETO Multicenter Integrals, Tallahasse, 1981*, Dordrecht, Holland, 1982, D. Reidel Publishing Company.

Chapter 17

ON THE ZERO POINT ENERGY DIFFICULTY OF QUASICLASSICAL TRAJECTORY SIMULATIONS

Song Ling and Robert Q. Topper

Department of Chemistry, Medical Technology, and Physics
Monmouth University
Thomas A. Edison Hall of Science
West Long Branch, NJ 07764-1898

Abstract

Following the work of Guo, Thompson, and Sewell (Y.Guo, D.L.Thompson, and T.D. Sewell, J.Chem.Phys. **104**, 576 (1996)) on the zero point energy correction of classical trajectories, we emphasize that the zero-point energy of a molecule is a quantum phenomenon with no classical counterpart, rooted soundly in the position-momentum uncertainty principle. As a consequence certain quantum "ingredients," such as those introduced using Heller's thawed Gaussian wavepacket dynamics (E.J. Heller, J.Chem.Phys. **62**, 1544 (1975)), are probably necessary to avoid the computational difficulties in applying zero-point energy corrections to classical molecular dynamics trajectories which have been described in the literature to date.

1. Introduction

Despite remarkable advances in computing technology and algorithms, the vibrational and rotational motions of medium-sized polyatomic molecules still defy full quantum-mechanical analysis, and so classical trajectory studies are still widely applied [1, 2]. However, in quantum mechanics the slowest possible motion of each rovibrational mode is not literally "standing still", i.e. it is not a fixed point in the classical phase space. This is the so-called zero point motion, and it leads to the zero-point energy (ZPE) for that mode. Since there are many rovibrational modes in a polyatomic molecule, setting the ZPE of one mode to be zero by resetting the energy scale does not reset the ZPE to be zero for all modes; there is thus no loss of generality in speaking of the ZPE (rather than the zero-point motion) problem for classical trajectory studies.

Even though conventionally the study of classical-quantum correspondence happens at high energies or large quantum numbers for polyatomic molecules, [3], the low energy

states of molecules are of great chemical interest as well. For example, if the ZPEs of several modes of a large molecule are "squeezed out" at the same time, the amount of that energy may be sufficient to break a chemical bond. Another example is the umbrella motion of NH_3, which is well-described by a double well potential. At low energies the umbrella motion is classically forbidden and is only achievable by quantum mechanical tunneling with a time scale inversely proportional to the energy splitting of the ground states. If an $-NH_2$ functional group is attached to a large polyatomic molecule which functions like a heat bath, the energies of the modes of the bath can flow into the attached $-NH_2$ group and make the umbrella motion more probable than it would be for the isolated NH_3 molecule.

Guo, Thompson, and Sewell (GTS)[4] pointed out that past efforts[5] to modify classical mechanics, either *passively* by abandoning trajectories with a mode energy lower than the ZPE after the trajectories are integrated or *actively* by modifying the equations of motion during the integration to enforce the ZPE condition lead to unphysical results. GTS emphasized that statistics (or probability) must be utilized in the comparison between classical trajectory and quantum studies. It is not the individual classical trajectory but the ensemble average of a swarm of them that should be compared to the quantities like the mode energy calculated by the propagation of a quantum wavefunction.

We note in the GTS paper, after they compared classical ensemble averages with quantum expectation values they concluded: "The search for practical solutions to the ZPE problem should focus upon ways for accounting for interference effects (i.e., semiclassical theories) and perhaps by improving the quasiclassical procedures, under the guidance of quantum mechanics, so as to obtain a better classical-quantum correspondence."[4]

Using the semiclassical Gaussian wavepackets that Heller[6] proposed for other studies to treat a single "stiff" mode while the "soft" modes were still treated classically, Alimi, Garcia-Vela, and Gerber[7] described the melting of some inert gas clusters. However, in their paper the cases studied for the "stiff" mode were one-dimensional. The ZPE issue troubles chemists the most in multi-mode systems, and in such systems there is likely more than one "stiff" mode.

Heller[6] proposed a multi-dimensional semiclassical scheme to integrate the time dependent Schrödinger equation, different from the conventional approach of letting a dimensionless parameter with $\hbar$ in the numerator go to zero. In this paper, Heller used a quadratic Taylor expansion of the potential function about the moving "center" of a Gaussian wavefunction. The resulting wavefunction remains Gaussian with determining parameters governed by a set of equations of motion, i.e., ordinary differential equations (ODE) in time. Interestingly, the time-dependent position and momentum expectation values fall out to follow exactly the classical equations of motion, while the other complex parameters account for interference effects (since the wavepacket corresponds to a swarm of classical trajectories moving in phase space), with a phase factor containing the classical action integral.

Computationally, this becomes an initial value problem of ODE integrations. In addition to integrating the classical equations of motion, the (complex) quantum parameters are also integrated along the way. We present a multi-dimensional Gaussian derivation in Section 2 and study the choice of both classical and quantum initial conditions in Section 3. Also in Section 3 we show that the thawed Gaussian helps avoid the ZPE difficulty by calculating the mode energy quantum mechanically as an expectation value of the propagating wavepacket, and the result contains the classical mode energy in the $\hbar -> 0$ limit.

2.   The Gaussian Wavefunction

We present a derivation for arbitrary dimensional systems of the Gaussian wavepacket in Cartesian coordinates, and then we derive the expression for the mode energy.

Follow Heller[6], we write the wavefunction as:

$$\psi(x_1, ..., x_n, t) = \exp\{\frac{i}{\hbar} \sum_{k=1}^{n} \sum_{j=1}^{n} \alpha_{jk}(t)(x_j - x_j(t))(x_k - x_k(t)) + \frac{i}{\hbar} \sum_{j=1}^{n} p_j(t)(x_j - x_j(t)) + \frac{i}{\hbar} \gamma(t)\}$$

(1)

where it is straightforward to show that $x_j(t)$ and $p_j(t)$ are the expectation values of $\hat{x}_j$ and $\hat{p}_j$, i.e., the jth position operator and momentum operator, respectively.

The Hamiltonian operator in a general time-independent potential is

$$H = -\frac{\hbar^2}{2} \sum_{j=1}^{n} \frac{1}{m_j} \frac{\partial^2}{\partial x_j^2} + V(x_1, ..., x_n)$$

(2)

and the potential function is Taylor-expanded up to quadratic about $(x_1(t), ..., x_n(t))$, i.e., the instantaneous "center" of the coordinate space wavefunction. Thus we obtain:

$$V(x_1, ..., x_n) \approx V(x_1(t), ..., x_n(t)) + \sum_{j=1}^{n} \frac{\partial V}{\partial x_j}|_{x_1(t),...,x_n(t)}(x_j - x_j(t)) +$$

$$+ \frac{1}{2} \sum_{k=1}^{n} \sum_{j=1}^{n} \frac{\partial^2 V}{\partial x_j \partial x_k}|_{x_1(t),...,x_n(t)}(x_j - x_j(t))(x_k - x_k(t))$$

(3)

The above ψ and the Taylor-expanded V are substituted into the time dependent Schrödinger equation:

$$i\hbar \frac{\partial \psi(x_1, ..., x_n, t)}{\partial t} = H\psi(x_1, ..., x_n, t)$$

(4)

Comparing like coefficients of the powers of $(x_j - x_j(t))^r (x_k - x_k(t))^s$, where the sum of r and s are less than or equal to 2, we get (where we apply the dot convention to denote $\frac{d}{dt}$, e.g., $\dot{\alpha} \equiv \frac{d\alpha}{dt}$)

$$\dot{x}_j(t) = \frac{p_j(t)}{m_j}$$

(5)

$$\dot{p}_j(t) = -\frac{\partial V}{\partial x_j}|_{x_1(t),...,x_n(t)}$$

(6)

$$\dot{\alpha}_{jk}(t) = -2 \sum_{l=1}^{n} \frac{\alpha_{jl}(t)\alpha_{kl}(t)}{m_l} - \frac{1}{2} \frac{\partial^2 V}{\partial x_j \partial x_k}|_{x_1(t),...,x_n(t)}$$

(7)

$$\dot{\gamma}(t) = \sum_{l=1}^{n} \frac{p_l^2(t)}{2m_l} - V(x_1(t), ..., x_n(t)) + i\hbar \sum_{l=1}^{n} \frac{\alpha_{ll}(t)}{m_l}$$

(8)

We note that the complex α matrix is symmetric, i.e., $\alpha_{jk}(t) = \alpha_{kj}(t)$ since $(x_j - x_j(t))(x_k - x_k(t)) = (x_k - x_k(t))(x_j - x_j(t))$. As a consequence, the real and imaginary parts of the α matrix form two real symmetric matrices. We count the number of *real* equations of motion for an n-dimensional system as below: n equations for the position expectation values $x_j(t)$, n equations for the momentum expectation values $p_j(t)$, $n(n+1)$ equations for the $\alpha_{jk}(t)$ matrix elements, and 2 equations for $\gamma(t)$. Therefore the total number of real equations of motion is $(n + 1)(n + 2)$ and increases as n^2 (as opposed to classical n-dependence). It must be noted that this behavior may limit the use of the Gaussian wavefunctions in place of classical trajectories for large n systems.

Since the time evolution of the position and momentum expectation values are classical as shown above, the choice of the initial positions and momenta can be done by any conventional method applied in classical trajectory studies[1]. When choosing the other initial conditions, the matrix of the imaginary part of $\alpha_{jk}(0)$ must be positive definite to ensure that the Gaussian wavefunction is square integrable throughout the time evolution. Without losing generality, the real part of the $\alpha_{jk}(0)$ matrix elements, $Re[\alpha_{jk}(0)]$, and the real part of $\gamma(0)$, $Re[\gamma(0)]$, can be chosen to be zero. The imaginary part of the diagonal α matrix elements, $Im[\alpha_{ll}(0)]$, can be chosen to mimic the ground state wavefunction of each mode, i.e.,

$$Im[\alpha_{ll}(0)] = \frac{1}{2}\sqrt{m_l \| \frac{\partial^2 V(x_1,...,x_n)}{\partial x_l^2}|_{x_1(0),...,x_n(0)}\|} \tag{9}$$

After the diagonal matrix elements are chosen, the off-diagonal imaginary α matrix elements can thus be selected to satisfy the matrix positive definite condition, reflecting the physical fact that the coupling between different modes are perturbative to the modes, not overtaking the modes. The imaginary part of $\gamma(0)$, $Im[\gamma(0)]$, can be determined by normalizing the initial Gaussian wavefunction. As a special case, if all of the imaginary parts of the off-diagonal elements of the initial $\alpha_{jk}(0)$ matrix are chosen to be zero, (this amounts to saying that at a moment of the wavepacket evolution there is no coupling between different modes so that *at that moment* the wavefunction is a product of the wavefunctions of each mode), the imaginary part of $\gamma(0)$ is

$$Im[\gamma(0)] = \frac{\hbar}{2}\ln\{(\frac{\pi\hbar}{2})^{\frac{n}{2}}\prod_{l=1}^{n}\frac{1}{Im[\alpha_{ll}(0)]}\} \tag{10}$$

3.   Applications to Generalized 2-Dimensional Systems and the Hénon-Heiles Potential

For purposes of discussion, at this juncture we develop and present the equations of motion for two-dimensional systems, with application to a model system widely known as the Hénon-Heiles potential.[8] The extension of these equations to multidimensional systems is straightforward but less illustrative.

The Gaussian wavefunction for a general 2-dimensional system is written as follows:

$$\psi(x,y,t) = \exp\{\frac{i}{\hbar}[\alpha_{xx}(t)(x - x(t))^2 + 2\alpha_{xy}(t)(x - x(t))(y - y(t)) + \alpha_{yy}(t)(y - y(t))^2 +$$
$$+ \ p_x(t)(x - x(t)) + p_y(t)(y - y(t)) + \gamma(t)]\} \tag{11}$$

Assuming the mass factor is scaled so that $m_x = m_y$, the $(n+1)(n+2) = 12$ real equations of motion read:

$$\dot{x}(t) = \frac{p_x(t)}{m} \tag{12}$$

$$\dot{y}(t) = \frac{p_y(t)}{m} \tag{13}$$

$$\dot{p}_x(t) = -\frac{\partial V}{\partial x}\Big|_{x(t),y(t)} \tag{14}$$

$$\dot{p}_y(t) = -\frac{\partial V}{\partial y}\Big|_{x(t),y(t)} \tag{15}$$

$$\dot{Re}[\alpha_{xx}(t)] = -\frac{2}{m}\{Re^2[\alpha_{xx}(t)] - Im^2[\alpha_{xx}(t)] + Re^2[\alpha_{xy}(t)] - Im^2[\alpha_{xy}(t)]\} - \frac{1}{2}\frac{\partial^2 V}{\partial x^2}\Big|_{x(t),y(t)} \tag{16}$$

$$\dot{Im}[\alpha_{xx}(t)] = -\frac{4}{m}\{Re[\alpha_{xx}(t)]Im[\alpha_{xx}(t)] + Re[\alpha_{xy}(t)]Im[\alpha_{xy}(t)]\} \tag{17}$$

$$\begin{aligned} \dot{Re}[\alpha_{xy}(t)] = & -\frac{2}{m}\{Re[\alpha_{xx}(t)]Re[\alpha_{xy}(t)] - Im[\alpha_{xx}(t)]Im[\alpha_{xy}(t)] \\ & + Re[\alpha_{xy}(t)]Re[\alpha_{yy}(t)] - Im[\alpha_{xy}(t)]Im[\alpha_{yy}(t)]\} - \frac{1}{2}\frac{\partial^2 V}{\partial x \partial y}\Big|_{x(t),y(t)} \end{aligned} \tag{18}$$

$$\begin{aligned} \dot{Im}[\alpha_{xy}(t)] = & -\frac{2}{m}\{Re[\alpha_{xx}(t)]Im[\alpha_{xy}(t)] + Im[\alpha_{xx}(t)]Re[\alpha_{xy}(t)] \\ & + Re[\alpha_{xy}(t)]Im[\alpha_{yy}(t)] + Im[\alpha_{xy}(t)]Re[\alpha_{yy}(t)]\} \end{aligned} \tag{19}$$

$$\dot{Re}[\alpha_{yy}(t)] = -\frac{2}{m}\{Re^2[\alpha_{yy}(t)] - Im^2[\alpha_{yy}(t)] + Re^2[\alpha_{xy}(t)] - Im^2[\alpha_{xy}(t)]\} - \frac{1}{2}\frac{\partial^2 V}{\partial y^2}\Big|_{x(t),y(t)} \tag{20}$$

$$\dot{Im}[\alpha_{yy}(t)] = -\frac{4}{m}\{Re[\alpha_{xy}(t)]Im[\alpha_{xy}(t)] + Re[\alpha_{yy}(t)]Im[\alpha_{yy}(t)]\} \tag{21}$$

$$\dot{Re}[\gamma(t)] = \frac{p_x^2(t) + p_y^2(t)}{2m} - V(x_1(t),...,x_n(t)) - \frac{\hbar}{m}\{Im[\alpha_{xx}(t)] + Im[\alpha_{yy}(t)]\} \tag{22}$$

$$\dot{Im}[\gamma(t)] = \frac{\hbar}{m}\{Re[\alpha_{xx}(t)] + Re[\alpha_{yy}(t)]\} \tag{23}$$

The choice of the initial conditions of $x(0)$, $y(0)$, $p_x(0)$, and $p_y(0)$ can be made based on established methods for choosing initial conditions for classical trajectory studies depending on the system of interest [1]. The choice of the initial α's and γ is as follows: $Re[\alpha_{xx}(0)] = Re[\alpha_{xy}(0)] = Re[\alpha_{yy}(0)] = Re[\gamma(0)] = 0$, and $Im[\alpha_{xx}(0)] = \frac{1}{2}\sqrt{m\|\frac{\partial^2 V}{\partial x^2}|_{x(0),y(0)}\|}$, $Im[\alpha_{yy}(0)] = \frac{1}{2}\sqrt{m\|\frac{\partial^2 V}{\partial y^2}|_{x(0),y(0)}\|}$, and $Im[\alpha_{xy}(0)] = 0.1\sqrt{Im[\alpha_{xx}(0)]Im[\alpha_{yy}(0)]}$ (to choose the coupling strength to be 10% of the average mode strength). The normalization of the initial wavefunction gives $Im[\gamma(0)] = \frac{\hbar}{2}\ln\frac{\pi\hbar}{2\sqrt{Im[\alpha_{xx}(0)]Im[\alpha_{yy}(0)]-Im^2[\alpha_{xy}(0)]}}$, where we notice the determinant of the imaginary part α matrix is under the square root and must be positive as mentioned previously.

Following GTS, the Hamiltonian (symbolically for both classical and quantum operators) of the Hénon-Heiles system [8] is written as:

$$H = \frac{p_x^2}{2} + \frac{p_y^2}{2} + \frac{1}{2}\omega_x^2 x^2 + \frac{1}{2}\omega_y^2 y^2 + x^2 y - \frac{1}{3}y^3 \tag{24}$$

Also following the GTS paper, the classical initial conditions are selected by the random phase method for the uncoupled 2-dimensional harmonic oscillator:

$$q_i(0) = \sqrt{\frac{(2n_i + 1)\hbar}{\omega_i}}\sin\phi_i \tag{25}$$

$$p_i(0) = \sqrt{(2n_i + 1)\hbar\omega_i}\cos\phi_i \tag{26}$$

where $i = x$ and y, ϕ_x and ϕ_y are each chosen randomly between 0 and 2π and the size of $\hbar$ is chosen as an adjustable parameter indicating the deviation from the classical regime. We note that these initial conditions do not correspond to picking up points from the constant energy shell, or the microcanonical ensemble, due to the anharmonic coupling terms. Therefore, generally speaking each classical trajectory has a different total energy to start with (but each energy stays constant over the propagation time).

The classical mode energy is

$$E_i^{cl}(t) = \frac{1}{2}p_i^2(t) + \frac{1}{2}\omega_i^2 q_i^2(t) \tag{27}$$

where $q_i(t)$ and $p_i(t)$ are the position-momentum expectation values of the Gaussian wavefunction at time t.

The quantum mode energy with the Gaussian wavefunction approximation can be calculated analytically, where we let the state vector propagate in time (this is a general formula, not specific to the Hénon-Heiles system):

$$E_i^{qu}(t) = \frac{1}{2} < \psi(t)|\hat{p_i^2} + \omega_i^2\hat{q_i^2}|\psi(t) > \tag{28}$$

Integrating over the coordinate space Gaussian wavefunction, we obtain for the x mode (replacing x by y will give the y-mode formula):

$$E_x^{qu}(t) = E_x^{cl}(t) \tag{29}$$
$$+ \frac{\hbar}{D_1(t)}\{\frac{1}{2}|\alpha_{xx}(t)|^2 Im[\alpha_{yy}(t)] + \frac{1}{2}|\alpha_{xy}(t)|^2 Im[\alpha_{xx}(t)] - Im[\alpha_{xy}(t)]D_2(t) + \frac{\omega_x^2}{8}Im[\alpha_{yy}(t)]\}$$

where $E_x^{cl}(t) = \frac{1}{2}p_x^2(t) + \frac{1}{2}\omega_x^2 x^2(t)$ is the classical x-mode energy as in eq. 27, $D_1(t) = Im[\alpha_{xx}(t)]Im[\alpha_{yy}(t)] - Im^2[\alpha_{xy}(t)]$ is the determinant of the imaginary part α matrix, and $D_2(t) = Re[\alpha_{xx}(t)]Re[\alpha_{xy}(t)] + Im[\alpha_{xx}(t)]Im[\alpha_{xy}(t)]$.

Even if the expectation values $x(t)$ and $p(t)$ happen to both be equal to zero at some time t (which results in zero classical mode energy), the quantum mode energy $E_x^{qu}(t)$ is still non-zero. Moreover, the comparison between the Gaussian wavefunction and the classical trajectory with the same initial position-momentum conditions is closer than comparing the time propagation of an unperturbed harmonic oscillator eigenfunction and a swarm of classical trajectories. First of all, the initial Gaussian already has its position and momentum expectation values chosen classically and these expectation values are integrated by classical equations of motion, i.e., their evolution is identical to that of classical trajectories. In stark contrast, the unperturbed quantum eigenfunctions tend to have a parity (either even or odd) and therefore have zero position and momentum expectation values. Secondly, the Gaussian wavefunction contains the classical trajectory as a special case, and when the size of the Gaussian shrinks to a point the position-momentum expectation values will trace out a classical phase space trajectory.

Similarly, the classical coordinate autocorrelation function is defined as

$$C_i^{cl}(t) = \lim_{T\to\infty} \frac{1}{T}\int_0^T dt' q_i(t')q_i(t'+t) \tag{30}$$

and its Fourier transform gives the power spectrum.

The quantum counterpart is defined as

$$
\begin{aligned}
C_i^{qu}(t) &= \lim_{T\to\infty} \frac{1}{T}\int_0^T dt' <\psi(0)|\hat{q}_i^\dagger(t')\hat{q}_i(t'+t)|\psi(0)> \\
&= \lim_{T\to\infty} \frac{1}{T}\int_0^T dt' <\psi(0)|\exp(\frac{i}{\hbar}\hat{H}t')\hat{q}_i\exp(\frac{i}{\hbar}\hat{H}t)\hat{q}_i\exp(-\frac{i}{\hbar}\hat{H}(t+t'))|\psi(0)> \\
&= \lim_{T\to\infty} \frac{1}{T}\int_0^T dt' <\psi(t')|\hat{q}_i\exp(\frac{i}{\hbar}\hat{H}t)\hat{q}_i|\psi(t+t')> \\
&= \lim_{T\to\infty} \frac{1}{T}\int_0^T dt' <\psi(t')|(\hat{q}_i - q_i(t') + q_i(t')) \\
&\qquad \exp(\frac{i}{\hbar}\hat{H}t)(\hat{q}_i - q_i(t+t') + q_i(t+t'))\psi(t+t')> \\
&= \lim_{T\to\infty} \frac{1}{T}\int_0^T dt' q_i(t')q_i(t+t') \\
&\quad + \lim_{T\to\infty} \frac{1}{T}\int_0^T dt' <\psi(t')|(\hat{q}_i - q_i(t')\exp(\frac{i}{\hbar}\hat{H}t)(\hat{q}_i - q_i(t+t'))|\psi(t+t')> \\
&= C_i^{cl}(t) + \lim_{T\to\infty} \frac{1}{T}\int_0^T dt' <\psi(t')|(\hat{q}_i - q_i(t') \\
&\qquad \exp(\frac{i}{\hbar}\hat{H}t)(\hat{q}_i - q_i(t+t'))|\psi(t+t')> \tag{31}
\end{aligned}
$$

We see that the quantum autocorrelation function is a sum of the classical autocorrelation function and a correction term which accounts for quantum interference effects (such as those which give rise to the zero-point energy). Unfortunately, since the time propagator operates on the linear term of the coordinate times the wavefunction, the resolution of the correction term is even beyond Gaussian wavefunction dynamics, and either Hamiltonian matrix diagonalization, Feynman path integration, or the numerical integration of the time dependent Schrödinger equation must be resorted to.

4. Conclusion

Heller's thawed Gaussian wavefunction seems to be able to help avoid the mode ZPE for classical trajectories. Its mode energy can be calculated analytically, as shown in Section 3, and is shown to be a sum of the classical mode energy plus a quantum correction term. Even though the classical mode energy often goes below the mode ZPE, the quantum correction term helps maintain the mode energy to be above the mode ZPE throughout the integration of the wavefunction.

Computationally, the Gaussian wavefunction provides a straightforward extension of integrating the classical equations of motion, i.e., all that is involved in principle is the solution of additional equations of motion to the classical ones. Since the method is based on integrating ordinary differential equations, upon which classical simulations are based, the computational effort of the Gaussian wavepacket need not necessarily be taxing if appropriate algorithms are used. The method formally scales as n^2, which may prevent its use for very large systems; however, simulations of intermediate-sized systems should be attainable.

Our understanding of the GTS paper is that it is both unnecessary and incorrect to abandon or modify individual trajectories, since the ZPE-violating trajectories are part of the statistics, without which the statistics would be skewed, biased, and untrue. In the results shown in the GTS paper, the unrestricted classical ensemble calculations match the quantum results far better than the other techniques that attempted to correct the ZPE by removing ZPE-violating trajectories (see Fig. 2 and Fig.5 of Ref. 1). The very presence of the ZPE violating trajectories is ostensibly responsible for this behavior. Generally speaking, a swarm of classical trajectories behaves differently from individual ones. In this regard it would seem that quasiclassical trajectory studies of reaction dynamics ought to be based on the statistical properties of a swarm of trajectories, and not solely the individual dissociating or isomerizing trajectories which are part of the statistics contributing to the overall probability distribution. Dissociating or isomerizing trajectories may correspond to a small probability amplitude of the quantum wavefunction in the relevant coordinate (or momentum) space regions. For classical trajectory studies such trajectories should not be abandoned or modified.

The fundamental cause of the classical ZPE difficulty is that the ZPE is a quantum concept with no classical counterpart. It is a consequence of our inability to simultaneously determine the position and momentum of a particle to an arbitrary precision as we may do in classical mechanics (at least in principle). Rather than a fixed point in phase space, when we try to minimize both the position and momentum at the same time, the closest we can get

is a ground state wavefunction with a finite position or momentum probability amplitude. There is a finite uncertainty in both the position and momentum, as if the motion, however low from the classical point of view, persists; thus, we have the so-called zero point motion and energy. To help "fix" such an issue from within the classical realm in a consistent way is unlikely. We believe that some quantum ingredients are needed to address the classical ZPE difficulty.

There are three final points worth emphasizing. One is that thawed Gaussian wavepackets extend to multiple dimensions in a straightforward way, as shown in section 2 (in coordinate space, they are simply multi-coordinate wavefunctions), and the computational effort scales rather modestly with the size of the system. There appears to be no fundamental reasons why they cannot be computationally applied to polyatomic molecules where ZPE effects are important. The second point is that a single time-evolving Gaussian wavepacket does not correspond to a single classical trajectory, even though its position-momenta expectation values trace out that trajectory. Rather, it corresponds to a swarm of trajectories which intefere with one another in the Feynman path-integral sense. The wavepacket itself is of quantum-mechanical nature, as it is an approximate solution to the time dependent Schrödinger equation. The wavefunction is much richer in information content than any single trajectory, requiring more than the position-momentum expectation values to describe the entire statistics. For example, other expectation values, like $< p^2 >$ and $< x^2 >$ (and higher order "moments") cannot be generated by the single trajectory that carries the position-momentum expectation values; as we saw in Section 3, it is the $< p^2 >$ vs. $< p >^2$ and $< x^2 >$ vs. $< x >^2$ difference that helps maintain the mode energy of which ZPE is a part. This helps bring out the last point we want to emphasize: a single thawed Gaussian already contains interference effects by its wave nature (as an approximate solution to the time dependent Schrödinger equation). More explicitly, a Gaussian can be expressed as a superposition of other waves. A well-known example is to express the coordinate space Gaussian as a weighted sum of plane waves, where the "weight" is the momentum space wavefunction. In the present context, a single Gaussian itself can be approximated by a weighted sum of other Gaussians. This illustrates that the interference effects necessary to consistently describe the pheonomenon of zero-point energy avoidance are indeed contained in a single, time-evolving Gaussian wavefunction.

Acknowledgments

References

[1] J. S. Hutchinson, in *Dynamics of Molecules and Chemical Reactions*, edited by R. E. Wyatt and J. Z. H. Zhang (Marcel Dekker, New York, 1996); H. R. Mayne, *ibid*.

[2] G. H. Peslherbe and W. L. Hase, *J. Chem. Phys.* **104**, 9445 (1996); ibid., **105**, 7432 (1996); D. A. McCormack and K. F. Lim, *J. Chem. Phys.* **106**, 572 (1997); A.J. Marks,

J. Chem. Phys. **108**, 1438 (1998); U. Mller and G. Stock, *J. Chem. Phys.* **111**, 77 (1999); E. Martinez-Núñez, A. Pea-Gallego, and S. A. Vázquez, *J. Chem. Phys.* **114**, 3546 (2001); E. Martinez-Núñez, J. M. C. Marques, and S. A. Vázquez, *J. Chem. Phys.* **115**, 7872 (2001); H. F. Busnengo, C. Crespos, W. Dong, J. C. Rayez, and A. Salin, *J. Chem. Phys.* **116**, 9005 (2002); P. Fleurat-Lessard, S. Y. Grebenshchikov, R. Schinke, C. Janssen, and D. Krankowsky, *J. Chem. Phys.* **119**, 4700 (2003); R. Schinke and P. Fleurat-Lessard, *J. Chem. Phys.* **122**, 94317 (2005); M. V. Ivanov, H. Zhu, and R. Schinke, *J. Chem. Phys.* **126**, 54304 (2007); J.Espinosa-Garcia, *J. Phys. Chem. A* **111**, 9654 (2007).

[3] R. L. Liboff, *Phys. Today,* **37**, 26 (1984).

[4] Y. Guo, D. L. Thompson, and T. D. Sewell, *J. Chem. Phys.* **104**, 576 (1996).

[5] G. Nyman and J. Davidsson, *J. Chem. Phys.* **92**, 2415 (1990); A. J. C. Varandas and J. M. C. Marques, *J. Chem. Phys.* **97**, 4050 (1992); A. J. C. Varandas, *J. Chem. Phys.* **99**, 1076 (1993); J. M. C. Marques, W. Wang, and A. J. C. Varandas, *J. Chem. Soc. Faraday Trans.* **90**, 2189 (1994); A. J. C. Varandas, *Chem. Phys. Lett.* **225**, 18 (1994); J. M. Bowman, B. Gazdy, and Q. Sun, *J. Chem. Phys.* **91**, 2859 (1989); W. H. Miller, W. L. Hase, and C. L. Darling, *J. Chem. Phys.* **91**, 2863 (1989); G. H. Peslherbe and W. L. Hase, *J. Chem. Phys.* **100**, 1179 (1994); F. E. Budenholzer, M. Y. Chang, and K. C. Huang, *J. Phys. Chem.* **98**, 12501 (1994); A. J. C. Varandas and J. M. C. Marques, *J. Chem. Phys.* **100**, 1908 (1994); M. Ben-Nun and R. D. Levine, *J. Chem. Phys* **101**, 8768 (1994); K. F. Lim and D. A. McCormack, *J. Chem. Phys.* **102**, 1705 (1995); T. D. Sewell and D. L. Thompson, J. D. Gezelter, and W. H. Miller, *Chem. Phys. Lett.* **193**, 512 (1992).

[6] E. J. Heller, *J. Chem. Phys.* **62**, 1544 (1975).

[7] R. Alimi, A. Garcia-Vela, and R. B. Gerber, *J. Chem. Phys.* **96**, 2034 (1992).

[8] M. Hénon and C. Heiles, *Astron. J.* **69**, 73 (1964).

Chapter 18

DYNAMICAL SYSTEMS APPROACH FOR THE CHAPMAN-CRUTZEN MECHANISM

F.J. Uribe and R.M. Velasco
Department of Physics
Universidad Autónoma Metropotitana
Iztapalapa, 09340, México.

Abstract

The dynamics of stratospheric ozone is studied using the ideas introduced by Chapman including the role of nitrogen oxides as proposed by Crutzen. We refer to these ideas as the Chapman–Crutzen mechanism that gives a system of five ordinary differential equations. This set of differential equations is studied using the ideas of the theory of dynamical systems. In particular, mass conservation is used to reduce the set to three differential equations by using certain constants of motion, we obtain the critical points of this reduced set of equations, analyze the eigenvalues of the Jacobian matrix evaluated at the critical points in order to determine whether or not they are hyperbolic, and compare them with the corresponding critical points of the Chapman mechanism. Several numerical methods, like Adams' method and the backward differentiation formula, are used to solve the initial value problem for the reduced set of ordinary differential equations seeking to obtain a more global picture of the orbits than that provided by the local analysis consisting in analyzing the nature of the critical points.

1. Introduction

The study of photochemical mechanisms to understand the formation and destruction of stratospheric ozone has received attention of many researches because of the relevance of this problem. It is well known that the planet atmosphere constitutes a very complex system, where a lot of phenomena take place and affect life in the planet surface. Nowadays, it is clear that the anthropogenic activities play a role in the atmosphere's natural evolution and this fact drives the researchers interest to this subject. Thought there are a huge quantity of works in the subject, the mathematical properties of mechanisms are not fully explored. It is our aim in this work, the application of some mathematical techniques in simple photochemical mechanisms in order to go deeper in their structure.

In 1930 Chapman [1] proposed the simplest mechanism to begin the study of ozone formation. In fact, the mechanism considered three species: atomic oxygen $[O]$, molecular oxygen $[O_2]$ and ozone $[O_3]$. There are two photolytic reactions which occur through the solar radiation and, consequently the corresponding rates depend on the solar spectrum, the geographical position and the time. Also, there are two thermochemical reactions depending on the temperature and pressure. This mechanism was successful in the qualitative understanding of the ozone concentration, however the numerical values predicted are not in agreement with the experimental observations. As an immediate result, it was clear that the Chapman mechanism did not take into account a lot of important reactions affecting the ozone concentration. There are several species participating in catalytic cycles which involve the ozone molecule as an ingredient in the mechanisms [2, 3], making the ozone concentration to vary according to a more complex kinetics than the one represented by Chapman. The main characteristic of catalytic cycles is that they drive to a reduction in the concentration of odd oxygens ($[O]$, $[O_3]$), and the reproduction of the original molecule producing the cycle. As examples of such effects we have the $[HO_x]$, the $[NO_x]$, the $CFC's$ cycles etc. In 1970, Crutzen [4] considered the influence of nitrogen oxides in the kinetics of stratospheric ozone and proposed a combined mechanism to take into account these species in the ozone formation. Though Crutzen considered several reactions we will consider the catalytic cycle which couples the Chapman mechanism with the nitrogen oxides $[NO, NO_2]$ and call the scheme as the "Chapman-Crutzen mechanism" (CCM). In this work we will concentrate our attention to the mathematical properties, instead of the practical consequences, since they have been extensively studied in the literature [2, 3, 5, 6, 7]. On the other hand, the mechanism equations can be studied with the tools provided by their approach as a dynamical system. This means that the set of equations constructed according to chemical kinetics is seen as a dynamical system, in which we can calculate the stationary points. Also, the stability characteristics of the linearized system are obtained [8], [9]. It is interesting to notice that this treatment can be done for several catalytic cycles in an unified scheme though the specific values are particular for each cycle. The numerical methods to solve differential equations give a picture of the time evolution of the concentrations and a global picture of the flow represented by the dynamical system. In section 2 we present the kinetic equations to be considered, section 3 will be devoted to the calculation of critical points and their stability. Section 4 gives the numerical results concerning the time evolution of ozone concentration and in section 5 we summarize the results obtained in this work.

2.   The General Scheme

The production and destruction of stratospheric ozone is dominated mainly by the presence of solar radiation, in such a way that for each geographical region in the planet, we have a set of chemical reactions occurring in daytime coupled with a nocturnal kinetics. This means that we will have a daily oscillation in the ozone concentration. The Chapman, the Chapman-Crutzen as well as some others mechanisms describe the behavior of ozone concentration for daytime conditions, then the calculations we will show in this work do not include the daily oscillations. Instead, we will consider the concentrations' time evolution with permanent solar radiation as it would happen in a laboratory setup. The tempera-

ture, pressure, species concentration and radiation with values according to stratospheric conditions. Also, we do not take into account transport phenomena, so we will work in a photochemical box model. The chemical species to be considered are the same as in the Chapman mechanism, $[O]$, $[O_2]$ $[O_3]$ and in this section we will consider a general scheme where the species participating in the catalytic cycle are added and can be interchanged. In this case the set of reactions in the mechanism can be written as follows,

$$
\begin{aligned}
(j_1) \quad & O_2 + h\nu \longrightarrow O + O, \\
(k_1) \quad & O + O_2 + M \longrightarrow O_3 + M, \\
(j_2) \quad & O_3 + h\nu \longrightarrow O_2 + O, \\
(k_2) \quad & O_3 + O \longrightarrow 2O_2, \\
(k_3) \quad & X + O_3 \longrightarrow XO + O_2, \\
(k_4) \quad & XO + O \longrightarrow X + O_2.
\end{aligned}
\tag{1}
$$
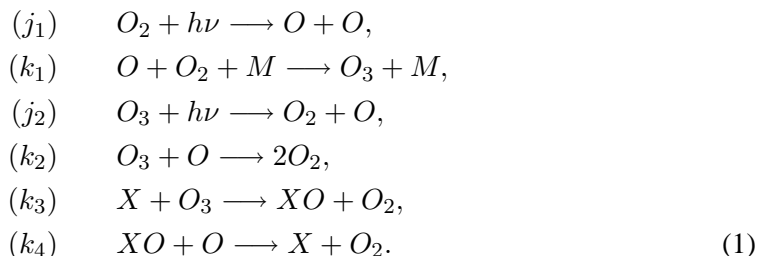
The quantity $[X]$ represents any radical in the stratosphere which participates in the catalytic cycle described by the last two reactions in the set (1), the possible species acting in the catalytic cycle are: $[H], [OH], [NO], [Cl], [Br]$. The photolytic as well as the rate constants corresponding to each reaction are specified in the set of Eqs. (1), j_1, j_2 are photolytic rates and $k_1, ..., k_4$ correspond to thermochemical reactions, all these quantities are considered as constants. The quantity $[M]$ indicates any molecule in air and this dependence means that the pressure plays a role in the calculation. In order to simplify the notation we will name the concentration of species as follows

$$
[O] = x, \quad [O_2] = y, \quad [O_3] = z, \quad [XO] = u, \quad [XO_2] = v,
\tag{2}
$$

also $K = k_1[M]$. Now the kinetics of the set is given by

$$
\begin{aligned}
\frac{dx}{dt} &= 2j_1 y + j_2 z - Kxy - k_2 xz - k_4 xv, \\
\frac{dy}{dt} &= -j_1 y - Kxy + j_2 z + 2k_2 xz + k_3 zu + k_4 xv, \\
\frac{dz}{dt} &= Kxy - j_2 z - k_2 xz - k_3 zu, \\
\frac{du}{dt} &= -k_3 zu + k_4 xv, \\
\frac{dv}{dt} &= k_3 zu - k_4 xv.
\end{aligned}
\tag{3}
$$

The set of kinetic equations (3) has two constants of motion which are a consequence of the balance in the reactions (1). In fact, those constants of motion represent the atoms conservation, as it should be, and can be written as

$$
\begin{aligned}
f_1 &= x(t) + 2y(t) + 3z(t) + v(t), \\
f_2 &= v(t) + u(t),
\end{aligned}
\tag{4}
$$

where f_1, f_2 are positive constants, whereas all concentrations depend explicitly on time. The presence of the constants of motion (4) allows us to reduce the independent variables, instead of five we will have three free concentrations to satisfy the kinetics. In order to compare the results of this mechanism with the results coming from the Chapman mechanism we will use the representation in which the concentration of atomic oxygen, molecular oxygen and ozone are independent. This means that we are going to eliminate the concentrations of $[X]$ and $[XO]$ by means of the conservation equations. In this case the set of equations to be solved are the following

$$\frac{dx}{dt} = 2j_1 y + j_2 z - Kxy - k_2 xz - k_4(f_1 - x - 2y - 3z)x,$$

$$\frac{dy}{dt} = j_2 z + 2k_2 xz - j_1 y - Kxy - k_3(f_2 - f_1 + x + 2y + 3z)z+$$
$$+ k_4 x(f_1 - x - 2y - 3z),$$

$$\frac{dz}{dt} = Kxy - j_2 z - k_2 xz - k_3 z(f_2 - f_1 + x + 2y + 3z). \tag{5}$$

This new set of equations does not contain explicitly the concentration of the species in the catalytic cycle, however their effect remains through the value of the constants f_1, f_2 and the rate constants k_3, k_4.

Now we will take advantage of the tools provided by the theory of dynamical systems, in the sense that the set of reduced equations (5) defines a dynamical system in a three dimensional phase space (x, y, z). The dynamics in phase space is determined by the solution of the set (5) given the initial conditions for the concentrations. As a first step in this direction we will find the coordinates of the stationary points, which will give us the steady states described by the mechanism. The conditions to find such coordinates are given by $\frac{dx}{dt} = 0$, $\frac{dy}{dt} = 0$ and $\frac{dz}{dt} = 0$. In this case there are six solutions for the critical points. It is a matter of algebraic manipulations to show that the coordinates (x_c, y_c, z_c) of the stationary points are given by

$$P = (f_1, 0, 0), \quad R = (0, 0, 0), \qquad Q_i = (x_c, y_c, z_c), \quad i = 1, 2, ..., 4 \tag{6}$$

where the coordinates of points Q_i satisfy the following set of equations,

$$y_c = \frac{j_2 k_4 x_c (f_1 - x_c)}{q(x_c)},$$

$$z_c = \frac{k_4 x_c (f_1 - x_c)(Kx_c - j_1)}{q(x_c)},$$

$$q(x_c) = Kx_c^2(3k_4 - k_2) + x_c[k_2 j_1 + k_4(2j_2 - 3j_1)] + j_1 j_2, \tag{7}$$

and x_c satisfies a fourth order polynomial which is obtained from Eq. (21) in the appendix by means of taking $j_3 = 0$. The specific values of coordinates for the critical points depend on the values for the rates constants, the photolytic rates and the constants of motion represented by f_1, f_2. The stability of critical points are determined by the linearized dynamical system around each critical point. The first step in this calculation corresponds to the determination of the eigenvalues, if the real part of these eigenvalues do not vanish the points are called hyperbolic. Then, the second step consists in the observation of the real part in

the eigenvalues, when the real part is negative we have a stable point and if it is positive the point is named as unstable. On the other hand, when the eigenvalues are complex we have a spiral behavior of trajectories near the critical point. Those spirals are stable or unstable according to the sign of the real part.

3.   The Chapman-Crutzen Mechanism

The general development done in the last section is now applied to the mechanism in which the nitrogen oxides play a role in the kinetics, as we said in the introduction. Besides, in the case of nitrogen oxides there exists the photolytic decomposition occurring in the stratosphere. It must be noted that the photolysis of of $[NO_2]$ was also considered by Crutzen [4], the reaction to be considered reads as follows

$$(j_3) \qquad NO_2 + h\nu \longrightarrow NO + O \tag{8}$$
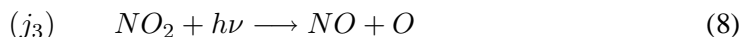
In this case the constants $f_1, \ f_2$ are the same as in Eq. (4), however the reduced kinetics is now given as follows

$$\frac{dx}{dt} = 2j_1 y + j_2 z + -Kxy - k_2 xz - (k_4 x - j_3)(f_1 - x - 2y - 3z),$$

$$\frac{dy}{dt} = j_2 z + 2k_2 xz - j_1 y - Kxy + k_3(f_2 - f_1 + x + 2y + 3z)z$$

$$+ k_4 x(f_1 - x - 2y - 3z),$$

$$\frac{dz}{dt} = Kxy - j_2 z - k_2 xz - k_3 z(f_2 - f_1 + x + 2y + 3z). \tag{9}$$

This dynamical system has six critical points with coordinates given by

$$P = (f_1, 0, 0), \qquad Q_i = (x_c, y_c, z_c), \qquad i = 1, 2, ..., 5 \tag{10}$$

where $y_c, \ z_c$ can be written as

$$y_c = \frac{x_c(f_1 - x_c)(j_2 k_4 - j_3 k_2)}{q(x_c)}, \quad z_c = \frac{(f_1 - x_c)(K k_4 x_c^2 - j_1 k_4 x_c - j_1 j_3)}{q(x_c)}, \tag{11}$$

$$q(x_c) = K x_c^2(3k_4 - k_2) + x_c[k_2(j_1 - 2j_3) + k_4(2j_2 - 3j_1)] + j_1(j_2 - 3j_3) \tag{12}$$

and x_c satisfies the polynomial given in the appendix. As an example of this kind of calculations we will take the specific values for the CCM in equinox conditions at noon and a height of about $25 \ km$ above the surface. The temperature dependence of rate constants are taken according to Arrhenius formula and all values refer to the standard atmosphere according to Seinfeld and Pandis [2]. The specific values used in this work are given in table 1, but the reader is warned that we have rounded off some of the values since our main objective are the qualitative features.

With these values for the constants, we can calculate the coordinates of the critical points taking Eqs. (10), Table 2 gives the corresponding results.

We recall that point $P = (f_1, 0, 0)$ is also a critical point in this dynamical system. From the results in Table 2 we notice that point Q_2 corresponds to positive concentrations,

Table 1. Values of rate constants, photolytic rates and concentrations taken as an example for the case of the CCM.

$k_1 \ cm^6/(molec^2 \times s)$	1.00×10^{-33}
$k_2 \ cm^3/(molec \times s)$	1.00×10^{-15}
$k_3 \ cm^3/(molec \times s)$	4.55×10^{-15}
$k_4 \ cm^3/(molec \times s)$	1.09×10^{-11}
$j_1 \ s^{-1}$	3.00×10^{-12}
$j_2 \ s^{-1}$	5.50×10^{-4}
$j_3 \ s^{-1}$	10^2
$n_M \ molec/cm^3$	5.99×10^{17}
$f_1 \ molec/cm^3$	2.40×10^{17}
$f_2 \ molec/cm^3$	6.00×10^8

Table 2. Coordinates for the five critical points Q_i, all of them are given in $molec/cm^3$.

$Q \ molec/cm^3$	x_c	y_c	z_c
Q_1	2.66×10^5	1.20×10^{17}	-2.20×10^{12}
Q_2	3.80×10^7	1.19×10^{17}	4.96×10^{12}
Q_3	-1.34×10^7	1.20×10^{17}	-1.71×10^{12}
Q_4	-9.04×10^7	1.20×10^{17}	-1.18×10^{13}
Q_5	-3.38×10^{13}	-2.20×10^{15}	8.14×10^{16}

in fact for this mechanism we have only two critical points with this characteristic P and Q_2. All other critical points have at least one negative concentration, those points are not physical. However, from the mathematical point of view they are present in the dynamical system and its behavior has an effect on the the mechanism. To begin with the study of the corresponding dynamics let us first compare these results with the Chapman mechanism. The Chapman mechanism only considers the reactions containing atomic oxygen, molecular oxygen and ozone, in set given by Eqs. (1) without the catalytic cycle. If we take the same rates as in Table 1 in the Chapman mechanism it can be shown that there are three critical points [8] and just one of them can be compared with the experimental measurements in the stratosphere and it is given as

$$P_{crit}(\text{Chapman}) = (5.24 \times 10^7, 1.19 \times 10^{17}, 6.86 \times 10^{12}) \ \frac{molec}{cm^3}. \qquad (13)$$

The ozone concentration given by the third coordinate of $P_{crit}(\text{Chapman})$ is approximately twice the measured concentration in the stratosphere. It means that the Chapman mechanism overestimates the production of ozone. On the other hand, with the Chapman-Crutzen mechanism we can observe that the ozone concentration at the critical point Q_2 has decreased as a consequence of the effect produced by the nitrogen oxides. We also notice that the atomic oxygen concentration has the same effect, it means that the presence of nitrogen

oxides drives to a reduction in the concentration of odd oxygens, as it should be according to the kinetic equations.

It is also interesting to consider the case of the previous section for nitrogen oxides ($j_3 = 0$), the results are given in table 3, In this case we see that the physical point, denoted by Q_2 in tables 2 and 3, has lower concentrations of ozone when compared with the case $j_3 \neq 0$.

Table 3. Coordinates for the four critical points Q_i for the case $j_3 = 0$, all of them are given in $molec/cm^3$. Recall that there are two additional critical points, those given by $(f_1, 0, 0)$ and $(0, 0, 0)$.

$Q\ molec/cm^3$	x_c	y_c	z_c
Q_1	4918.2	1.20×10^{17}	-1.18×10^7
Q_2	3.34×10^7	1.20×10^{17}	4.36×10^{12}
Q_3	-8.25×10^7	1.20×10^{17}	-1.07×10^{12}
Q_4	-3.40×10^{13}	-2.20×10^{15}	8.14×10^{16}

We now return to the mathematical properties of the mechanism, and we will study the stability of the critical points. This property is established once we calculate the eigenvalues of the linearized dynamical system around each critical point. In the Chapman mechanism, the point P_{crit}(Chapman) is a stable node because the three eigenvalues are real and negative. In this case all trajectories near the critical point are attracted to it. In the case of the critical points in the Chapman-Crutzen mechanism, point Q_2 is also a stable node.

4.   Local Analysis

The dynamical system given by Eqs. (9) can written as,

$$\frac{d\mathbf{y}}{dt} = \mathbf{F}(\mathbf{y}(t)), \tag{14}$$

where $\mathbf{F} = (F_1, F_2, F_3)$, $\mathbf{y}(t) \equiv (x(t), y(t), z(t))$ and,

$$
\begin{aligned}
F_1(x, y, z) &= 2j_1 y + j_2 z + -K x y - k_2 x z - (k_4 x - j_3)(f_1 - x - 2y - 3z), \\
F_2(x, y, z) &= j_2 z + 2k_2 xz - j_1 y - K xy + k_3(f_2 - f_1 + x + 2y + 3z)z \\
&+ k_4 x(f_1 - x - 2y - 3z), \\
F_3(x, y, z) &= K xy - j_2 z - k_2 xz - k_3 z(f_2 - f_1 + x + 2y + 3z). \tag{15}
\end{aligned}
$$

In order to have compact notation we will also use the notation $y_1 = x$, $y_2 = y$ and $y_3 = z$, so that $\mathbf{y} = (y_1, y_2, y_3) = (x, y, z)$.

We now consider the linearization of Eq. (14), around a point $\mathbf{y}_0$, by taking $\mathbf{y}(t) \approx \mathbf{y}_0 + \mathbf{u}(t)$, the result is,

$$\frac{d\mathbf{u}(t)}{dt} = \mathbf{F}(\mathbf{y}_0) + (JF(\mathbf{y}_0)\mathbf{u}(t)^T)^T, \tag{16}$$

where $JF(\mathbf{y}_0)$ is the Jacobian matrix of the vector field $\mathbf{F}$ evaluated at $\mathbf{y}_0$, it is defined by

$$JF(\mathbf{y})_{ij} = \frac{\partial F_i}{\partial y_i}(\mathbf{y}),\tag{17}$$

here $JF(\mathbf{y})_{ij}$ denotes the matrix element corresponding to the i row and column j, and the superscript T denotes the transpose. For simplicity we will take out the superscript T denoting the transpose and the meaning of our equations should be clear in the context used. In particular, if $\mathbf{y}_0$ is a critical point of $\mathbf{F}$ ($\mathbf{F}(\mathbf{y}_0) = 0$), we have the simpler problem $\frac{d\,\mathbf{u}(t)}{d\,t} = JF(\mathbf{y}_0)\mathbf{u}(t)$. The natural question is then what is the relation between the exact problem and its linearization. The answer to this question is given by the Hartman–Grobman [10] theorem which states that if the the critical point is hyperbolic, meaning that all the eigenvalues of the Jacobian matrix $JF(\mathbf{y}_0)$ have real parts different from zero, then there exists a neighborhood around $\mathbf{y}_0$ such that the solution curves of the exact problem can be mapped homeomorphically to the orbits of its linearization. In particular, if the critical point is a saddle or a node according to the linearization, then locally the critical point is also a saddle or a node. From the point of view of physics the theorem is of importance, to see this, suppose that the critical point is an unstable node, then it cannot be reached and although it can correspond to the observed values we are certain that the orbits of the chemical reactions will go away from it. Thus, it cannot represent a sound physical description. Such information is rather easy to obtain but apparently has not been studied in the literature.

For the vector field defined by Eqs. (15) we have that the elements of the Jacobian matrix are given by,

$$
\begin{aligned}
JF(x,y,z)_{11} &= -j_3 - K\,y - k_2\,z - k_4\,(f_1 - x - 2\,y - 3\,z) + k_4\,x, \\
JF(x,y,z)_{12} &= 2\,j_1 - 2\,j_3 - x\,K + 2\,k_4\,x, \\
JF(x,y,z)_{13} &= j_2 - 3\,j_3 - k_2\,x + 3\,k_4\,x, \\
JF(x,y,z)_{21} &= -K y + 2\,k_2\,z + k_3\,z + k_4\,(f_1 - x - 2\,y - 3\,z) - k_4\,x, \\
JF(x,y,z)_{22} &= -j_1 - x\,K + 2\,k_3\,z - 2\,k_4\,x, \\
JF(x,y,z)_{23} &= j_2 + 2\,k_2\,x + k_3\,(f_2 - f_1 + x + 2\,y + 3\,z) + 3\,k_3\,z - 3\,k_4\,x, \\
JF(x,y,z)_{31} &= K\,y - k_2\,z - k_3\,z, \\
JF(x,y,z)_{32} &= x\,K - 2\,k_3\,z, \\
JF(x,y,z)_{33} &= -j_2 - k_2\,x - k_3\,(f_2 - f_1 + x + 2\,y + 3\,z) - 3\,k_3\,z. \tag{18}
\end{aligned}
$$

For the physical point Q_2 given in table 2 the explicit form of the Jacobian matrix is,

$$JF(Q_2) = \begin{bmatrix} -71.89\,s^{-1} & -0.019\,s^{-1} & -0.0282\,s^{-1} \\ -71.84\,s^{-1} & +0.044\,s^{-1} & +0.0672\,s^{-1} \\ +71.85\,s^{-1} & -0.045\,s^{-1} & -0.0684\,s^{-1} \end{bmatrix},\tag{19}$$

and the corresponding eigenvalues are $\lambda_1 = -0.709 \times 10^{-3}/s$, $\lambda_2 = -0.295 \times 10^{-3}/s$, and $\lambda_2 = -73.225/s$. Therefore Q_2 is a hyperbolic critical point corresponding to a stable node, so there exists a neighborhood around Q_2, say W_{Q_2}, in which all solutions of the

dynamical system given by Eqs. (14)-(15) tend to Q_2 as $t \to \infty$. Another way to state the previous statement is by saying that the ω-limit set of any point in W_{Q_2} is Q_2. The previous result provides, in our opinion, a sound physical interpretation of the Chapman–Crutzen mechanism since it assures that Q_2 can be observed if the initial conditions are in W_{Q_2}. Unfortunately, the Hartman–Grobman theorem does not provide information about W_{Q_2}.

The same analysis can be done for the other five critical points of the Chapman–Crutzen mechanism and also for the case $j_3 = 0$, although we do not provide explicit forms of the corresponding Jacobian matrices or the explicit values of the eigenvalues. All of the critical points are hyperbolic and the eigenvalues of the corresponding Jacobian matrices are real. In table 4 we provide information about the nature of the critical points, the number of positive eigenvalues (the dimension of the unstable manifold, $\dim(W_{Q_i}^u)$), and the number of negative eigenvalues (the dimension of the stable manifold, $\dim(W_{Q_i}^s)$). Those readers interested in the stable manifold theorem may take a look at references [10, 11].

Table 4. Nature of the critical points of the the Chapman–Crutzen mechanism and the dimensions of the stable and unstable manifolds. See table 2 for the values of the critical points.

Q	$Type$	$\dim(W_{Q_i}^s)$	$\dim(W_{Q_i}^u)$
Q_1	Saddle	2	1
Q_2	Stable node	3	0
Q_3	Saddle	2	1
Q_4	Saddle	1	2
Q_5	Saddle	1	2
$(f_1, 0, 0)$	Saddle	2	1

It should be pointed out that the analysis done in this section refers to local considerations, mathematicians are also interested in global analysis that provides information about the existence of orbits connecting the critical points (the so–called heteroclinic orbits). In this work such analysis will not be considered. However, we would like to mention that such analysis, including Poincaré's compactification, has been done for the Chapman mechanism [9]. Another example of the information that global analysis can provide was obtained by us for the case of the Chapman mechanism were we showed that if we start from a physical initial condition, meaning that the concentrations are non negative, then the solution for all times greater than the initial one gives non negative concentrations.

5.   Numerical Results

In this section our interest will be to solve Eqs. (14) and (15) by numerical methods, this means that we will give an initial condition (say at $t = 0$) and obtain the solution at different times ($t > 0$). However, due to the very different values of the concentrations it is convenient to define the following reduced variables,

$$x_R(t) = x(t)/\alpha, \quad y_R(t) = y(t)/\beta, \quad z_R(t) = z(t)/\gamma, \tag{20}$$

where $\alpha \equiv 10^7 \, molec/cm^3$, $\beta \equiv 10^{17} \, molec/cm^3$, and $\gamma = 10^{12} \, molec/cm^3$. The numerical output, either in terms of numbers or in graphics form, will be expressed in terms of these reduced variables. There are several numerical methods and some of them can actually be implemented quite easily with a computer. However, it should be pointed out that the implementation of robust numerical methods can be a time consuming labor. Therefore, we decided to use canned subroutines because our interest is not in the numerics per se. We have found that using a code for systems that present rigidity, like the so–called Backward Differentiation Formula (BDF), can in some instances be several thousands faster than others not designed for systems with rigidity, such as Adams' method, see for example the last two rows in table 5. In the case considered here, we either use BDF or Adam's method to solve the differential equations in which we are interested in. We would like to stress that the numerical methods used in this section and the techniques from local analysis complement each other. It is interesting to solve numerically the differential equations and make some graphs to have an insight. On the other hand, in the previous section we were able to obtain the coordinates and type of the critical points. If we are "near" the stable node found in the previous section, Q_2, the numerical solution should go to it as time increases and also we can compare the results from solving the differential equations for large times with the results obtained in the previous section. An important quantity in the numerical methods is the tolerance which can be understood as the accuracy goal. To be more specific we give in table 5 the results of the numerical methods for solving differential equations starting from an initial condition.

Table 5. The solution for the concentrations x_R, y_R, z_R at the final time (FT) starting from the initial condition $x_0 = 10^9 \, molec/cm^3$,
$y_0 = 1.1984999935 \times 10^{17} \, molec/cm^3$, $z_0 = 10^{14} \, molec/cm^3$, **two different numerical methods (M), different tolerances (TOL), and the time required to obtain the solution with a computer (CT). All times are given in seconds. See Eq.(20) for the definition of the reduced quantities x_R, y_R, and z_R. For reference, we quote the reduced value of the stable node Q_2 (Q_2^R) with twelve figures which was obtained by calculating the roots of the polynomial given in the appendix using a computer algebra program; $Q_2^R = (3.80985768699, 1.19992543718, 4.97070440100)$.**

M	TOL	FT	CT	$x_R(FT)$	$y_R(FT)$	$z_R(FT)$
BDF	10^{-6}	5×10^{10}	0.09	3.810	1.1999	4.9707
BDF	10^{-6}	10^5	0.007	65.81	1.1987	86.017
BDF	10^{-10}	5×10^{10}	0.18	3.810	1.1999	4.9707
BDF	10^{-10}	10^5	0.009	65.81	1.1987	86.017
Adams	10^{-6}	10^5	14.426	65.81	1.1987	86.017
Adams	10^{-6}	10^6	120.380	28.586	1.1994	37.3531
Adams	10^{-6}	10^7	1321	7.895	1.1999	10.3086
Adams	10^{-6}	5×10^7	7105	3.8107	1.1999	4.97183
BDF	10^{-6}	5×10^7	0.017	3.8099	1.1999	4.97078
Adams	10^{-6}	10^8	11412	3.810716	1.1999254	4.97183
BDF	10^{-6}	10^8	0.009	3.809857	1.1999254	4.9707044
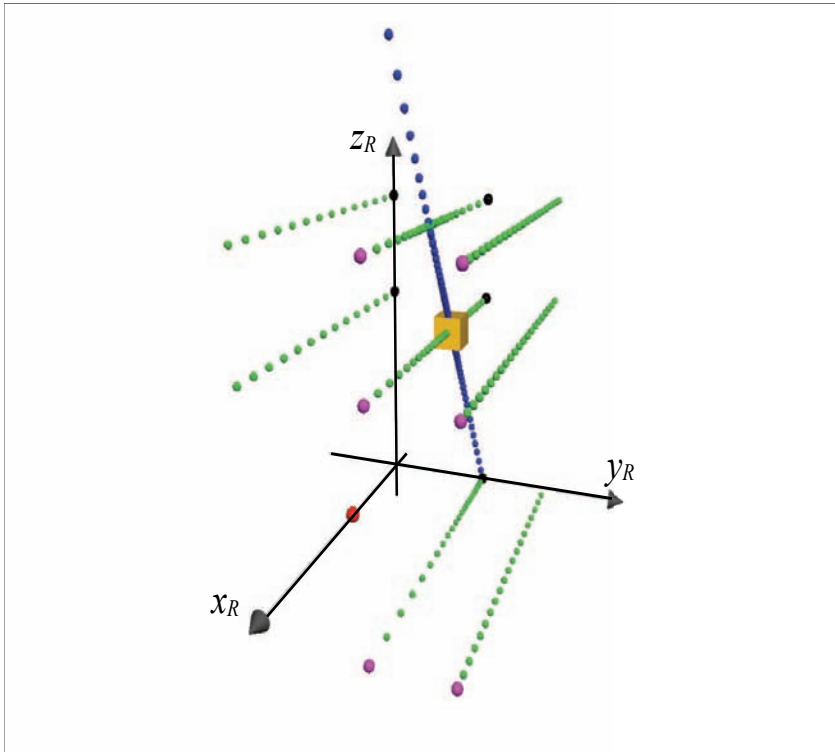
Figure 1. Numerical solutions obtained with the Adams and BDF methods. The black and purple spheres correspond to the initial points, the black ones lie on the plane $x_R = 0$ and the purple ones on the plane $x_R = 10$. The blue and green spheres are the numerical solutions using different time steps, the green ones were obtained with time intervals of orders of 10^{-2} seconds and the blue ones with time steps of order 10^7. The yellow box is centered at the stable node whose coordinates are $(3.8099, 1.1999, 4.9707)$. The red sphere on the x_R axis is located at $(3.8099, 0, 0)$, on the y_R axis the blue and green spheres meet at the point $(0, 1.1999, 0)$, and the black sphere with lower z_R on the z_R axis has coordinates $(0, 0, 5)$. The definitions of x_R, y_R, and z_R are given in caption of table 5.

The main point that we would like to bring to the fore from the results given in table 5, is that for "large" times the solution has reached approximately the stable node identified in the previous section, Q_2 in tables 2 and 4. This fact provides evidence that the numerical methods are robust. From table 5 we notice that Adams' method is slower than BDF, the difference in executing times is more apparent when considering larger final times. With respect to the tolerances used, it should be pointed out that with smaller tolerances the solution cannot be obtained at the final time requested. The reason is that with such tolerance, the numerical codes cannot guarantee the level of precision goal. Nevertheless, as seen from table 5 a change in six orders of magnitude for the tolerance is not important as long as one is interested in about five significant digits. For the generation of the numerical solutions we used the codes provided by the Numerical Algorithms Group (www.nag.com).

If we consider only numerical output there are some regularities that are hidden, but

become apparent when using graphical information. In figure 1 we provide a more global look at the orbits of the dynamical system under consideration by plotting the numerical solution for different initial points. For example, we have evidence of the existence of a slow manifold in which the solution move slowly (blue spheres) and the orbits are attracted to it, a similar behavior was observed for the Chapman mechanism [8]. Note also that the solutions seem to move in the planes y_R a constant and furthermore it looks that the solutions also lie on the planes z_R a constant with a notable exception. This exception is when the plane y_R constant contains the critical point since in this case the slow manifold given by the blue spheres is contained in such a plane. An important point to mention is that in figure 1 while all the concentrations shown are non negative the concentrations of nitrogen oxides can be negative and we also notice that the solution curves of the dynamical system under consideration lead to negative concentrations of monatomic oxygen as can be infered from figure 1. Note in particular that the initial points that lie on the plane $x_R = 10$ an whose y_R coordinate is larger than the corresponding y_R coordinate for the stable node, lead to negative concentrations of monatomic oxygen. So, there are initial conditions that lead to solutions that do not have physical sense. However, the important point, in our opinion, is that; if the initial conditions have physical sense then the solution always has physical sense. For the Chapman mechanism we were able to give a proof of such statement (initial conditions that have physical sense always give solutions that have physical sense) by showing that the physical region is a positively invariant set, but so far we have been unable to show a result of this type for the Chapman-Crutzen mechanism. In fact, what is the physical region remains elusive at this moment.

In figure 2 we have the solutions in the x_R–y_R plane for initial conditions such that its y_R is approximately the y_R coordinate of the critical point. The behavior of the orbits is quite similar to what we obtained for the Chapman mechanism [8] except that the critical point is different, see [8] for a broader description.

6. Conclusion

There are several features obtained in this work that we now summarize. First of all, we have considered some important catalytic cycles to the ozone dynamics in the stratosphere. In particular, we have obtained the critical points of the underlying differential equations that describe them, mass conservation of oxygen and the radical were used to reduce the original set of five to a system of three ordinary differential equations. From the analysis of such a set it turns out that there are only two points that have chemical and/or physical sense (none of the concentrations are negative). They correspond to a point $(f_1, 0, 0)$, with f_1 a constant of motion, that says that all oxygen is monatomic (not observed in atmosphere) and another critical point that roughly corresponds to the experimental values of ozone concentrations.

The second result was to consider the particular case in which the radical corresponds to $[NO]$ and furthermore we included the photolytic decomposition of $[NO_2]$. Using typical values in the stratosphere for the reaction rates and other quantities that need to be specified, we performed a local mathematical analysis of the six critical points for each two cases and determined the nature of the critical points. All the critical points turned out to be hyperbolic, the physical point $(f_1, 0, 0)$ corresponds to a saddle and the other physical point
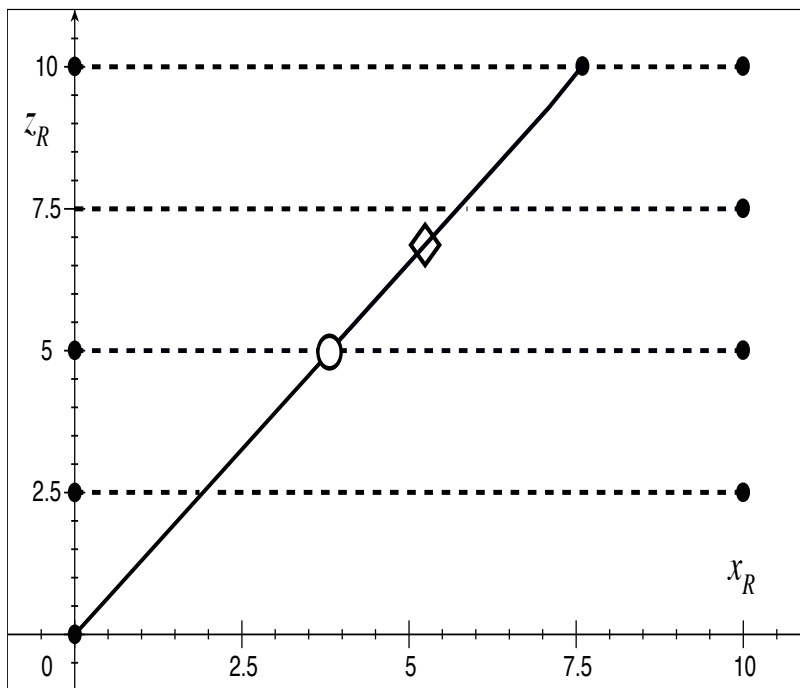
Figure 2. The orbits in the plane x_R–z_R for the Chapman–Crutzen mechanism for $y_R \approx$ 1.1999. Circle; the stable node for the Chapman–Crutzen mechanism, diamond; the stable node for the Chapman mechanism, solid circles; initial conditions, solid lines; orbits for a total time of value 5×10^7 seconds, dashed lines; orbits for a total time of value 5×10^{-2} seconds.

to a stable node. We argued that the stable node is what one expects to have because it can be observed. In this sense, the mechanisms considered in this work represent robust theoretical models.

The numerical methods used were tested against the results from local analysis showing that for large times, and with a specific initial condition, the numerical solution goes to the stable node. This allowed us to infer the internal consistency of the numerical methods and the results from the mathematical local analysis. Having tested consistency, we used graphical methods to infer that the orbits of the underlying dynamical systems move approximately in planes and conclude that the features of the Chapman–Crutzen mechanism resembles closely that of the Chapman mechanism in the plane that contains the Chapman–Crutzen stable node.

Finally we would like to point out that the mechanisms considered in this work are, so to speak, toy models and do not take into account the huge number of chemical reactions that may contribute to the stratospheric ozone dynamics [12]. Also, we have not attempted to give an account of the tremendous economic, scientific and social implications that stratospheric ozone dynamics, and climate change which in a way is closely related [13], has

on our present world [14]. Besides, global analysis and in particular Poincaré's compact-ification [9] have not been attempted because they deal with negative concentrations and therefore their scope is somewhat outside of a work in which chemistry and physics are emphasized. However, we expect that the reader will be convinced that the abstract mathe-matical theorems that have been obtained in the past by mathematicians, have implications with chemical and physical value.

Acknowledgments

Appendix

In this appendix we write the fifth order polynomial satisfied by the roots x_c of the critical points.

$$\Pi(x_c) = Ax_c^5 + Bx_c^4 + Dx_c^3 + Ex_c^2 + Fx_c + G, \tag{21}$$

where the coefficients are given by

$$A = K^2 k_2 k_4 (k_2 + k_3 - 3k_4), \tag{22}$$

$$\begin{aligned} B =& K^2 \big[k_2 k_3 k_4 (f_2 - f_1) + k_2 j_3 (k_2 - 3k_4) - 3k_4^2 k_3 f_2 \big] + \\ & K \big[2k_2 k_4 j_1 (3k_4 - k_3) + 2k_2 k_4 (k_2 j_3 - k_2 j_1 - k_4 j_2) \big], \end{aligned} \tag{23}$$

$$\begin{aligned} D =& K \big[k_4 j_1 j_2 (3k_4 - 2k_2 - k_3) + k_2 j_1 j_3 (9k_4 - k_3 - 2k_2) + 2k_3 k_4^2 f_2 (3j_1 - j_2) + \\ & 2k_2 k_3 k_4 (f_2 j_3 + f_1 j_1) + 2k_2 (k_2 j_3^2 - k_4 j_2 j_3 - k_3 k_4 j_1 f_2) \big] + \\ & k_2 k_4 \big[k_4 j_1 (2j_2 - 3j_1) + k_2 j_1 (j_1 - 2j_3) + k_3 j_1^2 \big] \end{aligned} \tag{24}$$

$$\begin{aligned} E =& K j_1 \big[k_2 k_3 j_3 (f_1 - f_2) + k_3 k_4 j_2 (f_1 - f_2) + j_2 j_3 (3k_4 - 2k_2) + \\ & 3j_3 (2k_3 k_4 f_2 + k_2 j_3) \big] + j_1^2 \big[k_2 k_3 k_4 (f_2 - f_1) + k_4 j_2 (2k_2 + k_3 - 3k_4) + \\ & j_3 (k_2^2 + k_2 k_3 - 6k_2 k_4) - 3k_3 k_4^2 f_2 \big] + 2k_4^2 j_1 j_2 (j_2 + k_3 f_2) - \\ & 2k_2 j_1 j_3 (k_2 j_3 + k_3 k_4 f_2) \end{aligned} \tag{25}$$

$$\begin{aligned} F =& j_1^2 \big[k_3 k_4 j_2 (f_2 - f_1) + k_2 k_3 j_3 (f_2 - f_1) + 2j_2 j_3 (k_2 - 3k_4) + \\ & j_2 (k_4 j_2 + k_3 j_3) - 3j_3 (k_2 j_3 + 2k_3 k_4 f_2) \big] - 2k_2 j_1 j_3^2 (j_2 + k_3 f_2) + \\ & 2k_4 j_1 j_2 j_3 (k_3 f_2 + j_2), \end{aligned} \tag{26}$$

$$G = j_1^2 j_3 \big[k_3 j_2 (f_2 - f_1) - 3k_3 f_2 j_3 + j_2 (j_2 - 3j_3) \big]. \tag{27}$$

The roots of the critical points corresponding to the case in which the photolytic de-composition of $[NO_2]$ is not considered can be obtained by taking $j_3 = 0$. With this value, the corresponding critical points of the chemical reactions considered in section 2 can be obtained by using the corresponding reaction rates for the catalytic cycle of interest.

References

[1] S. Chapman; *Mem. Roy. Met. Soc.* **3** (1930) 103-125.

[2] J. H. Seinfeld and S. N. Pandis; *Atmospheric Chemistry and Physics: from air pollution to climate change*, Wiley (1998).

[3] B. J. Finlayson-Pitts and J. N. Pitts; *Chemistry of the Upper and Lower Atmosphere*, Academic Press (2000).

[4] P. J. Crutzen; *Q. J. Roy. Met. Soc.* **96** (1970) 320-325.

[5] D. G. Andrews; *An Introduction to Atmospheric Physics* Cambridge (2000).

[6] A. Dessler; *The Chemistry and Physics of Stratospheric Ozone* Academic Press (2000).

[7] C. E. Wayne and R. P. Wayne; *Photochemistry* Oxford (1996).

[8] R. M. Velasco, F. J. Uribe, and E. Pérez-Chavela; *J. Math. Chem.* **44** (2008) 529-539.

[9] E. Pérez-Chavela, F. J. Uribe, and R. M. Velasco; The global flow in the Chapman mechanism, to appear in Nonlinear Analysis Series A: Theory, Methods and Applications.

[10] J. Guckenheimer and P. Holmes; *Nonlinear Oscillations, Dynamical Systems, and Bifurcations of Vector Fields*, Springer (1983).

[11] M. W. Hirsch and S. Smale, *Differential Equations, Dynamical Systems, and Linear Algebra*, Academic Press (1974).

[12] Scientific Assessment of Ozone Depletion: 2006. http://ozone.unep.org

[13] Intergovernmental Panel on Climate Change, Fourth Assessment Report. http://www.ipcc.ch/ipcc/reports.

[14] A. Irwing, An Environmental Fairy Tale. The Molina-Rowland Chemical Equations and the CFC Problem; in *It must be Beautiful*, ed. by G. Farmelo (Granta Books, London, 2003), pp. 87-109.

INDEX

D

I

J

N

O

P

W

X

Y